



---

# Università degli Studi di Catania

## Scuola Superiore di Catania

---

International PhD

in

Energetics

XXIV cycle

**SOLAR MIRRORS CHARACTERIZATION FOR CONCENTRATING SOLAR  
POWER TECHNOLOGY**

Dott. Ing. Alessandro Patrizio Contino

Coordinator of PhD

Prof. Alfio Consoli

Tutor

Prof. Luigi Marletta

*a.y 2009/2011*

## ABSTRACT

The increasing availability on the market of different types of solar reflectors such as: polymeric film mirrors, aluminum mirrors and thin glass mirrors, together with: the lack of available norms in this area, and a valid methodology to compare the performances of the candidate reflectors; highlights the necessity to conduct a more detailed analysis on these new technologies.

The objective of the present work is to suggest a valuable method to compare the reflectance performance of mirrors, evaluating also their performances in order to assess:

- the most durable to ageing and weathering effects;
- the different reflectance behavior with the variation of the solar incident angle.

.For these reasons the work here proposed was carried out with an experimental apparatus composed by:

- An Agilent Cary 5000 UV/Vis/NIR spectrophotometer to test the different performance of the mirrors at different characterization steps;
- An integrating sphere of 150 mm in diameter (DRA – Diffuse Reflectance Accessory);
- A VASRA (Variable Angle Specular Reflection Accessory);
- A UV chamber to accelerate the ageing process;
- A  $\mu$ Scan SMS Scatterometer for RMS Roughness and BDSF measurement;
- An outdoor bench

The work was completed with two modeling tools:

- An engineering equation solver (Mathcad) to dynamically evaluate the behavior;
- A ray tracing software (Soltrace) to evaluate the system's optical efficiency.

The analysis indicates that the candidate reflectors can be accurately characterized with five fundamental parameters:

- a)  $\rho_{\text{SWH}}$ , the solar-weighted hemispherical reflectance;
- b)  $\rho_{\text{SWS}}$ , the solar-weighted specular reflectance;
- c)  $\rho_{\text{SWS}}(\theta)$ , the solar weighted specular reflectance function of the variable angle of incidence;
- d) BDSF, Bi Directional Scattering Function;
- e) RMS Roughness

This evaluation will provide a valuable tool, for the companies who want to invest in concentrating solar power technology, to decide whether or not using a candidate reflectors to realize new plants, assessing their performances, their costs, and their durability.

Keywords: Specular Reflectance, Polymeric film reflector, Aluminum reflector, Thin glass reflector, high reflective mirrors, parabolic trough, BSDF, Scatterometer, UV/VIS NIR spectrophotometer, Integrating sphere, CSP, parabolic trough, renewable energy, optical efficiency, UV ageing test solar reflector, Solar Weighted Hemispherical Reflectance, Solar Weighted Specular Reflectance, RMS Roughness, Soltrace<sup>®</sup>, Mathcad<sup>®</sup>.

**Approved by**

**Coordinator of Ph.D.:** Prof. Alfio Consoli \_\_\_\_\_

**Tutor:** Prof. Luigi Marletta \_\_\_\_\_

## LIST OF CONTENTS

ABSTRACT.....	2
LIST OF FIGURES .....	10
1. INTRODUCTION .....	21
2. CONCENTRATING SOLAR POWER SYSTEMS.....	23
2.1 Technology Description and Status .....	24
2.2 Cost and Potential for Cost Reductions .....	26
2.3 Cost Overview.....	26
2.4 Linear Concentrator Systems .....	28
2.5 Parabolic Trough Systems .....	28
2.6 Linear Fresnel Reflector Systems .....	29
2.7 Dish/Engine Systems .....	30
2.8 Solar Concentrator .....	32
2.9 Power Conversion Unit.....	32
2.10 Power Tower Systems.....	33
2.11 Thermal Storage.....	34
2.12 Future R&D Efforts .....	35
3. SPETTROSCOPY .....	37
3.1 Reflection.....	39
3.1.1 Hemispheric Reflectance .....	42
3.2. Transmission .....	45
3.3 Emission.....	49
3.4 Correlation between emissivity and reflectance .....	51
3.5 The Mie theory.....	52
4. INSTRUMENTATION & MEASUREMENTS.....	55
4.1. Spectrophotometer.....	55

4.1.1 Introduction.....	55
4.1.2. Integrating sphere (Introduction) .....	63
4.1.3 Integrating Sphere (Measuring Sample Reflectance) .....	66
4.1.4 Description of the accessory .....	70
4.1.5 Optics .....	72
4.1.6 Specifications .....	74
4.1.6 Integrating Sphere Theory .....	75
4.2 VASRA (Variable Angle Specular Reflectance Accessory) .....	96
4.2.1 Specification.....	96
4.2.2 Optical Design.....	97
4.3 Experimental collection of reflectance data.....	98
4.3.1 Normative references .....	99
4.3.2 Terms and definitions.....	100
4.4 Relevance of the reflectance parameter for CSP applications .....	103
4.4.1 Reflective behaviour of solar mirrors .....	103
4.5 Preparation of measurement.....	104
4.5.1 Sample preparation .....	104
4.5.2 General.....	104
4.5.3 Cleaning .....	105
4.5.4 Glass mirrors.....	105
4.5.5 Aluminum sheets.....	106
4.5.6 Silver polymer films.....	106
4.6 Reference mirrors for integrating spheres.....	106
4.7 Measurement procedure.....	106
4.8 Measurement of hemispherical reflectance with spectrophotometer and integrating sphere	107
4.8.1 Configuration of the instrument.....	107

4.8.2	Auto corrections.....	107
4.8.3	Calibration.....	108
4.8.4	Procedure .....	108
4.9	Weighting with standard solar norm spectrum .....	108
4.9.1	Recommended solar norm .....	108
4.9.2	Irradiance spectrum tables .....	109
4.9.3	Solar-weighted hemispherical reflectance .....	110
4.9.4	Solar-weighted specular reflectance .....	121
4.10	Accuracy .....	121
5.	REFLECTANCE MEASUREMENTS.....	123
5.1	DRA (Diffuse Reflectance Accessory) Integrating Sphere .....	123
5.1.1	Thin Glass Mirrors.....	123
5.1.2	Aluminum Mirrors .....	129
5.1.3	Polymeric film mirrors.....	135
5.2	VASRA Reflectance Measurements.....	143
5.2.1	Thin Glass Mirrors.....	146
5.2.2	Aluminum Mirrors .....	151
5.2.3	Polymeric film mirrors.....	157
5.3	UV Accelerated Ageing Tests.....	163
5.3.1	Thin glass mirrors .....	172
5.3.2	Aluminum mirrors.....	177
5.3.3	Polymeric film mirror .....	181
5.4	Outdoor exposure measurements .....	185
5.4.1	Thin glass mirrors .....	189
5.4.2	Aluminum mirror .....	192
5.4.3	Polymeric film mirrors.....	196

5.5 Reflectance measurement after one month (Scatterometer) .....	199
5.5.1 Thin glass mirrors .....	200
5.5.2 Aluminum mirrors.....	203
5.5.3 Polymeric mirror .....	205
5.6 Comparison between the scatterometer measurement after one month.....	207
5.7 Reflectance measurement after one month (Spectrophotometer).....	210
5.7.1 Thin Glass mirrors .....	210
5.7.2 Aluminum mirrors.....	215
5.7.3 Polymeric film mirror .....	220
6. MODELING .....	225
6.1 Mathcad <sup>®</sup> .....	225
6.1.1 Direct Normal Insolation .....	225
6.1.2 Angle of incidence .....	226
6.1.3 Optical Efficiency and HCE Efficiency.....	232
6.1.4 Incidence Angle Modifier (IAM).....	234
6.1.5 Row Shadowing and End Losses .....	235
6.1.6 Solar Irradiation Absorption .....	238
6.1.7 Thin glass mirrors .....	241
6.1.8 Aluminum mirrors .....	244
6.1.9 Polymeric film mirrors.....	248
6.2 Soltrace <sup>®</sup> .....	252
6.2.1 Defining the Sun .....	255
6.2.2 Defining Optical Geometry.....	257
6.2.3 Defining System Geometry.....	259
6.2.4 Tracing Overview .....	263
6.2.5 Modeling with Soltrace.....	264

6.2.6	Thin glass mirrors .....	270
6.2.7	Aluminum mirrors .....	278
6.2.8	Polymeric Film mirrors.....	287
6.3	Comparison between Mathcad and Soltrace models.....	296
6.3.1	Thin glass mirrors .....	296
6.3.2	Aluminum mirrors .....	298
6.3.3	Polymeric film mirrors.....	300
7.	ENHANCING THE MODEL.....	303
7.2	Receiver Heat Loss .....	303
7.3	Analytical Heat Loss Derivation.....	303
7.3.1	Linear Regression Heat Loss Model.....	304
7.3.2	Solar Field Piping Heat Losses .....	308
7.4	Heat Transfer Fluid Energy Gain .....	309
7.5	Heat losses evaluation .....	309
7.5.1	Thin glass mirrors .....	311
7.5.2	Aluminum mirrors .....	313
7.5.3	Polymeric film mirrors.....	315
7.6	Results .....	317
7.6.1	Thin glass .....	317
7.6.2	Aluminum mirrors .....	327
7.6.3	Polymeric film mirror .....	337
7.7	Result improvement .....	347
8.	CONCLUSION.....	352
	BIBLIOGRAPHY .....	355

## LIST OF FIGURES

Figure 2. 1 A linear concentrator power plant using parabolic trough collectors.....	29
Figure 2. 2 A linear Fresnel reflector power plant.....	30
Figure 2. 3 SES Dish/Stirling system .....	31
Figure 2. 4 A dish/engine power plant.....	32
Figure 2. 5 A power tower power plant.....	33
Figure 3. 1 Typical material absorption process .....	37
Figure 3. 2 Spectrum division.....	38
Figure 3. 3 Optics Angles .....	39
Figure 3. 4 Bi-directional reflectance .....	40
Figure 3. 5 Hemispheric reflectance .....	42
Figure 3. 6 Transmission through a material .....	45
Figure 3. 7 Schematic diagram of an emission measurement.....	51
Figure 4. 1 Spectrophotometer Agilent Cary 5000.....	55
Figure 4. 2 Spectrophotometer optics: a) schematic diagram.....	56
Figure 4. 3 Spectrophotometer light sources .....	57
Figure 4. 4 Spectrophotometer sample holder, one for the reference beam and the other for the sample beam.....	58
Figure 4. 5 Diffraction grating geometry .....	60
Figure 4. 6 Overlap of the spectral orders.....	61
Figure 4. 7 Grating mounting on a dual monochromator .....	62
Figure 4. 8 The external DRA.....	63
Figure 4. 9 The external DRA viewed from the back.....	63
Figure 4. 10 Optical geometry of an integrating sphere .....	65
Figure 4. 11 PTFE reference disk .....	66
Figure 4. 12 Collection of scattered light by an integrating sphere. $I_o$ = incident light, $I_s$ = scattered light .....	67
Figure 4. 13 Some of the wide-angle scatter is lost when there is a space between the sample and the sphere wall .....	68
Figure 4. 14 Some of the wide-angle reflection is intercepted by the sphere wall.....	68
Figure 4. 15 Highly diffuse samples are measured against a flat PTFE reference plate .....	70

Figure 4. 16 A schematic view of the external DRA .....	71
Figure 4. 17 The optical design of the external DRA .....	71
Figure 4. 18 Mirror M1 .....	72
Figure 4. 19 Mirror M5 .....	72
Figure 4. 20 Mirror M2 .....	73
Figure 4. 21 Mirror M3 .....	73
Figure 4. 22 Mirror M4 .....	73
Figure 4. 23 Radiation exchange between two surfaces .....	75
Figure 4. 24 Angles relation between the two mentioned surfaces .....	76
Figure 4. 25 Schematics of the inside of the sphere.....	77
Figure 4. 26 Diagram of the magnitude of the sphere multiplier.....	79
Figure 4. 27 Diagram of the magnitude of radiance vs numbers of reflection .....	81
Figure 4. 28 Relative radiance plotted on different values of diameter .....	83
Figure 4. 29 Spectral reflectance of most used internal coatings.....	84
Figure 4. 30 Schematics on measurement of reflectance on the detector area .....	87
Figure 4. 31 Schematics on measurement of reflectance on the detector area .....	87
Figure 4. 32 measurement of omnidirectional flux.....	90
Figure 4. 33 measurement of unidirectional flux .....	90
Figure 4. 34 measurement of neither Omnidirectional or Unidirectional flux Detectors .....	91
Figure 4. 35 Human eye spectral response .....	91
Figure 4. 36 The optical design of the Variable Angle Specular Reflectance Accessory .....	97
Figure 4. 37 The beam profiles at 20° .....	98
Figure 4. 38 The beam profiles at 70° .....	98
Figure 4. 39 Diffuse reflectance.....	100
Figure 4. 40 Perfect specular reflection      Figure 4. 41 Specular reflection with offset.....	101
Figure 4. 42 Approximated reflection distribution for non-ideal specular mirror materials .....	104
Figure 4. 43 Direct + Circumsolar spectrum calculated with SMARTS model in a clear sky day at AM 1.5 .....	109
Figure 5. 1 Reflector type TG1              Figure 5. 2 Reflector type TG2 .....	124
Figure 5. 3 TG1 Reflectance Measurements.....	124
Figure 5. 4 Diffuse Reflectance .....	125
Figure 5. 5 Specular Reflectance .....	126
Figure 5. 6 TG2 Reflectance measurements .....	126

Figure 5. 7 Diffuse Reflectance .....	127
Figure 5. 8 Specular Reflectance .....	128
Figure 5. 9 Solar Weighted Hemispherical Reflectance .....	129
Figure 5. 10 Solar Weighted Specular Reflectance .....	129
Figure 5. 11 Aluminum mirror AL1     Figure 5. 12 Aluminum mirror AL2 .....	130
Figure 5. 13 Reflectance Measurements .....	131
Figure 5. 14 Diffuse Reflectance .....	131
Figure 5. 15 Specular Reflectance .....	132
Figure 5. 16 TG2 Reflectance measurement.....	132
Figure 5. 17 Diffuse Reflectance .....	133
Figure 5. 18 Specular Reflectance .....	133
Figure 5. 19 Solar Weighted Hemispherical Reflectance .....	134
Figure 5. 20 Solar Weighted Specular Reflectance .....	134
Figure 5. 21 PF1 mirror.....	135
Figure 5. 22 PF1 Global+Diffuse.....	136
Figure 5. 23 Diffuse Reflectance .....	137
Figure 5. 24 Specular Reflectance .....	137
Figure 5. 25 PF2 Global+Diffuse.....	138
Figure 5. 26 Diffuse Reflectance .....	139
Figure 5. 27 Specular Reflectance .....	139
Figure 5. 28 Solar Weighted Hemispherical Reflectance .....	140
Figure 5. 29 Solar Weighted Specular Reflectance .....	140
Figure 5. 30 Summary of the different Solar Weighted Hemispherical Reflectance .....	141
Figure 5. 31 Summary of the different Solar Weighted Specular Reflectance.....	141
Figure 5. 32 VASRA Reflectance Measurements for TG1 Samples .....	146
Figure 5. 33 VASRA Reflectance measurements for TG2 Samples .....	147
Figure 5. 34 Solar Weighted Specular Reflectance at different angles of incidence for TG1 Samples: a=20°,b=25°,c=30°,d=35°,e=40°,f=45°,g=50°,h=55°,l=60°,m=65°,n=70° .....	148
Figure 5. 35 Solar Weighted Specular Reflectance at different angles of incidence for TG2 Samples: a=20°,b=25°,c=30°,d=35°,e=40°,f=45°,g=50°,h=55°,l=60°,m=65°,n=70° .....	149
Figure 5. 36 Reflectance Vs Angle of Incidence .....	149
Figure 5. 37 Reflectance Vs Angle of Incidence .....	150
Figure 5. 38 TG1 Mirror Vs TG2 Mirror.....	150

Figure 5. 39 Comparison between the two thin glass mirrors .....	151
Figure 5. 40 VASRA Reflectance Measurements for AL1 Samples .....	152
Figure 5. 41 VASRA Reflectance measurements for TG2 Samples .....	153
Figure 5. 42 Solar Weighted Specular Reflectance at different angles of incidence for AL1 Samples: a=20°,b=25°,c=30°,d=35°,e=40°,f=45°,g=50°,h=55°,l=60°,m=65°,n=70° .....	154
Figure 5. 43 Solar Weighted Specular Reflectance at different angles of incidence for AL2 Samples: a=20°,b=25°,c=30°,d=35°,e=40°,f=45°,g=50°,h=55°,l=60°,m=65°,n=70° .....	154
Figure 5. 44 Reflectance Vs Angle of Incidence .....	155
Figure 5. 45 Reflectance Vs Angle of Incidence .....	155
Figure 5. 46 TG1 Mirror Vs TG2 Mirror.....	156
Figure 5. 47 Comparison between the two aluminum mirrors .....	157
Figure 5. 48 VASRA Reflectance Measurements for PF1 Samples.....	158
Figure 5. 49 Solar Weighted Specular Reflectance at different angles of incidence for PF Samples: a=20°,b=25°,c=30°,d=35°,e=40°,f=45°,g=50°,h=55°,l=60°,m=65°,n=70° .....	159
Figure 5. 50 Reflectance Vs Angles of incidence.....	159
Figure 5. 51 PF2 VASRA measurements .....	160
Figure 5. 52 Reflectance vs Angles of incidence.....	161
Figure 5. 53 Relative reflectance comparison.....	161
Figure 5. 54 Comparison between the two polymeric mirrors .....	162
Figure 5. 55 Comparison graph between all the mirrors tested .....	162
Figure 5. 56 UV Chamber.....	163
Figure 5. 57 Ultramed 2000 lamp .....	164
Figure 5. 58 LP UVA & LP UVB probes .....	164
Figure 5. 59 LP UVA 01 typical spectral response.....	166
Figure 5. 60 LP UVB 01 typical spectral response.....	167
Figure 5. 61 Positions of UVA + UVB measurements.....	168
Figure 5. 62 The wood board inside the UV chamber .....	171
Figure 5. 63 Schematic and real system constructed at the laboratory.....	171
Figure 5. 64 TG1 global and diffuse reflectance after the treatment in the UV chamber.....	172
Figure 5. 65 Specular reflectance spectrum comparison .....	173
Figure 5. 66 Diffuse reflectance comparison.....	173
Figure 5. 67 Solar weighted hemispherical ( $\rho$ SWH) and specular ( $\rho$ SWS) reflectance.....	174
Figure 5. 68 Spectral response for TG2 mirror after the UV exposure .....	175

Figure 5. 69 Specular reflectance comparison .....	175
Figure 5. 70 Diffuse reflectance comparison .....	176
Figure 5. 71 Solar weighted hemispherical ( $\rho$ SWH) and specular ( $\rho$ SWS) reflectance.....	176
Figure 5. 72 AL1 spectral response .....	177
Figure 5. 73 AL1 specular reflectance .....	178
Figure 5. 74 Diffuse reflectance comparison .....	178
Figure 5. 75 Solar weighted hemispherical and specular reflectance .....	179
Figure 5. 76 AL2 spectral response .....	179
Figure 5. 77 AL2 specular reflectance .....	180
Figure 5. 78 Diffuse reflectance comparison .....	180
Figure 5. 79 Comparison between the before and after condition for solar weighted hemispherical and specular reflectance .....	181
Figure 5. 80 PF1 Spectral response.....	182
Figure 5. 81 Specular reflectance variation .....	182
Figure 5. 82 Diffuse reflectance comparison .....	183
Figure 5. 83 Comparison of Solar weighted hemispherical and specular reflectance at time 0 and after the UV exposure .....	183
Figure 5. 84 Solar weighted hemispherical reflectance in the condition 0 and after one year of UV exposure .....	184
Figure 5. 85 Solar weighted specular reflectance in the condition 0 and after one year of UV exposure .....	184
Figure 5. 86 Aluminum structure for outdoor exposure .....	185
Figure 5. 87 External bench for outdoor exposure test .....	186
Figure 5. 88 SMS Scatterometer .....	187
Figure 5. 89 Instrument technical information.....	187
Figure 5. 90 Reference dielectric mirror .....	188
Figure 5. 91 Certificate of calibration and reference mirror value .....	188
Figure 5. 92 Reflectance at 25° (primary axis) and RMS Roughness (Secondary axis) .....	189
Figure 5. 93 BDSF at (0,0) and (50,180) for the TG1 sample .....	190
Figure 5. 94 Reflectance at 25° (primary axis) and RMS Roughness (Secondary axis) .....	191
Figure 5. 95 BDSF at (0,0) and (50,180) for the TG2 sample .....	192
Figure 5. 96 Reflectance at 25° (primary axis) and RMS Roughness (Secondary axis) .....	193
Figure 5. 97 BDSF at (0,0) and (50,180) for the TG1 sample .....	194

Figure 5. 98 Reflectance at 25° (primary axis) and RMS Roughness (Secondary axis) .....	195
Figure 5. 99 BDSF at (0,0) and (50,180) for the AL2 sample .....	195
Figure 5. 100 Reflectance at 25° (primary axis) and RMS Roughness (Secondary axis) .....	196
Figure 5. 101 BDSF at (0,0) and (50,180) for the TG1 sample .....	197
Figure 5. 102 Reflectance at 25° (primary axis) and RMS Roughness (Secondary axis) .....	198
Figure 5. 103 BDSF at (0,0) and (50,180) for the AL2 sample .....	199
Figure 5. 104 The mirror samples after one month of outdoor exposure .....	200
Figure 5. 105 Reflectance and RMS roughness values.....	201
Figure 5. 106 BDSF (0,0) and BDSF (50,180) values.....	201
Figure 5. 107 Reflectance and RMS roughness values.....	202
Figure 5. 108 BDSF (0,0) and BDSF (50,180) values.....	202
Figure 5. 109 Reflectance and RMS roughness values.....	203
Figure 5. 110 BDSF (0,0) and BDSF (50,180) values.....	204
Figure 5. 111 Reflectance and RMS roughness values.....	205
Figure 5. 112 BDSF (0,0) and BDSF (50,180) values.....	205
Figure 5. 113 Reflectance and RMS roughness values.....	206
Figure 5. 114 BDSF (0,0) and BDSF (50,180) values.....	206
Figure 5. 115 Comparison between the BDSF (0,0) and (50,180) at time 0 and after one month of outdoor exposure.....	207
Figure 5. 116 Reflectance values at 0 time and after 1 month of outdoor exposure.....	208
Figure 5. 117 RMS Roughness at 0 time and after 1 month of outdoor exposure.....	209
Figure 5. 118 TG1 spectral response after one month of outdoor exposure.....	211
Figure 5. 119 TG2 specular spectral response at 0 time and after one month of outdoor exposure	211
Figure 5. 120 Diffuse reflectance comparison between the sample in "before" and "after" condition .....	212
Figure 5. 121 Global + diffuse reflectance after one month of outdoor exposure.....	212
Figure 5. 122 Specular reflectance comparison between the "before" and "after" condition.....	213
Figure 5. 123 Diffuse reflectance comparison between the "before" and "after" condition.....	213
Figure 5. 124 Comparison between the solar weighted hemispherical reflectance for TG1 and TG2 sample in the "before" and "after" condition .....	214
Figure 5. 125 Comparison between the solar weighted specular reflectance for TG1 and TG2 sample in the "before" and "after" condition .....	215

Figure 5. 126 Global + diffuse reflectance spectral response after one month of outdoor exposure	216
Figure 5. 127 Specular reflectance comparison between the "before" and "after" condition	216
Figure 5. 128 Diffuse reflectance comparison	217
Figure 5. 129 Global + diffuse reflectance spectral response after one month of outdoor exposure	217
Figure 5. 130 Specular reflectance comparison between the "before" and "after" condition	218
Figure 5. 131 Diffuse reflectance comparison	219
Figure 5. 132 Comparison between the solar weighted hemispherical reflectance for AL1 and AL2 sample in the "before" and "after" condition	219
Figure 5. 133 Comparison between the solar weighted specular reflectance for AL1 and AL22 sample in the "before" and "after" condition	220
Figure 5. 134 Global + diffuse reflectance spectral response after one month of outdoor exposure	221
Figure 5. 135 Specular reflectance comparison between the "before" and "after" condition	221
Figure 5. 136 Diffuse reflectance comparison	222
Figure 5. 137 The solar weighted hemispherical reflectance for PF1 sample in the "before" and "after" condition	222
Figure 5. 138 Solar weighted specular reflectance for the PF1 mirror	223
Figure 5. 139 Solar weighted hemispherical reflectance at 0 time and after one month of outdoor exposure	223
Figure 5. 140 Solar weighted specular reflectance at 0 time and after one month of outdoor exposure	224
Figure 6. 1 Direct Normal Insolation as measured in Catania during the year 2009	226
Figure 6. 2 Angle of incidence between the collector normal and the beam radiation	227
Figure 6. 3 Declination angle due to Earth's tilt	227
Figure 6. 4 Shows the variation of the declination angle throughout the year	228
Figure 6. 5 Equation of time vs month of the year	229
Figure 6. 6 Solar altitude angles versus time, on June 21 and December 21 of the year, for Catania	230
Figure 6. 7 DNI and DNI cos ( $\theta$ ) in Catania on June 21	231
Figure 6. 8 Incidence angle modifier (IAM) versus $\theta$	235

Figure 6. 9 Collector tracking through morning, showing digression of collector shading as the day progresses.....	236
Figure 6. 10 RowShadow (Weff/Wh) versus time of day, for June 21 and December 21 .....	237
Figure 6. 11 End losses from an HCE.....	237
Figure 6. 12 End Losses versus incidence angle ( $\theta$ ).....	238
Figure 6. 13 Hourly average flux values collected from the HCE with the TG1 mirror .....	242
Figure 6. 14 Hourly average flux values collected from the HCE with the TG2 mirror .....	243
Figure 6. 15 Comparison between TG1 and TG2 mirrors .....	244
Figure 6. 16 Hourly average flux values collected from the HCE with the AL1 mirror .....	245
Figure 6. 17 Hourly average flux values collected from the HCE with the A12 mirror.....	247
Figure 6. 18 Comparison between the two aluminum mirrors .....	247
Figure 6. 19 Hourly average flux values collected from the HCE with the PF1 mirror .....	249
Figure 6. 20 Hourly average flux values collected from the HCE with the PF2 mirror .....	250
Figure 6. 21 Comparison between the two aluminum mirrors .....	251
Figure 6. 22 Comparison between all the typologies of mirrors.....	252
Figure 6. 23 Soltrace® coordinate system .....	254
Figure 6. 24 Generation of ( x, y, z ) system from the ( x, y, z ) system after translation of origin	254
Figure 6. 25 Defining the Sun Shape and Position .....	256
Figure 6. 26 A glass plane is actually constructed from two separate elements.....	258
Figure 6. 27 Illustration of surface slope and surface specularity error.....	259
Figure 6. 28 Optical geometry definition input page .....	259
Figure 6. 29 The trace setup parameters .....	263
Figure 6. 30 Soltrace model implemented on Google Sketch Up.....	266
Figure 6. 31 Soltrace geometric simulation .....	266
Figure 6. 32 100 sun rays hitting the parabolic surface .....	267
Figure 6. 33 100 sun rays hitting the heat collector element .....	268
Figure 6. 34 Flux collected on the receiver 2D.....	269
Figure 6. 35 Flux collected on the receiver 3D.....	269
Figure 6. 36 Average flux collected on the 172th day for the TG1 mirror.....	274
Figure 6. 37 Average flux collected on the 172th day for the TG2 mirror.....	277
Figure 6. 38 Comparison between the flux collected from TG1 and TG2 mirrors.....	278
Figure 6. 39 Average flux collected on the 172th day for the AL1 mirror.....	282

Figure 6. 40 Average flux collected on the 172th day for the AL2 mirror.....	286
Figure 6. 41 Comparison between the flux collected from AL1 and AL2 mirrors.....	287
Figure 6. 42 Average flux collected on the 172th day for the PF1 mirror.....	291
Figure 6. 43 Average flux collected on the 172th day for the PF2 mirror.....	295
Figure 6. 44 Comparison between the flux collected from PF1 and PF2 mirrors .....	296
Figure 6. 45 Comparison between TG1 Model and TG1 Soltrace .....	297
Figure 6. 46 Comparison between TG2 Model and TG2 Soltrace .....	298
Figure 6. 47 Comparison between AL1 Model and AL1 Soltrace .....	299
Figure 6. 48 Comparison between AL2 Model and AL2 Soltrace .....	300
Figure 6. 49 Comparison between PF1 Model and PF1 Soltrace .....	301
Figure 6. 50 Comparison between PF2 Model and PF2 Soltrace .....	302
Figure 7. 1 Heat transfer mechanisms acting on HCE surfaces.....	304
Figure 7. 2 Dependence of Heat Losses on the Heat Transfer Fluid in air annulus condition .....	310
Figure 7. 3 Values of Heat losse on the 172th day varying the HTF temperature in air condition .	310
Figure 7. 4 Dependence of Heat Losses on the Heat Transfer Fluid in vacuum annulus condition	311
Figure 7. 5 Values of Heat losses on the 172th day varying the HTF temperature in vacuum condition.....	311
Figure 7. 6 Variation of Heat losses for TG1 reflectance value at 290°C=(12,j) and at 390°C=(17,j) in vacuum and lost vacuum condition.....	312
Figure 7. 7 Values of Heat Losses in air and vacuum condition for TG1 mirror .....	312
Figure 7. 8 Variation of Heat losses for TG2 reflectance value at 290°C=(12,j) and at 390°C=(17,j) in vacuum and lost vacuum condition.....	313
Figure 7. 9 Values of Heat Losses in air and vacuum condition for TG2 mirror .....	313
Figure 7. 10 Variation of Heat losses for AL1 reflectance value at 290°C=(12,j) and at 390°C=(17,j) in vacuum and lost vacuum condition.....	314
Figure 7. 11 Values of Heat Losses in air and vacuum condition for AL1 mirror .....	314
Figure 7. 12 Variation of Heat losses for AL2 reflectance value at 290°C=(12,j) and at 390°C=(17,j) in vacuum and lost vacuum condition.....	314
Figure 7. 13 Values of Heat Losses in air and vacuum condition for AL2 mirror .....	315
Figure 7. 14 Variation of Heat losses for PF1 reflectance value at 290°C=(12,j) and at 390°C=(17,j) in vacuum and lost vacuum condition.....	315
Figure 7. 15 Values of Heat Losses in air and vacuum condition for PF1 mirror .....	316

Figure 7. 16 Variation of Heat losses for PF2 reflectance value at 290°C=(12,j) and at 390°C=(17,j) in vacuum and lost vacuum condition.....	316
Figure 7. 17 Values of Heat Losses in air and vacuum condition for PF2 mirror .....	316
Figure 7. 18 Value of total irradiance absorbed (Qabs), Total irradiance absorbed in vacuum condition (Qtotcollvac), Total irradiance absorbed in air condition (Qtotcollair) [W/m2] for the TG1 mirror.....	318
Figure 7. 19 Irradiance absorbed in different wind speed condition for the TG1 mirror .....	319
Figure 7. 20 Comparison along the year of the values of the 0.0 m/s wind speed and the different wind speed in vacuum and air condition for the TG1 mirror.....	320
Figure 7. 21 Values of yearly collected irradiance at different wind speed and in air or vacuum condition.....	321
Figure 7. 22 Value of total irradiance absorbed (Qabs), Total irradiance absorbed in vacuum condition (Qtotcollvac), Total irradiance absorbed in air condition (Qtotcollair) [W/m2] for the TG2 mirror .....	323
Figure 7. 23 Irradiance absorbed in different wind speed condition for the TG2 mirror .....	324
Figure 7. 24 Comparison along the year of the values of the 0.0 m/s wind speed and the different wind speed in vacuum and air condition for the TG2 mirror.....	325
Figure 7. 25 Values of yearly collected irradiance at different wind speed and in air or vacuum condition.....	326
Figure 7. 26 Value of total irradiance absorbed (Qabs), Total irradiance absorbed in vacuum condition (Qtotcollvac), Total irradiance absorbed in air condition (Qtotcollair) [W/m2] for the AL1 mirror .....	328
Figure 7. 27 Irradiance absorbed in different wind speed condition for the AL1 mirror .....	329
Figure 7. 28 Comparison along the year of the values of the 0.0 m/s wind speed and the different wind speed in vacuum and air condition for the AL1 mirror.....	330
Figure 7. 29 Values of yearly collected irradiance at different wind speed and in air or vacuum condition.....	331
Figure 7. 30 Value of total irradiance absorbed (Qabs), Total irradiance absorbed in vacuum condition (Qtotcollvac), Total irradiance absorbed in air condition (Qtotcollair) [W/m2] for the AL2 mirror .....	333
Figure 7. 31 Irradiance absorbed in different wind speed condition for the AL2 mirror .....	334
Figure 7. 32 Comparison along the year of the values of the 0.0 m/s wind speed and the different wind speed in vacuum and air condition for the AL2 mirror.....	335

Figure 7. 33 Values of yearly collected irradiance at different wind speed and in air or vacuum condition.....	336
Figure 7. 34 Value of total irradiance absorbed ( $Q_{abs}$ ), Total irradiance absorbed in vacuum condition ( $Q_{totcollvac}$ ), Total irradiance absorbed in air condition ( $Q_{totcollair}$ ) [ $W/m^2$ ] for the PF1 mirror .....	338
Figure 7. 35 Irradiance absorbed in different wind speed condition for the PF1 mirror .....	339
Figure 7. 36 Comparison along the year of the values of the 0.0 m/s wind speed and the different wind speed in vacuum and air condition for the PF1 mirror .....	340
Figure 7. 37 Values of yearly collected irradiance at different wind speed and in air or vacuum condition.....	341
Figure 7. 38 Value of total irradiance absorbed ( $Q_{abs}$ ), Total irradiance absorbed in vacuum condition ( $Q_{totcollvac}$ ), Total irradiance absorbed in air condition ( $Q_{totcollair}$ ) [ $W/m^2$ ] for the PF2 mirror .....	343
Figure 7. 39 Irradiance absorbed in different wind speed condition for the PF2 mirror .....	344
Figure 7. 40 Comparison along the year of the values of the 0.0 m/s wind speed and the different wind speed in vacuum and air condition for the PF2 mirror .....	345
Figure 7. 41 Values of yearly collected irradiance at different wind speed and in air or vacuum condition.....	346
Figure 7. 42 Collected energy values along the year between the different mirrors with constant reflectance .....	348
Figure 7. 43 Collected energy values along the year between the different mirrors with variable reflectance .....	349
Figure 7. 44 Values of total energy collected along the year in air in annulus condition for all the typologies of mirrors.....	349
Figure 7. 45 Values of total energy collected along the year in air in annulus condition for all the typologies of mirrors.....	350
Figure 7. 46 Values of total energy collected along the year with vacuum in annulus condition for all the typologies of mirrors .....	351

## 1. INTRODUCTION

The solar concentrating technology is far well known; during the eighties it had a great development due to the incentives given by the US government to develop an alternative source of energy capable of supplying enough power to face a possible energy crisis, therefore the SEGS plants were built.

Successively the US government discontinued the incentives and all the efforts done to build and develop these types of plants had to cease as well.

In 2006 the US congress has given the go-ahead with a new flow of incentives to build and develop new CSP plants with different technology. As a result, other countries such as Spain, Italy and Israel started to build and developed such plants.

All of the new plants were built with the same mirror technology as they were in the 80's, with thick glass mirrors.

They had an excellent reflectance but also great costs, not only for the product itself but also for all the logistics connected to the transportation, installation and maintenance.

As it was expected, new technologies were used to obtain mirrors with a high reflectance factor, easy bending and molding and low weight.

All of these characteristics lead the market to diffuse three different technologies that could cope with the needs mentioned above:

- Thin glass mirrors;
- Aluminum mirrors;
- Polymeric film mirrors.

The objective of the research here proposed is to better understand the optical behavior of these new technologies, with the evaluation of their specular reflectance near the normal angle ( $6^\circ$ ), their specular reflectance at different angles of incidence (from  $20^\circ$  to  $70^\circ$ ) and after an UV ageing process (able to irradiate the sample with a UV dose equal to a year of outdoor exposure at the Catania latitude) and an outdoor exposure to evaluate the soiling effects on reflectance.

Each of these reflectors appear to possess different characteristics that are not fully described in the commercial brochure, sometimes obtained with a non-precise methodology or worse, obtained with a non-precise instrumental apparatus.

To cope with this lack of information the companies concentrating on building solar power plants have to be able to decide whether to use a material or not.

Distinguishing between a good or a less good material such as mirrors (which is the heart of the entire project) is the key to building new and less expensive plants and can be critical for the initial cost assessment and the maintenance costs during the power plant's lifespan.

A good material will maintain the optical performances during the entire operational life, will have a good mechanical resistance, have a good weatherability and very high shape accuracy, furthermore it will be light weight, is easy to handle and possesses the quality to be produced in large sizes.

To achieve reliable results in research, different steps were necessary to conduct a measurement campaign with a CARY 5000 UV/VIS NIR spectrophotometer for the reflectance measurements (Chapter 5) in the optical and geometrical study of the systems with two modeling software tools: Mathcad and Soltrace (Chapter 6).

The results (Chapter 7) were used to obtain a quantitative analyses of the energy reflected from the mirrors and absorbed from the Heat Collector Element, maintaining firstly a constant reflectance of the mirrors and then introducing the VASRA experimental results inside the model to simulate the quantity of DNI reflected throughout a year, considering the contribution that the increase of mirrors reflectance show when varying the incidence angle.

## 2. CONCENTRATING SOLAR POWER SYSTEMS

Concentrating Solar Power (CSP) plants use all the technologies applied to transform sunlight into high-temperature heat and thus converting such heat into electrical energy. The general principle of a CSP plant entails using mirrors to concentrate the sun's rays on a fluid that vaporizes. The heat from this fluid is transferred into a heat exchanger to a water-steam cycle, which drives a turbine and a generator to generate electricity. The most widespread technology in the CSP sector is a CSP plant based on cylindrical -parabolic mirror technology (also called solar trough plants) with capacities ranging from 50 to 300 MW. Cylindrical-parabolic mirrors concentrate the sun's rays on an absorber tube containing a heat-transfer fluid that can be heated to temperatures of around 400°C and generate electricity based on heat transfer to a conventional water-steam cycle. Some plants are equipped with storage systems enabling unused, surplus energy to be stored in the form of heat in molten salt or some other phase-changing material.

The plant can then draw on the stored heat to generate electricity after sunset. Spain's Andasol 1 plant, for example, currently uses this system to operate for an additional 7½ hours every day.

Alternatively, solar power is harnessed in 10 to 50 MW-capacity solar tower CSP plants that use heliostats – huge, almost flat mirrors over 100 m<sup>2</sup> in surface area. They are arranged in large numbers (up to hundreds) to concentrate the sun's rays on a point at the top of a tower, heating the heat-transfer fluid (generally a salt) up to as much as 600°C.

Its designed storage capacity is for up to 15 hours which should support almost round-the-clock production, and enable the plant to supplement electricity generation based on fossil fuels or nuclear energy. There are other technologies in the stage of development and demonstration that are not yet used on an industrial scale. For instance, Fresnel linear collectors that are a variant on a CSP plant based on cylindrical-parabolic mirror technology, which instead of using a trough-shaped mirror, have sets of small flat mirrors arranged in parallel and longitudinally on an incline. Furthermore, the absorber tube that concentrates the rays is stationary and the mirrors follow the course of the sun.

The fluid is heated to a temperature of up to 450°C.

Development is under way on larger (150-MW and more) plants, but they are outside of Europe.

Another alternative technology is the dish Stirling system, based on a dish-shaped concentrator (comprising parabolic mirrors) to capture the sunlight and focus it on a receiver at the focal point of

the parabolic dish. The parabolic dish system, which tracks the sun, uses a gas (helium or hydrogen) that is heated in the receiver to temperatures in excess of 600°C to drive a Stirling engine coupled with a generator. The capacity of these units is limited to 10–25 kW, which will meet isolated production needs. Alternatively, parabolic dish CSP plants may be built as large-scale plants with thousands of parabolic dishes grouped together on a single site. Two projects with an aggregate capacity of 1.4 GW are under construction in the United States, but no industrial-scale ventures have been identified in Europe.

## 2.1 Technology Description and Status

There are three types of concentrating solar power (CSP) technology: trough, parabolic-dish and power tower.<sup>1</sup> Trough and power tower technologies apply primarily to large, central power generation systems, although trough technology can also be used in smaller systems for heating and cooling and for power generation.

The systems use either thermal storage or back-up fuels to offset solar intermittency and thus to increase the commercial value of the energy produced.

The conversion path of concentrating solar power technologies relies on four basic elements: concentrator, receiver, and transport-storage and power conversion.

The concentrator captures and concentrates solar radiation, which is then delivered to the receiver. The receiver absorbs the concentrated sunlight, transferring its heat to a working fluid. The transport-storage system passes the fluid from the receiver to the power-conversion system; in some solar-thermal plants a portion of the thermal energy is stored for later use.

The inherent advantage of CSP technologies is their unique capacity for integration into conventional thermal plants. Each technology can be integrated in parallel as “a solar burner” to a fossil burner into conventional thermal cycles. This makes it possible to provide thermal storage or fossil fuel backup firm capacity without the need of separate back-up power plants and without disturbances to the grid.

With a small amount of supplementary energy from natural gas or any other fossil fuel, solar thermal plants can supply electric power on a steady and reliable basis.

---

<sup>1</sup> CSP is used interchangeably with solar thermal power. D 0.72 per kWh by 2050.

Thus, solar thermal concepts have the unique capability to internally complement fluctuating solar burner output with thermal storage or a fossil back-up heater.

The efficiency and cost of such combined schemes, however, can be significant.

Current costs are about USD 0.10 per kWh and are expected to rise to about USD 0.72 per kWh by 2050. This technology relies on small-scale gas-fired power plants with low efficiency (40–45%), compared to 500-MW centralized plants with efficiencies of 60%. If the efficiency loss is allocated to the hybrid scheme, the economics would be less encouraging.

Fresh impetus was given to solar thermal-power generation by a Spanish law passed in 2004 and revised in 2005. The revised law provides for a feed-in-tariff of approximately EUR 0.22 (USD 0.27) per kWh for 500 MW of solar thermal electricity.

In several states in the United States and in other countries, the regulatory framework for such plants is improving. At present, solar plant projects are being developed in Spain (50 MW), in Nevada in the United States (68 MW) and elsewhere.

Two U.S. plants will also be constructed in southern California under the state's Renewable Portfolio Standard. A 500 MW solar thermal plant, expected to produce 1,047 GWh, is due for completion in 2012.

There is a current trend toward combining a steam-producing solar collector and a conventional natural gas combined-cycle plant. Projects in Algeria and Egypt, currently at the tendering stage, will combine a solar field with a combined-cycle plant. There are also plans to add a solar field to an existing coal plant in Australia.

On a long-term basis, the direct solar production of energy in transportable chemical fuels, such as hydrogen, also holds great promise.

## 2.2 Cost and Potential for Cost Reductions

Since concentrating solar power uses direct sunlight, the best conditions for this technology are in arid or semi-arid climates, including Southern Europe, Northern and Southern Africa, the Middle East, Western India, Western Australia, the Andean Plateau, Northeastern Brazil, Northern Mexico, and the Southwestern United States. The cost of concentrating solar power generated with up-to-date technology at superior locations is between USD 0.10 and USD 0.15 per kWh. CSP technology is still too expensive to compete in domestic markets without subsidies.

The goal of ongoing RD&D is to reduce the cost of CSP systems to USD 0.05–USD 0.08 per kWh within 10 years and to below USD 0.05 in the long term.

Improved manufacturing technologies are needed to reduce the cost of key components, especially for first plant applications where economies of scale are not yet available. Field demonstration of the performance and reliability of Stirling engines are critical.

The European Commission (EC) has undertaken a coordination activity, called the European Concentrated Solar Thermal Road-mapping (ECOSTAR), to harmonize the fragmented research methodology previously in place in Europe, which previously led to competing approaches on how to develop and implement CSP technology. Cost-targeted innovation approaches, as well as continuous implementation of this technology, are needed to realize cost-competitiveness in a timely manner.

## 2.3 Cost Overview

There is a wide range of costs for each renewable technology due mainly to varying resource quality and to the large number of technologies within each category. Investment includes all installation costs, including those of some demonstration plants in certain categories. Discount rates vary across regions.

Because of the wide range in costs, there is no specific year or CO<sub>2</sub> price level for which a renewable energy technology can be expected to become competitive.

A gradual increase in the penetration of renewable energy over time is more likely.

Energy policies can speed up this process by providing the right market conditions and to accelerate deployment so that costs can be reduced through technology learning.

Technology learning in bioenergy systems has been studied using experiences in Denmark, Finland, and Sweden (Junginger M et al, 2005) (al J. M., 2005). In the supply chain, learning rates for wood fuel-chips are 12–15%. For energy conversion in biogas or fluidized bed boiler plants, available data are much more difficult to interpret. An average learning rate of 5% for energy-producing plants appears to be a reasonable average estimate.

Technology learning is a key phenomenon that will determine the future cost of renewable power generation technologies. Unfortunately, the present state-of-heart does not allow reliable extrapolations. National data indicate learning rates between 4% and 8% for wind turbines in Denmark and Germany. Learning rates for installation costs are one or two percentage point's higher (L, 1999) (al N. L., 2004). From 1980 to 1995, the cost of electricity from wind energy in the European Union decreased at a considerably higher rate of 18%. Wind energy is a global technology and experience curves based on deployment in major manufacturing countries like Germany and Denmark may be much lower than learning rates elsewhere analyzed the installation cost of wind farms from a global learning perspective and found learning rates between 15% and 19% (Junginger M, 2004). Other recent studies quote learning rates of 5% for recent years.

Technology learning rates are better documented for photovoltaic than for other renewable energy sources. PV modules have shown a steady decrease in price over more than three decades, with a learning rate of about 20% (C, March 2000) (al P. S., 2004). In 1968, the price of one peak watt of PV module was about USD 100,000 per kW. Today the price is about USD 3,000 per kW. Learning for PV modules is a global phenomenon, but prices for balance-of-system components reflect national or regional conditions.

The EU-PHOTEX project found learning rates for balance-of-system in Germany, Italy, and the Netherlands to be from 15% to 18%.

	Learning rate (%)	Investment cost 2005 (USD/kW)	2030 (USD/kW)	2050 (USD/kW)	Production cost 2005 (USD/MWh)	2030 (USD/MWh)	2050 (USD/MWh)
Biomass	5	1,000–2,500	950–1,900	900–1,800	31–103	30–96	29–94
Geothermal	5	1,700–5,700	1,500–5,000	1,400–4,900	33–97	30–87	29–84
Large hydro	5	1,500–5,500	1,500–5,500	1,500–5,300	34–117	34–115	33–113
Small hydro	5	2,500	2,200	2,000	56	52	49
Solar PV	18	3,750–3,850	1,400–1,500	1,000–1,100	178–542	70–325	<60–290
Solar thermal	5	2,000–2,300	1,700–1,900	1,600–1,800	106–230	87–190	<60–175
Tidal	5	2,900	2,200	2,100	122	94	90
Wind onshore	5	900–1,100	800–900	750–900	42–221	36–208	35–205
Wind offshore	5	1,500–2,500	1,500–1,900	1,400–1,800	66–217	62–184	60–180

Note: Using 10% discount rate. The actual global range is wider as discount rates, investment cost and fuel prices vary. Wind and solar include grid connection cost learning rate implies

Table 2.1 Key cost and investment assumptions for renewables

## 2.4 Linear Concentrator Systems

Linear concentrating solar power (CSP) collectors are one of the three types of CSP systems in use today.

Linear CSP collectors capture the sun's energy with large mirrors that reflect and focus the sunlight onto a linear receiver tube.

The receiver contains a fluid that is heated by the sunlight and then used to create superheated steam that spins a turbine that drives a generator to produce electricity.

In few and rare applications, steam can be generated directly in the solar field, eliminating the need for costly heat exchangers, increasing on the other hand the cost for water demineralization.

Linear concentrating collector fields consist of a large number of collectors in parallel rows that are typically aligned in a north-south orientation to maximize both annual and summertime energy collection.

With a single-axis sun-tracking system, this configuration enables the mirrors to track the sun from east to west during the day, ensuring that the sun reflects continuously onto the receiver tubes.

## 2.5 Parabolic Trough Systems

The predominant CSP systems currently in operation are linear concentrators using parabolic trough collectors. In such a system, the receiver tube is positioned along the focal line of each parabola-shaped reflector (Fig.2.1).

The tube is fixed to the mirror structure and the heated fluid—either a heat-transfer fluid or water/steam flows through and out of the field of solar mirrors to where it is used to create steam (or, for the case of a water/steam receiver, it is sent directly to the turbine).

Currently, the largest individual trough systems generate 80 MW of electricity. However, individual systems being developed will generate 250 MW.

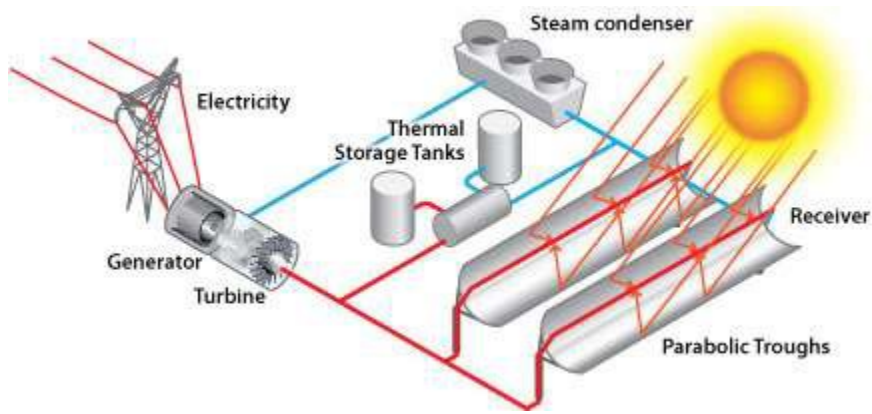


Figure 2. 1 A linear concentrator power plant using parabolic trough collectors

In addition, individual systems can be collocated in power parks.

This capacity would be constrained only by transmission capacity and availability of contiguous land area.

Trough designs can incorporate thermal storage.

In such systems, the collector field is oversized to heat a storage system during the day that can be used in the evening or during cloudy weather to generate additional steam to produce electricity.

Parabolic trough plants can also be designed as hybrids, meaning that they use fossil fuel to supplement the solar output during periods of low solar radiation.

## 2.6 Linear Fresnel Reflector Systems

A second linear concentrator technology is the linear Fresnel reflector system (Fig.2.2).

Flat or slightly curved mirrors mounted on trackers on the ground are configured to reflect sunlight onto a receiver tube fixed in space above the mirrors.

A small parabolic mirror is sometimes added atop of the receiver to further focus the sunlight.

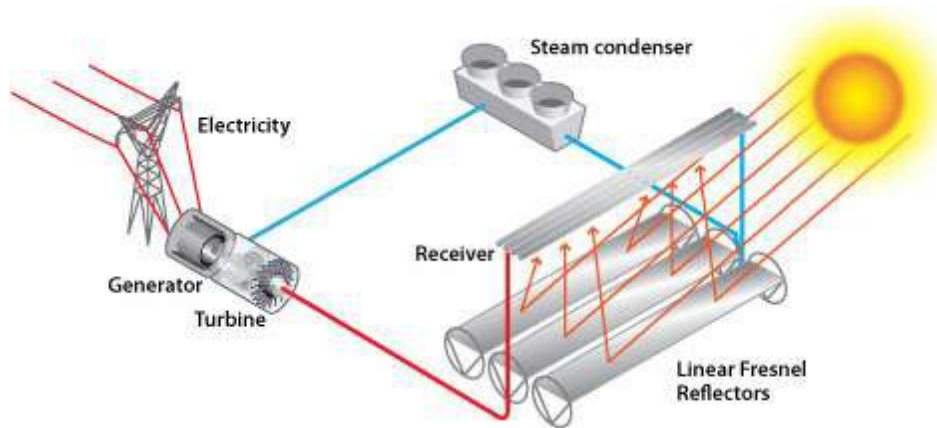


Figure 2. 2 A linear Fresnel reflector power plant

## 2.7 Dish/Engine Systems

The dish/engine system is a concentrating solar power (CSP) technology that produces relatively small amounts of electricity compared to other CSP technologies typically in the range of 3 to 25 kW.

A parabolic dish of mirrors directs and concentrates sunlight onto a central engine that produces electricity (Fig.2.3).

Currently, the most common type of heat engine used in dish/engine systems is the Stirling engine.

A Stirling engine uses the heated fluid to move pistons and create mechanical power.

The mechanical work, in the form of the rotation of the engine's crankshaft, drives a generator and produces electrical power.

Most current existing systems for low power thermodynamic solar energy conversion are based on the 'Dish/Stirling' technology (al B. e., 2006); (Diver, 1994) that relies on high temperature Stirling engines and requires a high solar energy concentration ratio.

It is clear that these systems are quite heavy, leading to high costs.

In the particular case of the concentrator, the sun tracking system and the engine fixation at the concentrator focus are quite expensive. Also the high pressure high temperature engine requires expensive technology.

Fig.2.3 presents an example of such a system, able to produce 25 kW of electric power.



**Figure 2. 3 SES Dish/Stirling system**

Initially developed and tested by McDonnell Douglas and Southern California Edison, it was acquired by Stirling Energy Systems in 1996 (SES, 2006).

This system, built in the years 1984-1985, is made up of a 10.57 m equivalent diameter concentrator with an efficiency of  $\eta_{\text{conc}} = 0.88$ , a cavity receiver with an opening of 0.2 m and an efficiency of 0.9 that leads to an overall solar energy collection efficiency of 0.79.

The Stirling engine is a kinematics 4-95 MkII engine built by United Stirling AB (USAB).

This engine has a 38-42% efficiency for a maximum hydrogen working fluid temperature of 720°C.

The whole system leads to a global solar to electric energy conversion efficiency of 29-30%.

This figure is more or less twice the efficiency of photovoltaic cells, but the corresponding structure is obviously heavier.

Most solar dish/Stirling systems built up to now were based on pre-existing engines, usually developed for external combustion applications.

This explains the high temperature level needed in the cavity receiver and therefore the high solar energy concentration level.

These high temperature engines use high pressure (typically 20 MPa) helium or hydrogen as a working fluid.

This is a quite high-tech, thus expensive, system.

However, it is possible to produce mechanical energy by means of a very low temperature differential thermal engine using direct solar energy without any concentration (Wongwises, 2003), (al B. e., 2006). But obviously these systems produce very low power per unit volume or unit mass of the system.

The two major parts of the system are the solar concentrator and the power conversion unit (Fig.2.4).

## 2.8 Solar Concentrator

The solar concentrator, or dish, gathers the solar energy coming directly from the sun. The resulting beam of concentrated sunlight is reflected onto a thermal receiver that collects the solar heat.

The dish is mounted on a structure that tracks the sun continuously throughout the day to reflect the highest percentage of sunlight possible onto the thermal receiver.

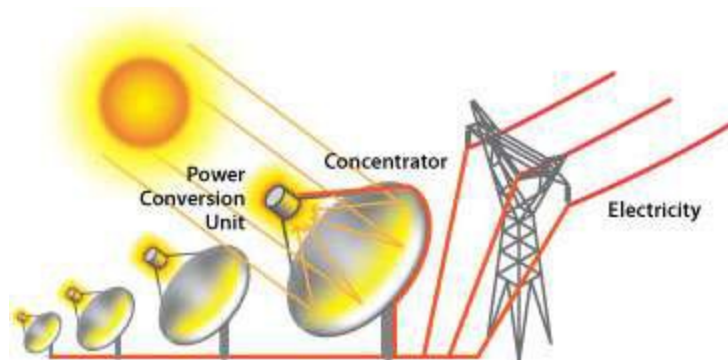


Figure 2. 4 A dish/engine power plant.

## 2.9 Power Conversion Unit

The power conversion unit includes the thermal receiver and the engine/generator.

The thermal receiver is the interface between the dish and the engine/generator.

It absorbs the concentrated beams of solar energy, converts them to heat, and transfers the heat to the engine/generator.

A thermal receiver can be a bank of tubes with a cooling fluid, usually hydrogen or helium, which typically is the heat-transfer medium and also the working fluid for an engine.

Alternate thermal receivers are heat pipes, where the boiling and condensing of an intermediate fluid transfers the heat to the engine.

The engine/generator system is the subsystem that takes the heat from the thermal receiver and uses it to produce electricity.

## 2.10 Power Tower Systems

Power tower systems are one of the three types of concentrating solar power (CSP) technologies in use today (Fig.2.5).

In this CSP technology, numerous large, flat, sun-tracking mirrors, known as heliostats, focus sunlight onto a receiver at the top of a tower.

A heat-transfer fluid heated in the receiver is used to generate steam, which, in turn, is used in a conventional turbine generator to produce electricity.

Some power towers use water/steam as the heat-transfer fluid.

Other advanced designs are experimenting with molten nitrate salt because of its superior heat-transfer and energy-storage capabilities.

Individual commercial plants can be sized to produce up to 200 megawatts of electricity.

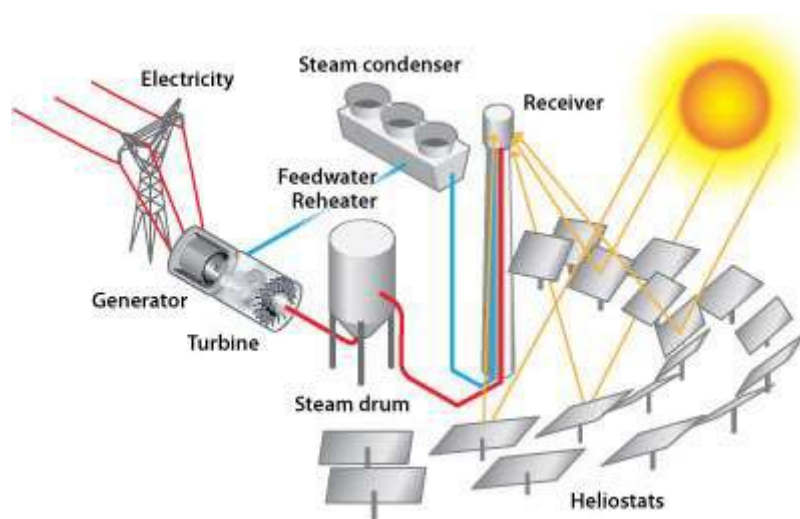


Figure 2. 5 A power tower power plant.

Two large-scale power tower demonstration projects have been deployed in the United States.

During its operation from 1982 to 1988, the 10-megawatt Solar One plant near Barstow, California, demonstrated the viability of power towers, producing more than 38 million kilowatt-hours of electricity.

The Solar Two plant was a retrofit of Solar One to demonstrate the advantages of molten salt for heat transfer and thermal storage.

Using its highly efficient molten-salt energy storage system, Solar Two successfully demonstrated efficient collection of solar energy and dispatch of electricity.

It also demonstrated the ability to routinely produce electricity during cloudy weather and at night.

In one demonstration, Solar Two delivered power to the grid for 24 hours a day for almost seven consecutive days before cloudy weather interrupted operation.

Currently, Spain has several power tower systems operating or under construction.

Planta Solar 10 and Planta Solar 20 are water/steam systems with capacities of 11 and 20 megawatts, respectively.

Solar Tres will produce some 15 megawatts of electricity and have the capacity for molten salt thermal storage.

Power towers also offer good longer-term prospects because of the high solar-to-electrical conversion efficiency.

Additionally, costs will likely drop as the technology matures.

## **2.11 Thermal Storage**

Thermal energy storage (TES) has become a critical aspect of any concentrating solar power (CSP) system deployed today.

One challenge facing the widespread use of solar energy is the reduced or curtailed energy production when the sun sets or is blocked by clouds.

Thermal energy storage provides a workable solution to this challenge.

In a CSP system, the sun's rays are reflected onto a receiver, creating heat that is then used to generate electricity.

If the receiver contains oil or molten salt as the heat-transfer medium, then the thermal energy can be stored for later use.

This allows CSP systems to be a cost-competitive option for providing clean, renewable energy.

Presently, steam-based receivers cannot store thermal energy for later use.

Thermal storage research in the United States and Europe seeks to develop such capabilities.

## **2.12 Future R&D Efforts**

Improvements in the concentrator performance and cost will have the most dramatic impact on the penetration of CSP. Because the concentrator is a modular component, it is possible to adopt a straightforward strategy that couples development of prototypes and benchmarks of these innovations in parallel with state-of-the-art technology in real solar-power plant operation conditions. Modular design also makes it possible to focus on specific characteristics of individual components, including reflector materials and supporting structures, both of which would benefit from additional innovation.

Research and development is aimed at producing reflector materials with the following traits (IEA, Renewable energy: RD&D priorities, 2005):

- Good outdoor durability.
- High solar reflectivity (>92%) for wavelengths within the range of 300–2,500 nm.
- Good mechanical resistance to withstand periodical washing.
- Low soiling co-efficient (<0.15%, similar to that of the back-silvered glass mirrors).

Scaling up to larger power cycles is an essential step for all solar thermal technologies (except for parabolic trough systems using thermal oil, which have already gone through the scaling in the nine solar electric generation stations installations in California, which range from 14 MW to 80 MW). Scaling up reduces unit investment cost, unit operation and maintenance costs and increases performance.

The integration into larger cycles, specifically for power tower systems, creates a significant challenge due to their less-modular design. Here the development of low risk scale-up concepts is still lacking.

Storage systems are another key factor for cost reduction of solar power plants.

Development needs are very much linked to the specific system requirements in terms of the heat-transfer medium utilized and the necessary temperature. In general, storage development requires several scale-up steps linked to an extended development time before market acceptance can be achieved. Research and development for storage systems is focused on improving efficiency in terms of energy and energy losses; reducing costs; increasing service life; and lowering parasitic power requirements.

### 3. SPETTROSCOPY

The spectroscopic analysis of the mirrors samples, that will be discussed in the following, encounter the major problem caused by the sample itself, in fact it is a non-perfectly smooth object. Furthermore, when the light hits the sample, part of the light beam pass through the material, part of the light is absorbed by the material, which is mostly reflected. The reflected or refracted photons from the material surface are called scattered.

After the reflection, the scattered photons can encounter another microscopic imperfection of the material or they can also be reflected outside of the material allowing for it to be measured.

The photons can also be originated by an object, this phenomenon is called emission.

Every surface which has a temperature higher than the absolute zero emits photons.

The emitted photons follow the physical laws of reflection, refraction and absorption as the incident ones should.

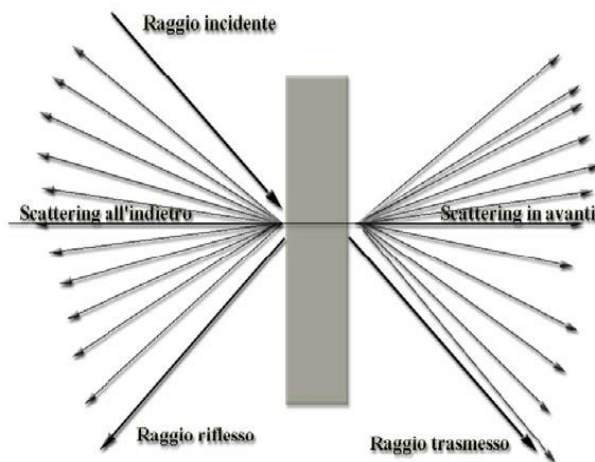


Figure 3. 1 Typical material absorption process

The photons are absorbed by different processes.

The specific type of absorption process and its direct correlation with the wavelength inform us of the exact chemical composition of a material analysing the emitted or reflected light.

The human eye is a reflection spectrometer: its configuration allows us to see a surface and its colour.

Our eyes and brain process the scattered light and due to the reflected photon wavelength they recognize the surface colour and shape.

A modern spectrophotometer can measure with great accuracy details on a broad range of wavelengths.

In this way a spectrophotometer can measure the absorption caused by many processes that can't be seen by the human eye.

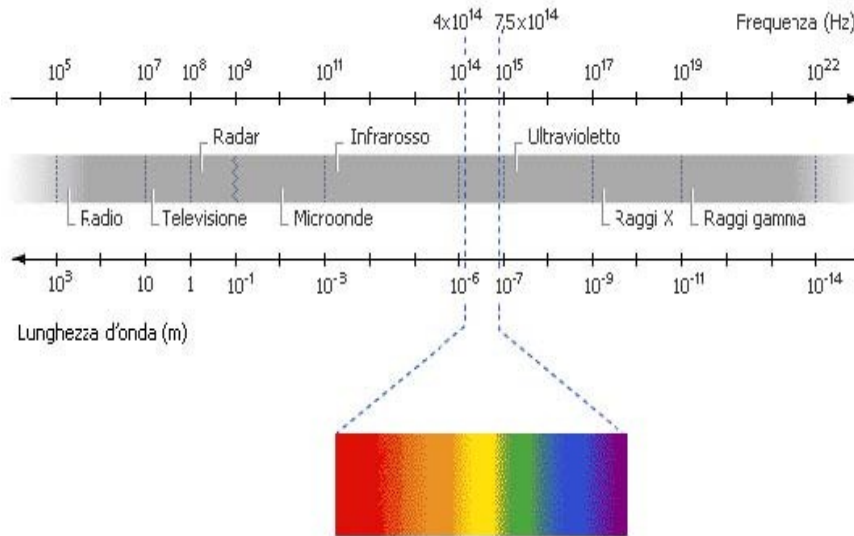


Figure 3. 2 Spectrum division

The electromagnetic spectrum is usually divided into different spectral range that is differentiated in way the radiation is analysed.

a)	X (XR),: from 0,001 to 1 nm;
b)	Ultraviolet (UV): from 0,001 to 0,4 $\mu\text{m}$ ;
c)	Visible : from 0.4 to 0.7 $\mu\text{m}$ ;
d)	Near-infraRed (NIR): from 0.7 to 3.0 $\mu\text{m}$ ;
e)	Mid-infraRed (MIR): from 3.0 to 30 $\mu\text{m}$ ;
f)	Far-infraRed (FIR): from 30 $\mu\text{m}$ to 1 mm;
g)	Millimetric, from 1 to 10 mm;
h)	Micro-Wave (MW), from 10 mm to 1 m;
i)	Radio, from 1 to 10 <sup>5</sup> m.

Table 3. 1 Spectrum division

The wavelength range from 0.4 to 1.0  $\mu\text{m}$  is usually called in literature remote sensing or VNIR (Visible-Near-InfraRed) while the wavelength from 1.0 to 2.5  $\mu\text{m}$  is usually called SWIR (Short Wave InfraRed).

It's important to note that these terms are not standard in the other field but only in the remote sensing.

The Mid-InfraRed cover the thermal energy emitted by the earth that goes from 2.5  $\div$  3.0  $\mu\text{m}$ , with a peak around 10  $\mu\text{m}$  decreasing thereafter with a trend similar to a grey body.

### 3.1 Reflection

The reflection spectroscopy is the study of the reflected light or diffused by a solid, a liquid or a gas, directly linked to the wavelength.

Considering a sample being hit by a monochromatic light beam  $J$  and the resulting reflected beam  $R$  ( see Fig.3.2)

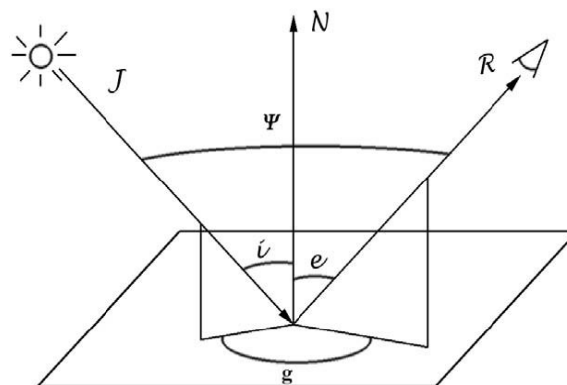


Figure 3. 3 Optics Angles

It is possible to recognize three planes:

<b>JN</b>	Incident plane
<b>RN</b>	Emersion plane
<b>JR</b>	Scattering plane

Having indicated with  $N$  the normal axis on the sample. If the  $g$  angle between the planes  $JN$  and  $JN$  is equal to 0 or  $\pi$  we obtain  $JN \equiv RN \equiv JR$  and the plane is called primary. (Hapcke, 1993).

In general the three different angles give a unique geometry. Commonly we use  $i$ ,  $e$ ,  $g$  (see Fig. 3.3.)

For simplicity we can assume  $\mu = \cos e$  and  $\mu_0 = \cos i$ .

The parameter used to measure the reflective capability of a material to reflect the incident beam is called Reflectance.

The reflectance is defined as the ratio between the diffused energy per unit of area of the mean and the incident energy on the unit of surface.

It is possible to distinguish different kinds of reflectance depending on the type of system we operate on:

- *Bi-directional reflectance*;
- *Bi-conic reflectance*;
- *Hemispheric reflectance*;
- *Spheris reflectance*;

In the following, a brief description of the different types of reflectance, the hemispheric reflectance will be discussed in a geometrical standpoint because it is the one used in the acquisition of data, and which will be discussed in depth successively.

The Bi-Directional reflectance is measured enlightening a sample with a light coming from a known source with a very little angular spreading and observing the diffused light with a mobile detector which also implies a small angle with the sample surface (see Fig. 3.4)

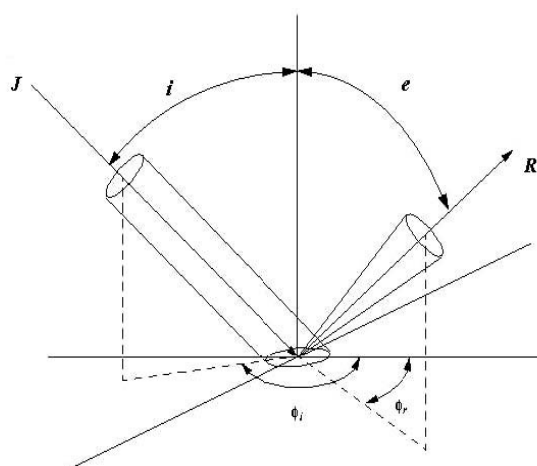


Figure 3. 4 Bi-directional reflectance

To obtain the most precise diffusion parameters, it's advisable to measure the reflectance with different values of  $i$ ,  $e$  and  $g$  ( $g = \phi_j - \phi$ ), even if normally it is measured with one set of angles.

The equation that describes the bi-directional reflectance function of the angles  $i$ ,  $e$  and  $g$  is the equation 2.1.

$$r(i, e, g) = \frac{w}{4\pi} \frac{\mu_0}{\mu_0 + \mu} \{p(g) + H(\mu_0)H(\mu) - 1\} \quad \text{Equation 3. 1}$$

With

$$H(x) \cong \frac{1 + 2x}{1 + 2\gamma x} \quad \text{Equation 3. 2}$$

And  $\gamma = \sqrt{1 - w}$

Indicating:

**r** Bi-directional reflectance;

**w** single scattering albedo;

**p(z)** Phase function (Hapke, 1993).

The Bi-conic reflectance it's the first integrated reflectance encountered.

This means that the detector doesn't occupy the entire solid angle saw from the sample surface.

The correct expression if this kind of reflectance could be found integrating the 3.1 equation on all the angular distribution of the radiation and the detector angular distribution response (Salisbury et al, 1991).

The Hemispheric reflectance is measured by an integrating sphere

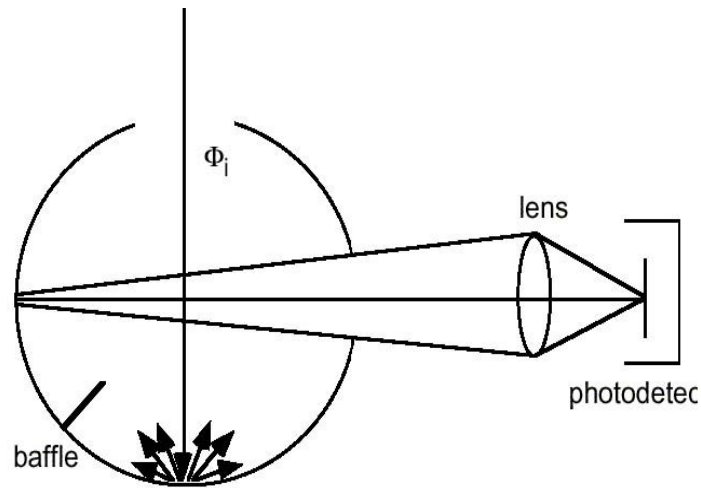


Figure 3.5 Hemispheric reflectance

This device (see Fig. 3.5) consists of a cavity covered with a highly reflective diffusion material, with two small openings, or ports, one to allow the incident beam to enter, the other to allow to observe the radiation in this sphere. Of course the expression that provides the hemispherical reflectance, as discussed in detail later, will be calculated from (3.1) integrated over a solid angle of  $2\pi$ .

As for the spherical reflectance it is, in principle, measured by an opaque sphere covered by the sample placed at the centre of the integrating sphere. One side of the sample is illuminated by a collimated beam of light, the radiation is diffused in all directions and is measured by a detector that doesn't see the target directly.

### 3.1.1 Hemispheric Reflectance

The importance of the hemispherical reflectance is mainly due to two reasons:

The quantity that is directly measured by many commercial spectrophotometers;

It is one of the properties of a material that determine radiative equilibrium temperature (see section 3.1.4.).

The incident energy per unit area is  $J\mu_0$ . The energy of the outgoing for a unit of solid angle per unit of area is:  $Y = Jr(i, e, g)\mu$ .

$$r_h = \frac{1}{J\mu_0} \int_{2\pi} Y(i, e, g) d\Omega_e = \frac{1}{\mu_0} \int_{2\pi} r(i, e, g) \mu d\Omega_e$$

Replacing to  $r(i, e, g)$  the equation (3.1) and being  $d\Omega_e = \sin e \, d\psi$ , it's possible to obtain the equation for the hemispheric reflectance:

$$r_h(i) = \frac{w}{4\pi} \int_{\psi=0}^{2\pi} \int_{e=0}^{\pi/2} \frac{\mu}{\mu_0 + \mu} [p(g) + H(\mu_0)H(\mu) - 1] \sin e \, d\psi$$

Hemispherical reflectance can be expressed as a contribution of two different elements  $r_h = r_{hi} + r_{ha}$  with  $r_{hi}$  isotropic hemispherical reflectance and  $r_{ha}$  anisotropic hemispherical reflectance, which can be expressed as:

$$r_{hi} = \frac{w}{2} \int_{\mu=0}^1 \frac{\mu}{\mu_0 + \mu} H(\mu_0)H(\mu) d\mu$$

$$r_{ha} = \frac{w}{4\pi} \int_{\psi=0}^{2\pi} \int_{\mu=0}^1 \frac{\mu}{\mu_0 + \mu} [p(g) - 1] d\mu d\psi$$

In this way we obtain:

$$r_{hi} = 1 - \gamma H(\mu_0) \quad r_{ha} = \frac{w}{2} \mu_0 b_1 \left[ \frac{1}{2} - \mu_0 + \mu_0^2 \ln \left( \frac{\mu_0 + 1}{\mu_0} \right) \right]$$

So

$$r_h(i) = 1 - \gamma H(\mu_0) + \frac{w}{2} \mu_0 b_1 \left( \frac{1}{2} - \mu_0 + \mu_0^2 \ln \frac{\mu_0 + 1}{\mu_0} \right)$$

Developing in Taylor series:

$$\mu_0^2 \ln \left( \frac{\mu_0 + 1}{\mu_0} \right) \cong \frac{2\mu_0}{1 + 2\mu_0}$$

Replacing  $H(\mu)$  from (2.2) we have:

$$r_h(i) = \frac{1 - \gamma}{1 + \gamma\mu_0} + b_1 \frac{w}{4} \frac{\mu_0}{1 + 2\mu_0}$$

Under appropriate simplifying assumptions we can define the reflectance  $r_0$ , called diffusive (Hapke, 1993), the ratio:

$$r_0 = \frac{P_{em}}{P_{in}}$$

Where  $P_{in}$  is the total energy incident on the material per unit area

$$P_{in} = \int_0^{\pi/2} I_0 \cos \vartheta 2\pi \sin \vartheta d\vartheta = \pi I_0$$

where  $I_0$  is the intensity of incident ray in the normal way.

$P_{em}$  is the total energy spread in all directions emerging per unit area:

$$P_{em} = \int_0^{\pi/2} I_1(0) \cos \vartheta 2\pi \sin \vartheta d\vartheta = \pi I_1(0) = \pi I_0 \frac{1-\gamma}{1+\gamma} = \pi I_0 r_0$$

$I_1(0)$  is the reflection in the normal direction

Then:

$$r_0 = \frac{1-\gamma}{1+\gamma}$$

Finally we find, inverting the (2.3) that  $\gamma = \frac{1-r_0}{1+r_0}$  and  $w = \frac{4r_0}{(1+r_0)^2}$ .

As a result it can be established that by introducing the parameters  $K'$  and  $S'$ , respectively the volumetric absorption coefficient and the coefficient of volumetric scattering Kubelka-Munk, the equation of Kubelka-Munk. The extinction coefficient is to be defined as  $(K' + S')$ . Through these parameters it's possible to redefine the single volume scattering albedo as

$$w' = \frac{2S'}{K'+2S'}$$

Hereupon

$$\gamma' = \sqrt{1-w'}$$

For analogy on (2.3) it's possible to state:

$$r'_0 = \frac{1 - \gamma'}{1 + \gamma'} = \frac{1 - \sqrt{1 - 2S'/(K' + 2S')}}{1 + \sqrt{1 - 2S'/(K' + 2S')}} = \frac{1 - \sqrt{K'/(K' + 2S')}}{1 + \sqrt{K'/(K' + 2S')}} \quad \text{Equation 3.3}$$

Combining the diffusive approximation, equation (3.3), the scattering law of Lambert we obtain the expression Lambert-diffusive:

$$r_{hL} = r_0$$

It's possible to recall briefly that the radiation emitted from the sphere towards the observer is given by:

$$I = \int_{\Lambda=-\pi/2}^{(\pi/2)-g} \int_{L=-\pi/2}^{\pi/2} JY(i, e, g) dA$$

With

$$Y(i, e, g) = \frac{1}{\pi} \cos i \cos e$$

Lambert law and L and  $\Lambda$  the latitude and longitude of the infinitesimal surface element dA of the sphere on the sphere.

### 3.2. Transmission

As was stated in the previous section the incident beam, noted by J in Figure 3.4. has an attenuated reflection. Denote by  $I_0$  as the energy difference between the incident and the reflected beam,  $I_0 = J - R$ . This energy may follow two processes: it could be transmitted through the sample or is absorbed by it. The two processes occur simultaneously and naturally, only if the optical depth of the material is low, otherwise the whole energy is absorbed.

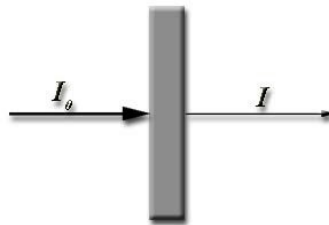


Figure 3.6 Transmission through a material

Suppose that our sample is optically thin. If  $I_0$  is the intensity of incident light on a material and  $I$  is the intensity of light the observer receives (see Figure 3.6.), these parameter are related by:

$$I = I_0 T$$

Where  $T$  is the transparency of the material.

The absorbance is defined by (3.4)

$$A(\lambda) = \log[T(\lambda)] \quad \text{Equation 3.4}$$

in differential form:

$$dI_\lambda = -k'_\lambda \rho_g I_\lambda dS \quad \text{Equation 3.5}$$

Where:

$dI_\lambda$  represent the absorbed radiation;

$k'_\lambda$  is the absorption coefficient per mass unit;

$\rho_g$  is the density of the crossed material;

$I_\lambda$  is the incoming Intensity of radiation;

$dS$  is the infinitesimal thickness of the crossed mean.

The absorption coefficient in the case of grain is given by:

$$k'_\lambda = \frac{3 C_{\text{ext}}(\lambda)}{4 \pi a^3} \frac{I}{\rho_M} \quad \text{Equation 3.6}$$

Where  $C_{\text{ext}}(\lambda)$  is called effective section of extinction,  $V$  has the matter particles volume and  $\rho_m$  the material density of the grains.

At this point two important conditions must be assumed:

Particles should be homogeneous both in composition and in density.

Particles all have the same shape, spherical, and the same size.

So if we assume that  $a$  is the radius of the spherical grain, the term  $V$  (3.6) is  $V = \frac{4}{3} \pi a^3$ , while the mass  $m_g$  is reported to be a consequence, in particular  $m_g = \frac{4}{3} \pi a^3 \rho_m$

The difference between the density  $\rho_g$  and  $\rho$  in the (3.5) and (3.6) respectively is now more clear, the first in fact is the density of a volume traversed by the radiation, while the second represents the density of individual spherical grain.

The extinction coefficient,  $C_{ext}(\lambda)$ , or effective section of extinction may be linked with energy extinct by the radiation:

$$C_{ext}(\lambda) = \frac{W_{abs}(\lambda) + W_{sca}(\lambda)}{I_0(\lambda)}$$

where  $W_{abs}(\lambda)$  is the energy absorbed by material per unit of time, while  $W_{sca}(\lambda)$  is the diffuse one. Since  $I_0(\lambda)$  energy per unit area and time, it is clear that  $C_{ext}(\lambda)$  is one dimensional surface. Through the equation:

$$Q_{ext}(\lambda) = \frac{C_{ext}(\lambda)}{\pi a^2} \quad \text{Equation 3.7}$$

$\pi a^2$  defined as effective extinction efficiency factor or factor of extinction.

The  $C_{ext}(\lambda)$  is related to the refractive index  $m(\lambda) = n(\lambda) + ik(\lambda)$ , where  $n(\lambda)$  is the refractive index usually used and neglects the absorption of radiation by the sample, and  $k(\lambda)$  takes precisely into account the absorption.

Resuming the (3.5):

$$dI_\lambda = -k'_\lambda \rho_g I_\lambda dS$$

Integrating we obtain:

$$I'_\lambda = I_\lambda e^{-\int_0^s k'_\lambda \rho_g dS} = I_\lambda e^{-\tau(\lambda)}$$

Being

$$\tau(\lambda) = \int_0^{\Delta S} k'_\lambda \rho_g dS = k'_\lambda \rho_g \Delta S$$

This optical thickness, supposing  $k'_\lambda$  and  $\rho_g$  constant.

Replacing in the definition of optical thickness the  $k'_\lambda$  value obtained with (3.6) we obtain:

$$\tau(\lambda) = \frac{3}{4} \frac{C_{ext}(\lambda)}{\pi a^3} \frac{\rho_g \Delta S}{\rho_M} = \frac{C_{ext}(\lambda) \rho_g \Delta S}{m_g} = n_g C_{ext}(\lambda) \Delta S$$

Knowing that  $n_g = \rho_g / m_g$

The transparency was defined as

$$T = \frac{I(\lambda)}{I_0(\lambda)} = e^{-\tau(\lambda)}$$

So  $\tau$  is

$$\tau(\lambda) = \ln[T(\lambda)]^{-1}$$

Consequently

$$C_{ext}(\lambda) = \frac{4}{3} \pi a^3 \frac{\rho_M S}{M} \ln \frac{1}{T(\lambda)}$$

Where M is the grain mass

$$M = \frac{4}{3} \pi a^3 \rho_M n_g S \Delta s$$

With:

$\frac{4}{3} \pi a^3$  volume of the grains

$\rho_M$  material density

$n_g$  number of grains

S beam section

$\Delta s$  sample thickness

The  $\rho_M$  value can be found using tabulated information while for M and S we are forced to make a hypothesis: it is assumed that all grains are distributed homogeneously throughout the volume  $S\Delta s$ . Once the thickness  $\Delta s$  is fixed, which is nothing more than the thickness of the sample, it's possible to replace it the  $C_{ext}$  formula instead of the  $S/M$  ratio the  $S'/M'$  ratio where  $S'$  is the section of the sample and  $M'$  is the total mass of the sample.

This replacement is possible because supposing the homogeneous composition of the sample, the proportion  $S : S' = M : M'$  is verified.

Recalling that the grains are approximated to spheres of radius  $a$ , the problem of estimating  $a$  remains, and actually this problem is passed by calculating the amount  $Q_{ext}/a$  or more precisely  $Q'_{ext}/a'$  because not all grains have the same radius.

It is possible to give a connection between  $Q_{ext}/a$  and the absorbance given by (3.6)

$$\frac{Q_{ext}(\lambda)}{a} = \xi \frac{A(\lambda)}{M}$$

$\xi$  is the constant made with all the constant values.

Although for technical reasons the thickness is constant and  $S'$  is the section of the sample, it is also settled that the only known parameter is  $M'$ .

### 3.3 Emission

As was mentioned in the introduction to this section, all surfaces above absolute zero temperature emit photons. The radiation is called thermal radiation. The radiation emitted by a body depends on the chemical and physical composition of the same sample, but there is a class body, purely theoretical, emitting thermal spectra of a universal character. These bodies are the so called black bodies and they have surfaces that absorb all incident radiation regardless of wavelength and re-emits it on a spectrum that depends only on temperature. The spectral distribution of these bodies is well known from the beginning of the century and follows the law:

$$I_{BB}(\lambda, T) = \frac{I}{\pi} B(\lambda, T)$$

Where  $B(\lambda, T)$  is the Planck function:

$$B(\lambda, T) = 2\pi h c^2 \lambda^{-5} e^{-\left(\frac{hc}{\lambda k T}\right)}$$

Where:

$h$  is the Planck constant

$k$  is the Boltzmann constant

$c$  is the light speed in the vacuum

The thermal power emitted by a surface is called emittance.

If we measure the emittance of a sample surface of infinite optical thickness it is generally recognized that the spectrum is similar to the Planck function, but is lower by an amount that varies with a wavelength change.

The relationship between the power emitted per unit area, from a surface temperature  $T$ ,  $U(\lambda, T)$ , and that one emitted by a blackbody at the same temperature, could define the spectral emissivity  $\varepsilon(\lambda)$  of a surface:

$$\varepsilon(\lambda) = \frac{U(\lambda, T)}{B(\lambda, T)}$$

If  $\varepsilon$  results independent from the wavelength the surface it is called a grey body.

In laboratory, it is possible to make measurements of a particular type of emissivity, the directional emissivity  $\varepsilon(\theta, \lambda)$ , which is the ratio of the thermal radiation emerging from the surface of the sample particles, at uniform temperature  $T$ , in the direction forming an angle  $\theta$  with the normal to the surface,  $I(\theta, \lambda, T)$ , and the thermal radiation emerging from a blackbody at the same temperature (the radiation of a black body is isotropic):

$$\varepsilon_d = \pi \frac{I(\theta, \lambda, T)}{B(\lambda, T)}$$

The measurements are issued by heating at a temperatures higher than room temperature, both the sample and the reference black body. The energy emitted is then recorded by the spectrophotometer and displayed as a function of wavelength (see schematic diagram in Figure 3.7.) (De Carlo, 1997).

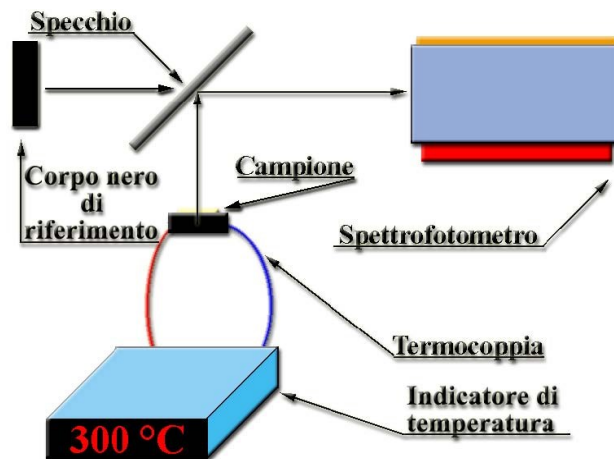


Figure 3. 7 Schematic diagram of an emission measurement

### 3.4 Correlation between emissivity and reflectance

Kirchhoff's law is an extremely powerful rule that states the existence of a functional relationship between the emissivity and reflectance. Under ideal conditions, where the surface is isothermal, and all the energy emitted can be measured, Kirchhoff's law is:

$$\varepsilon(\lambda) = 1 - R(\lambda)$$

Where:

$\varepsilon(\lambda)$  is the emissivity of the material;

$R(\lambda)$  is the hemispherical reflectance.

Kirchhoff's law was originally derived for opaque samples in thermal equilibrium with the environment. The thermal equilibrium reported here is a thermodynamic equilibrium, not simply a thermal constant condition. This implies that the sample is isothermal and at the same temperature of the background to which it radiates. Such a situation does not exist in most laboratory

measurements of emissivity and never exists in applications of remote sensing. This led to techniques to measure emissivity in the laboratory that use experimental configurations to ensure that the sample and its contour a temperature as uniform as possible.

However, a sample that radiates freely (for example, a sample that radiates independently from environmental radiation field) still follows Kirchhoff's law, if the energy states of the sample obey the Boltzmann distribution (Salisbury et al, 1994).

Where the sample surface radiates freely to a much colder background, there will be certainly a thermal gradient within the sample and this may limit the validity of the law. Laboratory measurements of hemispherical reflectance and directional emissivity performed on samples of solid rock and soil, these samples show that, even with a thermal gradient, follow the Kirchhoff's law within experimental error.

Only a selection of fine particulate material of an extremely low density was found a rather steep temperature gradient, in the thickness from which the infrared radiation is emitted from the sample, which could cause a divergence from the Kirchhoff's law, by 6% (Salisbury et al, 1994).

### 3.5 The Mie theory

The classical theory that interprets, with the electromagnetism described by Maxwell's equations, the processes of interaction of radiation with the particles is commonly known as Mie theory, it is valid for particles of spherical shape, homogeneous and optically isotropic (e.g. having optical properties, such as dielectric constant, refractive index, conductivity, not dependent on direction). Recall the coefficient  $C_{ext}$  (effective section of extinction) introduced in section 3.1.2..

It can also be expressed as:

$$C_{ext} = C_{abs} + C_{sca} = W_{ext} / F_0$$

where:

$C_{abs}$  is the effective section absorption of the grain, defined by the ratio of the power  $W_{abs}$  (energy per unit time) absorbed by the grain and flux  $F_0$  (energy per unit time and area) of the incident radiation;

$C_{sca}$  is the effective distribution section of the grain, defined by the ratio of power  $W_{sca}$  removed due to diffusion from the particle and the flux of incident radiation;

$W_{ext}$  is the power removed from the particle due to absorption and distribution of the incident beam,

$$(W_{ext} = W_{abs} + W_{sca}).$$

Of course all values are a function of wavelength  $\lambda$ .

From these quantities we can define the efficiency factors of diffusion and absorption, and  $Q_{sca}$   $Q_{abs}$  respectively, by formulas quite similar to (3.7).

Efficiency factors of a spherical particle of radius  $a$ , composed of material of refractive index (complex)  $m = n - ik$ , are given by the following developments in series:

$$Q_{sca} = \frac{2}{x^2} \sum_{n=1}^{\infty} (2n+1) \left[ |a_n|^2 + |b_n|^2 \right]$$

$$Q_{ext} = \frac{2}{x^2} \sum_{n=1}^{\infty} (2n+1) \text{Re}(a_n + b_n)$$

where  $n$  (not to be confused with the real part of complex refractive index) is the index on which the summation runs, the parameter  $x$  is given by:

$$x = \frac{2\pi a}{\lambda}$$

While  $a_n$  and  $b_n$  are defined as scattering coefficient and are given by:

$$a_n = \frac{m \psi_n(mx) \psi_n'(x) - \psi_n'(mx) \psi_n(x)}{m \psi_n(mx) \xi_n'(x) - \psi_n'(mx) \xi_n(x)}$$

$$b_n = \frac{\psi_n(mx) \psi_n'(x) - m \psi_n'(mx) \psi_n(x)}{\psi_n(mx) \xi_n'(x) - m \psi_n'(mx) \xi_n(x)}$$

In these formulas the functions of complex variable  $\psi_n(z)$  and  $\xi_n(z)$ , together with their conjugated  $\psi_n'(z)$  and  $\xi_n'(z)$  are the so-called Riccati-Bessel functions, they are defined through Bessel functions  $j_n(z)$  and  $h_n^{(1)}(z)$ , with the following relations:

$$\psi_n(z) = z j_n(z)$$

$$\xi_n(z) = z h_n^{(1)}(z)$$

Through this technique is then possible to calculate the optical constants of the material. Now it is possible to give approximations of the formulas (3.9) and (3.10) under the given assumption that:

$$2\pi a < \lambda \quad \text{Equation 3. 8}$$

The length of the incident wavelength is larger than the circumference of the particle.

We have:

$$Q_{sca} \cong \frac{8}{3} x^4 \left| \frac{m^2 - 1}{m^2 + 2} \right|^2 \quad \text{Equation 3. 9}$$

And

$$Q_{ext} \cong -4x \operatorname{Im} \left( \frac{m^2 - 1}{m^2 + 2} \right) + x^3 \operatorname{Im} \left[ -\frac{4}{15} \left( \frac{m^2 - 1}{m^2 + 2} \right) \frac{m^4 + 27m^2 + 38}{2m^2 + 3} \right] + x^4 \operatorname{Re} \left[ \frac{8}{3} \left( \frac{m^2 - 1}{m^2 + 2} \right)^2 \right] \quad \text{Equation 3. 10}$$

In the case of even smaller grains the (3.8) becomes:

$$2\pi a \ll \lambda$$

The (3.10) becomes:

$$Q_{ext} \cong -4x \operatorname{Im} \left( \frac{m^2 - 1}{m^2 + 2} \right)$$

As will be discussed in the next chapter, the spectrometer available can cover a range between 0.2 and 2.5  $\mu\text{m}$  while the diameter of the smallest grain is estimated to be around 1  $\mu\text{m}$ .

If we apply the hypothesis (3.8) in the latter sample we would find that the incident wavelength is less than 6.28  $\mu\text{m}$ .

It thus appears that the hypothesis (3.8) is not applicable in circumstances in which the measurement will be carried on.

## 4. INSTRUMENTATION & MEASUREMENTS

This chapter gives a detailed description of the spectrometer and accessories that will be used to make measurements.

### 4.1. Spectrophotometer



Figure 4. 1 Spectrophotometer Agilent Cary 5000

To make measurements the following will be used:

- UV/Vis/Nir spectrophotometer Agilent Cary 5000
- 150 mm integrating sphere
- VASRA (Variable Angle Specular Reflectance Accessory)

#### 4.1.1 Introduction

The spectrometer at our disposal is an Agilent, model Cary 5000.

Its spectral range covering the entire NIR, visible (using a PbS detector cooled Peltier cell) and the near-UV using a photomultiplier (from 185 to 3300 nm, purifying the instrument with N<sub>2</sub> the measurement can start at 175 nm).

Although the spectrometer needs particular climatic conditions (temperature between 15 and 35 ° C and humidity between 20 and 80%), the instrument is characterized by a wavelength accuracy of  $\pm$

0.1 nm in the UV / Vis and of  $\pm 0.4$  nm in the NIR, while the spectral resolution is  $< 0.05$  in the to 5.00 nm, 0.01 nm Step, and 0.20 to 20.00 nm, step 0.04 nm, respectively, in the UV / Vis and NIR.

Another important feature of the spectrometer is the signal to noise ratio, or noise level. For this instrument we have the standard deviation (RMS, root mean square) for a measure of absorbance of 0 with an integration time of 2 s 500 nm is 0.00005, while if the absorbance is 2, under the same conditions, it has an RMS of 0.002.

The structure of the spectrophotometer Cary 5000 is characterized by a double monochromator optical system. In each of monochromator are used reticles (grating) holographic both for the range UV/visible and the NIR.

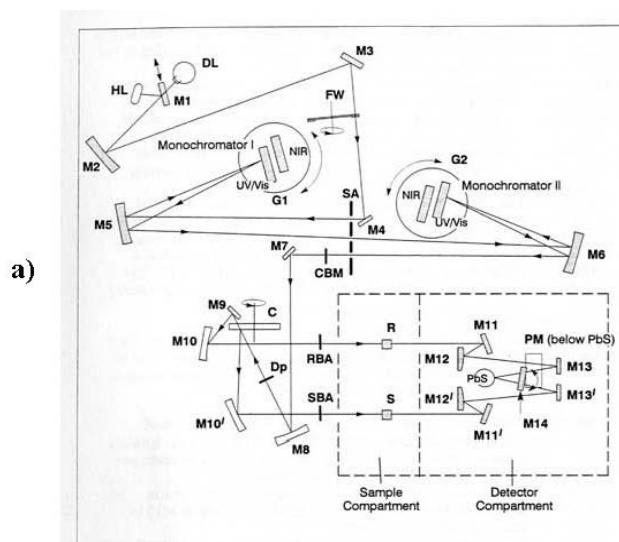


Figure 4. 2 Spectrophotometer optics: a) schematic diagram

The two sources of radiation, the deuterium lamp (DL) and the halogen lamp (HL), cover the entire working range of the spectrophotometer (see Figure 4.3).

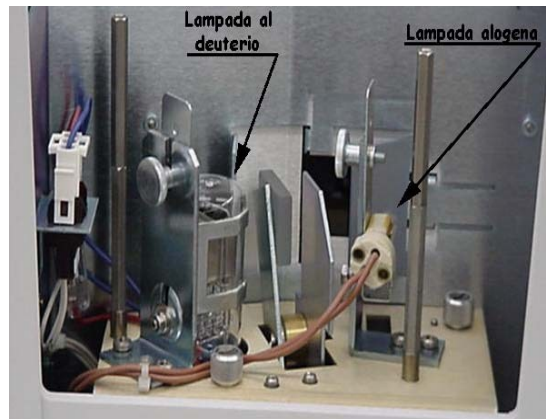


Figure 4. 3 Spectrophotometer light sources

For measurements in the NIR or visible, the mirror M1 reflects radiation from the halogen lamp on the mirror M2. At the same time M1 blocks the radiation from the deuterium lamp.

For measurements in the UV range, the mirror source M1 is lifted allowing the radiation from the deuterium lamp to strike the mirror M2. The change of source is automatic during the rotation of the monochromator.

The radiation from one of the lamps is reflected by the mirror M2 to M4 mirror after being reflected by the mirror M3 and after passing through an optical filter mounted on a filter wheel (FW). The filter wheel is driven by a stepper motor that is synchronized with monochromators.

Depending on the wavelength that will be produced, the appropriate filter is to be on the path of the radiation beam to prefilter before it enters the first monochromator and, fundamentally, allows to cut the higher orders.

The filter will automatically change during the rotation of the monochromator.

From the M4 mirror the radiation is reflected through the slit of the monochromator I.

All slits are located on a door crack (SA). The radiation is then collimated on the M5 mirror and reflected on the grating G1. Depending on the range of wavelengths currently in use, the radiation strikes the grating for the UV / Visible or the grating for the NIR.

The incident radiation on the grating produces a spectrum. The rotation of the grating selects a segment of the spectrum reflecting it on the mirror M5 and from this it goes on the output slit. The output slit has the task of restricting even further the segment of the spectrum, making the beam

more monochromatic as possible. The grating will automatically change during the rotation of the monochromator.

The exit slit of the monochromator I is also the entrance of the monochromator II. The radiation is reflected by the mirror M6 on the grating G2, and later, through the mirror M6 and the exit slit of the monochromator II arrives to the mirror M7. The rotation of G2 is synchronized with G1. The radiation emerging from the exit slit is characterized by high spectral purity and low noise.

In the range UV/Visible and NIR it's possible to choose between a fixed-width slit, a scheduled slit and a changeable slit. When the assisted slit is selected, the slit width changes automatically during the acquisition in order to maintain constant the energy to the detector.

From the M7 mirror the beam is reflected through a mirror M8 to a beam splitter (C, chopper).

The chopper consists of a mirror segment, a window segment and two dark segments, turning the radiation affect different segments.

When radiation encounters the window segment it passes through until it arrives at the M9 mirror and then, after meeting the mirror M10, create the reference beam (R, reference beam).

But when the beam meets the mirror segment it is reflected and creates the main beam (S, sample beam) through the mirror M10 '(see Figure 4.4).



Figure 4. 4 Spectrophotometer sample holder, one for the reference beam and the other for the sample beam

When the dark segment is on the path of the beam, no signal reaches the detector, allowing the detector to create a dark signal, e.g. a zero signal. The radiation, passing alternately through the sample and reference reaches, via the mirrors M11, M12 and M13 or M11, 'M12' and M13' alternatively, the appropriate detector, mounted on a door detector.

The M14 mirror can rotate allowing to select the detector required. A photomultiplier (PM) is used in the range of UV/Visible while a lead sulphide (PbS) detector is used in the NIR.

The detector will automatically change during the rotation of the monochromator. At the level of cells, each radiation beam is approximately 12 mm height. The beam width depends on the slit width. To a slit width of 5 nm corresponds a width of two beams of approximately 4.5 mm (other values of the beam as a function of the slit is shown in Table 4.1.).

<b>Slit</b>	<b>Beam width</b>	<b>Beam Height</b>
<b>0,05 nm</b>	0,04 mm	11,70 mm
<b>0,10 nm</b>	0,09 mm	11,70 mm
<b>0,50 nm</b>	0,45 mm	11,70 mm
<b>1,00 nm</b>	0,89 mm	11,70 mm
<b>2,00 nm</b>	1,00 mm	11,70 mm
<b>5,00 nm</b>	4,44 mm	11,70 mm

**Table 4. 1 Beam hitting section**

To allow the measurement of very small volume samples in microcells, the beam width must be reduced. A common beam mask (CBM), e.g. a mask that reduces the beam shape, is mounted between the door cracks (SA) and the mirror M7. The mask reduces the section of both the main beam and the reference beam in their cells. The beam can be increased from a maximum height of 11.7 mm at a minimum of 0.01 mm through 50 steps.

Obviously it can be chosen the wavelength at which the sources and detectors change in a well-defined range of wavelengths.

There is also a depolarizing filter (DP) option that can be placed on the beam path.

There are attenuators that can operate separately on the main beam (SBA) and on the reference beam (RBA). The values that the attenuators can assume are 0%, 1%, 10% and 100%.

#### 4.1.1.1. Diffraction grating

The diffraction grating is a collection of reflective (or transmissive) items separated by a distance comparable with the wavelength of light under consideration. A reflection grating is simply a grating overlaid with a reflective surface. An electromagnetic incident wave on the grating undergoes an expected change of amplitude of its electric field, or phase, or both.

The diffraction grating can be seen from the geometry in Figure 4.5., which shows a ray of light of wavelength  $\lambda$  incident at an angle  $\alpha$ , diffracted with an angle  $\beta_m$  on a grating pitch (groove spacing)  $d$ .

These angles are measured starting from the normal direction of the grating.

Usually we use the convention to indicate how positive angles of the diffracted light from the same side of the incident light while negative ones the opposite side. In figure the angles  $\beta_1$  and  $\alpha$  are positive and are measured clockwise from the normal to the grating, while  $\beta_0$  and  $\beta_{-1}$  are negative and are measured clockwise from the normal.

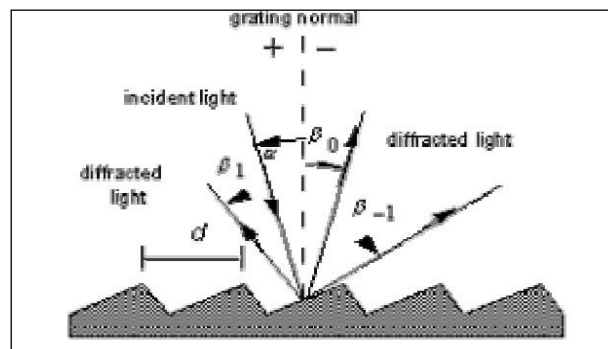


Figure 4. 5 Diffraction grating geometry

Now considering only the diffracted rays to the right. The path difference between rays from two adjacent channels is equal to  $d \sin \alpha + d \sin \beta$  ( $\beta$  being negative, the second term is negative). The interference principle states that only when this difference is equal to the wavelength  $\lambda$  of incident light, or a whole multiple thereof, the beams from two adjacent slits are in phase.

Consequently ray emerging angle  $\beta$  different from that complying with this condition suffers the effect of destructive interference. These relationships are expressed by the equation of gratings:

$$m\lambda = d(\sin \alpha + \sin \beta)$$

Which governs the angles of diffraction grating with a groove spacing  $d$ . In this case  $m$  represents the order of diffraction or spectral order, which is an integer.

Sometimes it is convenient to express the equation of the grid as:

$$Gm\lambda = \sin \alpha + \sin \beta$$

Where  $G=1/d$  is the grooves frequency, or density of grooves, more commonly known as "grooves per millimetre". Where the incident beam is not monochromatic what happens is that individual fringes normally diffracted from the grating can be solved as a sequence of monochromatic fringes. Using small angles it's possible to obtain a good resolution of these fringes. In this case, however, we also get the overlap, on some very specific wavelengths; between the rays emerging at different spectral orders (see Figure 4.6).

In that case we use optical filter to process the light before it arrives on the grating.

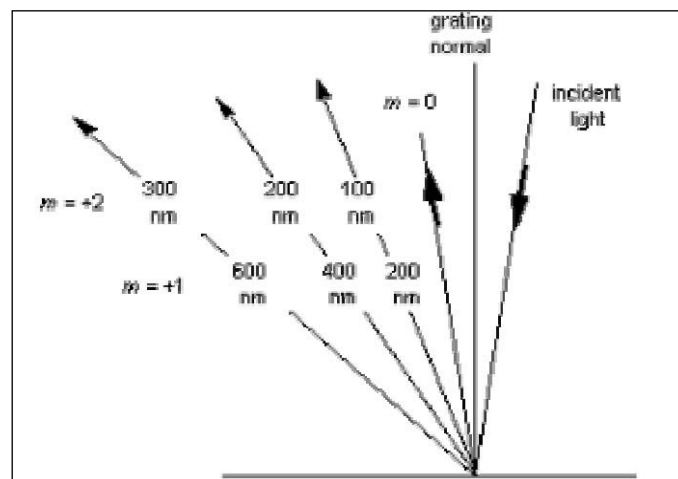


Figure 4. 6 Overlap of the spectral orders

Usually these fringes are projected onto a slit that selects a narrow range of wavelengths, in the case of a dual monochromator, as in our situation, the fringes end up on a second diffraction grating to undergo on a similar process and select as a "single" wavelength, where for single wavelength we means a range of wavelengths very limited. For our instrument this interval, as seen above, has a resolution of about 0.05 nm for UV / Vis and 0.20 nm for the NIR. (See Figure 4.7.) (Palmer, 2000).

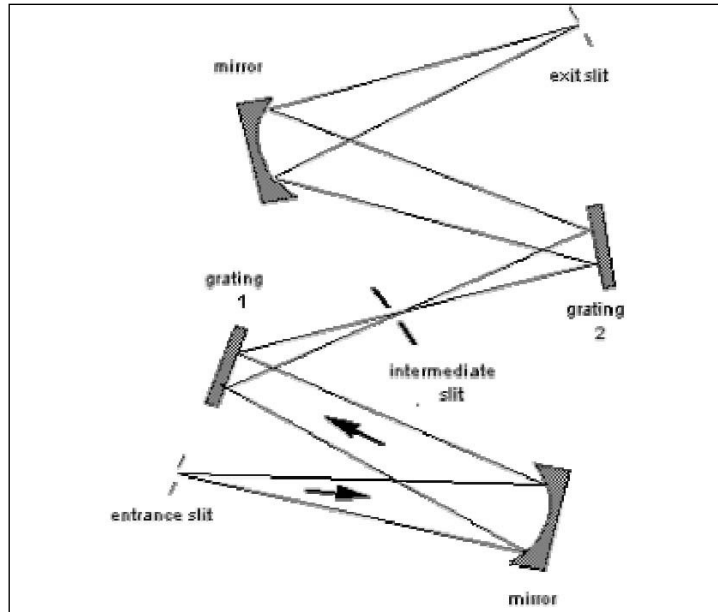


Figure 4. 7 Grating mounting on a dual monochromator

In many applications, such as monochromators, the analysis of various wavelengths  $\lambda$  is adjusted by turning the grating around an axis coincident with its central axis, leaving unchanged the direction of the incident ray and the emerging. The deviation angle  $2K$  between the incident direction and the emerging (also known as angular deviation) is:

$$2k = \alpha - \beta = \text{const.}$$

while the angle  $\varphi$  or acquisition angle, which is measured from the grating normal to the bisector ray is:

$$2\varphi = \alpha + \beta$$

Note that  $\varphi$  changes with  $\lambda$ . In this case the equation of the grating can be expressed in terms of  $\varphi$  and angular semi deviation  $K$  as:

$$m\lambda = d2 \sin K \sin \varphi$$

#### 4.1.2. Integrating sphere (Introduction)



Figure 4. 8 The external DRA

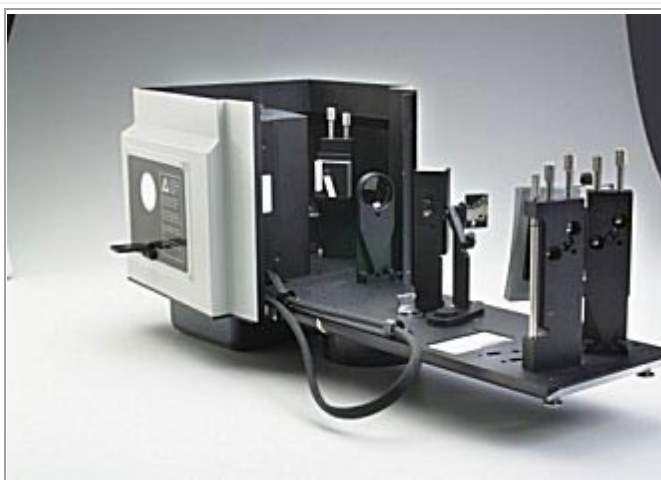


Figure 4. 9 The external DRA viewed from the back

Reflectance sampling accessories rely upon a light beam coming from the spectrometer to be focused upon the sample. In order to achieve the best signal-to-noise ratio (SNR), the smaller the focus is, the easier it is to refocus the illuminated sample spot back onto the detector. In order to measure light reflected at a larger angle, optical designs will allow only a small area of the sample to be projected onto the detector. This arrangement serves well if the sample is microscopically homogeneous, but will result in a larger sample position error. When the sample is moved, the focused beam will see a different portion of the sample resulting in measurement-to-measurement differences. This is called insertion error because the spectrum will be slightly different each time the sample is inserted.

Some industrial or natural samples are inhomogeneous either because they are mixtures of different substances or because they have a particle size comparable to the probing beam diameter. Clearly, if the probing beam could be larger and the reflected light could all be collected, a more representative spectrum could be measured.

Some other samples develop a directional scattering. For example, fibers wound on a mandrel are highly oriented, not just macroscopically as parallel, unidirectional filaments, but also in many cases the molecules of the drawn fibers are oriented within the fiber itself. Such a sample, when placed in a reflectance accessory will generate different results depending on the angle from which the detector is “viewing” the sample. When the overall reflectance needs to be measured reproducibly,

for example to measure the concentration of a minor ingredient in the sample, only isotropic optical systems, insensitive to such directionalities could be utilized.

Furthermore, in some cases, not just the reflectance in a small solid angle but the reflectance in all angles is sought. Most reflectance accessories measure at fixed or variable angles, narrower or wider collection angles, but there is a need for a device that uniformly collects all reflected light from a sample. In other words it measures the total reflectance of the sample.

Therefore the main reasons for using integrating spheres for the measurement of sample reflectance are the following:

- Efficient measurement of combined diffuse and specular reflectance
- Uniform detection of reflectance even when sample is inhomogeneous
- Isotropic detection of reflectance even on samples that reflect in preferred directions
- Reduction of polarization effects from the illuminating beam and the sample
- Measurement of absolute reflectance (with special integrating spheres)

All of the above concerns are addressed with integrating sphere based reflectometers.

**Integrating Sphere Optics** Integrating spheres are highly reflective enclosures that are placed in close proximity to the sample, such that the reflected light enters the sphere, bounces around the highly reflective diffuse surface of the sphere wall and finally impinges upon the detector – usually part of the integrating sphere assembly. The name, integrating sphere, refers to one of the main functions of the device, namely that it spatially integrates the light flux, in our application the light reflected from a sample. In spite of the long history of engineering and development of the sphere, the applications and further developments continue to this day. Advances in the theory, detector and electronics development and most of all, new applications, drive the progress.

As the name implies, the main part of the device is a sphere with a very highly reflecting inner surface. The surface should approach the ideal Lambertian scatterer, which means that the light falling on the surface is evenly scattered in all directions and the scattered light intensity is proportional to the cosine of the angle of observation.

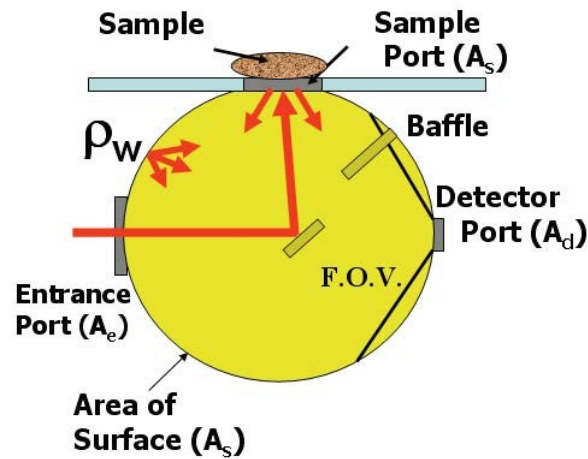


Figure 4. 10 Optical geometry of an integrating sphere

The infrared beam from the interferometer is directed through an entrance port onto the sample placed behind the sample port (shown above). Samples can be directly touching the sphere or separated from the sphere by a thin, infrared transparent window. The detector is placed close to the sphere, so that it can view the integrating sphere with a large solid angle. In order to improve the isotropy (non-directionality) of the detection, the detector is not directly in the line of sight of the sample. A small, also highly reflective and scattering baffle is placed in the sphere such that it blocks the first reflection of the sample from reaching the detector.

A well-designed sphere has the sample close to the sphere geometry so that the sphere will collect close to the full available hemispherical reflectance ( $2\pi$ steradians). A window to separate the sphere and sample may be important in some cases, but it will place the sample a small distance from the sphere, thereby somewhat reducing the collected high-angle reflectance. The integrating spheres are coated with the highest possible reflective surface for the desired wavelength region. The coating of the surface of the sphere has to be uniform and close to being a perfect Lambertian scatterer. These characteristics allow the light falling in the sphere to be uniformly distributed over the entire surface of the sphere. It is also important how much of this light is actually collected on the detector surface.

### 4.1.3 Integrating Sphere (Measuring Sample Reflectance)

First, a baseline is recorded with the PTFE reference disk covering the reflectance port (Fig.4.11).



Figure 4. 11 PTFE reference disk

The sample is then mounted over the port and the reflection off the sample surface is collected by the sphere. The reflectance is therefore measured relative to the PTFE disk.

This is the 'substitution' method.

The total (diffuse and specular) or the diffuse-only reflectance may be measured by using either the specular plug (specular included) or the light trap (specular excluded).

### 4.1.3.1 Transmittance measurements

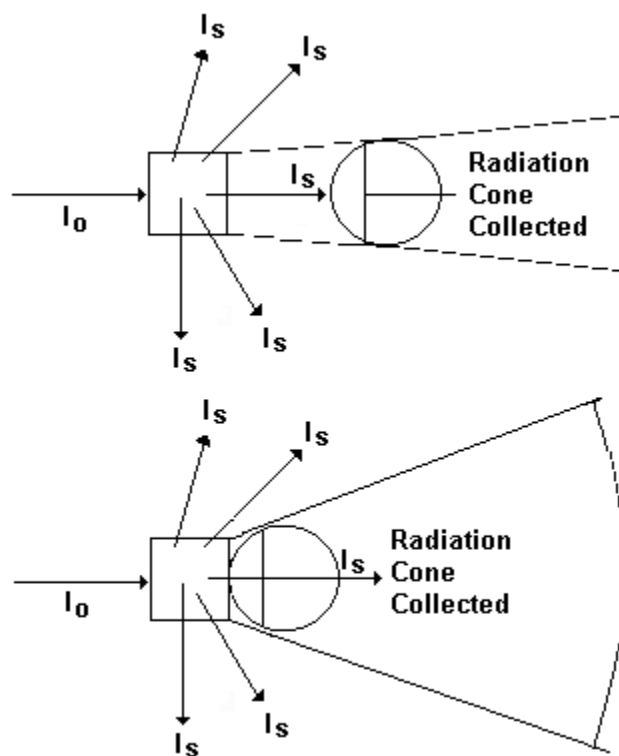


Figure 4. 12 Collection of scattered light by an integrating sphere.  $I_o$  = incident light,  $I_s$  = scattered light

In order to perform useful measurements on scattering samples, it is necessary to collect a high proportion of the scattered radiation. The integrating sphere is a highly efficient collector of scattered radiation. Because of its design, the Diffuse Reflectance accessory overcomes many of the problems associated with measuring turbid or scattering samples, which include sloping baseline, poor signal-to-noise ratio and high background absorbance.

### 4.1.3.2 Factors affecting accuracy or precision

Below are the major factors that may affect the accuracy of measurements when using the DRA.

#### Aperture area/total surface area ratio

Some of the reflected light escapes through the ports. This has the effect of reducing the signal to noise ratio, and thus the precision of the measurement.

The Commission Internationale de l' Eclairage (CIE) recommendation is a ratio of <10%.

This figure is < 10% for the Cary External DRA.

### Coating non-uniformity, ageing, or contamination

This accessory has been coated with PTFE via a unique process that ensures both a uniform coating on the inside of the sphere and the correct powder density. PTFE is durable, and does not yellow. The reflectivity of the PTFE is above 96% between 200– 2500 nm, and greater than 99% between 350–1800 nm. The sphere will maintain its reflectivity indefinitely if not subjected to smoke or other contaminants. Contact with plastic materials may also contaminate the coating.

### Incorrect sample placement

Theory assumes that the sample placement will coincide with the inside of the sphere wall. The sample is normally placed at a port on the outside of the sphere wall. Spacing between the sample and the sphere wall can lead to large errors due to loss of reflected light.

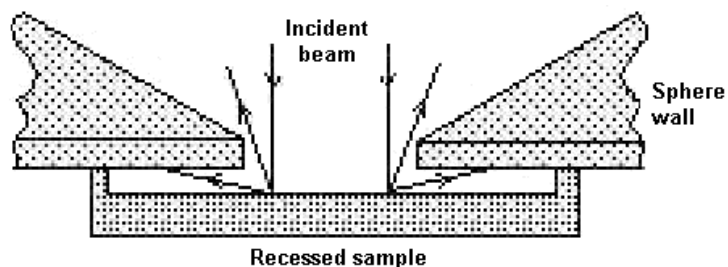


Figure 4. 13 Some of the wide-angle scatter is lost when there is a space between the sample and the sphere wall

### Sample recess

Theory assumes that the sample is placed coincident with the inside of the sphere wall, however the sample is placed against the outside of the sphere wall. The porthole edges have a finite thickness, and some part of the beam reflected at wide angles may be intercepted by the sphere wall.

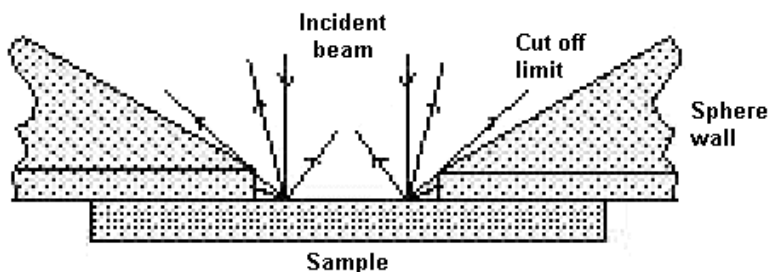


Figure 4. 14 Some of the wide-angle reflection is intercepted by the sphere wall

The edges of the reflectance port are feathered to reduce this error.

### Reference beam attenuation

Reference beam attenuation is most useful when the accessory or sample in the sample beam attenuates the light beam considerably. In such situations, attenuation of the reference beam will increase noise and considerably increase the dynamic range of the instrument, as the detector is not then 'seeing' two dramatically different signals. Clips are provided at the reference beam window for this purpose.

### Stray light

If the irradiating beam overfills the reflectance port, a proportion of sphere wall reflectance is mixed with that of the sample. This gives a high reading if this is not consistent between the baseline and the sample measurement.

### Gloss trap error

Gloss trap error is produced when the gloss trap is unable to completely absorb the specular component. In the measurement of diffuse-only reflectance, a 'gloss trap' is often used to absorb the specular component. Gloss traps are typically glossy black pyramidal light traps, matt black-coated cavities, or razor blade Fresnel light traps. However, the reflectance of many samples has broadened the specular peaks which cannot be excluded by standard sized light traps.

### Differences between the standard and sample

It is important that the reference material be of a similar reflectivity and have similar properties to the sample. Otherwise large errors can be introduced, if for example a poorly reflecting material is measured relative to a highly reflective PTFE reference plate. The table below lists the appropriate reference materials that are recommended for use.

Surface type	Reflectivity	Reference
Matt	High	PTFE reference plate
Matt	Low	Labsphere diffuse reflectance standards
Glossy	High	PTFE reference plate
Glossy	Low	NIST SRM 2021

Table 4. 2 Reference Material Table

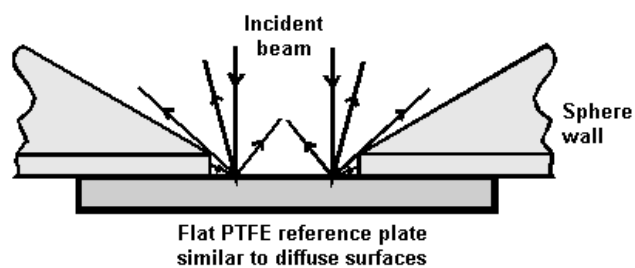


Figure 4. 15 Highly diffuse samples are measured against a flat PTFE reference plate

#### Inaccuracy in the standard

If the standard material used to calculate a value is not accurate, this will hamper the determination of the reflectance of the sample. Great care must be taken to keep reference materials clean and unscratched.

#### 4.1.4 Description of the accessory

##### Accessory design

The DRA accessories are designed specifically to measure the reflectance or transmission of solids, liquids, powders, or other small objects that can fit at the transmission or sample reflectance ports. Except for the sphere detectors, the construction of each version of the DRA is identical. Basic components of the accessory include the base plate, integrating sphere, optics chamber and detector chamber. The basic components are illustrated in the figure below.

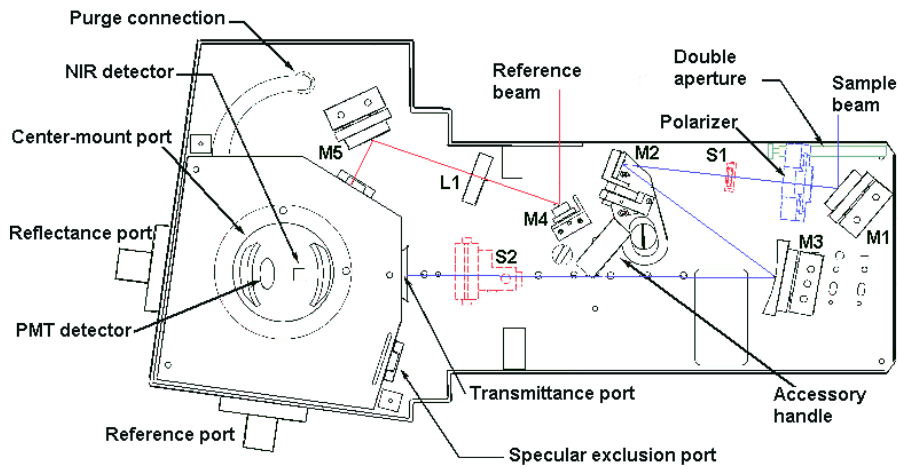


Figure 4.16 A schematic view of the external DRA

The optics chamber contains the transfer optics that direct the spectrophotometer beams to their final destinations. The integrating sphere collects and measures the radiation transmitted or reflected from the sample surface. A removable cover fits over the DRA to provide a light-tight operating environment. The sample reflectance and reference ports each are fitted with a separate magnetic port cover. The purposes of the covers are to reduce the potential for stray light when the accessory is in use and to keep the integrating sphere and standards clean when not in use.

Beam paths within the accessory are illustrated in the next figure. Light entering the accessory is directed to one of two entrance ports on the sphere: the reference beam and sample beam entrance ports. The sample beam entrance port is usually called the transmission port.

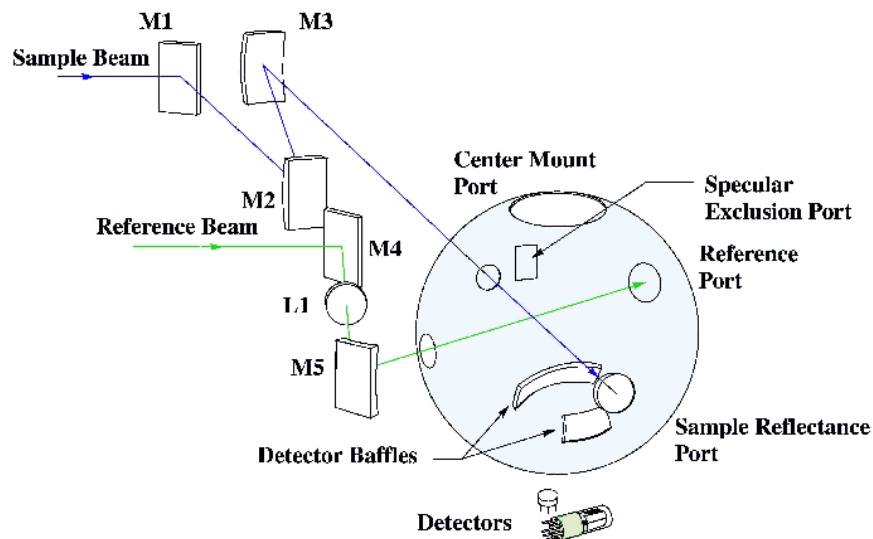
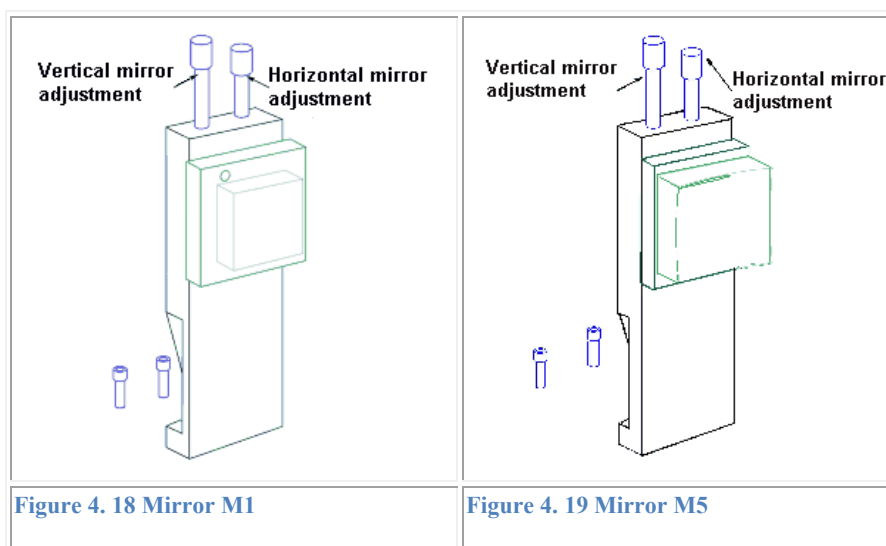


Figure 4.17 The optical design of the external DRA

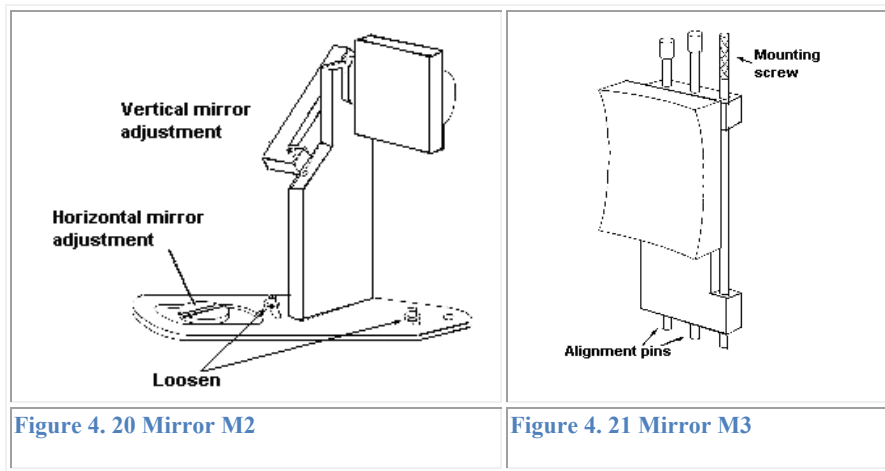
### 4.1.5 Optics

The optics chamber houses the transfer optics of the DRA accessory that directs the spectrophotometer reference and sample beams to their respective ports on the integrating sphere. The sample beam is the rear beam in the accessory. Mirrors labeled M1, M2 and M3 guide the sample beam through the sample transmission port of the integrating sphere and onto the sample reflectance port at an 8° angle of incidence. Mirrors M4 and M5 direct the reference beam through the reference beam entrance port onto the reference port.



Mirrors M1 and M5 are fixed mounted mirrors that are adjustable in the vertical and horizontal planes. Mirror M1, illustrated in the figure above, holds a flat mirror that helps direct the instrument sample beam into the integrating sphere transmission port. M5 holds a concave mirror surface that reflects the reference beam into the integrating sphere. The design of mirror M5, shown in the figure below, is very similar to mirror M1. The fixed mirrors are mounted to the base plate by two M5 bolts that can be adjusted using a 4 mm hex wrench. All mirror surfaces are coated with an Al/MgF<sub>2</sub> thin film.

Mirror M2 is a pivoting mirror assembly that positions a flat mirror surface into the sample beam path, directing the beam onto the movable mirror, M3. The mirror mounts pivots about a fixed point. To rotate the mirror assembly horizontally, loosen the two screws shown in the figure and rotate the floor adjustment with a large flathead screw driver. To adjust the mirror surface vertically, use a 3 mm allen wrench



Mirror M3 is a spherical mirror that condenses the sample beam onto the target sample.

The mirror can be mounted at any of three different positions on the base plate of the DRA. These positions correspond to the transmission port, center mount sample holder and sample reflectance port, and are labeled "T", "C" and "R" respectively. M3 features a knurled mounting screw for convenient installation and removal as well as the standard vertical and horizontal adjustments. The mirror is illustrated below.

Mirror M4 directs the raw reference beam through the collimating optic and onto mirror M5. The mirror mount is constructed in a manner to prevent stray light scattered from mirror M1 from reaching the integrating sphere. The mirror has a single adjustment in the vertical plane. If beam adjustment is required in the horizontal plane, loosen the cap screws at the base of the mirror mount and rotate the device slightly in either direction.

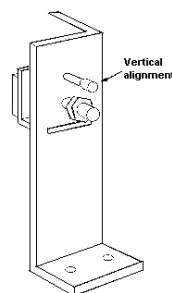


**Figure 4. 22 Mirror M4**

#### 4.16 Specifications

		<b>DRA 900</b>	<b>DRA 1800</b>	<b>DRA 2500</b>
Wavelength range	<b>Cary 4000</b>	200 nm to	200 nm to	200 nm to
	<b>Cary 5000</b>	200 nm to	200 nm to	200 nm to
	<b>Cary 6000i</b>	200 nm to	200 nm to	200 nm to
Detectors	<b>UV/VIS</b>	R928 PMT	R928 PMT	R928 PMT
	<b>NIR</b>		TE* cooled	TE* cooled
Sphere diameter		150 mm		
Internal coating		Polytetrafluoroethylene		
Coating density		1 g/cm <sup>3</sup>		
Coating thickness		4 mm		
Port area/total surface area ratio		<10% (CIE recommendation: <10%)		
Minimum sample size <sup>#</sup>		~ 20 mm (3/4")		
Maximum sample size		Unlimited		
Power input		Sample compartment DRA connector 15-pin D-range connector with two high voltage pins: -1000 volts DC.		
Purge gas connections		Clean flexible tubing of 6 mm (1/4") inside diameter (Tygon PVC or equivalent).		

Table 4. 3 Specification

\* Thermoelectrically cooled.

<sup>#</sup> The optional small spot kit, with the aperture kit, permits the measurement of samples down to approximately 5mm.

### 4.1.6 Integrating Sphere Theory

The integrating sphere is a simple, yet often misunderstood device for measuring optical radiation.

The function of an integrating sphere is to spatially integrate radiant flux.

How light passes through the sphere begins with a discussion of diffuse reflecting surfaces.

Then the radiance of the inner surface of an integrating sphere is derived and two related sphere parameters are discussed, the sphere multiplier and the average reflectance.

Finally, the time constant of an integrating sphere as it relates to applications involving fast pulsed or short lived radiant energy is discussed.

#### Radiation Exchange Within a Spherical Enclosure

The theory of the integrating sphere originates in the principles of radiation exchange within an enclosure of diffuse surfaces.

Although the general theory can be complex, the sphere is a simple solution to understand.

Consider the radiation exchange between two differential elements of diffuse surfaces.

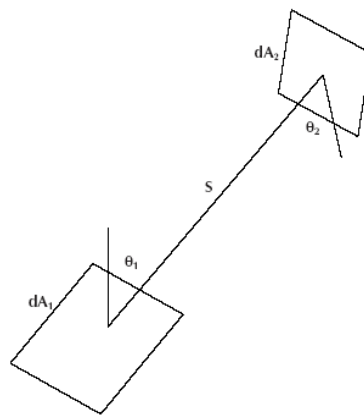


Figure 4. 23 Radiation exchange between two surfaces

The fraction of energy leaving  $dA_1$  that arrives at  $dA_2$  is known as the exchange factor  $dF_{d1-d2}$ .

Given by:

$$dF_{d1-d2} = \frac{\cos \theta_1 \cos \theta_2}{\pi s^2} dA_2 \quad \text{Equation 4. 1}$$

Where  $\theta_1$  and  $\theta_2$  are measured from the surface normal.

Consider two differential elements,  $dA_1$  and  $dA_2$  inside a diffuse surface sphere.

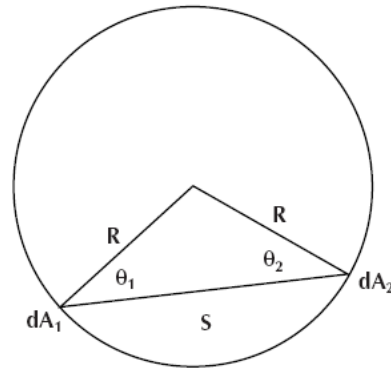


Figure 4. 24 Angles relation between the two mentioned surfaces

Since the distance  $S = 2R\cos \theta_1 = 2R\cos \theta_2$ :

$$dF_{d1-d2} = \frac{dA_2}{4\pi R^2} \quad \text{Equation 4. 2}$$

The result is significant since it is independent of viewing angle and the distance between the areas. Therefore, the fraction of flux received by  $dA_2$  is the same for any radiating point on the sphere surface.

If the infinitesimal area  $dA_1$  instead exchanges radiation with a finite area  $A_2$ , then Eq. 4.2 becomes:

$$dF_{d1-d2} = \frac{1}{4\pi R^2} \int_{A_2} dA_2 = \frac{A_2}{4\pi R^2} \quad \text{Equation 4. 3}$$

Since this result is also independent of  $dA_1$  :

$$F_{1-2} = \frac{A_2}{4\pi R^2} = \frac{A_2}{A_s} \quad \text{Equation 4. 4}$$

Where  $A_s$  is the surface area of the entire sphere. Therefore, the fraction of radiant flux received by  $A_2$  is the fractional surface area it consumes within the sphere.

### The Integrating Sphere Radiance Equation

Light incident on a diffuse surface creates a virtual light source by reflection. The light emanating from the surface is best described by its radiance, the flux density per unit solid angle.

Radiance is an important engineering quantity since it is used to predict the amount of flux that can be collected by an optical system that views the illuminated surface.

Deriving the radiance of an internally illuminated integrating sphere begins with an expression of the radiance,  $L$ , of a diffuse surface for an input flux,  $\Phi_i$ .

$$L = \frac{\Phi_i \rho}{\pi A} = [W/m^2/sr] \quad \text{Equation 4.5}$$

Where  $r$  is the reflectance,  $A$  the illuminated area and  $\rho$  the total projected solid angle from the surface. For an integrating sphere, the radiance equation must consider both multiple surface reflections and losses through the port openings needed to admit the input flux,  $\Phi_i$ , as well as view the resulting radiance. Consider a sphere with input port area  $A_i$  and exit port area  $A_e$ .

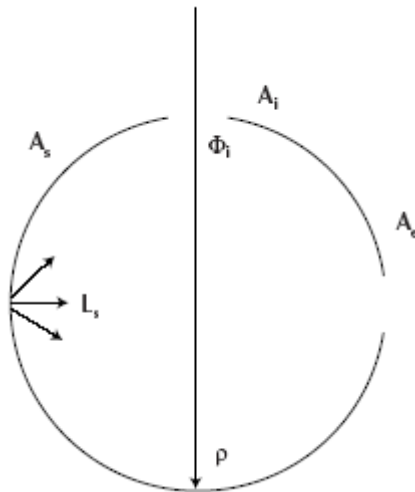


Figure 4.25 Schematics of the inside of the sphere

The input flux is perfectly diffused by the initial reflection.

The amount of flux incident on the entire sphere surface is:

$$= \Phi_i \rho \left( \frac{A_s - A_i - A_e}{A_e} \right) \quad \text{Equation 4.6}$$

Where the quantity in parenthesis denotes the fraction of flux received by the sphere surface that is not consumed by the port openings.

It is more convenient to write this term as  $(1-f)$  where  $f$  is the port fraction and  $f = (A_i + A_e)/A_s$ .

When more than two ports exist,  $f$  is calculated from the sum of all port areas.

By similar reasoning, the amount of flux incident on the sphere surface after the second reflection is:

$$= \Phi_i \rho^2 (1-f)^2 \quad \text{Equation 4. 7}$$

The third reflection produces an amount of flux equal to

$$= \Phi_i \rho^3 (1-f)^3 \quad \text{Equation 4. 8}$$

It follows that after  $n$  reflections, the total flux incident over the entire integrating sphere surface is:

$$\Phi_i \rho (1-f) \{1 + \rho(1-f) + \dots + \rho^{n-1} (1-f)^{n-1}\} \quad \text{Equation 4. 9}$$

Expanding to an infinite power series, and given that  $\rho(1-f) < 1$ , this reduces to a simpler form:

$$= \frac{\Phi_i \rho (1-f)}{1 - \rho(1-f)} \quad \text{Equation 4. 10}$$

The 4.10 equation indicates that the total flux incident on the sphere surface is higher than the input flux due to multiple reflections inside the cavity.

It follows that the sphere surface radiance is given by:

$$L_s = \frac{\Phi_i}{\pi A_s (1-f)} \frac{\rho(1-f)}{1 - \rho(1-f)} \quad \text{Equation 4. 11}$$

$$= \frac{\Phi_i}{\pi A_s} \frac{\rho}{1 - \rho(1-f)} \quad \text{Equation 4. 12}$$

This equation is used to predict integrating sphere radiance for a given input flux as a function of sphere diameter, reflectance, and port fraction. Note that the radiance decreases as sphere diameter increases.

### The Sphere Multiplier

The 4.12 equation is purposely divided into two parts. The first part is approximately equal to the 4.5 equation, the radiance of a diffuse surface. The second part of the equation is a unitless quantity which can be referred to as the sphere multiplier.

$$M = \frac{\rho}{1 - \rho(1 - f)} \quad \text{Equation 4. 13}$$

It accounts for the increase in radiance due to multiple reflections.

The following chart illustrates the magnitude of the sphere multiplier, M, and its strong dependence on both the port fraction, f, and the sphere surface reflectance r.

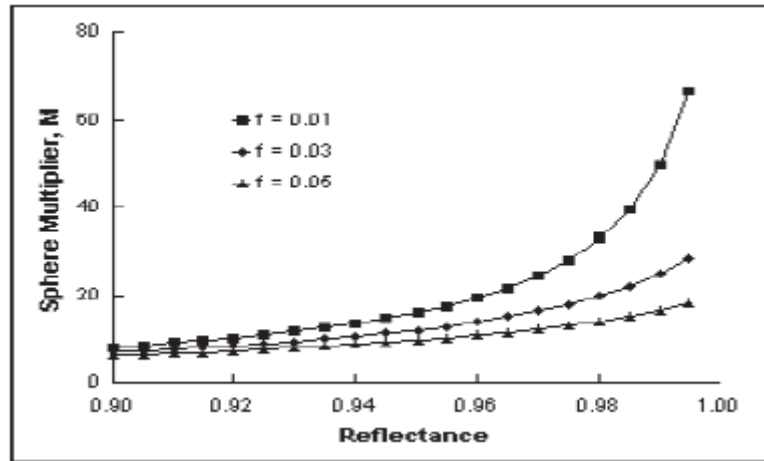


Figure 4. 26 Diagram of the magnitude of the sphere multiplier

A simplified intuitive approach to predicting flux density inside the integrating sphere might be to simply divide the input flux by the total surface area of the sphere.

However, the effect of the sphere multiplier is that the radiance of an integrating sphere is at least an order of magnitude greater than this simple intuitive approach. A handy rule of thumb is that for most real integrating spheres ( $0.94 < r < 0.99$ ;  $0.02 < f < 0.05$ ), the sphere multiplier is in the range of 10 to 30.

### The Average Reflectance

The sphere multiplier in Eq. 4.13 is specific to the case where the incident flux impinges on the sphere wall, the wall reflectance is uniform and the reflectance of all port areas is zero.

The general expression is:

$$M = \frac{\rho_s}{1 - \rho_w \left( 1 - \sum_{i=0}^n f_i \right) - \sum_{i=0}^n \rho_i f_i} \quad \text{Equation 4. 14}$$

where;  $\rho_0$  = the initial reflectance for incident flux

$\rho_w$  = the reflectance of the sphere wall

$\rho_i$  = the reflectance of port opening  $i$

$f_i$  = the fractional port area of port opening  $i$

The quantity  $\rho_w \left( 1 - \sum_{i=0}^n f_i \right) + \sum_{i=0}^n \rho_i f_i$  can also be described as the average reflectance  $\bar{\rho}$  for the entire integrating sphere.

Therefore, the sphere multiplier can be rewritten in terms of both the initial and average reflectance:

$$M = \frac{\rho_0}{1 - \bar{\rho}} \quad \text{Equation 4. 15}$$

### Spatial Integration

An exact analysis of the distribution of radiance inside an actual integrating sphere depends on the distribution of incident flux, the geometrical details of the actual sphere design, and the reflectance distribution function for the sphere coating as well as all surfaces of every device mounted at a port opening or inside the integrating sphere.

Design guidelines for optimum spatial performance are based on maximizing both the coating reflectance and the sphere diameter with respect to the required port openings and system devices.

The effect of the reflectance and port fraction on the spatial integration can be illustrated by considering the number of reflections required to achieve the total flux incident on the sphere surface given by Eq. 4.10. The total flux on the sphere wall after only  $n$  reflections can be written as:

$$= \theta_i \sum_{n=1}^n \rho^n (1 - f)^n \quad \text{Equation 4. 16}$$

The radiance produced after  $n$  reflections can be compared to the steady state condition.

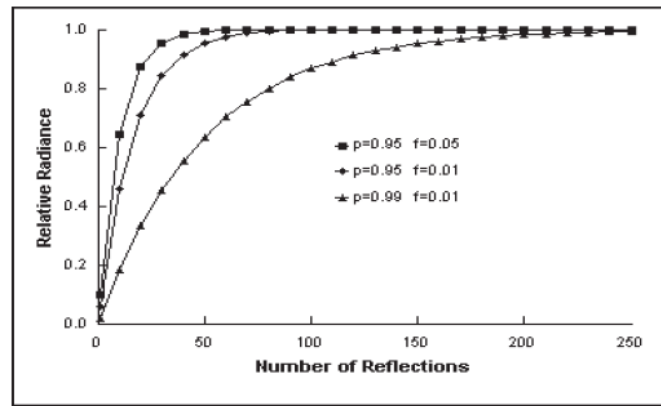


Figure 4. 27 Diagram of the magnitude of radiance vs numbers of reflection

Since the integrating sphere is most often used in the steady state condition, a greater number of reflections produce steady state radiance as  $\rho$  increases and  $f$  decreases.

Therefore, integrating sphere designs should attempt to optimize both parameters for the best spatial integration of radiant flux.

#### Temporal Response of an Integrating Sphere

Most integrating spheres are used as steady state devices.

The previous analysis of their performance and application assumes that the light levels within the sphere have been constant for enough time so that all transient response has disappeared.

If rapidly varying light signals, such as short pulses or those modulated at high (radio) frequencies, are introduced into an integrating sphere, the output signal may be noticeably distorted by the “pulse stretching” caused by the multiple diffuse reflections.

The shape of the output signal is determined by convolving the input signal with the impulse response of the integrating sphere.

This impulse response is of the form:

$$e^{-t/\tau} \quad \text{Equation 4. 17}$$

where the time constant,  $\tau$ , is calculated as:

$$\tau = -\frac{2 D_s}{3 c \ln \rho} \quad \text{Equation 4. 18}$$

and

$\bar{\rho}$  = the average wall reflectance

$c$  = the velocity of light

$D_s$  = the diameter of the integrating sphere

Time constants of typical integrating spheres range from a few nanoseconds to a few tens of nanoseconds.

### Integrating Sphere Design

The design of an integrating sphere for any application involves a few basic parameters.

These include selecting the optimum sphere diameter based upon the number and size of port openings and peripheral devices.

Selecting the proper sphere coating considers spectral range, as well as performance requirements.

The use of baffles with respect to incident radiation and detector field-of-view is discussed.

Radiometric equations are presented for determining the coupling efficiency of an integrating sphere to a detection system.

### Integrating Sphere Diameter

Figure 4.28 shows that decreasing the port fraction have a dramatic effect on increasing the sphere multiplier.

For port fractions larger than 0.05, one begins to lose the advantage offered by the high reflectance coatings available for integrating spheres.

The first rule of thumb for integrating spheres is that no more than 5% of the sphere surface area be consumed by port openings.

Integrating spheres are designed by initially considering the diameter required for the port openings. Port diameter is driven by both the size of devices, as well as the geometrical constraints required by a sphere system.

Consider the case of a two port integrating sphere with both ports of unit diameter.

The relative radiance produced as a function of sphere diameter,  $D_s$ , for an equivalent input flux is proportional to:

$$L_s \propto \frac{M}{D^2} \quad \text{Equation 4.19}$$

The equation can be plotted as a function of reflectance for different sphere diameters.

The resulting port fraction for each is shown in Figure 4.28.

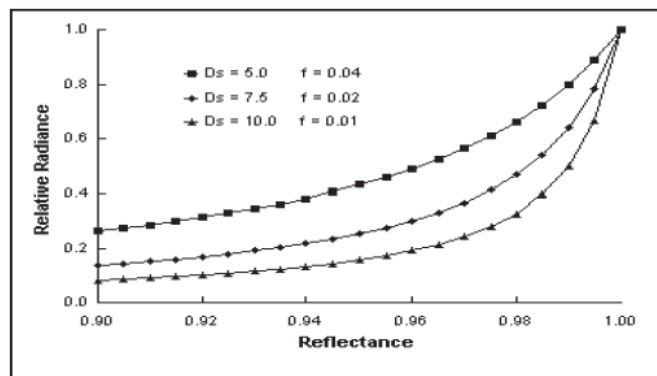


Figure 4.28 Relative radiance plotted on different values of diameter

The smallest sphere produces the highest radiance in general.

However, since the integrating sphere is usually employed for its ability to spatially integrate input flux, a larger sphere diameter and smaller port fraction will improve the spatial performance.

Notice in Figure 4.28 that all three sphere designs converge on the same unit flux density as the reflectance approaches 1.0.

Therefore, high reflectance integrating sphere materials such as Spectralon can optimize spatial performance at only a slight trade-off in radiance efficiency.

### Integrating Sphere Coatings

When choosing a coating for an integrating sphere two factors must be taken into account: reflectance and durability.

For example, if there seems to be plenty of light, and the sphere will be used in an environment that may cause the sphere to collect dirt or dust, a more durable, less reflective coating can be chosen.

Items located inside the sphere, including baffles, lamps, and lamp sockets absorb some of the energy of the radiant source and decrease the throughput of the sphere.

This decrease in throughput is best avoided by coating all possible surfaces with a highly reflective coating.

The sphere multiplier as illustrated by Figure 4.22 is extremely sensitive to the sphere surface reflectance. The selection of sphere coating or material can make a large difference in the radiance produced for a given sphere design.

The typical spectral reflectance of Spectralon and Spectralect are shown in Figure 4.29.

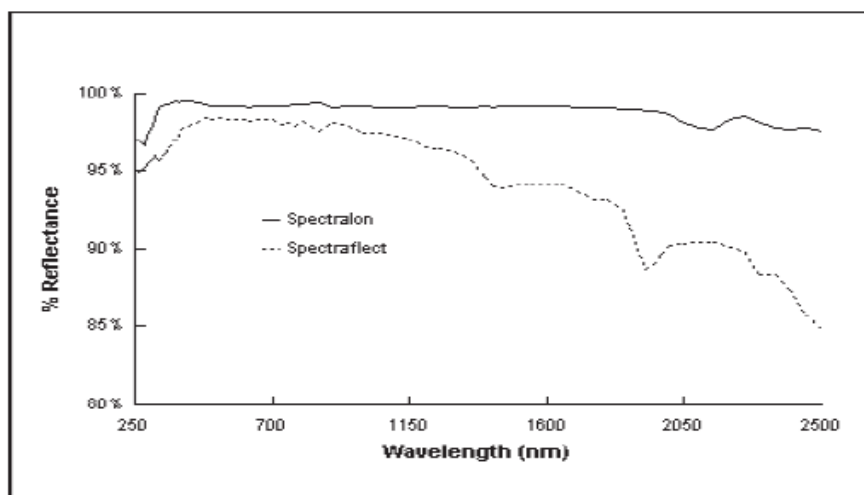


Figure 4. 29 Spectral reflectance of most used internal coatings

Both coatings are highly reflective, over 95% from 350 nm to 1350 nm, therefore, intuitively one might expect no significant increase in radiance for the same integrating sphere.

However, the relative increase in radiance is greater than the relative increase in reflectance by a factor equal to the newsphere multiplier,  $M_{new}$ .

$$\frac{\Delta L_s}{L_s} \approx \frac{\Delta \rho}{\rho_0} M_{new} \quad \text{Equation 4. 20}$$

Although Spectralon offers a 2% to 15% increase in reflectance over Spectralect within the wavelength range, an identical integrating sphere design would offer 40% to 240% increased radiance. The largest increase occurs in the NIR spectral region above 1400 nm.

Available Sphere Coatings

Modern coatings include barium sulfate based spray coatings, packed PTFE coatings, and Labsphere's proprietary reflectance materials and coatings: Spectralon®, Spectraflect®, Duraflect™, and Infragold™.

### Spectralon Reflectance Material

Spectralon is a highly Lambertian, thermoplastic material that is suitable for applications ranging from the UV-VIS to the NIR-MIR wavelength regions.

Spectralon spheres offer excellent reflectance values over the wavelength range from 250 nm to 2500 nm. This high reflectance in the ultraviolet and near-infrared regions makes Spectralon the ideal material for a wide range of integrating sphere applications.

Spectralon expands the temperature region for effective use of an integrating sphere and is stable to above 350°C.

The material exhibits reflectance greater than 99% over the wavelength range from 400 to 1500 nm and greater than 95% from 250 to 2500 nm.

The material is not well suited for applications above 2500 nm.

There are three grades of spectralon material — optical, laser, and space quality.

Spectralon space-grade material has undergone extensive stringent materials testing.

Upon exposure to UV flux for over 100 hours (tests were performed under vacuum conditions), Spectralon showed minimal damage.

In addition to UV radiation, Spectralon was tested for susceptibility to proton damage.

Samples were irradiated with  $10^{10}$  protons/cm<sup>2</sup> at consecutive energy levels of 100 keV, 1 MeV and 10 MeV.

### Spectraflect Reflectance Coating

Spectraflect is a specially formulated barium sulfate coating which produces a nearly perfect diffuse reflectance surface.

Spectraflect employs an alcohol-water mixture as a vehicle and is generally used in UV-VIS-NIR although most effectively in the 300 nm to 1400 nm wavelength range.

The reflectance properties of Spectrafect depend on the thickness of the coating.

Although the number of coats needed to attain maximum reflectance varies with the type of component, Labsphere typically applies more than twenty coats to each sphere.

At a thickness above 0.4 mm, Spectrafect is opaque with reflectance of greater than 98% over the 400 nm to 1100 nm wavelength range.

Spectrafect, sprayed onto degreased, sandblasted surfaces, exhibits thermal stability to 100°C.

The coating is inexpensive, safe, and highly Lambertian.

Spectrafect is not usable in very humid environments and is not stable in changing environments.

In these cases, Duraflect coating is preferred.

#### Duraflect Reflectance Coating

Duraflect, a durable white reflectance coating, is best used in applications from the VIS to NIR, 350 nm to 1200 nm.

The coating is opaque with reflectance values of 94 to 96% over its effective wavelength range.

Is preferred to use Duraflect in place of Spectrafect for applications involving outdoor exposure, humid environments and underwater applications.

Although Duraflect exhibits more environmentally stable properties than Spectrafect it does have some limitations and does not preclude the use of Spectrafect.

Duraflect is unsuitable for use in the UV range and may be incompatible with certain plastic substrates.

#### Infragold Reflectance Coating

Infragold is an electrochemically plated, diffuse, gold metallic reflectance coating that exhibits excellent reflectance properties over the wavelength range from 0.7 mm to 20 mm.

Reflectance data is traceable to the National Institute of Standards and Technology (NIST).

The reflectivity of Infragold is 92 to 96% over the wavelength region from 1mm to greater than 20 mm.

## Flux on the Detector

The sphere wall determines the total flux incident on a photodetector mounted at or near a port of the integrating sphere.

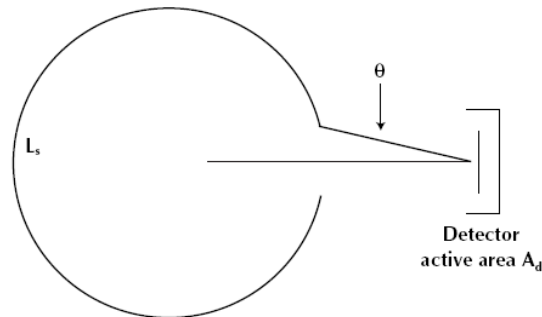


Figure 4. 30 Schematics on measurement of reflectance on the detector area

By definition, the total flux incident on the detector active area,  $A_d$  ( $m^2$ ) is:

$$\Phi_d = L_s A_d \Omega \quad \text{Equation 4. 21}$$

where:  $\Omega$  = projected solid angle (sr) of the detector field of view.

A good approximation for  $\Omega$  in almost cases is:

$$\Omega = \pi \sin^2 \theta \text{ (sr)} \quad \text{Equation 4. 22}$$

In the case of imaging optics used with detector, the angle  $\theta$  is subtended from the exit pupil of the system.

The detector is the field stop of the system.

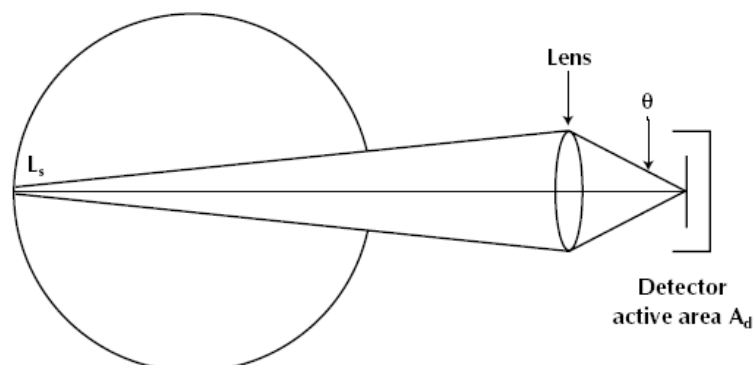


Figure 4. 31 Schematics on measurement of reflectance on the detector area

The f-number ( $f/\#$ ) of an optical system is also used to express its light gathering power.

Therefore:

$$\Omega = \frac{\pi}{(2f/\#)^2} \quad \text{Equation 4. 23}$$

The efficiency of the optical system, which is generally a function of the transmittance and reflectance of individual components, must also be considered. Therefore the detector incident flux is:

$$\Phi_d = L_s A_d \frac{\pi}{(2f/\#)^2} \varepsilon_0 \quad \text{Equation 4. 24}$$

where;  $\varepsilon_0$  = optical system efficiency (unitless).

### Integrating Sphere Baffles

In general, the light entering an integrating sphere should not directly illuminate either the detector element or the area of the sphere wall that the detector views directly.

In order to accomplish this baffles are often used in integrating sphere design.

Baffles, however, will cause certain inaccuracies simply because the integrating sphere is no longer a perfect sphere.

Light incident on a baffle does not uniformly illuminate the remainder of the sphere. It is advisable to minimize the number of baffles used in a sphere design.

### Geometric Considerations of Sphere Design

There are four primary considerations that must be taken into account in the design of an integrating sphere system: source geometry, detector geometry, coating, and calibration.

In many cases these topics become inter-related, but for this discussion they will be described separately.

## Source Geometry

Sources can be separated into three types:

- Omnidirectional- sources that emit light in all directions
- Unidirectional - sources that emit in one direction;
- Partially directional - those that fit somewhere between unidirectional and omnidirectional.

The design challenge is to make spheres for each type of source that allow for accurate and repeatable measurements.

The first consideration related to source geometry is ensuring that the source does not directly illuminate the detector.

This may mean that the designer will place a shield or “baffle” between the source and the detector.

In other cases, it simply means that the detector needs to be located in a portion of the sphere that is not illuminated by the source.

The following are some typical designs that can be used for these types of sources.

Most sphere designs can be based on one of these designs as long as the source geometry is correctly defined and identified.

### Omnidirectional Sources

Many light sources, including commercial lamps, provide general illumination.

The total luminous flux emitted by these lamps is more significant than the intensity in a single direction.

The integrating sphere offers a simple solution to the measurement of total luminous flux (Figure 4.26).

In this design, the test source is placed inside an integrating sphere in order to capture all the light emitted from it.

With a properly calibrated system, this geometry yields very accurate measurement results.

### Unidirectional Sources

Some light sources, including lasers, are highly directional.

These sources may be directed through an entrance port on the sphere (Figure 4.27).

Although extremely highly directional sources could be measured directly by focusing the laser on the detector, the integrating sphere offers several advantages over the simple detector approach.

First, the integrating sphere eliminates the need for precise alignment of the laser beam.

Second, the sphere uniformly illuminates the detector eliminating effects of non-uniformity of the detector response. Third, the sphere naturally attenuates the energy from the laser.

This attenuation protects the detector from the full strength of the laser and allows the use of faster, more sensitive detectors.

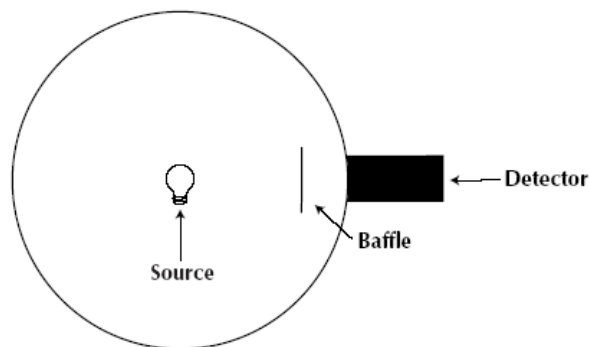


Figure 4. 32 measurement of omnidirectional flux

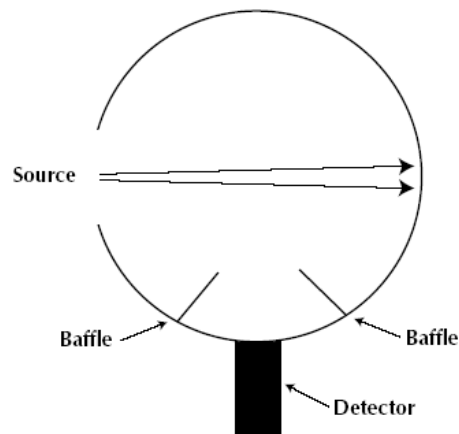


Figure 4. 33 measurement of unidirectional flux

### Sources that are neither Omnidirectional nor Unidirectional

Other light sources, including laser diodes, fiber optic illuminators, fiber optics, and reflector lamps are neither highly directional nor omnidirectional.

These light sources can be placed near the entrance port of the sphere so that all of the light is directed into the sphere. The sphere spatially integrates the light before it reaches the detector (Figure 4.28).

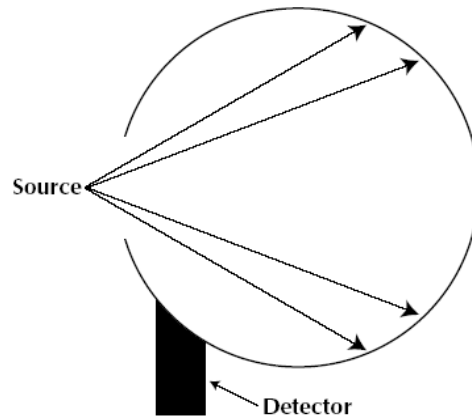


Figure 4. 34 measurement of neither Omnidirectional or Unidirectional flux Detectors

It is important to understand the type of measurement to be made: Photometric, Radiometric, Spectroradiometric, or Colorimetric (i.e. power, visible power, spectrum, or colour).

Each uses a different detector or detector/filter combination as described below.

### Photometers

Photometers measure the energy as perceived by the human eye. Matching the results of a physical photometer to the spectral response of the human eye is quite difficult. In 1924, the Commission Internationale de l'Eclairage (CIE) recorded the spectral response of 52 experienced observers.

The data resulted in a standard luminosity curve, commonly called the photopic response of the standard observer.

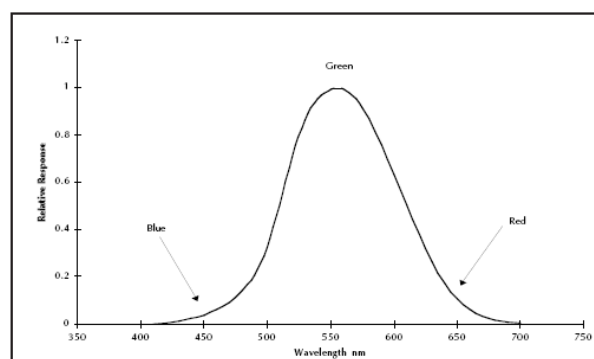


Figure 4. 35 Human eye spectral response

Generally, photometers will use a silicon detector that has a filter placed in front of it.

The combined response of the detector/filter combination will be approximately that of the human eye,  $V(\lambda)$ .

### Radiometers

A radiometer is an instrument that measures the power of a radiant source. Power is described in units of watts, or joules per second. There are a variety of detectors that can be used depending on the wavelength range to be measured. A silicon detector allows measurements over the UV/VIS/NIR wavelength range (from 0.2 to 1.1  $\mu\text{m}$ ).

A germanium detector allows measurements over the NIR wavelength range (from 0.8 to 1.8  $\mu\text{m}$ ). Other detectors are available for use over longer wavelengths.

One must be careful when specifying and using a radiometer. Due to the fact that detectors do not typically have a flat response (e.g. silicon has a response of about 0.6 A/W at 900 nm, but about 0.4 A/W at 600 nm) specifying a broad band measurement is very difficult. Typically they will be calibrated for use at a variety of wavelengths.

Each wavelength will have an associated calibration factor, which will not give accurate results unless only light near that wavelength is entering the sphere. Alternatively, a narrow band filter can be placed in front of the detector so that only light of a specific wavelength band reaches it (the calibration must be performed with this filter in place).

In this case, the result will be accurate regardless of the input, but the system may only be used for one wavelength band.

### Spectroradiometer

A spectroradiometer is a device that measures power per wavelength interval as a function of wavelength. It is used to obtain detailed spectral information about the source.

In addition, a spectroradiometer can be used to create a highly accurate photometer for sources such as arc and fluorescent lamps. Although a filter photometer is accurate over much of the photopic response curve, some divergence occurs in small sections of the spectrum. Therefore, the potential error associated with lamps with high emissions at those sections could be significant. A better approximation to this curve is obtained with spectroradiometers.

Spectroradiometers typically come in two varieties:

- scanning monochromators
- diode array spectrometers.

### Colorimeter

A colorimeter measures and quantifies the colour of the source. The detector consists of a combination of three or four filtered detectors. These detectors are used to simulate the x, y, and z CIE functions. The signal received from the detectors is used by a signal processor to calculate the chromaticity coordinates, x and y.

### Sources of Error

Measurement uncertainty is a function of the measurement process. Uncertainty analysis, as applied to any scientific experiment or physical measurement, provides an estimate of the size of the error that may be expected. Both random and systematic errors are considered.

Random errors provide a measure of the precision or repeatability of a measurement process. Random errors can be reduced by repeating a measurement.

Systematic errors cannot be reduced by repeating a measurement.

Reduction of systematic errors often depends on the ability of the system operator or experimenter to recognize and quantify these errors. In total luminous flux measurements, the most obvious systematic error is the calibration uncertainty stated for the working standard lamp. Other systematic errors are discussed below.

### Geometry

Geometric errors within the integrating sphere are associated with comparing test and standard lamps of different physical dimensions and flux distributions. The errors are minimized when comparing lamps of similar characteristics.

Geometric error arises from the spatial distribution of luminous flux inside the sphere. The total luminous flux from an internal lamp illuminates the sphere wall directly.

This direct luminance distribution may be non-uniform.

From a port on the sphere wall, a photodetector can be sensitive to the luminance distribution within its field-of-view. Therefore, the ratio of viewed luminance may not be exactly proportional to the

ratio of the total luminous flux for two lamps being compared. A detector which can receive light from over the entire sphere will minimize this effect. A diffuser window or small auxiliary sphere in front of the photodetector best achieves the required angular and spatial response.

Quantifying geometric errors to an acceptable degree of precision is a very difficult exercise.

The presence of baffles, mounting fixtures, and the lamp itself affect the performance of the sphere photometer.

Although a detailed analysis has not been performed, an allowance of 1% for geometric errors is included in the uncertainty analysis of NIST transfer calibrations of total luminous flux. It is the largest of the associated systematic errors within assigned NIST uncertainties.

### Spectral Response

A photometer incorporates a detector characterized by a spectral responsivity which approximates the CIE luminous efficiency function. An exact match to the CIE luminous efficiency function is not entirely possible.

Spectral response errors with photopic response detectors occur for test lamps of different spectral distribution than those used as calibration standards. A goodness-of-fit value is often expressed to quantify the associated error. The goodness-of-fit is based on both the calibration source spectral distribution as well as the spectral response of the photopic detector.

In total luminous flux measurements, the spectral efficiency of the integrating sphere must be included in the spectral response analysis of the complete system. Integrating sphere efficiency decreases slightly towards the blue wavelengths of the visible spectrum due to the nature of the sphere coating. As the coating ages, the decrease in efficiency becomes more pronounced. Pale blue glass filters may be added to the photodetector assembly to correct for the induced spectral response shift of the sphere.

The spectral efficiency of the integrating sphere is determined by rationing the spectral distribution measured at the detector port for a lamp operating within the sphere to that measured directly of the lamp operating on the outside the sphere.

A spectroradiometer is used for this measurement.

The required spectral transmittance of the correcting blue filter is determined by:

$$T(\lambda) \propto \frac{S_0(\lambda)}{S_i(\lambda)}$$

Where;

$T(\lambda)$  = filter transmittance

$S_0(\lambda)$  = lamp distribution outside the sphere

$S_i(\lambda)$  = lamp distribution inside the sphere

The spectral correction required may also be specified by measuring the induced shift in the lamp's correlated colour temperature. The difference between the apparent colour temperature within the sphere and the actual lamp colour temperature is used to calculate the filter's colour balancing power expressed as a transformation value in units of "reciprocal mega-Kelvins". Blue filter glasses have negative mired values. The filter's mired value is given by:

$$\left[ \frac{1}{CCT_0} - \frac{1}{CCT_i} \right] * 10^6$$

Where;

$CCT_0$  = lamp correlated colour temperature outside the sphere

$CCT_i$  = lamp correlated colour temperature inside the sphere

### Linearity

The output data displayed on a photometer must be linear with respect to input light levels. Linearity means that the output is exactly proportional to the input. The linearity of a photometer may be measured by multiple source, multiple aperture, or inverse-square methods.

### Lamp Absorption

A lamp placed within the integrating sphere affects the sphere efficiency through self-absorption. When measuring lamps of different absorption properties, a constant sphere efficiency is not achieved. The effect can be significant when measuring test lamps of a different type than those used for calibration. Correcting for lamp absorption requires the use of an auxiliary lamp.

## Electrical Measurements

When calibrating with a standard lamp, operating current must be accurately set. The variation in total luminous flux for a tungsten filament lamp is approximately proportional to the variation in operating current to the sixth power.

## **4.2 VASRA (Variable Angle Specular Reflectance Accessory)**

The Variable Angle Specular Reflectance accessory (VASRA) allows to measure the specular or mirror-like reflectance off a sample surface. It is installed in the sample compartment of the instrument.

The accessory has several unique features:

- The sample mounting platform is moved as the angle is changed. This ensures that the center of the image is always in the same position.
- The accessory is supplied with several different aperture masks. These allow to change the height of the image to suit the sample size.
- The sample is mounted at the slit image position. Can be changed the width of the image to suit the sample by simply selecting the appropriate spectral bandwidth (SBW).
- Angles in  $0.5^\circ$  increments can be set.
- The accessory is motor driven and is completely controlled from the Cary WinUV software.

### **4.2.1 Specification**

The Variable Angle Specular Reflectance Accessory is suitable for Installation category II and Pollution degree 2.

- Wavelength range: 175–3300 nm
- Maximum horizontal beam divergence:  $\pm 2.5^\circ$
- Maximum Vertical ray divergence:  $\pm 2.2^\circ$
- Sample sizes: Maximum sample size

Angle	Length	Height	Thickness
20	150	140	65
45	235	140	53
70	243	140	35

Table 4. 4 Specification

#### 4.2.2 Optical Design

The Variable Angle Specular Reflectance accessory features a five mirror design with two cylindrical, two torodial and one flat mirror. The powered mirrors are used to ensure that correct imaging is maintained in both the vertical and horizontal planes. The design is symmetrical, taking advantage of the already symmetrical beam profile throughout the sample compartment.

The slit image is positioned at the sample mounting position. This achieves a very small beam size at that point, allowing small samples to be measured. The horizontal ray divergence at the sample is  $\pm 2.5^\circ$  (5 nm SBW). The vertical ray divergence is  $\pm 2.2^\circ$ .

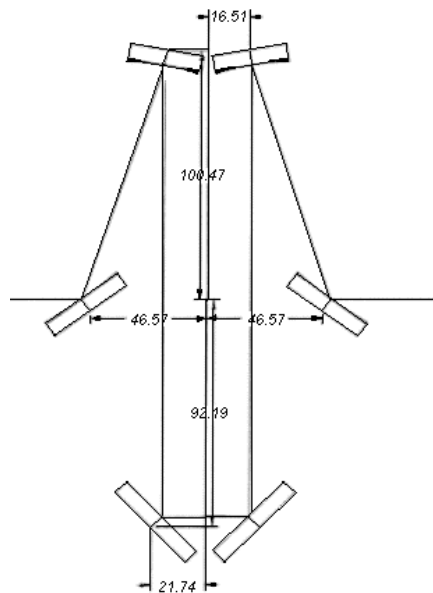


Figure 4. 36 The optical design of the Variable Angle Specular Reflectance Accessory

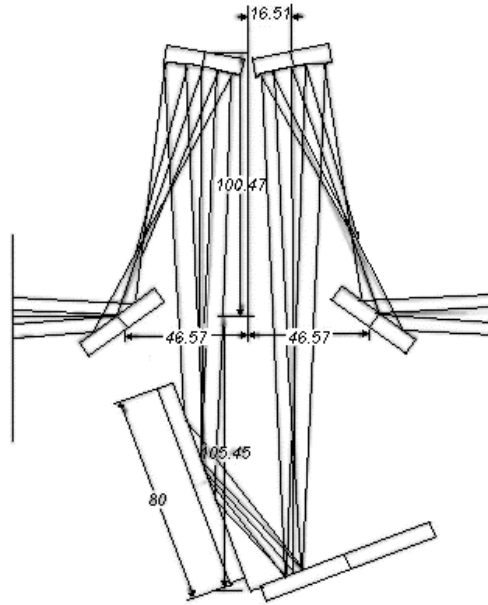


Figure 4.37 The beam profiles at 20°

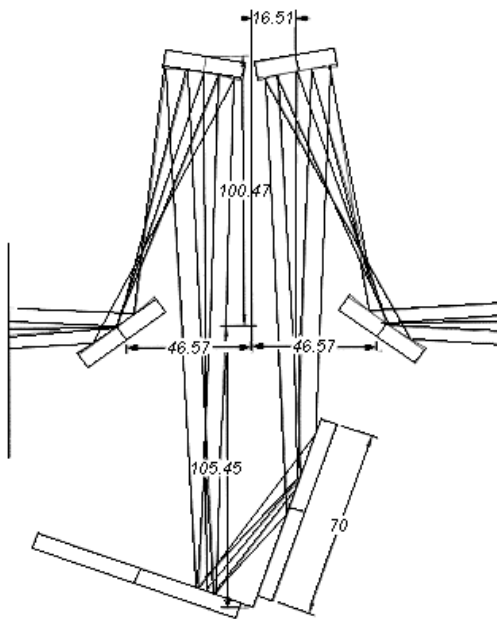


Figure 4.38 The beam profiles at 70°

### 4.3 Experimental collection of reflectance data

The reflector quality in a CSP system directly influences the amount of solar radiation that can be converted into power. The efficiency of a CSP collector can be characterized by the solar flux that reaches the receiver, is absorbed and converted into heat, in relation to the solar incident flux at the aperture plane. The net solar flux intercepting the receiver is influenced by the sun shape, the

concentrator quality, the tracking system accuracy, and the receiver position in relation to the ideal focal position. To determine the quality of the concentrator, first the reflector material needs to reflect the majority of the incident sunlight. This can be quantified by the solar weighted hemispherical reflectance. Second, the reflected sunlight needs to be directed to the focal plane without major losses, which are the result of macroscopic and microscopic optical concentrator errors. These are namely the contour errors of the concentrator module and specular errors of the reflector material. In addition, cost issues and the stability of the hemispherical and specular reflectance following decades of outdoor exposure must also be considered for the reflector. All these properties and influences need to be measured and evaluated independently.

This procedure concentrates only on the measurement of the solar-weighted hemispherical reflectance and the solar-weighted specular reflectance of the reflector material itself

The specular reflectance is evaluated with a simplified characterization of mirror reflectance properties, which gives results that can be used to compare mirror materials.

This procedure applies to the common solar mirror material types, surface mirrors with reflective layers of silver or aluminum.

#### **4.3.1 Normative references**

The following referenced documents are indispensable for the measurement of the reflectance. For dated references, only the edition cited applies. For undated references, the latest edition of the referenced document (including any amendments) applies.

DIN/ISO normative references:

1. EN ISO 9488:1999; Solar energy - Vocabulary
2. DIN 5036 Part 3; Radiometric and photometric properties of materials: Methods of measurement for photometric and spectral radiometric characteristic factors
3. ISO 9845-1:1992; Solar energy - Reference solar spectral irradiance at the ground at different receiving conditions - Part 1: Direct normal and hemispherical solar irradiance for air mass 1.5
4. ISO 9050; Glass in building, Determination of light transmittance, solar direct transmittance, total solar energy transmittance, ultraviolet transmittance and related glazing factors

5. ISO/IEC 98:1995; Guide to the Expression of Uncertainty in Measurement; Geneva: International Organization for Standardization, 1995

Other:

6. ASTM E 903-96; Standard Test Method for Solar Absorptance, Reflectance and Transmittance of Materials Using Integrating Spheres (withdrawn because not updated for eight years)
7. ASTM G 173-03; Terrestrial Reference Spectra for Photovoltaic Performance Evaluation – American Society for Testing and Materials
8. ASTM E 891-87; Standard Tables for Terrestrial Direct Normal Solar Spectral Irradiance for Air Mass 1.5 (withdrawn because outdated and replaced by ASTM G173)

### 4.3.2 Terms and definitions

#### Diffuse reflectance

If a parallel bundle of light rays is incident on an object with a rough or microscopically structured surface, each incident beam encounters a different surface slope and therefore the law of reflection takes effect for a different angle  $\theta$  to the surface normal at this point. The light is diffusely scattered in all directions in the plane of incidence (Figure 4.39).

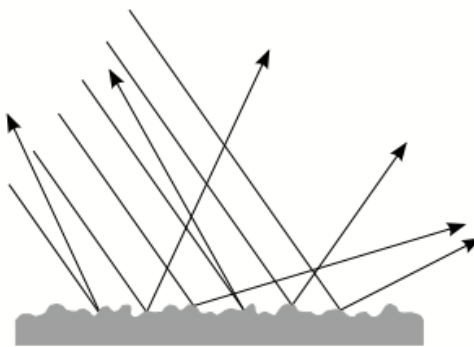


Figure 4. 39 Diffuse reflectance

## Specular reflectance

As shown in Figure 4.39, the specular reflectance describes the case of reflection on a microscopically perfectly smooth surface, where a parallel bundle of incident rays is reflected as a parallel bundle of rays according to the law of reflection.

On the atomic level, a perfectly smooth surface does not exist in reality, so the specular reflection is always mixed with a certain (even if infinitesimal) amount of scattering. Vice versa, any polished material can produce a certain amount of specular reflection mixed with scattering. For nearly perfectly smooth surfaces, the scattering effect results in a slight widening of the beam cone that is reflected in the specular direction. Of the reflected bundle of rays, the majority are reflected with the reflectance angle  $\theta_r$  and a number of reflected rays have an offset of plus or minus  $\phi_0$  to the specular direction (Figure 4.40). In an instrument designed to measure specular reflectance, the instrument's design and detector size define the maximum offset angle  $\phi_0$  within which the reflected light rays are still detected. This angle is called the acceptance angle  $\phi$ .

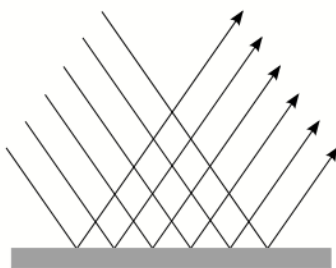


Figure 4. 40 Perfect specular reflection

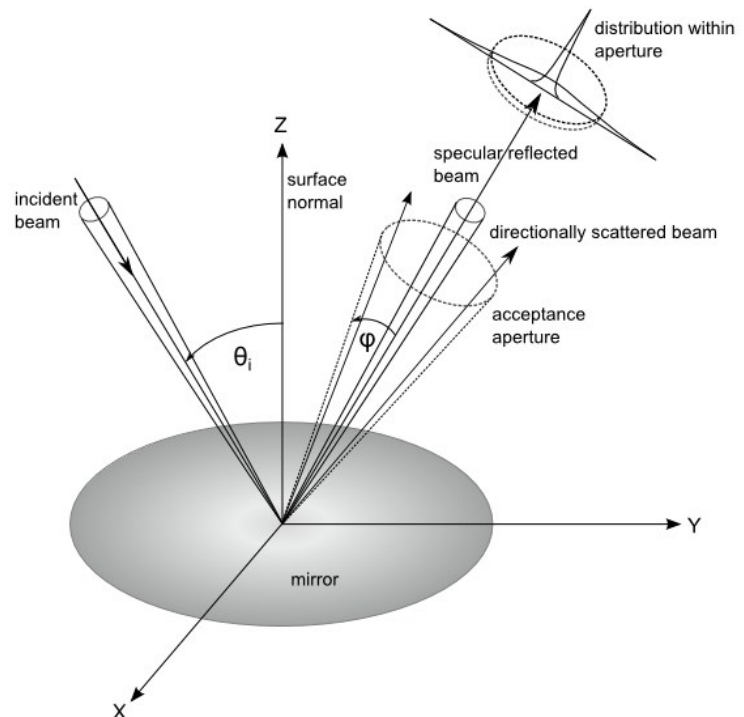


Figure 4. 41 Specular reflection with offset

The specular reflectance can be understood as the amount of light reflected into the acceptance angle  $\phi$ . Specular reflectance is written as  $\rho_s(\lambda, \theta, \phi)$  where  $\rho_s$  is dependent on the wavelength  $\lambda$  and the incident angle  $\theta$  of the light and the acceptance angle  $\phi$ .

### Hemispherical reflectance

A detector that covers the entire hemisphere above the reflective surface captures both, the specular reflected light and all of the diffusely scattered light. It measures the hemispherical reflectance  $\rho_h(\lambda, \theta, h)$  and is dependent on the wavelength  $\lambda$  and the incident angle  $\theta$  of the light.

### Specularity

Specularity describes the quality of a mirror surface. A mirror with good specularity has no losses of the specular reflectance value (compared to the hemispherical reflectance value) due to scattering or beam spread. The parameter can be quantified by the ratio of the specular reflectance to the hemispherical reflectance and for perfect specularity is equal to 1.

### Specular beam diversion or beam spread

If a surface displays a very good but not perfect specularity, an incident bundle of rays is reflected with not exactly the same shape, instead the beam shape is slightly widened. It can still be considered a beam cone with specular reflectance, but the offset to the original shape is referred to as the specular beam diversion or beam spread.

### Air Mass (AM)

Air mass (AM) is the optical path sunlight travels through the Earth's atmosphere. As sunlight passes through the atmosphere, it is attenuated by scattering and absorption; the thicker the atmosphere through which it passes, the greater the attenuation. The attenuation of solar radiation by the atmosphere is not the same for all wavelengths; consequently, passage through the atmosphere not only reduces intensity but also alters the spectral irradiance. The term "air mass" normally indicates the relative air mass, the path length relative to that at the zenith at sea level. Or the ratio of the mass of atmosphere in the observer-sun path relative to the mass that would exist if the observer were at sea level and the sun were directly overhead, at standard barometric pressure. By definition the sea-level air mass at zenith is 1. The value of the air mass is appended to the acronym AM, so an AM1 indicates an air mass of 1, AM1.5 indicates an air mass of 1.5, and AM2

indicates an air mass of 2. The region above the earth's atmosphere, where there is no atmospheric attenuation of sunlight is considered to have "air mass zero" (AM0).

## 4.4 Relevance of the reflectance parameter for CSP applications

In this chapter the challenges for reflectance measurements are explained along with the reasons for certain specifications made in this document. A discussion about the adequate acceptance angle for specular measurements is presented in chapter 4.4.2.

### 4.4.1 Reflective behaviour of solar mirrors

A typical mirror for CSP applications is either a second-surface glass mirror, where the light beam has to pass the glass before it is reflected on the reflective layer, or a first (or front) surface mirror, where the reflective layer is applied to a substrate. Low-iron glass of 3- or 4-mm thickness can be produced with a very good flatness quality (in both the glass surfaces and in the reflective layer deposited on the back-side of the glass) and therefore these 2nd-surface mirrors have a very good specularity. The double reflection occurring on the glass does not influence the energy conversion process because the beam displacement is small enough for the receiver acceptance function and its effect is diminished by the distance to the receiver. On the other hand, for alternative mirror materials like polished/anodized aluminum mirrors, metalized polymer film, and some front surface mirrors, a slight loss of specular reflectance due to scattering is typical. This can be the result of the production process, which causes microscopic surface structures or a wavy surface. Also, some material types are coated with different protective layers, which might have local variances in thickness and quality and introduce alternating constructive and destructive interference effects in the reflection spectrum. The exact distribution of the reflected beam profile on these materials is still not fully investigated and can currently only be approximated.

The reflection from ideal specular mirrors can be adequately represented by a Gaussian bell curve, with the standard deviation  $\sigma$  and the amplitude  $R$ . Glass mirrors usually display a very small beam spread of  $\sigma < 0.2$  mrad. However, for non-ideal specular mirrors (i.e., metallized films and polished/anodized aluminum mirrors) this description is not sufficient. They are less specular than glass mirrors and the different material and surface properties lead to characteristic scattering profiles in addition to the beam spread. They are most accurately characterized by two fundamental parameters: the hemispherical reflectance and the reflected light distribution function. A simple approach of describing this reflected beam distribution is with a combination of two Gaussian

distributions (see Figure 4.41). This approximation assumes one Gaussian distribution with high amplitude and a narrow standard deviation, which contains the majority of the reflected radiance, and one Gaussian distribution with low amplitude and a very wide standard deviation, which describes the scattered part.

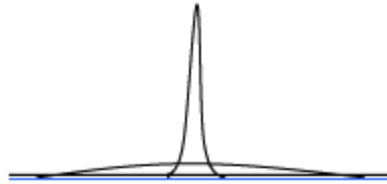


Figure 4.42 Approximated reflection distribution for non-ideal specular mirror materials

## 4.5 Preparation of measurement

The measurement procedure shall be valid for the reflectance measurements of all types of solar mirror materials. These have very varying material properties. A careful preparation of the mirror samples as well as the appropriate selection of reference standards is necessary to ensure a high measurement accuracy and comparability within the solar community.

### 4.5.1 Sample preparation

The preparation of samples is an essential part of the measurement process. The important points to be considered for the different types of mirror materials are explained in the following.

### 4.5.2 General

For laboratory measurements, the samples should be cut to a size that allows measurement on different points on the surface, but also fits into the instrument's sample holder. Typically a size between 80x80 mm<sup>2</sup> and 100x100 mm<sup>2</sup> is advised. The sample must not be smaller than the sample port.

To evaluate a product, samples should be taken out of the production line to be measured rather than prototype samples specifically made for the analysis. At least three replicate samples of one product should be analyzed, so that anomalies can be identified.

There must not be any structure, protective edge envelope or any other element that rises above the front plane of the mirror. There must not be any protrusion changing the angle between the reflective surface and the measurement port of the instrument.

Regular recalibration of instruments and reference standards are essential for a performance with constant high accuracy.

### 4.5.3 Cleaning

The mirror's front surface should be cleaned very carefully with a soft lens tissue and deionized water or according to the manufacturer's recommendation prior to measurement.

If the mirrors cannot be cleaned sufficiently with the normal cleaning procedure because of heavy soiling or because air-blown dirt has bonded and baked onto the mirror surface for samples exposed outdoors, slightly more aggressive methods may need to be used. Depending on the type of solar reflectors, contact washing with a cotton swap and an extremely dilute solution of a mild detergent and deionized water (1/100) followed by a copious rinse of deionized water can be used. Careful utilization of ethyl alcohol can be used for glass, protected aluminum, and some front surface mirrors. Isopropanol is not advised because it leaves a residual coating which smears on the mirror. Many alcohols (e.g., toluene, acetone benzene) are not advised for use with silvered polymers because the alcohol can soften and damage the polymer surface. Commercial glass cleaner and chlorine- and ammonia-based cleaners are not recommended with sensitive metals like silver. If a smear is left on the mirror, it should be carefully removed with demineralized water.

The samples should be allowed sufficient time to dry (i.e., overnight), particularly if the mirror's surface can absorb water (i.e., silvered polymers) during cleaning. Any remaining dust should be removed with pressurized air. The sample should be free of grease and particles and perfectly dry before measurement.

### 4.5.4 Glass mirrors

Thin glass mirrors (i.e. 1-mm thickness) are more flexible than thick glass mirrors and care needs to be taken to not break or deform an unsupported mirror when cleaning and positioning the sample in the instrument for measurement. To prevent breakage and avoid introducing deformation of the mirror during mounting the sample can be bonded to a substrate or a fixing structure can be used.

#### **4.5.5 Aluminum sheets**

Measurement errors due to deformation can be avoided by applying flexible aluminum sheets onto a flat substrate (glass is recommended, heavier-gauge aluminum or steel have also been used) before measurement.

#### **4.5.6 Silver polymer films**

Silvered polymer films must be applied to a flat substrate (glass is recommended, heavy-gauge aluminum or steel have also been used) so that a stable surface is provided for measurement. Application of the film to the substrate must be performed with great care according to the manufacturer recommendations. Loose films and any air bubbles encapsulated between the film and the substrate introduce specular reflectance measurement errors.

#### **4.6 Reference mirrors for integrating spheres**

Especially for hemispherical measurements, the measurement accuracy strongly depends on the reference mirror. Depending on the type of sample, the appropriate reference mirror needs to be chosen. Instead of a reference mirror it was used the absolute white sample reference tested by the Varian and certified to properly be used for relative reflectance measurements.

Due to the previously motivation all the measurement are intended to be only for comparison and won't be used as an absolute measurement.

#### **4.7 Measurement procedure**

This measurement procedure is a combination of a variety of standards and methods developed and used by the working group for reflectance measurements of solar mirrors. It is partially based on the ASTM standard E903 that was withdrawn not because its content was outdated, but because the standard was not reapproved by the committee within 8 years. A round robin test partly validated the procedure and partly revealed essential points that were taken into account to obtain more accurate results.

## 4.8 Measurement of hemispherical reflectance with spectrophotometer and integrating sphere

In the following subchapters the procedure for measuring the hemispherical reflectance with a spectrophotometer and integrating sphere is described. This includes the necessary instrument parameters, the measurement steps and data treatment.

### 4.8.1 Configuration of the instrument

The significant wavelength range for solar applications is the solar wavelength range of  $\lambda = 280 - 2500$  nm, which should also be used for measurements of solar mirrors. The wavelength interval is determined by the correct balance between accuracy and measurement duration. An interval of 5 nm was used. The wavelength intervals of the reference mirror calibration spectrum should be the same as the measurement intervals for better accuracy.

To cover the wide range of the spectrum, normally two detectors and light sources are used in the instrument. The signal response can therefore vary and become weaker in the portion of the spectrum where the detector's sensitivity decreases. The instrument parameters like slit-width, gain and integrating time should be set to obtain optimum detector response and smooth transitions between changes of detector, lamp and grating. A longer integrating time in the wavelength areas where detector changes take place was used to reduce the gap.

### 4.8.2 Auto corrections

At the beginning of the measurement session these can be utilized to regulate the two beams within the instrument to ensure equal intensity. The diffuse white tiles (usually supplied with the instrument and typically match the sphere's Lambertian coating) should be placed in both ports of the instrument during the auto corrections.

The diffuse white tiles will be replaced with the reference mirrors in the ports when the 100%-baseline.

A graph of the raw and uncorrected data does not represent the actual reflectance values, but the measured flux intensity in combination with the detector response curve. A great decrease or increase in the wavelength area near the detector change point is normal and will be corrected later with the data treatment.

### 4.8.3 Calibration

Calibration is the key issue to keep a high accuracy. Characteristic peaks at known wavelengths in the spectrum of the lamp or special monochromatic transmittance samples can be used to localize the exact positions of gratings and slits.

### 4.8.4 Procedure

The instrument should be turned on 120 minutes before starting the baseline to ensure proper and stable operating temperature. Using the integrating sphere as detector, the instrument should not be turned on without the white plates in the ports to ensure that positioning errors of gratings and slits do not occur due to a missing signal from an empty port. Care must be taken to properly place the references and samples in the ports and to close the integrating sphere external cover, to ensure that no intrusion of external stray light affects the measurement. The 100%-baseline correction should be performed with the reference standard at the beginning of every measurement session.

#### 4.8.4.1 Baseline

A baseline (100%) measurement needs to be taken before each measurement session and at the end of it. The second measurement ensures that no changes have occurred during the session concerning the instrument performance.

## 4.9 Weighting with standard solar norm spectrum

For evaluation of the quality of a mirror for application in concentrating solar power technology, the reflectance spectrum needs to be weighted with a standardized solar irradiance spectrum. This allows an averaged evaluation of the solar radiation that is reflected by the mirror material. In the CSP context, the solar weighted specular reflectance  $\rho_s(SW,\theta,\phi)$  is the significant value, with  $\phi = 12.5$  mrad for parabolic-trough technology.

### 4.9.1 Recommended solar norm

The solar irradiance spectrum is taken from international norm tables which represent an average irradiance spectrum for the northern hemisphere at an elevation level typical for the United States or Europe with Air Mass 1.5 (AM1.5). Tables that have been commonly used in the past and up to now were taken from ISO 9845-1, ASTM G173, and ASTM E891. Within the glass industry, ISO

9050 is a common standard that is currently also being used to evaluate glass mirror solar reflectance.

The standard E891 was withdrawn by ASTM and was replaced with G173, which is calculated with a new algorithm and uses atmospheric conditions more indicative of the modern industrial society. ISO 9845-1 has not been withdrawn but the tables are calculated with the same algorithms and atmospheric conditions as in E891, which makes its tables equally outdated. Considering that the tables given in ISO 9050 are based on ISO 9845-1 and only include the global solar irradiance instead of the direct solar irradiance, all of these solar norms except the current ASTM G173, are not recommended for evaluating the solar reflectance of CSP mirrors.

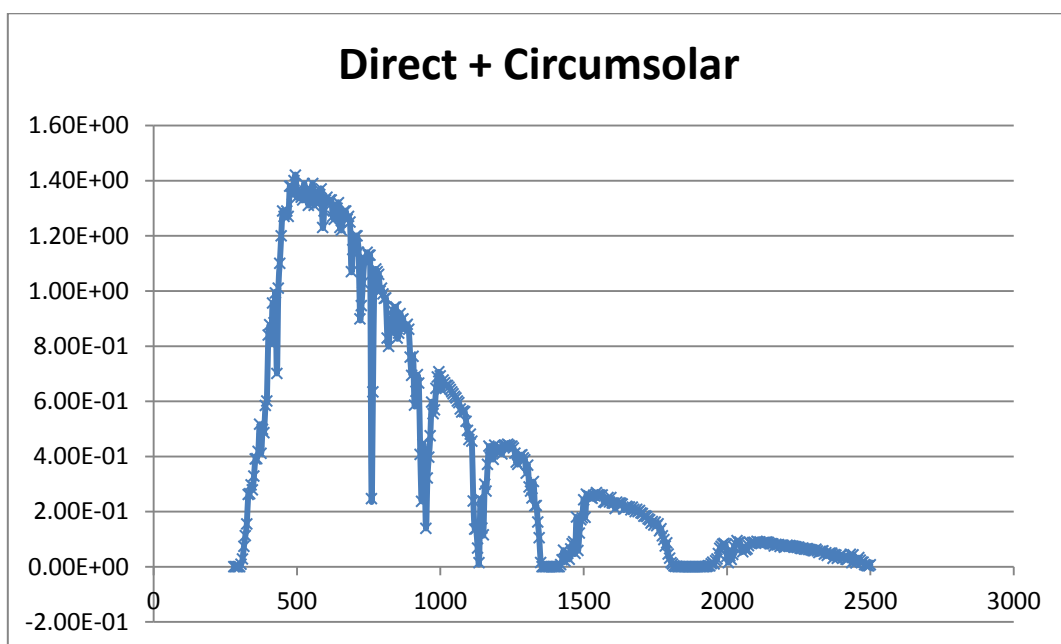


Figure 4. 43 Direct + Circumsolar spectrum calculated with SMARTS model in a clear sky day at AM 1.5

#### 4.9.2 Irradiance spectrum tables

The solar norm tables represent the solar irradiance in Watts per m<sup>2</sup> per wavelength. The column for global or hemispherical irradiance at a tilted surface is not appropriate for evaluation in the context of CSP technology. It is essential to use the values for direct + circumsolar irradiance.

### 4.9.3 Solar-weighted hemispherical reflectance

The solar-weighted reflectance  $\rho(SW)$  of a mirror represents the convolution of the spectral reflectance function  $\rho(\lambda)$  with the solar irradiance function  $E(\lambda)$ , according to the following expression:

$$\rho(SW) = \frac{\int_0^{\infty} \rho(\lambda) E_{\lambda}(\lambda) d\lambda}{\int_0^{\infty} E_{\lambda}(\lambda) d\lambda}$$

Since these functions are generally only known with discrete values, the integration is performed as a summation. Therefore, the solar-weighted hemispherical reflectance  $\rho_h(SW, \theta, h)$  of a solar mirror is calculated using the values of the measured hemispherical reflectance spectrum  $\rho_h(\lambda, \theta, h)$  and the direct solar irradiance spectrum  $E_{\lambda}$  at wavelength intervals of  $\Delta\lambda$  with the following formula:

$$\rho_h(SW, \theta, h) = \frac{\sum_{i=0}^{2500} \rho_h(\lambda_i, \theta, h) E_{\lambda}(\lambda_i) \Delta\lambda_i}{\sum_{i=0}^{2500} E_{\lambda}(\lambda_i) \Delta\lambda_i}$$

Results are influenced by the way the total integral of the solar irradiance is calculated from the discrete values. To ensure higher repeatability within the solar community, the weighting table following gives weighting factors  $F(\lambda_i)$  for the interval of  $\Delta\lambda = 5$  nm.

Wavelength $\lambda$ [nm]	Direct + Circumsolar $E_{\lambda}$ [ $W m^{-2} nm^{-1}$ ]	Integrated Irradiance $E_{0 \rightarrow \lambda_i}$ [ $W m^{-2}$ ]	Weighting Factor $F(\lambda_i)$
280	2.54E-26	0.0000	1.42E-28
285	9.00E-17	0.0000	5.04E-19
290	5.15E-10	0.0000	2.88E-12
295	3.22E-06	0.0012	1.80E-08
300	4.56E-04	0.0246	2.55E-06
305	8.93E-03	0.1165	5.00E-05
310	2.78E-02	0.3703	1.56E-04
315	7.37E-02	0.8365	4.12E-04
320	1.13E-01	1.5060	6.31E-04
325	1.55E-01	2.5484	8.68E-04
330	2.62E-01	3.8651	1.47E-03
335	2.65E-01	5.2685	1.48E-03
340	2.97E-01	6.7063	1.66E-03
345	2.79E-01	8.2255	1.56E-03
350	3.29E-01	10.0268	1.84E-03

355	3.91E-01	11.9863	2.19E-03
360	3.92E-01	14.0126	2.20E-03
365	4.18E-01	16.3495	2.34E-03
370	5.17E-01	18.6683	2.89E-03
375	4.11E-01	20.9393	2.30E-03
380	4.98E-01	23.3990	2.78E-03
385	4.86E-01	26.0764	2.72E-03
390	5.85E-01	29.0402	3.27E-03
395	6.01E-01	32.6423	3.36E-03
400	8.40E-01	36.9383	4.70E-03
405	8.78E-01	41.1572	4.92E-03
410	8.09E-01	45.5692	4.53E-03
415	9.56E-01	50.1701	5.35E-03
420	8.85E-01	54.8646	4.95E-03
425	9.93E-01	59.1007	5.56E-03
430	7.01E-01	63.3716	3.92E-03
435	1.01E+00	68.6373	5.64E-03
440	1.10E+00	74.3836	6.15E-03
445	1.20E+00	80.6018	6.71E-03
450	1.29E+00	86.9858	7.21E-03
455	1.27E+00	93.3473	7.08E-03
460	1.28E+00	99.7713	7.16E-03
465	1.29E+00	106.1848	7.22E-03
470	1.27E+00	112.8108	7.13E-03
475	1.38E+00	119.7058	7.70E-03
480	1.38E+00	126.5263	7.74E-03
485	1.35E+00	133.3826	7.53E-03
490	1.40E+00	140.4341	7.82E-03
495	1.42E+00	147.3413	7.97E-03
500	1.34E+00	154.0886	7.49E-03
505	1.36E+00	160.8623	7.61E-03
510	1.35E+00	167.5828	7.55E-03
515	1.34E+00	174.2663	7.49E-03
520	1.33E+00	181.0683	7.47E-03
525	1.39E+00	187.9326	7.76E-03
530	1.36E+00	194.7573	7.61E-03
535	1.37E+00	201.4566	7.67E-03
540	1.31E+00	208.1448	7.33E-03
545	1.37E+00	214.9711	7.64E-03
550	1.36E+00	221.8538	7.64E-03
555	1.39E+00	228.6041	7.77E-03
560	1.31E+00	235.2723	7.34E-03
565	1.36E+00	241.9711	7.59E-03

570	1.32E+00	248.5873	7.41E-03
575	1.32E+00	255.2573	7.40E-03
580	1.35E+00	262.0553	7.53E-03
585	1.37E+00	268.5686	7.69E-03
590	1.23E+00	274.8651	6.89E-03
595	1.29E+00	281.4021	7.20E-03
600	1.33E+00	288.0761	7.43E-03
605	1.34E+00	294.7398	7.51E-03
610	1.32E+00	301.3626	7.41E-03
615	1.33E+00	308.0008	7.42E-03
620	1.33E+00	314.4923	7.44E-03
625	1.27E+00	320.8063	7.09E-03
630	1.26E+00	327.2198	7.05E-03
635	1.31E+00	333.7266	7.31E-03
640	1.30E+00	340.2596	7.25E-03
645	1.32E+00	346.6268	7.37E-03
650	1.23E+00	352.7566	6.88E-03
655	1.22E+00	358.9786	6.84E-03
660	1.27E+00	365.3633	7.09E-03
665	1.29E+00	371.7943	7.20E-03
670	1.29E+00	378.1673	7.19E-03
675	1.26E+00	384.4896	7.07E-03
680	1.27E+00	390.7656	7.08E-03
685	1.25E+00	396.5656	6.97E-03
690	1.07E+00	402.1366	6.01E-03
695	1.15E+00	407.9301	6.46E-03
700	1.16E+00	413.8363	6.51E-03
705	1.20E+00	419.8221	6.71E-03
710	1.20E+00	425.6676	6.69E-03
715	1.14E+00	430.7731	6.40E-03
720	8.99E-01	435.3901	5.03E-03
725	9.47E-01	440.3321	5.30E-03
730	1.03E+00	445.6809	5.76E-03
735	1.11E+00	451.2359	6.21E-03
740	1.11E+00	456.8666	6.22E-03
745	1.14E+00	462.5359	6.38E-03
750	1.13E+00	468.1844	6.31E-03
755	1.13E+00	471.6325	6.34E-03
760	2.47E-01	473.8349	1.38E-03
765	6.34E-01	478.0808	3.55E-03
770	1.06E+00	483.4425	5.96E-03
775	1.08E+00	488.8145	6.04E-03
780	1.07E+00	494.1485	5.98E-03

785	1.06E+00	499.3220	5.96E-03
790	1.00E+00	504.3498	5.62E-03
795	1.01E+00	509.3378	5.63E-03
800	9.89E-01	514.2410	5.53E-03
805	9.73E-01	519.1099	5.44E-03
810	9.75E-01	523.6203	5.46E-03
815	8.29E-01	527.6910	4.64E-03
820	7.99E-01	531.9322	4.47E-03
825	8.98E-01	536.2993	5.02E-03
830	8.49E-01	540.7455	4.75E-03
835	9.29E-01	545.4215	5.20E-03
840	9.41E-01	550.1302	5.27E-03
845	9.42E-01	554.5584	5.27E-03
850	8.29E-01	558.7495	4.64E-03
855	8.47E-01	563.1623	4.74E-03
860	9.18E-01	567.6936	5.14E-03
865	8.95E-01	572.1791	5.01E-03
870	8.99E-01	576.5825	5.03E-03
875	8.62E-01	580.9234	4.82E-03
880	8.74E-01	585.3071	4.89E-03
885	8.79E-01	589.6569	4.92E-03
890	8.61E-01	593.7077	4.82E-03
895	7.60E-01	597.3424	4.25E-03
900	6.94E-01	600.9865	3.89E-03
905	7.63E-01	604.3588	4.27E-03
910	5.86E-01	607.4113	3.28E-03
915	6.36E-01	610.7415	3.56E-03
920	6.97E-01	614.1485	3.90E-03
925	6.66E-01	616.8310	3.73E-03
930	4.07E-01	618.4402	2.28E-03
935	2.37E-01	620.1427	1.33E-03
940	4.44E-01	622.1212	2.49E-03
945	3.47E-01	623.3380	1.94E-03
950	1.39E-01	624.4917	7.80E-04
955	3.22E-01	626.2890	1.80E-03
960	3.97E-01	628.4678	2.22E-03
965	4.75E-01	631.1468	2.66E-03
970	5.97E-01	634.0274	3.34E-03
975	5.55E-01	636.8393	3.11E-03
980	5.69E-01	639.8812	3.19E-03
985	6.47E-01	643.2206	3.62E-03
990	6.88E-01	646.7085	3.85E-03
995	7.07E-01	650.2043	3.96E-03

1000	6.92E-01	653.5368	3.87E-03
1005	6.41E-01	656.8327	3.59E-03
1010	6.77E-01	660.1919	3.79E-03
1015	6.67E-01	663.5048	3.73E-03
1020	6.58E-01	666.7940	3.68E-03
1025	6.57E-01	670.0644	3.68E-03
1030	6.51E-01	673.3004	3.64E-03
1035	6.43E-01	676.4933	3.60E-03
1040	6.34E-01	679.6452	3.55E-03
1045	6.27E-01	682.7581	3.51E-03
1050	6.18E-01	685.8342	3.46E-03
1055	6.12E-01	688.8671	3.43E-03
1060	6.01E-01	691.8554	3.36E-03
1065	5.95E-01	694.7714	3.33E-03
1070	5.72E-01	697.6022	3.20E-03
1075	5.61E-01	700.4165	3.14E-03
1080	5.65E-01	703.2336	3.16E-03
1085	5.62E-01	705.9540	3.14E-03
1090	5.27E-01	708.5045	2.95E-03
1095	4.94E-01	710.8914	2.76E-03
1100	4.61E-01	713.2459	2.58E-03
1105	4.81E-01	715.5849	2.69E-03
1110	4.55E-01	717.3181	2.55E-03
1115	2.38E-01	718.2530	1.33E-03
1120	1.36E-01	718.9369	7.59E-04
1125	1.38E-01	719.4506	7.72E-04
1130	6.76E-02	719.6566	3.78E-04
1135	1.48E-02	720.3048	8.29E-05
1140	2.44E-01	721.2654	1.37E-03
1145	1.40E-01	721.9060	7.82E-04
1150	1.16E-01	722.9448	6.52E-04
1155	2.99E-01	724.3766	1.67E-03
1160	2.74E-01	725.9879	1.53E-03
1165	3.71E-01	728.0082	2.08E-03
1170	4.37E-01	730.1800	2.45E-03
1175	4.31E-01	732.3099	2.41E-03
1180	4.21E-01	734.3339	2.35E-03
1185	3.89E-01	736.4097	2.18E-03
1190	4.41E-01	738.5795	2.47E-03
1195	4.27E-01	740.7160	2.39E-03
1200	4.28E-01	742.8286	2.39E-03
1205	4.17E-01	744.9531	2.33E-03
1210	4.33E-01	747.0561	2.42E-03

1215	4.09E-01	749.1705	2.29E-03
1220	4.37E-01	751.3671	2.45E-03
1225	4.41E-01	753.5688	2.47E-03
1230	4.39E-01	755.7772	2.46E-03
1235	4.44E-01	757.9877	2.49E-03
1240	4.40E-01	760.1786	2.46E-03
1245	4.36E-01	762.3612	2.44E-03
1250	4.37E-01	764.5305	2.44E-03
1255	4.31E-01	766.6386	2.41E-03
1260	4.12E-01	768.6162	2.31E-03
1265	3.79E-01	770.4902	2.12E-03
1270	3.71E-01	772.4037	2.08E-03
1275	3.95E-01	774.3998	2.21E-03
1280	4.04E-01	776.4239	2.26E-03
1285	4.06E-01	778.4264	2.27E-03
1290	3.95E-01	780.3844	2.21E-03
1295	3.88E-01	782.2008	2.17E-03
1300	3.39E-01	783.9668	1.89E-03
1305	3.68E-01	785.6091	2.06E-03
1310	2.89E-01	787.0179	1.62E-03
1315	2.74E-01	788.3257	1.54E-03
1320	2.49E-01	789.7209	1.39E-03
1325	3.09E-01	791.0458	1.73E-03
1330	2.21E-01	792.1532	1.23E-03
1335	2.22E-01	793.1147	1.24E-03
1340	1.62E-01	793.7831	9.08E-04
1345	1.05E-01	794.0848	5.89E-04
1350	1.55E-02	794.1236	8.67E-05
1355	3.48E-06	794.1236	1.95E-08
1360	2.07E-06	794.1236	1.16E-08
1365	8.78E-12	794.1236	4.92E-14
1370	2.83E-07	794.1244	1.58E-09
1375	3.13E-04	794.1253	1.75E-06
1380	7.90E-05	794.1255	4.42E-07
1385	2.03E-06	794.1267	1.13E-08
1390	4.78E-04	794.1279	2.68E-06
1395	6.51E-07	794.1279	3.65E-09
1400	3.15E-09	794.1279	1.76E-11
1405	3.54E-07	794.1291	1.98E-09
1410	4.53E-04	794.1307	2.54E-06
1415	1.79E-04	794.1512	9.99E-07
1420	8.04E-03	794.2342	4.50E-05
1425	2.51E-02	794.4468	1.41E-04

1430	5.99E-02	794.6487	3.35E-04
1435	2.08E-02	794.7972	1.17E-04
1440	3.85E-02	795.0147	2.16E-04
1445	4.84E-02	795.2025	2.71E-04
1450	2.67E-02	795.4303	1.49E-04
1455	6.44E-02	795.7992	3.60E-04
1460	8.32E-02	796.2344	4.65E-04
1465	9.09E-02	796.5826	5.09E-04
1470	4.84E-02	797.1525	2.71E-04
1475	1.80E-01	797.7490	1.00E-03
1480	5.91E-02	798.2008	3.31E-04
1485	1.22E-01	798.9299	6.81E-04
1490	1.70E-01	799.7983	9.51E-04
1495	1.77E-01	800.8504	9.93E-04
1500	2.43E-01	801.9060	1.36E-03
1505	1.79E-01	803.0099	1.00E-03
1510	2.63E-01	804.3117	1.47E-03
1515	2.58E-01	805.5990	1.44E-03
1520	2.57E-01	806.8697	1.44E-03
1525	2.51E-01	808.1179	1.41E-03
1530	2.48E-01	809.3857	1.39E-03
1535	2.59E-01	810.6773	1.45E-03
1540	2.57E-01	811.9937	1.44E-03
1545	2.69E-01	813.3224	1.51E-03
1550	2.62E-01	814.6282	1.47E-03
1555	2.60E-01	815.9239	1.46E-03
1560	2.58E-01	817.2188	1.45E-03
1565	2.60E-01	818.4556	1.45E-03
1570	2.35E-01	819.6253	1.31E-03
1575	2.33E-01	820.8020	1.30E-03
1580	2.38E-01	822.0247	1.33E-03
1585	2.51E-01	823.2402	1.41E-03
1590	2.35E-01	824.4544	1.31E-03
1595	2.51E-01	825.6598	1.40E-03
1600	2.31E-01	826.8134	1.29E-03
1605	2.30E-01	827.9173	1.29E-03
1610	2.11E-01	829.0314	1.18E-03
1615	2.34E-01	830.1865	1.31E-03
1620	2.28E-01	831.3338	1.28E-03
1625	2.31E-01	832.4861	1.29E-03
1630	2.30E-01	833.6285	1.29E-03
1635	2.27E-01	834.7192	1.27E-03
1640	2.09E-01	835.7724	1.17E-03

1645	2.12E-01	836.8503	1.19E-03
1650	2.19E-01	837.9384	1.23E-03
1655	2.16E-01	839.0219	1.21E-03
1660	2.17E-01	840.0801	1.22E-03
1665	2.06E-01	841.1346	1.15E-03
1670	2.16E-01	842.1937	1.21E-03
1675	2.08E-01	843.2140	1.16E-03
1680	2.00E-01	844.2335	1.12E-03
1685	2.08E-01	845.2523	1.16E-03
1690	2.00E-01	846.2628	1.12E-03
1695	2.04E-01	847.2600	1.14E-03
1700	1.95E-01	848.2285	1.09E-03
1705	1.93E-01	849.1683	1.08E-03
1710	1.83E-01	850.0884	1.03E-03
1715	1.85E-01	851.0065	1.03E-03
1720	1.82E-01	851.8964	1.02E-03
1725	1.74E-01	852.7551	9.72E-04
1730	1.70E-01	853.5735	9.50E-04
1735	1.58E-01	854.3776	8.82E-04
1740	1.64E-01	855.1653	9.18E-04
1745	1.51E-01	855.9470	8.45E-04
1750	1.62E-01	856.7243	9.04E-04
1755	1.49E-01	857.4878	8.36E-04
1760	1.56E-01	858.2022	8.73E-04
1765	1.30E-01	858.8721	7.26E-04
1770	1.38E-01	859.4982	7.74E-04
1775	1.12E-01	860.0239	6.28E-04
1780	9.81E-02	860.4573	5.49E-04
1785	7.52E-02	860.8623	4.21E-04
1790	8.68E-02	861.1941	4.86E-04
1795	4.59E-02	861.3865	2.57E-04
1800	3.11E-02	861.5005	1.74E-04
1805	1.45E-02	861.5604	8.11E-05
1810	9.48E-03	861.5921	5.30E-05
1815	3.21E-03	861.6026	1.80E-05
1820	9.66E-04	861.6081	5.40E-06
1825	1.25E-03	861.6112	6.97E-06
1830	5.09E-06	861.6112	2.85E-08
1835	6.28E-06	861.6113	3.51E-08
1840	6.13E-08	861.6113	3.43E-10
1845	6.13E-06	861.6113	3.43E-08
1850	2.93E-06	861.6113	1.64E-08
1855	2.78E-07	861.6113	1.56E-09

1860	1.09E-05	861.6114	6.11E-08
1865	1.66E-05	861.6114	9.31E-08
1870	2.61E-10	861.6114	1.46E-12
1875	4.43E-10	861.6116	2.48E-12
1880	7.61E-05	861.6119	4.26E-07
1885	4.31E-05	861.6126	2.41E-07
1890	2.20E-04	861.6135	1.23E-06
1895	1.27E-04	861.6138	7.13E-07
1900	8.49E-07	861.6138	4.75E-09
1905	5.58E-07	861.6138	3.12E-09
1910	2.27E-05	861.6139	1.27E-07
1915	1.97E-05	861.6151	1.10E-07
1920	4.45E-04	861.6185	2.49E-06
1925	9.23E-04	861.6222	5.17E-06
1930	5.45E-04	861.6324	3.05E-06
1935	3.54E-03	861.6494	1.98E-05
1940	3.24E-03	861.6842	1.81E-05
1945	1.07E-02	861.7522	5.99E-05
1950	1.65E-02	861.8181	9.22E-05
1955	9.89E-03	861.8967	5.53E-05
1960	2.16E-02	862.0210	1.21E-04
1965	2.81E-02	862.2114	1.57E-04
1970	4.81E-02	862.4983	2.69E-04
1975	6.67E-02	862.8508	3.73E-04
1980	7.42E-02	863.2404	4.15E-04
1985	8.16E-02	863.6548	4.57E-04
1990	8.41E-02	864.0645	4.71E-04
1995	7.98E-02	864.3577	4.47E-04
2000	3.75E-02	864.4883	2.10E-04
2005	1.47E-02	864.6229	8.25E-05
2010	3.91E-02	864.7861	2.19E-04
2015	2.62E-02	864.9622	1.47E-04
2020	4.42E-02	865.2547	2.48E-04
2025	7.28E-02	865.6453	4.07E-04
2030	8.35E-02	866.0910	4.67E-04
2035	9.48E-02	866.5489	5.31E-04
2040	8.83E-02	866.9938	4.94E-04
2045	8.96E-02	867.3852	5.02E-04
2050	6.69E-02	867.6876	3.74E-04
2055	5.41E-02	867.9932	3.03E-04
2060	6.82E-02	868.3160	3.81E-04
2065	6.10E-02	868.6302	3.41E-04
2070	6.47E-02	868.9828	3.62E-04

2075	7.63E-02	869.3874	4.27E-04
2080	8.55E-02	869.8108	4.79E-04
2085	8.38E-02	870.2399	4.69E-04
2090	8.78E-02	870.6804	4.91E-04
2095	8.84E-02	871.1136	4.95E-04
2100	8.49E-02	871.5552	4.75E-04
2105	9.18E-02	872.0054	5.14E-04
2110	8.83E-02	872.4520	4.94E-04
2115	9.03E-02	872.8935	5.05E-04
2120	8.63E-02	873.3274	4.83E-04
2125	8.73E-02	873.7667	4.89E-04
2130	8.84E-02	874.2095	4.95E-04
2135	8.87E-02	874.6547	4.96E-04
2140	8.94E-02	875.0985	5.00E-04
2145	8.81E-02	875.5272	4.93E-04
2150	8.34E-02	875.9445	4.67E-04
2155	8.36E-02	876.3607	4.68E-04
2160	8.29E-02	876.7560	4.64E-04
2165	7.52E-02	877.1458	4.21E-04
2170	8.08E-02	877.5459	4.52E-04
2175	7.93E-02	877.9456	4.44E-04
2180	8.06E-02	878.3307	4.51E-04
2185	7.35E-02	878.7091	4.11E-04
2190	7.79E-02	879.0984	4.36E-04
2195	7.78E-02	879.4685	4.36E-04
2200	7.02E-02	879.8263	3.93E-04
2205	7.29E-02	880.2041	4.08E-04
2210	7.82E-02	880.5875	4.37E-04
2215	7.52E-02	880.9670	4.21E-04
2220	7.66E-02	881.3446	4.29E-04
2225	7.44E-02	881.7174	4.16E-04
2230	7.47E-02	882.0875	4.18E-04
2235	7.33E-02	882.4510	4.10E-04
2240	7.21E-02	882.8062	4.04E-04
2245	6.99E-02	883.1585	3.91E-04
2250	7.10E-02	883.5033	3.98E-04
2255	6.69E-02	883.8358	3.74E-04
2260	6.61E-02	884.1695	3.70E-04
2265	6.74E-02	884.4983	3.77E-04
2270	6.41E-02	884.8169	3.59E-04
2275	6.33E-02	885.1390	3.54E-04
2280	6.56E-02	885.4589	3.67E-04
2285	6.24E-02	885.7712	3.49E-04

2290	6.25E-02	886.0790	3.50E-04
2295	6.06E-02	886.3760	3.39E-04
2300	5.82E-02	886.6679	3.26E-04
2305	5.85E-02	886.9722	3.28E-04
2310	6.32E-02	887.2740	3.54E-04
2315	5.75E-02	887.5465	3.22E-04
2320	5.15E-02	887.8143	2.88E-04
2325	5.56E-02	888.0940	3.11E-04
2330	5.62E-02	888.3780	3.15E-04
2335	5.74E-02	888.6348	3.21E-04
2340	4.54E-02	888.8754	2.54E-04
2345	5.09E-02	889.1053	2.85E-04
2350	4.11E-02	889.3256	2.30E-04
2355	4.70E-02	889.5674	2.63E-04
2360	4.97E-02	889.8139	2.78E-04
2365	4.89E-02	890.0125	2.74E-04
2370	3.05E-02	890.1980	1.71E-04
2375	4.37E-02	890.4126	2.45E-04
2380	4.21E-02	890.5943	2.36E-04
2385	3.05E-02	890.7624	1.71E-04
2390	3.67E-02	890.9548	2.06E-04
2395	4.02E-02	891.1646	2.25E-04
2400	4.37E-02	891.3572	2.45E-04
2405	3.33E-02	891.5241	1.86E-04
2410	3.35E-02	891.6755	1.88E-04
2415	2.71E-02	891.8091	1.51E-04
2420	2.64E-02	891.9570	1.48E-04
2425	3.28E-02	892.1508	1.84E-04
2430	4.47E-02	892.2995	2.50E-04
2435	1.48E-02	892.4437	8.26E-05
2440	4.29E-02	892.6027	2.40E-04
2445	2.07E-02	892.6881	1.16E-04
2450	1.35E-02	892.7837	7.57E-05
2455	2.47E-02	892.9283	1.38E-04
2460	3.32E-02	893.0712	1.86E-04
2465	2.40E-02	893.1728	1.34E-04
2470	1.66E-02	893.2554	9.31E-05
2475	1.64E-02	893.3163	9.16E-05
2480	8.00E-03	893.3502	4.48E-05
2485	5.58E-03	893.3729	3.13E-05
2490	3.50E-03	893.3888	1.96E-05
2495	2.86E-03	893.4136	1.60E-05
2500	7.03E-03	893.4312	3.94E-05

Table 5. 1 Standard reference spectrum at AM 1.5

Using these weighting factors, the solar weighted hemispherical reflectance is obtained by the sum of a simple multiplication:

$$\rho_h(SW, \theta, h) = \sum_{i=280}^{2500} \rho_h(\lambda_i, \theta, h) \cdot F(\lambda_i)$$

#### 4.9.4 Solar-weighted specular reflectance

If the specular reflectance is acquired with a spectrophotometer and an appropriate accessory, unfortunately we don't have such an accessory so always with the integrating sphere we were able also to collect not only the Global hemispherical reflectance but also the diffuse reflectance.

With a simple subtraction we were able to construct the relative specular reflectivity at  $6^\circ$  due to the conformation of the integrating sphere which present the possibility to detach a part of the sphere itself to make this type of measurement.

This procedure it also correct for this type of measurement always because we are doing these measurement for comparison scope only.

The results obtained are valid to calculate the solar-weighted specular reflectance  $\rho_s(SW, \theta, \phi)$ , when replacing  $\rho_h(\lambda_i, \theta, h)$  with  $\rho_s(\lambda_i, \theta, \phi)$ .

Another important assumption is that the ratio between specular and hemispherical reflectance at one wavelength in the spectrum is basically constant over the entire spectrum. Therefore, the ratio at one wavelength is proportional to the ratio between the solar-weighted specular reflectance and the solar-weighted hemispherical reflectance.

This means that a possible specular reflectance loss due to scattering at one wavelength is also assumed to be lost with a similar amount at another wavelength. In reality, this has been measured to be true within  $\pm 0.015$ .

#### 4.10 Accuracy

After obtaining the reflectance results with the procedure previously exposed, the reported parameters and information should also be uniform.

Global uncertainty of a measurement is calculated by the convolution of type A and type B uncertainties. Type A uncertainties only take into account measurement statistics. However, type B

uncertainties depend on several factors, such as measurement instrument (which is affected by various sources of uncertainties like stability, reproducibility, sensitivity, etc.), sample quality, reference standard quality, calibration status, and operator experience. In particular, the accuracy of specular reflectance measurements decreases for mirror samples with a low specular surface quality.

A global measurement accuracy of about  $\pm 0.013$  is achievable following the procedure presented in this document. Within one laboratory the solar weighted reflectance values should be repeatable by at least  $\pm 0.005$  and the results of the spectrophotometer by  $\pm 0.003$ .

## 5. REFLECTANCE MEASUREMENTS

### 5.1 DRA (Diffuse Reflectance Accessory) Integrating Sphere

In the following the core of our research will be presented. It involves three big families of mirrors:

1. Thin Glass silvered mirrors
2. Polymeric Film mirrors
3. Aluminum mirrors

For the Thin Glass mirrors we have two types of high reflective mirrors which for privacy we will call TG1 and TG2.

For the Polymeric film mirrors we will use the acronym of PF1 and PF2.

For the Aluminum mirrors we have two types of high reflective mirrors that we will call with the acronym of AL1 and AL2.

#### 5.1.1 Thin Glass Mirrors

Thin glass mirrors have a durability, which is comparable to that for thick glass mirrors because they are made by using the same wet silvering processes, but use a relatively lightweight glass that is  $\leq 1$  mm thick; they also have greater material costs, are more difficult to handle, and have higher associated labor costs (25% - 40%) than other advanced reflector technologies. Their unweathered solar-weighted hemispherical reflectance is  $\sim 93$  to  $96\%$  and their cost is  $\sim 20$  to  $60$   $\$/\text{m}^2$ .

The choice of adhesive, which is used to bond the mirror to a structural substrate, can adversely affect the performance of weathered thin glass mirrors; corrosion has been detected in thin glass mirrors deployed in the field.

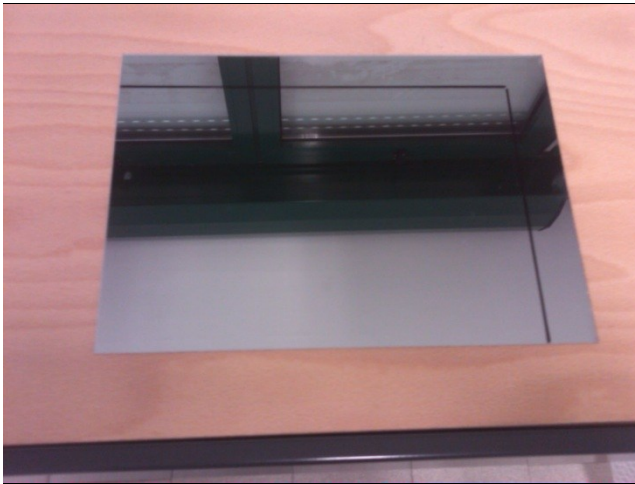


Figure 5. 1 Reflector type TG1

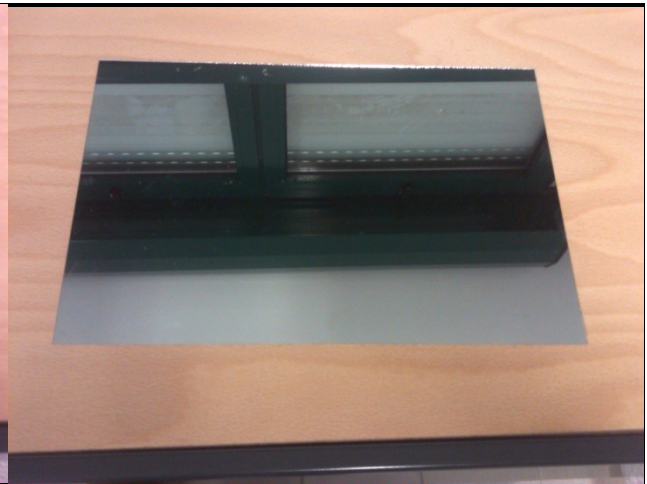


Figure 5. 2 Reflector type TG2

For each family were conducted a measurement campaign of ten measurements for the global and ten measurements for the diffuse reflectivity to achieve a good average of the standard deviation.

The raw measurement of TG1 is described in figure 5.3.

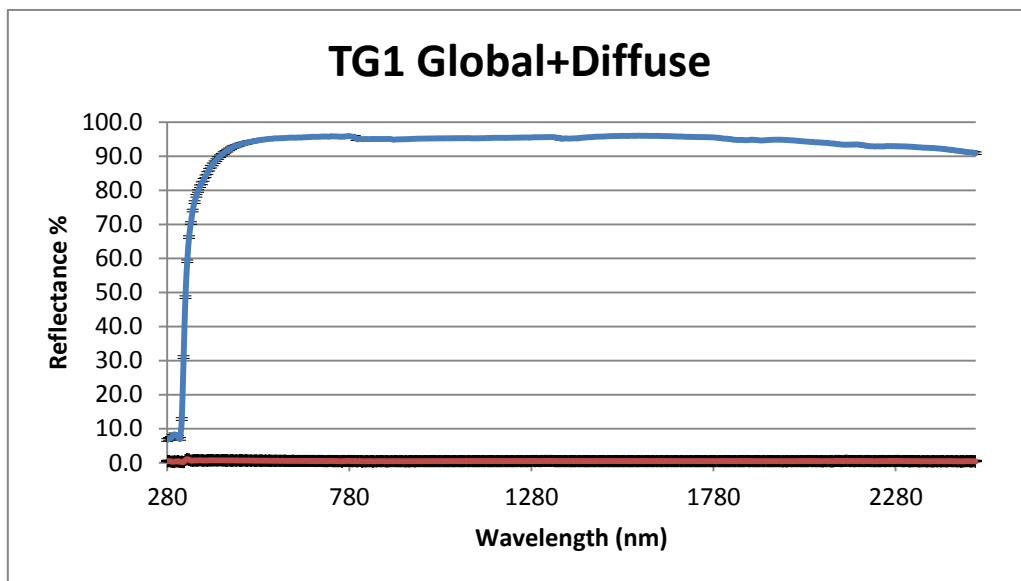


Figure 5. 3 TG1 Reflectance Measurements

We are reporting just a single measurement but we conducted an experimental campaign of measurements composed of three measurements on each sample for four samples for a total of twelve measurements for each kind of mirrors.

For each sample was measured the Global Reflectance with the complete integrating sphere so we obtained the upper curve which is a scan all over the entire spectrum covered by the sphere.

The resulting standard deviation for all the measurements of global reflectance is equal to a mean of 0.38528 with a maximum of 1.117921 and a minimum value of 0.072879 along the wavelength range.

The lowest curve is the Diffuse Reflectance (figure 5.4.) which is obtained removing the quarter of the integrating sphere placed at 6° from the normal to the sample surface, and replacing it with a light trap.

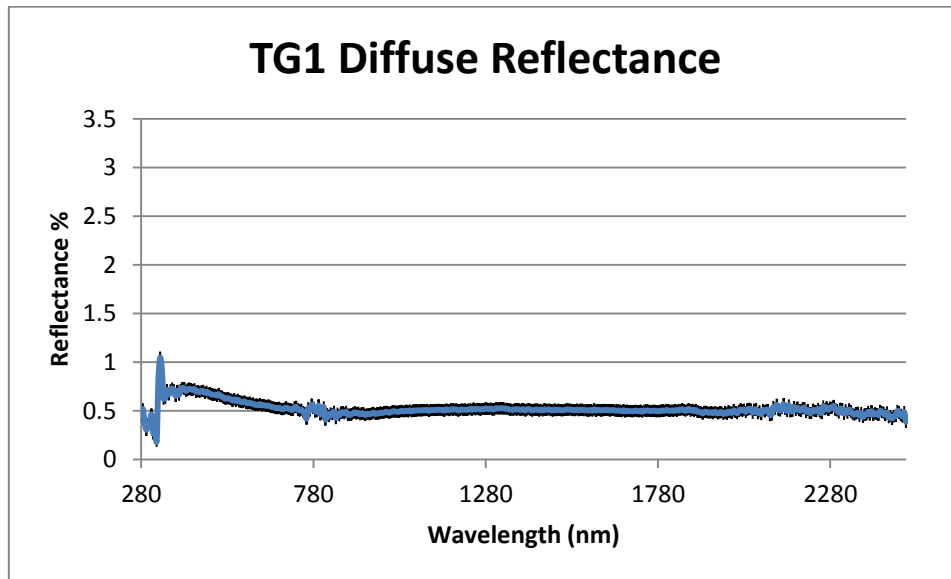


Figure 5. 4 Diffuse Reflectance

The resulting standard deviation for all the measurements of diffuse reflectance is equal to a mean of 0.075917 with a maximum of 0.267867 and a minimum value of 0.03911 along the wavelength range.

To obtain the most important value for our purpose we complete the evaluation subtracting the lower curve from the upper curve to obtain the specular reflectance which is reported in the following figure 5.5

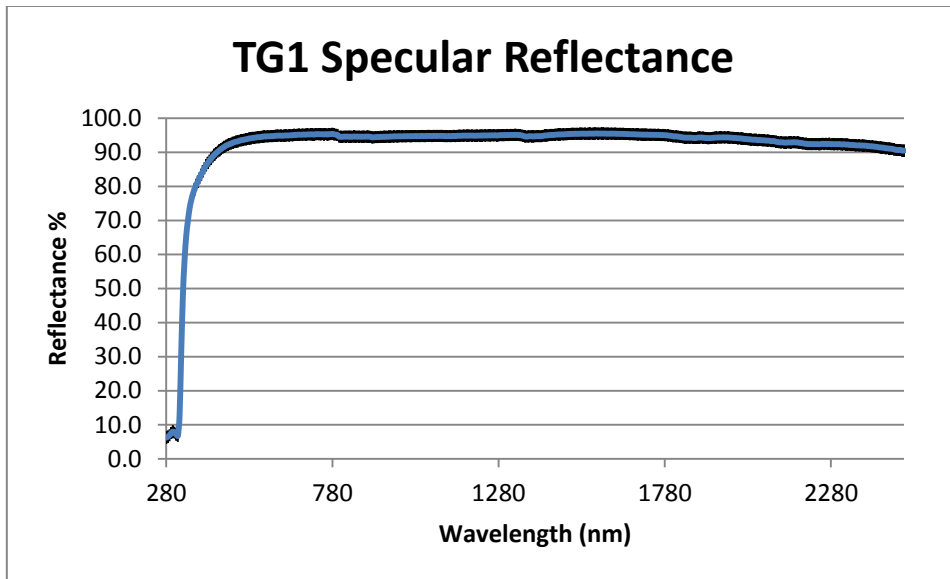


Figure 5. 5 Specular Reflectance

In the previous graph nothing seems to be changed from the values of the global reflectance but is slightly lower of exactly the values of the diffuse reflectance

While the raw measurement of TG2 is described in figure 5.6.

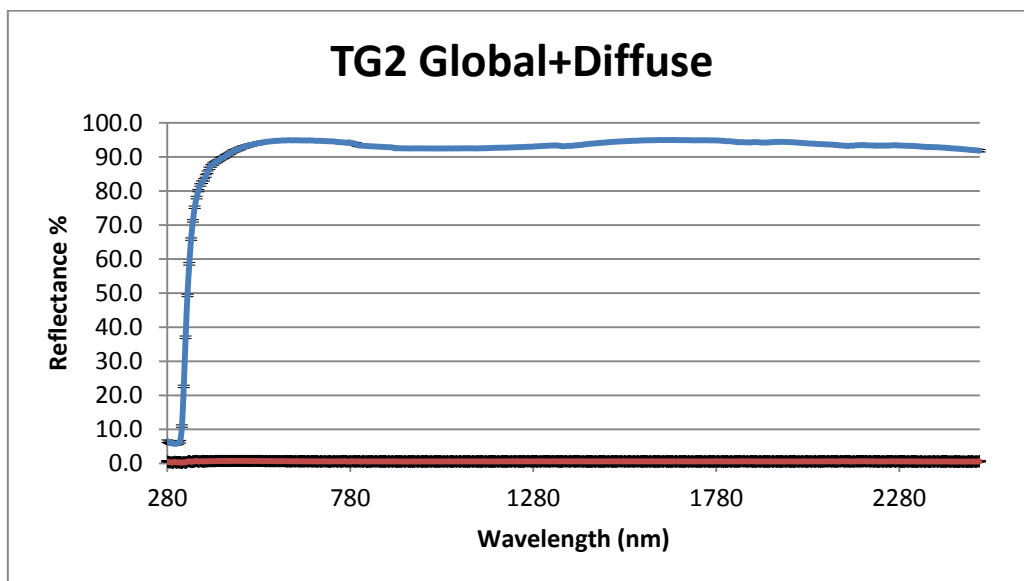


Figure 5. 6 TG2 Reflectance measurements

Using the same methodology above mentioned we obtained that the resulting standard deviation for the global reflectance measurements is equal to a mean of 0.394081 with a maximum of 1.007866 and a minimum value of 0.10266 along the wavelength range. It's clear, observing the graph, that almost all the incident radiation along the wavelength that goes from the upper limit 2500 nm, to

440 nm is reflected with a little scattering effect, after the 440 nm the mirror result in a complete opaque element till it reaches the 280 nm lower limit, in fact the reflectance drops very quickly.

The Diffuse Reflectance which is obtained removing the quarter of the integrating sphere is showed in figure 5.7.

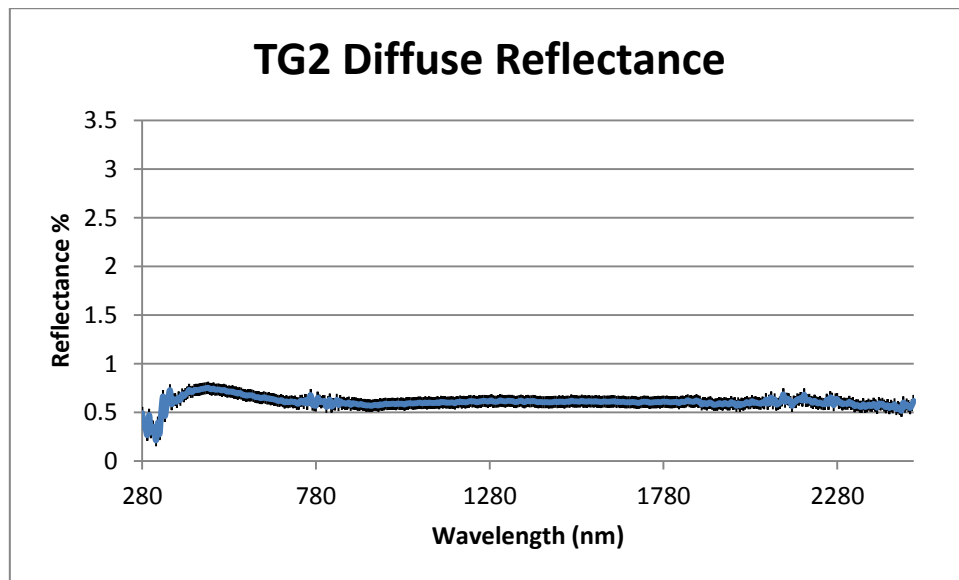


Figure 5. 7 Diffuse Reflectance

The resulting standard deviation for the diffuse reflectance measurements is equal to a mean of 0.061623 with a maximum of 0.039199 and a minimum value of 0.261434 along the wavelength range.

Always subtracting the lower curve from the upper curve we obtained the specular reflectance which is reported in the following figure 5.8.

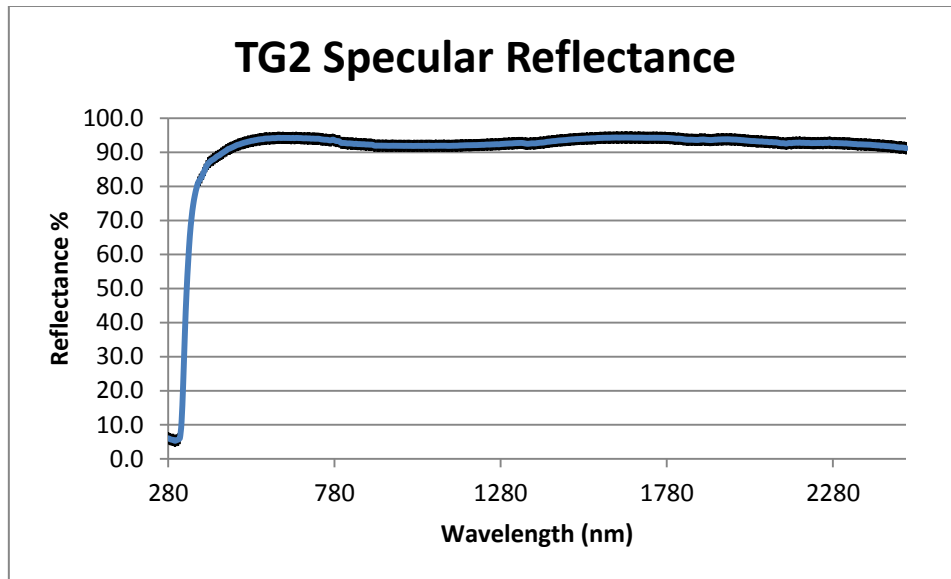


Figure 5. 8 Specular Reflectance

Following the procedure all the data collected was normalized first on the baseline automatically by the instrument and second by calculating the Solar Weighted Hemispherical Reflectance and using the specular reflectance curve it was possible to achieve also the Solar Weighted Specular Reflectance.

As it was previously exposed, the way to calculate the Solar weighted Hemispherical and specular reflectance is to normalize the entire reflectivity field with the solar spectrum at AM 1.5.

To achieve this result all the evaluation on the Mathcad Engineering Equation Software was implemented.

For each sample the values of the  $\rho_{SWH}$  and  $\rho_{SWS}$  were retrieved and then compared and averaged to obtain a single value to be inserted in the simulations.

The final values for these two typologies of thin glass mirrors for the Solar Weighted Hemispherical Reflectance are represented in the next figure 5.9.

While the final values for these two typologies of thin glass mirrors for the Solar Weighted Specular Reflectance are represented in the next figure 5.10.

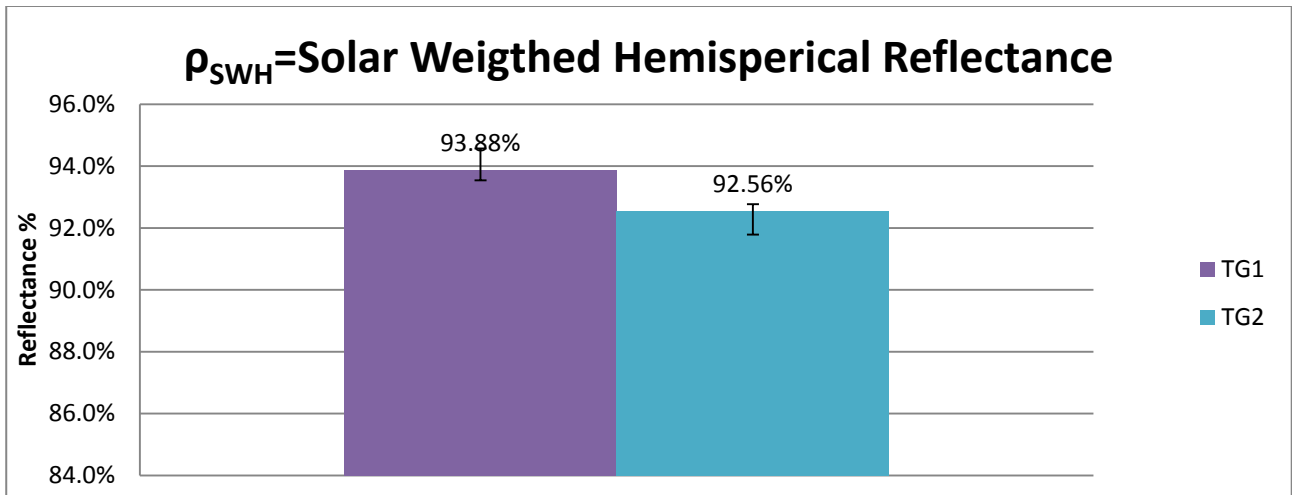


Figure 5. 9 Solar Weighted Hemispherical Reflectance

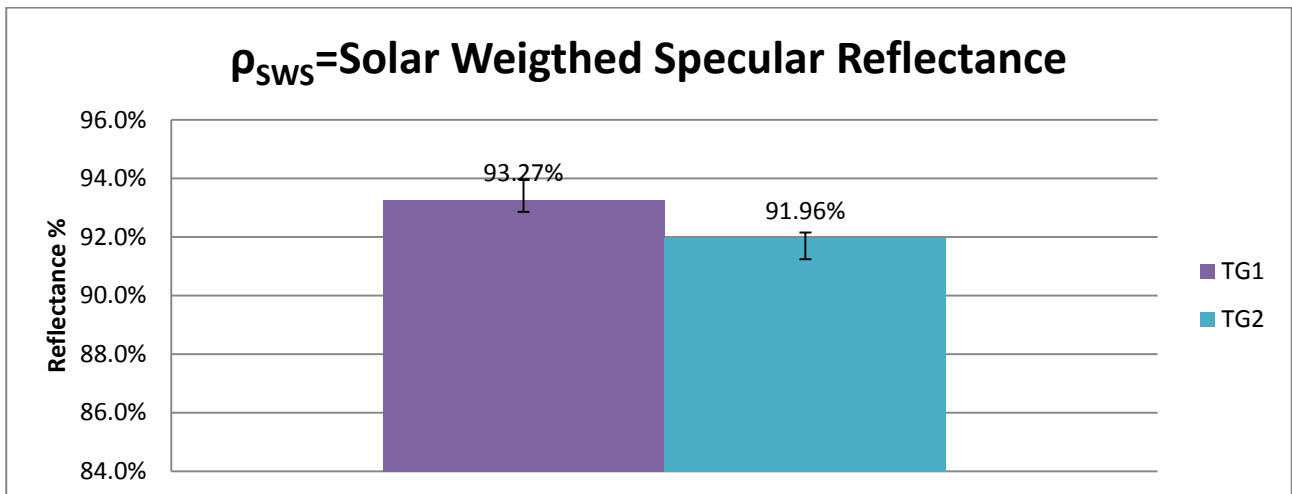


Figure 5. 10 Solar Weighted Specular Reflectance

In the upper graphs it's possible to deduce that the TG1 Mirror maintain the highest reflectance in the parts of the spectrum which contains the major contribute to the total solar radiation at AM 1.5 obtaining an averaged  $\rho_{SWH}$  and  $\rho_{SWS}$  of respectively 93.88% and 93.27%.

Although the TG2 mirror has a slightly lower reflectance it remains a high performance mirror with a  $\rho_{SWH}$  and  $\rho_{SWS}$  of respectively 92.56% and 91.96%.

### 5.1.2 Aluminum Mirrors

In the following are presented the spectrophotometer results for the Aluminum mirrors AL1 and AL2.

Silver has the highest reflectance, but has to be protected against weathering, which is expensive. Silver thin films are formed on a glass or polymeric substrates with additional corrosion-protection and reflectance enhancing coatings.

Aluminum is suitable for lower concentration factors or lower efficiency. Low-end products are simply anodized for corrosion protection.

For corrosion protection, high-end reflectors are coated with a reflective metal layer (silver or aluminum) and additional dielectric coatings are formed using physical deposition techniques such as reactive sputtering or evaporation and applying a transparent polymeric corrosion protection.

Depending upon how the structural support of the mirrors is provided, high winds can cause significant breakage. Their unweathered solar-weighted hemispherical reflectance is ~ 88 to 92% and their cost is ~ 15 to 40 \$/m<sup>2</sup>.



**Figure 5.11 Aluminum mirror AL1**

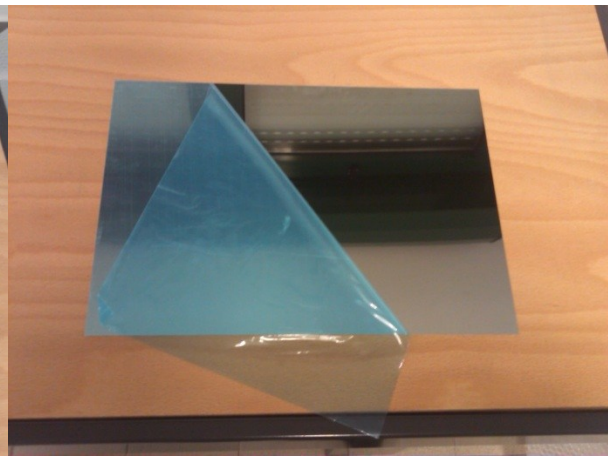


**Figure 5.12 Aluminum mirror AL2**

For each family were conducted a measurement campaign of ten measure for the global and ten measure for the diffuse reflectivity to achieve a good average of the standard deviation as done before for the TG1 and TG2 mirrors

The raw measurement of AL1 is described in figure 5.13.

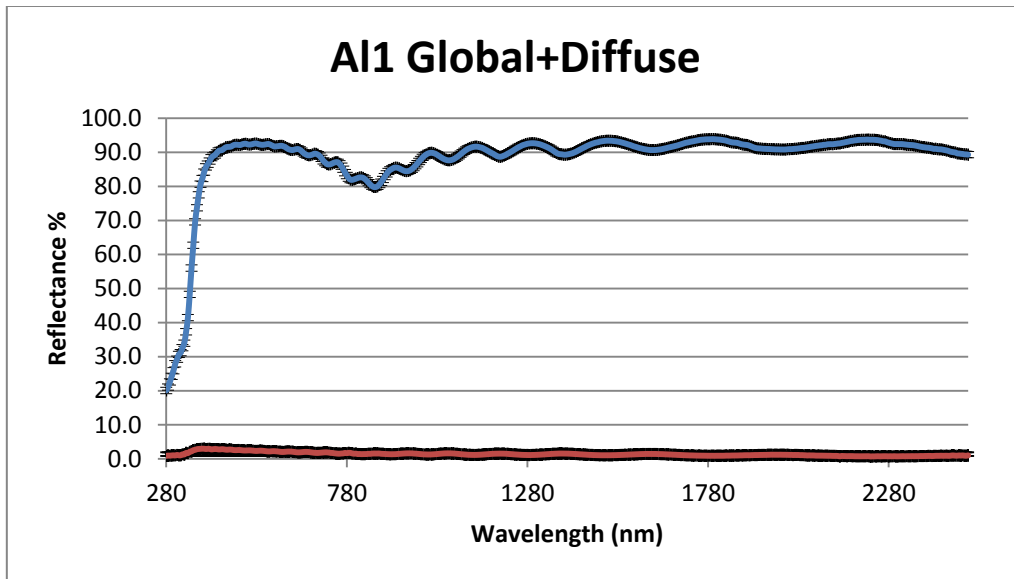


Figure 5. 13 Reflectance Measurements

For each sample was measured the Global Reflectance with the complete integrating sphere.

The resulting standard deviation for the global reflectance measurements is equal to a mean of 0.920682 with a maximum of 2.008495 and a minimum value of 0.124527 along the wavelength range.

The lowest curve is the Diffuse Reflectance which is obtained removing the quarter of the integrating sphere showed in the next figure 5.14.

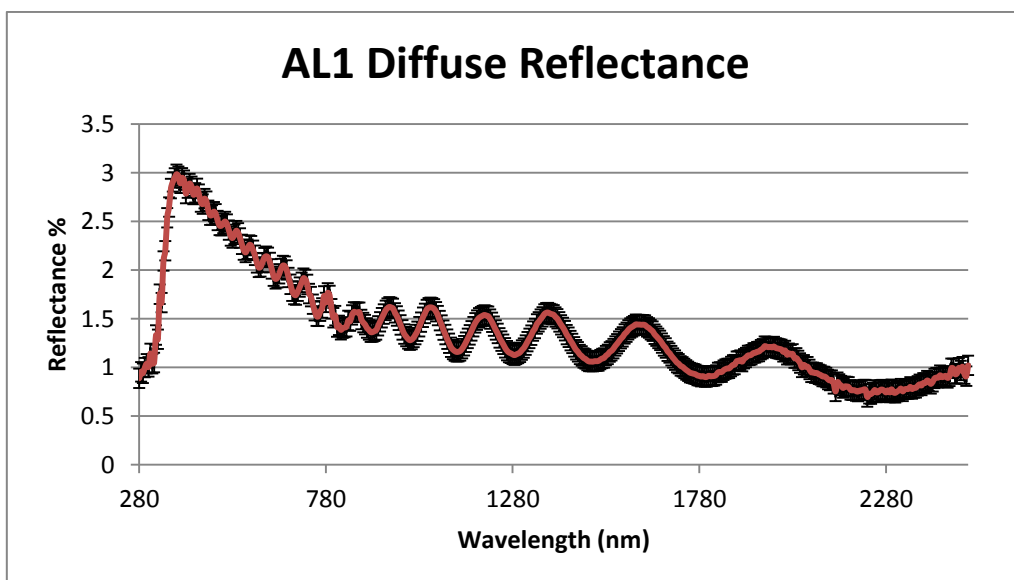


Figure 5. 14 Diffuse Reflectance

The resulting standard deviation for all the measurements of diffuse reflectance is equal to a mean of 0.148712 with a maximum of 0.44726 and a minimum value of 0.015296 along the wavelength range.

The specular reflectance obtained is showed in the following figure 5.15

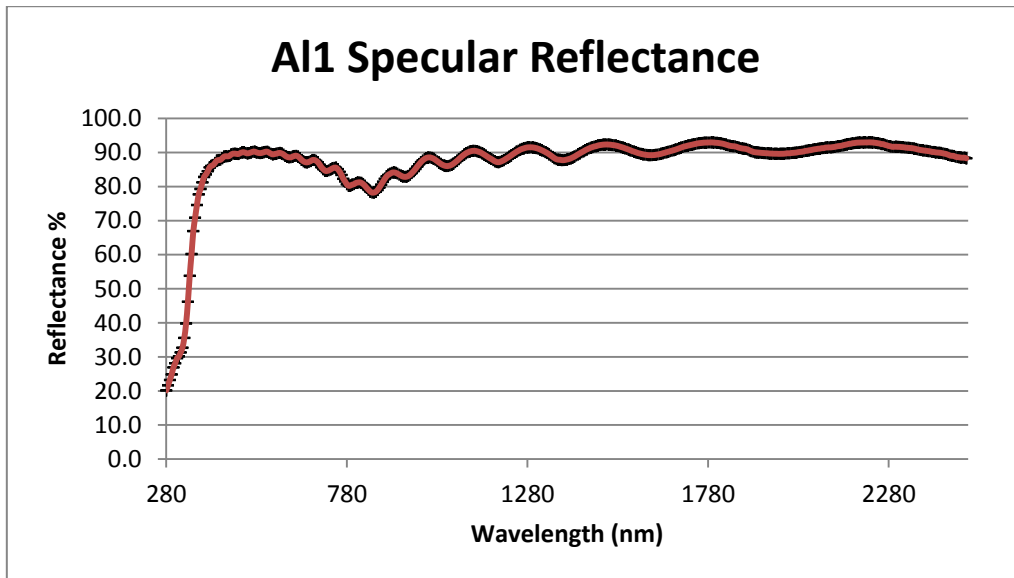


Figure 5. 15 Specular Reflectance

The raw measurement of AL2 is described in figure 5.16.

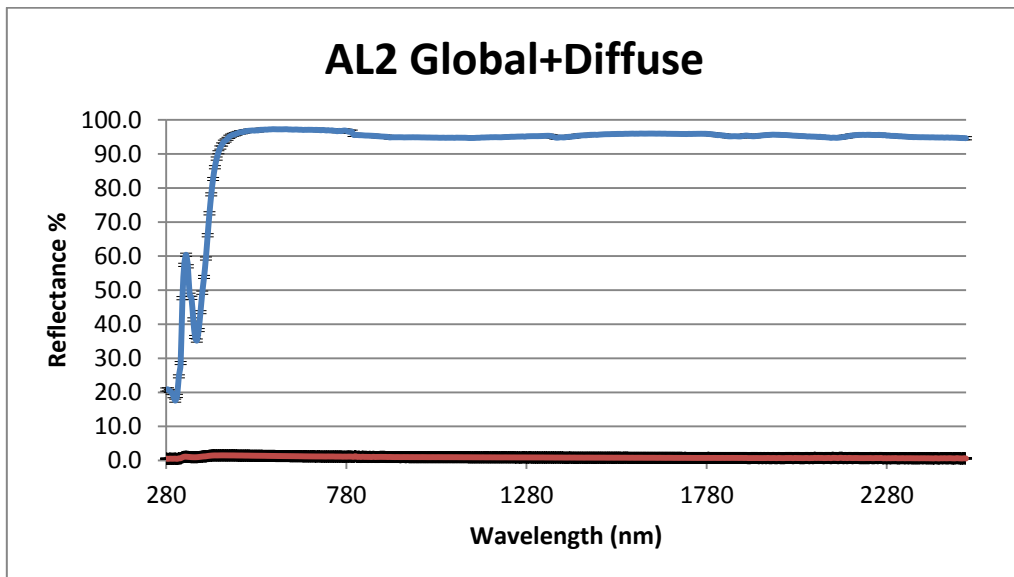


Figure 5. 16 TG2 Reflectance measurement

The resulting standard deviation for all the global reflectance measurements is equal to a mean of 0.460541 with a maximum of 0.080496 and a minimum value of 1.679228 along the wavelength range.

The Diffuse Reflectance obtained is showed in figure 5.17.

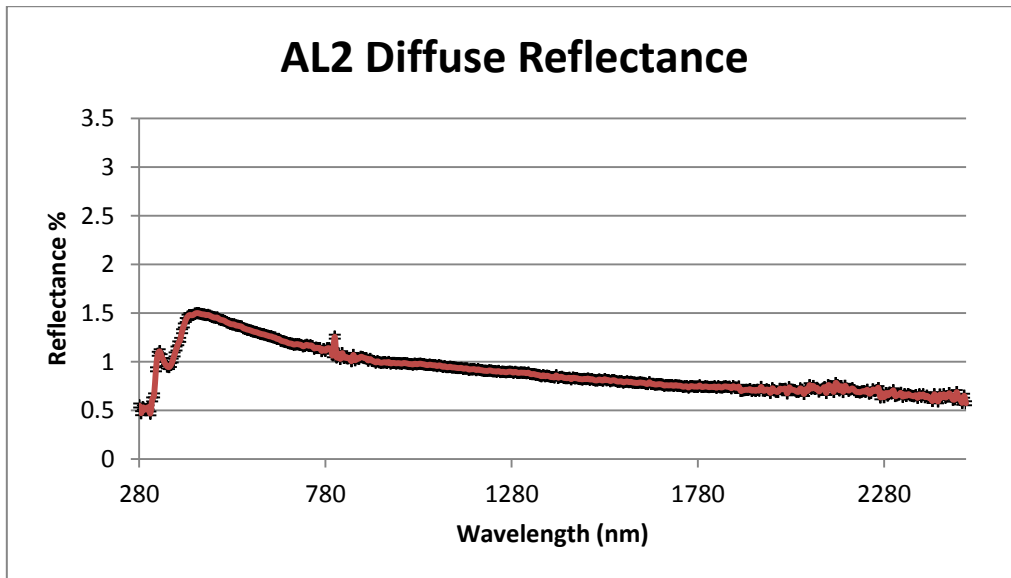


Figure 5. 17 Diffuse Reflectance

The resulting standard deviation for the above measurements is equal to a mean of 0.020431 with a maximum of 0.007162 and a minimum value of 0.226039 along the wavelength range.

The specular reflectance which is showed in the following figure 5.18.

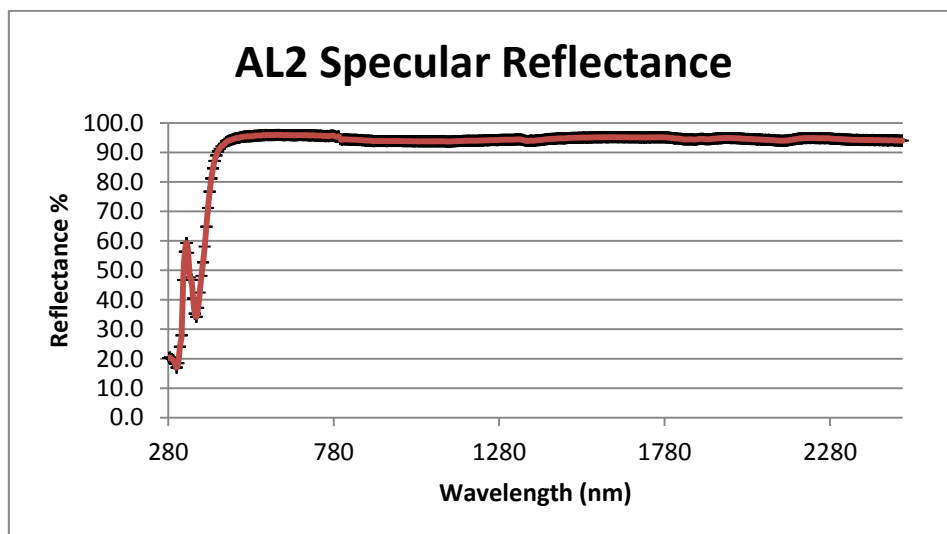


Figure 5. 18 Specular Reflectance

The final values for these two typologies of aluminum mirrors for the Solar Weighted Hemispherical Reflectance are represented in the next figure 5.19.

The final values for these two typologies of aluminum mirrors for the Solar Weighted Specular Reflectance are represented in the next figure 5.20.

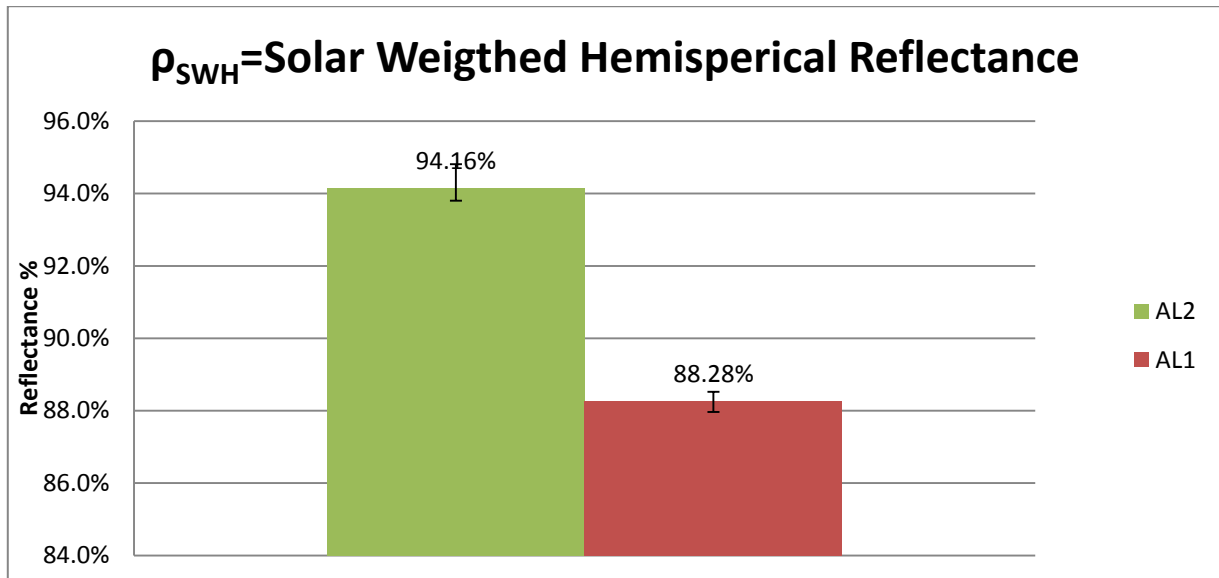


Figure 5. 19 Solar Weighted Hemispherical Reflectance

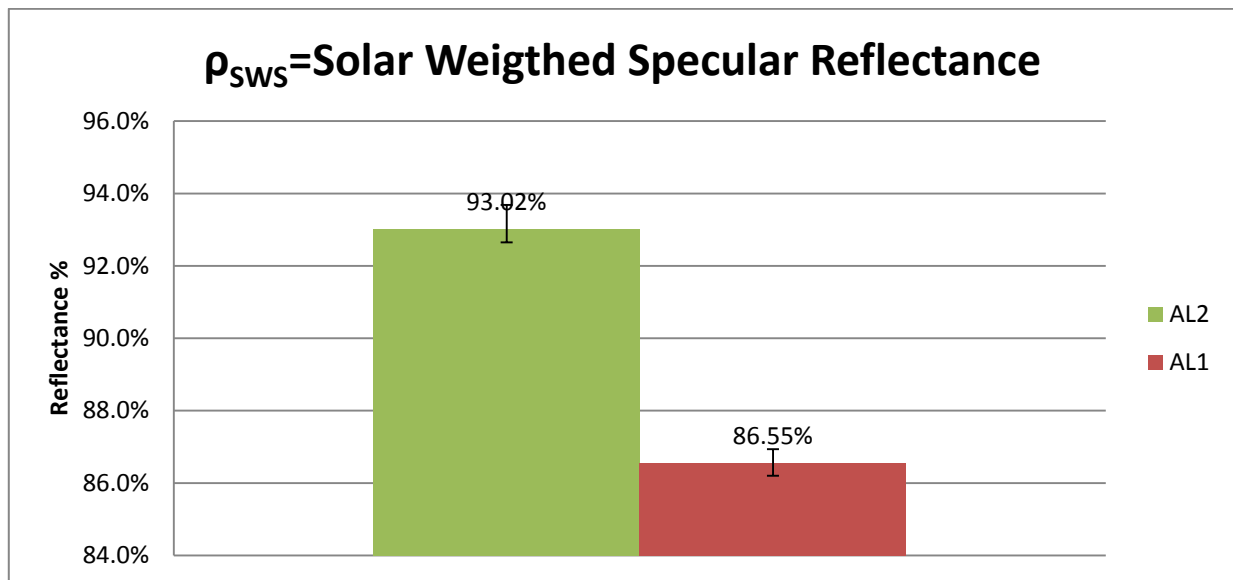


Figure 5. 20 Solar Weighted Specular Reflectance

In the upper graphs it's possible to deduct that the AL2 Mirror maintain the highest reflectance in the parts of the spectrum which contains the major contribute to the total solar radiation at AM 1.5 obtaining an averaged  $\rho_{SWH}$  and  $\rho_{SWS}$  of respectively 94.16% and 88.28%.

While the AL1 mirrors demonstrate a poor performance due to the sinusoidal behavior that maintain all over the wavelength range.

### 5.1.3 Polymeric film mirrors

Polymer reflector constructions are attractive for solar application because they minimize weight and cost and allow for ease of handling during manufacture, transport, and field installation. However, because polymers are significantly more permeable than glass to water, oxygen, and pollutants, corrosion of the metal reflective layer and subsequent loss in reflectance is a difficult problem that must be overcome (Schissel and Czanderna, 1980).

A number of advanced metalized polymer constructions have been developed (Jorgensen and Schissel, 1989; Scissel et al., 1994); these may have lifetime of 5 to 10 years depending on where they are used.

Their unweathered solar-weighted hemispherical reflectance is ~ 92 to 94%.

Uncertainty regarding commercial availability exist but cost estimates range from 15 to 45 \$/m<sup>2</sup>.

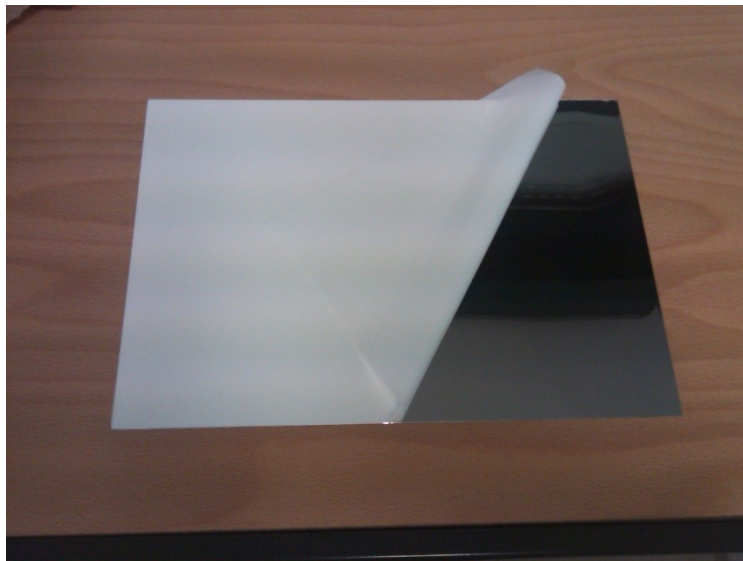


Figure 5. 21 PF1 mirror

In particular the results are summarized in the next figure 5.22

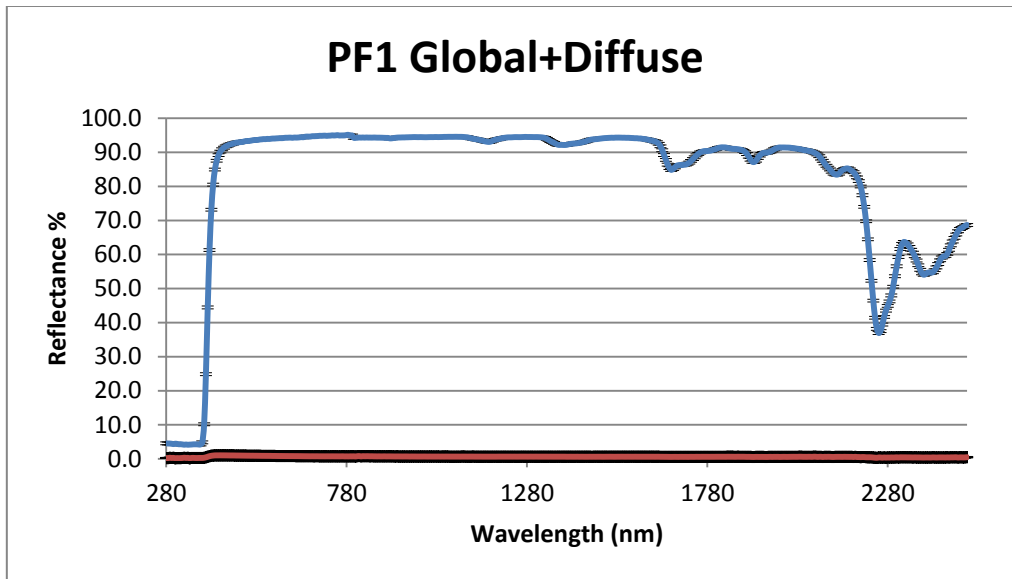


Figure 5. 22 PF1 Global+Diffuse

From the previous graph it's possible to analyze the behavior of this particular and innovative type of mirror more in depth. As it can be seen it has a cut off wavelength at about 2250 nm and at a value of about 380 nm. For the remaining part of the spectrum it maintains a slightly constant value.

The resulting standard deviation for all the measurements of global reflectance is equal to a mean of 0.413341 with a maximum of 0.846709 and a minimum value of 0.03455 along the wavelength range.

The Diffuse Reflectance obtained removing the quarter of the integrating sphere is showed in the next figure 5.23.

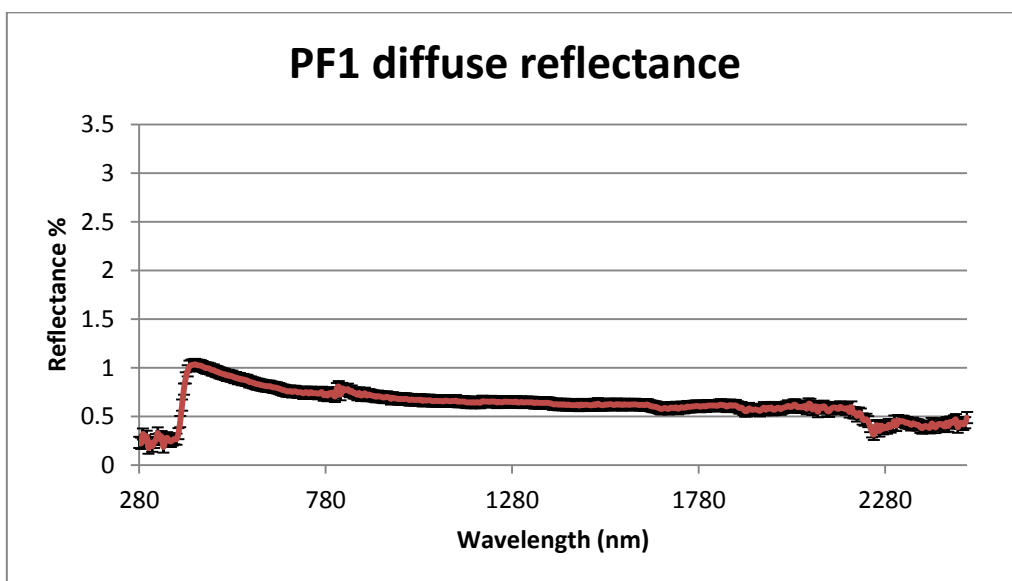


Figure 5. 23 Diffuse Reflectance

The resulting standard deviation for all the measurements of diffuse reflectance is equal to a mean of 0.148712 with a maximum of 0.44726 and a minimum value of 0.015296 along the wavelength range.

The specular reflectance is showed in the following figure 5.24

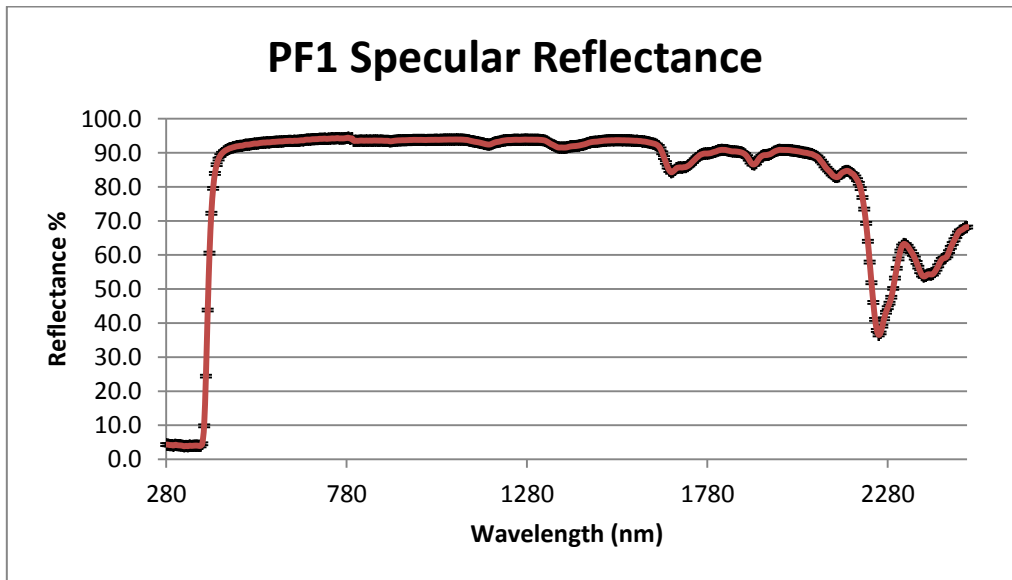


Figure 5. 24 Specular Reflectance

For what concern the second polymeric thin film mirror sample the same measurements were carried on, in particular the results are summarized in the next figure 5.25.

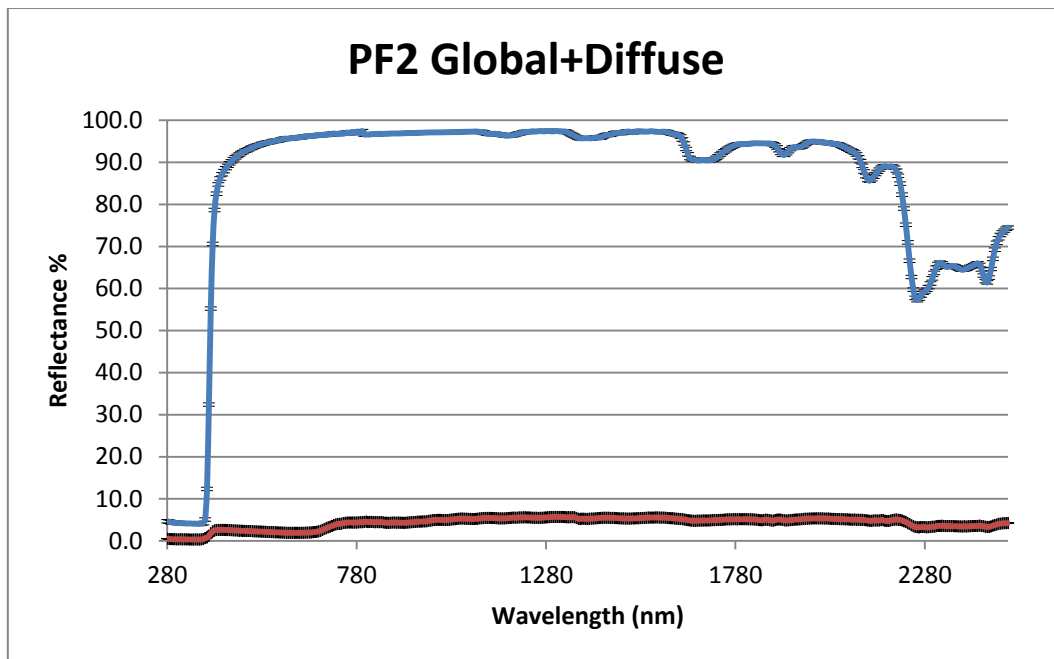


Figure 5. 25 PF2 Global+Diffuse

From the previous graph it's possible to observe the behavior of this particular and innovative type of mirror. As it can be seen it has a cut off wavelength at about 2250 nm and at a value of about 390 nm. For the remaining part of the spectrum it maintains a slightly constant value.

The resulting standard deviation for all the measurements of global reflectance is equal to a mean of 0.028502 with a maximum of 0.101275 and a minimum value of 0.007687 along the wavelength range.

The Diffuse Reflectance obtained is showed in the next figure 5.26.

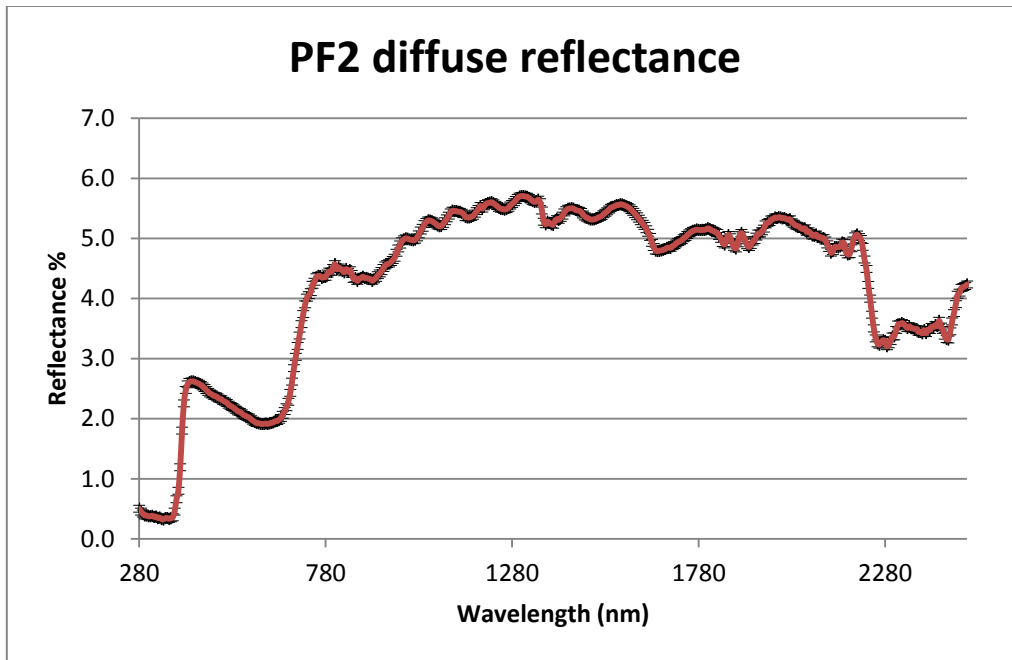


Figure 5. 26 Diffuse Reflectance

The resulting standard deviation for all the measurements of diffuse reflectance is equal to a mean of 0.023208 with a maximum of 0.064102 and a minimum value of 0.001148 along the wavelength range.

We obtained the specular reflectance which is showed in the following figure 5.27

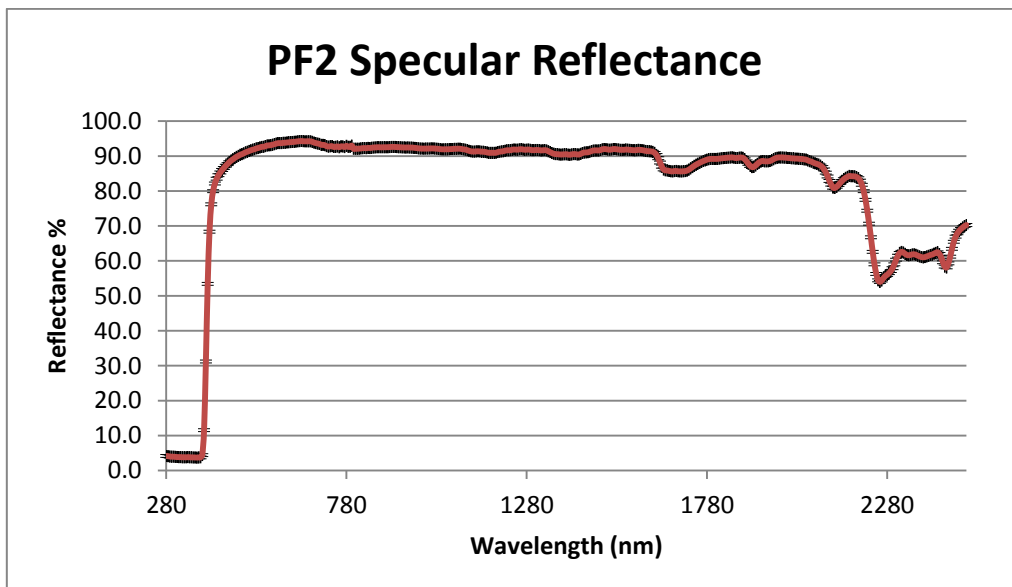


Figure 5. 27 Specular Reflectance

The final values for these two typologies of polymeric mirrors for the Solar Weighted Hemispherical Reflectance are represented in the next figure 5.28.

While the final values for these two typologies of polymeric film mirrors for the Solar Weighted Specular Reflectance are represented in the next figure 5.29.

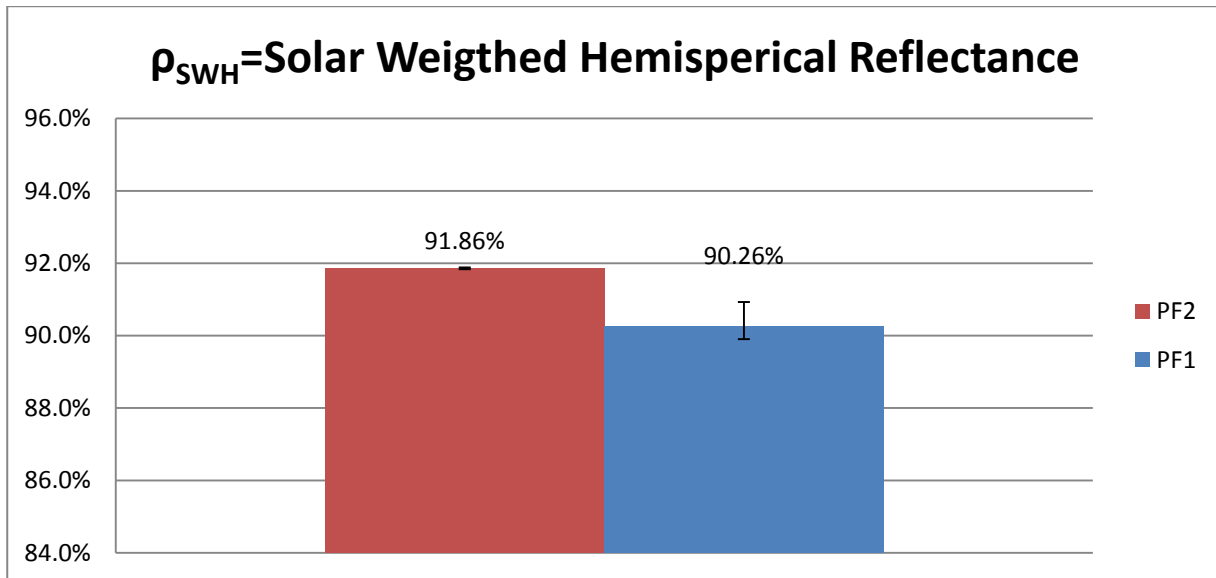


Figure 5. 28 Solar Weighted Hemispherical Reflectance

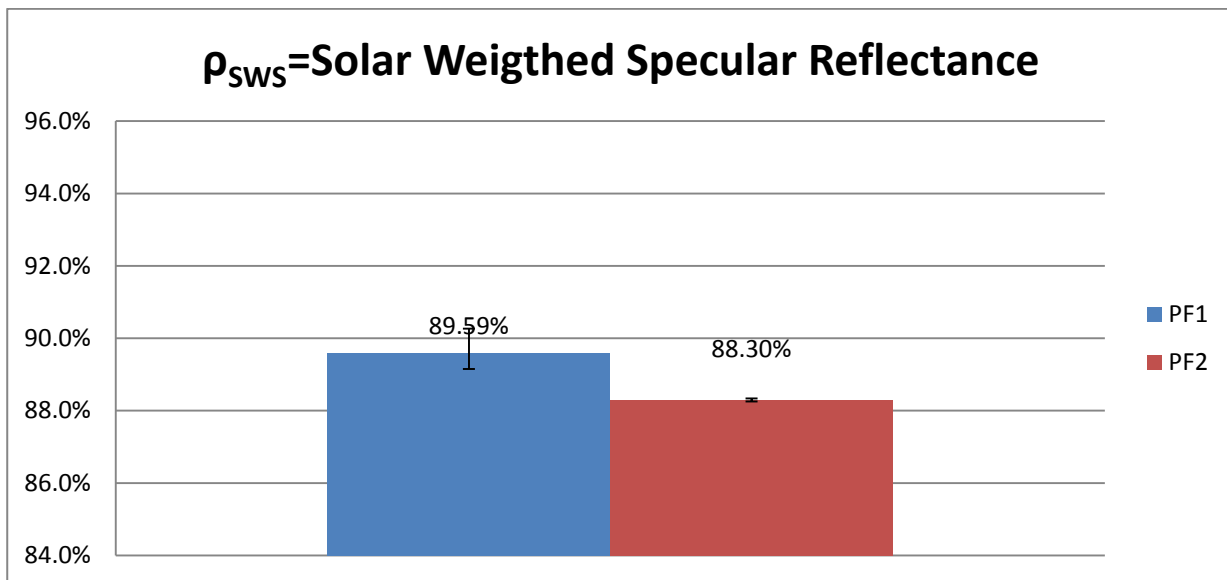


Figure 5. 29 Solar Weighted Specular Reflectance

In the above graph it's clear that the major quantity of diffuse reflectance lead to a very low specular reflectance compared with the PF1 sample

To summarize the results obtained till now we propose a comparison graph where are represented the different mirrors weighted reflectance (Figure 5.30 and 5.31).

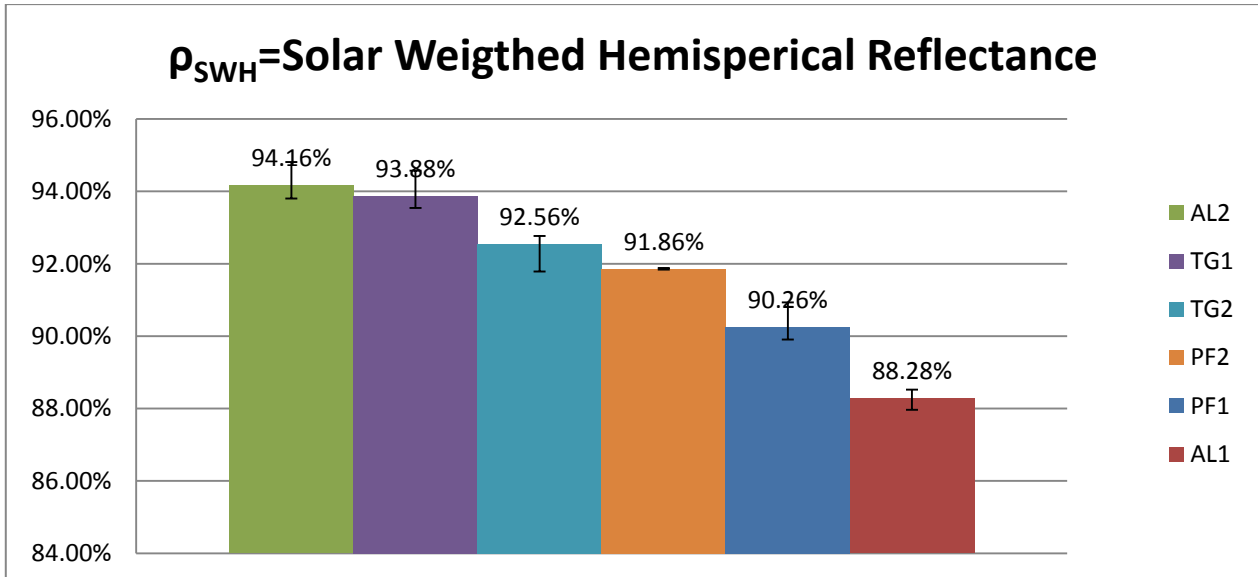


Figure 5. 30 Summary of the different Solar Weighted Hemispherical Reflectance

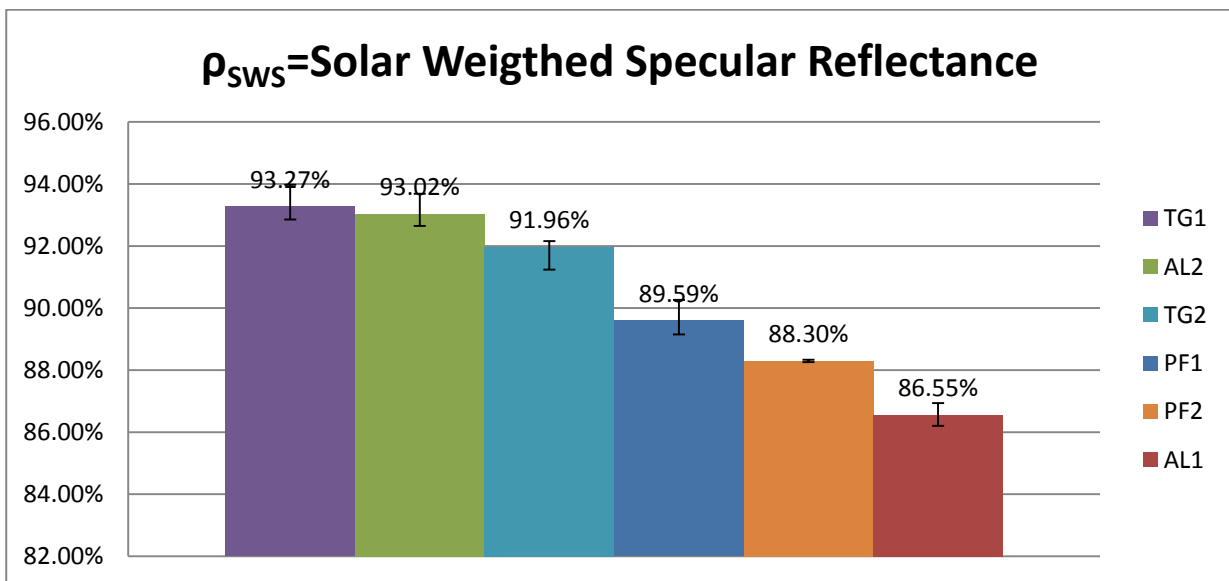


Figure 5. 31 Summary of the different Solar Weighted Specular Reflectance

What appears different between the first and the second graph is the rank of the Aluminum Mirror type 2 which results with a Hemispherical Reflectance of 94.16% making this mirror the best reflector of the solar irradiance, but taking into account the specular reflectance it has a value slightly lower than the Thin Glass mirror type 1.

This is significant because it means that the thin glass mirror has a diffuse reflectance very low that makes it the best mirror for CSP application.

Of course we are experimenting a difference of just 0.25% but in a more extensive way in the total cycle of production it involves a loss of produced energy as it can be seen in the following equation.

The equation for the absorbed solar radiation is:

$$Q_{Absorbed} = DNI \cdot \cos\theta \cdot IAM \cdot RowShadow \cdot EndLoss \cdot \eta_{mirrors} \cdot \eta_{HCE}$$

where

- $Q_{Absorbed}$  = solar radiation absorbed by the receiver tubes [W/m<sup>2</sup>]
- DNI = direct normal insolation [W/m<sup>2</sup>]
- $\theta$  = angle of incidence [deg]
- IAM = incidence angle modifier [-]
- RowShadow = performance factor that accounts for mutual shading of parallel collector rows during early morning and late evening [-]
- EndLoss = performance factor that accounts for losses from ends of HCEs [-]
- $\eta_{mirrors}$  = efficiency that accounts for losses due to mirror optics and imperfections [-]
- $\eta_{HCE}$  = HCE efficiency that accounts for losses due to HCE optics and imperfections [-]

Thus, the solar radiation absorbed by the receiver tubes is directly proportional to the mirror efficiency, described in the following equation.

$$\eta_{mirrors} = \sum_{i=1}^{NumCol} ColFrac_i \cdot TrkTwstErr_i \cdot GeoAcc_i \cdot MirRef_i \cdot MirCln_i$$

where

- NumCol = the number of collector types in the field
- ColFrac = the fraction of collector type in the field
- TrkTwstErr = twisting and tracking error associated with the collector type
- GeoAcc = geometric accuracy of the collector mirrors
- MirRef = mirror reflectivity
- MirCln = mirror cleanliness

## 5.2 VASRA Reflectance Measurements

The second part of our research consists of measuring the variation of specular reflectance with the Variable Angle Specular Reflectance Accessory.

Were conducted several measurement on the samples; in particular for a matter of time three measurements for each sample with the angle variation from  $20^\circ$  to  $70^\circ$  with a step of  $5^\circ$ , so we had ten measurements for each mirror repeated three times.

Due to the fact that we didn't own a reference mirror all the measurements has a lack of base measurement so they are not comparable one on another.

With the DRA we previously obtained the values of solar weighted specular reflectance at  $6^\circ$  from the normal to the sample surface.

Predicting the value of specular reflectance at  $6^\circ$  with the previous method allow us to obtain a correction number to scale up the predicted value with the known specular reflectance.

This method due to the high linearity of behavior of the mirrors in the range from  $20^\circ$  to  $70^\circ$  gave us the approximate behavior of the sample even in the range uncovered by the machine between  $6^\circ$  and  $20^\circ$  obtaining a measurement in absolute value.

To use this particular accessory was necessary to cut the mirror samples in several strips.

The major problem encountered was how to treat the different materials without:

1. Scratching the samples;
2. Bending the samples;
3. Cracking the samples.

In order to cut the thin glass mirrors we tried the water cutting machinery, but the result was, due to the high pressure on the sample, a completely cracked mirror.

Finally we achieved the best result using a diamond glass cutter. The two typologies of thin mirrors responded in different ways to the cutting procedure.

The TG1 sample was the most fragile and even if a very tiny pressure was applied on the surface the edges of the cut presented micro-jagged and chipped cut lines, but finally a pretty good accuracy and linearity.

While for the TG2 sample we experimented no problem at all while cutting.

For the AL1, AL2, and PF samples we found the best ways to cut them with a numeric controlled aluminum cutting machinery.

In every attempt we made the problem of this type of machinery was that, usually this machinery is used to cut very thick aluminum sheets and are not properly suitable for such thin aluminum sheets.

During the first try we tested bending problems on the strip cut, which resulted in a non-suitable sample to be inserted in the experimental measurement with the spectrophotometer.

The PF sample is usually applied on a thin aluminum sheet that allows this material to achieve the necessary mechanical properties to be installed on the parabolic trough.

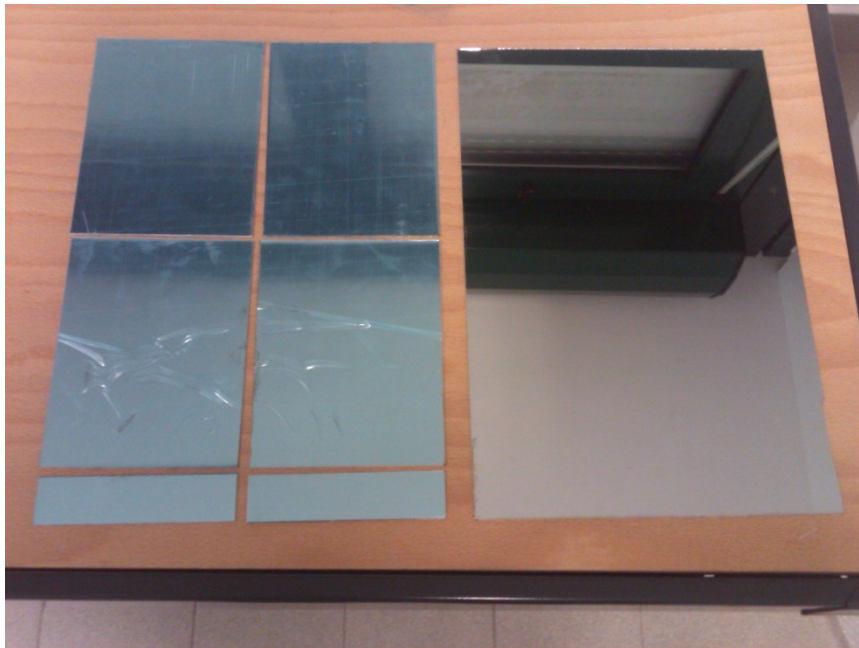
Being that the aluminum sheet was cut directly on site they use a laser cutter before applying the film, but after the deposition of the polymeric film it had some problems during further cutting procedures.

To obviate the problem we used another thin (1mm) aluminum sheet on the sample to give stiffness to the mirror, to obtain a clean cut.

Here in the following are some pictures of the cutting procedure.



Picture 5. 1 Some shots while cutting the aluminum mirrors and the PF mirror



Picture 5. 2 Example of cutting methodology

### 5.2.1 Thin Glass Mirrors

As previously seen in the 5.1 subchapter this family holds the first and third highest value of specular reflectance of all the typologies of mirrors.

As said before by closely analyzing without a reference mirror it's impossible to evaluate the baseline of the VASRA measurements, so we collected all the results using the zero line as baseline correction.

The Specular reflectance in all the samples gave us all the same behavior along the spectrum. From the first collected curve at 20° (which is the lowest) till the 70° curve.

Starting with TG1 we obtained the following curves reported in figure 5.32.

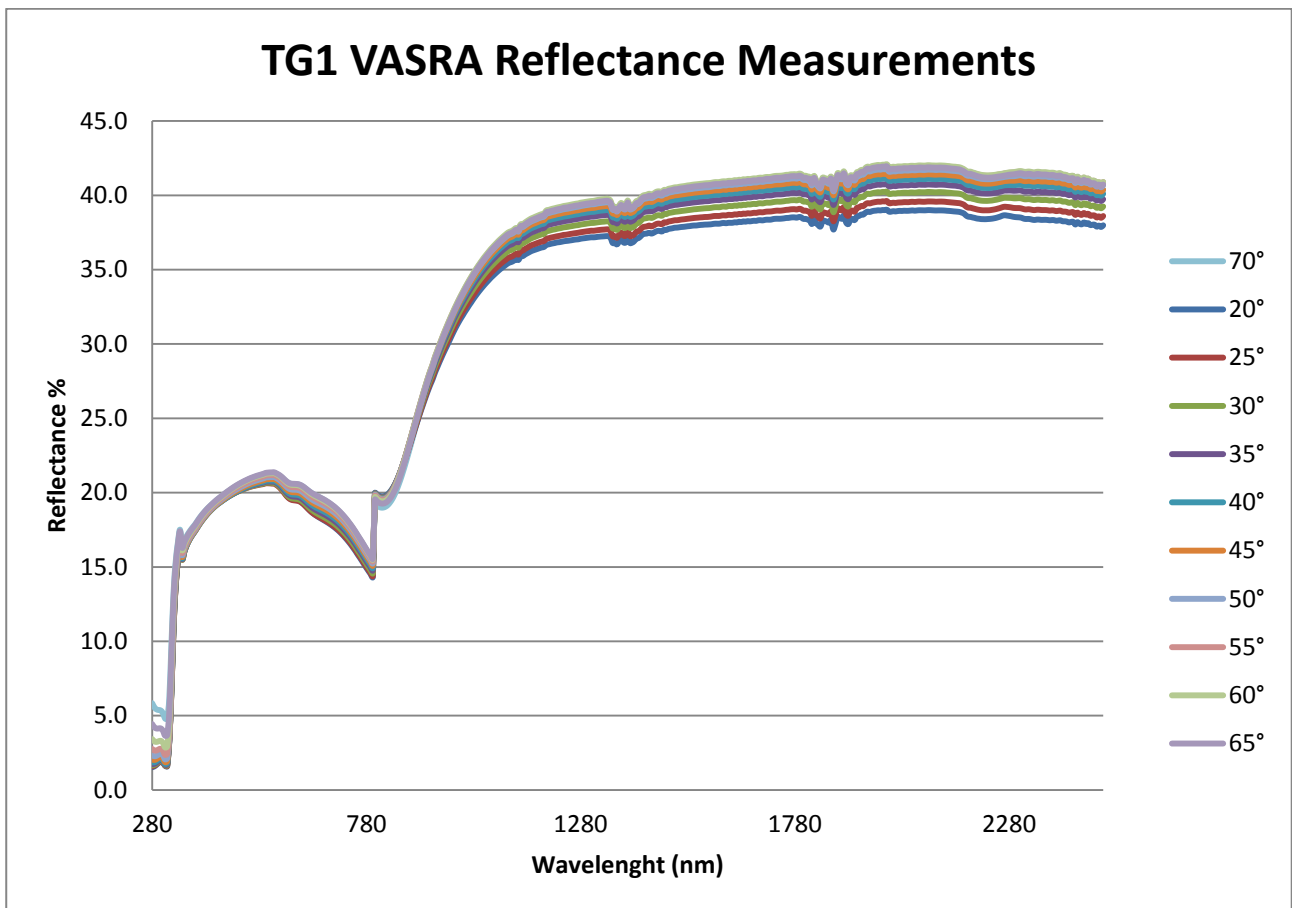


Figure 5. 32 VASRA Reflectance Measurements for TG1 Samples

In the next table are summarized the values of standard deviation for these measurements with values of minimum, maximum and average.

	20°	25°	30°	35°	40°	45°	50°	55°	60°	65°	70°
mean	0.0511	0.0387	0.0467	0.0518	0.0410	0.0265	0.0226	0.0161	0.0175	0.0090	0.0195
min	0.0005	0.0006	0.0009	0.0009	0.0004	0.0010	0.0006	0.0007	0.0004	0.0005	0.0015
max	0.1293	0.1117	0.1219	0.1244	0.1050	0.0980	0.0676	0.0735	0.0786	0.0864	0.0751

Table 5. 2 Values of Standard Deviation for TG1 samples

It is noticeable that all the values obtained with the spectrophotometer lead us to see an increasing value of R% with the increasing of the values of the incidence angle.

In the same way we conducted the experimentation on the TG2 samples obtaining the measurements in the following figure 5.33.

What can immediately be seen is the similarity of the two behaviors all along the spectrum which is the same behavior these samples had with the integrating sphere measurements.

They differ in the order of 0.05% in the average, starting obviously with two different values of specular reflectance.

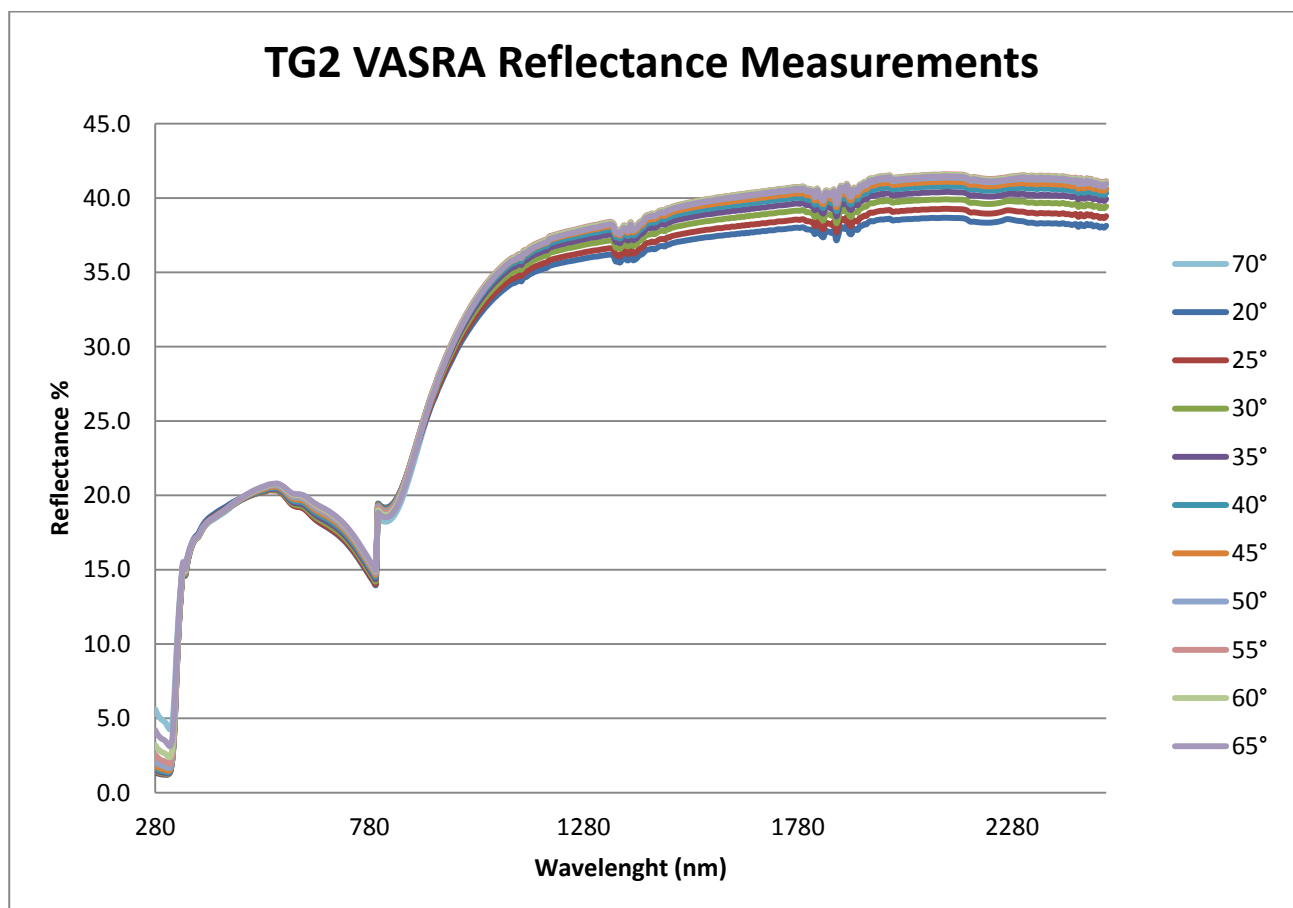


Figure 5. 33 VASRA Reflectance measurements for TG2 Samples

Here in the following table 5.3 the values of the standard deviation for the TG2 sample.

	20°	25°	30°	35°	40°	45°	50°	55°	60°	65°	70°
mean	0.0261	0.0318	0.0347	0.0388	0.0459	0.0518	0.0589	0.0617	0.0702	0.0777	0.0789
min	0.0020	0.0071	0.0032	0.0046	0.0049	0.0022	0.0060	0.0116	0.0141	0.0088	0.0078
max	0.1034	0.1102	0.1231	0.1359	0.1553	0.1742	0.1903	0.1991	0.1990	0.2288	0.2293

Table 5. 3 Values of Standard Deviation for TG2 samples

In order to evaluate the differences between the behavior of these two mirrors the Solar Weighted Specular Reflectance for each value of the incident angles was calculated.

Unfortunately without any reference mirrors all the results are presented as a relative value to allow a better comparison between the mirrors. The results are represented in the following two figures 5.34 and 5.35.

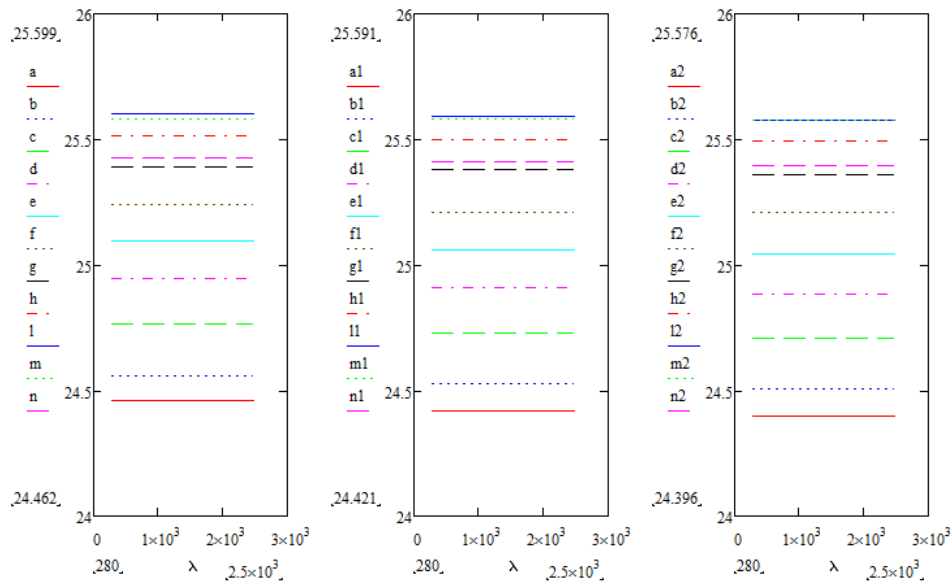


Figure 5. 34 Solar Weighted Specular Reflectance at different angles of incidence for TG1 Samples:  
a=20°,b=25°,c=30°,d=35°,e=40°,f=45°,g=50°,h=55°,i=60°,m=65°,n=70°

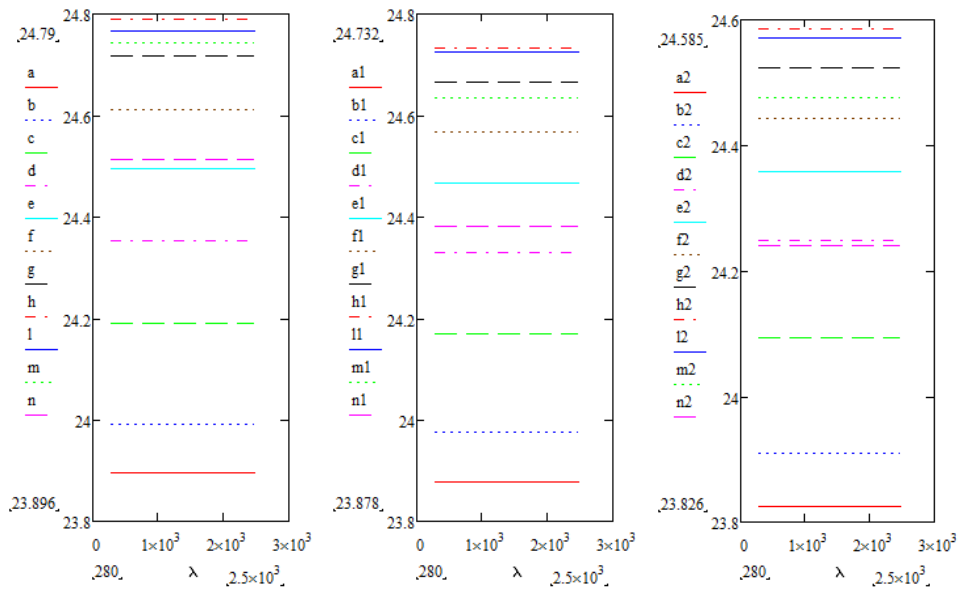


Figure 5.35 Solar Weighted Specular Reflectance at different angles of incidence for TG2 Samples: a=20°,b=25°,c=30°,d=35°,e=40°,f=45°,g=50°,h=55°,l=60°,m=65°,n=70°

Positioning all the points obtained after the normalization it is possible to draw the graphs that give the idea of the behavior of these two types of mirror.

In figure 5.36 the TG1 mirror behavior is summarized evaluating its angular response as a ratio between its starting value at 20° and its ending value at 70°.

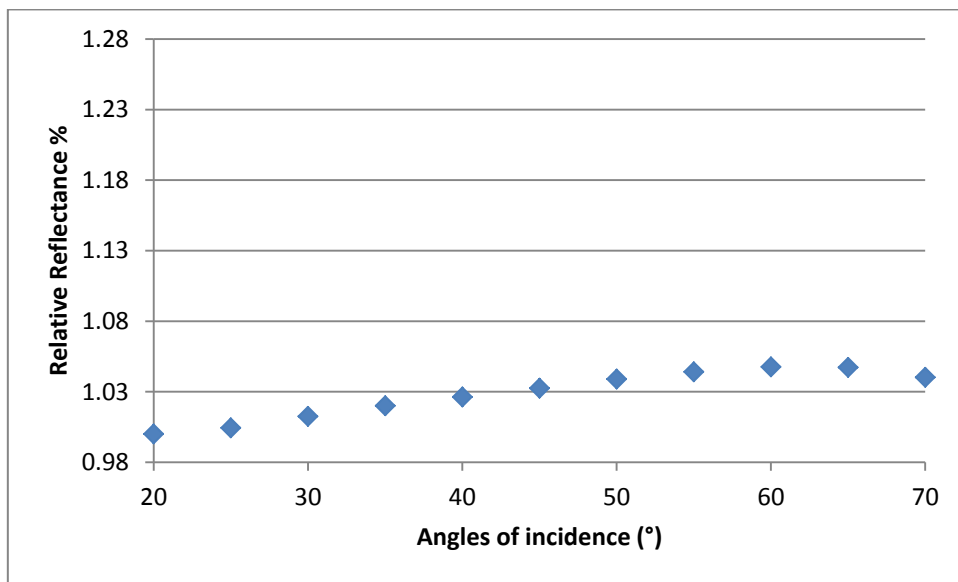


Figure 5.36 Reflectance Vs Angle of Incidence

While in figure 5.37 the TG2 mirror behavior is represented.

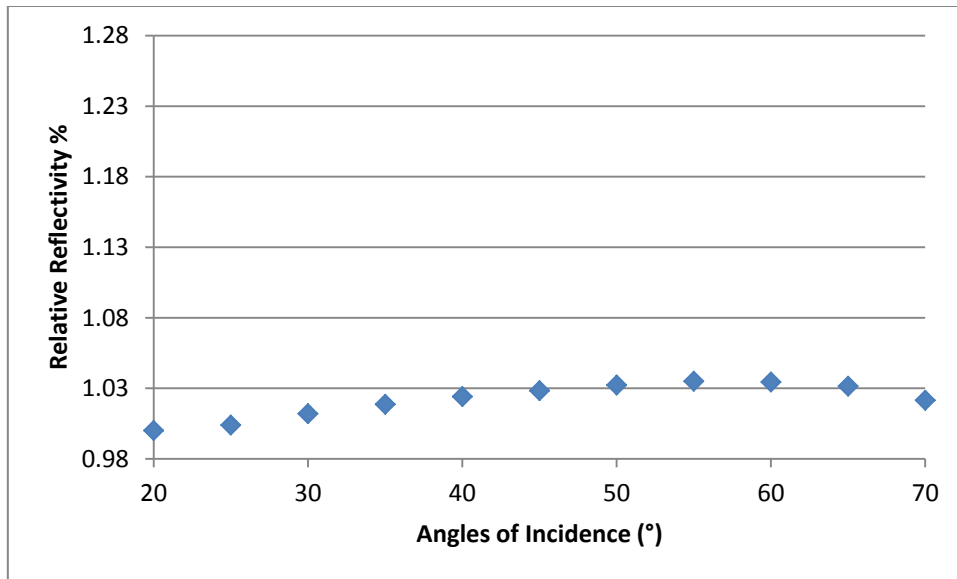


Figure 5.37 Reflectance Vs Angle of Incidence

Then a comparison between the two mirrors in figure 5.38 is reported.

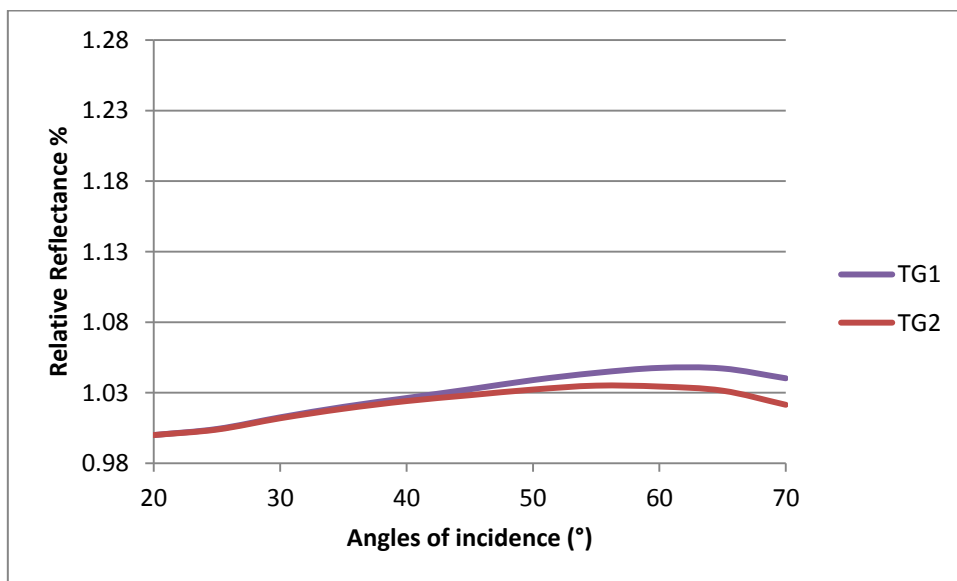


Figure 5.38 TG1 Mirror Vs TG2 Mirror

It is noticeable that TG1 and TG2 have the same behavior along the angles of incidence but the first increases the value of its reflectance from the 20° measurements in the order of 4.761 % at 60° while the TG2 reaches at the maximum an increased value of 3.502 % at 55° then they fall.

Using the method described at the beginning of this chapter it was possible to obtain the linear correlation between the specular reflectance obtained with the DRA and the relative values obtained with the VASRA.

In the next fig. 5.39 are represented the presumed values of reflectance varying the incidence angle.

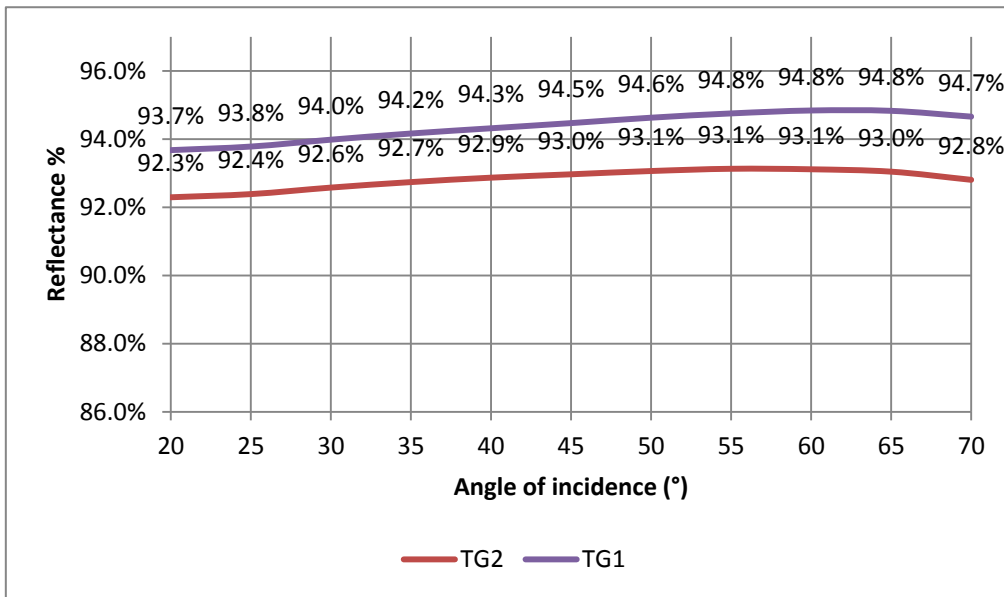


Figure 5.39 Comparison between the two thin glass mirrors

### 5.2.2 Aluminum Mirrors

As previously seen in the 5.1 subchapter this family holds the second and the latter value of specular reflectance of all the typologies of mirrors.

The Specular reflectance in all the samples gave us all the same behavior along the spectrum. From the first collected curve at 20° (which is the lowest) till the 70° curve.

Starting with AL1 we obtained the following curves reported in figure 5.40.

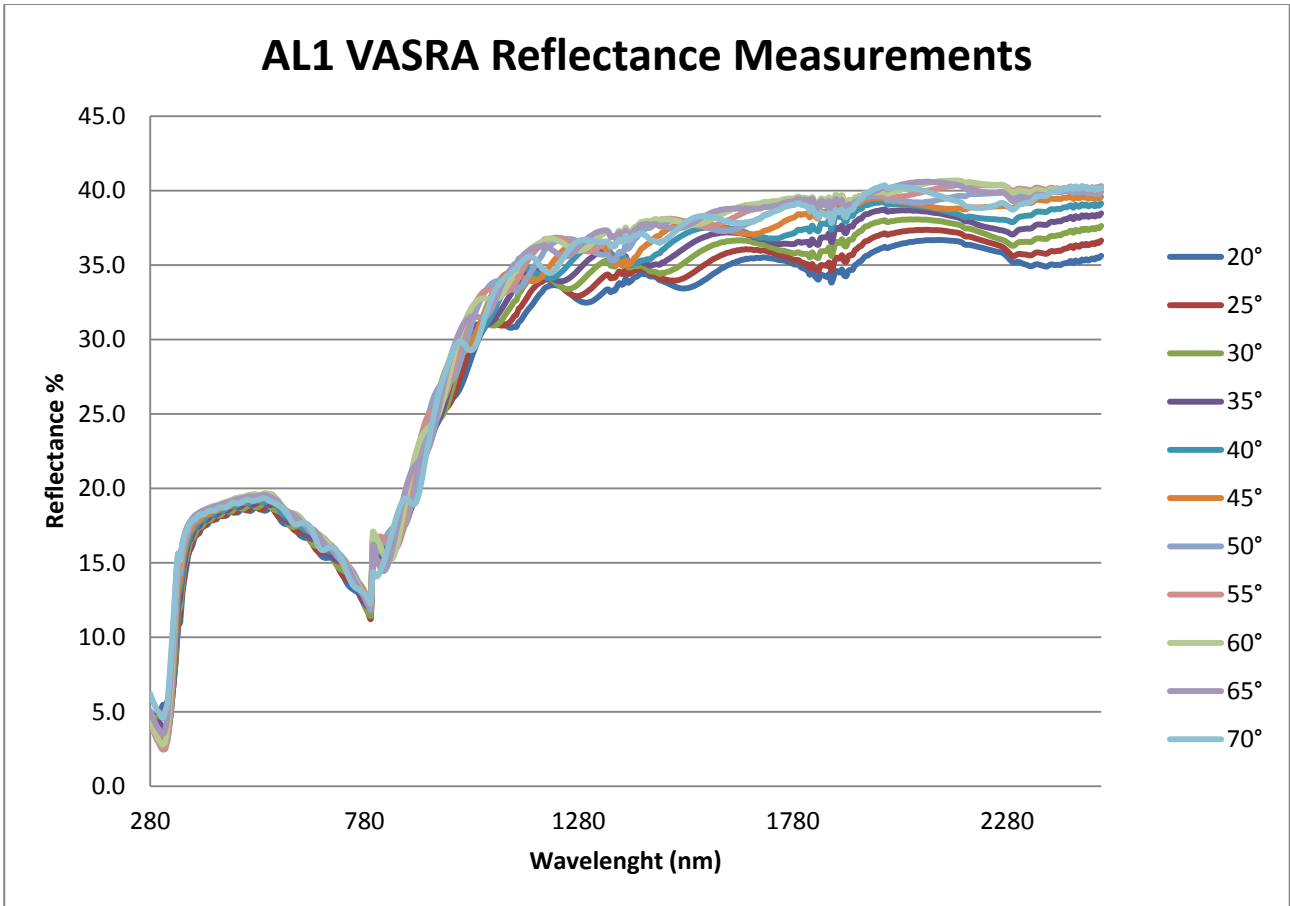


Figure 5. 40 VASRA Reflectance Measurements for AL1 Samples

In the next table 5.4 are summarized the values of standard deviation for these measurements with values of minimum, maximum and average.

	20°	25°	30°	35°	40°	45°	50°	55°	60°	65°	70°
mean	0.0376	0.0300	0.0596	0.0517	0.0336	0.0454	0.0402	0.0388	0.0334	0.0238	0.0113
min	0.0033	0.0014	0.0003	0.0034	0.0029	0.0043	0.0033	0.0080	0.0011	0.0010	0.0000
max	0.0827	0.0870	0.2166	0.1872	0.1077	0.1711	0.1499	0.1636	0.2176	0.1688	0.0443

Table 5. 4 Values of Standard Deviation for AL1 samples

It is noticeable that all the values obtained with the spectrophotometer lead us to see an increasing value of R% with the increasing of the values of the incidence angle.

In the same way we conducted the experimentation on the AL2 samples obtaining the measurements in the following figure 5.41.

What can immediately be seen is the similarity of the two behaviors all along the spectrum which is the same behavior these samples had with the integrating sphere measurements.

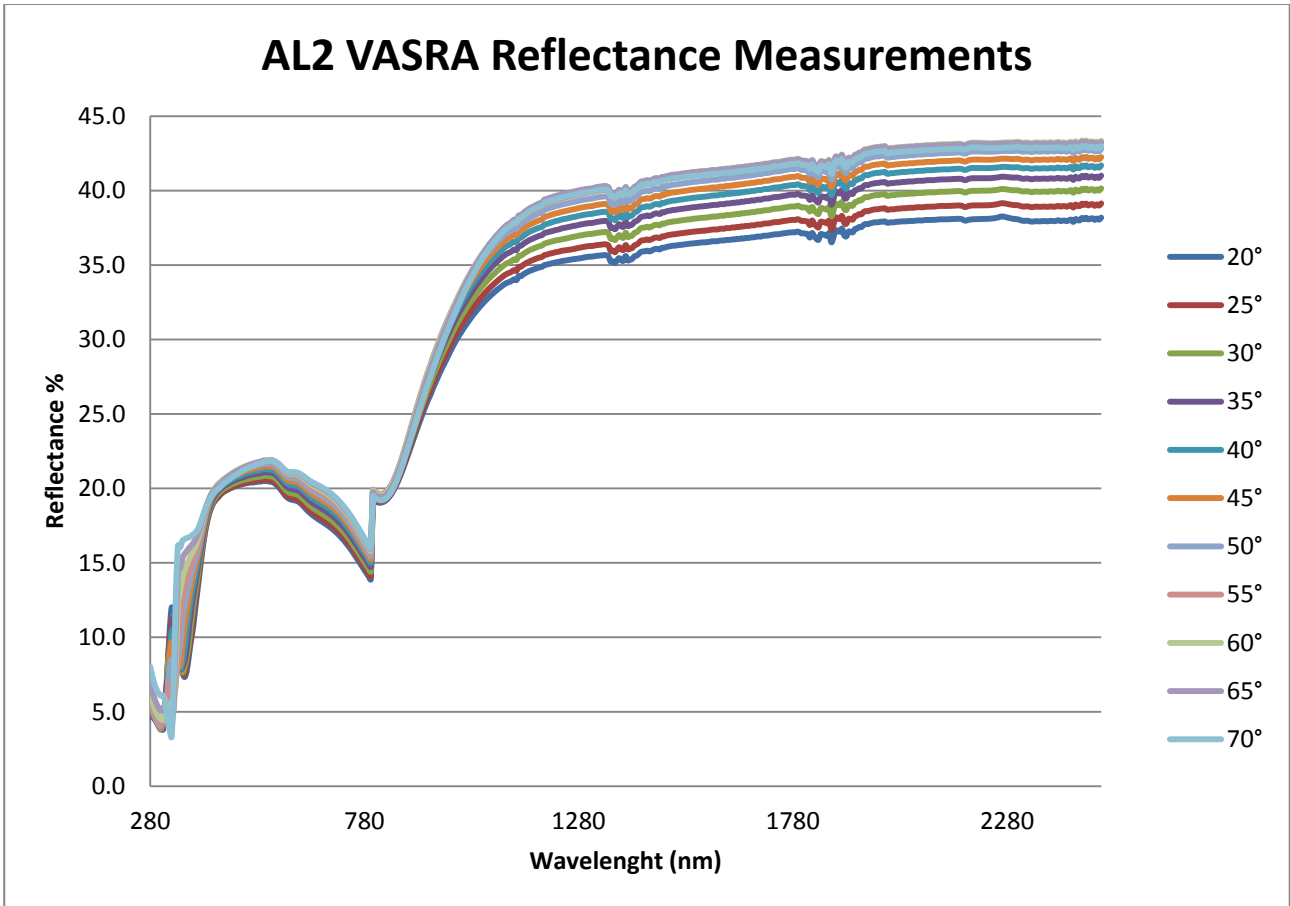


Figure 5. 41 VASRA Reflectance measurements for TG2 Samples

Here in the following table the values of the standard deviation for the TG2 sample.

	20°	25°	30°	35°	40°	45°	50°	55°	60°	65°	70°
mean	0.0118	0.0064	0.0059	0.0101	0.0173	0.0250	0.0217	0.0285	0.0227	0.0151	0.0121
min	0.0003	0.0003	0.0002	0.0004	0.0042	0.0014	0.0031	0.0007	0.0017	0.0017	0.0012
max	0.0228	0.0269	0.0240	0.0425	0.0545	0.0576	0.0590	0.0633	0.0640	0.0628	0.0422

Table 5. 5 Values of Standard Deviation for AL2 samples

In order to evaluate the differences between the behavior of this two mirrors was calculated the Solar Weighted Specular Reflectance for each value of the incident angles.

Unfortunately without any reference mirrors all the results are presented as a relative value to allow a better comparison between the mirrors. The results are represented in the following two figures 5.42 and 5.43.

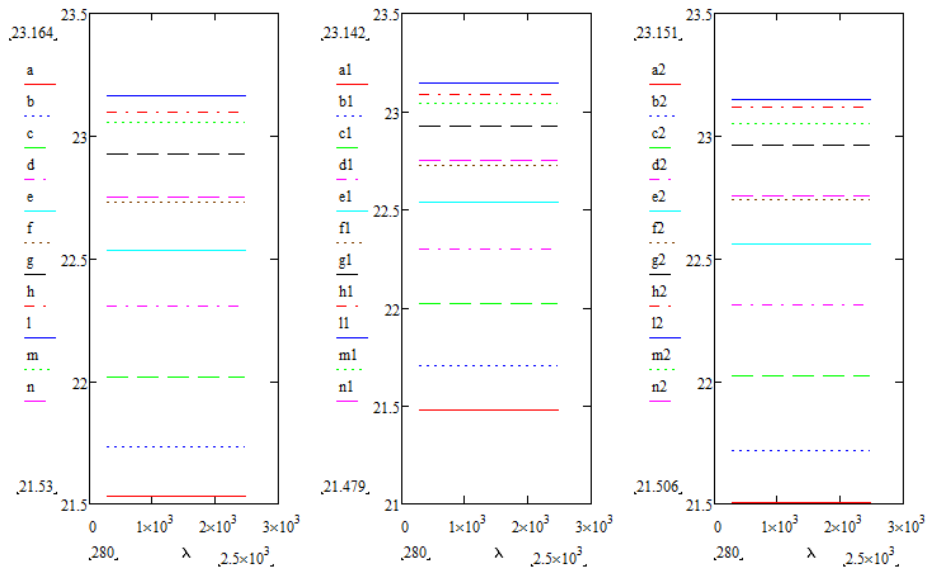


Figure 5.42 Solar Weighted Specular Reflectance at different angles of incidence for AL1 Samples:  
 $a=20^\circ, b=25^\circ, c=30^\circ, d=35^\circ, e=40^\circ, f=45^\circ, g=50^\circ, h=55^\circ, i=60^\circ, m=65^\circ, n=70^\circ$

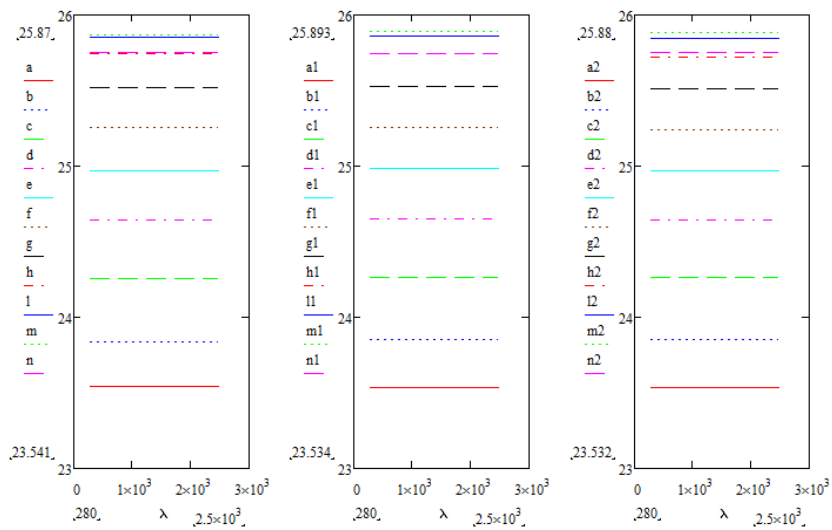


Figure 5.43 Solar Weighted Specular Reflectance at different angles of incidence for AL2 Samples:  
 $a=20^\circ, b=25^\circ, c=30^\circ, d=35^\circ, e=40^\circ, f=45^\circ, g=50^\circ, h=55^\circ, i=60^\circ, m=65^\circ, n=70^\circ$

Positioning all the points obtained after the normalization it is possible to draw the graphs that give the idea of the behavior of these two types of mirror.

In figure 5.44 the AL1 mirror behavior is summarized.

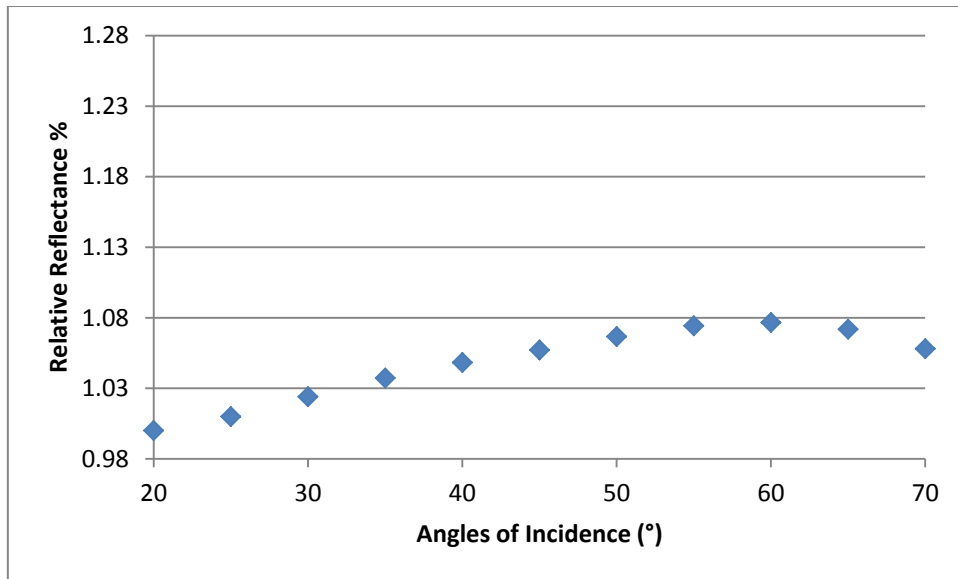


Figure 5. 44 Reflectance Vs Angle of Incidence

While in figure 5.45 the TG2 mirror behavior is represented.

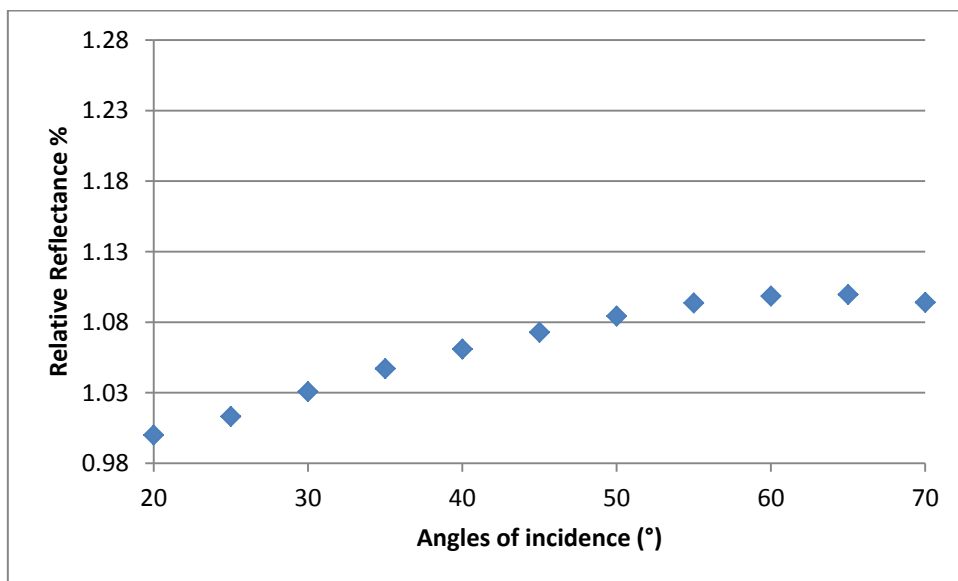


Figure 5. 45 Reflectance Vs Angle of Incidence

Then a comparison between the two mirrors in figure 5.46.

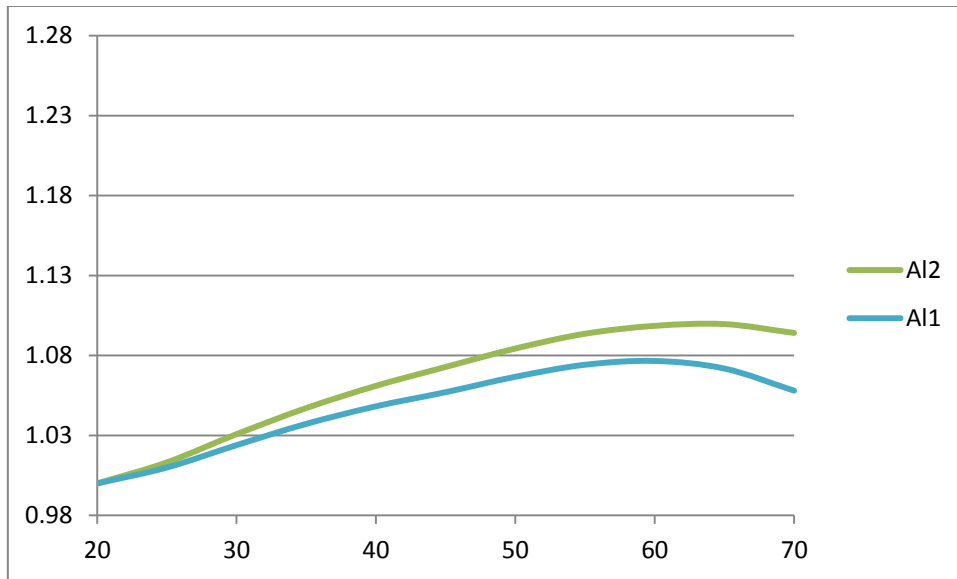


Figure 5. 46 TG1 Mirror Vs TG2 Mirror

In the graph above is represented the behavior of the two aluminum mirrors it's easy to notice that the AL2 mirror maintain a higher value than the AL1 mirror along the variation of the incidence angle. The AL2 follows a linear increasing till it reaches 65° then it has a drop in the reflectance as the thin glass mirror does. The difference between the first and the highest value is in the order of 9.963%. The AL1 mirror has a peak at 60° with a relative value respect the 20° initial point in the order of 7.658%.

Looking at the above shown curves it's possible to assume that the aluminum mirror behavior is almost linear, so, as it was done for the thin glass mirrors it was possible to estimate their absolute reflectance values. In the next figure the comparison is represented .

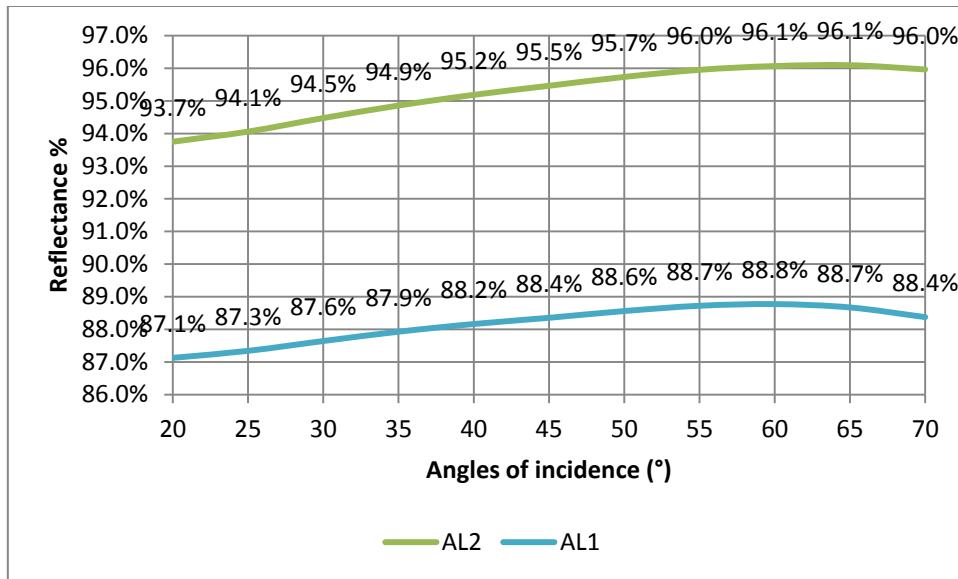


Figure 5. 47 Comparison between the two aluminum mirrors

### 5.2.3 Polymeric film mirrors

As previously seen in the 5.1 subchapter this family holds the fourth value of specular reflectance of all the typologies of mirrors.

The Specular reflectance in all the samples gave us all the same behavior along the spectrum. From the first collected curve at 20° (which is the lowest) till the 70° curve, see figure 5.48.

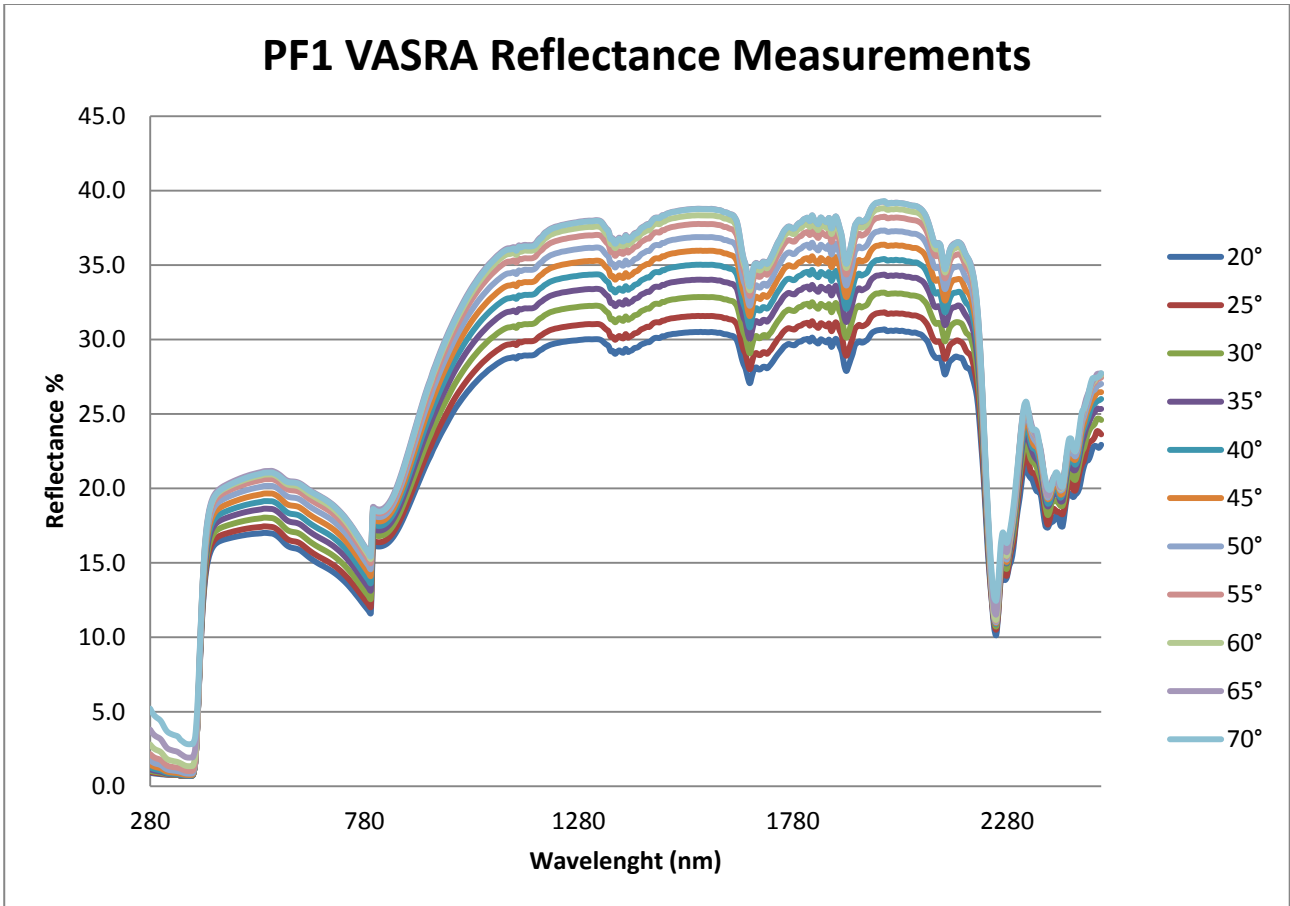


Figure 5. 48 VASRA Reflectance Measurements for PF1 Samples

In the next table 5.6 are summarized the values of standard deviation for these measurements with values of minimum, maximum and average.

	20°	25°	30°	35°	40°	45°	50°	55°	60°	65°	70°
mean	0.0573	0.0363	0.0381	0.0402	0.0296	0.0293	0.0227	0.0247	0.0146	0.0177	0.0261
min	0.0002	0.0002	0.0004	0.0002	0.0001	0.0002	0.0002	0.0002	0.0001	0.0005	0.0004
max	0.2213	0.2246	0.2213	0.2227	0.1951	0.1940	0.1747	0.1650	0.1397	0.1414	0.1588

Table 5. 6 Values of Standard Deviation for PF1 samples

It is noticeable that all the values obtained with the spectrophotometer lead us to see an increasing value of R% with the increasing of the values of the incidence angle. The next figure 5.49, represents the values of calculated solar weighted specular reflectance.

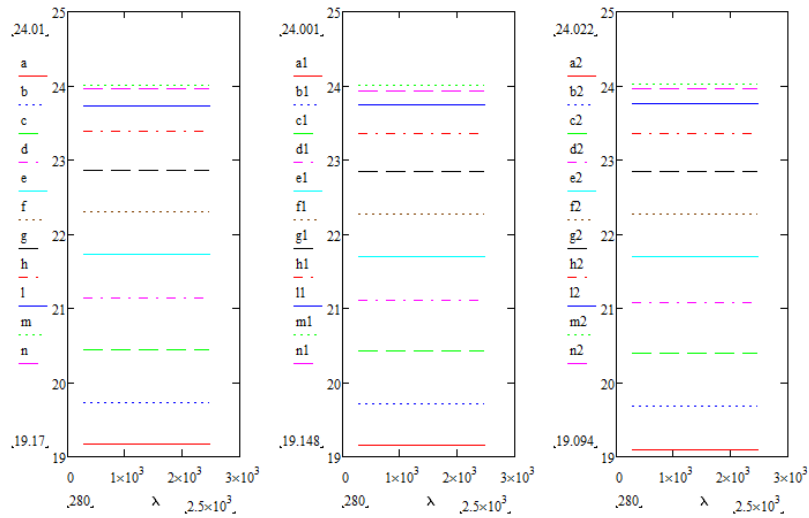


Figure 5.49 Solar Weighted Specular Reflectance at different angles of incidence for PF Samples: a=20°,b=25°,c=30°,d=35°,e=40°,f=45°,g=50°,h=55°,l=60°,m=65°,n=70°

In the next figure 5.50 is summarized the behavior of this typology of mirror.

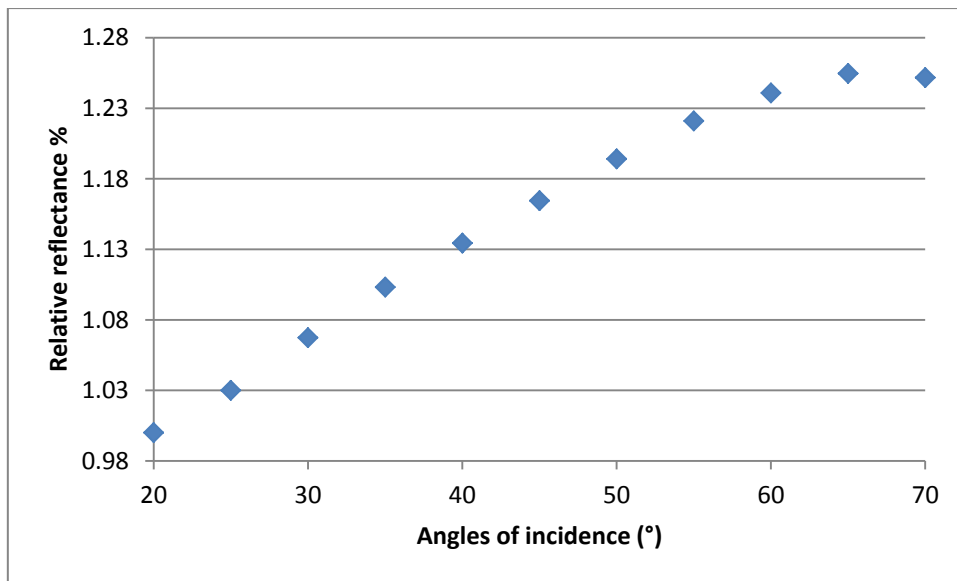


Figure 5.50 Reflectance Vs Angles of incidence

As all the other types of mirrors it maintains a linear behavior from 20° to 65° and then it falls at a lower value. The difference between the highest and the lowest value is of the order of 24.084%.

In the same way are summarized the results of the PF2 mirror in the next figure 5.51.

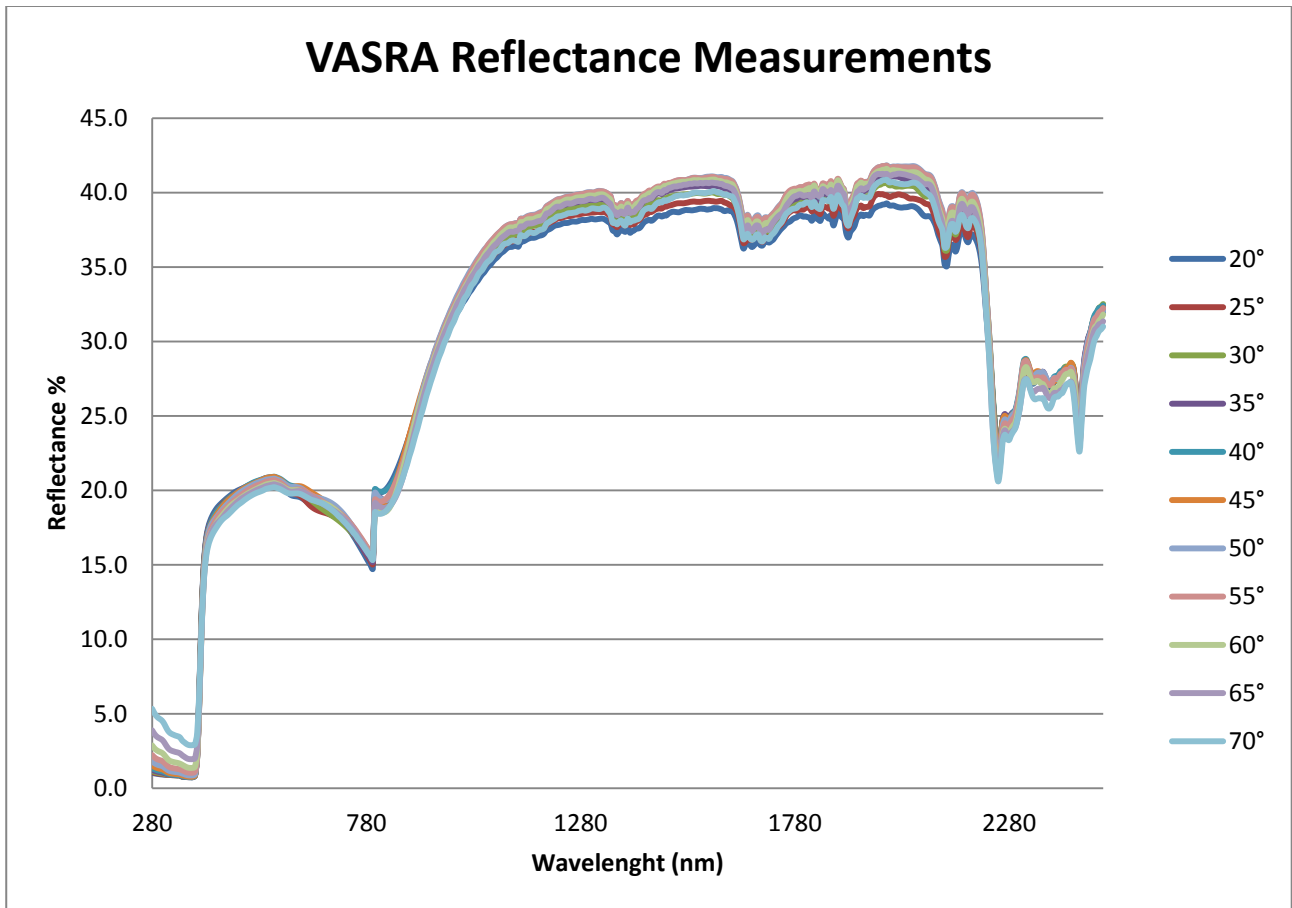


Figure 5. 51 PF2 VASRA measurements

It conserves the same behaviour of the DRA measurements and as the others do it has a slight improvement of reflectance along the angle of incident variation till it reaches the value of 45°, but it has also a decreasing of reflectance after the angle the lead to a minor value when we reach the 70° value.

This behavior is represented in the next figure 5.52.

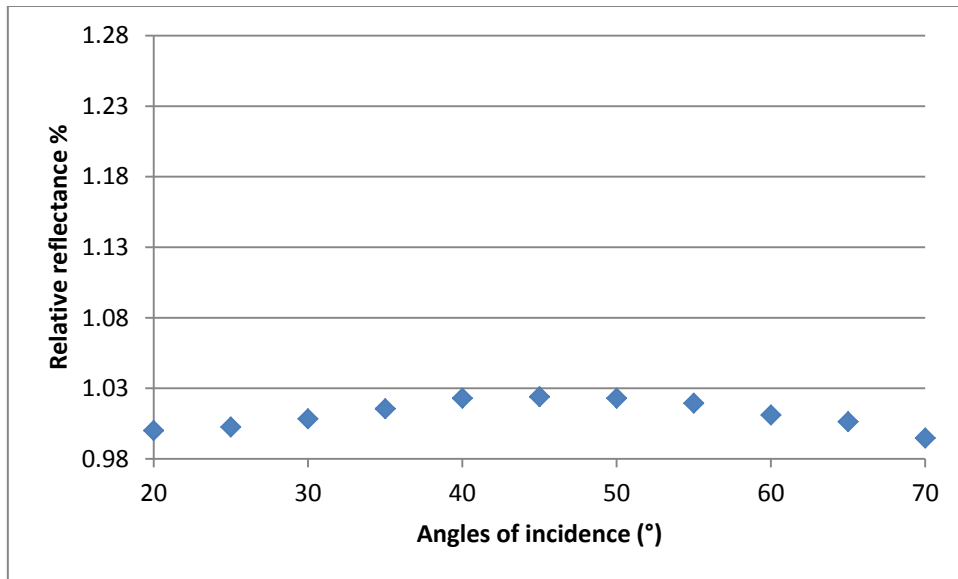


Figure 5.52 Reflectance vs Angles of incidence

So we compared the results in relative and absolute values in the figure 5.53.

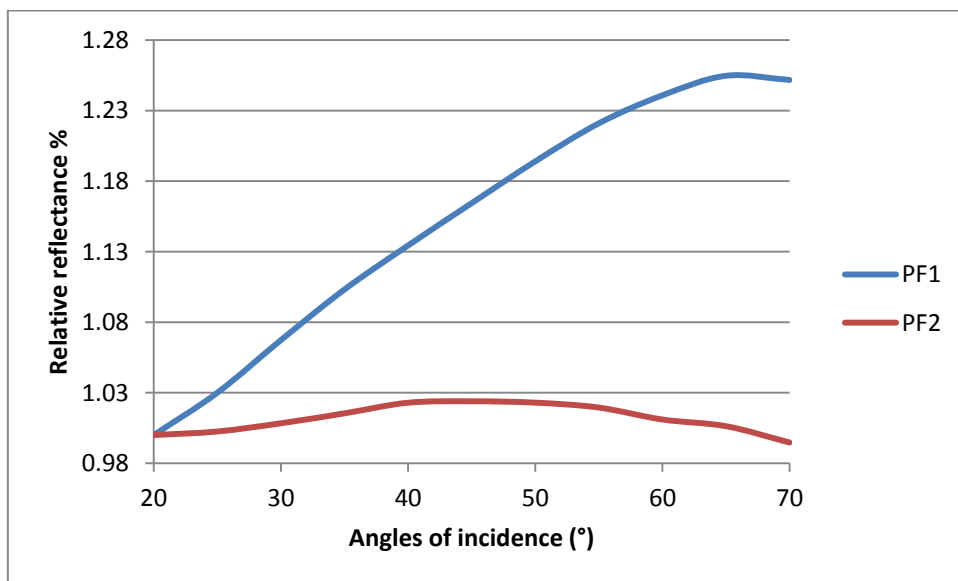


Figure 5.53 Relative reflectance comparison

It's easy to observe that the PF1 mirrors have a better increase compared to the PF2 mirror, the above values are better described in the absolute comparison where the PF1 mirror reaches the best values of the AL2 mirror around 65° to 70°.

A comparison between the two mirrors are represented in the next figure 5.54.

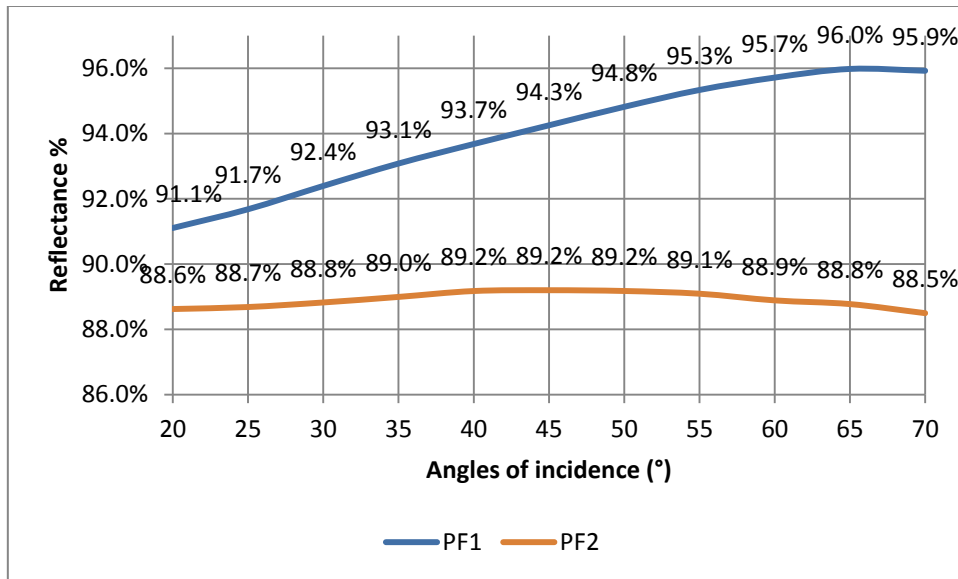


Figure 5. 54 Comparison between the two polymeric mirrors

At last it is possible to obtain an overview comparing all the above results in the next figure 5.55.

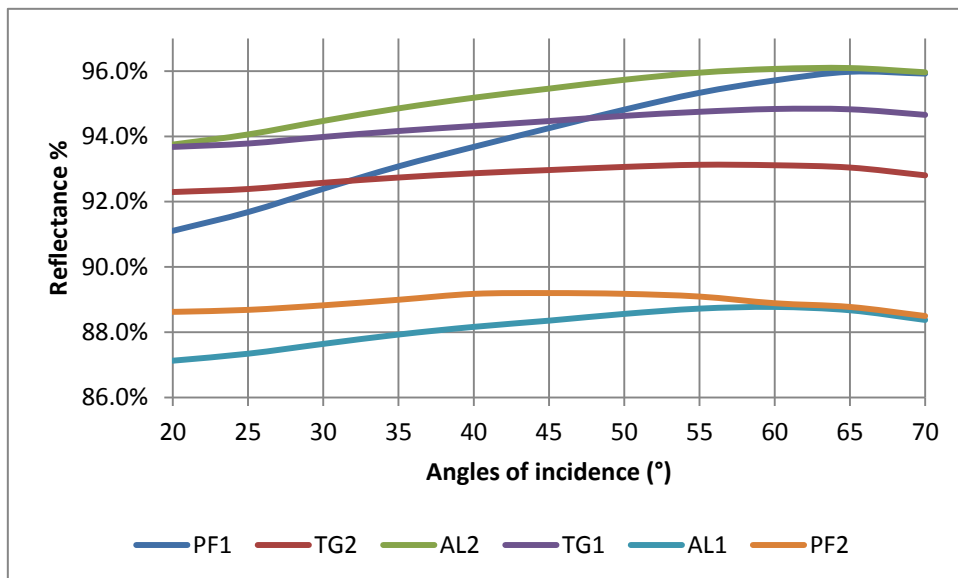


Figure 5. 55 Comparison graph between all the mirrors tested

For all of the above mentioned mirrors it was possible to characterize not only the unique Brewster angles but also their behaviour along different angles of incidence.

### 5.3 UV Accelerated Ageing Tests

As a natural exposure during the operational time over the years, generally a loss of reflectance is involved, the same condition could be replicated by laboratory-controlled testing; it may be possible to accelerate these failure mechanisms by exposing materials to a combination of higher temperatures, higher relative humidity, and increased UV doses. This allows for early screening of developmental materials.

To obtain this results an experimental campaign of measurements with a UV chamber model TC 22-72/20-40D (1992) was conducted, as reported in Fig.5.56.



**Figure 5. 56 UV Chamber**

This unit uses 4 UV lamp type OSRAM Ultramed 2000W. This typology of lamp give a close match to the terrestrial air-mass AM 1.5 global solar spectrum with a spectral width of 280-440nm this type of lamp is shown in figure 5.57.

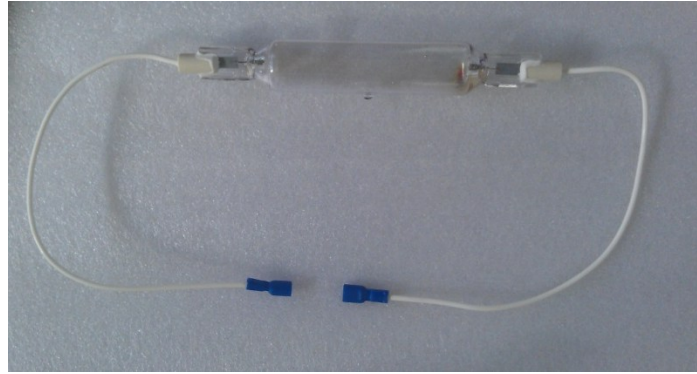


Figure 5. 57 Ultramed 2000 lamp

Technical - Electrical Data	
Nominal wattage	2000 W
Construction wattage	2000 W
Construction voltage	400 V
Lamp voltage	400 V
Technical - Light Technical Data	
Radiated power 315...400 nm (UVA)	490 W
Radiated power 280...315 nm (UVB)	60 W
Technical - Lifespan	800 h

As outdoor weather conditions vary continuously, accelerated exposure conditions can also change as well, for example a loss of light intensity due to aging of the bulb. Consequently, all relevant parameters must be known and measured as a function of time.



Figure 5. 58 LP UVA & LP UVB probes

To control the level of irradiance on the work plane was necessary to conduct a measurement campaign with the probes shown in figure 5.58.

To measure the uniformity of irradiance on the work plane we used two probes that measure the UVA and the UVB contribution provided by the Delta Ohm industries so that the spectral content and spatial uniformity of artificial light sources can be subjected to accelerated testing in known and controlled laboratory environments.

The probes were:

- LP UVA 01
- LP UVB 01

The LP UVA 01 probe measures irradiance ( $\text{W}/\text{m}^2$ ) defined as the ratio between the radiant flux (W) passing through a surface and the surface area ( $\text{m}^2$ ) in the UVA (315 nm ÷ 400 nm) spectral range. Thanks to a new type of photodiode, LP UVA 01 is blind to visible and infrared light.

Probe calibration is carried out by using a 365 nm line of a Xe-Hg lamp, filtered through a special interferential filter. Measurement is carried out by comparison with the primary standards, assigned to Delta Ohm Metrological Laboratory.

The technical specifications are reported in the next 5.7 table, while the spectral response is shown in figure 5.59.

<b>Technical Specification</b>	
Typical sensitivity:	$2.6\mu\text{V}/(\mu\text{W}/\text{cm}^2)$
Measuring range:	0-200 $\text{mW}/\text{cm}^2$
Typical spectral range:	Peak at 360 nm and FWHM 60 nm
Calibration accuracy	<6%
Working temperature:	0-50°C
Output impedance:	1k $\Omega$

**Table 5. 7 LP UVA 01 technical specification**

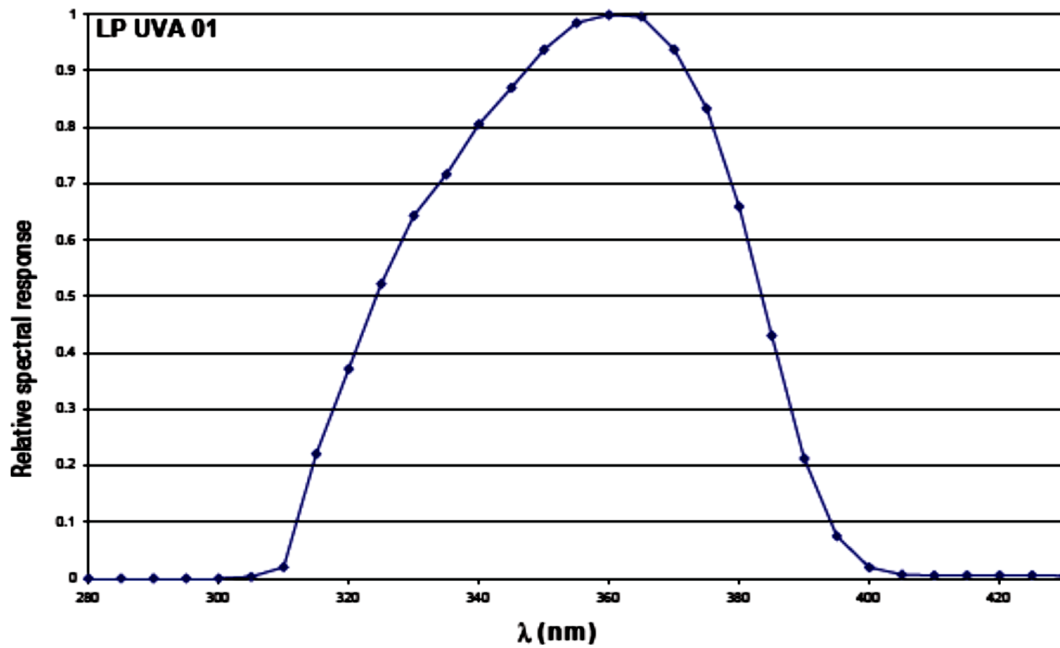


Figure 5.59 LP UVA 01 typical spectral response

LP UVB 01 probe measures irradiance ( $W/m^2$ ) defined as the ratio between the radiant flux (W) passing through a surface and the surface area ( $m^2$ ) in the UVB (280 nm – 315 nm) spectral range. Thanks to a new type of photodiode, LP UVB 01 is blind to visible and infrared light.

Probe calibration is carried out by using a 313 nm line of a Xe-Hg lamp, filtered through a special interferential filter. Measurement is carried out by comparison with the primary standards, assigned to Delta Ohm Metrological Laboratory.

The technical specification are reported in the next table 5.8, while the spectral response is shown in figure 5.60.

Technical Specification	
Typical sensitivity:	$0.19\mu V/(\mu W/cm^2)$
Measuring range:	0-200 $mW/cm^2$
Typical spectral range:	Peak at 305 nm and FWHM 31 nm
Calibration accuracy	<8%
Working temperature:	0-50°C
Output impedance:	2kΩ

Table 5.8 LP UVB 01 Technical specification

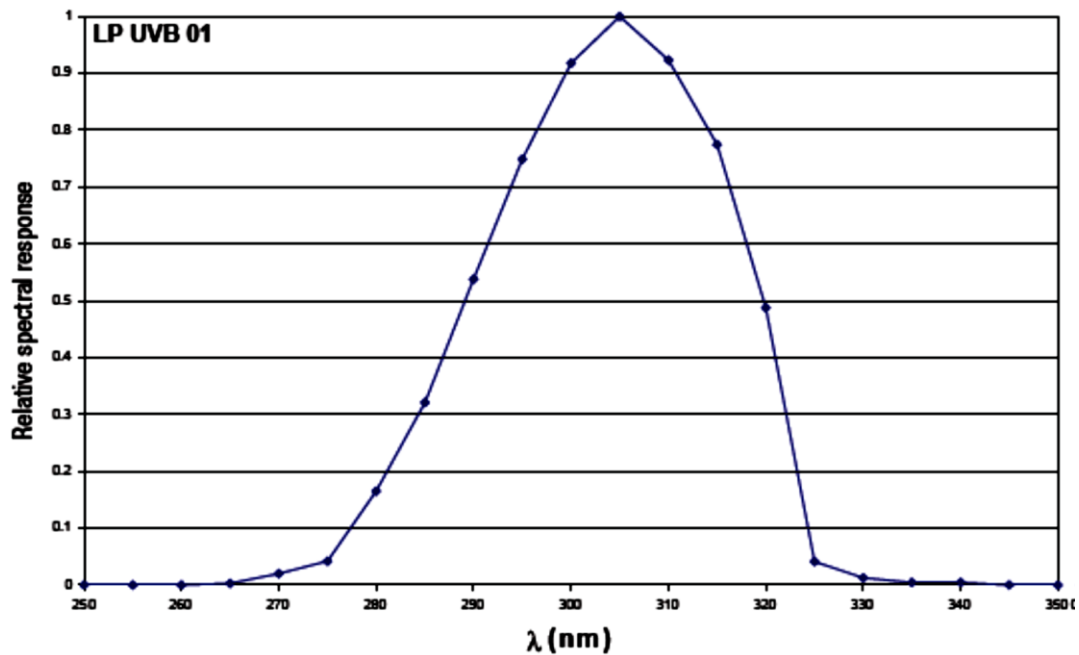


Figure 5.60 LP UVB 01 typical spectral response

To evaluate the right quantity of UV dose necessary to simulate an accelerated ageing process we referred to the norm CEI EN 61345 UV test for photovoltaic modules.

The test shall be carried out according to the procedure outlined below.

- a) Use the calibrated radiometer to measure the irradiance at the proposed plane and ensure that, at wavelengths between 280 nm and 400nm, the test spectral irradiance is never more than 5 times the corresponding standard spectral irradiance specified in the standard AM 1.5 solar irradiance distribution as reported in the previous table 5.1.

Ensure that there is no appreciable irradiance at wavelength below 280 nm and it has a uniformity of  $\pm 15\%$  over the test plane.

The experimental result of a previously done campaign of radiometer measurements show that at the Passo Martino Location the global UV dose along the year is 72200 kWh/m<sup>2</sup> per year.

The results are reported below:

We took in exam 5 points all over the work plane distributed as the next figure 5.61 shows.

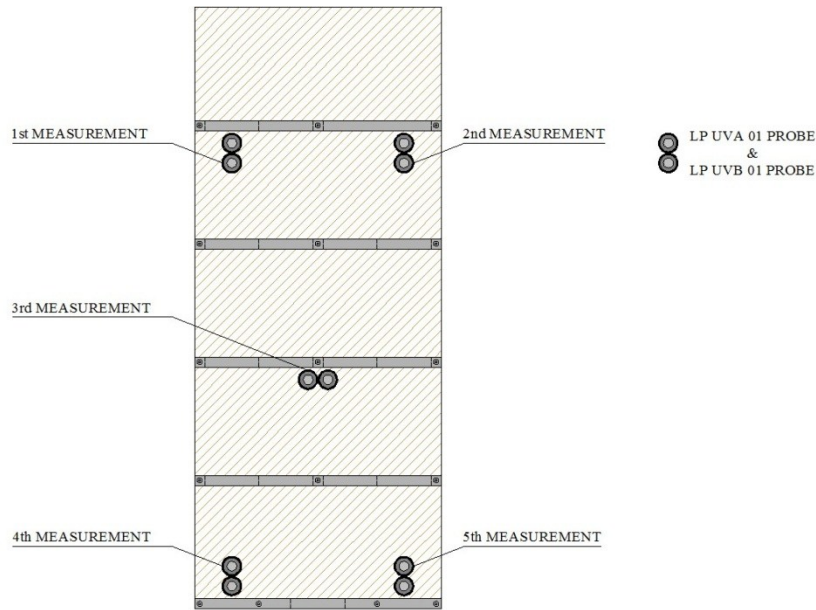


Figure 5. 61 Positions of UVA + UVB measurements

We find the followings values shown in the next tables 5.9 and 5.10 in  $W/m^2$ . The measurements were carried on in two different planes of work respectively at 1 m from the inox steel shield and at 10 cm from the shields to collect the maximum and the minimum values of UVA + UVB irradiance.

Maximum height Irradiance values measured			Minimum height Irradiance values measured		
First	Second		First	Second	
182.7	170.2	Row 5	148.9	150.2	Row 5
		Row 4			Row 4
158.1		Row 3	148.9		Row 3
Third		Row 2	Third		Row 2
170.7	168	Row 1	144.7	143.5	Row 1
Fourth	Fifth		Fourth	Fifth	
UV chamber door			UV chamber door		

Table 5. 9 Values measured of the maximum and minimum values of UVA + UVB irradiance

Minimum height						
	First	Second	Third	Fourth	Fifth	
UVA [W/m <sup>2</sup> ]	123.60	125.00	123.70	119.40	118.20	± 6%
UVB [W/m <sup>2</sup> ]	25.30	25.20	25.20	25.30	25.30	± 8%
Total	148.90	150.20	148.90	144.70	143.50	

Maximum height						
	First	Second	Third	Fourth	Fifth	
UVA [W/m <sup>2</sup> ]	151.50	140.60	133.00	141.40	138.70	± 6%
UVB [W/m <sup>2</sup> ]	31.20	29.60	29.30	29.30	29.30	± 8%
Total	182.70	170.20	162.30	170.70	168.00	

**Table 5. 10 Summary of the values collected**

Considering the probes accuracy respectively of <6% for the LP UVA 01 and <8% for the LP UVB 01 the values obtained could be judged in the 15% interval of uniformity on the plane dictated by the norm, so the uniformity has been verified.

The value of total UV dose along a year of exposure was measured in a previous campaign of measurement with a radiometer.

The total UV dose is assumed to be 72200 Wh/m<sup>2</sup> per year, in this way was possible to define the total time the samples were taken inside the UV chamber. In the next table 5.11 has been proposed the operative summary.

Days to cover 1 year of UV irradiation		
<b>First</b>	<b>Second</b>	
16.5	17.7	Row 5
		Row 4
	19.0	Row 3
	<b>Third</b>	
		Row 2
17.6	17.9	Row 1
<b>Fourth</b>	<b>Fifth</b>	
		Maximum height (10 cm from the top)
		UV chamber door

**Table 5. 11 Operative summary**

The mirrors were deployed in rows with the use of a wood boards to allow a perfect alignment with a major uniformity of UV irradiation along the rows and the main duty to maintain the mirrors fixed in the same point without the movement that the ventilation inside the chamber can induce (figure 5.62). The following figure 5.63 gives an idea of the schematic and real system constructed at the laboratory.



Figure 5. 62 The wood board inside the UV chamber

We introduced also a thick glass mirror that for the NDA (non-disclosure agreement) will be called TGM that in the figures is the biggest one in the upper right corner.

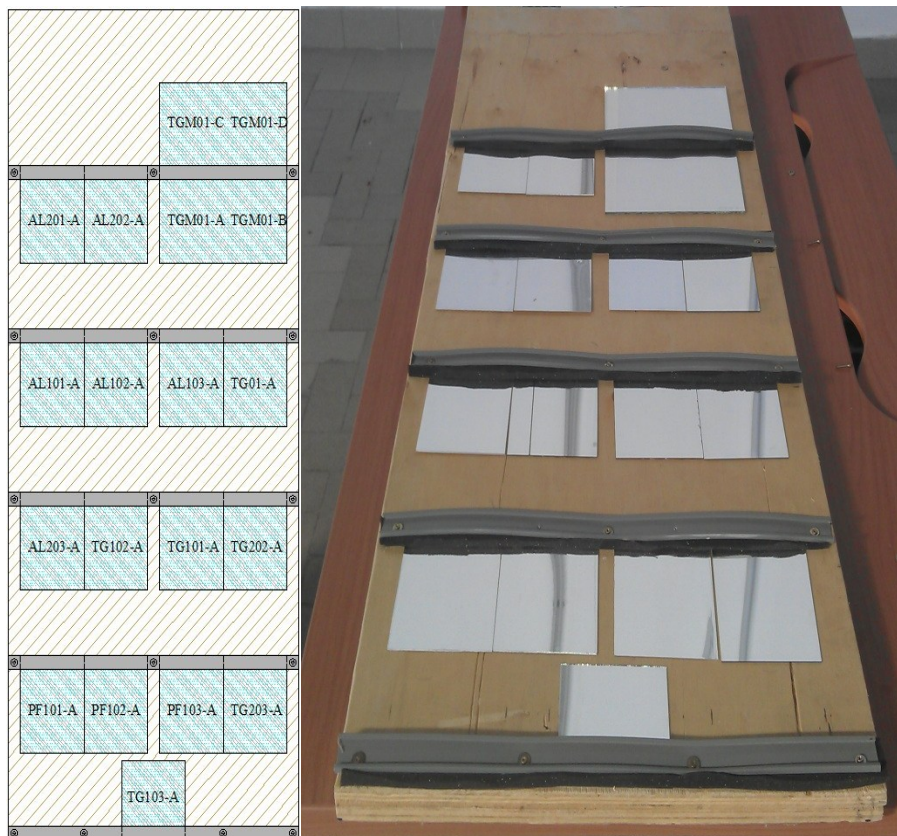


Figure 5. 63 Schematic and real system constructed at the laboratory

The results obtained after an accelerated year of UV exposure are described in the next subchapters.

### 5.3.1 Thin glass mirrors

After almost 18 days it was possible to test with the spectrophotometer the TG1 and TG2 mirrors.

For what the reflectance is concerned, as it was expected, the values resulted almost similar to the 0 time, just because all of these mirrors are designed to last at least 20 25 years.

The loss of reflectance is due to the normal effect that the UV radiation does to every material, and in particular these losses could be localized in the UV spectrum reflected from the mirrors.

A measurement campaign was conducted with four measurements on each sample, for each family there were three sample for a total of twelve measurements.

In only one year of exposure to the UV radiation the losses are so little that the differences can only be evaluated weighting the mirror spectral response with the solar norm spectrum as done for the initial measurements. In the next figure 5.64 is represented the TG1 mirror behavior.

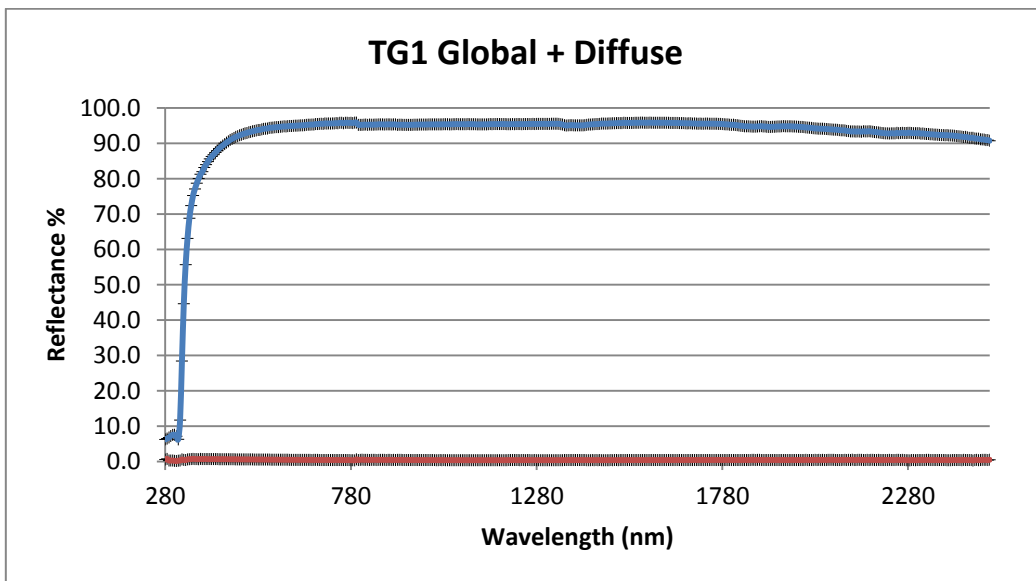


Figure 5. 64 TG1 global and diffuse reflectance after the treatment in the UV chamber

Here in the following figure 5.65 is represented the comparison between the specular reflectance at time 0 and the specular reflectance after the UV chamber test.

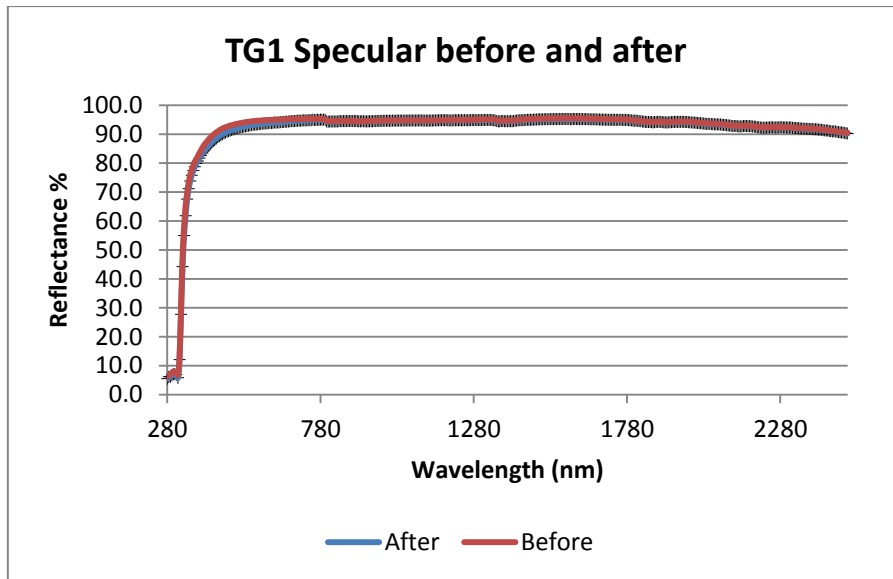


Figure 5. 65 Specular reflectance spectrum comparison

As can be seen in the above graph the specular reflectance obtained with the spectrophotometer after the UV exposure is slightly lower than the time 0 spectral response.

To evaluate the difference it is useful to examine the diffuse reflectance spectrum obtained compared to the time 0 diffuse reflectance.

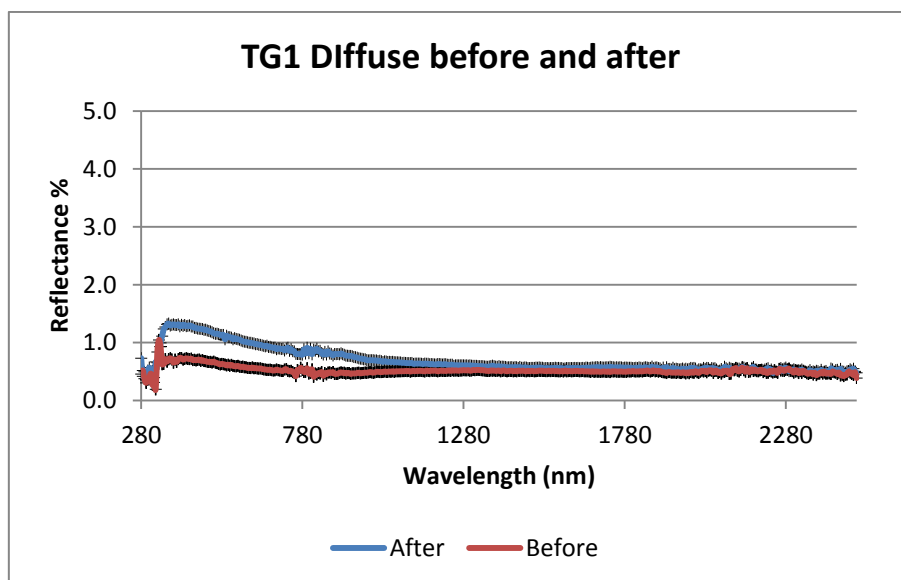


Figure 5. 66 Diffuse reflectance comparison

The figure 5.66 shows how the diffuse reflectance has increased all over the spectrum leading to a consequently lower specular reflectance.

Evaluating the solar weighted hemispherical reflectance and the solar weighted specular reflectance we obtained the following figure comparing the “after” condition to the 0 time condition for both values.

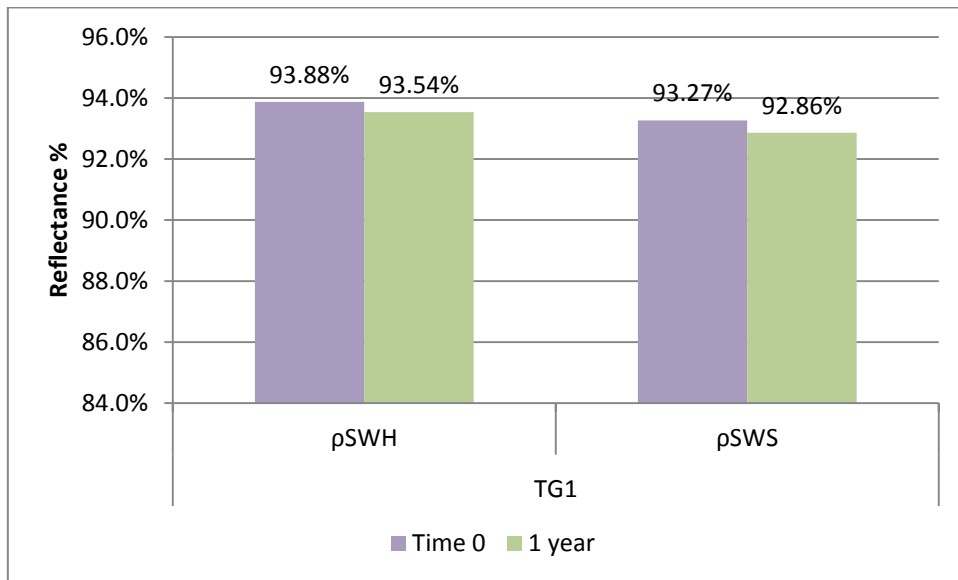


Figure 5. 67 Solar weighted hemispherical (ρSWH) and specular (ρSWS) reflectance

We experienced a loss of hemispherical reflectance of 0.34% while for the specular reflectance we have a loss of 0.41%.

The same evaluation was conducted on the TG2 samples obtaining the following figure 5.68 for the spectrum measured.

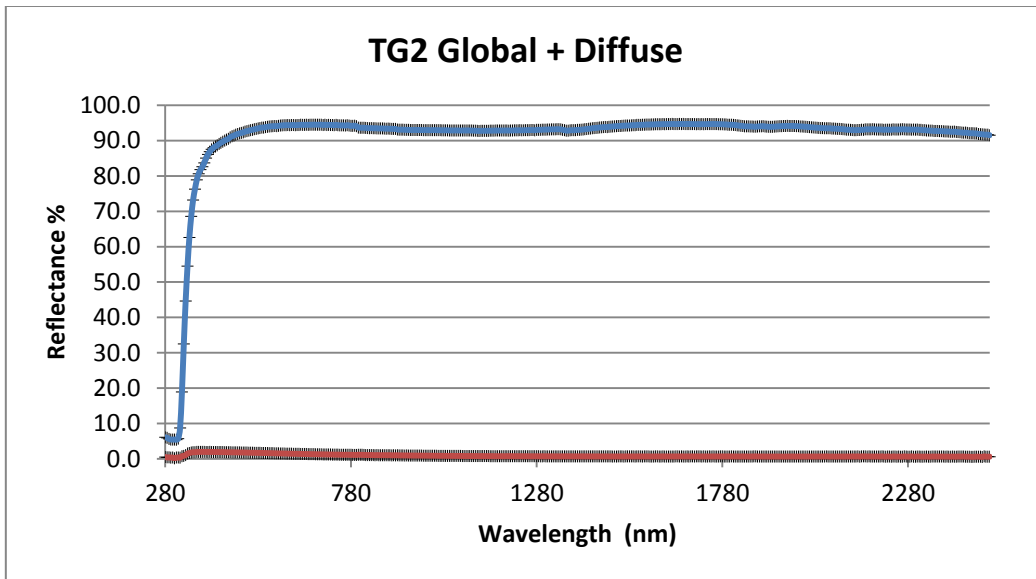


Figure 5. 68 Spectral response for TG2 mirror after the UV exposure

Here in the following figure 5.69 is represented the comparison between the specular reflectance at time 0 and the specular reflectance after the UV chamber test.

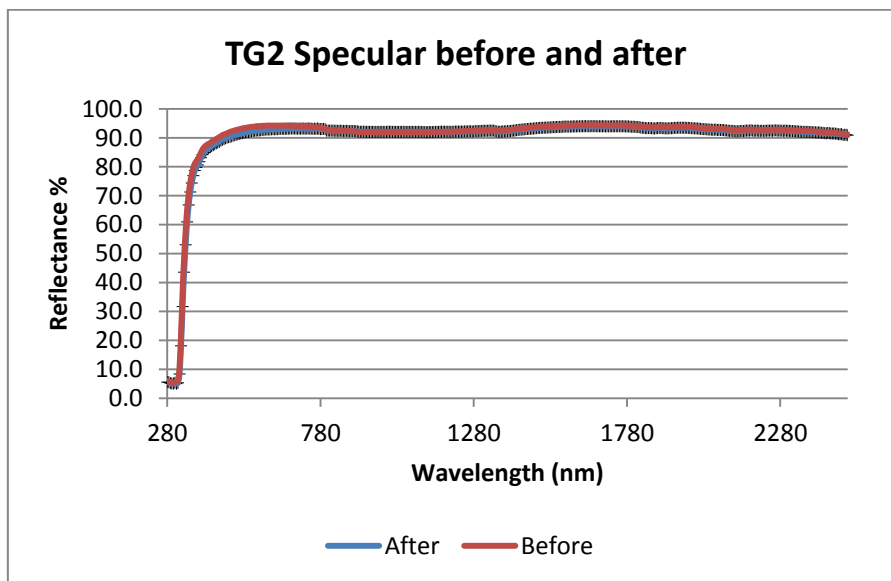


Figure 5. 69 Specular reflectance comparison

As it can be seen in the above graph the specular reflectance obtained with the spectrophotometer after the UV exposure is slightly lower than the time 0 spectral response.

To evaluate the difference is useful to examine the diffuse reflectance spectrum obtained compared to the time 0 diffuse reflectance.

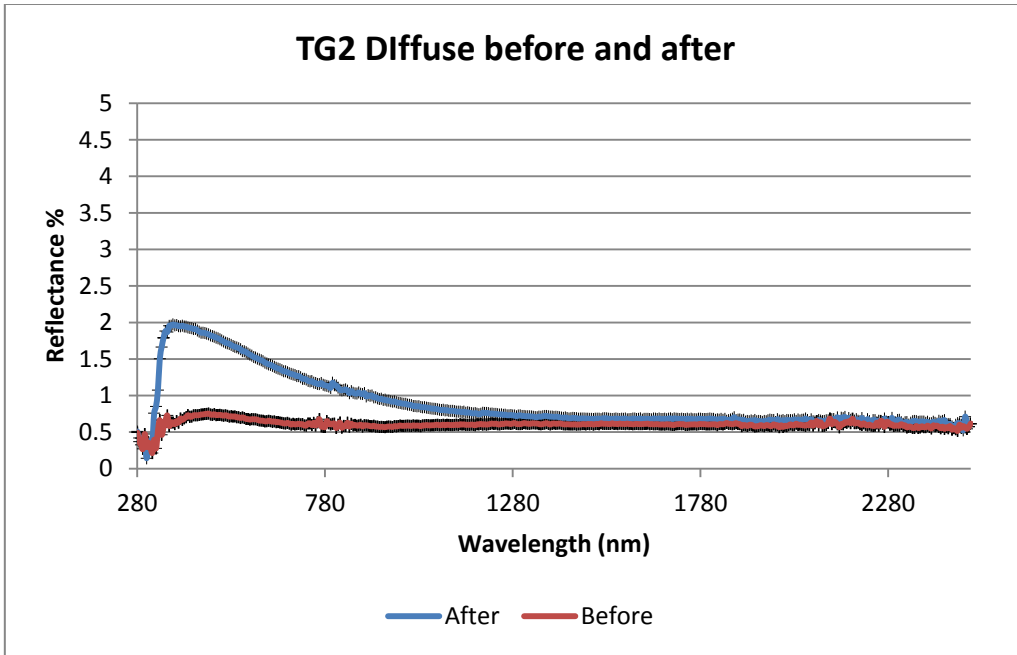


Figure 5.70 Diffuse reflectance comparison

The figure 5.70 shows how the diffuse reflectance has increased all over the spectrum leading to a consequently lower specular reflectance.

Evaluating the solar weighted hemispherical reflectance and the solar weighted specular reflectance we obtained the following figure comparing the “after” condition to the 0 time condition for both values.

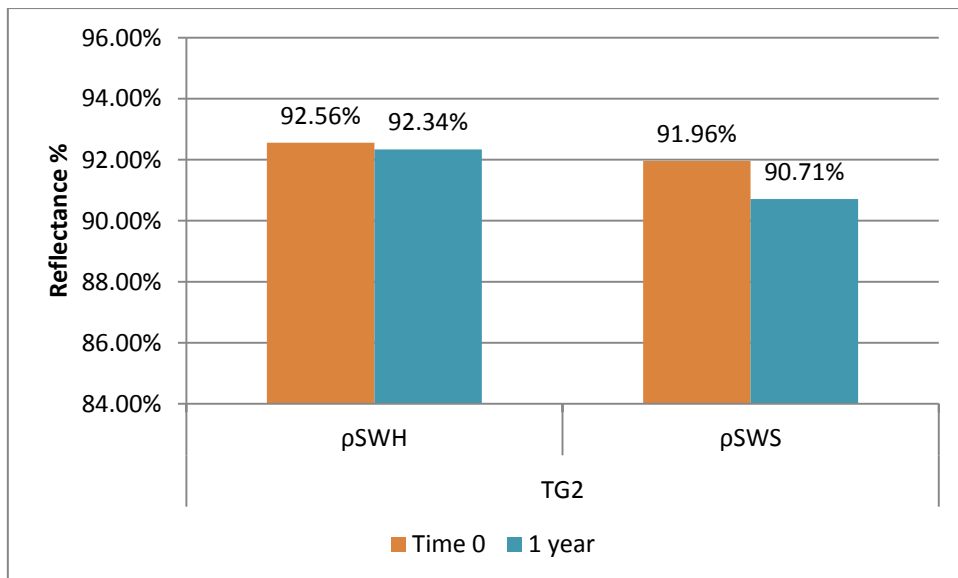


Figure 5.71 Solar weighted hemispherical (ρSWH) and specular (ρSWS) reflectance

In this case we experienced a loss of hemispherical reflectance of 0.22% while for the specular reflectance we have a loss of 1.25%.

### 5.3.2 Aluminum mirrors

For the aluminum mirrors AL1 we obtained the following results for what concern the global and diffuse reflectance (figure 5.72).

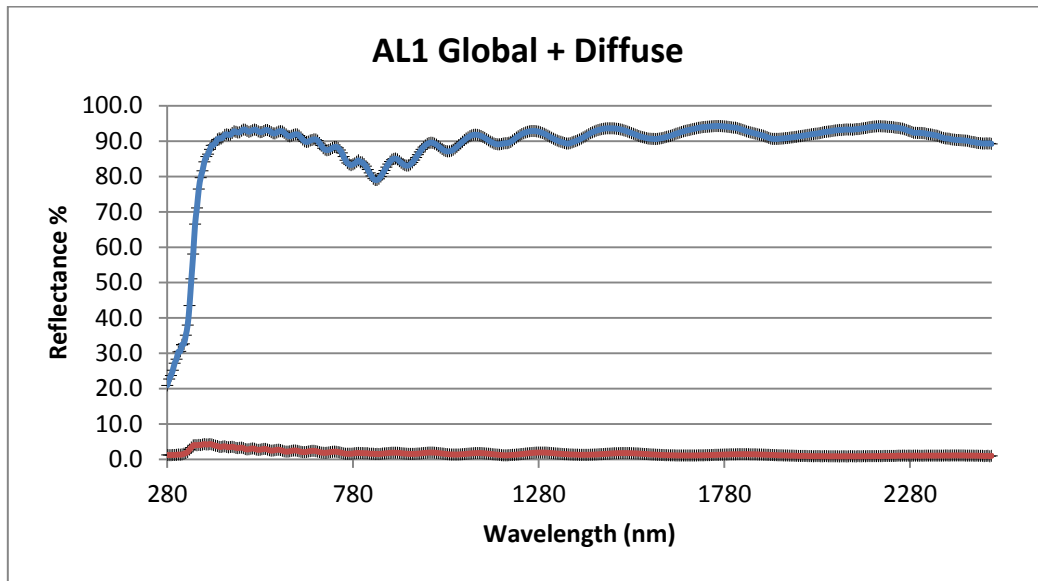


Figure 5.72 AL1 spectral response

Here in the following figure 5.73 is represented the comparison between the specular reflectance at time 0 and the specular reflectance after the UV chamber test.

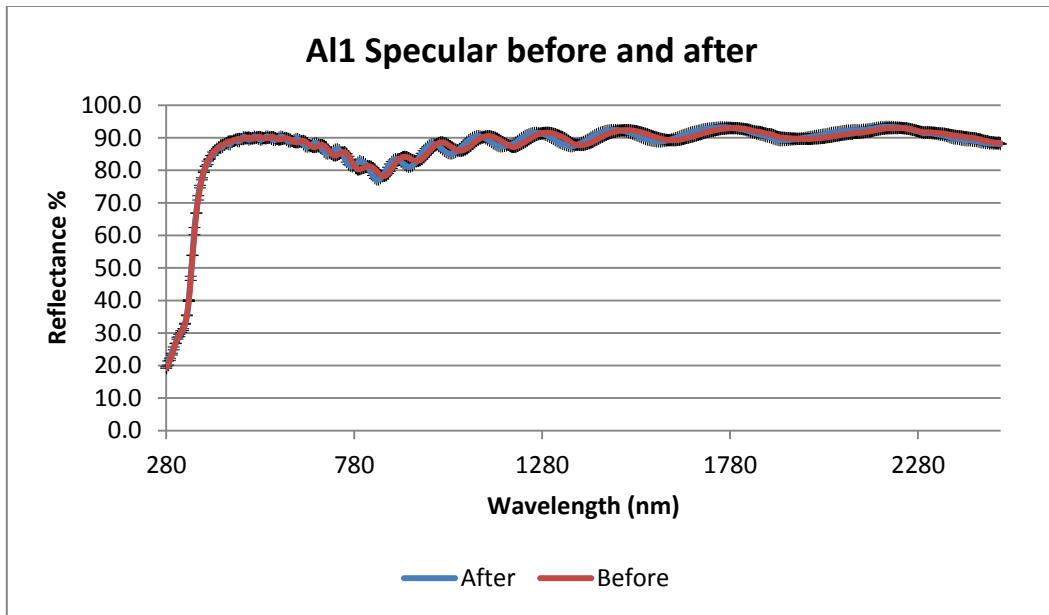


Figure 5. 73 AL1 specular reflectance

For the AL1 mirror the comparison between the diffuse reflectance is shown in the next figure 5.74.

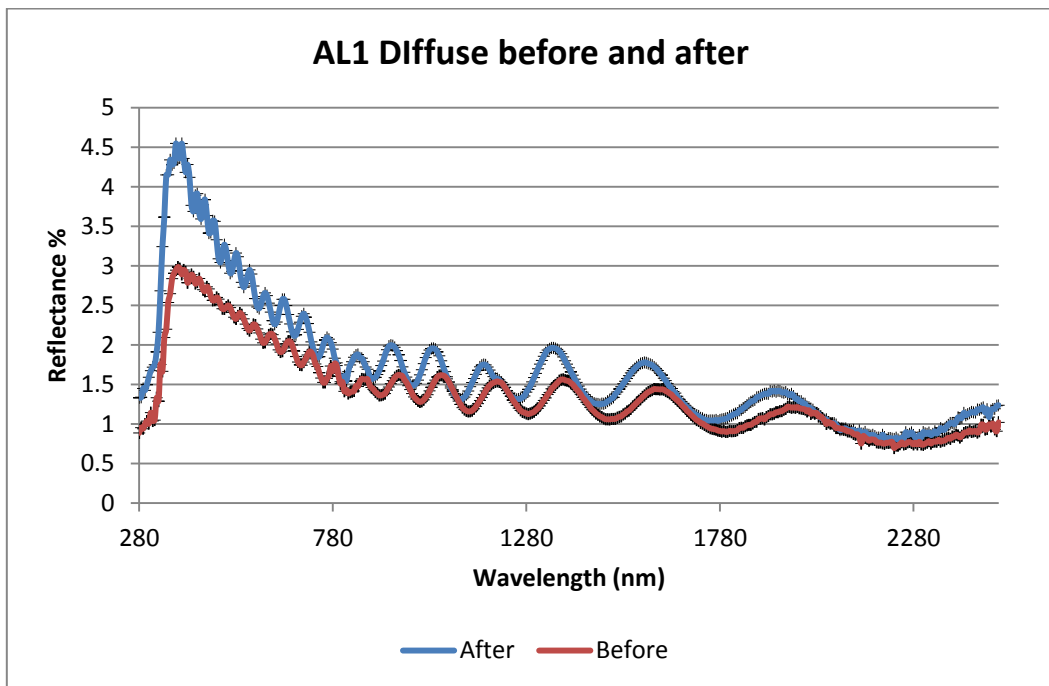


Figure 5. 74 Diffuse reflectance comparison

Finally after the weighting procedure in the following graph are shown the results of specular and hemispherical reflectance.

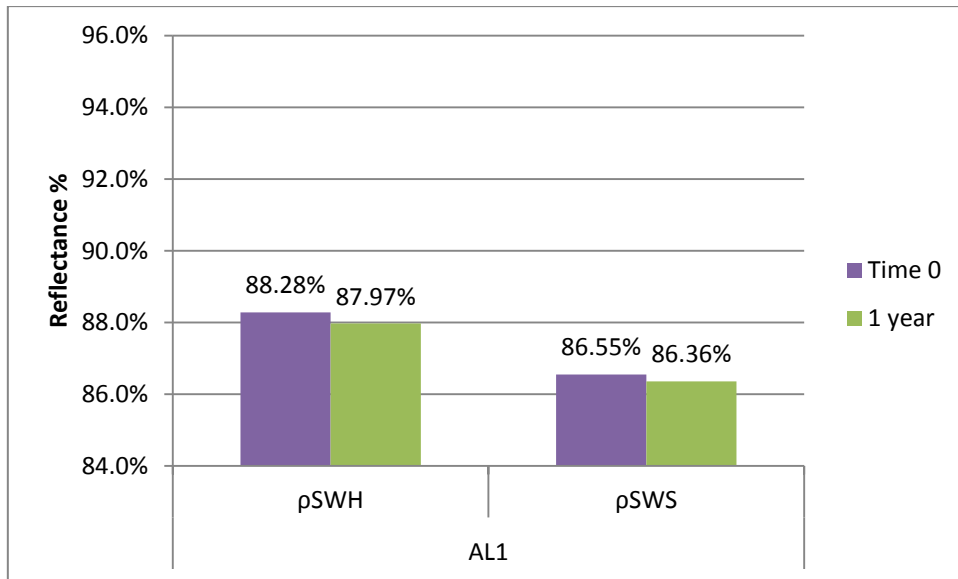


Figure 5. 75 Solar weighted hemispherical and specular reflectance

As can be seen the loss of hemispherical reflectance for all the samples tested is 0.31% and for the specular reflectance is 0.19 %.

In the same way we obtained the results for the AL2 mirror where the spectral response is indicated in the next figure 5.76.

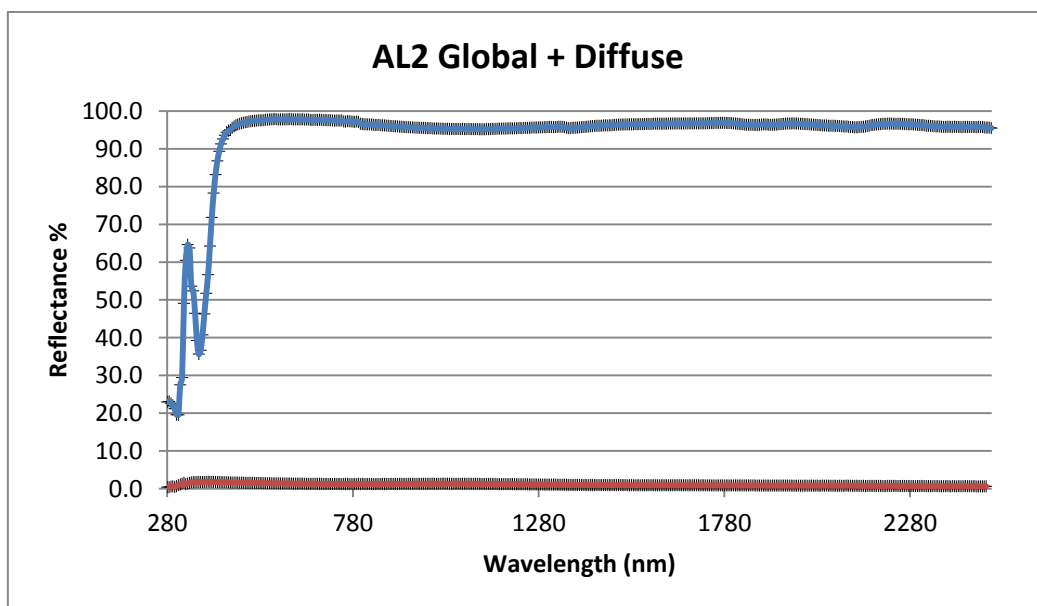


Figure 5. 76 AL2 spectral response

In the next graph it is possible to see the comparison between the specular reflectance in the after and before condition.

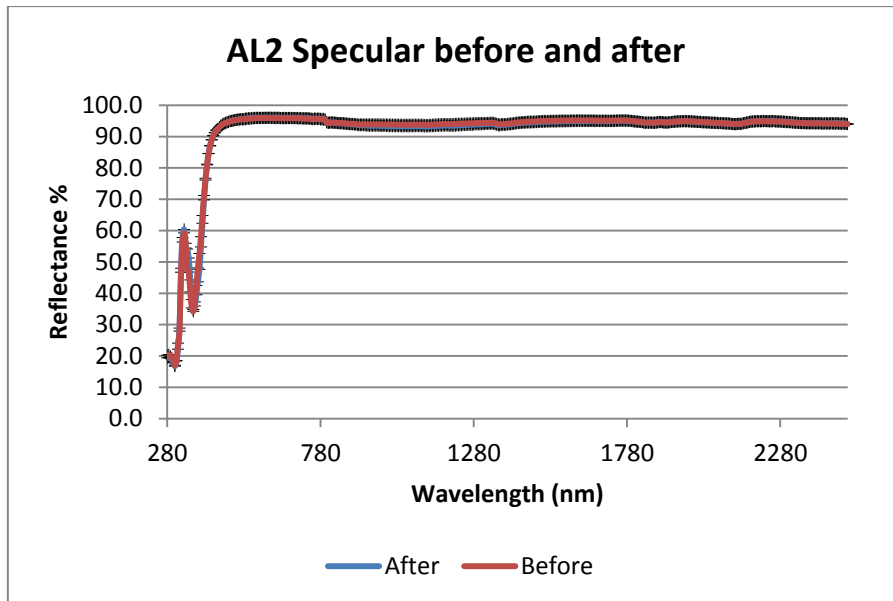


Figure 5. 77 AL2 specular reflectance

While in the next graph is represented the diffuse reflectance always in the time 0 and after the UV exposure.

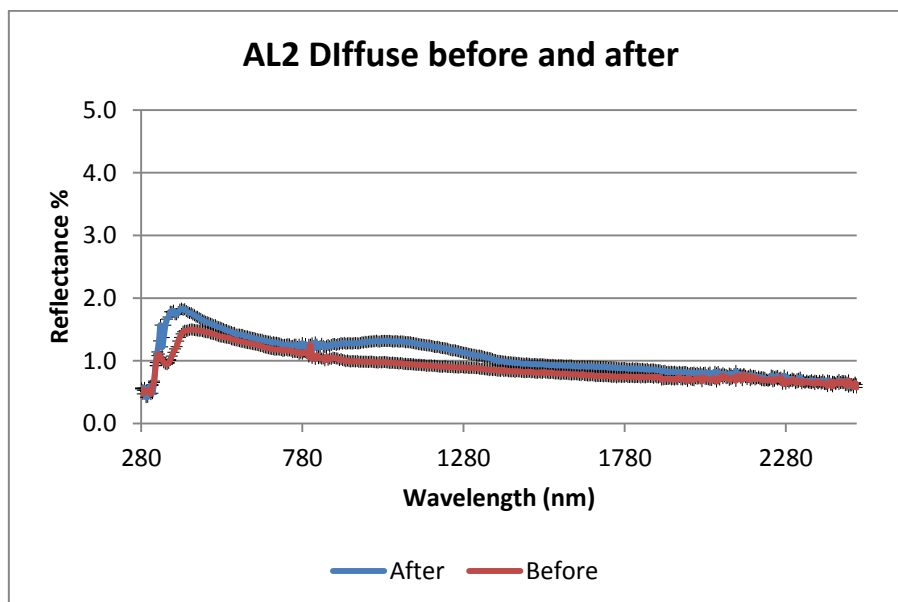


Figure 5. 78 Diffuse reflectance comparison

The diffuse reflectance here appears to have a peak between 800 and 1350 nm and the highest peak in the range between 350 and 580 nm.

As previously done it's possible to make a comparison between the solar weighted hemispherical and specular reflectance in the next graph.

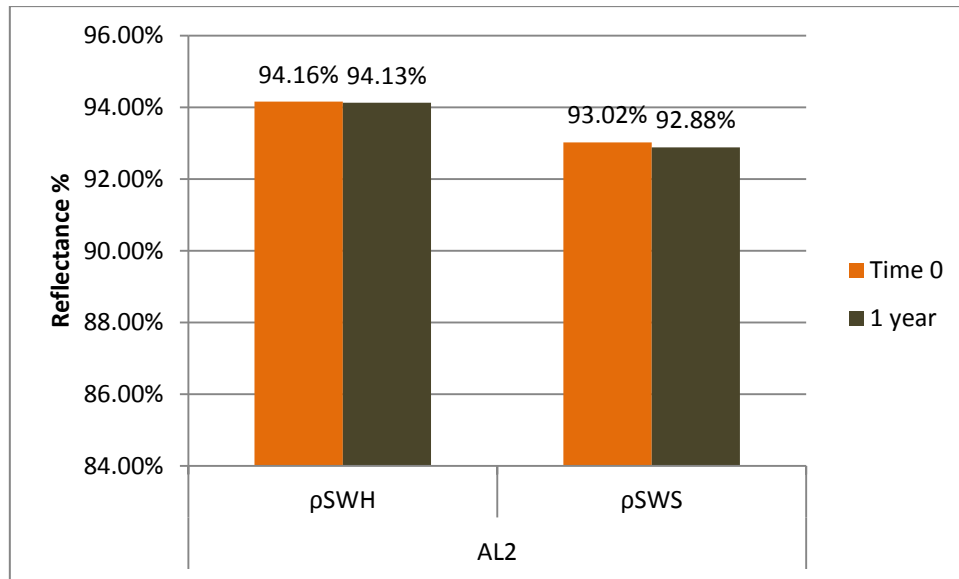


Figure 5. 79 Comparison between the before and after condition for solar weighted hemispherical and specular reflectance

In the above graph it is possible to see the loss of hemispherical reflectance of 0.03% while we have a loss of specular reflectance of 0.14%.

### 5.3.3 Polymeric film mirror

Unfortunately this test could be carried out only for the PF1 sample, because we had only a single sample for the PF2 mirror type.

For the PF1 sample the measurement lead to the spectral response shown in the next graph.

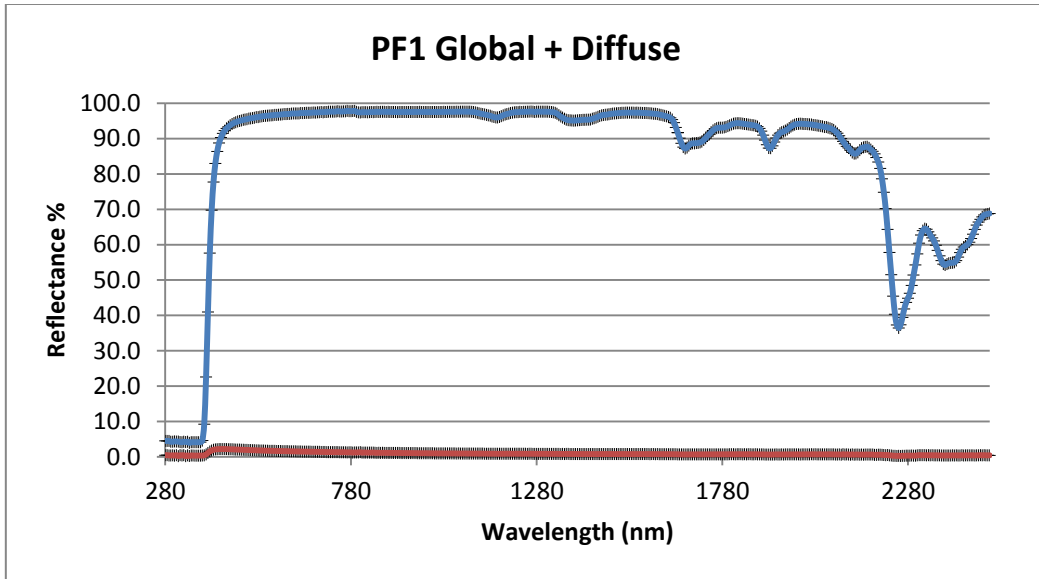


Figure 5. 80 PF1 Spectral response

While the variation of specular reflectance is shown in the next figure 5.81.

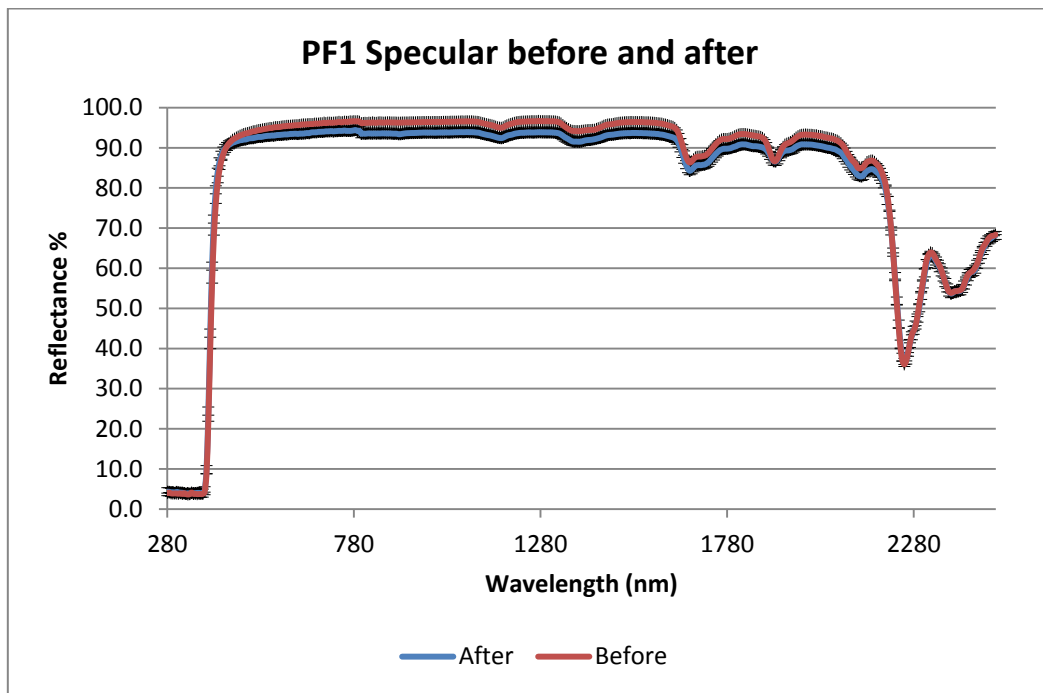


Figure 5. 81 Specular reflectance variation

In order to evaluate the decreasing of performance the diffuse reflectance comparison is proposed in the next graph.

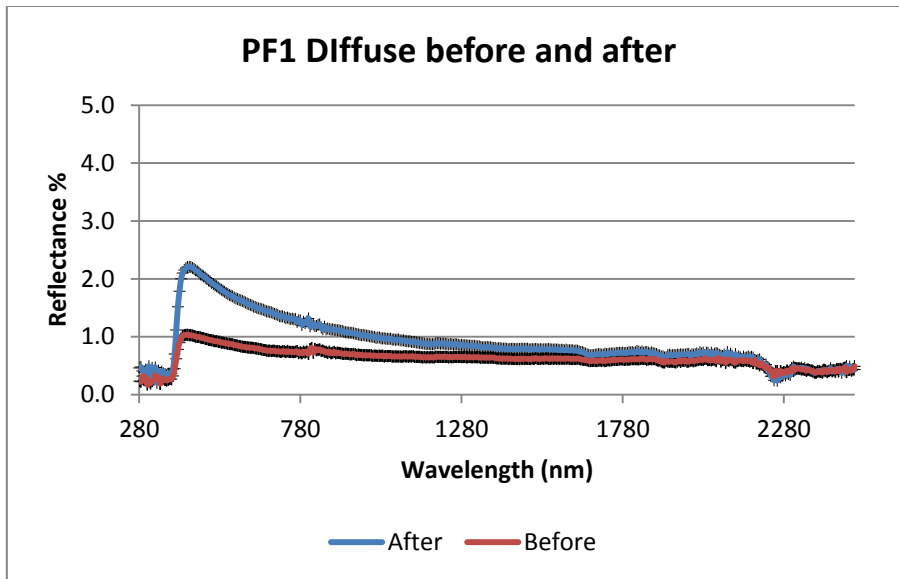


Figure 5. 82 Diffuse reflectance comparison

Then the differences between the time 0 and the 1 year UV radiation exposure.

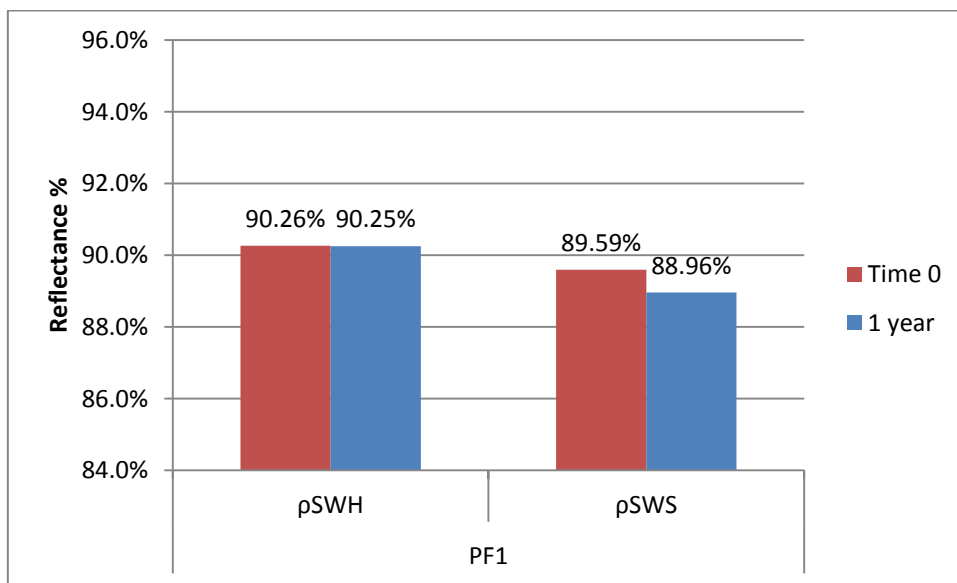


Figure 5. 83 Comparison of Solar weighted hemispherical and specular reflectance at time 0 and after the UV exposure

As far as the hemispherical reflectance is concerned, it is almost similar to the time 0 value while for the specular reflectance we experienced a loss of 0.63%

Finally is proposed a general comparison between the solar weighted hemispherical reflectance and the solar weighted specular reflectance for each typology of mirrors at the time 0 and after the UV exposure.

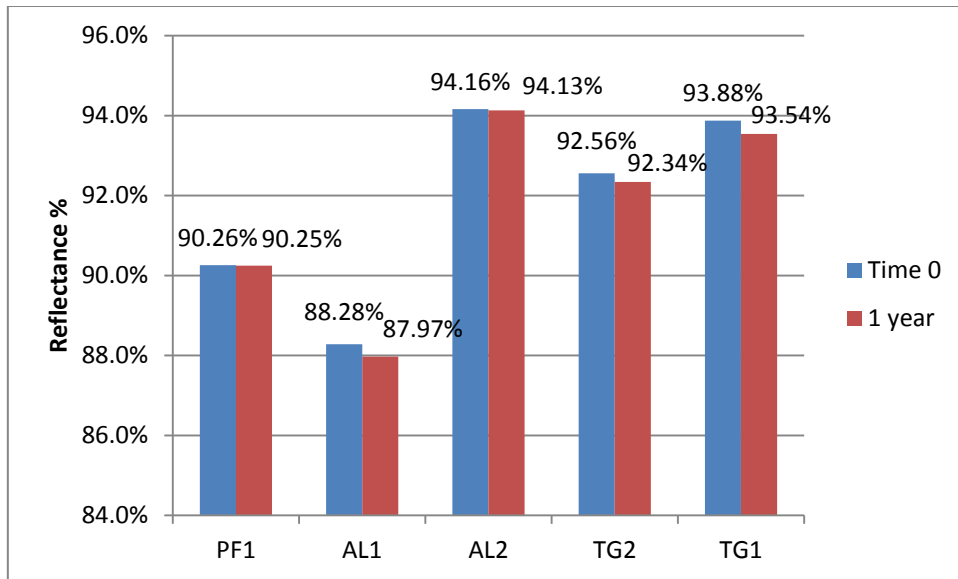


Figure 5. 84 Solar weighted hemispherical reflectance in the condition 0 and after one year of UV exposure

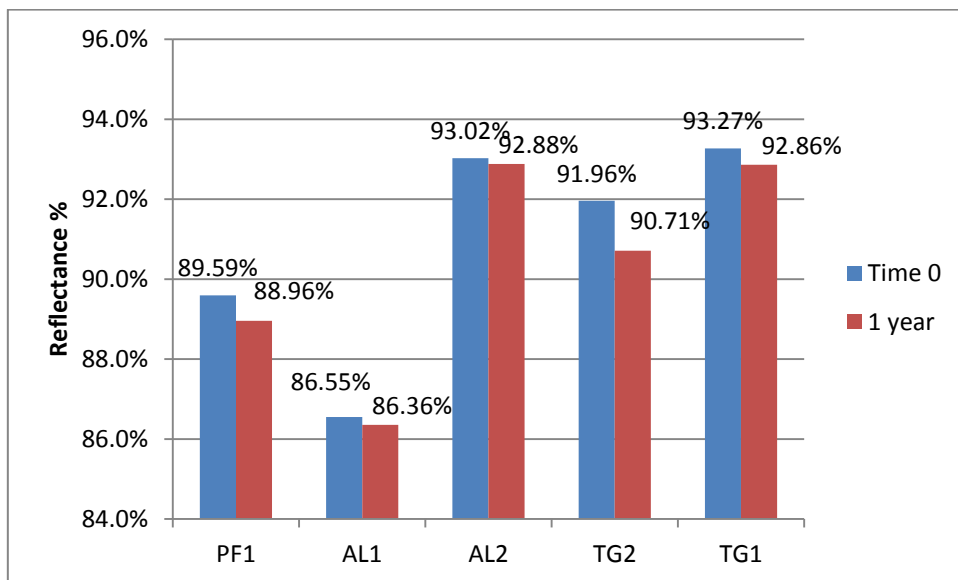
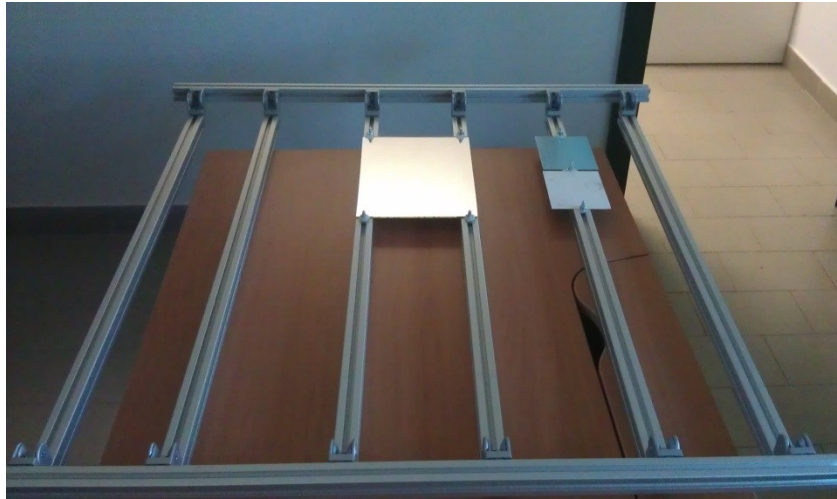


Figure 5. 85 Solar weighted specular reflectance in the condition 0 and after one year of UV exposure

## 5.4 Outdoor exposure measurements

In order to assess the mirror behaviors in an outdoor environment it was necessary to build an experimental bench placed at the research site.

The bench was primarily built with aluminum profiles as it can be seen in the next picture and then mounted on an existing bench outdoor.



**Figure 5. 86 Aluminum structure for outdoor exposure**

The exposure test started on 13<sup>th</sup> October and it was carried on for a month to assess the losses of reflectance for each type of mirror the samples used were all cleaned before the beginning of experimentation.

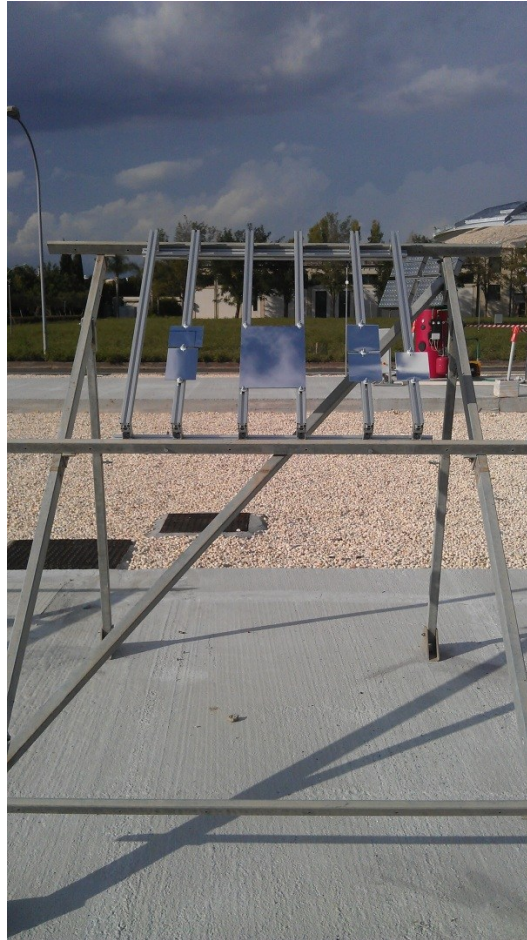


**Figure 5.87 External bench for outdoor exposure test**

All the samples were linked to the structure using screws and nuts chosen for the objective with washers in pvc capable of not scratching the samples end ensure the stability of the sample itself with all atmosphere conditions. During the first month of exposure we had several days of rain and strong wind with the relative transport of dust and soil on the sample surfaces.

In order to compare the soiling effect on the samples we used a field scatterometer at the beginning of the experimentation and after one month.

The SMS  $\mu$ Scan System consists of a hand held Control Unit (CU), an interchangeable measurement head, and a separate charging unit. The CU controls all aspects of the system operation.

To perform a measurement, the operator places the measurement head on the surface to be measured and presses the button. Each measurement takes less than five seconds.

Software is available for control, analysis and file conversion.

The SMS  $\mu$ Scan System allows the operator to rapidly take measurements at the sample - where is needed – in seconds. From a single measurement, a user can determine RMS surface roughness, reflectance and scattered light level (BRDF) on flat or curved surfaces under any lighting conditions.

In the following figure are shown the SMS scatterometer, technical information and performance.



Figure 5. 88 SMS Scatterometer

$\mu$ Scan® Technical Information		CE COMPLIANT	ISO 9001 TÜV CERTIFIED
<b>Measurements</b>			
Range:	(Ra, RMS, P-V) (Reflectance) (BRDF)	From 1Å up to 1100Å From 0.1 up to 100.0% From 1 <sup>st</sup> to 1 <sup>60</sup> (sr <sup>-1</sup> )	.01 to 5 $\mu$ m.
Spatial Bandwidth:	Upper Lower	10 to 999 $\mu$ m (selectable) 1.0 $\mu$ m	
<b>Measurement Head</b>			
Dimensions	5"h x 3½"d		
Weight	1¼ lbs.		
Time of Measurement	< 5 seconds		
Spot Size	1 mm		
Repeatability	±0.5%		
Accuracy	±2% Reflectance ±3% Scatter		
Wavelength	670nm (1300nm available)		
	1.Laser diode 2.Reflectance detector and specular beam trap 3.Scatter detectors		
<b>Control Unit</b>			
Dimensions	1¼" h x 4¼" w x 9¼" d	Storage	-40C to +50C
Weight	2 lbs.	Temperature Coefficient	
Power Source		Scatter detectors	±0.1% per °C
Batteries		Reflectance detector	±0.15% per °C
- Type	Rechargeable NiCd	Non-Volatile Memory	
- Duration	> 5 hours	Storage capacity	700 measurements
- Charge Time	Turbo < 3 hours, trickle 15 hours	Number of files	255
External	9 VDC to 11 VDC	Real Time Clock	
Data Transfer	Baud rate selectable to 9600, 4800, 2400, 1200, 300 bps (no parity, 8 bits, 1 stop bit)	Display	
Temperature Range		Size	4 line x 20 character LCD
Operations	-10C to +45C (LCD Limited)	Lighting	LED backlit
		Contrast Control	Keypad controllable

Figure 5. 89 Instrument technical information

It's noticeable that this instrument works at only one wavelength in particular at 670 nm.

The instrument is calibrated upon a reference dielectric mirror shown in the next picture 5.90.



Figure 5.90 Reference dielectric mirror

With the certificate of calibration reported in the next figure 5.91.



Figure 5.91 Certificate of calibration and reference mirror value

It's also important to define the sensitivity of this instrument which is  $\pm 2\%$  for the dielectric mirror measurement. In the followings will be introduced also the value of the BDSF which is the bi-directional scattering distribution function.

In the followings the values measured for the different typologies of mirrors are reported.

### 5.4.1 Thin glass mirrors

For the thin glass mirrors TG1 and TG2 with the scatterometer we obtained the following roughness and BDSF.

For the TG1 mirror we did 30 measurements along the middle line of the sample a value of reflectance at 670 nm and at 25° equal to a mean of respectively:

**Reflectance:** 95.00%

**RMS Roughness:** 33.50  $\mu\text{m}$

With a behaviour reported in the next figure 5.92.

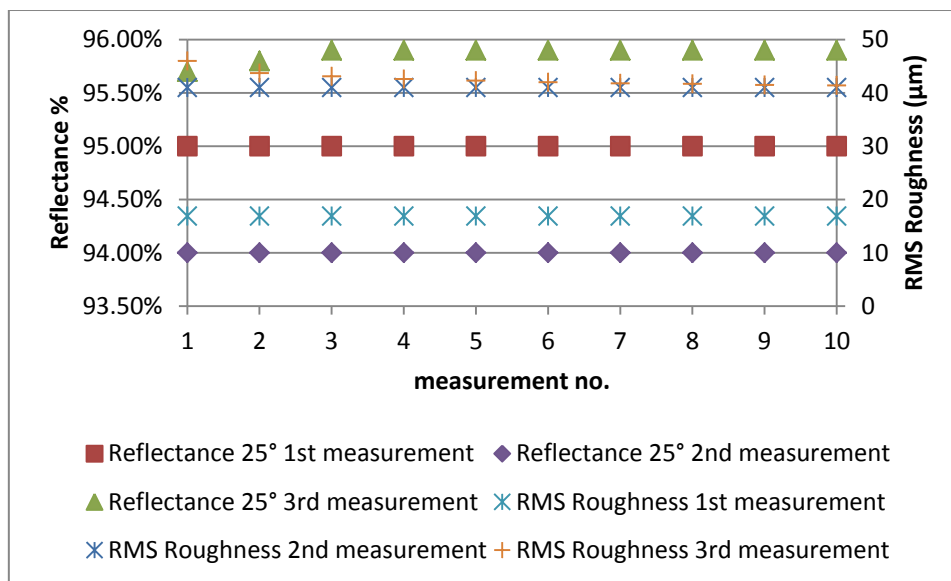


Figure 5.92 Reflectance at 25° (primary axis) and RMS Roughness (Secondary axis)

With a BDSF measured on two different planes, the first at 0,0 that means that detectors in the measurement head are located using beam coordinates, thus,  $\theta_s$  is 0° and  $\phi_s$  is 0° (indicating that detector is in the incident plane), while the second measurement is taken at  $\theta_s$  is 50° and  $\phi_s$  is 180°.

$\theta_s$  is the receiver theta angle which is the same between the beam coordinates and the scatter coordinates.

$\theta_i$  is the incident theta angle which is the same between the beam coordinates and have the same nomenclature

$\phi_s$  is the angle that correlates the scatter (receiver) azimuthal angles in the beam coordinates and the scatter coordinates with the relation  $\phi_s = \Phi_s + \alpha$

$\phi_i$  is the angle that correlates the incident azimuthal angle in the beam coordinates and the scatter coordinates with the relation  $\phi_i = \Phi_i + \alpha = 180^\circ$

The incident angle of source is reported in the instrument display and it is always  $\theta_i = 25^\circ$  at 670 nm.

The standard deviation for the above measurements is equal to 0.78 % for the reflectance and 11.9850  $\mu\text{m}$  for the RMS roughness.

In the next graph (figure 5.93) it's possible to see the values of BDSF, along the middle line of the sample, in the two different plane with a mean value for the first measurement equal to  $1.008\text{E-}03 \text{ sr}^{-1}$  and for the second measurement is equal to  $1.873\text{E-}04 \text{ sr}^{-1}$ .

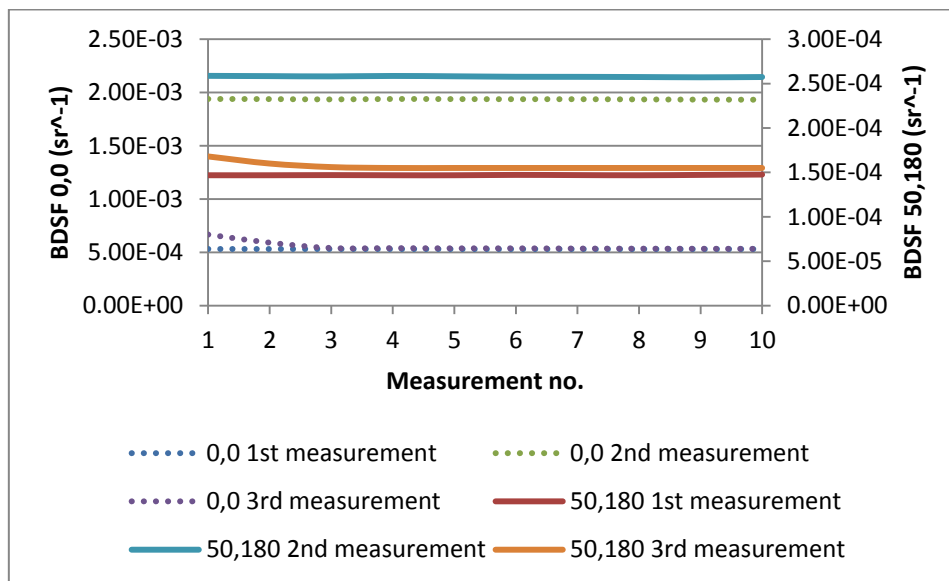


Figure 5. 93 BDSF at (0,0) and (50,180) for the TG1 sample

The standard deviation for the above measurements is equal to  $6.6844\text{E-}04 \text{ sr}^{-1}$  for the BDSF (0,0) and  $6.1030\text{E-}05 \text{ sr}^{-1}$  for the BDSF (50,180).

For the TG2 mirror we did 30 measurements along the middle line of the sample a value of reflectance at 670 nm and at  $25^\circ$  equal to a mean of respectively:

**Reflectance:** 93.00%

**RMS Roughness:** 23.427  $\mu\text{m}$

With a behaviour reported in the next figure 5.94.

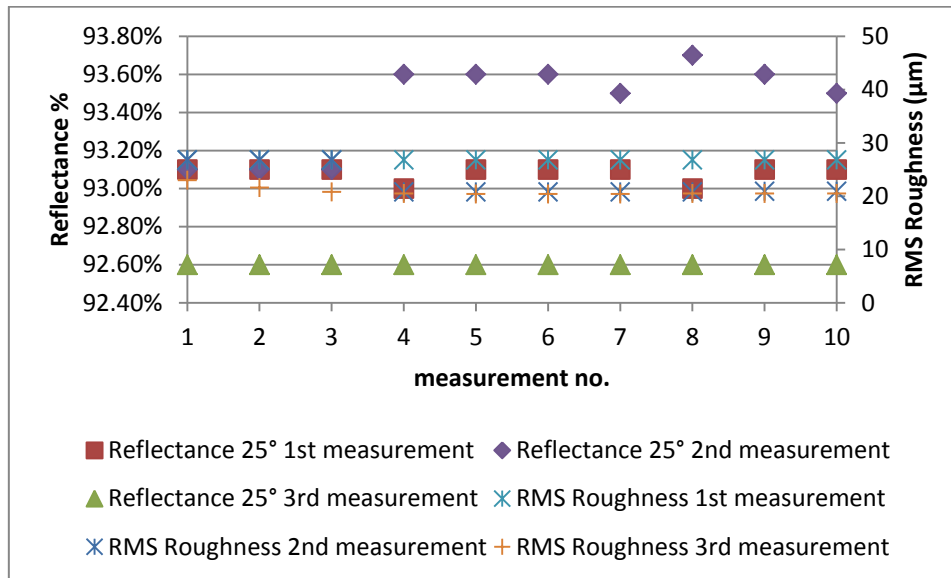


**Figure 5. 94 Reflectance at 25° (primary axis) and RMS Roughness (Secondary axis)**

The standard deviation for the above measurements is equal to 0.4 % for the reflectance and 3.036  $\mu\text{m}$  for the RMS roughness.

In the next graph (figure 5.95) it's possible to see the values of BDSF, along the middle line of the sample, in the two different plane with a mean value for the first measurement equal to  $1.057\text{E}-03 \text{ sr}^{-1}$  and for the second measurement is equal to  $3.936\text{E}-04 \text{ sr}^{-1}$ .

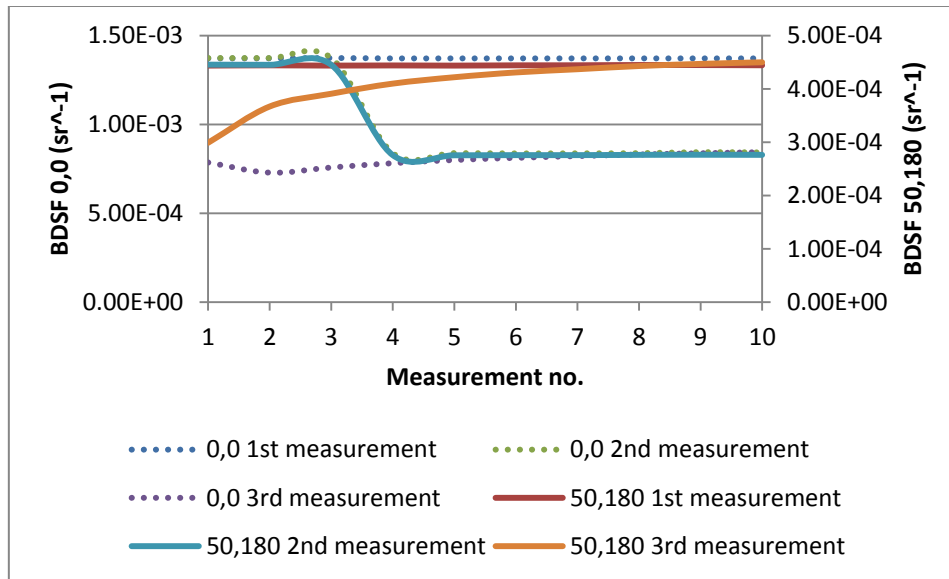


Figure 5.95 BDSF at (0,0) and (50,180) for the TG2 sample

The standard deviation for the above measurements is equal to  $1.057E-03 \text{ sr}^{-1}$  for the BDSF (0,0) and  $3.936E-04 \text{ sr}^{-1}$  for the BDSF (50,180).

#### 5.4.2 Aluminum mirror

For the aluminum mirrors AL1 and AL2 we obtained with the scatterometer the following roughness and BDSF.

For the AL1 mirror we did 30 measurements along the middle line of the sample a value of reflectance at 670 nm and at  $25^\circ$  equal to a mean of respectively:

**Reflectance:** 91.30%

**RMS Roughness:** 53.70  $\mu\text{m}$

With a behaviour reported in the next figure 5.96.

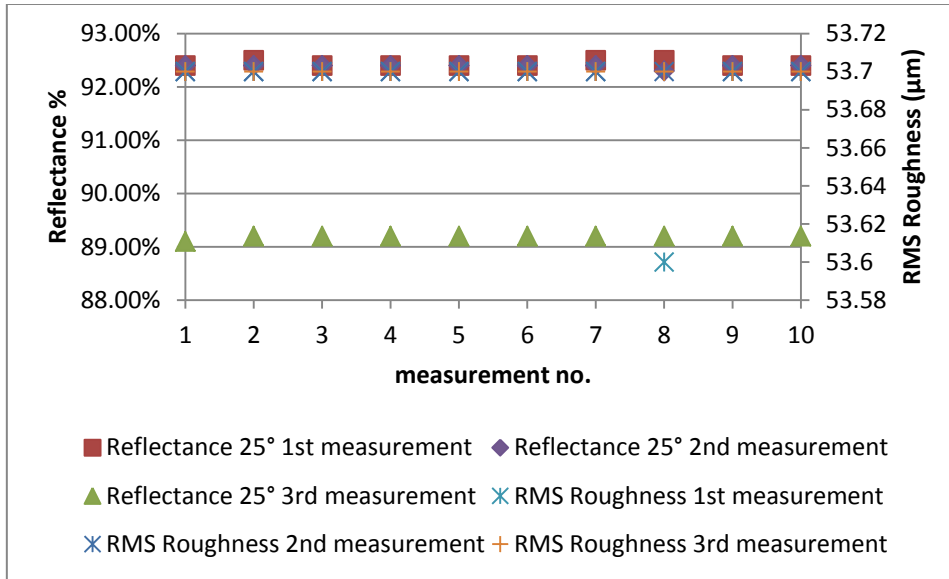


Figure 5.96 Reflectance at 25° (primary axis) and RMS Roughness (Secondary axis)

The standard deviation for the above measurements is equal to 1.54 % for the reflectance and 0.0183 µm for the RMS roughness.

With a BDSF measured on two different plane, the first at 0,0 that means that detectors in the measurement head are located using beam coordinates, thus,  $\theta_s$  is 0° and  $\phi_s$  is 0° (indicating that detector is in the incident plane), while the second measurement is taken at  $\theta_s$  is 50° and  $\phi_s$  is 180°.

$\theta_s$  is the receiver theta angle which is the same between the beam coordinates and the scatter coordinates.

$\theta_i$  is the incident theta angle which is the same between the beam coordinates and have the same nomenclature

$\phi_s$  is the angle that correlates the scatter (receiver) azimuthal angles in the beam coordinates and the scatter coordinates with the relation  $\phi_s = \Phi_s + \alpha$

$\phi_i$  is the angle that correlates the incident azimuthal angle in the beam coordinates and the scatter coordinates with the relation  $\phi_i = \Phi_i + \alpha = 180^\circ$

The incident angle of source is reported in the instrument display and it is always  $\theta_i = 25^\circ$  at 670 nm.

In the next graph (figure 5.97) it's possible to see the values of BDSF, along the middle line of the sample, in the two different plane with a mean value for the first measurement equal to  $3.55E-03 \text{ sr}^{-1}$  and for the second measurement is equal to  $4.80E-04 \text{ sr}^{-1}$ .

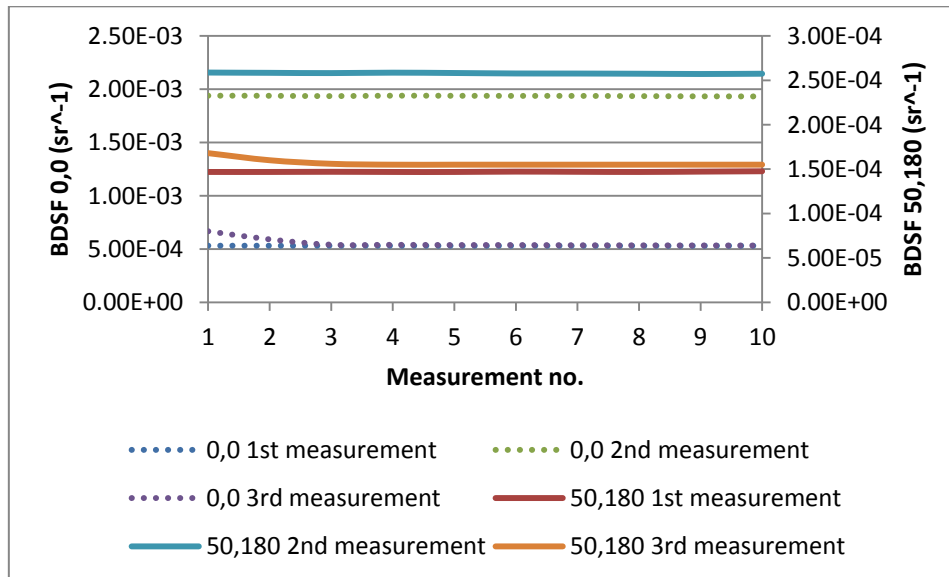


Figure 5. 97 BDSF at (0,0) and (50,180) for the TG1 sample

The standard deviation for the above measurements is equal to  $1.12E-03 \text{ sr}^{-1}$  for the BDSF (0,0) and  $2.33E-04 \text{ sr}^{-1}$  for the BDSF (50,180).

For the AL2 mirror we did 30 measurements along the middle line of the sample a value of reflectance at 670 nm and at  $25^\circ$  equal to a mean of respectively:

**Reflectance:** 96.40%

**RMS Roughness:** 72.44  $\mu\text{m}$

With a behaviour reported in the next figure 5.98.

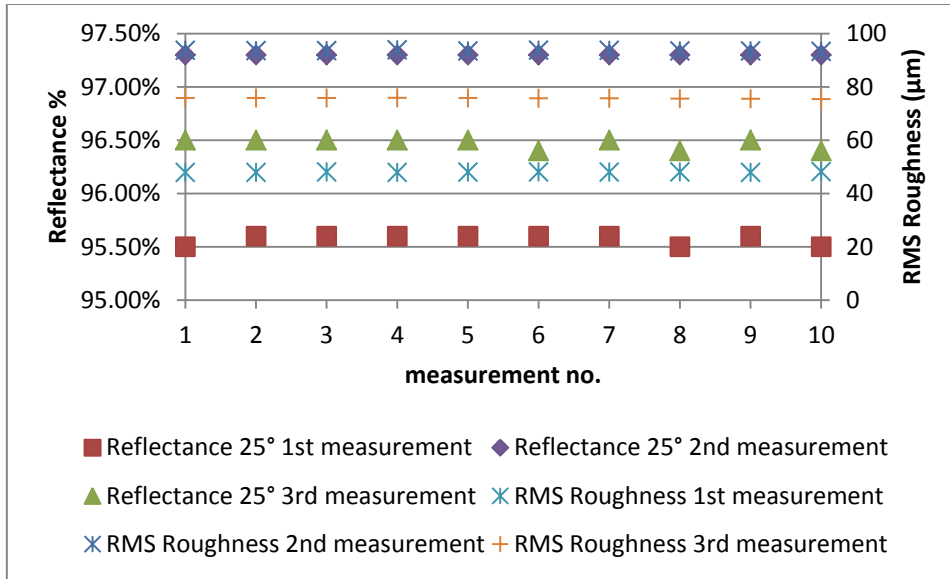


Figure 5.98 Reflectance at 25° (primary axis) and RMS Roughness (Secondary axis)

The standard deviation for the above measurements is equal to 0.7 % for the reflectance and 19.08  $\mu\text{m}$  for the RMS roughness.

In the next graph (figure 5.99) it's possible to see the values of BDSF, along the middle line of the sample, in the two different plane with a mean value for the first measurement equal to  $6.59\text{E-}03 \text{ sr}^{-1}$  and for the second measurement is equal to  $4.15\text{E-}04 \text{ sr}^{-1}$ .

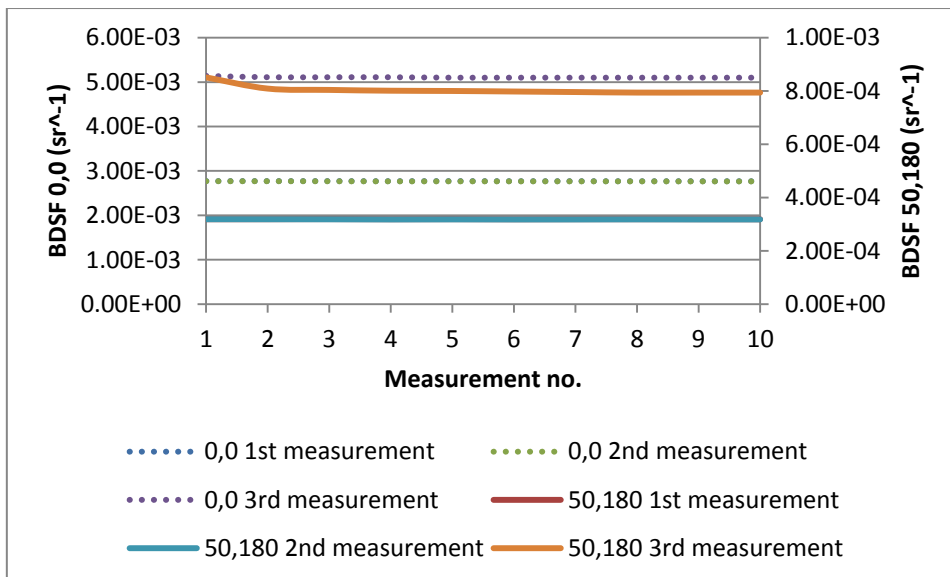


Figure 5.99 BDSF at (0,0) and (50,180) for the AL2 sample

The standard deviation for the above measurements is equal to  $6.06\text{E-}03 \text{ sr}^{-1}$  for the BDSF (0,0) and  $3.56\text{E-}04 \text{ sr}^{-1}$  for the BDSF (50,180).

### 5.4.3 Polymeric film mirrors

Unfortunately the PF2 sample was the only one in our possess so it wasn't possible to measure the values with the scatterometer after one month of outdoor exposure.

Anyway was possible to characterize this mirror at the zero time without any contamination of the external weather agents.

For the polymeric mirrors PF1 and PF2 we obtained with the scatterometer the following roughness and BDSF.

For the PF1 mirror we did 30 measurements along the middle line of the sample a value of reflectance at 670 nm and at 25° equal to a mean of respectively:

**Reflectance:** 98.9%

**RMS Roughness:** 87.50  $\mu\text{m}$

With a behaviour reported in the next figure 5.100.

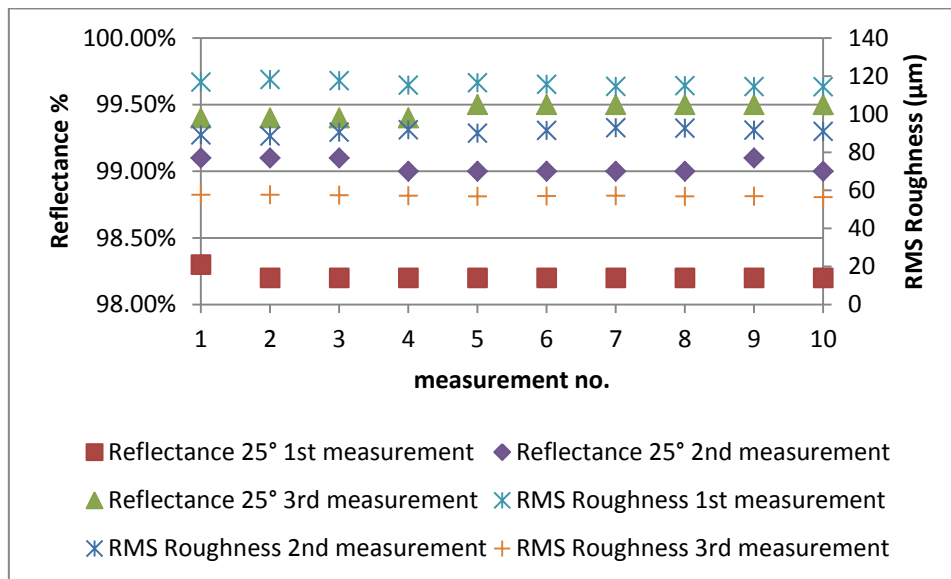


Figure 5. 100 Reflectance at 25° (primary axis) and RMS Roughness (Secondary axis)

The standard deviation for the above measurements is equal to 0.5 % for the reflectance and 24.53  $\mu\text{m}$  for the RMS roughness

With a BDSF measured on two different plane, the first at 0,0 that means that detectors in the measurement head are located using beam coordinates, thus,  $\theta_s$  is  $0^\circ$  and  $\phi_s$  is  $0^\circ$  (indicating that detector is in the incident plane), while the second measurement is taken at  $\theta_s$  is  $50^\circ$  and  $\phi_s$  is  $180^\circ$ .

$\theta_s$  is the receiver theta angle which is the same between the beam coordinates and the scatter coordinates.

$\theta_i$  is the incident theta angle which is the same between the beam coordinates and have the same nomenclature

$\phi_s$  is the angle that correlates the scatter (receiver) azimuthal angles in the beam coordinates and the scatter coordinates with the relation  $\phi_s = \Phi_s + \alpha$

$\phi_i$  is the angle that correlates the incident azimuthal angle in the beam coordinates and the scatter coordinates with the relation  $\phi_i = \Phi_i + \alpha = 180^\circ$

The incident angle of source is reported in the instrument display and it is always  $\theta_i = 25^\circ$  at 670 nm.

In the next graph (figure 5.101) it's possible to see the values of BDSF, along the middle line of the sample, in the two different plane with a mean value for the first measurement equal to  $2.24E-03 \text{ sr}^{-1}$  and for the second measurement is equal to  $1.45E-04 \text{ sr}^{-1}$ .

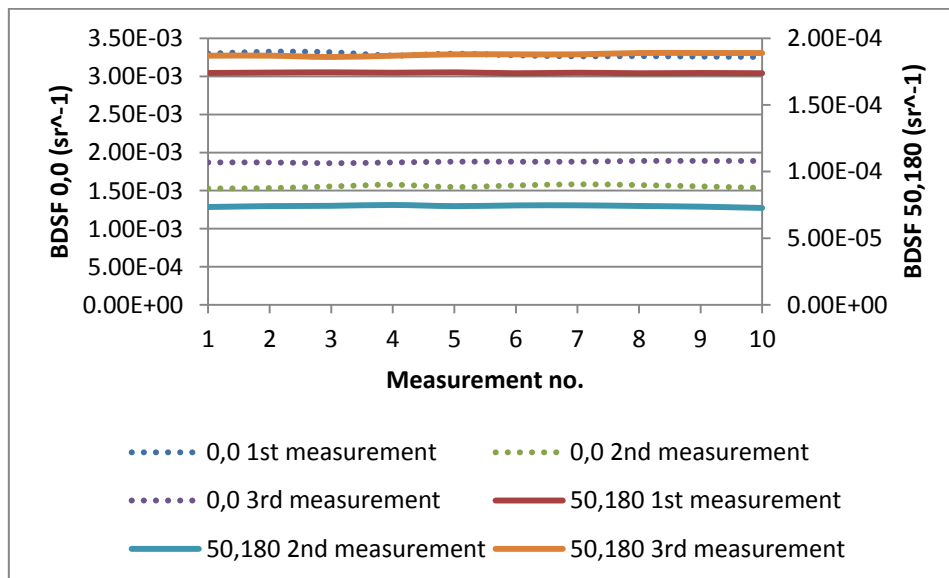


Figure 5. 101 BDSF at (0,0) and (50,180) for the TG1 sample

The standard deviation for the above measurements is equal to  $7.63E-04 \text{ sr}^{-1}$  for the BDSF (0,0) and  $5.20E-05 \text{ sr}^{-1}$  for the BDSF (50,180).

For the PF2 mirror we did 30 measurements along the middle line of the sample a value of reflectance at 670 nm and at  $25^\circ$  equal to a mean of respectively:

**Reflectance:** 91.90%

**RMS Roughness:** 78.41  $\mu\text{m}$

With a behaviour reported in the next figure 5.102.

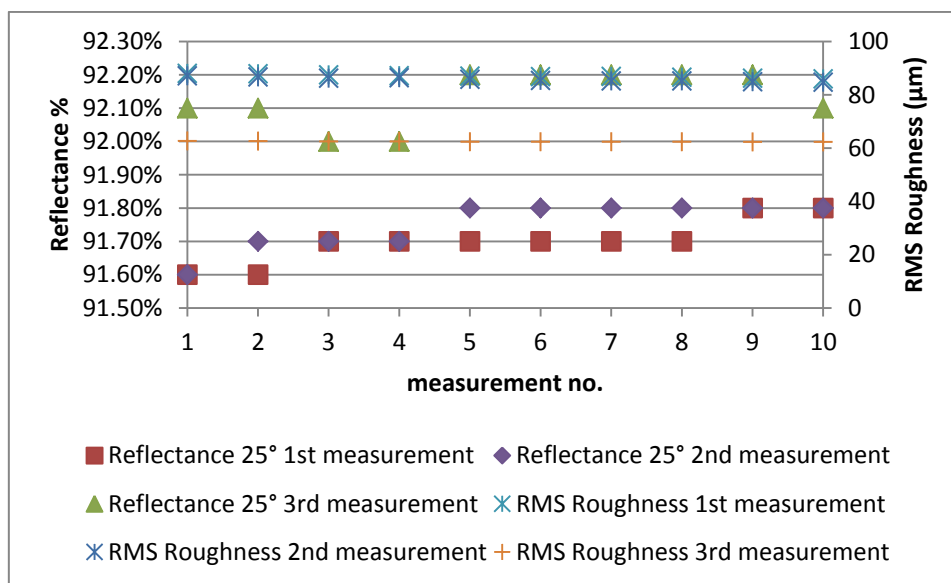


Figure 5.102 Reflectance at  $25^\circ$  (primary axis) and RMS Roughness (Secondary axis)

The standard deviation for the above measurements is equal to 0.2 % for the reflectance and 11.50  $\mu\text{m}$  for the RMS roughness

In the next graph (figure 5.103) it's possible to see the values of BDSF, along the middle line of the sample, in the two different plane with a mean value for the first measurement equal to  $6.53E-03 \text{ sr}^{-1}$  and for the second measurement is equal to  $7.92E-04 \text{ sr}^{-1}$ .

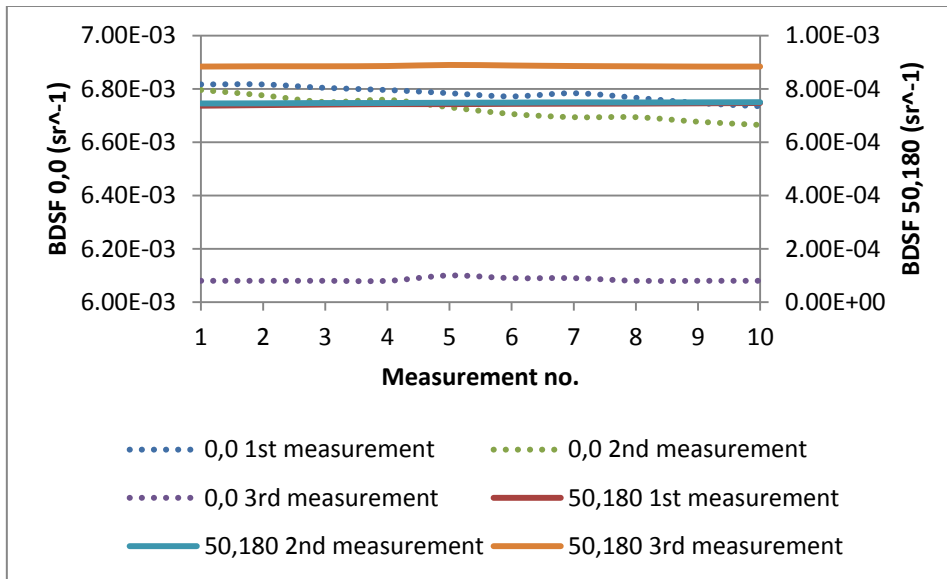


Figure 5. 103 BDSF at (0,0) and (50,180) for the AL2 sample

The standard deviation for the above measurements is equal to  $6.53E-03 \text{ sr}^{-1}$  for the BDSF (0,0) and  $7.92-04 \text{ sr}^{-1}$  for the BDSF (50,180).

In the next table will be reported the meteorological condition along the month of October.

### 5.5 Reflectance measurement after one month (Scatterometer)

With a visual inspection after the first month of outdoor exposure we noticed that the AL2 mirror despite the other samples behavior was covered with fouling on its surface determining a huge loss of the reflectance capacity.

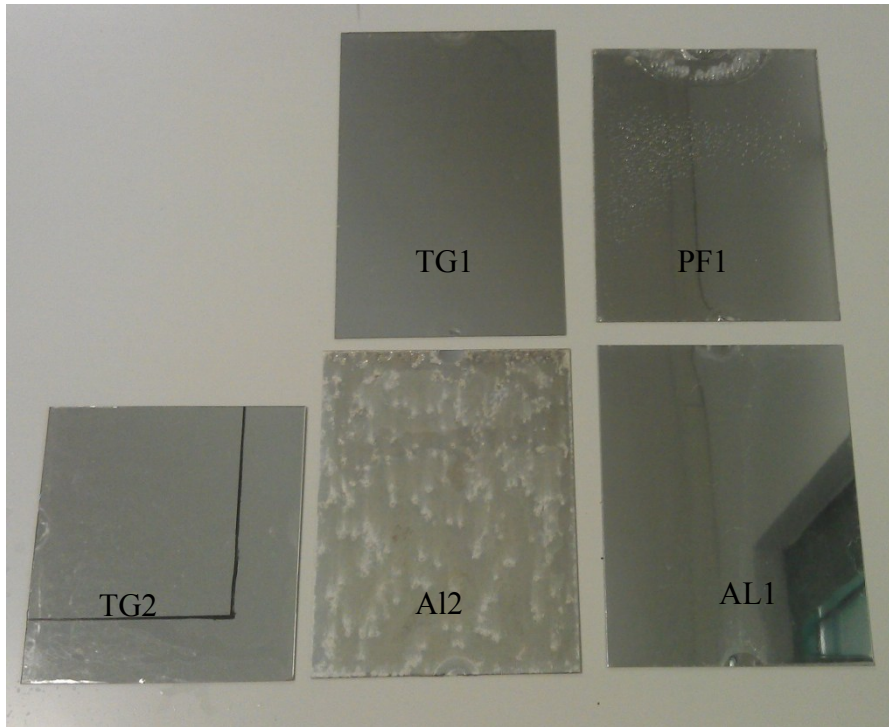


Figure 5.104 The mirror samples after one month of outdoor exposure

In the followings will be reported the values of reflectance, BDSF, and RMS roughness for all the typologies of mirrors.

### 5.5.1 Thin glass mirrors

So we obtained measuring the TG1 sample with the scatterometer the following average values of reflectance and RMS roughness with the values of BDSF in all the two cases shown in the previous subchapter.

Reflectance: 94.00%;

RMS Roughness: 63.54  $\mu\text{m}$ ;

BDSF (0,0): 5.21 E-03;

BDSF (50,180): 7.84 E-04;

As previously graphically represented here in the following the relative graph (figure 5.105 and 5.106)

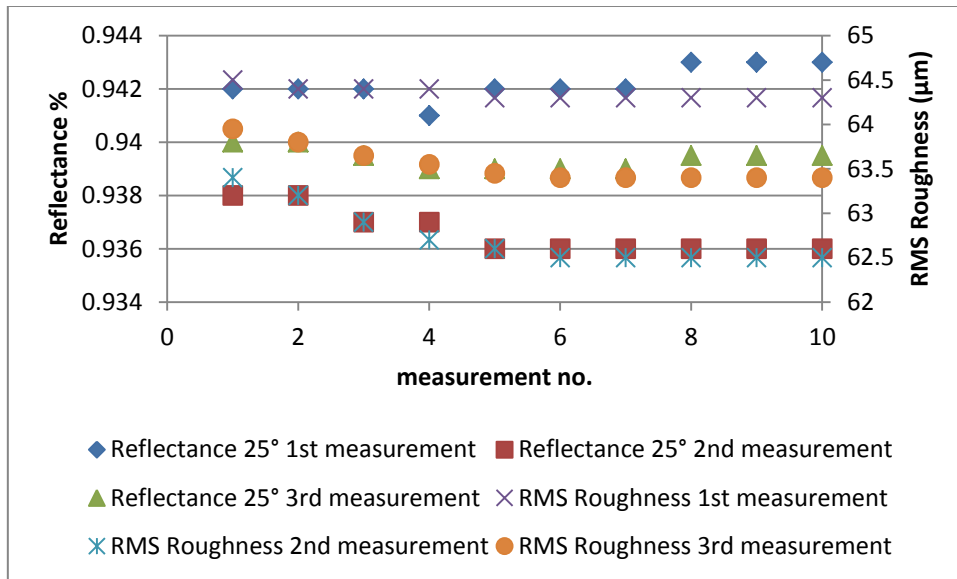


Figure 5.105 Reflectance and RMS roughness values

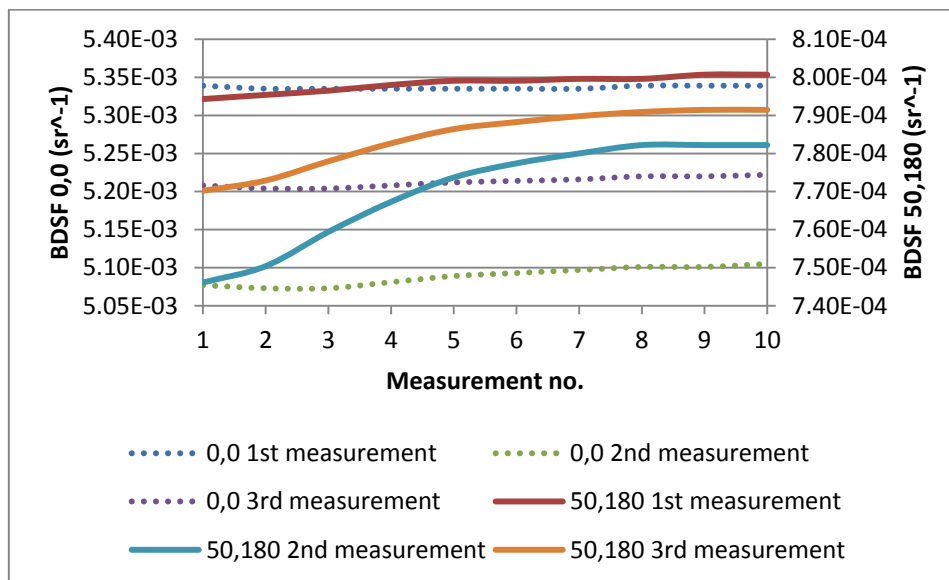


Figure 5.106 BDSF (0,0) and BDSF (50,180) values

The standard deviation of the above measurements are respectively 0.2% for the reflectance, 0.707  $\mu\text{m}$  for the RMS roughness,  $1.03\text{E-}04 \text{ sr}^{-1}$  for the BDSF (0,0) and  $1.50\text{E-}05 \text{ sr}^{-1}$  for the BDSF (50,180).

For the TG2 mirror we obtained the following results

Reflectance: 91.00%;

RMS Roughness: 69.79  $\mu\text{m}$ ;

BDSF (0,0): 7.66 E-03;

BDSF (50,180): 1.61 E-04;

As previously graphically represented here in the following the relative graph (figure 5.107 and 5.108)

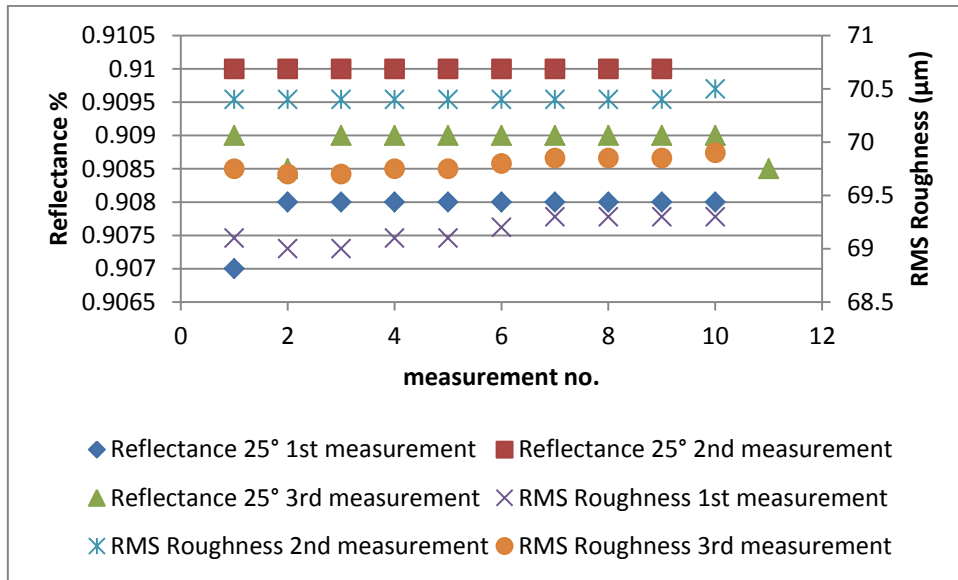


Figure 5. 107 Reflectance and RMS roughness values

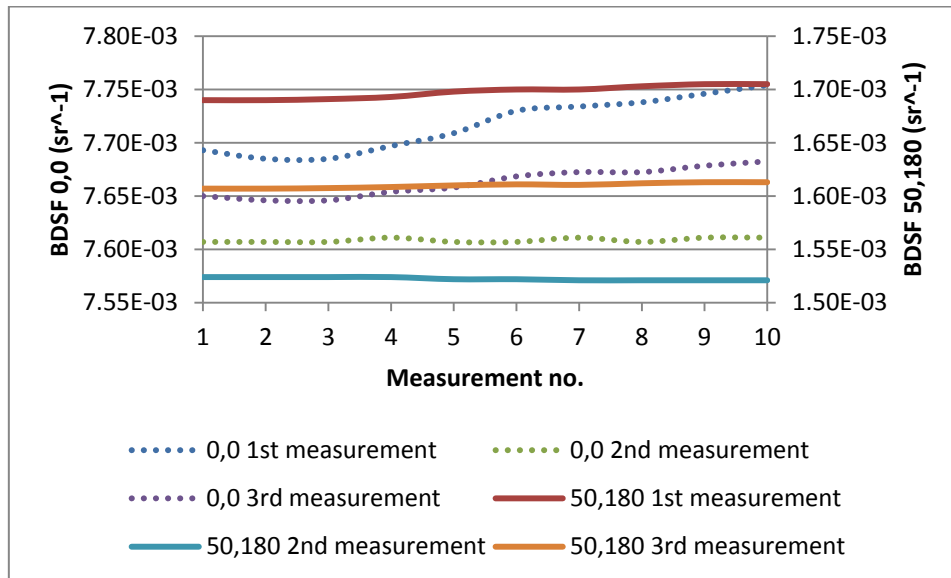


Figure 5. 108 BDSF (0,0) and BDSF (50,180) values

The standard deviation of the above measurements are respectively 0.1% for the reflectance, 0.521  $\mu\text{m}$  for the RMS roughness,  $4.80\text{E-}05 \text{ sr}^{-1}$  for the BDSF (0,0) and  $7.30\text{E-}05 \text{ sr}^{-1}$  for the BDSF (50,180).

### 5.5.2 Aluminum mirrors

For the aluminum mirror we obtained the following average values of reflectance, BDSF and RMS roughness.

Reflectance: 82.00%;

RMS Roughness: 126.50  $\mu\text{m}$ ;

BDSF (0,0): 2.14 E-02;

BDSF (50,180): 3.89 E-03;

As previously graphically represented here in the following the relative graph (figure 5.109 and 5.110)

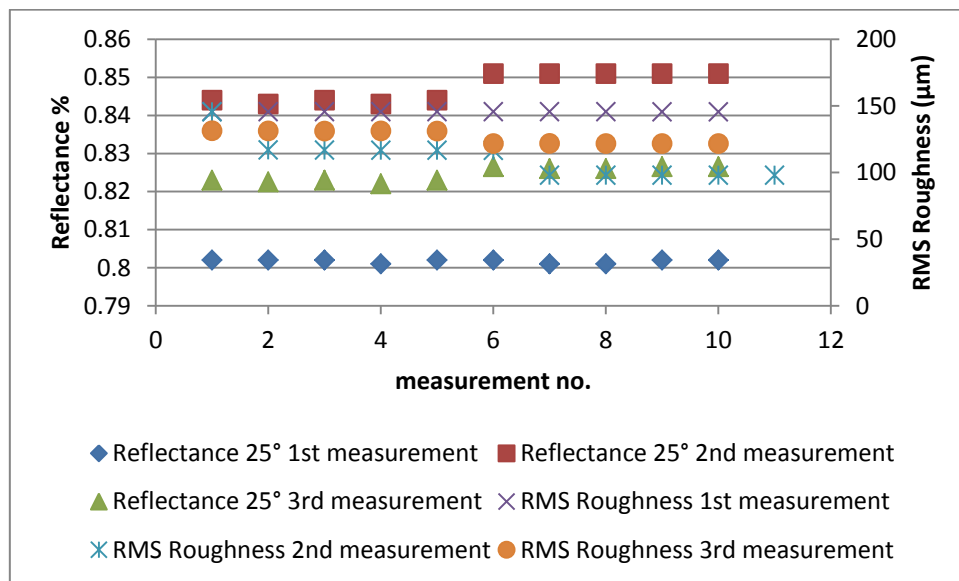


Figure 5. 109 Reflectance and RMS roughness values

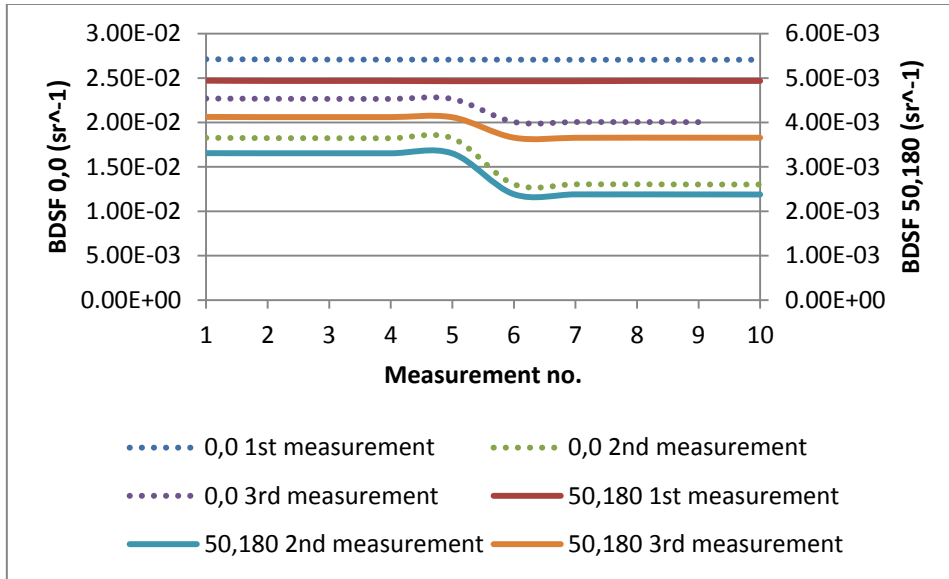


Figure 5. 110 BDSF (0,0) and BDSF (50,180) values

The standard deviation of the above measurements are respectively 1.9% for the reflectance, 17.04  $\mu\text{m}$  for the RMS roughness,  $4.80\text{E-}05 \text{ sr}^{-1}$  for the BDSF (0,0) and  $7.30\text{E-}05 \text{ sr}^{-1}$  for the BDSF (50,180).

For the AL2 mirror we obtained the following results.

Reflectance: 51.00%;

RMS Roughness: 330.91  $\mu\text{m}$ ;

BDSF (0,0): 1.12 E-01;

BDSF (50,180): 3.32 E-02;

As previously graphically represented here in the following the relative graph (figure 5.111 and 5.112)

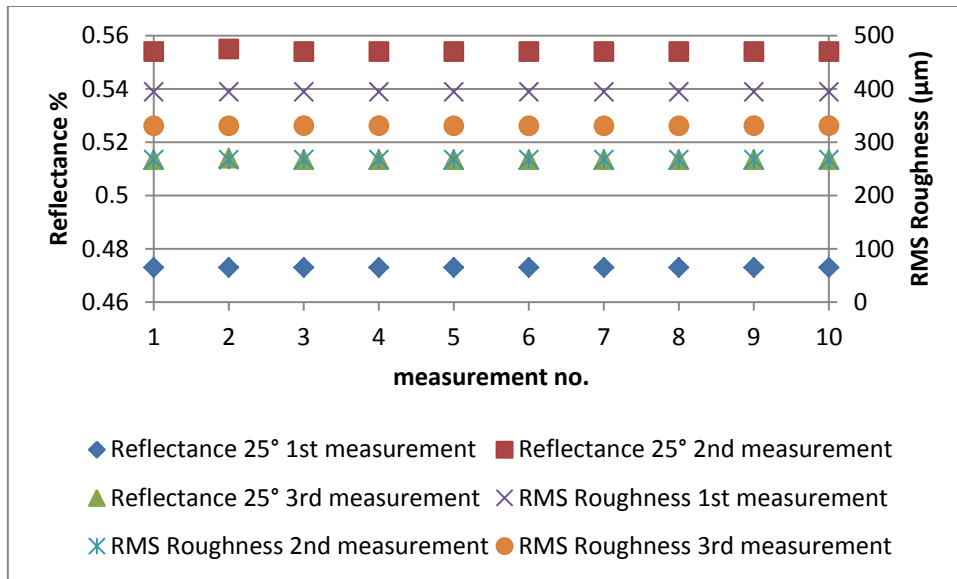


Figure 5.111 Reflectance and RMS roughness values

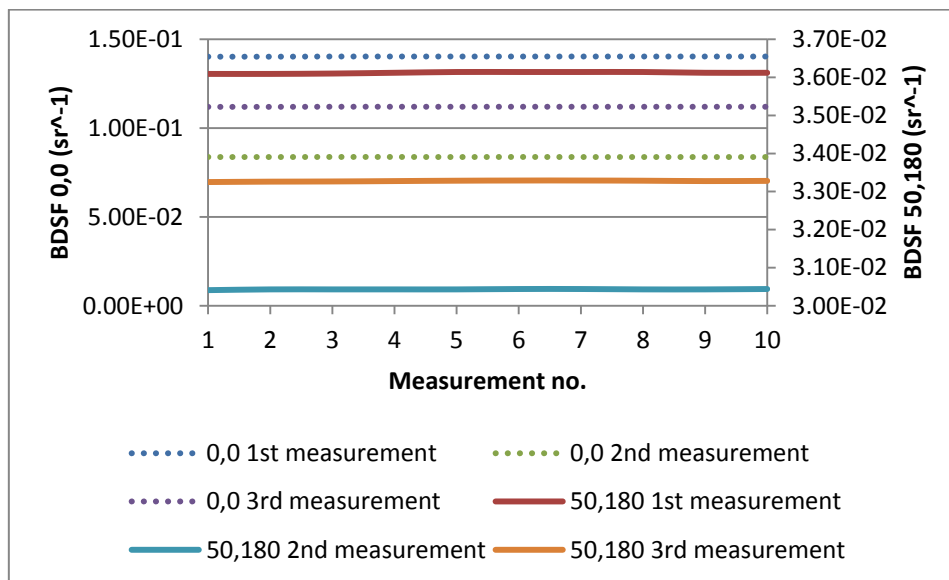


Figure 5.112 BDSF (0,0) and BDSF (50,180) values

The standard deviation of the above measurements are respectively 3.4% for the reflectance, 52.75  $\mu\text{m}$  for the RMS roughness,  $2.35\text{E-}02 \text{ sr}^{-1}$  for the BDSF (0,0) and  $2.36\text{E-}03 \text{ sr}^{-1}$  for the BDSF (50,180).

### 5.5.3 Polymeric mirror

As said before the only polymeric film mirror exposed outdoor was the PF1 sample and here in the followings are reported the results obtained.

Reflectance: 93.00%;

RMS Roughness: 91.20  $\mu\text{m}$ ;

BDSF (0,0): 1.28 E-02;

BDSF (50,180): 2.49 E-03;

As previously graphically represented here in the following the relative graph (figure 5.113 and 5.114)

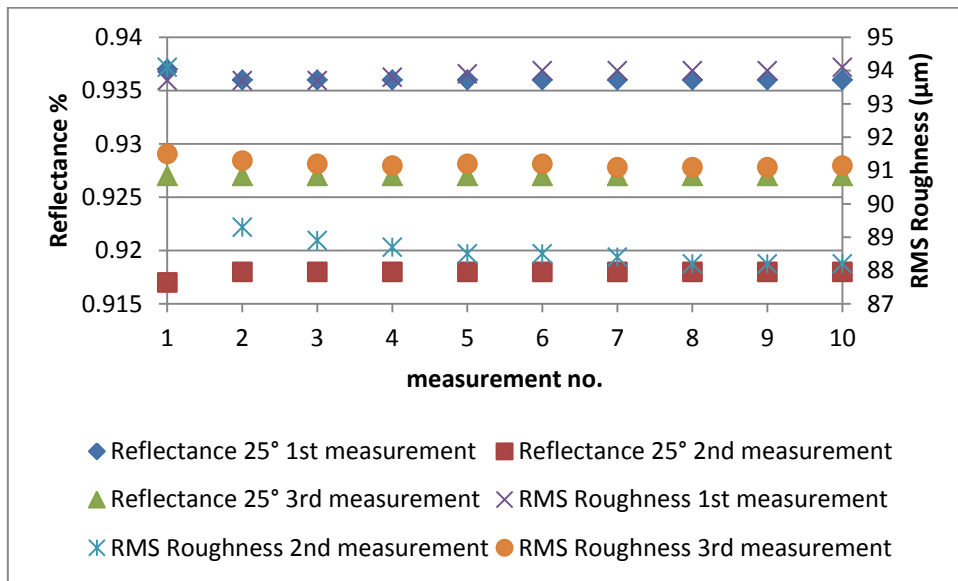


Figure 5. 113 Reflectance and RMS roughness values

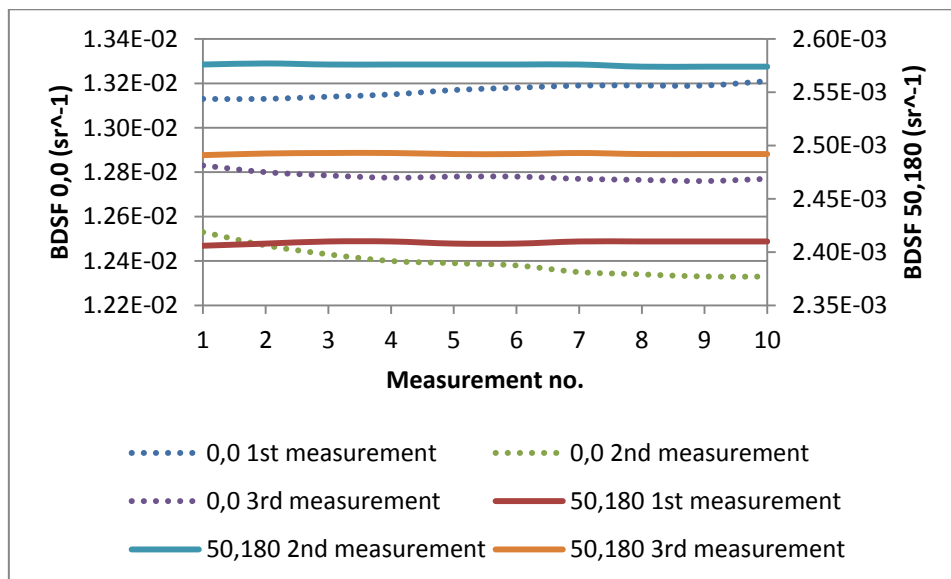


Figure 5. 114 BDSF (0,0) and BDSF (50,180) values

The standard deviation of the above measurements are respectively 0.756% for the reflectance, 2.245  $\mu\text{m}$  for the RMS roughness, 3.24E-04  $\text{sr}^{-1}$  for the BDSF (0,0) and 6.91E-05  $\text{sr}^{-1}$  for the BDSF (50,180).

## 5.6 Comparison between the scatterometer measurement after one month

In the followings will be shown the variation of the values up above evaluated with the scatterometer in order to compare and evaluate the soiling effect on the mirrors surfaces.

For what concern the BDSF in the two cases shown before, the (0,0) and the (50,180), we compared the results obtained so we had as it was expected an increase of the scattering function due to the soiling effects that is far more evident in the AL2 mirror as it was seen in figure 5.115 in the previous subchapter.

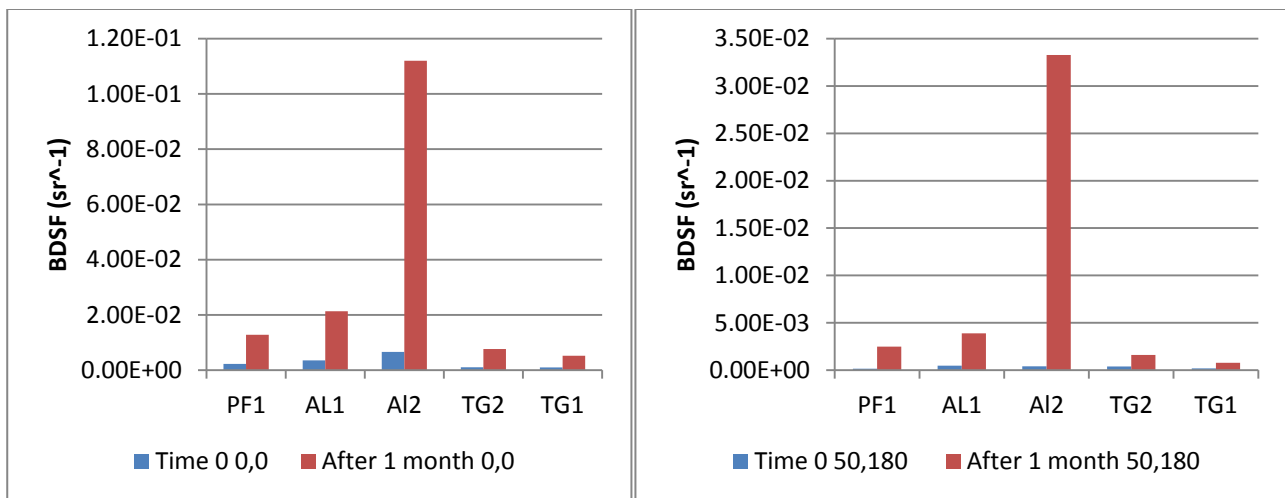


Figure 5. 115 Comparison between the BDSF (0,0) and (50,180) at time 0 and after one month of outdoor exposure

It is possible to compare the values and obtain the following tables:

	BDSF(0,0) [ $\mu\text{m}$ ]	
	Time 0	After 1 month
PF1	2.24E-03	1.28E-02
AL1	3.55E-03	2.14E-02
AL2	6.59E-03	1.12E-01
TG2	1.06E-03	7.66E-03
TG1	1.01E-03	5.21E-03

Table 5. 12 BDSF (0,0) time 0 and after one month

BDSF (50,180) [ $\mu\text{m}$ ]		
	Time 0	After 1 month
PF1	1.45E-04	2.49E-03
AL1	4.80E-04	3.89E-03
AL2	4.15E-04	3.33E-02
TG2	3.94E-04	1.61E-03
TG1	1.87E-04	7.84E-04

Table 5. 13 BDSF (50,180) time 0 and after one month

Here in the followings the comparison of reflectance measurement and the RMS roughness measurements.

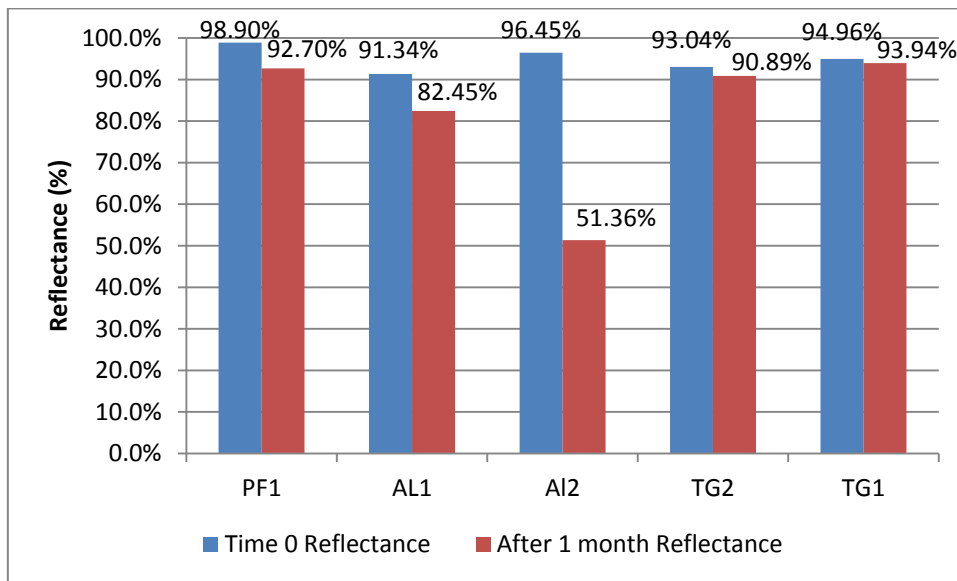


Figure 5. 116 Reflectance values at 0 time and after 1 month of outdoor exposure

The accuracy of the scatterometer should be considered, which is far more accurate in scatter measurement than reflectance measurement, but it is obvious considering that this instrument is made for on field measurement so most of the values has to be considered indicative and not as precise as a laboratory instrument such as the Cary 5000 UV/VIS NIR spectrophotometer. In the following table 5.14 is possible to see a numerical comparison between the two time condition.

	Time 0	After 1 month	
	Reflectance	Reflectance	% of variation
PF1	98.90%	92.70%	-6.69%
AL1	91.34%	82.45%	-10.78%
AL2	96.45%	51.36%	-87.80%
TG2	93.04%	90.89%	-2.37%
TG1	94.96%	93.94%	-1.08%

Table 5. 14 Reflectance measurement comparison

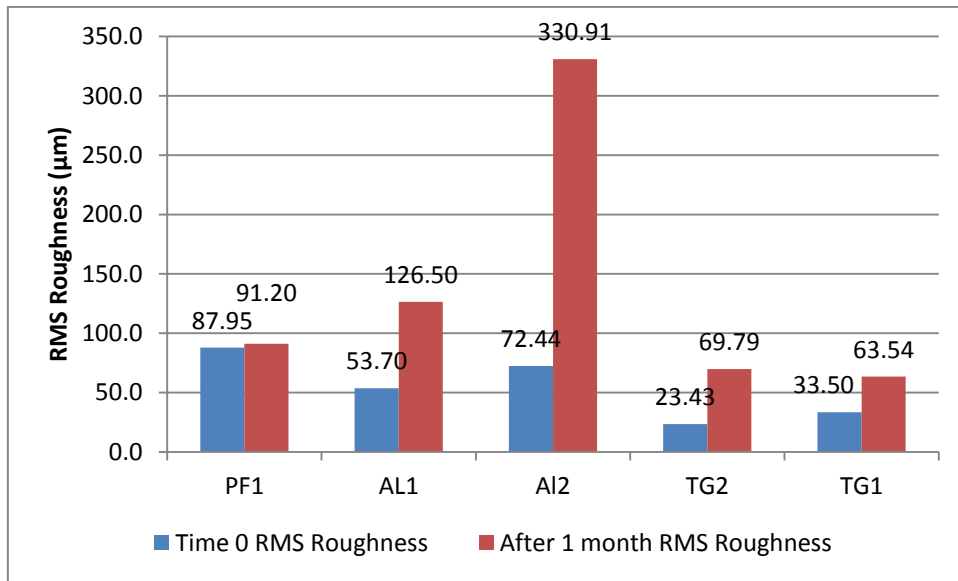


Figure 5. 117 RMS Roughness at 0 time and after 1 month of outdoor exposure

The instrument gave us results coherent with the visual inspection so that is clean that the fouling on the AL2 mirror will have increased the roughness on the mirror surface in the next table 5.15 is reported the values measured and the percentage of variation.

	Time 0	After 1 month	
	RMS Roughness	RMS Roughness	% of variation
PF1	87.95	91.2	103.70%
AL1	53.70	126.49	235.57%
AL2	72.44	330.90	456.80%
TG2	23.43	69.79	297.91%
TG1	33.50	63.54	189.65%

Table 5. 15 RMS Roughness measurement [µm]

In the next subchapter we find the values of the solar weighted Hemispherical reflectance and the solar weighted specular reflectance obtained with a far more accurate instrument, the spectrophotometer.

## 5.7 Reflectance measurement after one month (Spectrophotometer)

In this chapter a comparison between the different mirrors (all except the PF2 mirror) at time 0 and after a month of outdoor exposure measuring with the UV/VIS NIR spectrophotometer Cary 5000 will be made.

Fundamentally, the way of measuring, preparing samples and weighting the spectral response with the solar norm spectrum has not been changed to allow the measurement to be compared.

In the next subchapter the results of the measurement campaign after one month with the spectral response global + diffuse will be presented as it was shown in the previous chapter, a comparison between the new diffuse and specular reflectance and finally the new ranking of mirrors as it was done before.

### 5.7.1 Thin Glass mirrors

All of the sample tested are the same of the scatterometer testing.

As for the TG1 mirror its response was quite similar to its “0 time “ response but as it was seen with the scatterometer it presented a decreasing of reflectance due to the soiling effect.

For the soiling effect it’s important to evaluate the maintenance plan (washing) of the entire plant.

What we are trying to obtain is that along a number of months of operating life every each type of mirrors response, according to its RMS roughness, in different ways to the soiling effect.

What will be expected will be an asymptotic curve that will converge to a limit value of reflectance after which the soiling effect won’t affect the decrease of performance of the mirror.

In this case a month is just an initial condition to fit the curves behavior but we started collecting this data in order to achieve a greater results in about a year.

In the next figure 5.118 it is possible to see the new spectral response of the TG1 mirror, and then the “before” and “after” conditions will be compared, both for the specular and the diffuse reflectance.

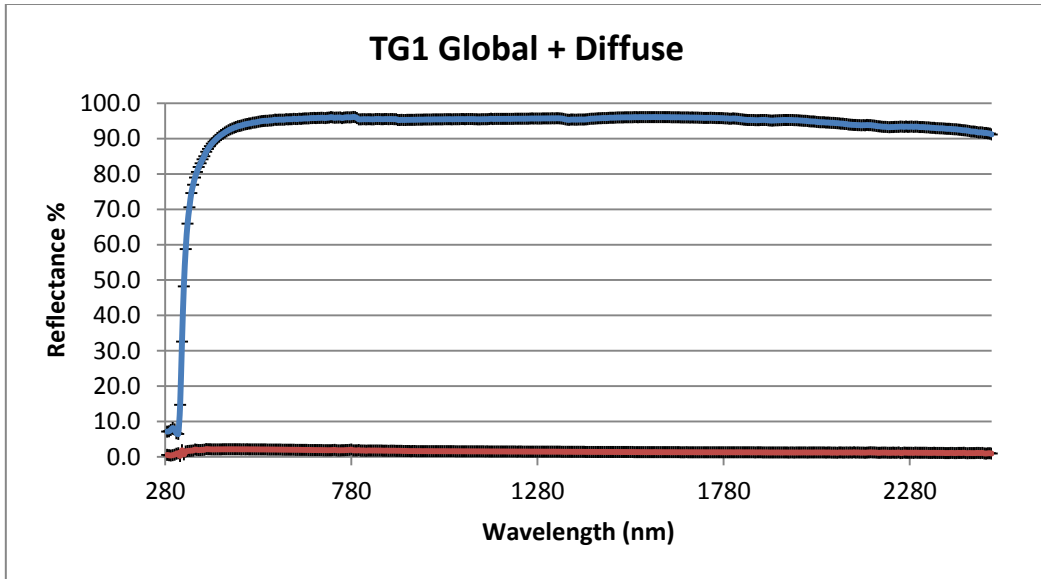


Figure 5. 118 TG1 spectral response after one month of outdoor exposure

Comparing the specular response in the two cases till now examined we obtained the following figure 5.119 the blue curve is always the aged sample with a standard deviation equal to a mean of 0.030508 with a maximum value of 0.282119 and a minimum value of 0.013524 for the global reflectance, while for the diffuse it's equal to a mean of 0.022294 with a maximum value of 1.058328 and a minimum value of 0.000448 for the diffuse reflectance.

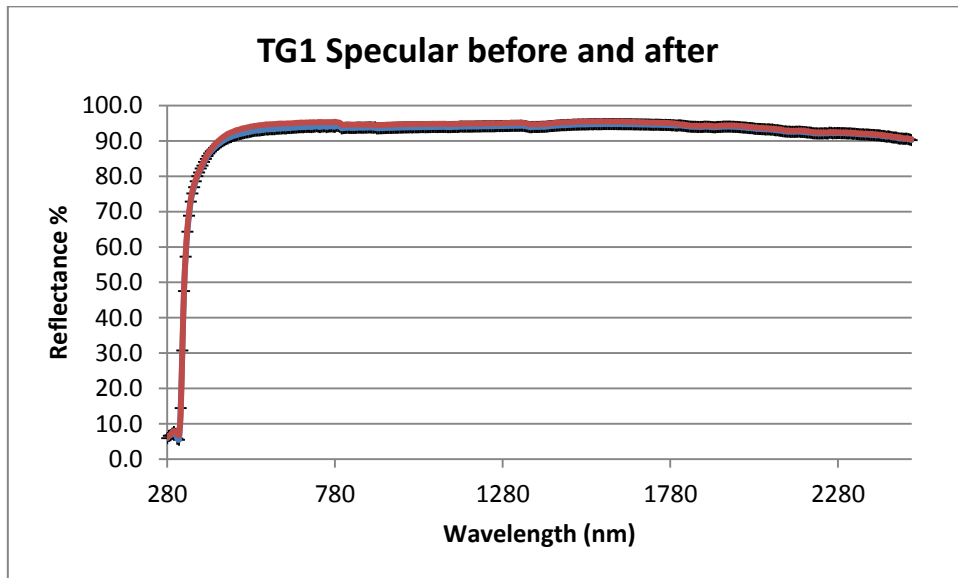


Figure 5. 119 TG2 specular spectral response at 0 time and after one month of outdoor exposure

While in the next figure 5.120 we have a comparison between the “before” and “after” diffuse reflectance, main responsible for the decreasing of the specular reflectance due to the soiling effect.

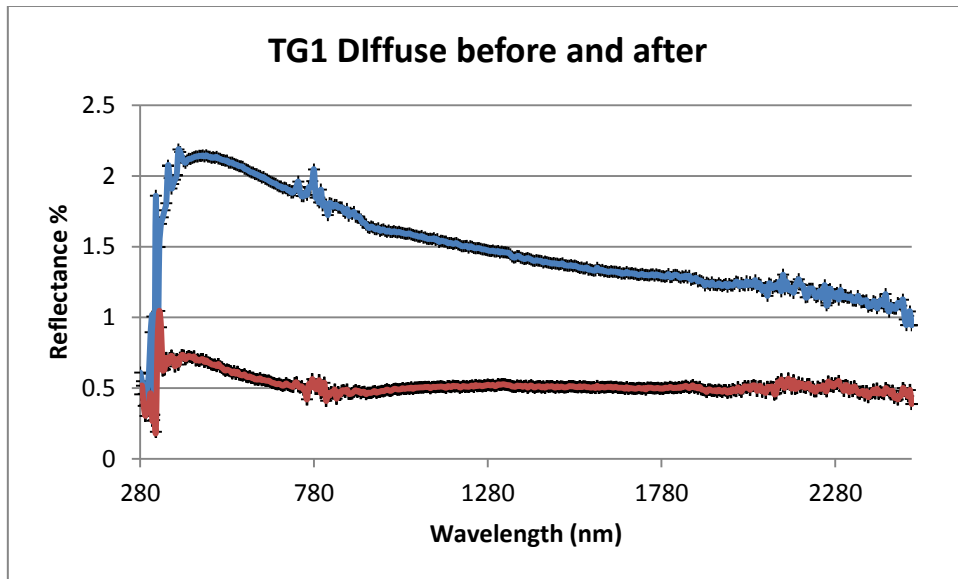


Figure 5.120 Diffuse reflectance comparison between the sample in "before" and "after" condition

It's simple to see that the diffuse reflectance increased up to the 2% along the spectrum examined.

For the TG2 sample were conducted the same evaluations in order to compare the results in the two time conditions, obtaining the following figures.

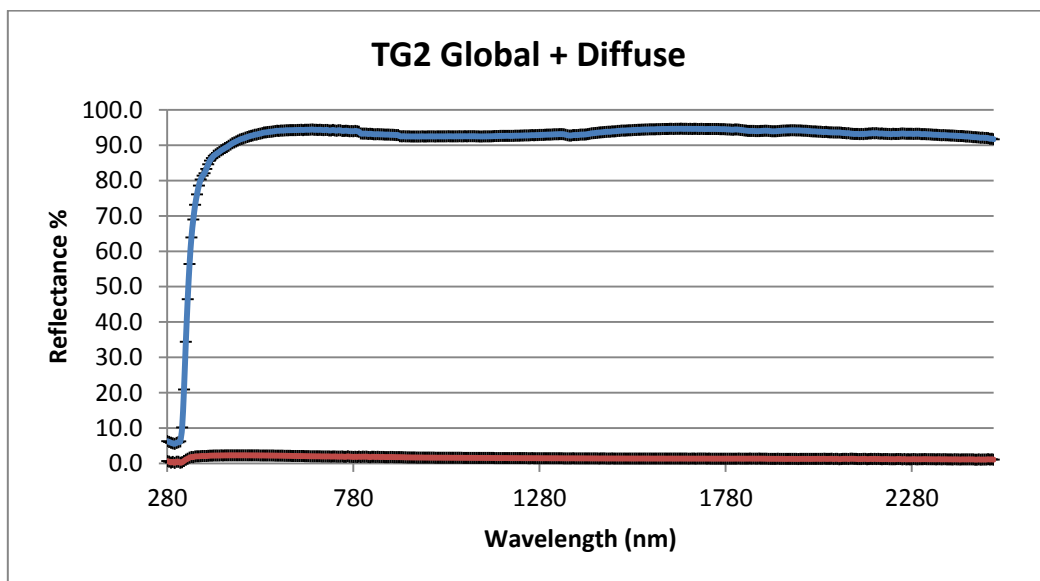


Figure 5.121 Global + diffuse reflectance after one month of outdoor exposure

With a standard deviation equal to a mean of 0.021203 with a maximum value of 0.328214 and a minimum value of 0.003632 for the global reflectance, while for the diffuse is equal to a mean of 0.015325 with a maximum value of 0.153443 and a minimum value of 0.001443 for the diffuse reflectance.

Thus the specular comparison is the one shown in the next figure 5.122.

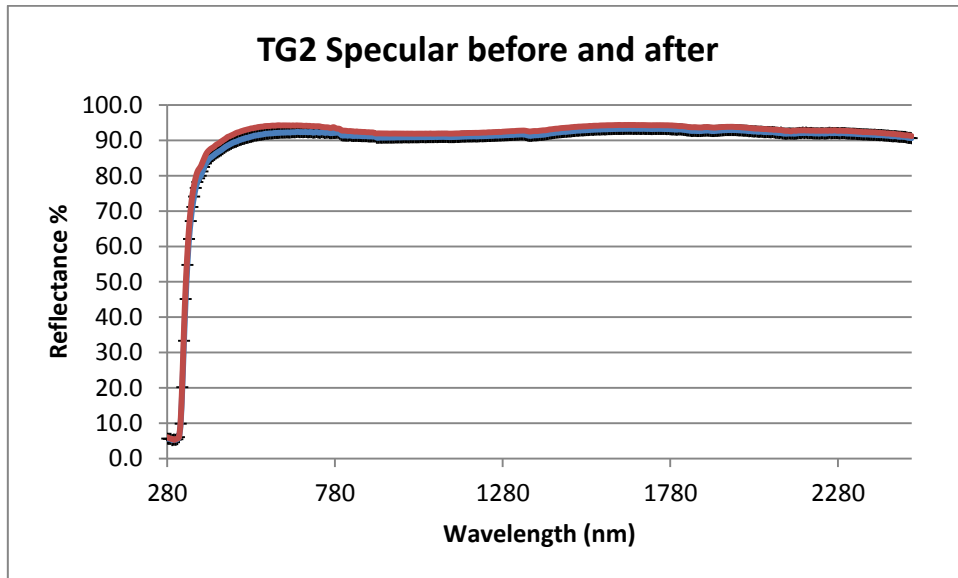


Figure 5. 122 Specular reflectance comparison between the "before" and "after" condition

It's possible to see a slightly decrease of the spectral response due to the diffuse reflectance shown in the next figure 5.123.

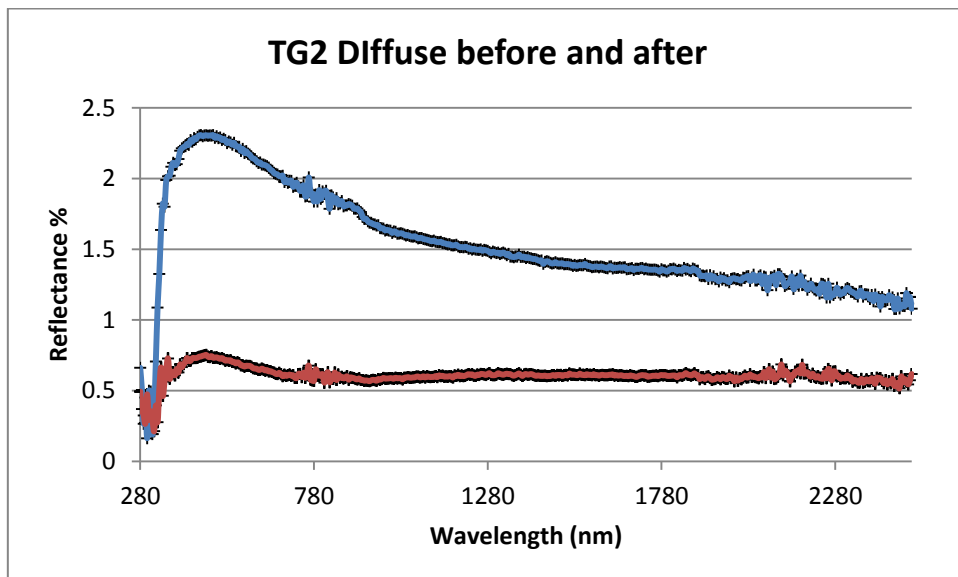


Figure 5. 123 Diffuse reflectance comparison between the "before" and "after" condition

Also in this case the increasing of the diffuse reflectance is simple to be seen, with a value higher than the TG1 sample.

Weighting the global (Hemispherical) along the solar norm spectrum is possible to compare the TG1 and TG2 sample in the “before” and “after” condition.

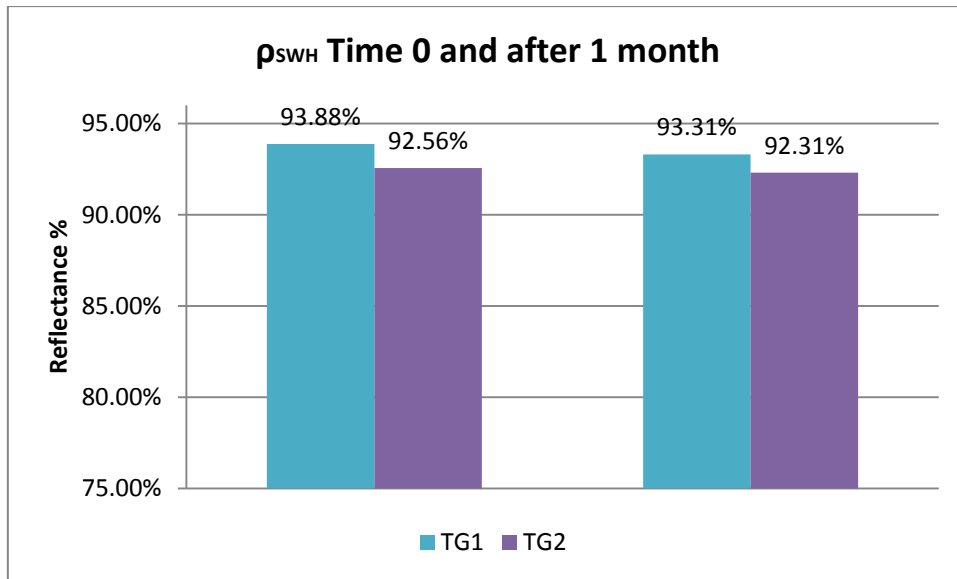


Figure 5. 124 Comparison between the solar weighted hemispherical reflectance for TG1 and TG2 sample in the "before" and "after" condition

The TG1 sample presents a loss of weighted reflectance in the order of 0.57% while the TG2 mirrors has a loss of reflectance equal to 0.25% which is a good results in the point of view of field maintenance.

As far as the specular reflectance it is possible to conduct the same weighting as above and obtain the following figure 5.125.

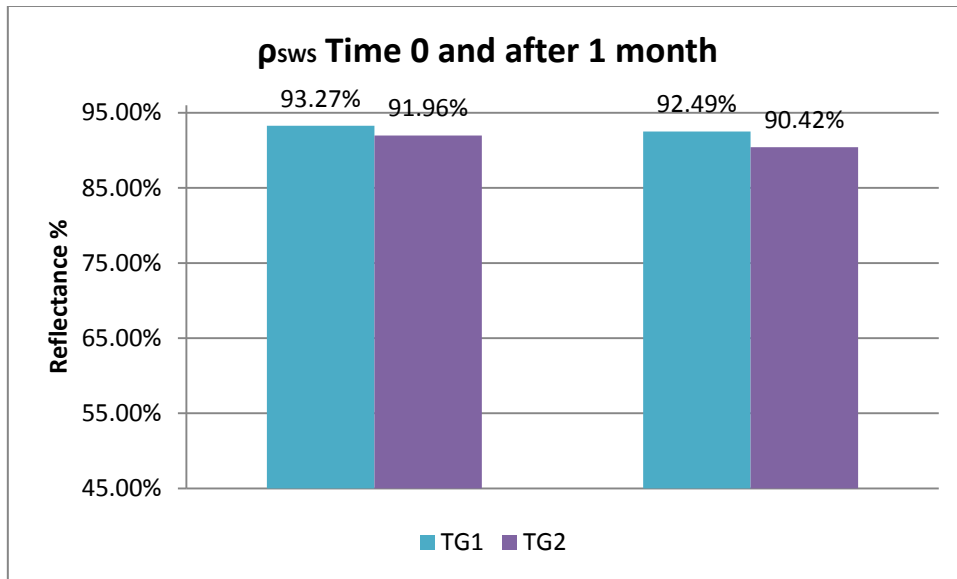


Figure 5. 125 Comparison between the solar weighted specular reflectance for TG1 and TG2 sample in the "before" and "after" condition

In this comparison we can affirm that the loss of specular reflectance for the TG1 mirror between the 0 condition and the 1 month condition is equal to 0.77% while for the TG2 is equal to 1.54%.

### 5.7.2 Aluminum mirrors

For what involves the aluminum mirrors as already written in the previous chapters we are going to see how the outdoor exposure deteriorated the AL2 mirror in less than a month. While for AL1 mirror there was a little effect on its reflectance decreasing.

Here in the followings is shown the spectral response for the AL1 mirror after the month of natural exposure.

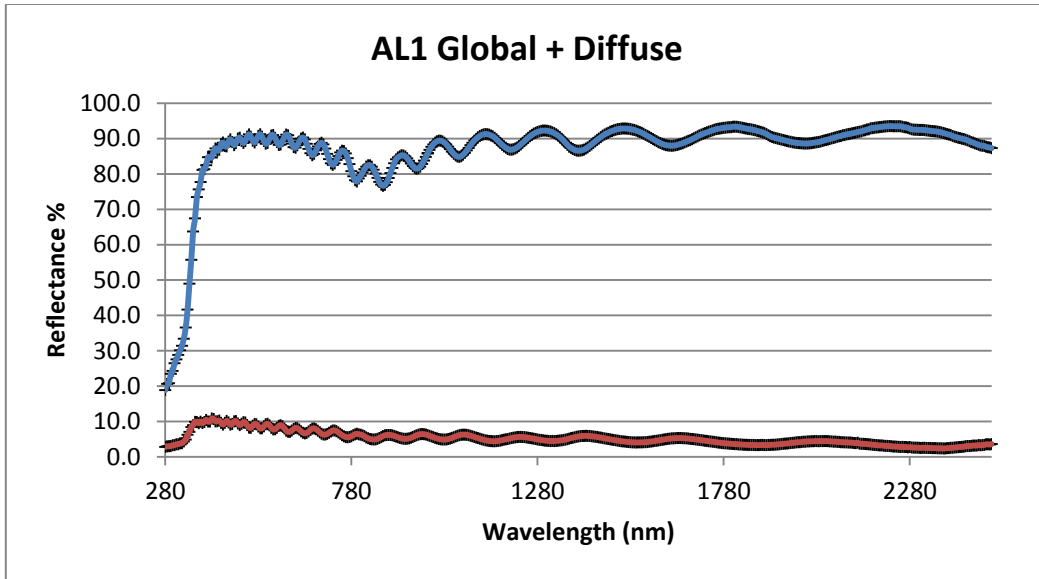


Figure 5.126 Global + diffuse reflectance spectral response after one month of outdoor exposure

With a standard deviation equal to a mean of 0.023194 with a maximum value of 0.131798 and a minimum value of 0.003463 for the global reflectance, while for the diffuse it's equal to a mean of 0.012172 with a maximum value of 0.076885 and a minimum value of 0.001667 for the diffuse reflectance.

While in the next figure 5.127 is described the specular spectral response at zero time and after a month.

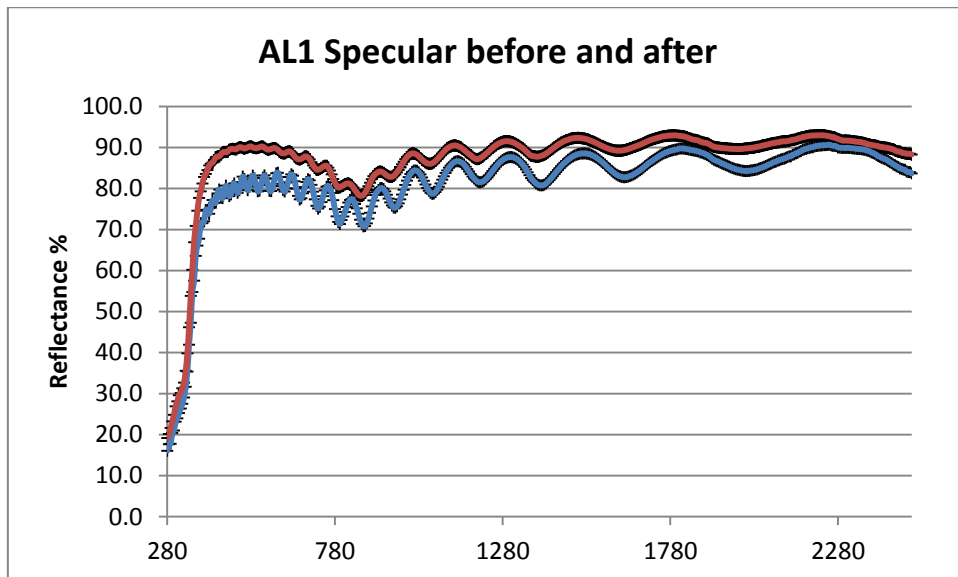


Figure 5.127 Specular reflectance comparison between the "before" and "after" condition

As for the diffuse reflectance, comparing a month of outdoor exposure and the zero time the results are shown in the next figure 5.128

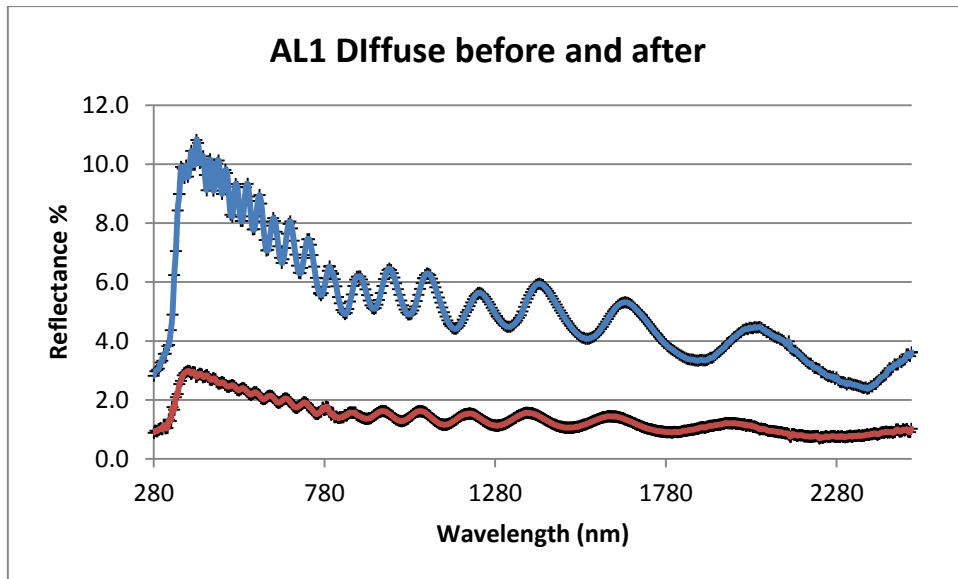


Figure 5. 128 Diffuse reflectance comparison

Here the value of diffuse light is far higher compared to the thin glass mirrors, in fact it is in the order of the 10% in the highest point.

For the AL2 mirror we had the following behavior after the exposure.

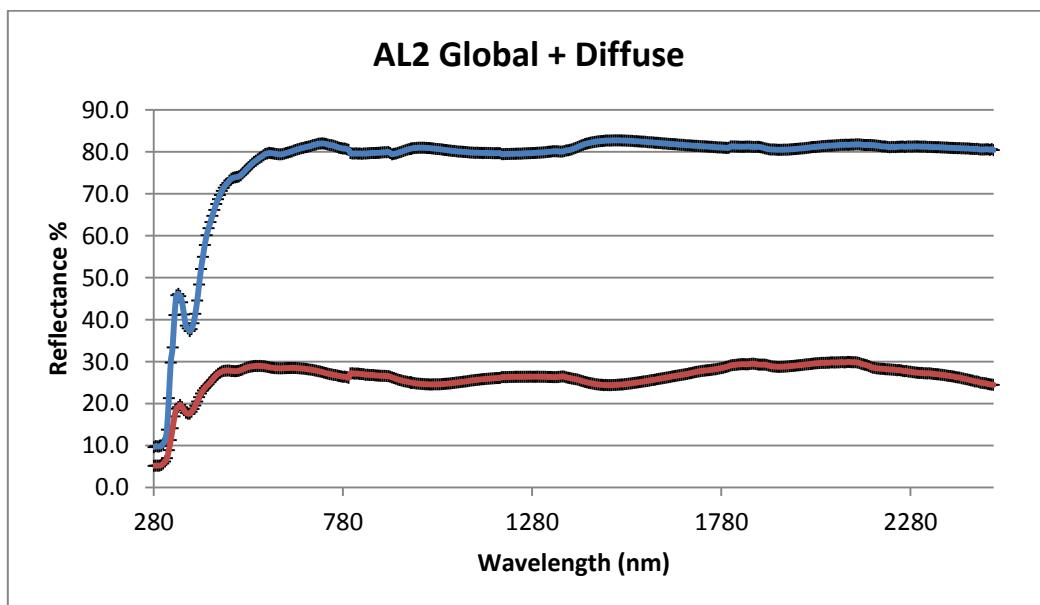


Figure 5. 129 Global + diffuse reflectance spectral response after one month of outdoor exposure

It's clear to see how high the spectral values of diffuse reflectance are in the case of Al2 mirrors. The fouling on the surface mirror contributes in a consistent way to the increase of scattering and thus the diffuse reflectance.

The values above present a standard deviation equal to a mean of 0.019138 with a maximum value of 0.116101 and a minimum value of 0.002238 for the global reflectance, while for the diffuse it's equal to a mean of 0.013308 with a maximum value of 0.088066 and a minimum value of 0.00063 for the diffuse reflectance.

In particular comparing the specular reflectance of this type of mirror in the "before" and "after" we obtain the following figure 5.130.

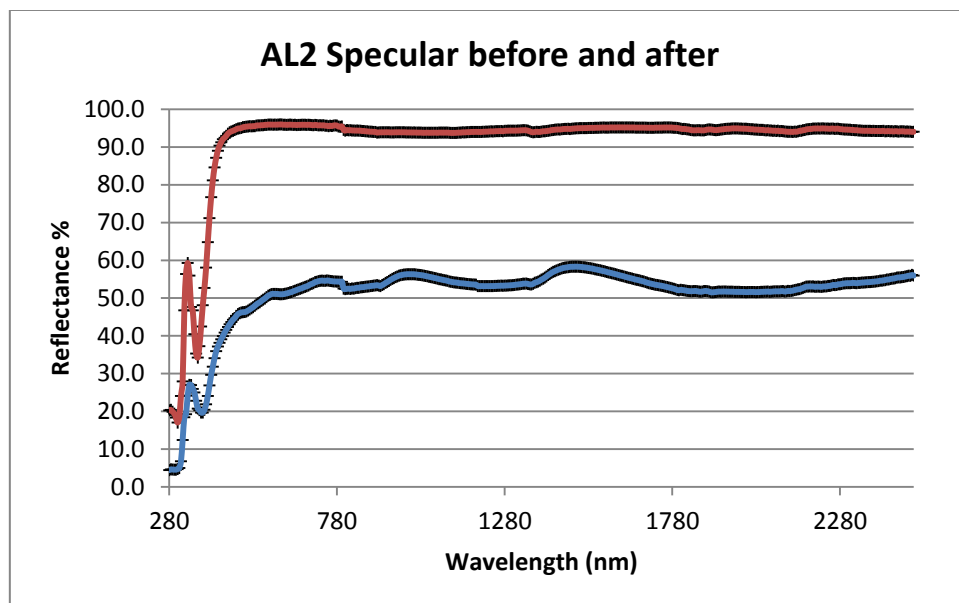


Figure 5. 130 Specular reflectance comparison between the "before" and "after" condition

While for the diffuse contribute we can look at the following figure 5.131.

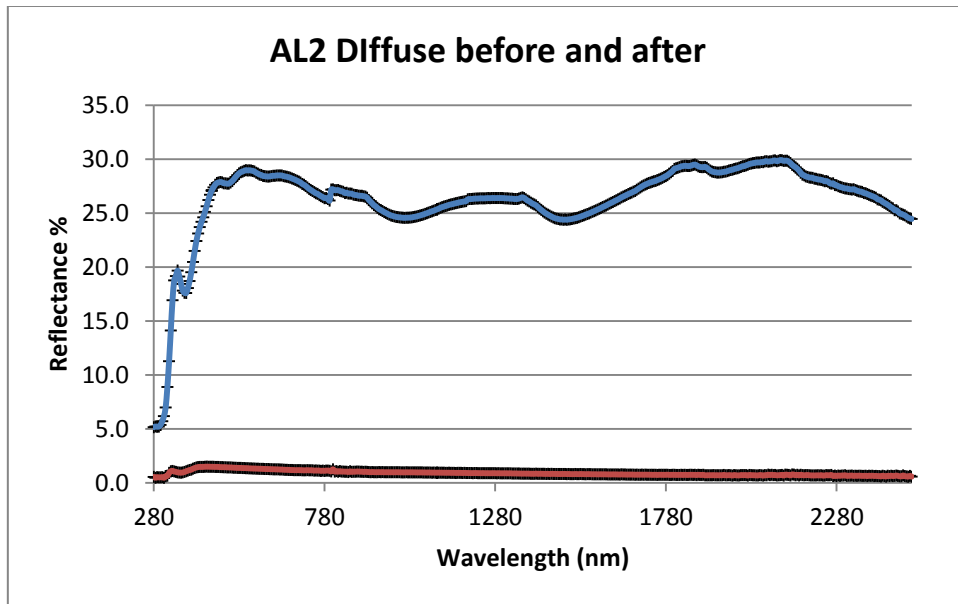


Figure 5. 131 Diffuse reflectance comparison

Also in this case the contribute of diffuse reflectance along all the spectrum is very high, definitively compromising the high reflectance of this type of mirror.

In the following the comparison between the two aluminum mirror analyzing the solar weighted hemispherical and specular reflectance will be carried on.

The hemispherical reflectance is shown in the following figure 5.132.



Figure 5. 132 Comparison between the solar weighted hemispherical reflectance for AL1 and AL2 sample in the "before" and "after" condition

In this case the losses of reflectance for the AL1 is equal to 1.64% while for the TG2 is equal to 17.20% which is the highest loss we have encountered till now.

As for the solar weighted specular reflectance the situation is far heavier as can be seen in the next figure 5.133.

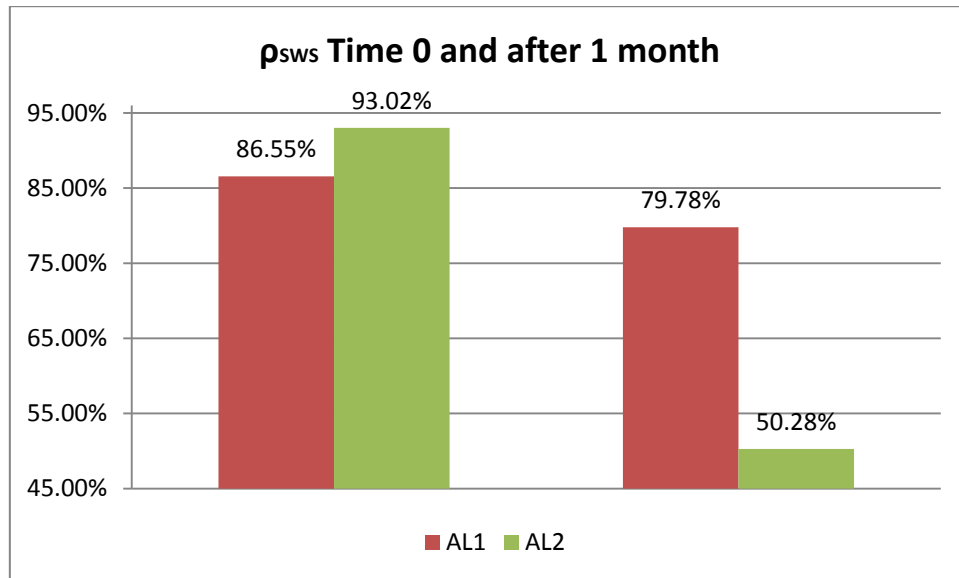


Figure 5. 133 Comparison between the solar weighted specular reflectance for AL1 and AL22 sample in the "before" and "after" condition

Which indicates a loss for the AL1 mirror equal to 6.77% and for the AL2 mirror is equal to 42.75%.

### 5.7.3 Polymeric film mirror

Unfortunately as previously stated we didn't have at our disposal different samples of the PF2 mirror so we couldn't carry on the experimental outdoor exposure campaign for this mirror so the next results will be relative only for the PF1 mirror.

For this particular type of mirror we obtained after the month of natural exposure the following spectral response.

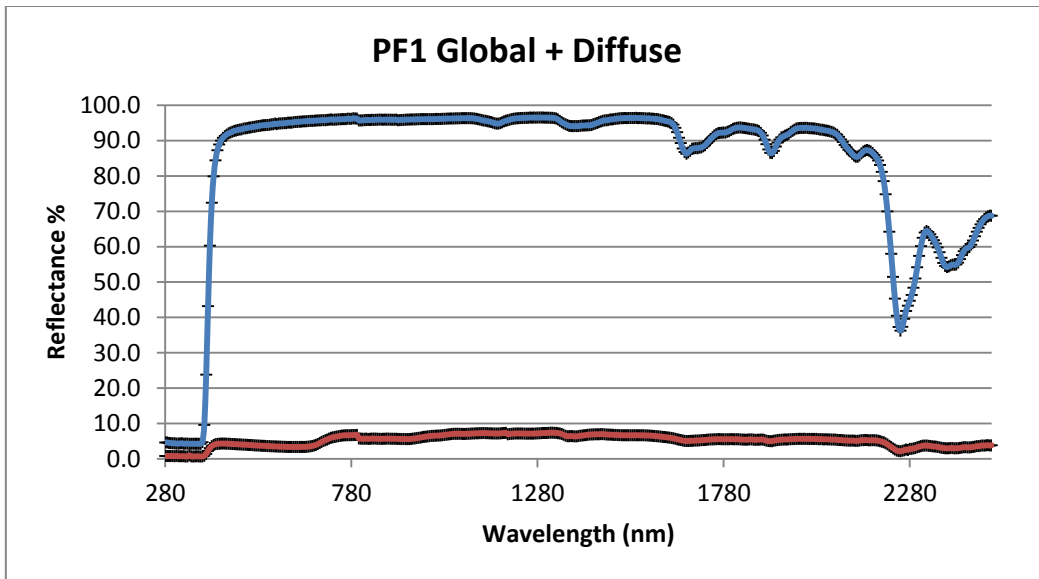


Figure 5. 134 Global + diffuse reflectance spectral response after one month of outdoor exposure

The resulting standard deviation is equal to a mean of 0.018675 with a maximum value of 0.105154 and a minimum value of 0.003688 for the global reflectance, while for the diffuse it's equal to a mean of 0.013242 with a maximum value of 0.115759 and a minimum value of 0.001414 for the diffuse reflectance.

Thus we can compare the specular spectral response for the AL2 mirror in the case of 0 time and 1 month outdoor exposure.

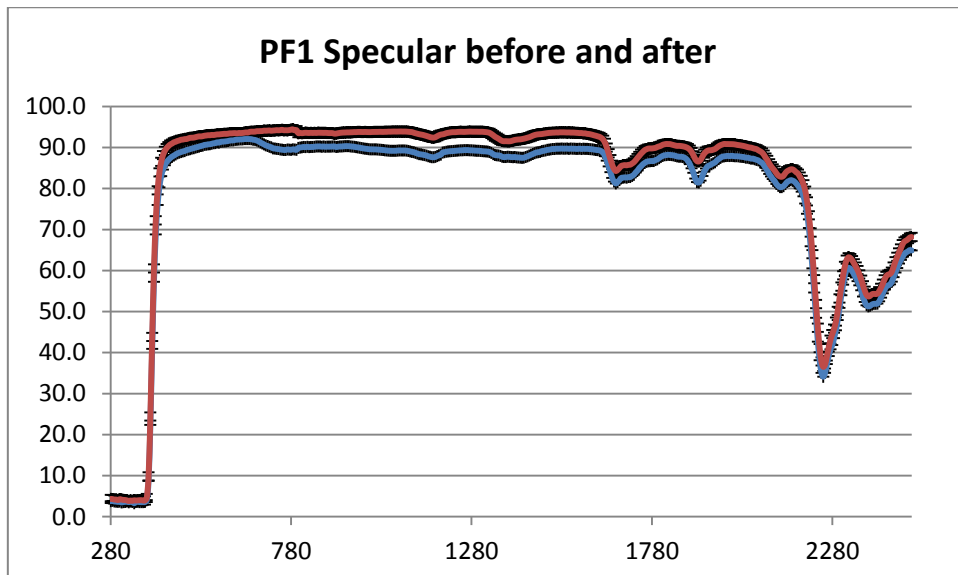


Figure 5. 135 Specular reflectance comparison between the "before" and "after" condition

The specular response after one month results in a slightly decreased curve.

As before it's possible to determine the diffuse reflectance and compare it with the 0 time diffuse reflectance.

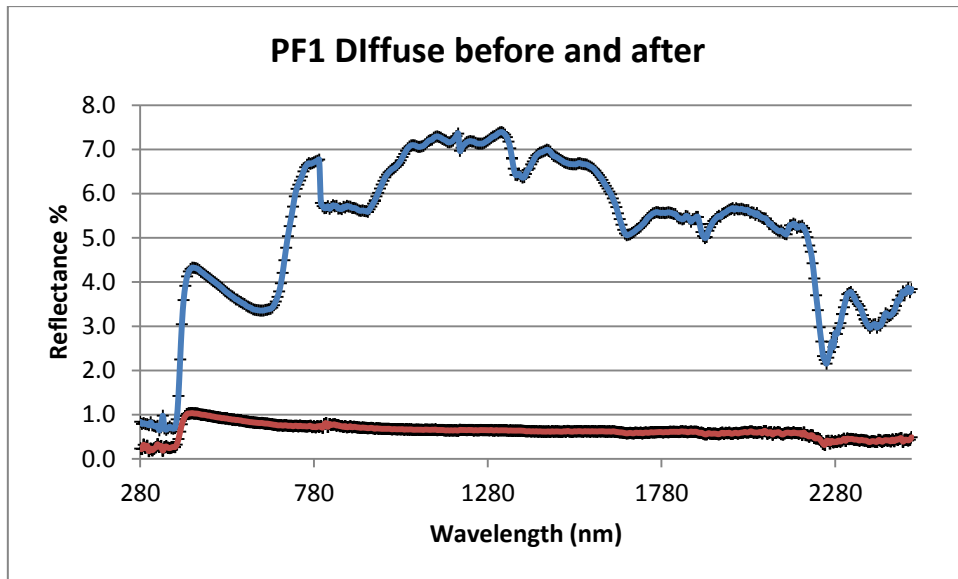


Figure 5. 136 Diffuse reflectance comparison

The above graph shows the increase of the diffuse reflectance along the spectrum with a maximum value of about 7%.

In particular weighting the specular and the hemispherical reflectance we obtained the following figures

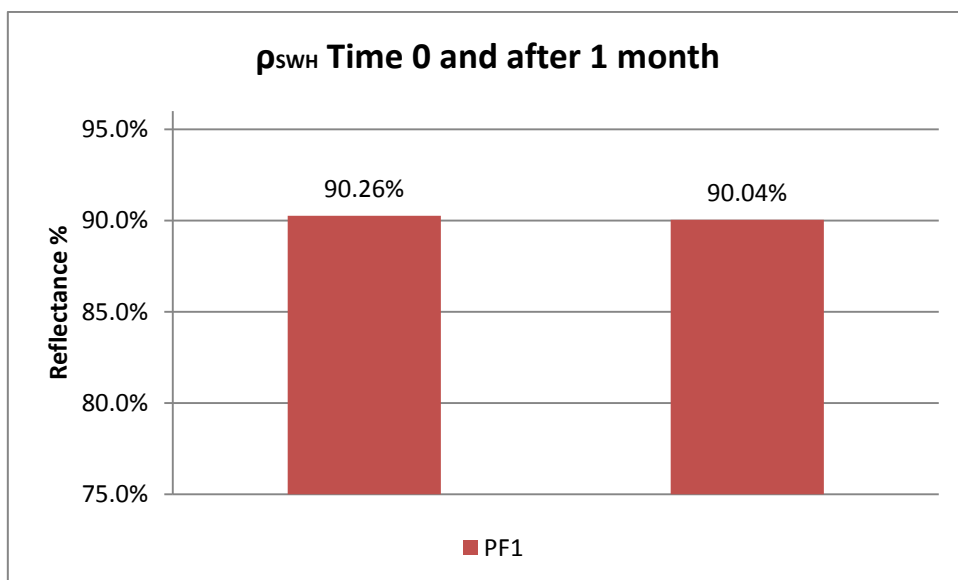


Figure 5. 137 The solar weighted hemispherical reflectance for PF1 sample in the "before" and "after" condition

Which consist in a loss of reflectance equal to 0.22%.

While for the case of specular reflectance it has the following behavior, shown in the next figure 5.138

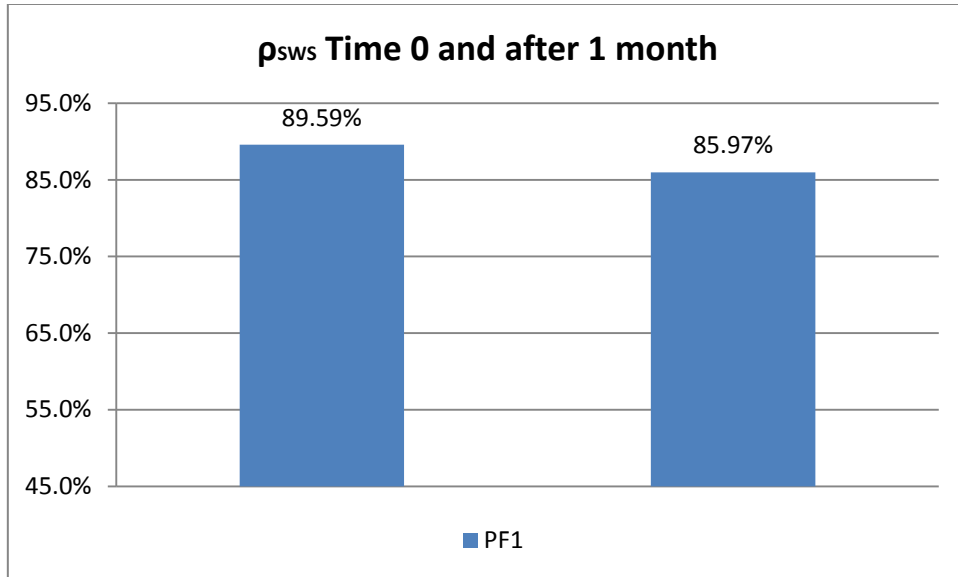


Figure 5. 138 Solar weighted specular reflectance for the PF1 mirror

With a loss of reflectance equal to 3.63%.

At last, it is interesting to note the comparison between the reflectance performance and ranking of the examined mirrors comparing the ρ<sub>SWH</sub> and the ρ<sub>SWS</sub> at the 0 measurements and the 1 month of outdoor exposure condition.

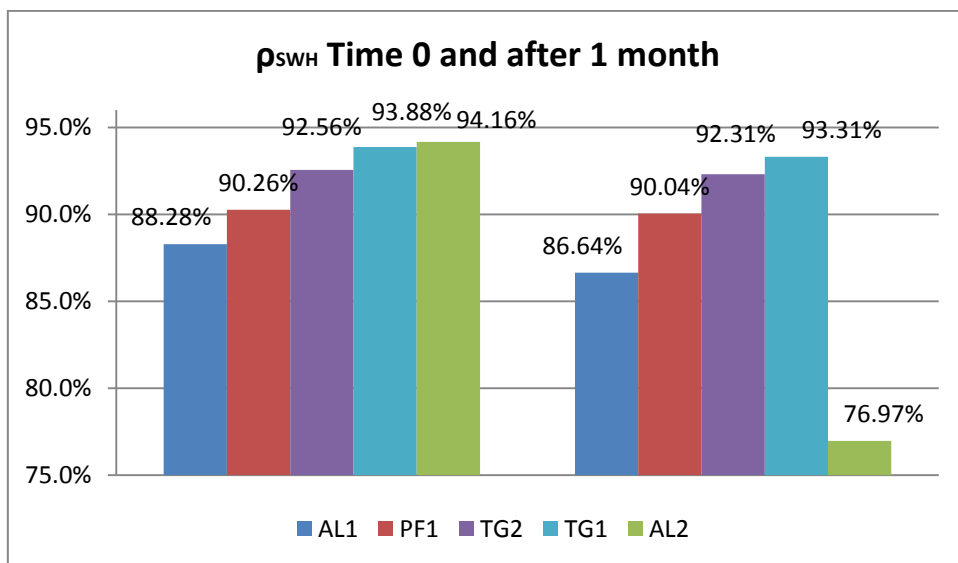


Figure 5. 139 Solar weighted hemispherical reflectance at 0 time and after one month of outdoor exposure

While for the specular reflectance we obtained the following comparison always in the same conditions.

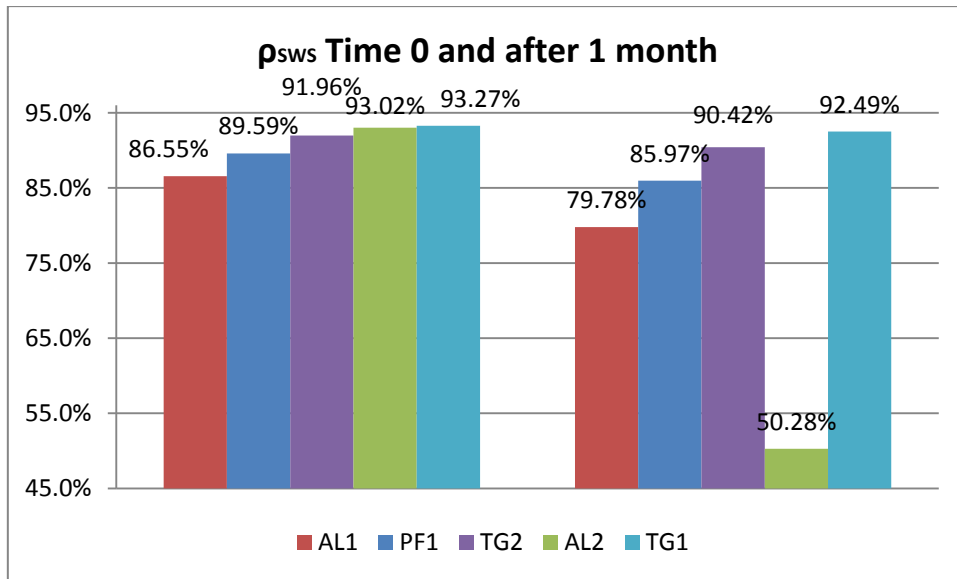


Figure 5. 140 Solar weighted specular reflectance at 0 time and after one month of outdoor exposure

In the above figure are represented the values of solar weighted specular reflectance after one month of outdoor exposure, so the new ranking is proposed.

The most significant meaning is that the AL2 mirror is not suitable for outdoor operation and it is synthesized by the loss of 42.75% of specular reflectance.

## 6. MODELING

The research was conducted by implementing a software evaluation of the solar radiation absorbed by the HCE (Heat Collector Element) with an Engineering Equation Solver, in particular the MATHCAD<sup>®</sup> Software to allow us to proceed with a more detailed evaluation of the formulas.

To validate the model it was used a NREL Software on ray tracing called Soltrace.

The main research was focused on the reflectivity variation due to the typologies of mirrors (Thin, Polymeric or Aluminum) and the reflectivity values associated to the mirrors itself.

### 6.1 Mathcad<sup>®</sup>

With this software we were able to simulate the variation of the sun angle's during all the year to see how these parameters would affect the entire quantity of the solar radiation absorbed.

In the following the various step occurred to obtain the entire simulation.

#### 6.1.1 Direct Normal Insolation

Extraterrestrial solar radiation follows a direct line from the sun to the Earth. Upon entering the earth's atmosphere, some solar radiation is diffused by air, water molecules, and dust within the atmosphere (Duffie and Beckman, 1991). The direct normal insolation represents that portion of solar radiation reaching the surface of the Earth that has not been scattered or absorbed by the atmosphere. The adjective "normal" refers to the direct radiation as measured on a plane normal to its direction.

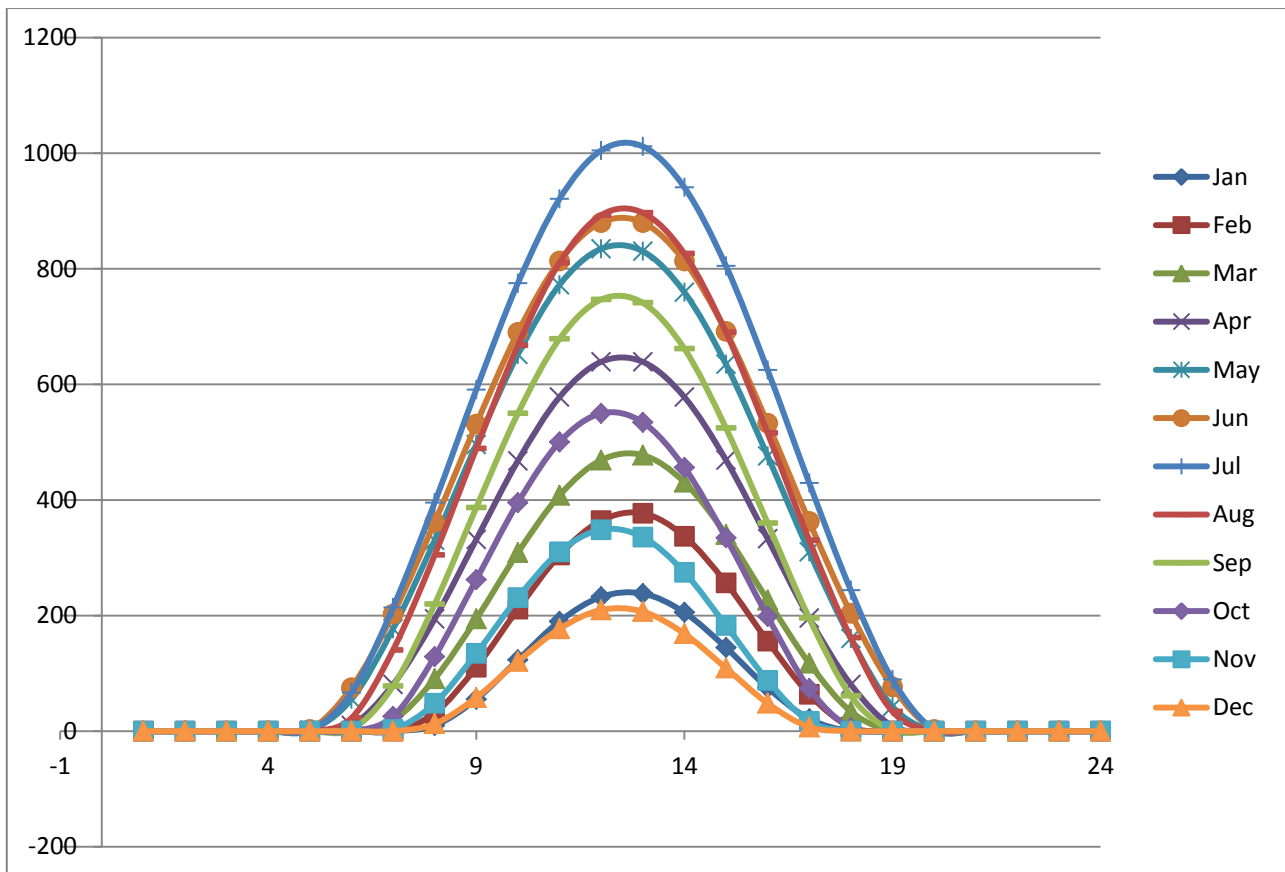


Figure 6. 1 Direct Normal Insolation as measured in Catania during the year 2009

The dome shape of the graphs in Figure 6.1 results from the atmosphere scattering and absorbing radiation with time, as atmospheric conditions and effective air mass change throughout the day (Duffie and Beckman, 1991).

### 6.1.2 Angle of incidence

Only the insolation that is directly normal to the collector surface can be focused and thus be available to warm the absorber tubes. The angle of incidence ( $\theta$ ) represents the angle between the beam radiation on a surface and the plane normal to that surface. The angle of incidence will vary over the course of the day (as well as throughout the year) and will heavily influence the performance of the collectors.

Figure 6.2 illustrates the angle of incidence between the collector normal and the beam radiation on a parabolic trough. The angle of incidence results from the relationship between the sun's position in the sky and the orientation of the collectors for a given location.

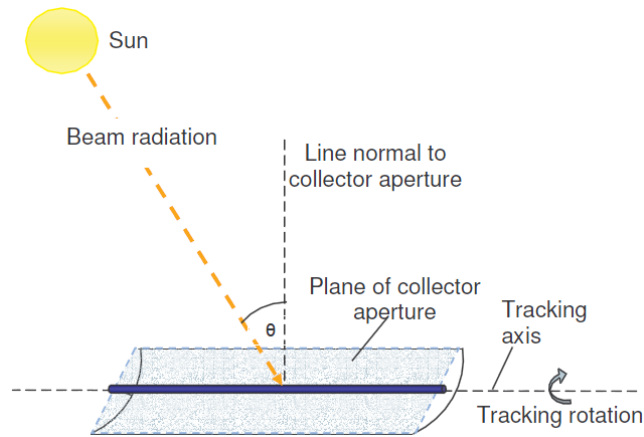


Figure 6. 2 Angle of incidence between the collector normal and the beam radiation

The position of the sun varies throughout the year. The declination angle is the angular position of the sun at solar noon, with respect to the plane of the equator. If the earth rotated upright on its axis, there would be no change in declination angle as the earth revolved around the sun.

However, the earth is tilted on its axis at an angle of  $23.45^\circ$ . As the earth rotates around the sun through the course of a year, the declination angle will change, within a range of  $-23.45^\circ \leq \delta \leq 23.45^\circ$ .

See Figure 6.3 for a pictorial representation of the declination angle.

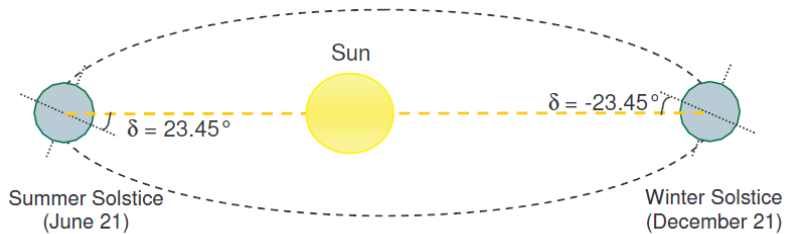


Figure 6. 3 Declination angle due to Earth's tilt

The following expression for declination angle was developed by P.I. Cooper in 1969 (Cooper, as cited by Duffie and Beckman, 1991):

$$\delta = 23.45 \sin \left( 360 \frac{284 + n}{365} \right)$$

where

$n$  = the day number of the year, from 1 (corresponding to January 1) to 365 (corresponding to December 31).

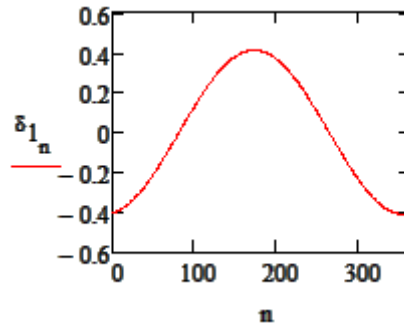


Figure 6. 4 Shows the variation of the declination angle throughout the year

The position of the sun depends on the hour angle, or the angular displacement of the sun east or west of the local meridian. The hour angle is negative when the sun is east of the local meridian (in the morning), positive when the sun is west of the local meridian (afternoon), and zero when the sun is in line with the local meridian (noon).

The hour angle comes as a result of the rotation on the earth, which spins on its axis at a rate of 15° per hour:

$$\omega = (SolarTime - 12) \cdot 15 \text{ } ^\circ/hr$$

Where  $\omega$  is the hour angle [deg] and SolarTime is the solar time [hr].

There is an important distinction between standard time and solar time. In solar time, the sun aligns with the local meridian ( $\omega = 0$ ) at exactly 12:00, or “solar noon.” However, standard time is based not on the local meridian, but on a standard meridian for the local time zone. The length of the solar day also varies; this variation is due primarily to the fact that the earth follows an elliptical path around the sun (Stine and Harrigan, 1985). As a result, the standard time must be adjusted to reflect the current time of day in solar time. The relationship between solar time and standard time, in hours, is:

$$SolarTime = StandardTime - DST + \frac{(Lst - Lloc)}{15} + E \cdot \frac{1 \text{ hr}}{60 \text{ min}}$$

Where

DST = Daylight Savings Time adjustment (1 [hr] during Daylight Savings Time, 0 [hr] during standard time)

Lst = standard meridian for the local time zone [deg]

Lloc = the local meridian of the collector site [deg]

$E$  = equation of time [min]

$E$ , the equation of time, accounts for the small irregularities in day length that occur due to the Earth's elliptical path around the sun. The equation of time used here, in minutes, comes from Spencer (as cited by Iqbal, 1983):

$$E = 229.18(0.000075 + 0.001868 \cos B - 0.032077 \sin B - 0.014615 \cos 2B - 0.04089 \sin 2B)$$

where

$$B = \frac{360}{365} (n - 1) [deg]$$

$n$  = day number of the year (1 for January 1, 365 for December 31)

The variation in the equation of time over the year is given in Figure 6.5. The equation of time may offset solar time from standard time by as much as fifteen minutes during the year.

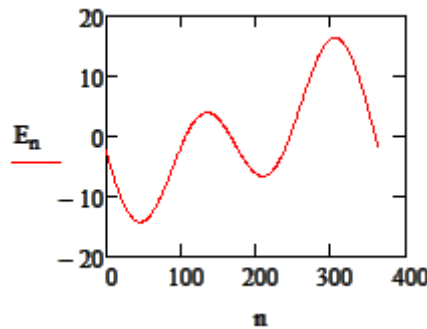


Figure 6.5 Equation of time vs month of the year

The final angle required to solve for the angle of incidence is the zenith angle. The zenith angle is the angle between the line of sight to the sun and the vertical.

Its complement, the angle between the line of sight to the sun and the horizon, is the solar altitude angle. The zenith angle is related to both the declination angle and the hour angle by the following relationship (Duffie and Beckman, 1991):

$$\cos\theta_z = \cos(\delta) \cos(\varphi) \cos(\omega) + \sin(\delta) \sin(\varphi)$$

where

$\delta$  = declination angle

$\omega$  = hour angle

$\varphi$  = latitude location of the plant

Figure 6.6 shows solar altitude angle variation throughout the day on the two extreme days of the year: the summer solstice (June 21 n=172) and the winter solstice (December 21 n=355) and their paragon.

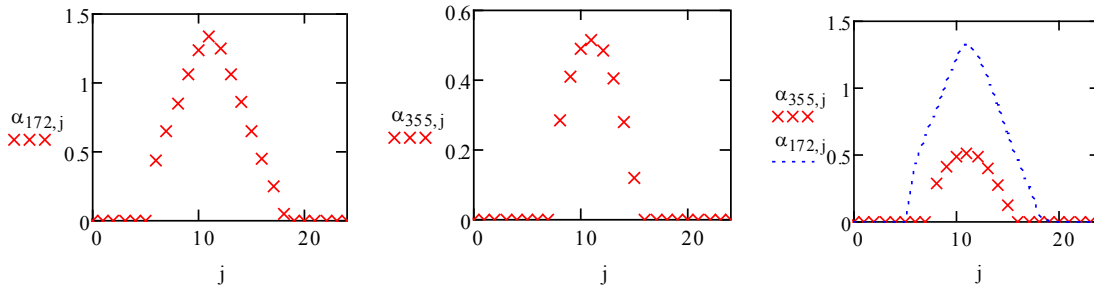


Figure 6. 6 Solar altitude angles versus time, on June 21 and December 21 of the year, for Catania

Clearly, the sun reaches a much higher position above the horizon in the summer than it does in the winter. This natural occurrence will prove to have large impact on the solar resource collected by the field in the winter months as compared to the summer months.

Once the declination angle, hour angle, and zenith angle are known, the angle of incidence on the collectors can be calculated. The solar field collectors modeled are at level with the ground (no vertical tilt) and are oriented due north-south. With a single-axis tracking system, the collectors are capable of tracking the sun from a position  $10^\circ$  above the eastern horizon to  $10^\circ$  above the western horizon. In the model, the assumption is made that the collectors are tracking during all times the sun is above the horizon.

The incidence angle for a plane rotated about a horizontal north-south axis with continuous east-west tracking to minimize the angle of incidence is given by (Duffie and Beckman, 1991):

$$\cos\theta = \sqrt{\cos^2 \theta_z + \cos^2 \delta \sin^2 \omega}$$

Figure 6.7 show variation of  $\text{DNI} \cos\theta$  throughout the day, as calculated for the solar collector location, orientation, and tracking capability. For reference, the direct normal insolation and cosine of the incidence angle are shown on the graphs as well. The summer solstice and the winter solstice (June 21 n=172, December 21 n=355) are shown in Figure 6.7.

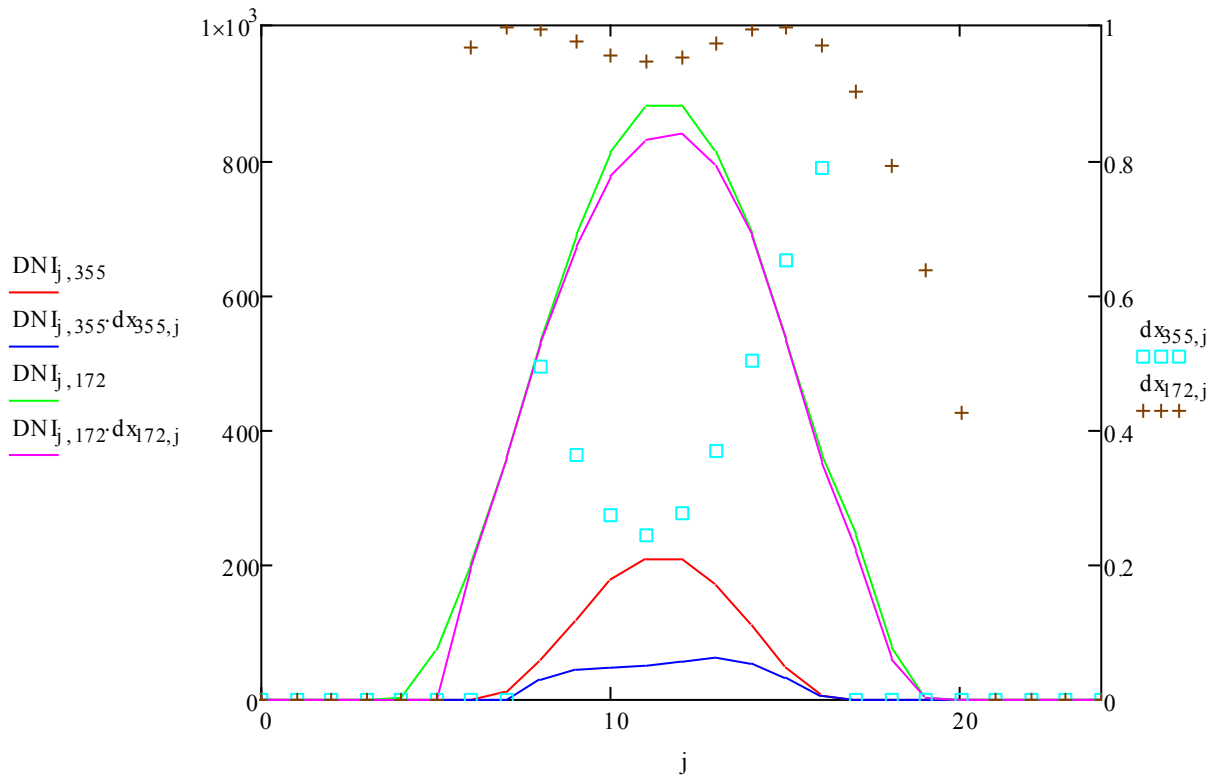


Figure 6. 7 DNI and DNI cos ( $\theta$ ) in Catania on June 21

The impact of the lower solar altitude angle in the winter is clearly seen in comparing Figure 6.7.

There is also a noticeable sag in DNI cos( $\theta$ ) around noon in Figure 6.8. The sun rises above the southeast horizon and sets beneath the southwest horizon. With a fixed north-south orientation and east-west single-axis tracking system, the incidence angle is much larger at noon in December than it is during morning or afternoon hours, which results in the shape of the plot seen in Figure 1.8. Over the course of an entire year, the north-south oriented single-axis tracking receives slightly more energy than an east-west single-axis tracking aperture in the same location (Stine and Harrigan, 1984). Also, the north-south oriented tracking aperture receives more energy in the summertime, when electricity demand is highest and the solar collectors are designed for their peak performance.

These were the initial steps to achieve the final results.

From here after what concur to obtain the results are what was achieved with the spectrophotometer.

We started with implementation of some correlation between the production expected and the losses that can vary the results.

We defined 4 typologies of losses:

- The incident angle modifier;

- The row shadowing (when present);
- End losses;
- Optical losses

The work on the incident angle modifier was already conducted by Dudley et al in 1994 then developed at the NREL Laboratory on a particular type of mirror, parabolic shape, absorber etc... Unfortunately we don't have such a technology and instrumentation to achieve these results so we took their result to take into account the losses due to the angle of incidence.

In second place we took into account the losses due to the parallel rows that once in the evening.

In the followings these two parameters are described, and the results discussed.

In third place we analyzed the losses due to the unenlightened part of the absorber which is for geometric needs out of the reflection field.

To validate the simulation conducted with Mathcad it was necessary to input each soft wares with the same parameter, so the IAM, the row shadowing and the end losses are considered equal to one.

To understand better the optical behavior of the different mirrors we used the previously described equation of the optical efficiency further described in the followings.

### 6.1.3 Optical Efficiency and HCE Efficiency

The final category of solar radiation losses lays in the surface properties and inaccuracies of the solar collector trough mirrors, glass envelope, and receiver tube materials. Insolation may be absorbed or scattered by dirt on the mirrors, or mis-reflected due to small mirror inaccuracies or tracking error. The transmissivity of the glass envelope, the absorbtivity of the receiver tube selective coating, and other surface properties will also contribute to the final solar radiation absorption.

Over time, as older malfunctioning collectors could be gradually replaced with the next generation of HCEs and mirrors, the makeup of the field may include two or three or more types of solar collector assemblies and receiver tubes. Surface properties and correction factors may vary from one type or generation of equipment to the next. The resultant efficiency for the mirrors as a whole is assumed in the model to be the weighted average of the performance of each type of component found in the field.

The sum effect of surface and correction parameters for the collector assembly and mirrors is accounted for in the mirrors efficiency term,  $\eta_{\text{mirrors}}$  :

$$\eta_{mirrors} = \sum_{i=1}^{NumCol} ColFrac_i \cdot TrkTwstErr_i \cdot GeoAcc_i \cdot MirRef_i \cdot MirCln_i$$

where

- NumCol = the number of collector types in the field
- ColFrac = the fraction of collector type in the field
- TrkTwstErr = twisting and tracking error associated with the collector type
- GeoAcc = geometric accuracy of the collector mirrors
- MirRef = mirror reflectivity
- MirCln = mirror cleanliness

To evaluate the difference between the model and the Soltrace results the followings terms are used in the above equation:

- NumCol = 1
- ColFrac = 1
- TrkTwstErr = 1
- GeoAcc = 1
- MirRef = equal to the Solar Weighted Specular Reflectance obtained with the spectrophotometer.
- MirCln = 1

In the first approximation the  $\eta_{HCE}$  term is hypothesized equal to 1 but is however described in the followings.

The sum effect of surface and correction parameters for the heat collection element is accounted for in the HCE efficiency term,  $\eta_{HCE}$  :

$$\eta_{HCE} = \sum_{i=1}^{NumHCE} HCEFrac_i \cdot HCEdust_i \cdot BelShad_i \cdot EnvTrans_i \cdot HCEabs_i \cdot HCEEmisc_i$$

where

- NumHCE = the number of HCE types in the field
- HCEFrac = the fraction of HCE type in the field
- HCEdust = losses due to shading of HCE by dust on the envelope
- BelShad = losses from shading of ends of HCEs due to bellows
- EnvTrans = transmissivity of the glass envelope

HCEabs = absorptivity of the HCE selective coating  
HCEmisc = miscellaneous factor to adjust for other HCE losses

Typical surface properties and correction parameters for the collector field and HCE are shown in Table 6.1 but used in the second step phase.

Name	Value	Name	Value
TrkTwstErr	0,99	HCEdust	0,98
GeoAcc	0,98	BelShad	0,97
MirRef	0.93	EnvTrans	0,96
MirCln	0,95	HCEabs	0,95
		HCEmisc	0,96

Table 6.1 Typical optical parameters and correction values for solar field (Source: Price, 2005, and Forristall, 2003)

Using the parameters listed in Table 6.1, the field efficiency calculated is 0.857, and the HCE efficiency calculated is 0.832.

Together, the incident radiation losses due to surface properties and focusing and cleanliness correction factors are 0.7133.

#### 6.1.4 Incidence Angle Modifier (IAM)

In addition to losses due to the angle of incidence, there are other losses from the collectors that can be correlated to the angle of incidence. These losses occur due to additional reflection and absorption by the glass envelope when the angle of incidence increases. The incidence angle modifier (IAM) corrects for these additional reflection and absorption losses. The incidence angle modifier is given as an empirical fit to experimental data for a given collector type, but unfortunately these experiment haven't been already carried out for the Archimede solar plant.

In this phase of the research we are using the incidence angle modifier based on performance tests conducted at Sandia National Laboratories on an LS-2 collector, the incidence angle modifier for the collector is (Dudley, 1994):

$$K = \cos(\theta) + 0.000884(\theta) - 0.00005369(\theta)^2$$

where  $\theta$ , the incidence angle, is provided in degrees.

It is desirable to distinguish between losses in available radiation due to the angle of incidence itself and the reflection/absorption corrections empirically correlated to the angle of incidence. For this

purpose, the incidence angle modifier is defined for this work as the incidence angle modifier defined by Dudley et al, divided by the cosine of the incidence angle:

$$IAM = \frac{K}{\cos(\theta)}$$

The equation for the incidence angle modifier used in the solar field component model is:

$$IAM = 1 + 0.000884 \cdot \frac{\theta}{\cos\theta} - 0.00005369 \cdot \frac{\theta^2}{\cos\theta}$$

The variation of the incidence angle modifier (IAM) is shown versus the incidence angle ( $\theta$ ) in Figure 6.8. The cosine of the incidence angle is provided in Figure 6.8 for reference.

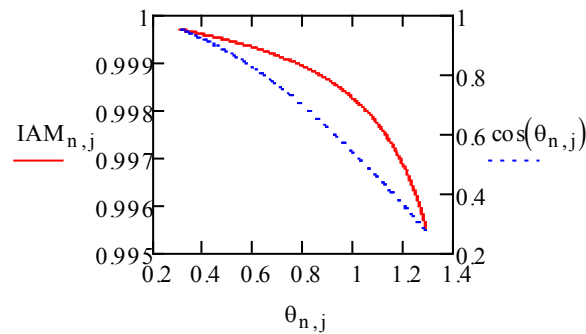


Figure 6.8 Incidence angle modifier (IAM) versus  $\theta$

### 6.1.5 Row Shading and End Losses

The positioning and geometry of the collector troughs and HCEs can introduce further losses, due to shading of parallel rows in the morning and evening as well as end losses from the HCE.

The following discussion of collector shading is based on Stuetzle (2002). At the Archimede Plant, the collectors are arranged in parallel rows, with about 15 [m] of spacing between each row. In the early morning, all of the collectors face due east. Due to the low solar altitude angle of the sun in the morning, the eastern-most row of collectors will receive full sun, but this row will shade all subsequent rows to the west. As the sun rises and the collectors track the sun, this mutual row shading effect decreases, until a critical zenith angle is reached at which no row shading occurs. Collector rows remain un-shaded through the middle of the day, from late morning through early afternoon.

Mutual row shading then re-appears in the late afternoon and evening, when the solar altitude angle is again very low. Figure 6.9 depicts tracking of solar collectors from early to mid-morning, and the consequent row shading that occurs over this period.

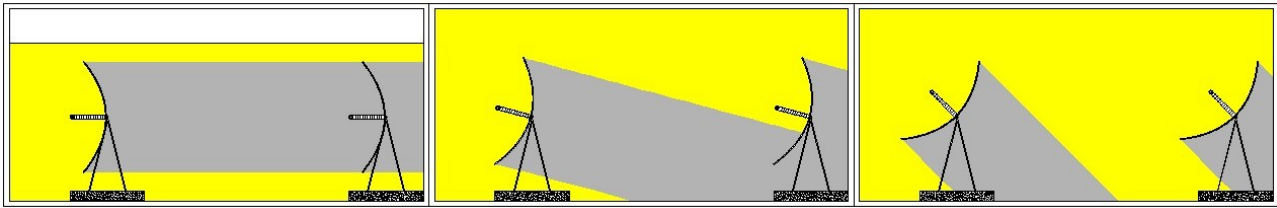


Figure 6. 9 Collector tracking through morning, showing digression of collector shading as the day progresses

Row shading decreases collector performance by decreasing the amount of radiation incident on the collectors. The width of the mirror aperture which receives incident radiation (that is, the width of the aperture that is not shaded) is defined as the “effective mirror width.” The row shadow factor is the ratio of the effective mirror width to the actual mirror width. This ratio can be derived from the geometry of the solar zenith angle, the incidence angle, and the layout of the collectors in a field (Stuetzle, 2002):

$$RowShadow = \frac{W_{eff}}{W} = \frac{L_{spacing}}{W} \cdot \frac{\cos \theta_z}{\cos \theta}$$

Where

- RowShadow = row shadow factor [-]
- W<sub>eff</sub> = effective (unshaded) width of mirror aperture [m]
- L<sub>spacing</sub> = length of spacing between troughs (15 [m])
- W = collector aperture width (5.78 [m])
- θ<sub>z</sub> = zenith angle
- θ = angle of incidence

The previous equation is bounded with a minimum value of 0 (rows are fully shaded) and a maximum value of 1 (rows are not shaded). Figure 6.10 shows variation of the row shadow factor through the day, both for the summer solstice and the winter solstice. As seen in Figure 6.10, losses are introduced by collector shading during approximately the first and last 90 minutes of operation each day. Because the collectors are single-axis tracking in a north-south orientation, the length of time over which row shading occurs does not vary significantly throughout the year.

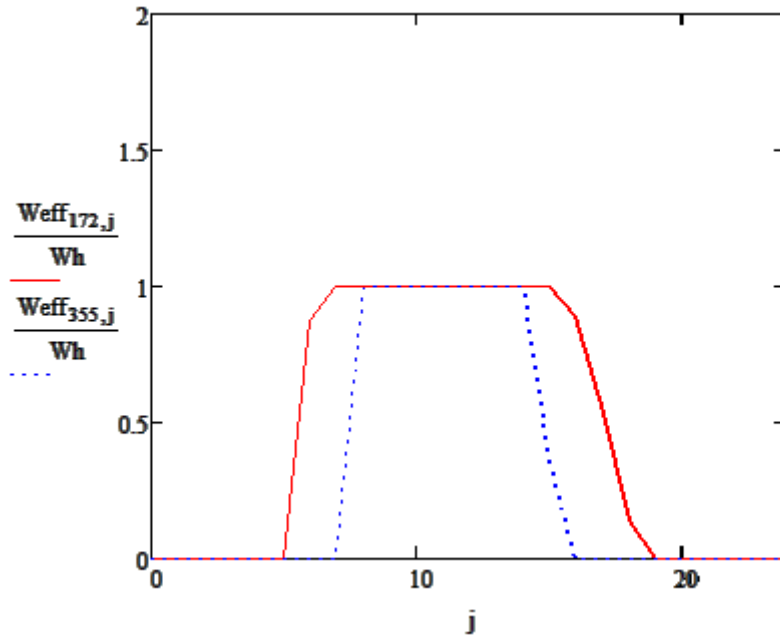


Figure 6.10 RowShadow ( $W_{eff}/W_h$ ) versus time of day, for June 21 and December 21

End losses occur at the ends of the HCEs, where, for a nonzero incidence angle, some length of the absorber tube is not illuminated by solar radiation reflected from the mirrors. Figure 6.11 depicts the occurrence of end losses for an HCE with a nonzero angle of incidence.

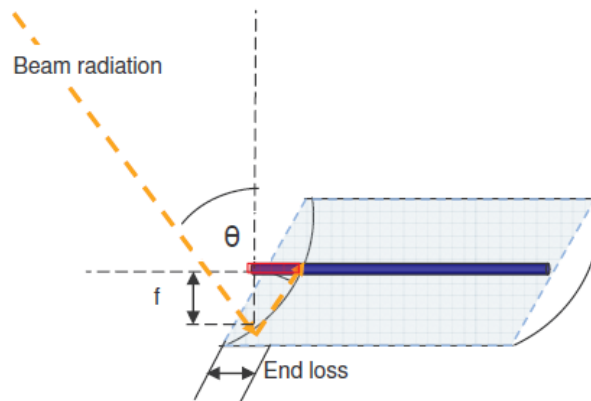


Figure 6.11 End losses from an HCE

The end losses are a function of the focal length of the collector, the length of the collector, and the incident angle (Lippke, 1995):

$$EndLoss = 1 - f \frac{\tan \theta}{L_{SCA}}$$

Where

- f = focal length of the collectors (1.81 [m])
- $\theta$  = incident angle
- $L_{SCA}$  = length of a single solar collector assembly (12.18 m)

Figure 6.12 shows variation of end losses with incidence angle.

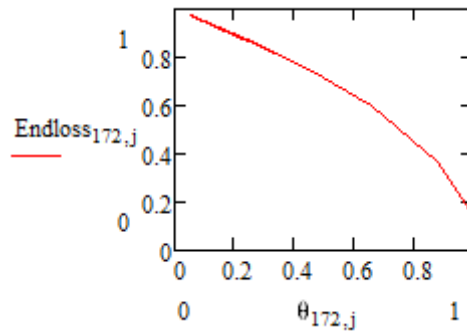


Figure 6. 12 End Losses versus incidence angle ( $\theta$ )

### 6.1.6 Solar Irradiation Absorption

To obtain a comparable value between the Mathcad and the Soltrace software we calculated the following relation and then compare the results.

Now we will start to describe the results obtained with the values of mirror reflectance for each type of mirrors.

The equation for the absorbed solar radiation is:

$$Q_{Absorbed} = DNI \cdot \cos\theta \cdot IAM \cdot RowShadow \cdot EndLoss \cdot \eta_{mirrors} \cdot \eta_{HCE}$$

where

- $Q_{Absorbed}$  = solar radiation absorbed by the receiver tubes [W/m<sup>2</sup>]
- DNI = direct normal insolation [W/m<sup>2</sup>]
- $\theta$  = angle of incidence [deg]
- IAM = incidence angle modifier [-]
- RowShadow = performance factor that accounts for mutual shading of parallel collector rows during early morning and late evening [-]
- EndLoss = performance factor that accounts for losses from ends of HCEs [-]
- $\eta_{mirrors}$  = efficiency that accounts for losses due to mirror optics and imperfections [-]

$\eta_{HCE}$  = HCE efficiency that accounts for losses due to HCE optics and imperfections [-]

Thus, summarizing the different terms used in the simulation we have:

For the DNI direct normal insolation were evaluated for the day 172 (solstice of summer) 21<sup>st</sup> of June, which consists in the following values in table 6.2:

HOUR(h)	DNI VALUE (W/m <sup>2</sup> )
0	0.000
1	0.000
2	0.000
3	0.000
4	2.830
5	75.104
6	202.640
7	361.35
8	531.400
9	690.110
10	813.390
11	880.000
12	880.000
13	813.390
14	691.520
15	532.81
16	362.769
17	244.050
18	76.520
19	2.830
20	0.000
21	0.000
22	0.000
23	0.000

Table 6. 2 Hourly DNI values for the 172<sup>th</sup> day

For the angle incidence  $\theta$  were used the following values shown in table 6.3:

HOUR (h)	$\theta$ (rad)
0	0
1	0

2	0
3	0
4	0
5	0
6	0.253
7	0.064
8	0.099
9	0.225
10	0.305
11	0.333
12	0.307
13	0.23
14	0.106
15	0.055
16	0.243
17	0.448
18	0.658
19	0.881
20	1.13
21	0
22	0
23	0

Table 6. 3 Hourly values of incident angle ( $\theta$ )

For the IAM values, the RowShadow, the EndLoss were firstly used the values of 1  
For the values of  $\eta_{\text{mirrors}}$  were used the followings values (table 6.4):

Name	Solar Weighted Specular Reflectance
TG1	93.27%
TG2	91.96%
AL1	86.55%
AL2	93.02%
PF1	89.59%
PF2	88.30%

Table 6. 4 Solar weighted specular reflectance obtained with the spectrophotometer

While for the  $\eta_{\text{HCE}}$  was first used 1 to let us compare the model.

Being aware that the concentration factor rules a fundamental importance in the solar collection it was necessary to calculate this factor which is a geometric parameter obtained with the followings equation:

$$Conc = \frac{Wh}{\pi d}$$

Where:

Wh is equal to 5.90 m that is the width of the parabolic aperture;

D is the diameter of the inner absorber tube where all the rays are collected and concentrated.

Using the geometric characteristic of the Schott solar 2008 PTR which will be used in the followings to calculate also the heat losses, the diameter is equal to 0.07 m.

Thus the concentrating ratio is equal to 26.829.

So finally we will use the following equation to obtain the value the Soltrace is able to calculate.

$$Q_{Absorbed} = DNI \cdot \eta_{mirrors} \cdot Conc$$

### 6.1.7 Thin glass mirrors

For TG1 samples we used the value of 93.27% of Solar Weighted Specular Reflectance in the model obtaining the following results (table 6.5):

HOUR (h)	Q <sub>Absorbed</sub> (W/m <sup>2</sup> )
0	0
1	0
2	0
3	0
4	71.053
5	1.89E+03
6	5.09E+03
7	9.07E+03
8	1.33E+04
9	1.73E+04
10	2.04E+04
11	2.21E+04
12	2.21E+04
13	2.04E+04
14	1.74E+04
15	1.34E+04
16	9.11E+03
17	6.13E+03

18	1.92E+03
19	7.11E+01
20	0
21	0
22	0
23	0

Table 6. 5 Hourly irradiance absorbed from the Heat Collector Element values for the 172th day with the TG1 mirror

Graphically shown in the next figure 6.13.

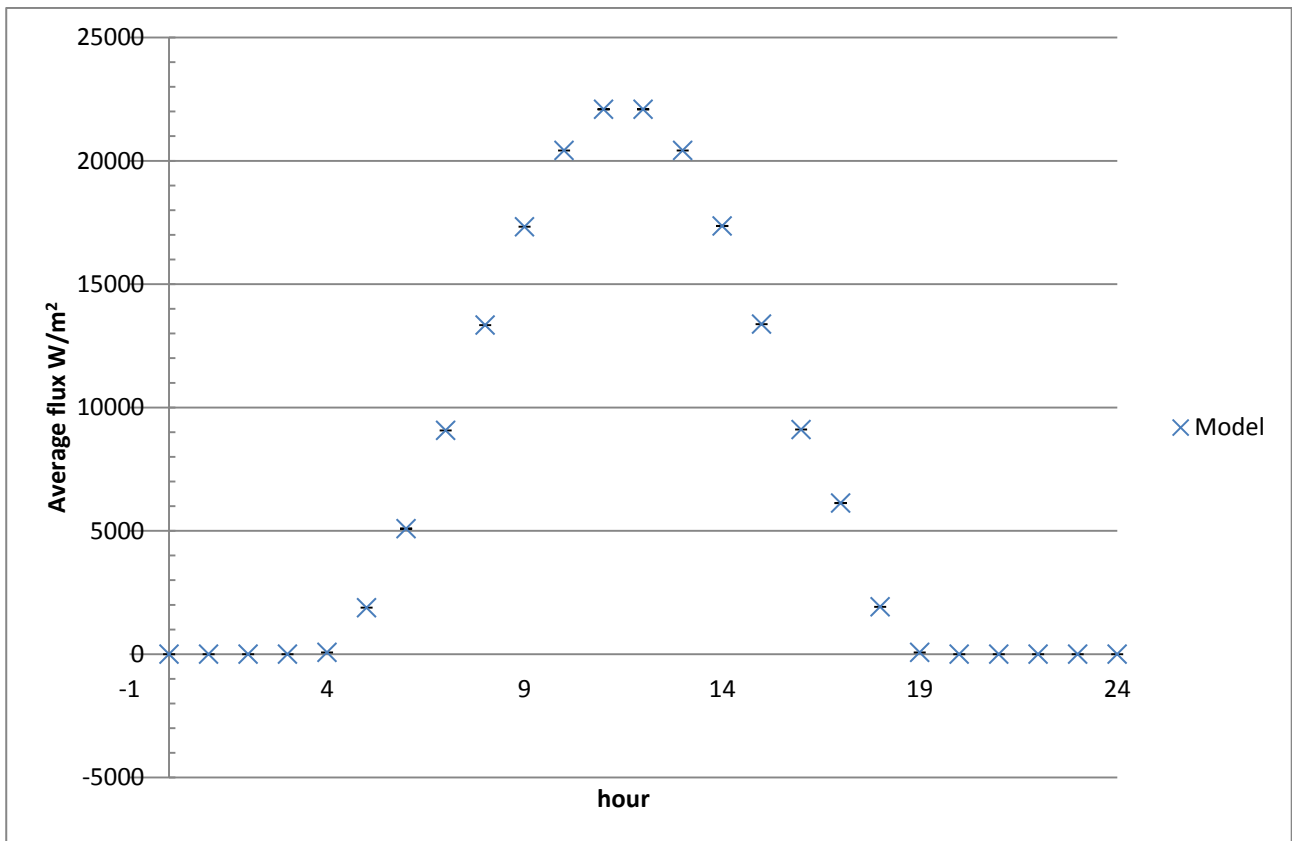


Figure 6. 13 Hourly average flux values collected from the HCE with the TG1 mirror

In the same way the TG2 mirror was modeled with a Solar Weighted Specular Reflectance of 91.96% where the results are shown in the next figure and described in the table 6.6 below.

HOUR (h)	$Q_{\text{Absorbed}} \text{ (W/m}^2\text{)}$
0	0
1	0
2	0
3	0
4	70.528
5	1.87E+03
6	5.05E+03
7	9.01E+03

8	1.32E+04
9	1.72E+04
10	2.03E+04
11	2.19E+04
12	2.19E+04
13	2.03E+04
14	1.72E+04
15	1.33E+04
16	9.04E+03
17	6.08E+03
18	1.91E+03
19	7.05E+01
20	0
21	0
22	0
23	0

Table 6. 6 Hourly irradiance absorbed from the Heat Collector Element values for the 172th day with the TG2 mirror

Graphically represented in figure 6.14

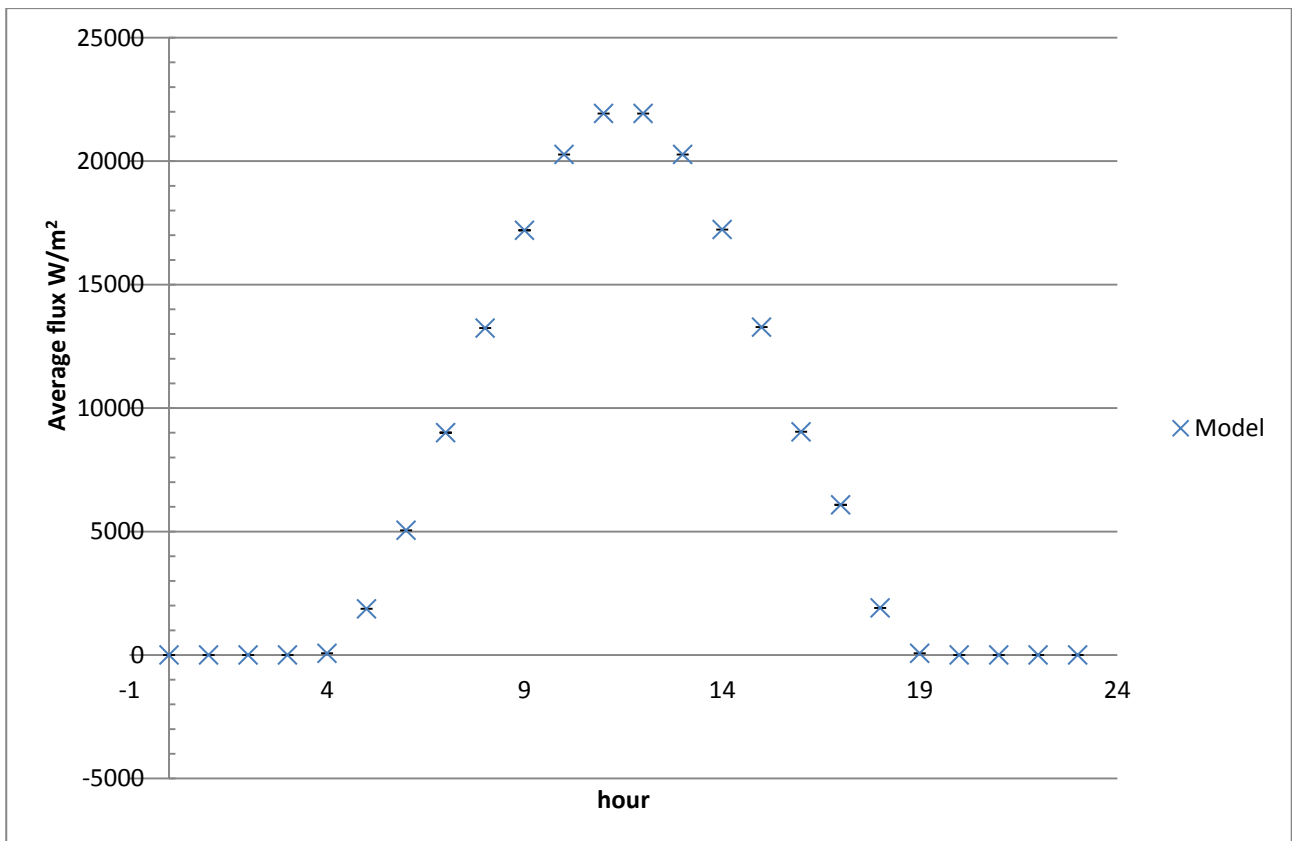


Figure 6. 14 Hourly average flux values collected from the HCE with the TG2 mirror

In the following figure 6.15 is proposed a comparison between the two mirrors.

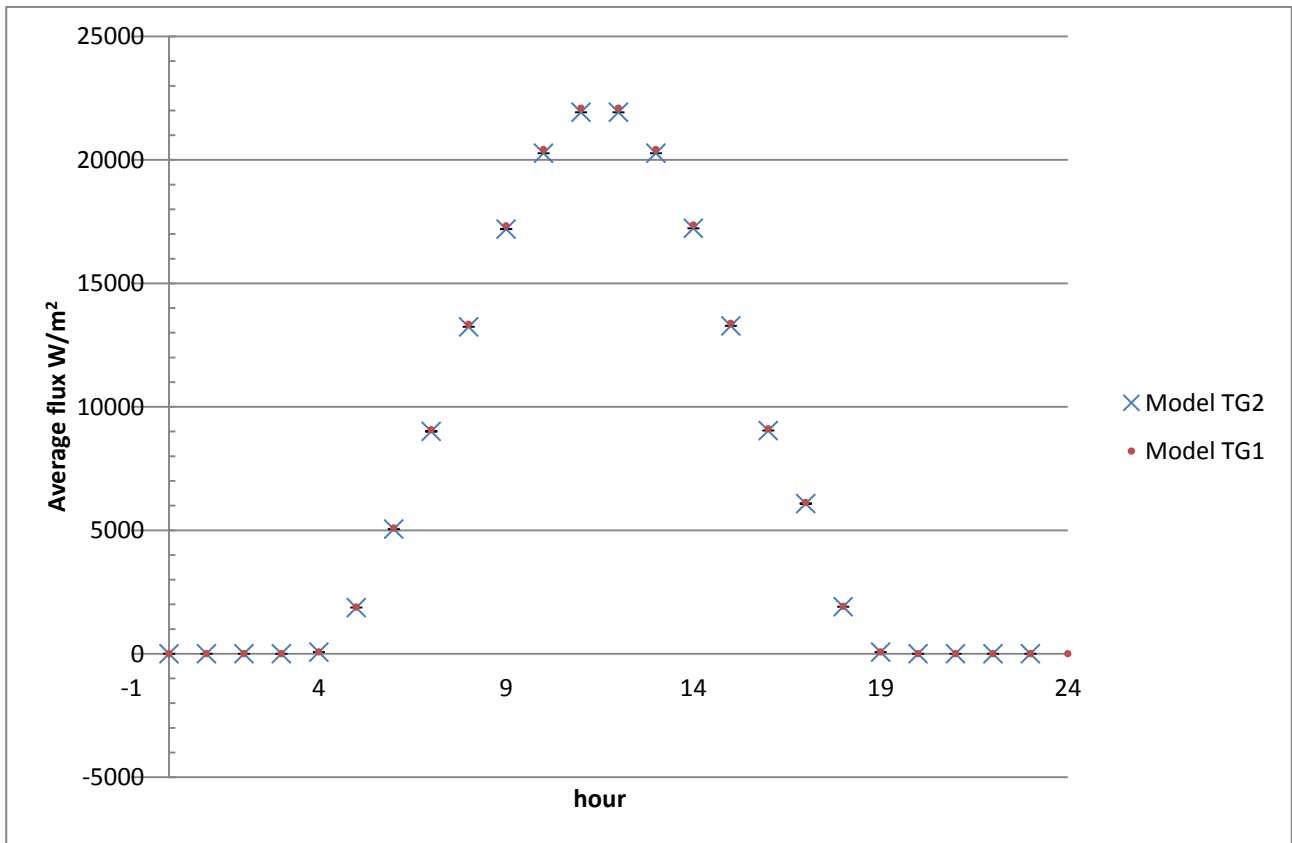


Figure 6. 15 Comparison between TG1 and TG2 mirrors

There is little difference between the values of reflected irradiance due to the reflectivity difference.

### 6.1.8 Aluminum mirrors

For the All mirrors we used the value of 86.55 % of Solar Weighted Specular Reflectance obtaining the values reported in the table and shown in the next table 6.7.

HOUR (h)	$Q_{\text{Absorbed}} \text{ (W/m}^2\text{)}$
0	0
1	0
2	0
3	0
4	66.807
5	1.77E+03
6	4.78E+03
7	8.53E+03
8	1.25E+04

9	1.63E+04
10	1.92E+04
11	2.08E+04
12	2.08E+04
13	1.92E+04
14	1.63E+04
15	1.26E+04
16	8.56E+03
17	5.76E+03
18	1.81E+03
19	66.807
20	0
21	0
22	0
23	0

Table 6. 7 Hourly irradiance absorbed from the Heat Collector Element values for the 172th day with the AL1 mirror

With a graph shown in the next figure.

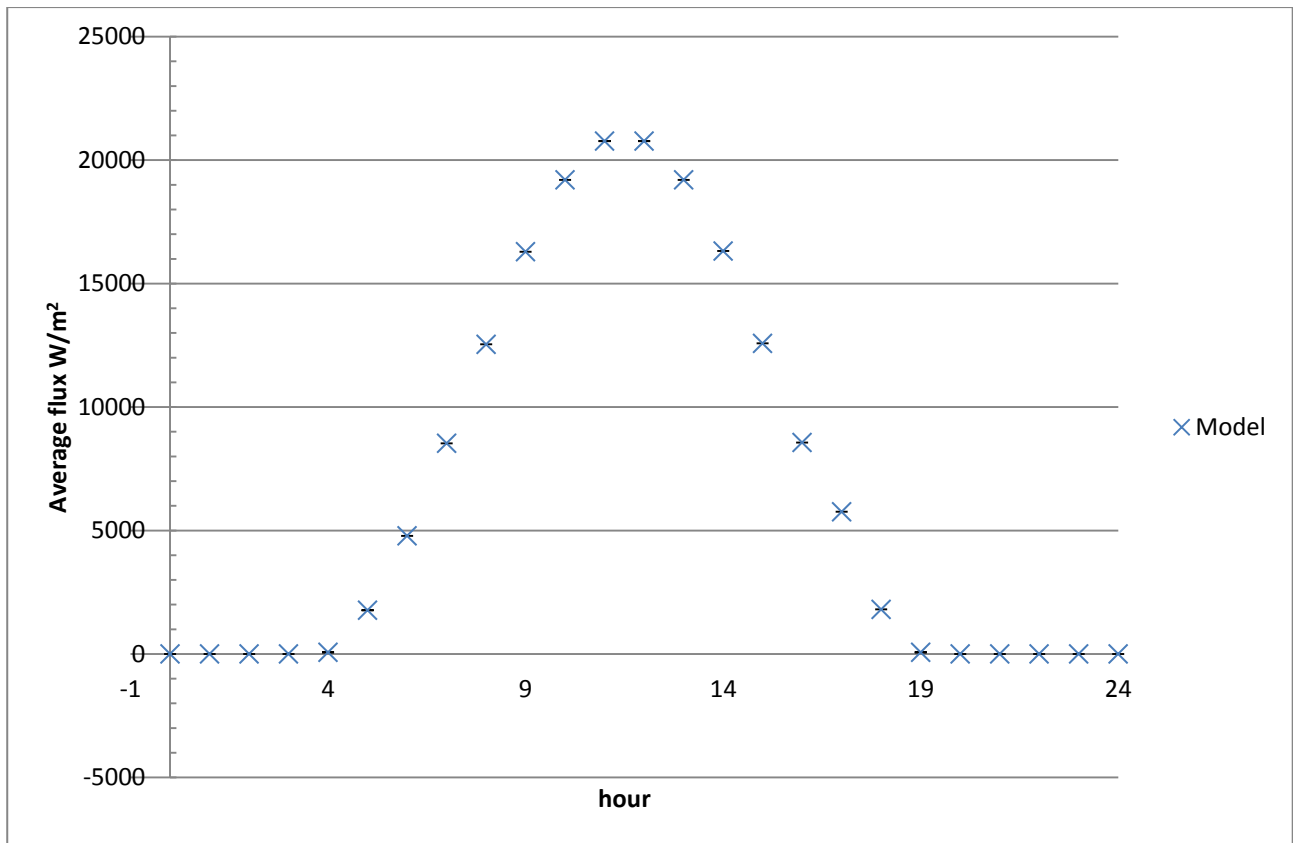


Figure 6. 16 Hourly average flux values collected from the HCE with the AL1 mirror

For the AL2 we obtained the following data.

HOUR (h)	$Q_{\text{Absorbed}} \text{ (W/m}^2\text{)}$
0	0
1	0
2	0
3	0
4	71.02
5	1.89E+03
6	5.09E+03
7	9.07E+03
8	1.33E+04
9	1.73E+04
10	2.04E+04
11	2.21E+04
12	2.21E+04
13	2.04E+04
14	1.74E+04
15	1.34E+04
16	9.10E+03
17	6.13E+03
18	1.92E+03
19	7.10E+01
20	0.00E+00
21	0
22	0
23	0

Table 6. 8 Hourly irradiance absorbed from the Heat Collector Element values for the 172th day with the AL2 mirror

Graphically shown in the following graph (Fig 6.17).

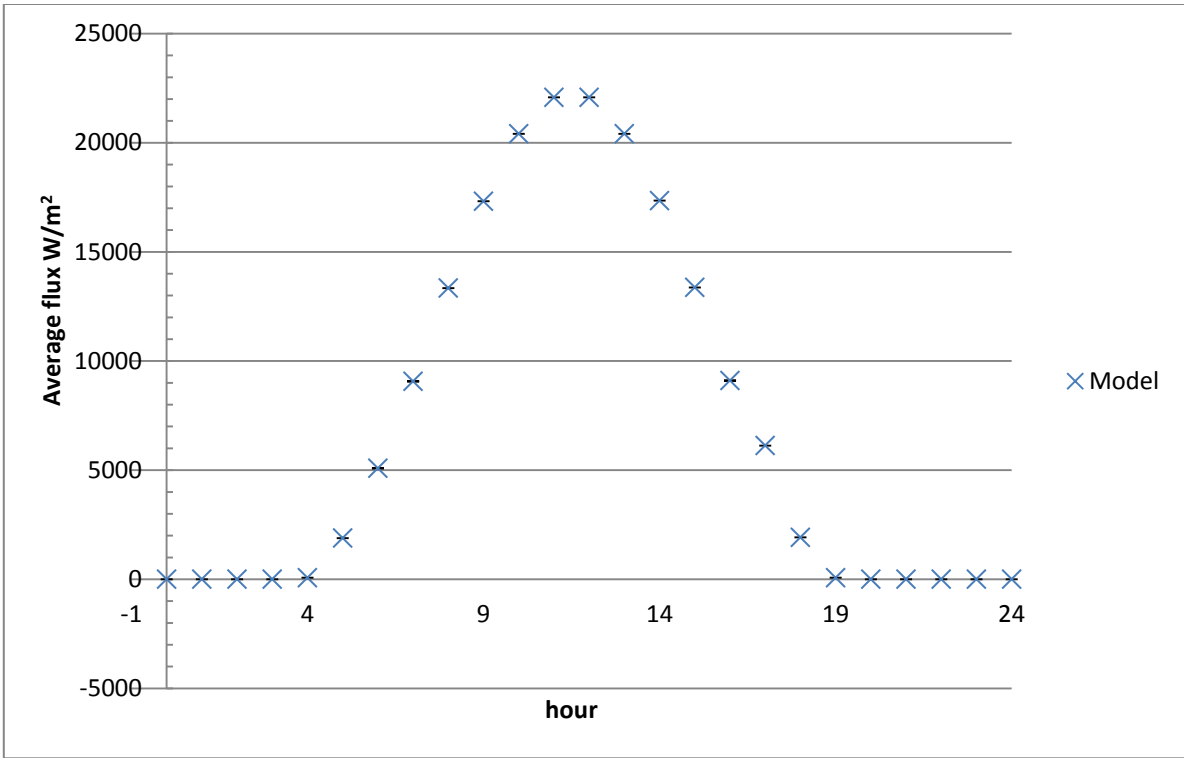


Figure 6.17 Hourly average flux values collected from the HCE with the A12 mirror

Finally we obtained a comparison graph (Fig 6.18).

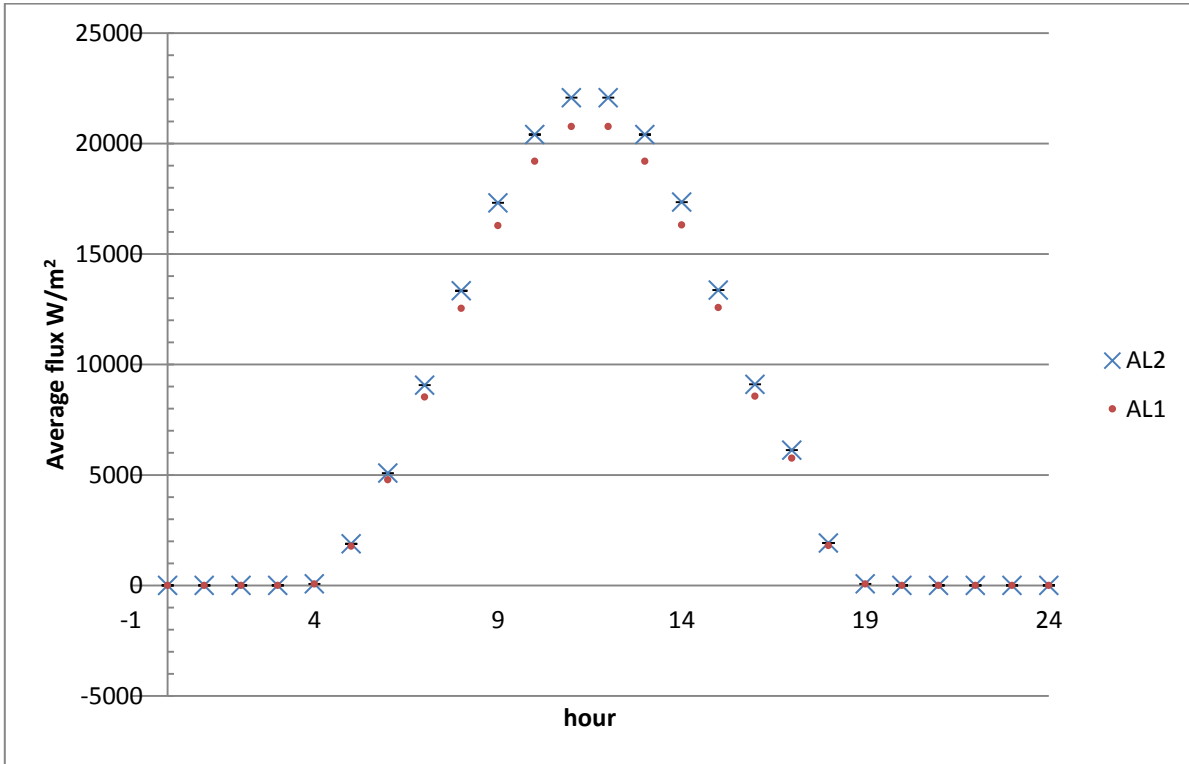


Figure 6.18 Comparison between the two aluminum mirrors

Here the differences between the collected irradiance from one mirror to another are apparent, with the highest difference at the highest values of DNI.

### 6.1.9 Polymeric film mirrors

For PF samples we used the value of 89.59% of Solar Weighted Specular Reflectance in the model obtaining the following results shown in the next table 6.9:

HOUR (h)	Q <sub>Absorbed</sub> (W/m <sup>2</sup> )
0	0
1	0
2	0
3	0
4	70.102
5	1.86E+03
6	5.02E+03
7	8.95E+03
8	1.32E+04
9	1.71E+04
10	2.02E+04
11	2.18E+04
12	2.18E+04
13	2.02E+04
14	1.71E+04
15	1.32E+04
16	8.99E+03
17	6.05E+03
18	1.90E+03
19	70.102
20	0
21	0
22	0
23	0
	0

Table 6. 9 Hourly irradiance absorbed from the Heat Collector Element values for the 172th day with the PF1 mirror

Graphically these values are represented in the following graph (fig 6.19).

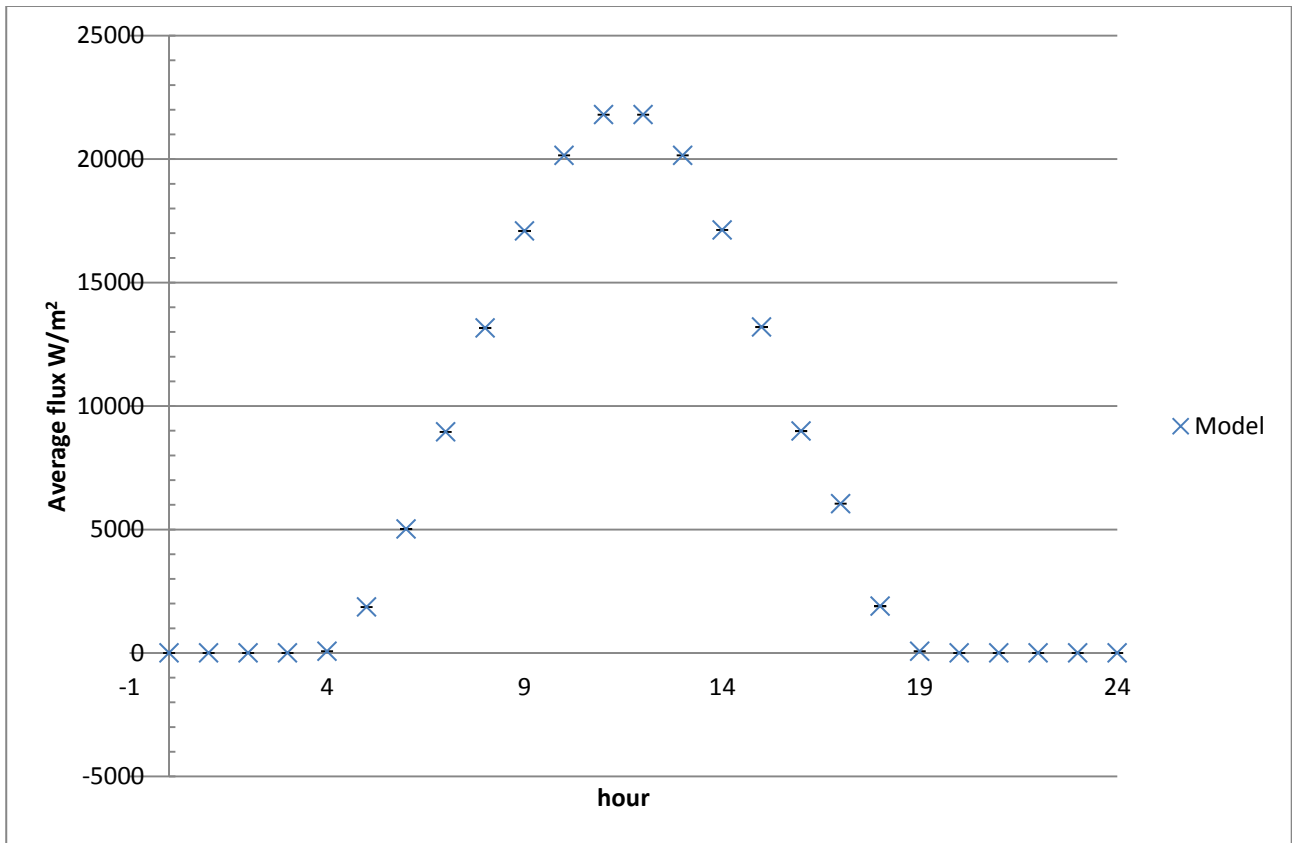


Figure 6. 19 Hourly average flux values collected from the HCE with the PF1 mirror

For the PF2 we obtained the following data shown in the table 6.10.

HOUR (h)	$Q_{\text{Absorbed}} \text{ (W/m}^2\text{)}$
0	0
1	0
2	0
3	0
4	67.043
5	1.78E+03
6	4.80E+03
7	8.56E+03
8	1.26E+04
9	1.64E+04
10	1.93E+04
11	2.09E+04
12	2.09E+04
13	1.93E+04
14	1.64E+04
15	1.26E+04
16	8.59E+03

17	5.78E+03
18	1.81E+03
19	6.70E+01
20	0
21	0
22	0
23	0

Table 6. 10 Hourly irradiance absorbed from the Heat Collector Element values for the 172th day with the PF2 mirror

Graphically represented in the next figure 6.20.

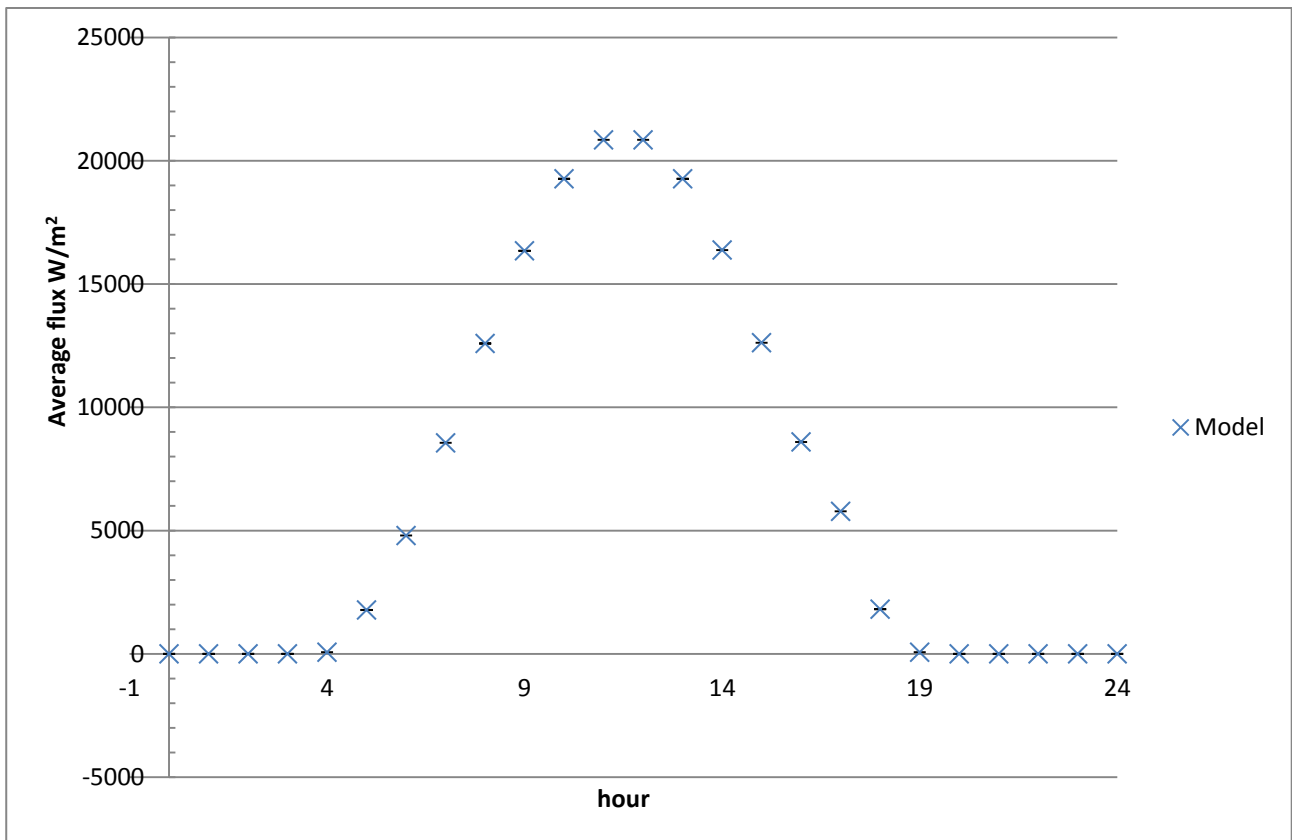


Figure 6. 20 Hourly average flux values collected from the HCE with the PF2 mirror

Finally we obtained a comparison graph (figure 6.21) between the two aluminum mirrors.

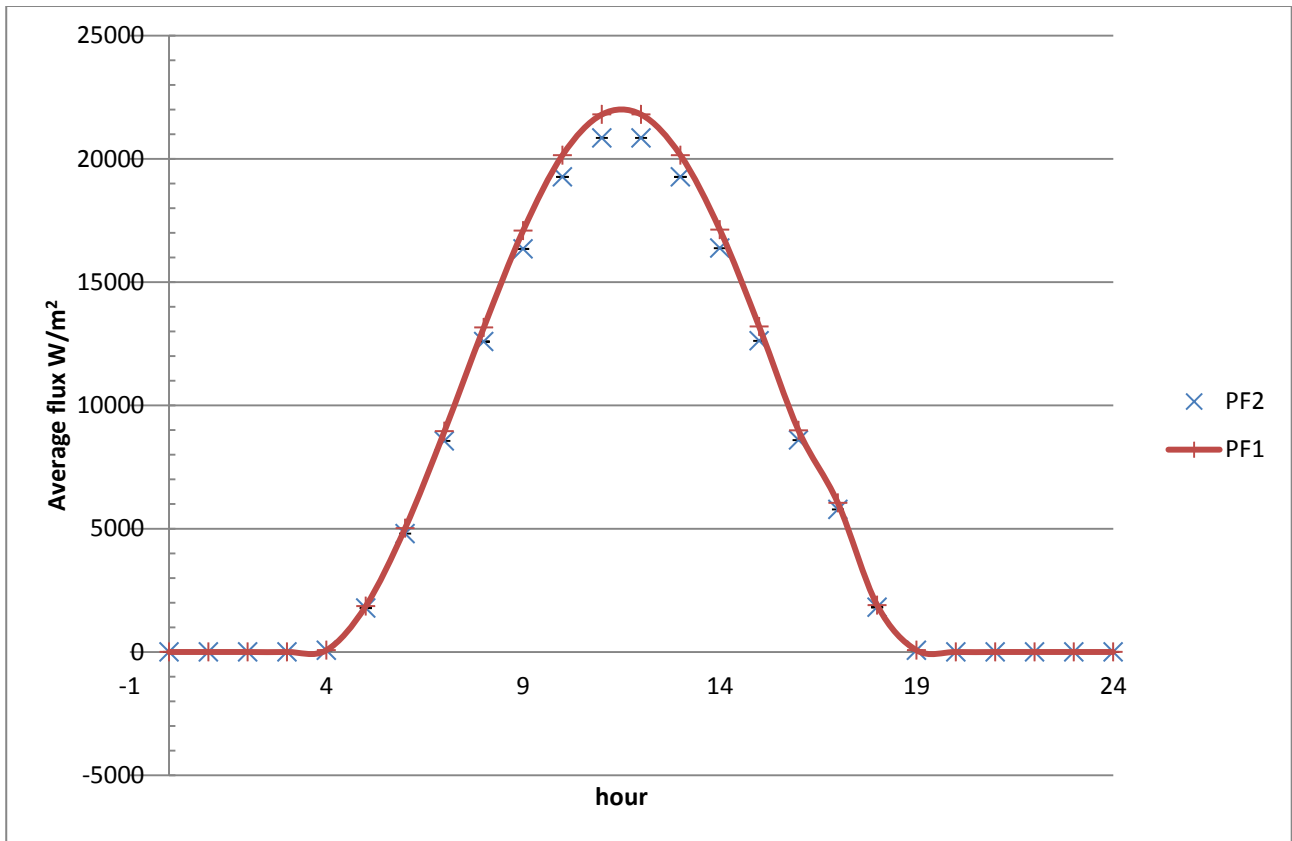


Figure 6. 21 Comparison between the two aluminum mirrors

Here the differences between the collected irradiance from one mirror to another are apparent, with the highest difference at the highest values of DNI.

Finally it's interesting to compare all the typologies of mirrors behavior in a graph (figure 6.22)

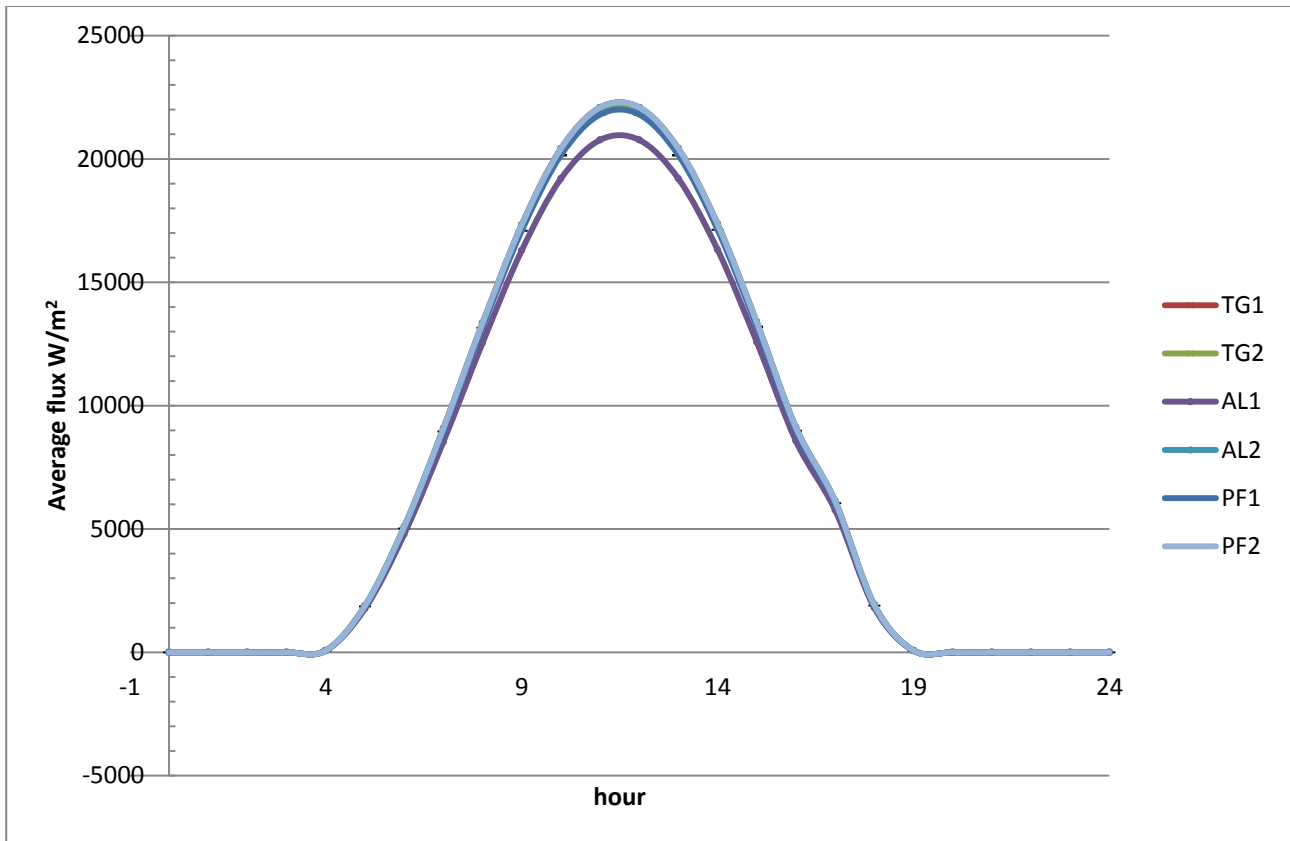


Figure 6. 22 Comparison between all the typologies of mirrors

In the next subchapter we will show the results of the Soltrace simulation and then the comparison between the model and the Soltrace simulation.

## 6.2 Soltrace®

Soltrace is software package developed at the National Renewable Energy Laboratory (NREL) to model solar power optical systems and analyze their performance. Although originally intended for solar optical applications, the code can also be used to model and characterize general optical systems. The creation of the code evolved out of a need to model more complex optical systems than could be modeled with existing tools such as OPTDSH (Steele et al., 1991) and CIRCE (Ratzel and Boughton, 1987).

The code utilizes ray-tracing methodology (Spencer and Murty, 1962). The user selects a given number of rays to be traced. Each ray is traced through the system while encountering various optical interactions. Some of these interactions are probabilistic in nature (e.g. selection of sun angle from sun angular intensity distribution) while others are deterministic (e.g. calculation of ray intersection with an analytically described surface and resultant redirection.) Such a code has the

advantage over codes based on convolution of moments in that it replicates real photon interactions and therefore can provide accurate results for complex systems that cannot be modeled otherwise. The disadvantage is longer processing time. Accuracy increases with the number of rays traced and larger ray numbers means more processing time. Also, complex geometries translate into longer run times. However, the required number of rays is also a function of the desired result. For example, fewer rays (and therefore less time) are needed to determine relative changes in optical efficiency for different sun angles on a given solar concentrator than say are needed to accurately assess the flux distribution on the receiver of that same concentrator.

In Soltrace, an optical system is organized into “stages” within a global coordinate system. A stage is loosely defined as a section of the optical geometry which, once a ray exits the stage, will not be re-entered by the ray on the remainder of its path through the system. A complete system geometry may consist of one or more stages. It is incumbent on the user to define the stage geometry accordingly. The motivation behind the stage concept is to employ efficient tracing and therefore save processing time. A stage is comprised of “elements”. Each element consists of a surface, an optical interaction type, an aperture shape and, if appropriate, a set of optical properties. The other significant benefit of stages is that they can also be saved and employed in other system geometries without the need for recalculating element positions and orientations. The location and orientation of stages are defined within the global coordinate system whereas the location and orientation of elements are specified within the coordinate system of the particular stage in which they are defined. Stages can be one of two types: optical or virtual. An optical stage is defined as one that physically interacts with the rays. Conversely, a virtual stage is defined as one that does not physically interact with the rays. The virtual stage is useful for determining ray locations and directions at various positions along the optical path without physically affecting ray trajectory. Elements defined within a virtual stage therefore have no optical properties because they do not interact with the rays. Optical stages consist of elements which interact with the rays potentially altering their trajectories. These elements have optical properties and interaction types associated with them. Beyond this, optical and virtual stages are identical in how they are defined and used. Stages can be duplicated and moved around as groups of elements and then saved for use in other system geometries.

Soltrace uses three right-handed coordinate systems: the global coordinate system, the stage coordinate system and the element coordinate system. These are illustrated in Figure 6.23. Each element in a stage has a local coordinate system (i.e. location and orientation) defined relative to the

stage coordinate system. Each stage has a coordinate system defined relative to the global coordinate system. As shall be described later, the direction of the sun is defined relative to the global coordinate system. Currently, the sun direction is input in either vector form, or in time-of-day, day-of-year format with latitude specified. Light rays are generated from the sun and then traced sequentially through each stage in the geometry. The position and direction of each ray in each stage is stored in memory for later processing and output.

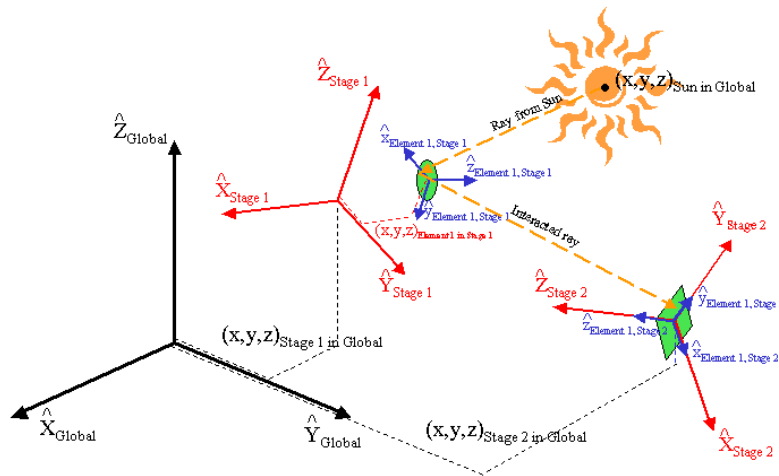


Figure 6. 23 Soltrace® coordinate system

The stage and element coordinate systems are translated from the global coordinate system and stage coordinate system origins respectively and then oriented via three Euler angle rotations. These rotations are shown in Figure 6.24.

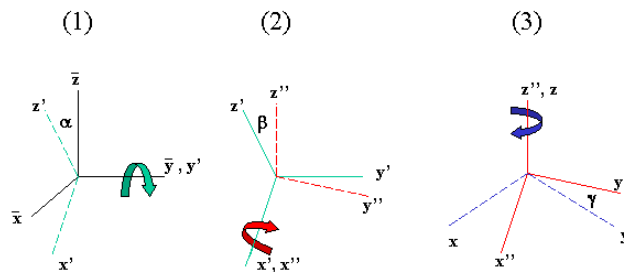


Figure 6. 24 Generation of ( x, y, z ) system from the ( x, y, z ) system after translation of origin

The first rotation is by angle  $\alpha$  about the y-axis, the second rotation by angle  $\beta$  about the x-axis and the last rotation by angle  $\gamma$  about the z-axis. After translation of the child coordinate system origin from the parent coordinate system, these three rotations completely specify the orientation of the child coordinate system within the parent. The first two rotations are automatically determined by specifying a point in the parent coordinate system toward which the z-axis of the child coordinate system is aligned. The last rotation of the child coordinate system about the z-axis is then specified.

### 6.2.1 Defining the Sun

Two characteristics completely define the “sun” as the light source: the angular intensity distribution of light across the sun’s disk (referred to as the sun shape) and the sun’s position. The area in the upper left of the window shown in Figure 6.25 is the first step in defining the sun shape. The first step is to determine the sun's direction. One option is to define a point in the global coordinate system such that a vector from this point to the global coordinate system origin defines the sun direction.

The other option is to define a particular site latitude and time (day of year and local solar hour.) From this information, the sun direction is determined assuming the z-axis of the global coordinate system points due north, the y-axis points towards zenith and the x-axis points due west.

This is critical to remember when defining the stage and element geometry. Soltrace calculates the sun position in azimuth and elevation and determines a corresponding unit vector based on the following equations. In the case where the element geometry depends on sun position (e.g., for a heliostat in a tower geometry), we must use these same equations (Duffie, 2006) to determine element aim points.

Note that these equations are based on solar time and come from the spherical geometric relationship of the earth and sun and do not account for longitude, eccentricity of the earth's orbit or impacts due to atmospheric effects.

The next step is to determine the sun shape. Three options are available. The first two are commonly used probabilistic distributions. Although the sun shapes varies widely with terrestrial location, sky conditions and time it is neither truly Gaussian nor pillbox in nature although the pillbox approximation is adequate for a large class of problems. For highly

accurate systems, the use of a Gaussian sun is not recommended unless the system includes relatively large optical errors (either based on geometry or optical property definitions).

The parameter defining a Gaussian distribution for the sun's disk is the standard deviation,  $\sigma$ .

The parameter for the pillbox, being a flat distribution, is simply the half-angle width.

The third option allows the user to define the sun shape profile as a series of intensity datum points. Since the sun shape is axisymmetric, only half of the profile (from the sun's center to the edge) is required. This can be manually entered into the table seen in the lower left corner of the window.

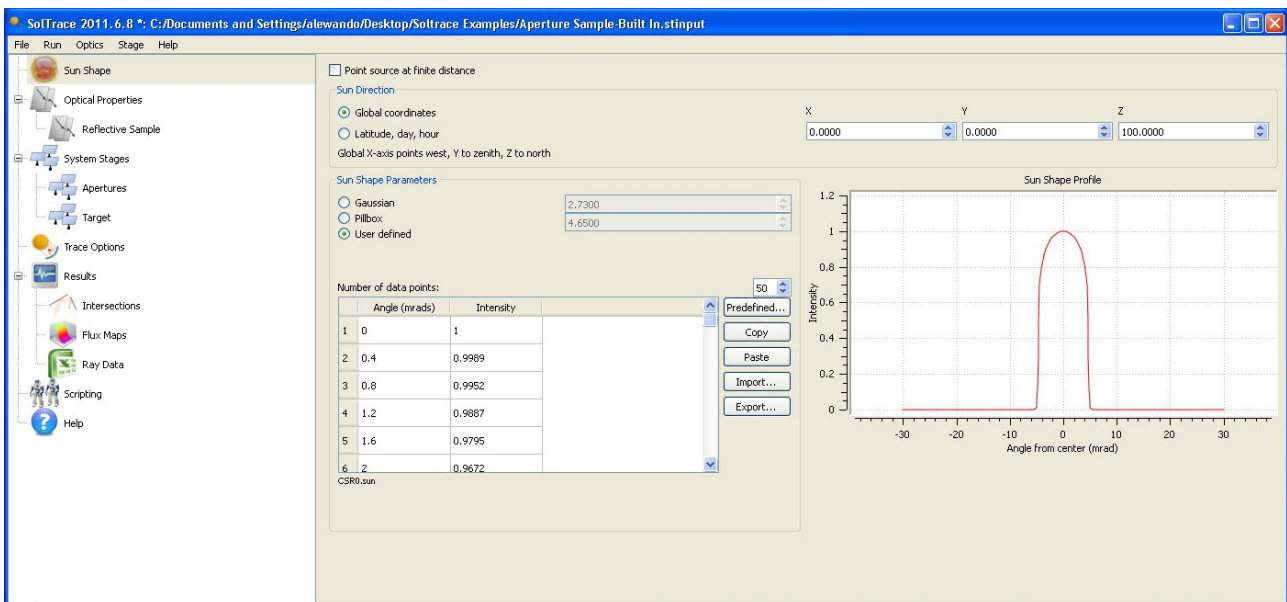


Figure 6. 25 Defining the Sun Shape and Position

There are some situations where defining the sun as a point source is useful (e.g., checking the performance of ideal optical elements). A point source can be specified with a check in the box in the upper left of this window. When using Global Coordinates with a point source, the distance to the elements is important so, for example, setting a point source at infinity requires a very large distance be specified. The Latitude, day and hour option is not available for a point source.

The impact of the solar distribution is much greater on high concentration systems. In fact, for many high concentration systems the choice of a pillbox sun is more than adequate. Tests of run time for User Defined and Pillbox sun shapes have shown essentially no difference. For

low concentration systems, the impact is much less since the system has a high acceptance angle and much of the circumsolar will find its way to the target or aperture.

### 6.2.2 Defining Optical Geometry

Each optical property set contains a separate set of parameters for the front and back of the surface, accessed from the selection options under Editing.

Element surfaces have a front and back side defined by the z-axis vector.

Surface selection and the coordinate system definitions will be covered in the next section on Geometry.

The front side of a surface faces toward the positive z-axis and the back side away from the positive z-axis. For most surfaces the front and back are relatively straightforward however some, like the cylinder, can be confusing.

Elements can be either reflective or refractive with the selection entered in the element data geometry.

For refractive optics, only the transmissivity and the real component of the refraction indices are relevant and used at this time.

The imaginary refractive index is not used. A real physical refractive component is actually constructed from two elements or surfaces. In Figure 6.26 for example, a plane of glass consists of two surfaces (or elements) separated by the glass media between. A ray passes from one media (air for example) through one surface (or element) to the glass media, is refracted and then passes through the other surface back to the air. The first element would be defined with the index of refraction of air on the back side and the index of refraction of glass on the front side. The second surface would be defined with the index of refraction of glass on the back side and the index of refraction of air on the front side. Surfaces other than flat would construct lenses.

The transmissivity is the fraction of rays (0 to 1.0) that pass through an element.

Currently, for refractive surfaces there is no reflective component nor is there any direct input for absorption through the media.

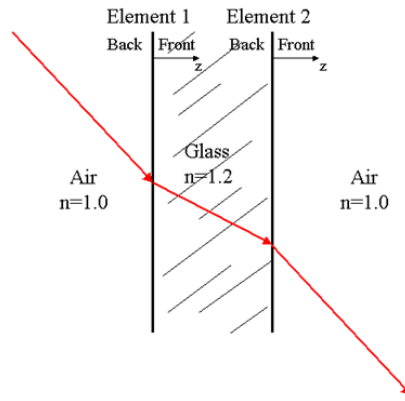


Figure 6. 26 A glass plane is actually constructed from two separate elements

For reflective optics, one element is sufficient to model a mirror since no transmission is allowed. The relevant parameter is the reflectivity and the element still possesses both back and front side values. For example, a mirror could have rays which intersect the back side (e.g., a heliostat in a field); the back should then be assigned a reflectance of zero.

For both refractive and reflective optics another set of parameters applies that define the optical accuracy of the surface. In addition to the effects of the element surface shape on ray direction, two random errors can be included which affect ray interaction at the surface of an element.

They are surface slope error and surface specularity.

Surface slope error is a macro feature while specularity is a micro structure effect.

Both are illustrated in Figure 6.27 for the case of a reflective surface with Gaussian error distribution having a standard deviation of  $\sigma$ . The total error is given by

$$\sigma_{\text{optical}} = (4\sigma_{\text{slope}}^2 + \sigma_{\text{specularity}}^2)^{1/2}$$

Specularity error is already in terms of the reflected vector, thus the factor of 4 on the  $\sigma_{\text{slope}}$  term.

Select the distribution type in the box on the lower center of the Property Values window and enter appropriate values for the errors to the right.

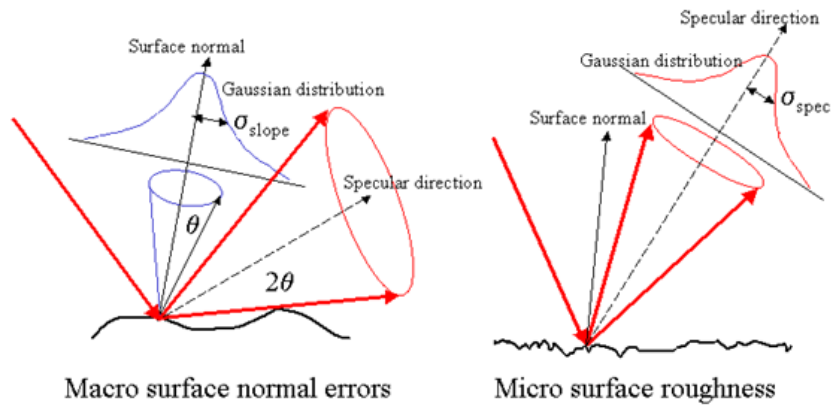


Figure 6.27 Illustration of surface slope and surface specular error

### 6.2.3 Defining System Geometry

Once the sun is defined the next step is defining the optical geometry of the system.

The system geometry is defined on a selected System Stage page, shown below in Figure 6.28.

En.	X-Coord.	Y-Coord.	Z-Coord.	X-AimPt.	Y-AimPt.	Z-AimPt.	Z-Rot.	Aperture	Surface	Interaction	Optics	Comment
1	-1.32144	1.5748	0.337323	1.83577	0.157399	9.71938	0	h-0.8799,0,0,0,0,0,0	s-0.06892,0.06892,0,0,0,0,0	Reflection	primary facet	
2	-1.32144	0.7874	0.337323	1.89885	-0.11253	9.76175	0	h-0.8799,0,0,0,0,0,0	s-0.06889,0.06889,0,0,0,0,0	Reflection	primary facet	
3	-1.32144	0	0.337323	1.93805	-0.355782	9.7845	0	h-0.8799,0,0,0,0,0,0	s-0.06823,0.06823,0,0,0,0,0	Reflection	primary facet	
4	-1.32144	-0.7874	0.337323	1.95002	-0.584572	9.78488	0	h-0.8799,0,0,0,0,0,0	s-0.06811,0.06811,0,0,0,0,0	Reflection	primary facet	
5	-1.32144	-1.5748	0.337323	1.93356	-0.813122	9.76201	0	h-0.8799,0,0,0,0,0,0	s-0.068,0.068,0,0,0,0,0	Reflection	primary facet	
6	-0.660721	1.1811	0.168661	2.12162	-0.0110794	9.69952	0	h-0.8799,0,0,0,0,0,0	s-0.06859,0.06859,0,0,0,0,0	Reflection	primary facet	
7	-0.660721	0.3937	0.168661	2.1694	-0.257396	9.7377	0	h-0.8799,0,0,0,0,0,0	s-0.06811,0.06811,0,0,0,0,0	Reflection	primary facet	
8	-0.660721	-0.3937	0.168661	2.19352	-0.481112	9.75228	0	h-0.8799,0,0,0,0,0,0	s-0.06835,0.06835,0,0,0,0,0	Reflection	primary facet	
9	-0.660721	-1.1811	0.168661	2.19165	-0.696651	9.74098	0	h-0.8799,0,0,0,0,0,0	s-0.06806,0.06806,0,0,0,0,0	Reflection	primary facet	
10	-0.660721	-1.9695	0.168661	2.1638	-0.919691	9.70397	0	h-0.8799,0,0,0,0,0,0	s-0.06833,0.06833,0,0,0,0,0	Reflection	primary facet	
11	0	1.5748	0	2.31639	0.100116	9.61559	0	h-0.8799,0,0,0,0,0,0	s-0.06859,0.06859,0,0,0,0,0	Reflection	primary facet	
12	0	0.7874	0	2.36754	-0.156593	9.66973	0	h-0.8799,0,0,0,0,0,0	s-0.06823,0.06823,0,0,0,0,0	Reflection	primary facet	
13	0	0	0	0.239967	-0.0382958	0.970025	0	h-0.8799,0,0,0,0,0,0	s-0.06811,0.06811,0,0,0,0,0	Reflection	primary facet	
14	0	-0.7874	0	2.40976	-0.592645	9.70336	0	h-0.8799,0,0,0,0,0,0	s-0.06811,0.06811,0,0,0,0,0	Reflection	primary facet	

Figure 6.28 Optical geometry definition input page

The input page is shown with data already entered for the sake of example. The form can now be used to design every aspect of the optical problem to be analyzed.

Each stage is displayed as a tab, much like worksheets in a spreadsheet. For each stage, there is a set of stage properties, position and orientation information in the global coordinate system, as well as a table of optical elements in the stage coordinate system.

### Stage Properties

The tracing of rays is modified by several choices under Stage Properties. The first is a choice of Virtual Stage which, if checked, defines the stage and its elements so as not to interact with the rays. However, rays intersections with elements are determined and provide a useful means of determining power and flux passing through the element.

This allows the rays to interact with the elements depending on aperture, shape and optical properties.

### Global Coordinates

The first set of three inputs is the location (in  $x,y,z$ ) of the stage coordinate system origin within the global coordinate system. Every stage must have these parameters defined within the global coordinate system. The set of four numbers below this determines the orientation of the stage coordinate system within the global coordinate system. The first three numbers of this set define a special point within the global coordinate system. A vector from the stage origin to this point defines the  $z$ -axis of the stage coordinate system. The last degree of freedom to be defined is then the rotation of the stage coordinate system about this  $z$ -axis. This is entered as the fourth number in degrees (Z Rotation).

### Element Definition

Each element is defined on one row of the table and is identified by its row number and by the stage in which it exists.

The next three columns are the  $x,y,z$  coordinates of the element coordinate system origin within the stage coordinate system. The next three columns define the  $x,y,z$  coordinates of the aim point. A vector from the element origin to this aim point defines the  $z$ -axis of the element coordinate system. The ninth column is the rotation of the element coordinate system about its  $z$ -axis in degrees. This set of seven numbers describing the location and orientation of the element within the

stage is exactly analogous to the set described above for the stage within the global coordinate system.

### Apertures

The Aperture column contains the description of the projected shape of the element opening in a plane perpendicular to the element z-axis.

A variety of aperture shapes are available table 6.11. The column entry is a text string that encodes the aperture description. The code format for the different apertures is shown in Table 5.4. The code can be entered manually as a string of text. A code begins with a lower case letter denoting the type of aperture shape, followed by a hyphen, and then a list of eight numbers separated by commas. Some aperture shapes require all eight parameters, while others may only require one. Shape parameters that are unused can be set to 0 and are ignored.

<i>Aperture Type</i>	<i>Code</i>	<i>Special Considerations</i>
Circular	c-# (# = diameter of circular aperture)	
Hexagonal	h-# (# = diameter of the circle which circumscribes a hexagonal aperture)	
Triangular	t-# (# = diameter of the circle which circumscribes an equilateral triangle)	
Rectangular	r-# <sub>1</sub> ,# <sub>2</sub> (# <sub>1</sub> ,# <sub>2</sub> = width, height of rectangle)	
Single Axis Curvature Section	l-# <sub>1</sub> ,# <sub>2</sub> ,# <sub>3</sub> (# <sub>1</sub> ,# <sub>2</sub> ,# <sub>3</sub> = distance to inner edge in x dir, distance to outer edge in x dir, length of section in y dir; # <sub>1</sub> < # <sub>2</sub> )	Used to represent surfaces with curvature in the x direction only. Also used with cylindrical surfaces with # <sub>1</sub> =# <sub>2</sub> =0 and # <sub>3</sub> = length of cylinder. It is important that the user ensure that the surface used includes single axis curvature only otherwise unpredictable results may occur.
Annular	a-# <sub>1</sub> ,# <sub>2</sub> ,# <sub>3</sub> (# <sub>1</sub> ,# <sub>2</sub> ,# <sub>3</sub> = inner radius, outer radius, included angle in degrees; # <sub>1</sub> < # <sub>2</sub> , 0 < # <sub>3</sub> ≤ 360)	
Irregular Triangle	i-# <sub>1</sub> ,# <sub>2</sub> ,# <sub>3</sub> ,# <sub>4</sub> ,# <sub>5</sub> ,# <sub>6</sub> (# <sub>1</sub> ,# <sub>2</sub> are the x-y pair of one corner of the triangle followed by the other two pairs)	These apertures need not have the element origin within its boundaries; can be used for off-axis sections of various
	i-# <sub>1</sub> ,# <sub>2</sub> ,# <sub>3</sub> ,# <sub>4</sub> ,# <sub>5</sub> ,# <sub>6</sub> ,# <sub>7</sub> ,# <sub>8</sub> (# <sub>1</sub> ,# <sub>2</sub> are the x-	

Irregular Quadilateral	y pair of one corner of the quadrilateral followed by the other three pairs)	surfaces. Can be used with all surface types, except with spheres there is no option for different curvatures in x and y directions.
------------------------	--	--

Table 6. 11 Aperture types and corresponding codes

## Surfaces

Each element's surface is defined by a text code in the Surface column of the table, similar to how the aperture is defined. A variety of surface options are available. Table 6.12 lists the surface options and respective text codes with more detailed descriptions following the table where needed.

Surface Type	Code	Special Considerations
Zernike Series	m:*.mon (surface described by Zernike series equation with coefficients in file "*.mon")	The $B_{0,0}$ term is a piston term and would normally be set to zero; any offset in the surface should be accounted for in the element position
VSHOT Data Set	v:*.sht (surface described by VSHOT data file "*.sht")	It is important to insure that the coordinate systems and orientation of panels tested by VSHOT are equivalent to those used in SolTrace when these data files are utilized.
Polynomial Series	r:*.ply (surface described by coefficients of polynomial equation in file "*.ply")	Can be used with all apertures except Single Axis Curvature Section to represent a surface of revolution. When used with the Single Axis Curvature Section the surface is curved in only the x direction. It is critical that the user assure that the aperture limits defined for the element match the data in these files. With polynomial files any aperture location outside the outside the nominal range will result in z values extrapolated. For cubic spline files the aperture range cannot be outside the data range indicated in the file.
Cubic Spline Interpolation	i:*.csi (surface described by discrete data points and 1 <sup>st</sup> derivative boundary conditions in file "*.csi")	
Finite Element Data Set (not yet available)	*.fed (surface described by finite element data file "*.fed")	This feature will be implement in the near future.
Parabolic	p-#1,#2 (#1,#2 = 1/radii of curvature in x, y directions of a parabolic surface)	Both #1 and #2 values can be entered as separate values. The different curvatures are utilized for all apertures except the single axis curvature where #2 is internally set to zero to provide for curvature in the x direction only.
Spherical	s-#1,#2 (#1,#2 = 1/radii of curvature in x, y directions of a spherical surface)	Currently the code cannot handle elliptical surfaces defined with #1 ≠ #2. The input window only allows for entry of the $C_x$ value (#1). However, the user can manually enter a non-zero value for $C_y$ (#2) in the worksheet portion of the inputs. Unless this value is the same as $C_x$ or zero, the code will find this error on Tracing and alert the user. If used with single axis curvature apertures the $C_y$ will be set to 0 internally. For spherical surfaces there is clearly a maximum aperture defined by the diameter of the sphere. The user must be careful not to define the aperture with dimensions greater than the diameter.
Hyperboloids and Hemellipsoids	o-#1,#2,#3 (#1,#2 = 1/radii of curvature in x, y directions, #3= k parameter that determines specific surface)	The surfaces described by $k=0$ or $k=1$ are either parabolas or spheres, respectively. If the user enters either of these values for k, the code alerts the user on Tracing. The allowed values for hyperboloids of revolution are $k<0$ and for ellipsoids either $0<k<1$ or $k>1$ . For elliptical surfaces, the user must be careful to define the aperture with dimensions not larger than the diameters described by the surface parameters.
Flat	f	
Conical	c-#1 (#1 = half angle of conical surface)	Note the element origin of this surface is the vertex of the cone.
		The user must be careful to note the element origin is on the surface of the cylinder not the central axis of revolution. If the central axis

Cylinder	t-# <sub>1</sub> (# <sub>1</sub> = 1 / radius of curvature; use in conjunction with aperture code "1-0,0,# <sub>2</sub> " where # <sub>2</sub> is length of cylinder)	represents a focal point (e.g. for a parabolic trough receiver) then the element origin must be offset by the radius and care must be taken to specify the direction of the z axis consistently. By definition the inside of the cylinder is the Front surface for optical properties. Must be used with a Single Axis Curvature Section with # <sub>1</sub> =# <sub>2</sub> =0 and # <sub>3</sub> = length of cylinder.
Torus (not yet available)	d-# <sub>1</sub> ,# <sub>2</sub> (# <sub>1</sub> = radius from origin to center of toric ring, # <sub>2</sub> = radius of the toric ring)	This surface option has not be completely debugged but may be available in the future.

Table 6. 12 Surface types and corresponding codes

## 6.2.4 Tracing Overview

When the user specifies a certain number of rays to be traced (how this is done will be described later), rays continue to be randomly generated until that number of intersections has occurred somewhere on the elements of Stage 1. A vector is calculated which connects the origin of Stage 1 and the source (e.g. the sun) and ray locations are generated on a plane normal to this vector and within a rectangle which encompasses all the projected shapes of the elements within Stage 1 that are selected. This narrows down the random ray generation region and saves execution time. The actual application of the sun direction and the sun shape occurs after these intersections have been determined, not before as might be expected. Mathematically it makes no difference when they are applied, but functionally it is more efficient to do so in this way in order to eliminate needless ray generation and increased execution time. Once the requested number of rays has intersected Stage 1 somewhere, they are traced to subsequent stages. Figure 6.29 shows a Trace Options window.

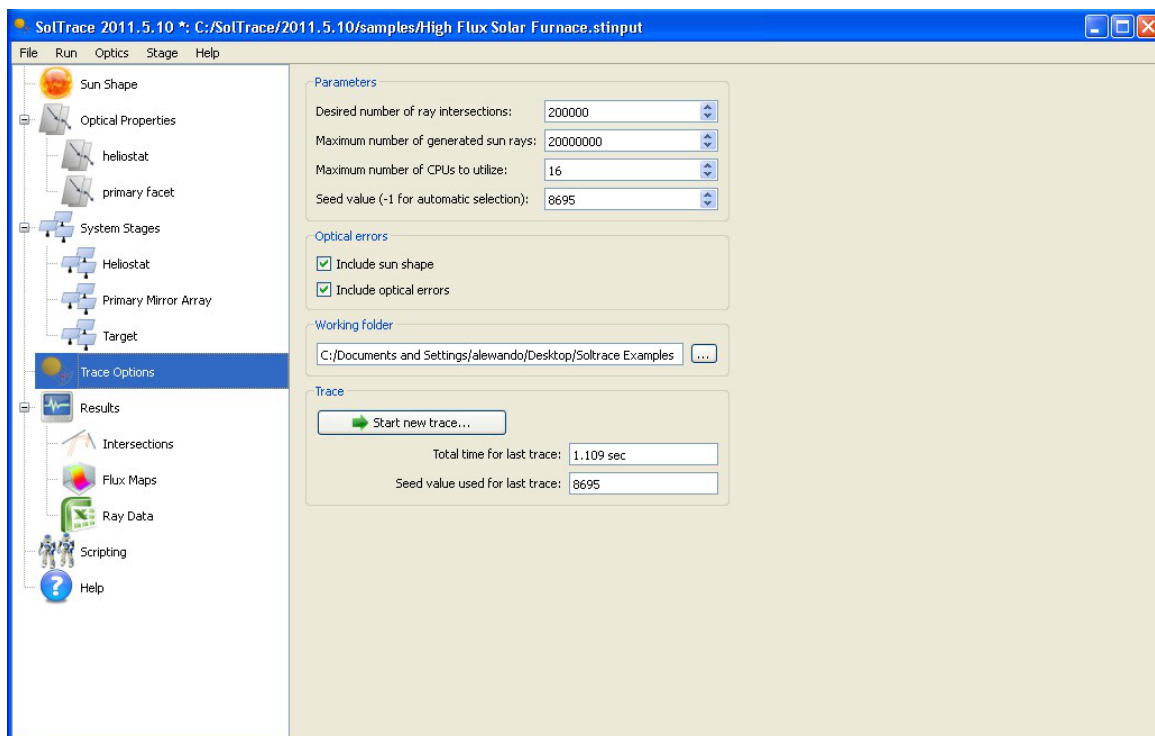


Figure 6. 29 The trace setup parameters

## Parameters

The first input box is the number of rays to be traced. Recall from previous discussions that this many rays will actually interact with elements of Stage 1. The code continues to generate rays until the numbers of requested rays have fallen on elements of Stage 1. The code tallies the total number of rays generated within the rectangle, both those that fell on an element and those that did not, divides this number into the area of the rectangle and multiplies the result by the Direct Normal Insolation value (described in the Visualization section). This result in a unit power/ray value subsequently used to calculate power and flux values.

The maximum number of rays to generate allows the user to limit the maximum number of rays generated, regardless of how many have actually hit Stage 1.

This prohibits a trace to spin forever due to an implausibly defined geometry. To avoid hitting this limit in normal operation, it is incumbent upon the user to make sure the number is large enough.

## Optical Errors

In most cases the user will want to use the selected sun shape and optical errors from element properties. It is often instructive to see the direct impact of the sun shape and/or optical errors on the power and flux distribution within geometry.

### **6.2.5 Modeling with Soltrace**

After an extensive overview of the software, now will be described the methodology used to validate the Mathcad® model.

To compare the two models it was necessary to define the same initial parameter, geometry, optical properties and so on.

As the sun was defined as it varies throughout the year in the Mathcad® model, in the Soltrace model was fundamental to indicate the global coordinates.

As it was previously carried on with the Mathcad® model was taken into account a day of the year exactly the 172<sup>th</sup> day, the summer solstice and the 355<sup>th</sup> day of the year, the winter solstice.

For each component were taken into account the different optical properties.

In particular was implemented a single stage with different component, in particular:

1. The mirror
2. The Absorber
3. The Inner envelope of the external tube
4. The outer envelope of the external tube

All of these components have an influence on each other, in particular a ray is reflected on the mirror to the external envelope, the external envelope diffract the light rays that exits trough the inner envelope to hits the absorber.

Every single component was modeled with the different specifics given by the manufacturer.

For the geometric characteristics of the parabolic trough it was taken in consideration the data in table 6.13, while for the HCE it was used the data provided by the Schott solar 2008 PTR 70.

Each receiver was 4.06 m long at 25°C, with absorber inner/outer diameters of 6.6 cm/7.0 cm and glass envelope inner/outer diameters of about 11.5cm/12.0 cm.

---

***Mechanical and geometrical characteristics***

---

<i>Parabolic aperture</i>	mm	5.900
<i>Focus of parabolic trough</i>	mm	1.810
<i>Transversal nr of panels</i>	-	4 / 2
<i>Longitudinal nr of panels</i>	-	10
<i>Panel dimension</i>	mm x mm	1.200x1.600/ 1.200x3.200
<i>Ray of curvature on the panel surface: min</i>	mm	3.620
<i>max</i>		7.771

---

**Table 6. 13 Mechanical and geometric characteristics**

A single module of parabolic trough with the length of 12.18 m and the aperture of 5.9 m was examined as it can be seen in figure 6.30.

Although the mirrors have a maximum thickness of 0.85 mm it wasn't taken into account in this simulation because it is assumed that they have no transmittance.

In the same way it is clear that also the inner HCE doesn't have any optical transmissivity.

The software is able to calculate the amount of energy flux that hits the absorber after all the others optical interactions.

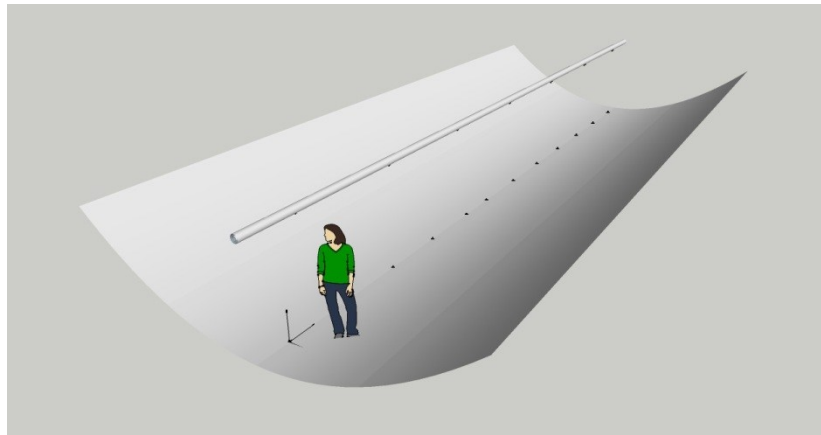


Figure 6. 30 Soltrace model implemented on Google Sketch Up

The heat collector element was, in order to evaluate all optical interaction implemented on Soltrace divided in to two parts each one of 2.03 m length see figure 6.31.

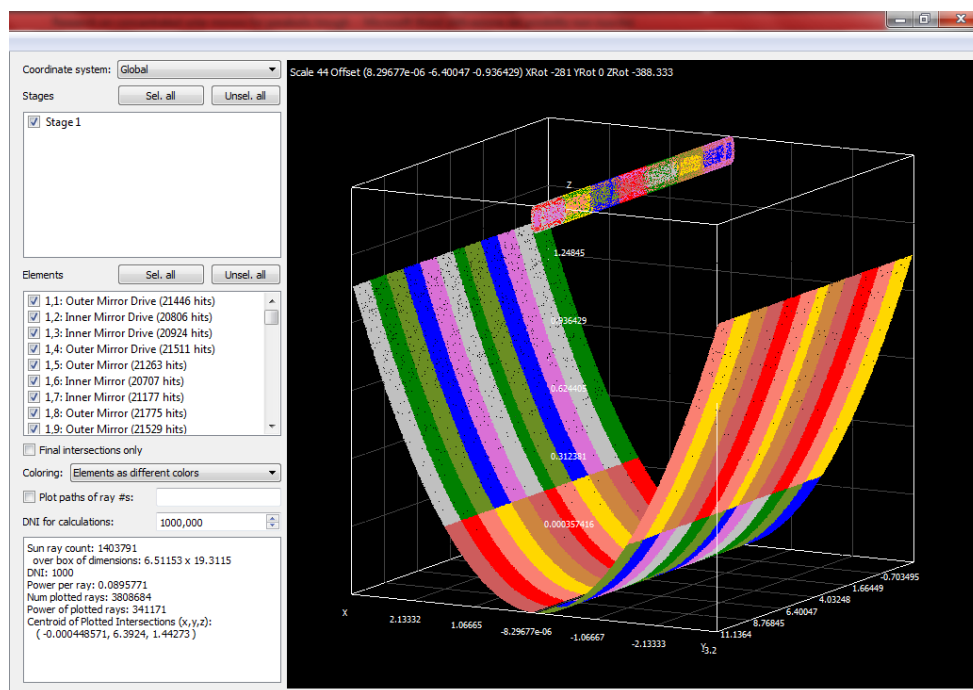


Figure 6. 31 Soltrace geometric simulation

As an optical characteristic of the reflecting mirrors the different values obtained with the Spectrophotometer were chosen every time (table 6.14).

Name	Solar Weighted Specular Reflectance
TG1	93.27%
TG2	91.96%
AL1	86.55%
AL2	93.02%
PF1	89.59%
PF2	88.30%

Table 6. 14 Solar weighted specular reflectance measured with the spectrophotometer

The code generates a number of user defined light rays that hit the entire component in front of the emitting source.

All the simulations were conducted with a number of 3.000.000 rays, this was dictated from the 8 processor and the RAM mounted on the station. Raising the number of rays would give a more accurate result but a very long time of processing.

The hitting rays are shown (the hitting rays from 1 to 100, because more would result in quite a homogeneous distribution along the image) in the next figures 6.32 and 6.33.

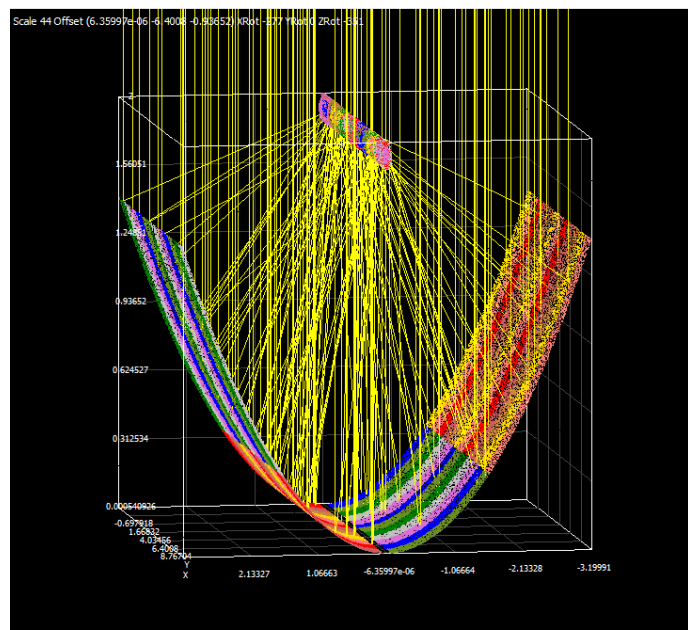
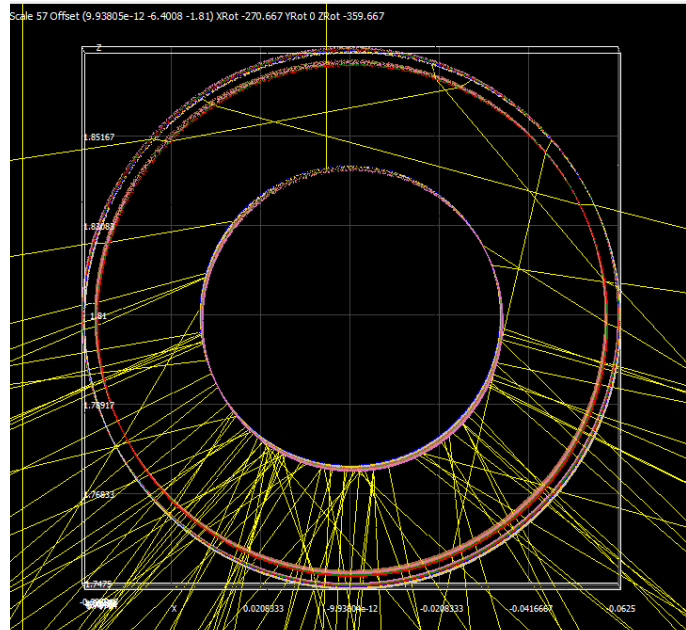


Figure 6. 32 100 sun rays hitting the parabolic surface



**Figure 6. 33 100 sun rays hitting the heat collector element**

In the last picture it's possible to see how not all the rays hits the inner absorber tube, due to the geometric and the optical imperfection of the reflecting mirror.

It is also taken into account the diffraction, due to the outer glass, that suffer from passing between two different media.

It is also possible to have data on the flux that arrives on the inner tube section per section.

To better understand what can be obtained there are some picture (fig 6.34 and 6.35) that show the graph obtained section per section.

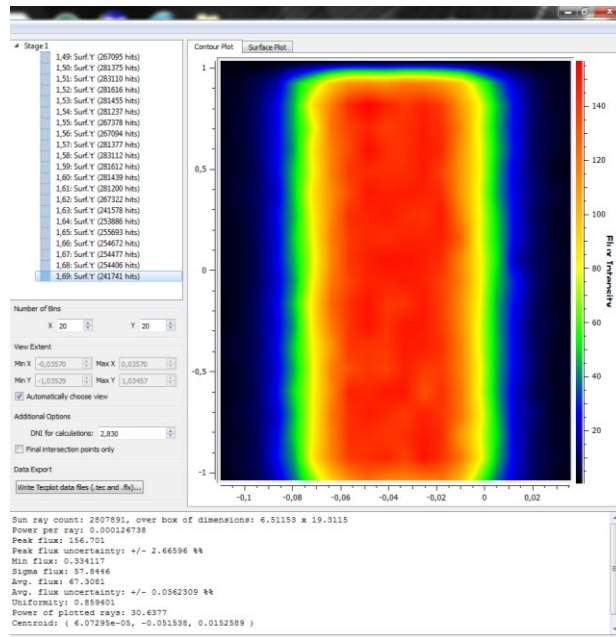


Figure 6. 34 Flux collected on the receiver 2D

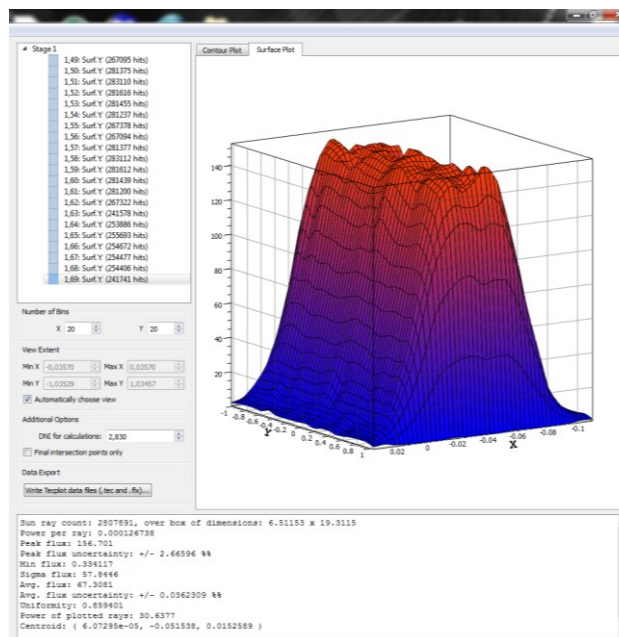


Figure 6. 35 Flux collected on the receiver 3D

These two images represent the initial section of the absorber tube.

The first 12 centimeter are not involved in the collection of the irradiance due to the tube geometry.

After we have a flux which is distributed uniformly along the linearization of the circumference of the inner tube, in fact the right and the left part of the graph corresponds to the upper part of the

absorber, which is not involved in the collection of the concentrated rays but only involved in the direct irradiance absorption.

The simulation has its limitation, it can't emulate the different value of the DNI during all the day but only a single hour.

To make possible a comparison between this model and the Mathcad model it was necessary to input the value of the DNI on the 172<sup>th</sup> day as done before in Mathcad.

In the followings the results for each type of mirror is tabulated and represented with a graph.

### 6.2.6 Thin glass mirrors

With Soltrace there are a lot of information at our disposal in particular:

- Peak flux [ $\text{W}/\text{m}^2$ ];
- Uncertainty of peak flux;
- Min flux [ $\text{W}/\text{m}^2$ ];
- $\sigma$  flux [ $\text{W}/\text{m}^2$ ];
- Avg. Flux [ $\text{W}/\text{m}^2$ ];
- Avg. Flux uncertainty

Manipulating the data obtained it was possible to write the following table 6.15 for TG1 mirror.

Peak flux	Uncertainty	Min flux	$\sigma$ flux	Avg. Flux	Avg. Flux uncertainty	Section: from-to (m)
<b>DNI 2.83</b>						
157.441	0.00265747	0.222899	58.6396	68.1193	0.0362309	0.31
157.308	0.00265747	2.00534	58.2546	72.1077	0.0362309	2.34
154.56	0.00265747	1.8568	58.2104	71.8668	0.0362309	4.37
157.606	0.00265747	1.48545	58.0077	71.8174	0.0362309	6.4
156.863	0.00265747	1.48544	58.0837	71.7743	0.0362309	8.43
155.155	0.00265747	2.1539	58.0967	71.9019	0.0362309	10.46
155.985	0.00265747	0.297114	58.4901	68.1116	0.0362309	12.49
<b>DNI 75.104</b>				<b>70.81414</b>		
4178.25	0.00265747	5.91541	1556.21	1807.78	0.0362309	0.31
4174.72	0.00265747	53.2189	1545.99	1913.63	0.0362309	2.34
4101.79	0.00265747	49.2767	1544.82	1907.24	0.0362309	4.37
4182.62	0.00265747	39.4215	1539.44	1905.93	0.0362309	6.4
4162.9	0.00265747	39.4214	1542.46	1904.78	0.0362309	8.43
4117.59	0.00265747	57.1614	1541.8	1908.17	0.0362309	10.46
4139.6	0.00265747	7.88496	1552.24	1807.58	0.0362309	12.49

DNI 202.64					1879.301	
11273.5	0.00265747	15.9605	4198.84	4877.63	0.0362309	0.31
11263.9	0.00265747	143.591	4171.28	5163.22	0.0362309	2.34
11067.1	0.00265747	132.955	4168.11	5145.96	0.0362309	4.37
11285.2	0.00265747	106.364	4153.6	5142.43	0.0362309	6.4
11232	0.00265747	106.364	4159.04	5139.34	0.0362309	8.43
11109.8	0.00265747	154.229	4159.97	5148.48	0.0362309	10.46
11169.2	0.00265747	21.2746	4188.14	4877.08	0.0362309	12.49
DNI 361.35					5070.591	
20103	0.00265747	28.461	7487.42	8697.85	0.0362309	0.31
20086	0.00265747	256.053	7438.27	9207.11	0.0362309	2.34
19735	0.00265747	237.086	7432.63	9176.34	0.0362309	4.37
20124	0.00265747	189.67	7406.75	9170.04	0.0362309	6.4
20029.1	0.00265747	189.669	7416.45	9164.53	0.0362309	8.43
19811.1	0.00265747	275.022	7418.1	9180.83	0.0362309	10.46
19917	0.00265747	37.9371	7468	8696.87	0.0362309	12.49
DNI 531.4					9041.939	
29563.3	0.00265747	41.8546	11011	12791	0.0362309	0.31
29538.3	0.00265747	376.551	10938.7	13539.9	0.0362309	2.34
29022.3	0.00265747	348.658	10930.4	13494.7	0.0362309	4.37
29594.2	0.00265747	278.928	10892.3	13485.4	0.0362309	6.4
29454.7	0.00265747	278.927	10906.6	13477.3	0.0362309	8.43
29134.1	0.00265747	404.446	10909	13501.3	0.0362309	10.46
29289.8	0.00265747	55.7902	10982.9	12789.6	0.0362309	12.49
DNI 690.11					13297.03	
38392.8	0.00265747	54.3551	14299.6	16611.2	0.0362309	0.31
38360.4	0.00265747	489.013	14205.7	17583.8	0.0362309	2.34
37690.2	0.00265747	452.789	14194.9	17525.1	0.0362309	4.37
38433	0.00265747	362.234	14145.5	17513	0.0362309	6.4
38251.7	0.00265747	362.232	14164	17502.5	0.0362309	8.43
37835.4	0.00265747	525.24	14167.2	17533.6	0.0362309	10.46
38037.7	0.00265747	72.4527	14263.1	16609.4	0.0362309	12.49
DNI 813.39					17268.37	
45251.2	0.00265747	64.065	16854	19578.6	0.0362309	0.31
45213	0.00265747	576.37	16743.4	20725	0.0362309	2.34
44423.1	0.00265747	533.675	16730.7	20655.7	0.0362309	4.37
45298.6	0.00265747	426.942	16672.4	20641.5	0.0362309	6.4
45085	0.00265747	426.941	16694.2	20629.1	0.0362309	8.43
44594.2	0.00265747	619.068	16698	20665.8	0.0362309	10.46
44832.6	0.00265747	85.3955	16811.1	19576.4	0.0362309	12.49
DNI 880					20353.16	
48957	0.00265747	69.2114	18234.2	21182	0.0362309	0.31
48915.6	0.00265747	623.57	18114.5	22422.2	0.0362309	2.34
48061	0.00265747	577.378	18100.8	22347.3	0.0362309	4.37
49008.2	0.00265747	461.905	18037.7	22331.9	0.0362309	6.4

48777	0.00265747	461.904	18061.4	22318.5	0.0362309	8.43
48246.1	0.00265747	669.765	18065.4	22358.2	0.0362309	10.46
48504.1	0.00265747	92.3887	18187.7	21179.6	0.0362309	12.49
DNI 880				22019.96		
48957	0.00265747	69.2114	18234.2	21182	0.0362309	0.31
48915.6	0.00265747	623.57	18114.5	22422.2	0.0362309	2.34
48061	0.00265747	577.378	18100.8	22347.3	0.0362309	4.37
49008.2	0.00265747	461.905	18037.7	22331.9	0.0362309	6.4
48777	0.00265747	461.904	18061.4	22318.5	0.0362309	8.43
48246.1	0.00265747	669.765	18065.4	22358.2	0.0362309	10.46
48504.1	0.00265747	92.3887	18187.7	21179.6	0.0362309	12.49
DNI 813.39				22019.96		
45251.2	0.00265747	64.065	16854	19578.6	0.0362309	0.31
45213	0.00265747	576.37	16743.4	20725	0.0362309	2.34
44423.1	0.00265747	533.675	16730.7	20655.7	0.0362309	4.37
45298.6	0.00265747	426.942	16672.4	20641.5	0.0362309	6.4
45085	0.00265747	426.941	16694.2	20629.1	0.0362309	8.43
44594.2	0.00265747	619.068	16698	20665.8	0.0362309	10.46
44832.6	0.00265747	85.3955	16811.1	19576.4	0.0362309	12.49
DNI 691.52				20353.16		
38471.3	0.00265747	54.4662	14328.8	16645.2	0.0362309	0.31
38438.8	0.00265747	490.013	14234.7	17619.8	0.0362309	2.34
37767.2	0.00265747	453.715	14223.9	17560.9	0.0362309	4.37
38511.5	0.00265747	362.974	14174.4	17548.8	0.0362309	6.4
38329.9	0.00265747	362.972	14192.9	17538.3	0.0362309	8.43
37912.7	0.00265747	526.313	14196.1	17569.5	0.0362309	10.46
38115.4	0.00265747	72.6007	14292.3	16643.3	0.0362309	12.49
DNI 532.81				17303.69		
29641.8	0.00265747	41.9657	11040.2	12825	0.0362309	0.31
29616.7	0.00265747	377.55	10967.7	13575.9	0.0362309	2.34
29099.3	0.00265747	349.583	10959.4	13530.5	0.0362309	4.37
29672.8	0.00265747	279.668	10921.2	13521.2	0.0362309	6.4
29532.8	0.00265747	279.667	10935.5	13513.1	0.0362309	8.43
29211.4	0.00265747	405.52	10938	13537.1	0.0362309	10.46
29367.6	0.00265747	55.9382	11012.2	12823.5	0.0362309	12.49
DNI 362.769				13332.33		
20181.9	0.00265747	28.5728	7516.82	8732	0.0362309	0.31
20164.8	0.00265747	257.059	7467.48	9243.27	0.0362309	2.34
19812.5	0.00265747	238.017	7461.82	9212.38	0.0362309	4.37
20203	0.00265747	190.415	7435.83	9206.05	0.0362309	6.4
20107.7	0.00265747	190.414	7445.57	9200.52	0.0362309	8.43
19888.9	0.00265747	276.102	7447.24	9216.88	0.0362309	10.46
19995.2	0.00265747	38.0861	7497.67	8731.02	0.0362309	12.49
DNI 244.05				9077.446		
13577.2	0.00265747	19.2221	5056.88	5874.39	0.0362309	0.31

13565.7	0.00265747	172.934	5023.69	6218.33	0.0362309	2.34
13328.7	0.00265747	160.124	5019.88	6197.56	0.0362309	4.37
13591.4	0.00265747	128.1	5002.4	6193.3	0.0362309	6.4
13527.3	0.00265747	128.1	5008.95	6189.58	0.0362309	8.43
13380.1	0.00265747	185.745	5010.07	6200.58	0.0362309	10.46
13451.6	0.00265747	25.6221	5044	5873.73	0.0362309	12.49
DNI 76.52				6106.781		
4257.03	0.00265747	6.02694	1585.55	1841.87	0.0362309	0.31
4253.43	0.00265747	54.2222	1575.14	1949.71	0.0362309	2.34
4179.12	0.00265747	50.2057	1573.94	1943.2	0.0362309	4.37
4261.48	0.00265747	40.1648	1568.46	1941.86	0.0362309	6.4
4241.39	0.00265747	40.1646	1570.52	1940.7	0.0362309	8.43
4195.22	0.00265747	58.2391	1570.87	1944.15	0.0362309	10.46
4217.65	0.00265747	8.03362	1581.51	1841.66	0.0362309	12.49
DNI 2.83				1914.736		
157.441	0.00265747	0.222899	58.6396	68.1193	0.0362309	0.31
157.308	0.00265747	2.00534	58.2546	72.1077	0.0362309	2.34
154.56	0.00265747	1.8568	58.2104	71.8668	0.0362309	4.37
157.606	0.00265747	1.48545	58.0077	71.8174	0.0362309	6.4
156.863	0.00265747	1.48544	58.0837	71.7743	0.0362309	8.43
155.155	0.00265747	2.1539	58.0967	71.9019	0.0362309	10.46
155.985	0.00265747	0.297114	58.4901	68.1116	0.0362309	12.49
70.81414						

Table 6. 15 Values obtained after the Ray tracing simulation Run for the TG1 mirror

We took into consideration the average value of the averages for each DNI value.

Thus, we obtained the following graph (fig 6.36).

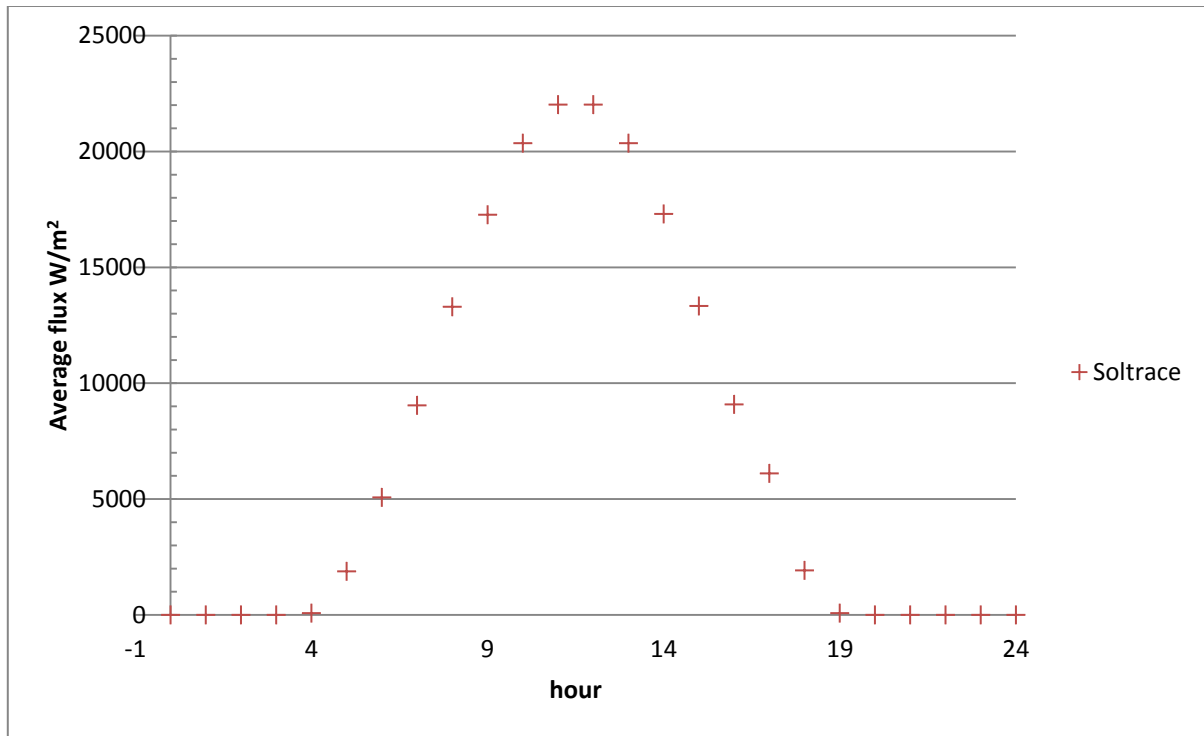


Figure 6. 36 Average flux collected on the 172th day for the TG1 mirror

For the TG2 we obtained the following results summarized in the following table 6.16.

Peak flux	Uncertainty	Min flux	$\sigma$ flux	Avg. Flux	Avg. Flux uncertainty	Section: from-to (m)
<b>DNI 2.83</b>						
155.635	2.16625	0.297298	58.2254	67.6672	0.0294663	0.31
153.875	2.16625	1.8575	57.6241	71.4267	0.0294663	2.34
153.133	2.16625	1.9318	57.56	71.3041	0.0294663	4.37
158.036	2.16625	2.0804	57.6239	71.2889	0.0294663	6.4
156.029	2.16625	1.63459	57.513	71.2197	0.0294663	8.43
159.002	2.16625	2.0804	57.8417	71.4152	0.0294663	10.46
157.146	2.16625	0.148602	58.3216	67.8879	0.0294663	12.49
<b>DNI 75.104</b>				<b>70.31567</b>		
4130.33	2.16625	7.88984	1545.21	1795.79	0.0234663	0.31
4083.63	2.16625	49.2953	1529.26	1895.56	0.0234663	2.34
4063.91	2.16625	51.2672	1527.56	1892.21	0.0234663	4.37
4194.04	2.16625	55.2106	1529.25	1891.9	0.0234663	6.4
4140.79	2.16625	43.3797	1526.31	1890.06	0.0234663	8.43
4219.68	2.16625	55.2108	1535.03	1895.25	0.0234663	10.46
4170.43	2.16625	3.94367	1547.77	1801.65	0.0234663	12.49
<b>DNI 202.64</b>				<b>1866.06</b>		
11144.2	2.16625	21.2878	4169.18	4845.26	0.0234663	0.31
11018.1	2.16625	133.0005	4126.13	5114.45	0.0234663	2.34
10964.9	2.16625	138.325	4121.54	5105.68	0.0234663	4.37
11316	2.16625	148.965	4126.11	5104.59	0.0234663	6.4

11172.4	2.16625	117.044	4118.18	5099.63	0.0234663	8.43
11385.2	2.16625	148.966	4141.71	5113.63	0.0234663	10.46
11252.3	2.16625	10.6405	4176.08	4861.06	0.0234663	12.49
DNI 361.35				5034.9		
19872.4	2.16625	37.9606	7434.54	8640.12	0.0234663	0.31
19647.7	2.16625	237.176	7357.76	9120.15	0.0234663	2.34
19552.8	2.16625	246.663	7349.57	9104.51	0.0234663	4.37
20178.9	2.16625	265.637	7357.73	9102.56	0.0234663	6.4
19922.7	2.16625	208.714	7343.58	9093.72	0.0234663	8.43
20302.3	2.16625	265.637	7385.55	9118.68	0.0234663	10.46
20065.3	2.16625	18.9743	7446.83	8668.31	0.0234663	12.49
DNI 531.4				8978.293		
29224.3	2.16625	55.8248	10933.2	12706.1	0.0234663	0.31
28893.8	2.16625	348.79	10820.3	13412.1	0.0234663	2.34
28754.3	2.16625	362.742	10808.3	13389.1	0.0234663	4.37
29675	2.16625	390.644	10820.3	13386.2	0.0234663	6.4
29298.3	2.16625	306.934	10799.4	13373.2	0.0234663	8.43
29856.4	2.16625	390.645	10861.2	13409.9	0.0234663	10.46
29508	2.16625	27.9035	10951.3	12747.6	0.0234663	12.49
DNI 690.11				13203.46		
37952.5	2.16625	72.4976	14198.6	16501	0.0234663	0.31
37523.3	2.16625	452.961	14051.9	17417.8	0.0234663	2.34
37342.1	2.16625	471.08	14036.3	17387.9	0.0234663	4.37
38537.9	2.16625	507.315	14051.9	17384.2	0.0234663	6.4
38048.6	2.16625	398.604	14024.8	17367.3	0.0234663	8.43
38773.5	2.16625	507.317	14105	17415	0.0234663	10.46
38320.9	2.16625	36.2673	14222	16554	0.0234663	12.49
DNI 813.39				17146.74		
44732.3	2.16625	85.4484	16735	19448.7	0.0234663	0.31
44226.4	2.16625	533.877	16562.1	20529.2	0.0234663	2.34
44012.9	2.16625	555.233	16543.7	20494	0.0234663	4.37
45422.2	2.16625	597.941	16562.1	20489.6	0.0234663	6.4
44845.5	2.16625	469.81	16530.2	20469.7	0.0234663	8.43
45699.9	2.16625	597.943	16624.7	20525.9	0.0234663	10.46
45166.5	2.16625	42.7106	16762.6	19512.1	0.0234663	12.49
DNI 880				20209.89		
48395.5	2.16625	92.446	18105.4	21041.4	0.0234663	0.31
47848.2	2.16625	577.598	17918.4	22210.4	0.0234663	2.34
47617.2	2.16625	600.702	17898.5	22172.3	0.0234663	4.37
49141.9	2.16625	646.908	17918.4	22167.6	0.0234663	6.4
48518	2.16625	508.284	17883.9	22146	0.0234663	8.43
49442.4	2.16625	646.909	17986.1	22206.8	0.0234663	10.46
48865.3	2.16625	46.2083	18135.3	21110	0.0234663	12.49
DNI 880				21864.93		
48395.5	2.16625	92.446	18105.4	21041.4	0.0234663	0.31

47848.2	2.16625	577.598	17918.4	22210.4	0.0234663	2.34
47617.2	2.16625	600.702	17898.5	22172.3	0.0234663	4.37
49141.9	2.16625	646.908	17918.4	22167.6	0.0234663	6.4
48518	2.16625	508.284	17883.9	22146	0.0234663	8.43
49442.4	2.16625	646.909	17986.1	22206.8	0.0234663	10.46
48865.3	2.16625	46.2083	18135.3	21110	0.0234663	12.49

DNI 813.39 21864.93

44732.3	2.16625	85.4484	16735	19448.7	0.0234663	0.31
44226.4	2.16625	533.877	16562.1	20529.2	0.0234663	2.34
44012.9	2.16625	555.233	16543.7	20494	0.0234663	4.37
45422.2	2.16625	597.941	16562.1	20489.6	0.0234663	6.4
44845.5	2.16625	469.81	16530.2	20469.7	0.0234663	8.43
45699.9	2.16625	597.943	16624.7	20525.9	0.0234663	10.46
45166.5	2.16625	42.7106	16762.6	19512.1	0.0234663	12.49

DNI 691.52 20209.89

38030	2.16625	72.6457	14227.6	16534.7	0.0234663	0.31
37600	2.16625	453.887	14080.6	17453.4	0.0234663	2.34
37418.4	2.16625	472.042	14065	17423.4	0.0234663	4.37
38616.6	2.16625	508.352	14080.6	17419.7	0.0234663	6.4
38126.3	2.16625	399.419	14053.5	17402.8	0.0234663	8.43
38852.7	2.16625	508.353	14133.8	17450.5	0.0234663	10.46
38399.2	2.16625	36.3113	14251.1	16588.6	0.0234663	12.49

DNI 532.81 17181.87

29301.8	2.16625	55.9729	10962.2	12739.8	0.0234663	0.31
28970.5	2.16625	349.716	10849	13447.7	0.0234663	2.34
28830.6	2.16625	363.705	10836.9	13424.6	0.0234663	4.37
29753.7	2.16625	391.681	10849	13421.7	0.0234663	6.4
29376	2.16625	307.749	10828.1	13408.7	0.0234663	8.43
29935.7	2.16625	391.682	10890	13445.5	0.0234663	10.46
29586.3	2.16625	27.9776	10980.3	12781.4	0.0234663	12.49

DNI 362.769 13238.49

19950.4	2.16625	38.1097	7463.73	8674.05	0.0234663	0.31
19724.8	2.16625	238.107	7386.65	9155.97	0.0234663	2.34
19629.6	2.16625	247.632	7378.43	9140.26	0.0234663	4.37
20258.1	2.16625	266.68	7386.62	9138.3	0.0234663	6.4
20000.9	2.16625	209.534	7372.42	9129.43	0.0234663	8.43
20382	2.16625	266.68	7414.55	9154.49	0.0234663	10.46
20144.1	2.16625	19.0488	7476.07	8702.35	0.0234663	12.49

DNI 244.05 9013.55

13421.5	2.16625	25.638	5021.17	5835.4	0.0234663	0.31
13269.7	2.16625	160.185	4969.31	6159.61	0.0234663	2.34
13205.7	2.16625	166.592	4963.78	6149.04	0.0234663	4.37
13628.5	2.16625	179.407	4969.29	6147.72	0.0234663	6.4
13455.5	2.16625	140.962	4959.74	6141.75	0.0234663	8.43
13711.8	2.16625	179.407	4988.08	6158.61	0.0234663	10.46

13551.8	2.16625	12.8149	5029.47	5854.44	0.0234663	12.49
DNI 76.52				6063.796		
4208.21	2.16625	8.0386	1574.35	1829.65	0.0234663	0.31
4160.62	2.16625	50.2247	1558.09	1931.3	0.0234663	2.34
4140.53	2.16625	52.2338	1556.36	1927.98	0.0234663	4.37
4273.11	2.16625	56.2516	1558.08	1927.57	0.0234663	6.4
4218.86	2.16625	44.1976	1555.09	1925.7	0.0234663	8.43
4299.24	2.16625	56.2517	1563.98	1930.99	0.0234663	10.46
4249.06	2.16625	4.01802	1576.95	1835.61	0.0234663	12.49
DNI 2.83				1901.257		
155.635	2.16625	0.297298	58.2254	67.6672	0.0294663	0.31
153.875	2.16625	1.8575	57.6241	71.4267	0.0294663	2.34
153.133	2.16625	1.9318	57.56	71.3041	0.0294663	4.37
158.036	2.16625	2.0804	57.6239	71.2889	0.0294663	6.4
156.029	2.16625	1.63459	57.513	71.2197	0.0294663	8.43
159.002	2.16625	2.0804	57.8417	71.4152	0.0294663	10.46
157.146	2.16625	0.148602	58.3216	67.8879	0.0294663	12.49
70.31567						

Table 6. 16 Values obtained after the Ray tracing simulation Run for the TG1 mirror

Thus, we obtained the following graph (fig 6.37).

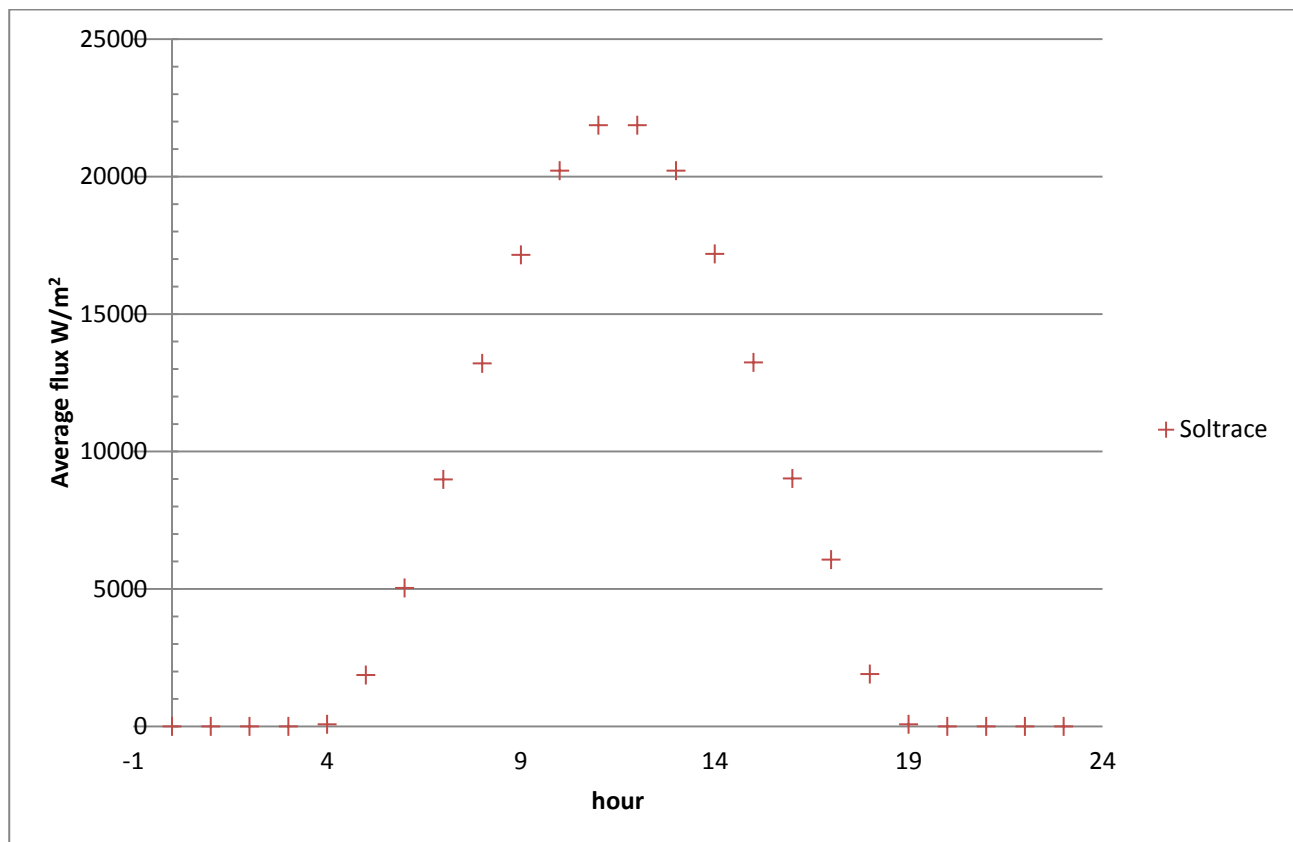


Figure 6. 37 Average flux collected on the 172th day for the TG2 mirror

With a comparison between the two thin glass mirrors in the next graph.

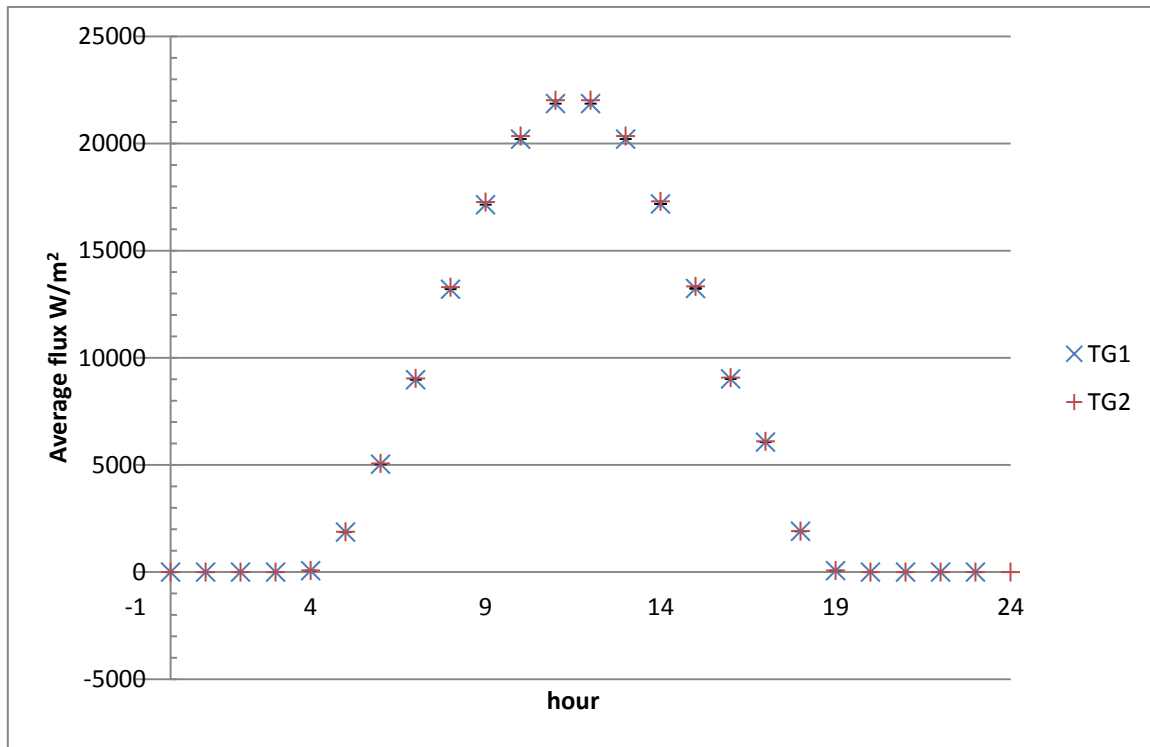


Figure 6. 38 Comparison between the flux collected from TG1 and TG2 mirrors

### 6.2.7 Aluminum mirrors

We conducted the same modeling on the aluminum mirrors and we obtained the following results (table 6.17).

Peak flux	Uncertainty	Min flux	$\sigma$ flux	Avg. Flux	Avg. Flux uncertainty	Section: from-to (m)
<b>DNI 2.83</b>						
146.024	2.5532	0.222823	55.2317	64.2401	0.0300984	0.31
149.27	2.5532	1.55954	54.4846	67.5237	0.0300984	2.34
148.379	2.5532	1.93086	54.4391	67.5246	0.0300984	4.37
148.453	2.5532	2.07938	54.5102	67.6041	0.0300984	6.4
146.078	2.5532	2.00513	54.5959	67.7377	0.0300984	8.43
146.82	2.5532	1.93086	54.6221	67.5944	0.0300984	10.46
149.58	2.5532	0.445842	55.2071	64.1677	0.0300984	12.49
<b>DNI 75.104</b>				<b>66.62747</b>		
3875.25	2.5532	5.9134	1465.77	1704.84	0.0300984	0.31
3961.4	2.5532	41.878	1445.94	1791.98	0.0300984	2.34
3937.76	2.5532	51.2421	1444.73	1792	0.0300984	4.37
3939.73	2.5532	55.1837	1446.62	1794.11	0.0300984	6.4
3876.68	2.5532	53.2133	1448.89	1797.66	0.0300984	8.43
3896.38	2.5532	51.2422	1449.59	1793.86	0.0300984	10.46

3969.64	2.5532	11.832	1465.11	1702.92	0.0300984	12.49
DNI 202.64				1768.196		
10455.9	2.5532	15.9551	3954.82	4599.87	0.0300984	0.31
10680.4	2.5532	111.669	3901.33	4834.98	0.0300984	2.34
10624.6	2.5532	138.257	3898.07	4835.05	0.0300984	4.37
10629.9	2.5532	148.893	3903.16	4840.74	0.0300984	6.4
10459.8	2.5532	143.576	3909.3	4850.3	0.0300984	8.43
10512.9	2.5532	138.258	3911.18	4840.05	0.0300984	10.46
10710.6	2.5532	31.9242	3953.06	4594.68	0.0300984	12.49
DNI 361.35				4770.81		
18645.1	2.5532	28.4513	7052.29	8202.53	0.0300984	0.31
19059.6	2.5532	199.13	6956.9	8621.8	0.0300984	2.34
18945.8	2.5532	246.542	6951.09	8621.92	0.0300984	4.37
18955.3	2.5532	265.507	6960.17	8632.06	0.0300984	6.4
18652	2.5532	266.026	6971.11	8649.12	0.0300984	8.43
18746.8	2.5532	246.543	6974.46	8630.83	0.0300984	10.46
19059.2	2.5532	56.9276	7049.15	8193.28	0.0300984	12.49
DNI 531.4				8507.363		
27419.4	2.5532	41.8404	10371.1	12062.6	0.0300984	0.31
28029	2.5532	292.84	10230.8	12679.2	0.0300984	2.34
27861.7	2.5532	362.564	10222.2	12679.4	0.0300984	4.37
27875.6	2.5532	390.454	10235.6	12694.3	0.0300984	6.4
27429.6	2.5532	376.512	10251.7	12719.4	0.0300984	8.43
27568.9	2.5532	362.565	10256.6	12692.5	0.0300984	10.46
28087.2	2.5532	83.7176	10366.4	12049	0.0300984	12.49
DNI 690.11				12510.91		
35608.6	2.5532	54.3366	13.468.5	15665.3	0.0300984	0.31
36400.3	2.5532	380.301	13286.4	16466	0.0300984	2.34
36182.9	2.5532	470.849	13275.3	16466.2	0.0300984	4.37
36201.1	2.5532	507.068	13292.6	16485.6	0.0300984	6.4
35621.8	2.5532	488.962	13313.5	16518.2	0.0300984	8.43
35802.7	2.5532	470.85	13319.9	16483.3	0.0300984	10.46
36475.9	2.5532	108.721	13462.5	15647.6	0.0300984	12.49
DNI 813.39				16247.46		
41969.6	2.5532	64.0432	15874.5	18463.7	0.0300984	0.31
42902.7	2.5532	448.238	15659.8	19407.5	0.0300984	2.34
42646.6	2.5532	554.961	15646.7	19407.7	0.0300984	4.37
42667.9	2.5532	597.65	15667.2	19430.6	0.0300984	6.4
41985.2	2.5532	576.309	15091.8	19469	0.0300984	8.43
42198.5	2.5532	554.962	15699.3	19427.8	0.0300984	10.46
42991.9	2.5532	128.143	15867.5	18442.9	0.0300984	12.49
DNI 880				19149.89		
45406.6	2.5532	69.2878	17174.5	19975.7	0.0300984	0.31
46416.1	2.5532	484.944	16942.2	20966.8	0.0300984	2.34
46139	2.5532	600.408	16928.1	20997.1	0.0300984	4.37

46162.1	2.5532	646.593	16950.2	21021.8	0.0300984	6.4
45423.4	2.5532	623.504	16976.8	21063.3	0.0300984	8.43
45654.2	2.5532	600.409	16985	21018.8	0.0300984	10.46
46512.6	2.5532	138.637	17166.9	19953.2	0.0300984	12.49

DNI 880 20713.81

45406.6	2.5532	69.2878	17174.5	19975.7	0.0300984	0.31
46416.1	2.5532	484.944	16942.2	20966.8	0.0300984	2.34
46139	2.5532	600.408	16928.1	20997.1	0.0300984	4.37
46162.1	2.5532	646.593	16950.2	21021.8	0.0300984	6.4
45423.4	2.5532	623.504	16976.8	21063.3	0.0300984	8.43
45654.2	2.5532	600.409	16985	21018.8	0.0300984	10.46
46512.6	2.5532	138.637	17166.9	19953.2	0.0300984	12.49

DNI 813.39 20713.81

41969.6	2.5532	64.0432	15874.5	18463.7	0.0300984	0.31
42902.7	2.5532	448.238	15659.8	19407.5	0.0300984	2.34
42646.6	2.5532	554.961	15646.7	19407.7	0.0300984	4.37
42667.9	2.5532	597.65	15667.2	19430.6	0.0300984	6.4
41985.2	2.5532	576.309	15091.8	19469	0.0300984	8.43
42198.5	2.5532	554.962	15699.3	19427.8	0.0300984	10.46
42991.9	2.5532	128.143	15867.5	18442.9	0.0300984	12.49

DNI 691.52 19149.89

35681.3	2.5532	54.4476	13496	15697.3	0.0300984	0.31
36474.6	2.5532	381.078	13313.5	16499.9	0.0300984	2.34
36256.9	2.5532	471.811	13302.4	16499.9	0.0300984	4.37
36275	2.5532	508.104	13319.8	16519.3	0.0300984	6.4
35694.6	2.5532	489.961	13340.7	16551.9	0.0300984	8.43
35875.9	2.5532	471.812	13347.1	16516.9	0.0300984	10.46
36550.4	2.5532	108.943	13490	15679.6	0.0300984	12.49

DNI 532.81 16280.69

532.81	2.5532	41.9514	10398.6	12094.6	0.0300984	0.31
28103.4	2.5532	293.617	10257.9	12712.8	0.0300984	2.34
27935.6	2.5532	363.526	10249.4	12713	0.0300984	4.37
27949.6	2.5532	391.49	10262.8	12728	0.0300984	6.4
27502.3	2.5532	377.511	10278.9	12753.1	0.0300984	8.43
27642.1	2.5532	363.527	10283.8	12726.1	0.0300984	10.46
28161.8	2.5532	83.9397	10394	12081	0.0300984	12.49

DNI 362.769 12544.09

18718.3	2.5532	28.563	7079.98	8234.75	0.0300984	0.31
19134.5	2.5532	199.912	6984.22	8655.66	0.0300984	2.34
19020.2	2.5532	247.511	6978.38	8655.79	0.0300984	4.37
19029.7	2.5532	266.55	6987.5	8665.96	0.0300984	6.4
18725.2	2.5532	257.032	6998.48	8683.08	0.0300984	8.43
18820.4	2.5532	247.511	7001.84	8664.72	0.0300984	10.46
19174.2	2.5532	57.1512	7076.83	8225.46	0.0300984	12.49

DNI 244.05 8540.774

12592.6	2.5532	19.2156	4763	5539.86	0.0300984	0.31
12872.6	2.5532	134.489	4698.58	5823.02	0.0300984	2.34
12795.7	2.5532	166.511	4700.78	5829.96	0.0300984	4.37
12802.1	2.5532	179.319	4700.78	5829.96	0.0300984	6.4
12597.3	2.5532	172.916	4708.17	5841.48	0.0300984	8.43
12661.3	2.5532	166.511	4710.44	5829.13	0.0300984	10.46
12899.3	2.5532	38.448	4760.88	5533.61	0.0300984	12.49
DNI 76.52				5746.717		
3986.94	2.5532	8.03819	1486.51	1732.37	0.0300984	0.31
3970.67	2.5532	46.2173	1475.38	1828.03	0.0300984	2.34
4040.99	2.5532	46.2172	1480.24	1832.97	0.0300984	4.37
3998.77	2.5532	44.2075	1474.26	1825.85	0.0300984	6.4
3912.41	2.5532	54.2553	1474.24	1830.16	0.0300984	8.43
3952.56	2.5532	54.2547	1480.64	1828.87	0.0300984	10.46
4027.15	2.5532	10.0478	1493.89	1739.83	0.0300984	12.49
DNI 2.83				1802.583		
146.024	2.5532	0.222823	55.2317	64.2401	0.0300984	0.31
149.27	2.5532	1.55954	54.4846	67.5237	0.0300984	2.34
148.379	2.5532	1.93086	54.4391	67.5246	0.0300984	4.37
148.453	2.5532	2.07938	54.5102	67.6041	0.0300984	6.4
146.078	2.5532	2.00513	54.5959	67.7377	0.0300984	8.43
146.82	2.5532	1.93086	54.6221	67.5944	0.0300984	10.46
149.58	2.5532	0.445842	55.2071	64.1677	0.0300984	12.49
				66.62747		

Table 6. 17 Values obtained after the Ray tracing simulation Run for the AL1 mirror

Taking always the mean of the average flux for each value of DNI it was possible to obtain the following graph (fig. 6.39).

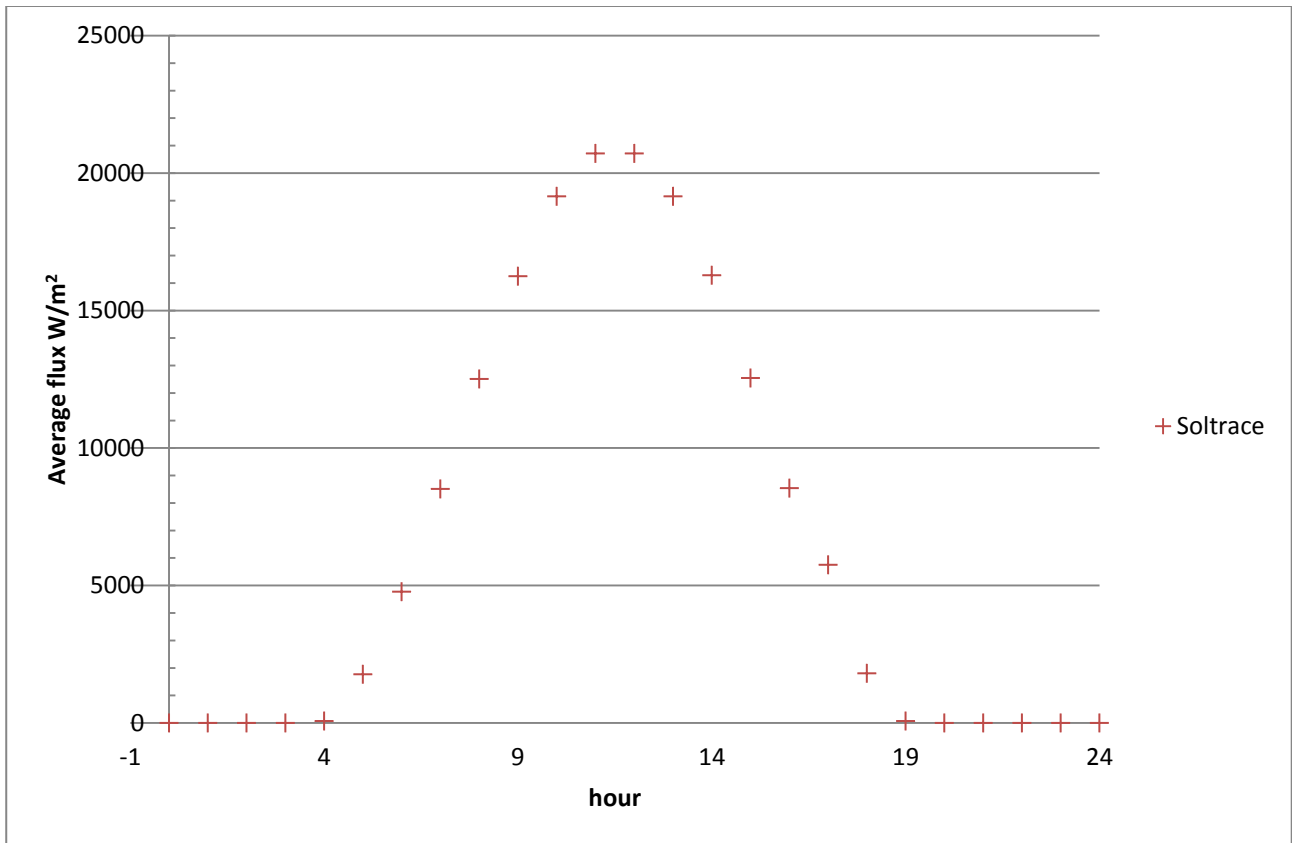


Figure 6.39 Average flux collected on the 172th day for the AL1 mirror

For the AL2 we obtained (table 6.18):

Peak flux	Uncertainty	Min flux	$\sigma$ flux	Avg. Flux	Avg. Flux uncertainty	Section: from-to (m)
<b>DNI 2.83</b>						
155.605	2.18062	0.371196	58.3825	67.9393	0.0300588	0.31
156.15	2.18062	1.78118	58.0666	71.7775	0.0300588	2.34
157.19	2.18062	1.92962	58.0021	71.6885	0.0300588	4.37
155.334	2.18062	1.8554	57.9197	71.7671	0.0300588	6.4
156.744	2.18062	1.63275	58.0977	71.8947	0.0300588	8.43
157.785	2.18062	2.22651	58.3828	71.9123	0.0300588	10.46
156.51	2.18062	0.371228	58.5587	68.1564	0.0300588	12.49
<b>DNI 75.104</b>				<b>70.73369</b>		
4129.54	2.18062	9.851	1549.39	1803.01	0.0300588	0.31
4143.99	2.18062	47.2699	1541	1904.87	0.0300588	2.34
4171.58	2.18062	51.2092	1539.29	1902.51	0.0300588	4.37
4122.33	2.18062	49.2394	1537.1	1904.59	0.0300588	6.4
4159.76	2.18062	43.3308	1541.83	1907.98	0.0300588	8.43
4187.39	2.18062	59.0882	1549.39	1908.45	0.0300588	10.46
4153.54	2.18062	9.85185	1554.06	1808.77	0.0300588	12.49
<b>DNI 202.64</b>				<b>1877.169</b>		
11142	2.18062	26.5792	4180.44	4864.74	0.0300588	0.31

11181	2.18062	127.54	4157.81	5139.57	0.0300588	2.34
11255.4	2.18062	138.169	4153.2	5133.2	0.0300588	4.37
11122.5	2.18062	132.854	4147.29	5138.83	0.0300588	6.4
11223.5	2.18062	116.912	4160.04	5147.96	0.0300588	8.43
11298.1	2.18062	159.427	4180.46	5149.23	0.0300588	10.46
11206.8	2.18062	26.5815	4193.05	4880.29	0.0300588	12.49
DNI 361.35				5064.831		
19868.6	2.18062	47.3964	7454.6	8674.86	0.0300588	0.31
19938.1	2.18062	227.431	7414.26	9164.94	0.0300588	2.34
20070.8	2.18062	246.384	7406.03	9153.58	0.0300588	4.37
19833.9	2.18062	236.907	7395.5	9163.61	0.0300588	6.4
20013.9	2.18062	208.479	7418.23	9179.91	0.0300588	8.43
20146.9	2.18062	284.293	7454.64	9182.16	0.0300588	10.46
19984	2.18062	47.4005	7477.1	8702.59	0.0300588	12.49
DNI 531.4				9031.664		
29218.6	2.18062	69.7009	10962.7	12757.2	0.0300588	0.31
29320.9	2.18062	334.459	10903.4	13477.9	0.0300588	2.34
29516.1	2.18062	362.332	10891.3	13461.2	0.0300588	4.37
29167.6	2.18062	348.395	10875.8	13476	0.0300588	6.4
29432.4	2.18062	306.588	10909.2	13499.9	0.0300588	8.43
29627.9	2.18062	418.08	10962.8	13503.3	0.0300588	10.46
29388.5	2.18062	69.707	10995.8	12798	0.0300588	12.49
DNI 690.11				13281.93		
37945.2	2.18062	90.5181	14236.9	16567.3	0.0300588	0.31
38078	2.18062	434.35	14159.8	17503.3	0.0300588	2.34
38331.5	2.18062	470.547	14144.1	17481.6	0.0300588	4.37
37878.9	2.18062	452.448	14124	17500.8	0.0300588	6.4
38222.8	2.18062	398.155	14167.4	17531.9	0.0300588	8.43
38476.7	2.18062	542.945	14237	17536.2	0.0300588	10.46
38165.7	2.18062	90.5259	14279.9	16620.3	0.0300588	12.49
DNI 813.39				17248.77		
44723.6	2.18062	106.688	16780.1	19526.9	0.0300588	0.31
44880.2	2.18062	511.941	16689.3	20630.1	0.0300588	2.34
45179	2.18062	554.605	16670.8	20604.5	0.0300588	4.37
44645.5	2.18062	533.272	16647.1	20627.1	0.0300588	6.4
45050.9	2.18062	469.28	16698.3	20663.7	0.0300588	8.43
45350.2	2.18062	639.936	16780.2	20668.8	0.0300588	10.46
44983.6	2.18062	106.697	16830.8	19589.3	0.0300588	12.49
DNI 880				20330.06		
48386.1	2.18062	115.425	18154.3	21126	0.0300588	0.31
48555.5	2.18062	553.865	18056	22319.5	0.0300588	2.34
48878.8	2.18062	600.023	18036	22291.8	0.0300588	4.37
48301.6	2.18062	576.943	18010.4	22316.3	0.0300588	6.4
48740.2	2.18062	507.711	18065.7	22355.9	0.0300588	8.43
49064	2.18062	692.342	18154.4	22361.4	0.0300588	10.46

48667.4	2.18062	115.435	18209.1	21193.5	0.0300588	12.49
DNI 880				21994.91		
48386.1	2.18062	115.425	18154.3	21126	0.0300588	0.31
48555.5	2.18062	553.865	18056	22319.5	0.0300588	2.34
48878.8	2.18062	600.023	18036	22291.8	0.0300588	4.37
48301.6	2.18062	576.943	18010.4	22316.3	0.0300588	6.4
48740.2	2.18062	507.711	18065.7	22355.9	0.0300588	8.43
49064	2.18062	692.342	18154.4	22361.4	0.0300588	10.46
48667.4	2.18062	115.435	18209.1	21193.5	0.0300588	12.49
DNI 813.39				21994.91		
44723.6	2.18062	106.688	16780.1	19526.9	0.0300588	0.31
44880.2	2.18062	511.941	16689.3	20630.1	0.0300588	2.34
45179	2.18062	554.605	16670.8	20604.5	0.0300588	4.37
44645.5	2.18062	533.272	16647.1	20627.1	0.0300588	6.4
45050.9	2.18062	469.28	16698.3	20663.7	0.0300588	8.43
45350.2	2.18062	639.936	16780.2	20668.8	0.0300588	10.46
44983.6	2.18062	106.697	16830.8	19589.3	0.0300588	12.49
DNI 691.52				20330.06		
38022.7	2.18062	90.703	14266	16601.2	0.0300588	0.31
38155.8	2.18062	435.237	14188.8	17539.1	0.0300588	2.34
38409.8	2.18062	471.509	14173	17517.3	0.0300588	4.37
37956.3	2.18062	453.372	14152.9	17536.5	0.0300588	6.4
38300.9	2.18062	398.968	14196.4	17567.7	0.0300588	8.43
38555.3	2.18062	544.055	14266	17572	0.0300588	10.46
38243.7	2.18062	90.7109	14309	16654.3	0.0300588	12.49
DNI 532.81				17284.01		
29296.2	2.18062	69.8859	10991.8	12791.1	0.0300588	0.31
29398.7	2.18062	335.346	10932.3	13513.7	0.0300588	2.34
29594.4	2.18062	363.293	10920.2	13496.9	0.0300588	4.37
29245	2.18062	349.319	10904.7	13511.7	0.0300588	6.4
29510.5	2.18062	307.401	10938.2	13535.8	0.0300588	8.43
29706.6	2.18062	419.189	10991.9	13539.1	0.0300588	10.46
29466.4	2.18062	69.8919	11025	12832	0.0300588	12.49
DNI 362.769				13317.19		
19946.6	2.18062	47.5825	7483.87	8708.93	0.0300588	0.31
20016.4	2.18062	228.324	7443.37	9200.93	0.0300588	2.34
20149.7	2.18062	247.352	7435.11	9189.53	0.0300588	4.37
19911.7	2.18062	237.837	7424.54	9199.6	0.0300588	6.4
20092.5	2.18062	209.297	7447.36	9215.96	0.0300588	8.43
20226	2.18062	285.409	7483.92	9218.22	0.0300588	10.46
20062.5	2.18062	47.5866	7506.47	8736.76	0.0300588	12.49
DNI 244.05				9067.133		
13418.9	2.18062	32.0108	5034.72	5858.86	0.0300588	0.31
13465.9	2.18062	153.603	5007.47	6189.86	0.0300588	2.34
13555.5	2.18062	166.404	5001.91	6182.18	0.0300588	4.37

13395.5	2.18062	160.003	4994.8	6188.96	0.0300588	6.4
13517.1	2.18062	140.803	5010.16	6199.96	0.0300588	8.43
13606.9	2.18062	192.007	5034.75	6201.49	0.0300588	10.46
13496.9	2.18062	32.0135	5049.92	5877.59	0.0300588	12.49
DNI 76.52				6099.843		
4207.4	2.18062	10.0367	1578.6	1837	0.0300588	0.31
4222.12	2.18062	48.1611	1570.05	1940.78	0.0300588	2.34
4250.23	2.18062	52.1747	1568.31	1938.38	0.0300588	4.37
4200.05	2.18062	50.1678	1566.08	1940.5	0.0300588	6.4
4238.18	2.18062	44.1477	1570.9	1943.95	0.0300588	8.43
4266.33	2.18062	60.2023	1578.61	1944.43	0.0300588	10.46
4231.85	2.18062	10.0376	1583.36	1842.87	0.0300588	12.49
DNI 2.83				1912.559		
155.605	2.18062	0.371196	58.3825	67.9393	0.0300588	0.31
156.15	2.18062	1.78118	58.0666	71.7775	0.0300588	2.34
157.19	2.18062	1.92962	58.0021	71.6885	0.0300588	4.37
155.334	2.18062	1.8554	57.9197	71.7671	0.0300588	6.4
156.744	2.18062	1.63275	58.0977	71.8947	0.0300588	8.43
157.785	2.18062	2.22651	58.3828	71.9123	0.0300588	10.46
156.51	2.18062	0.371228	58.5587	68.1564	0.0300588	12.49
				70.73369		

Table 6. 18 Values obtained after the Ray tracing simulation Run for the AL2 mirror

With the following graph fig 6.40.

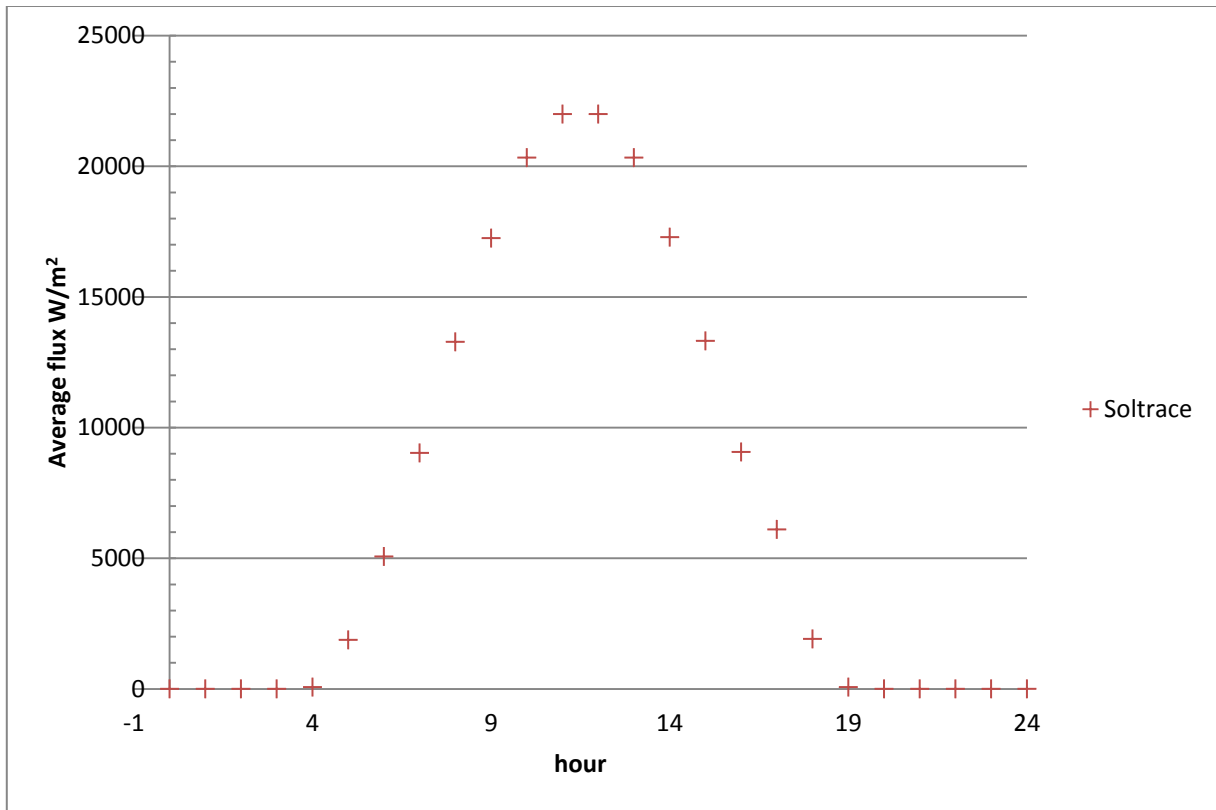


Figure 6. 40 Average flux collected on the 172th day for the AL2 mirror

Comparing the two mirrors we obtained fig. 6.41:

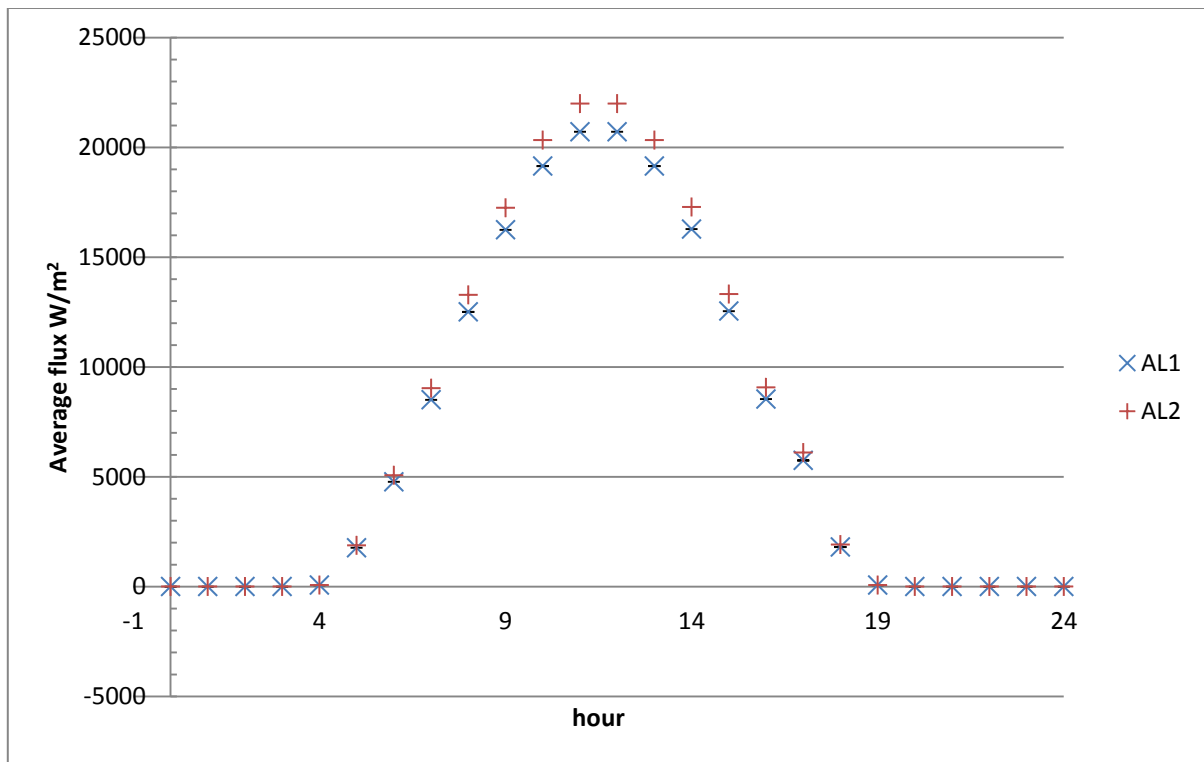


Figure 6.41 Comparison between the flux collected from AL1 and AL2 mirrors

### 6.2.8 Polymeric Film mirrors

Still in the same way we obtained table 6.19:

Peak flux	Uncertainty	Min flux	$\sigma$ flux	Avg. Flux	Avg. Flux uncertainty	Section: from-to (m)
DNI 2.83						
155.955	0.00265747	0.148599	58.0915	67.4443	0.0362309	0.31
154.425	0.00265747	1.78269	57.5096	71.0095	0.0362309	2.34
156.134	0.00265747	1.85697	57.2615	70.8671	0.0362309	4.37
153.534	0.00265747	1.93124	57.1823	70.8657	0.0362309	6.4
153.98	0.00265747	2.0798	57.2175	70.7459	0.0362309	8.43
153.162	0.00265747	2.15407	57.3086	70.9915	0.0362309	10.46
156.228	0.00265747	0.222864	57.844	67.4109	0.0362309	12.49
DNI 75.104				69.90499		
4186.15	0.00265747	2.95632	1534.94	1785.45	0.0362309	0.31
4127.58	0.00265747	50.2283	1516.38	1875.33	0.0362309	2.34
4192.59	0.00265747	44.3191	1526.39	1888.68	0.0362309	4.37
4092.17	0.00265747	41.3649	1520.74	1881.16	0.0362309	6.4
4263.48	0.00265747	41.3644	1520.84	1879.69	0.0362309	8.43
4124.68	0.00265747	47.2742	1516.33	1879.19	0.0362309	10.46
4158.6	0.00265747	8.86696	1535.11	1786.26	0.0362309	12.49
DNI 202.64				1853.68		
11294.7	0.00265747	7.97652	4141.45	4817.38	0.0362309	0.31

11136.7	0.00265747	135.522	4091.38	5059.88	0.0362309	2.34
11312.1	0.00265747	119.579	4118.38	5095.9	0.0362309	4.37
11041.2	0.00265747	11.608	4103.13	5075.6	0.0362309	6.4
11503.4	0.00265747	11.606	4103.41	5071.64	0.0362309	8.43
11128.9	0.00265747	127.552	4091.25	5070.3	0.0362309	10.46
11220.4	0.00265747	23.9242	4141.92	4819.54	0.0362309	12.49
<b>DNI 361.35</b>				<b>5001.463</b>		
20140.9	0.00265747	14.2238	7385.09	8590.4	0.0362309	0.31
19859.2	0.00265747	241.665	7295.8	9022.84	0.0362309	2.34
20171.9	0.00265747	213.234	7343.95	9087.07	0.0362309	4.37
19685.8	0.00265747	199.02	7316.76	9050.87	0.0362309	6.4
20513	0.00265747	199.017	7317.24	9043.82	0.0362309	8.43
19845.2	0.00265747	227.452	7295.57	9041.42	0.0362309	10.46
20008.4	0.00265747	42.6618	7385.92	8594.27	0.0362309	12.49
<b>DNI 531.4</b>				<b>8918.67</b>		
29596.9	0.00265747	20.918	10852.3	12623.5	0.0362309	0.31
29182.8	0.00265747	355.124	10721.1	13259	0.0362309	2.34
29642.4	0.00265747	313.345	10791.9	13353.3	0.0362309	4.37
28932.5	0.00265747	292.458	10751.9	13300.2	0.0362309	6.4
30143.7	0.00265747	292.454	10752.6	13289.3	0.0362309	8.43
29162.3	0.00265747	334.238	10720.8	13286.3	0.0362309	10.46
29402.1	0.00265747	62.6911	10853.5	12629.2	0.0362309	12.49
<b>DNI 690.11</b>				<b>13105.83</b>		
38390.3	0.00265747	27.1501	14100.6	16397.2	0.0362309	0.31
37901.6	0.00265747	461.552	13934	17232.6	0.0362309	2.34
38526	0.00265747	407.252	14025.8	17355.2	0.0362309	4.37
37630.1	0.00265747	380.102	13974	17285.9	0.0362309	6.4
39150.5	0.00265747	380.102	13975.1	17272.7	0.0362309	8.43
37874.4	0.00265747	434.402	13933.4	17267.9	0.0362309	10.46
38200.2	0.00265747	81.4504	14104.2	16408.3	0.0362309	12.49
<b>DNI 813.39</b>				<b>17031.4</b>		
45336.7	0.00265747	32.017	16625.6	19336.8	0.0362309	0.31
44702.5	0.00265747	543.982	16422.7	20310.2	0.0362309	2.34
45406.5	0.00265747	479.984	16531	20454.8	0.0362309	4.37
44319	0.00265747	447.99	16469.8	20373.3	0.0362309	6.4
46174.3	0.00265747	447.983	16470.9	20357.4	0.0362309	8.43
44671	0.00265747	511.988	16422.1	20352	0.0362309	10.46
45038.4	0.00265747	96.0308	16625.5	19345.5	0.0362309	12.49
<b>DNI 880</b>				<b>20075.71</b>		
47833.9	0.00265747	92.4326	18027.4	20938.2	0.0362309	0.31
48129.2	0.00265747	346.586	17846.9	22076.6	0.0362309	2.34
48106	0.00265747	623.853	17937.9	22115.9	0.0362309	4.37
47875.1	0.00265747	577.643	17810.6	22028.9	0.0362309	6.4
47898.3	0.00265747	577.644	17733.4	22031.7	0.0362309	8.43
48661.2	0.00265747	623.861	17841.2	22071	0.0362309	10.46

48064.6	0.00265747	92.432	17983.4	20916	0.0362309	12.49
DNI 880				21739.76		
47833.9	0.00265747	92.4326	18027.4	20938.2	0.0362309	0.31
48129.2	0.00265747	346.586	17846.9	22076.6	0.0362309	2.34
48106	0.00265747	623.853	17937.9	22115.9	0.0362309	4.37
47875.1	0.00265747	577.643	17810.6	22028.9	0.0362309	6.4
47898.3	0.00265747	577.644	17733.4	22031.7	0.0362309	8.43
48661.2	0.00265747	623.861	17841.2	22071	0.0362309	10.46
48064.6	0.00265747	92.432	17983.4	20916	0.0362309	12.49
DNI 813.39				21739.76		
45336.7	0.00265747	32.017	16625.6	19336.8	0.0362309	0.31
44702.5	0.00265747	543.982	16422.7	20310.2	0.0362309	2.34
45406.5	0.00265747	479.984	16531	20454.8	0.0362309	4.37
44319	0.00265747	447.99	16469.8	20373.3	0.0362309	6.4
46174.3	0.00265747	447.983	16470.9	20357.4	0.0362309	8.43
44671	0.00265747	511.988	16422.1	20352	0.0362309	10.46
45038.4	0.00265747	96.0308	16625.5	19345.5	0.0362309	12.49
DNI 691.52				20075.71		
37588.7	0.00265747	72.6353	14166.2	16453.6	0.0362309	0.31
37820.8	0.00265747	272.353	14024.4	17348.2	0.0362309	2.34
37802.6	0.00265747	490.235	14091.2	17379.1	0.0362309	4.37
37621.1	0.00265747	453.922	13995.9	17310.7	0.0362309	6.4
37639.3	0.00265747	453.924	13935.3	17312.9	0.0362309	8.43
38238.8	0.00265747	490.241	14019.9	17343.8	0.0362309	10.46
37770.1	0.00265747	72.6347	14131.7	16436.4	0.0362309	12.49
DNI 532.81				17083.53		
28961.8	0.00265747	55.9648	10914.9	12677.4	0.0362309	0.31
29140.6	0.00265747	209.846	10805.7	13366.6	0.0362309	2.34
29126.5	0.00265747	377.722	10857.1	13390.4	0.0362309	4.37
28986.7	0.00265747	349.743	10783.7	13337.7	0.0362309	6.4
29000.8	0.00265747	349.744	10737	13339.4	0.0362309	8.43
29462.7	0.00265747	377.727	10862.2	13363.2	0.0362309	10.46
29101.5	0.00265747	55.9644	10888.3	12664.1	0.0362309	12.49
DNI 362.769				13162.69		
19718.9	0.00265747	38.1042	7431.55	8631.51	0.0362309	0.31
19840.7	0.00265747	142.876	7357.17	9100.8	0.0362309	2.34
19831.1	0.00265747	257.176	7392.18	9117.02	0.0362309	4.37
19735.9	0.00265747	238.126	7342.21	9081.13	0.0362309	6.4
19745.5	0.00265747	238.127	7310.39	9082.3	0.0362309	8.43
20060	0.00265747	257.179	7354.8	9098.49	0.0362309	10.46
19814	0.00265747	38.1039	8622.47	8622.47	0.0362309	12.49
DNI 244.05				8961.96		
13265.8	0.00265747	25.6343	4999.52	5806.78	0.0362309	0.31
13347.6	0.00265747	96.1184	4949.48	6122.49	0.0362309	2.34
13341.2	0.00265747	173.013	4973.03	6133.4	0.0362309	4.37

13277.2	0.00265747	160.188	4939.42	6109.26	0.0362309	6.4
13283.6	0.00265747	160.198	4918.01	6110.04	0.0362309	8.43
13495.2	0.00265747	173.015	4947.88	6120.94	0.0362309	10.46
13329.7	0.00265747	25.6341	4987.33	5800.7	0.0362309	12.49
DNI 76.52				6029.087		
4159.37	0.00265747	8.03744	1567.56	1820.67	0.0362309	0.31
4185.05	0.00265747	30.1372	1551.87	1919.66	0.0362309	2.34
4183.04	0.00265747	54.2469	1559.26	1923.08	0.0362309	4.37
4162.95	0.00265747	50.2287	1548.72	1915.51	0.0362309	6.4
4164.97	0.00265747	50.2288	1542	1915.76	0.0362309	8.43
4231.31	0.00265747	54.2476	1551.37	1919.17	0.0362309	10.46
4179.44	0.00265747	8.03738	1563.74	1818.76	0.0362309	12.49
DNI 2.83				1890.373		
155.955	0.00265747	0.148599	58.0915	67.4443	0.0362309	0.31
154.425	0.00265747	1.78269	57.5096	71.0095	0.0362309	2.34
156.134	0.00265747	1.85697	57.2615	70.8671	0.0362309	4.37
153.534	0.00265747	1.93124	57.1823	70.8657	0.0362309	6.4
153.98	0.00265747	2.0798	57.2175	70.7459	0.0362309	8.43
153.162	0.00265747	2.15407	57.3086	70.9915	0.0362309	10.46
156.228	0.00265747	0.222864	57.844	67.4109	0.0362309	12.49

69.90499

Table 6. 19 Values obtained after the Ray tracing simulation Run for the PF1 mirror

With the following graph (fig. 6.42).

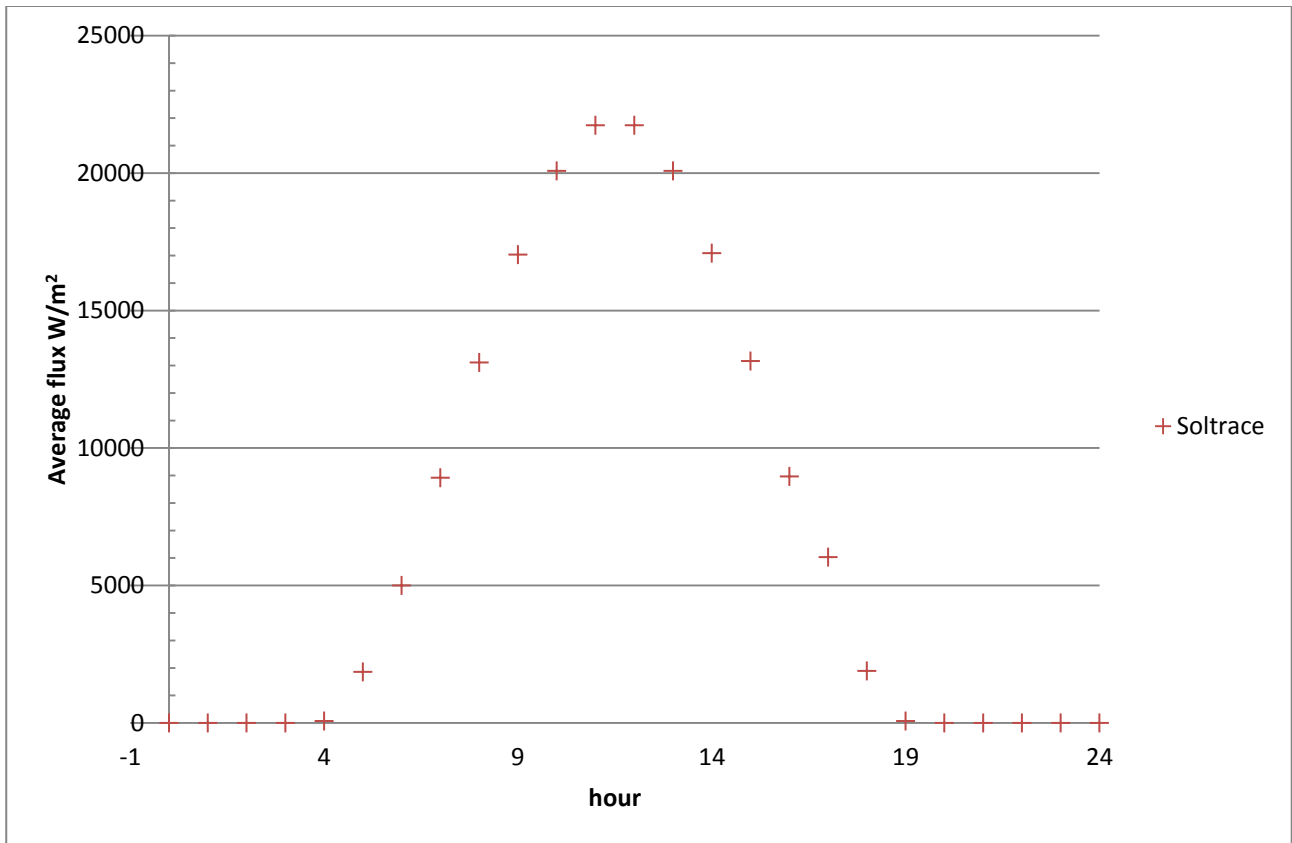


Figure 6.42 Average flux collected on the 172th day for the PF1 mirror

For the PF2 we obtained the following data (table 6.20).

Peak flux	Uncertainty	Min flux	$\sigma$ flux	Avg. Flux	Avg. Flux uncertainty	Section: from-to (m)
<b>DNI 2.83</b>						
146.427	2.25246	0.148581	551.1358	64.3127	0.030058	0.31
148.797	2.25246	2.00575	54.7635	67.8457	0.030058	2.34
147.089	2.25246	2.00576	54.8544	67.8707	0.030058	4.37
146.717	2.25246	2.00576	54.9604	68.0671	0.030058	6.4
146.792	2.25246	1.93147	54.7313	67.7548	0.030058	8.43
148.129	2.25246	2.08004	54.9431	68.0009	0.030058	10.46
147.836	2.25246	0.297157	55.3479	64.4688	0.030058	12.49
<b>DNI 75.104</b>				<b>66.90296</b>		
3885.96	2.25246	3.94313	1463.22	1706.76	0.030058	0.31
3948.84	2.25246	53.2295	1453.34	1800.52	0.030058	2.34
3903.52	2.25246	53.2298	1455.75	1801.19	0.030058	4.37
3893.96	2.25246	53.2298	1458.57	1806.4	0.030058	6.4
3895.63	2.25246	51.2583	1452.49	1798.11	0.030058	8.43
3931.12	2.25246	55.2012	1458.11	1804.64	0.030058	10.46
3923.34	2.25246	7.88611	1468.85	1710.91	0.030058	12.49
<b>DNI 202.64</b>				<b>1775.504</b>		
10484.8	2.25246	10.6391	3947.96	4605.06	0.030058	0.31

10654.5	2.25246	143.62	3921.3	4858.04	0.030058	2.34
10532.2	2.25246	143.621	3927.81	4859.83	0.030058	4.37
10505.6	2.25246	143.621	3935.4	4873.89	0.030058	6.4
10510.9	2.25246	138.301	3918.99	4851.53	0.030058	8.43
10606.6	2.25246	148.94	3934.16	4869.15	0.030058	10.46
10585.7	2.25246	21.2777	3963.14	4616.24	0.030058	12.49
DNI 361.35				4790.534		
18696.6	2.25246	18.9717	7040.05	8211.8	0.030058	0.31
18999.2	2.25246	256.105	6992.5	8662.91	0.030058	2.34
18781.1	2.25246	256.106	7004.11	8666.1	0.030058	4.37
18733.7	2.25246	256.106	7017.65	8691.18	0.030058	6.4
18743.2	2.25246	246.621	6988.39	8651.31	0.030058	8.43
18913.9	2.25246	265.591	7015.44	8682.72	0.030058	10.46
18876.5	2.25246	37.9427	7067.12	8231.73	0.030058	12.49
DNI 531.4				8542.536		
27495.2	2.25246	27.8997	10353.1	12076.3	0.030058	0.31
27940.1	2.25246	376.627	10283.2	12739.6	0.030058	2.34
27619.4	2.25246	376.628	10300.2	12744.3	0.030058	4.37
27549.7	2.25246	376.629	10320.1	12781.2	0.030058	6.4
27563.6	2.25246	362.679	10277.1	12722.6	0.030058	8.43
27814.7	2.25246	390.578	10316.9	12768.8	0.030058	10.46
27759.7	2.25246	55.7983	10392.9	12105.6	0.030058	12.49
DNI 690.11				12562.63		
35707	2.25246	36.2323	13445.2	15683	0.030058	0.31
36284.8	2.25246	489.111	13354.4	16544.5	0.030058	2.34
35868.3	2.25246	489.114	13376.5	16550.6	0.030058	4.37
35777.8	2.25246	489.114	13402.4	16598.5	0.030058	6.4
35795.9	2.25246	470.999	13346.5	16522.4	0.030058	8.43
36121.9	2.25246	507.229	13398.2	16582.4	0.030058	10.46
36050.5	2.25246	72.4633	13496.9	15271	0.030058	12.49
DNI 813.39				16250.34		
42085.6	2.25246	42.7048	15847	18484.6	0.030058	0.31
42766.7	2.25246	576.485	15740	19500	0.030058	2.34
42275.8	2.25246	576.488	15766.1	19507.2	0.030058	4.37
42169.1	2.25246	576.489	15796.6	19563.6	0.030058	6.4
42190.4	2.25246	555.137	15730.7	19473.9	0.030058	8.43
42574.7	2.25246	597.839	15791.6	19544.6	0.030058	10.46
42490.5	2.25246	85.408	15907.9	18529.4	0.030058	12.49
DNI 880				19229.04		
45532.1	2.25246	46.202	17144.7	19998.3	0.030058	0.31
46268.9	2.25246	623.695	17028.9	21096.9	0.030058	2.34
45737.8	2.25246	623.698	17057.2	21104.7	0.030058	4.37
45622.4	2.25246	623.698	17090.2	21165.7	0.030058	6.4
45645.5	2.25246	600.598	17018.9	21068.6	0.030058	8.43
46061.2	2.25246	646.798	17084.8	21145.1	0.030058	10.46

45970.1	2.25246	92.4022	17210.6	20046.8	0.030058	12.49
DNI 880				20803.73		
45532.1	2.25246	46.202	17144.7	19998.3	0.030058	0.31
46268.9	2.25246	623.695	17028.9	21096.9	0.030058	2.34
45737.8	2.25246	623.698	17057.2	21104.7	0.030058	4.37
45622.4	2.25246	623.698	17090.2	21165.7	0.030058	6.4
45645.5	2.25246	600.598	17018.9	21068.6	0.030058	8.43
46061.2	2.25246	646.798	17084.8	21145.1	0.030058	10.46
45970.1	2.25246	92.4022	17210.6	20046.8	0.030058	12.49
DNI 813.39				20803.73		
42085.6	2.25246	42.7048	15847	18484.6	0.030058	0.31
42766.7	2.25246	576.485	15740	19500	0.030058	2.34
42275.8	2.25246	576.488	15766.1	19507.2	0.030058	4.37
42169.1	2.25246	576.489	15796.6	19563.6	0.030058	6.4
42190.4	2.25246	555.137	15730.7	19473.9	0.030058	8.43
42574.7	2.25246	597.839	15791.6	19544.6	0.030058	10.46
42490.5	2.25246	85.408	15907.9	18529.4	0.030058	12.49
DNI 691.52				19229.04		
35779.9	2.25246	36.3064	13472.6	15715	0.030058	0.31
36359	2.25246	490.111	13381.6	16578.3	0.030058	2.34
35941.6	2.25246	490.113	13403.9	16584.4	0.030058	4.37
35850.9	2.25246	490.114	13429.8	16632.4	0.030058	6.4
35869	2.25246	471.961	13373.8	16556.1	0.030058	8.43
36195.8	2.25246	508.265	13425.5	16616.2	0.030058	10.46
36124.1	2.25246	72.6113	13524.4	15753.2	0.030058	12.49
DNI 532.81				16347.94		
27568.1	2.25246	27.9737	10380.5	12108.3	0.030058	0.31
28014.3	2.25246	377.626	10310.4	12773.4	0.030058	2.34
27692.7	2.25246	377.628	10327.6	12778.2	0.030058	4.37
27622.8	2.25246	377.628	10347.5	12815.1	0.030058	6.4
27636.8	2.25246	363.642	10304.4	12756.3	0.030058	8.43
27888.5	2.25246	391.614	10344.3	12802.7	0.030058	10.46
27833.3	2.25246	55.9464	10420.5	12137.7	0.030058	12.49
DNI 362.769				12595.96		
18770	2.25246	19.0462	7067.69	8244.05	0.030058	0.31
19073.8	2.25246	257.11	7019.96	8696.93	0.030058	2.34
18854.9	2.25246	257.112	7031.62	8700.14	0.030058	4.37
18807.3	2.25246	257.112	7045.21	8725.31	0.030058	6.4
18816.8	2.25246	247.589	7015.83	8685.28	0.030058	8.43
18988.2	2.25246	266.634	7042.99	8716.82	0.030058	10.46
18950.6	2.25246	38.0917	7094.87	8264.06	0.030058	12.49
DNI 244.05				8576.084		
12627.4	2.25246	12.8132	4754.74	5546.12	0.030058	0.31
12831.7	2.25246	172.969	4722.63	5850.79	0.030058	2.34
12684.5	2.25246	172.97	4730.47	5852.95	0.030058	4.37

12652.4	2.25246	172.97	4739.61	5869.88	0.030058	6.4
12658.8	2.25246	166.564	4719.85	5842.96	0.030058	8.43
12774.1	2.25246	179.376	4738.12	5864.17	0.030058	10.46
12748.9	2.25246	25.6259	4773.02	5559.58	0.030058	12.49
DNI 76.52				5769.493		
3959.22	2.25246	4.01747	1490.81	1738.94	0.030058	0.31
4023.29	2.25246	54.2331	1480.74	1834.47	0.030058	2.34
3977.11	2.25246	54.2334	1483.2	1835.15	0.030058	4.37
3967.07	2.25246	54.2334	1486.07	1840.46	0.030058	6.4
3969.08	2.25246	52.2247	1479.87	1832.01	0.030058	8.43
4005.23	2.25246	56.242	1485.6	1838.67	0.030058	10.46
3997.31	2.25246	8.03479	1496.54	1743.16	0.030058	12.49
DNI 2.83				1808.98		
146.427	2.25246	0.148581	551.1358	64.3127	0.030058	0.31
148.797	2.25246	2.00575	54.7635	67.8457	0.030058	2.34
147.089	2.25246	2.00576	54.8544	67.8707	0.030058	4.37
146.717	2.25246	2.00576	54.9604	68.0671	0.030058	6.4
146.792	2.25246	1.93147	54.7313	67.7548	0.030058	8.43
148.129	2.25246	2.08004	54.9431	68.0009	0.030058	10.46
147.836	2.25246	0.297157	55.3479	64.4688	0.030058	12.49
				66.90296		

Table 6. 20 Values obtained after the Ray tracing simulation Run for the PF2 mirror

Graphically we obtained for the PF2 mirror the following graph (fig 6.43).

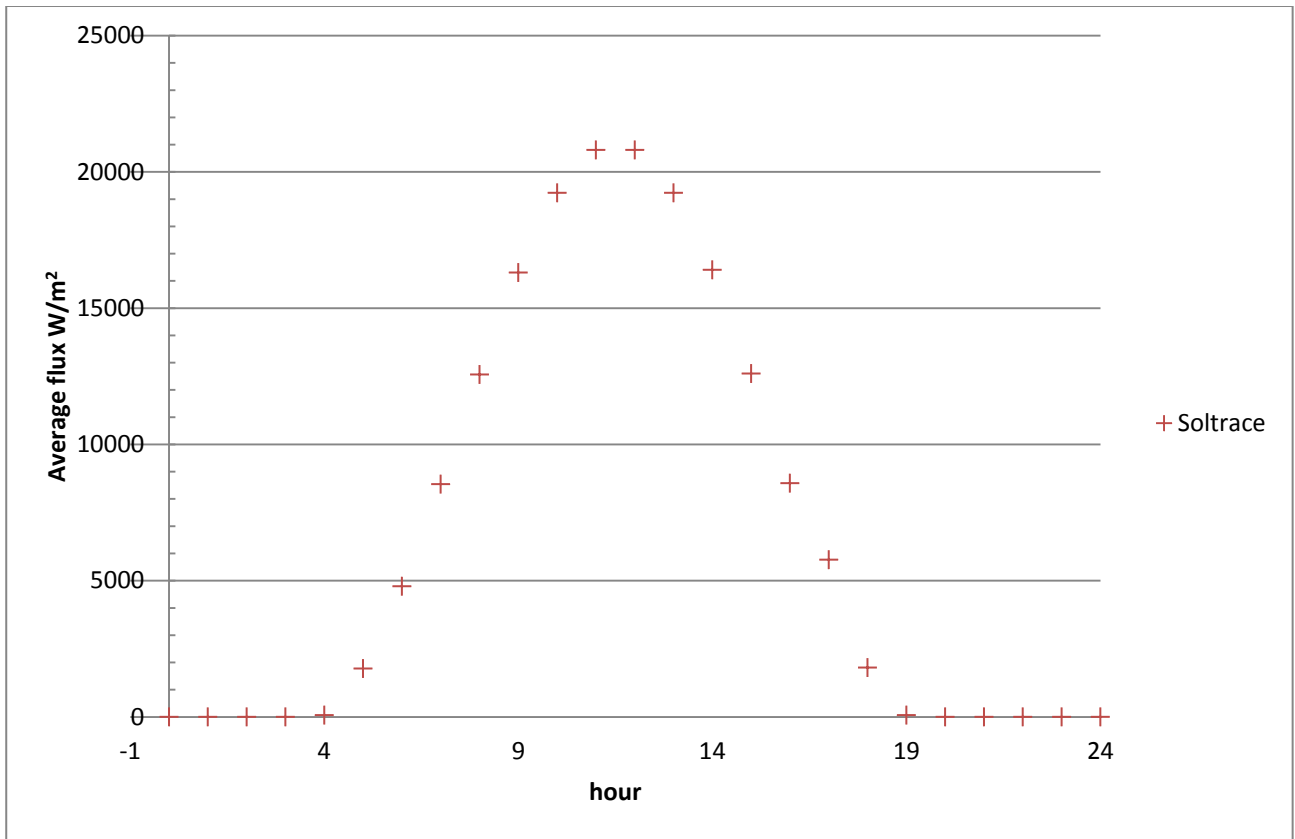


Figure 6. 43 Average flux collected on the 172th day for the PF2 mirror

Comparing the two mirrors we obtained the following figure 6.44:

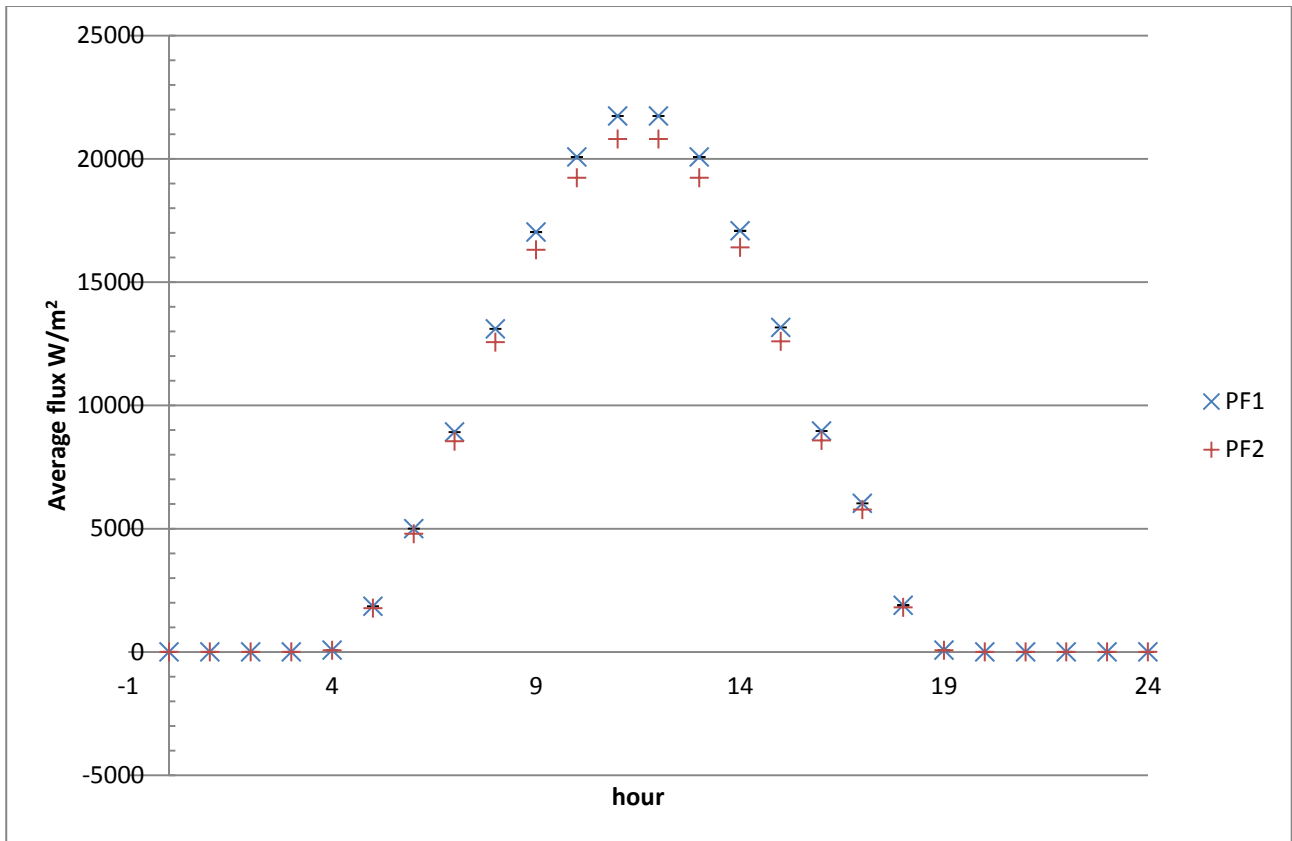


Figure 6. 44 Comparison between the flux collected from PF1 and PF2 mirrors

### 6.3 Comparison between Mathcad and Soltrace models

To validate the Mathcad model now we will compare the result obtained with the Soltrace simulation, to find the errors between the two methodologies.

#### 6.3.1 Thin glass mirrors

The results obtained in the two modeling methods are summarized in the next graph (fig 6.45) . On the secondary axis reports the value in percentage of the difference between one and the other models.

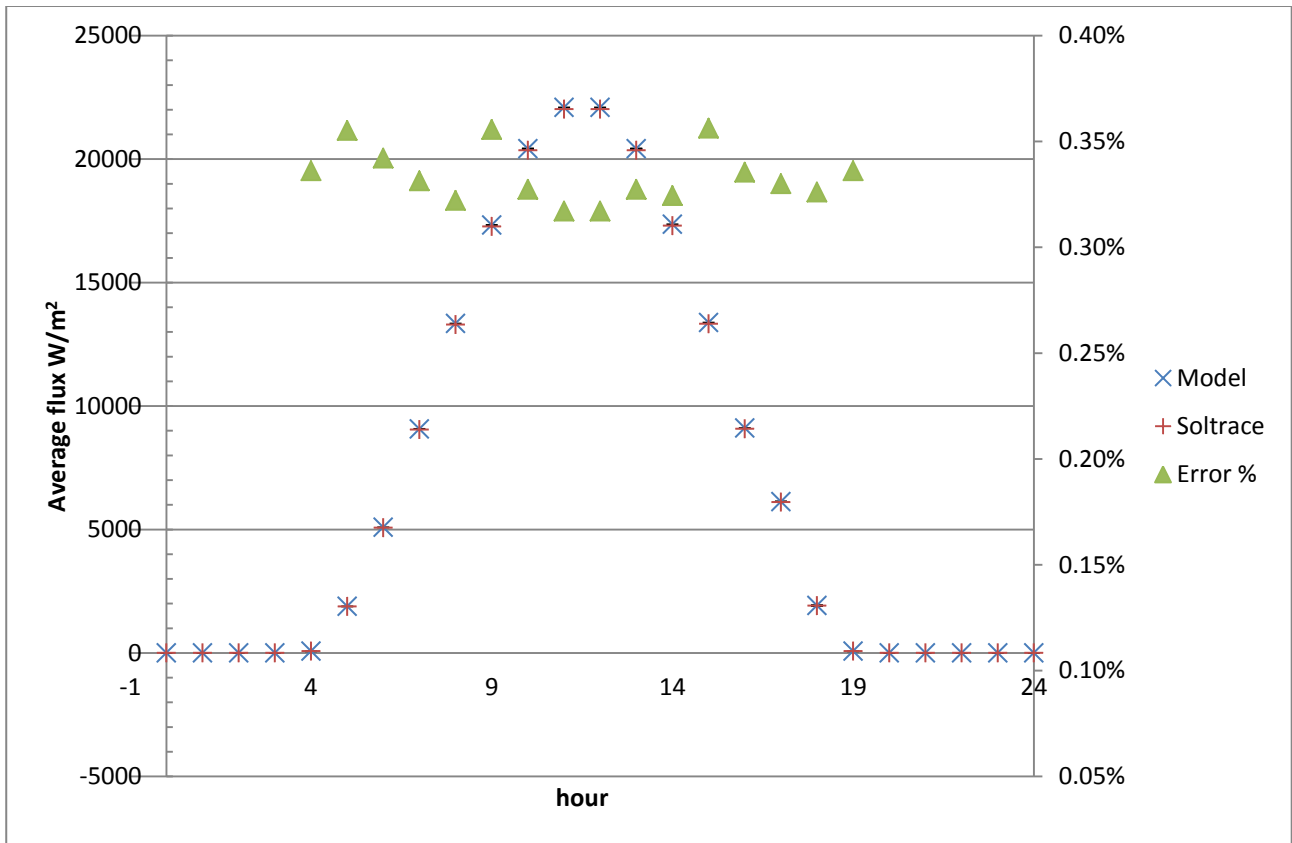


Figure 6. 45 Comparison between TG1 Model and TG1 Soltrace

In this case we didn't have almost any difference between the two methods so the error is at maximum equal to 0.36% which means that the Mathcad simulation with all the parameters inserted are a very good approximation of the real systems with the entire hypothesis done before.

We obtained the same graph with the TG2 mirror which is shown in the next figure 6.46.

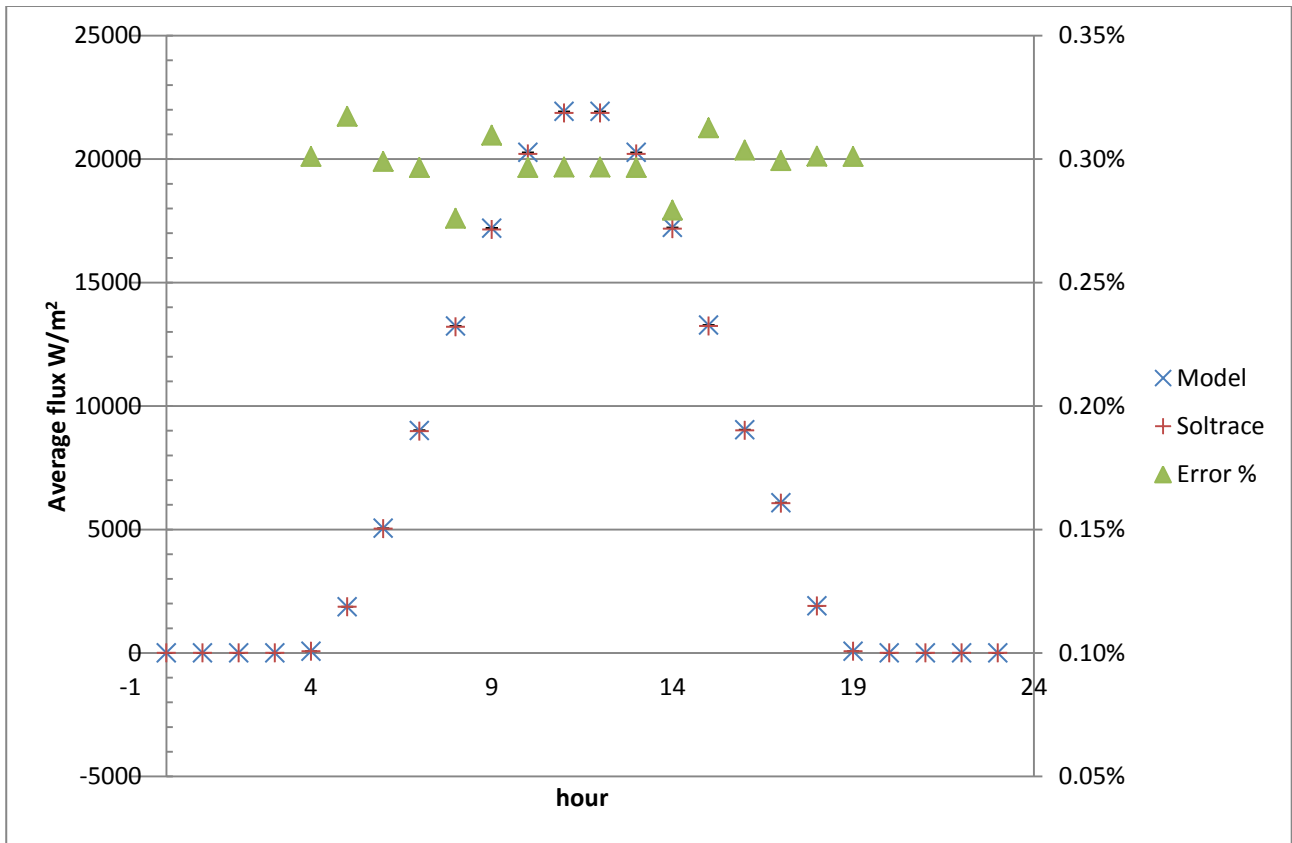


Figure 6.46 Comparison between TG2 Model and TG2 Soltrace

It can be easily seen that the simulation is as good as the TG1 with a maximum error of 0.32% at maximum.

It has to be said that the Soltrace simulation also returns the average flux uncertainty which is in the order of the error, so it is also hypnotizable that the two modeling correspond completely.

### 6.3.2 Aluminum mirrors

As shown previously it was possible to compare the two simulations also for the other mirrors such as the aluminum mirrors.

The results are presented in the following graph 6.47.

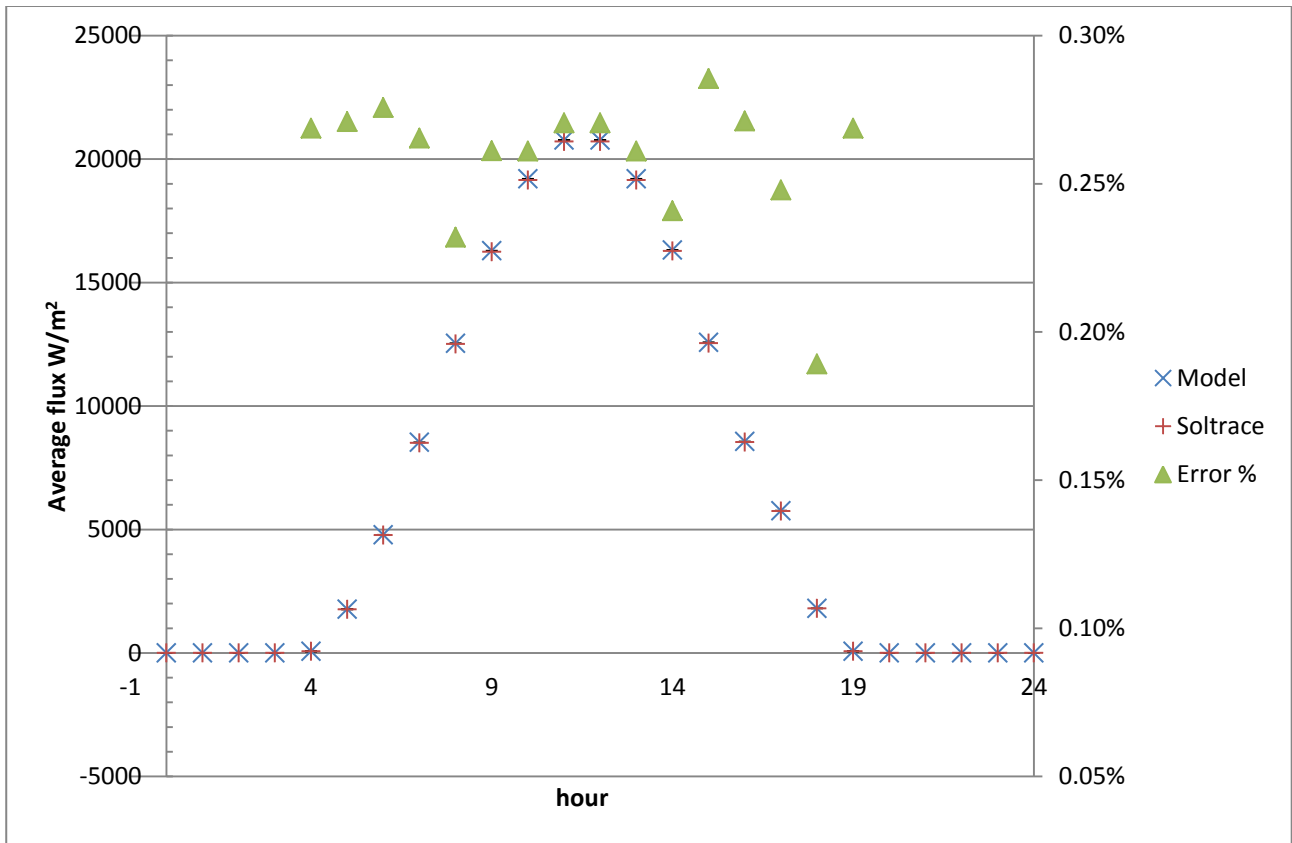


Figure 6. 47 Comparison between AL1 Model and AL1 Soltrace

In this case we can see that we have some discordance between the models with a minimum error of 0.19% and a maximum error equal to 0.29%.

It means that also in this case the simulations are very similar.

The same graph was built for the AL2 mirror with the following result in figure 6.48.

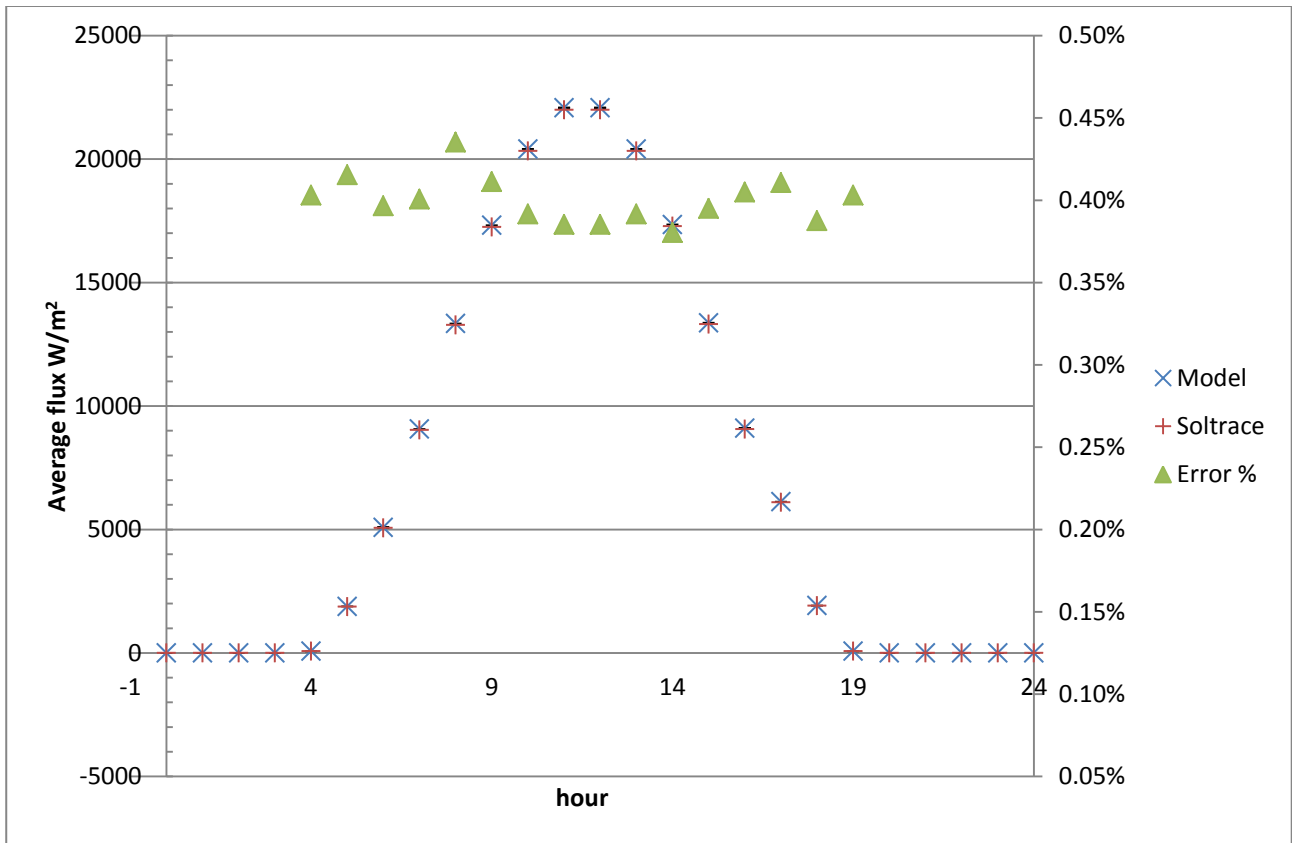


Figure 6. 48 Comparison between AL2 Model and AL2 Soltrace

In this case the simulations differ from one each other of a maximum error equal to 0.44% and a minimum error of 0.38%.

### 6.3.3 Polymeric film mirrors

In order to evaluate the goodness of the Mathcad simulation it was conducted the same data evaluation as above. The next figure 6.49 shows the comparison.

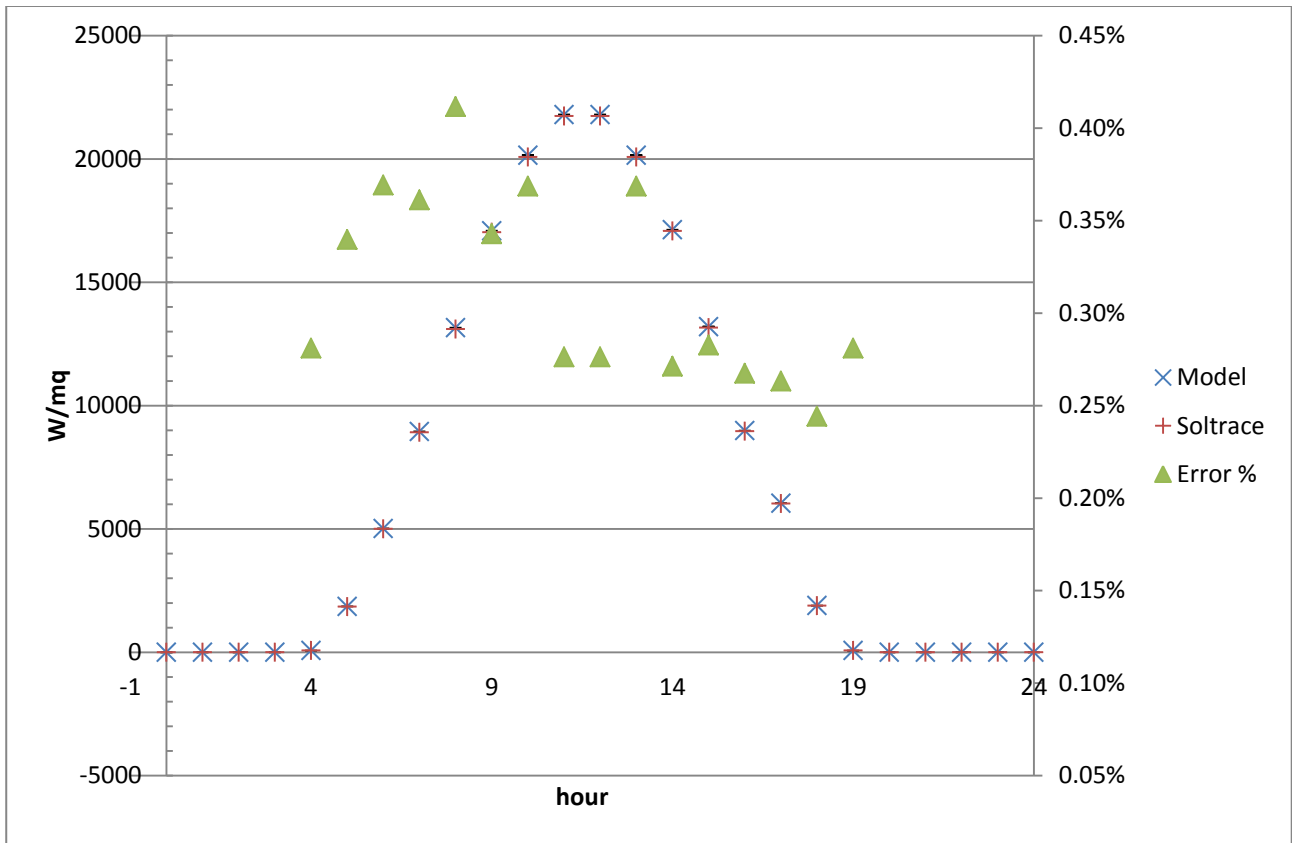


Figure 6. 49 Comparison between PF1 Model and PF1 Soltrace

As it can be seen in the above graph the error evaluation (secondary axis) lead to a maximum error of 0.41% and a minimum error equal to 0.24%.

We obtained the same graph with the PF2 mirror which is shown in the next figure 6.50.

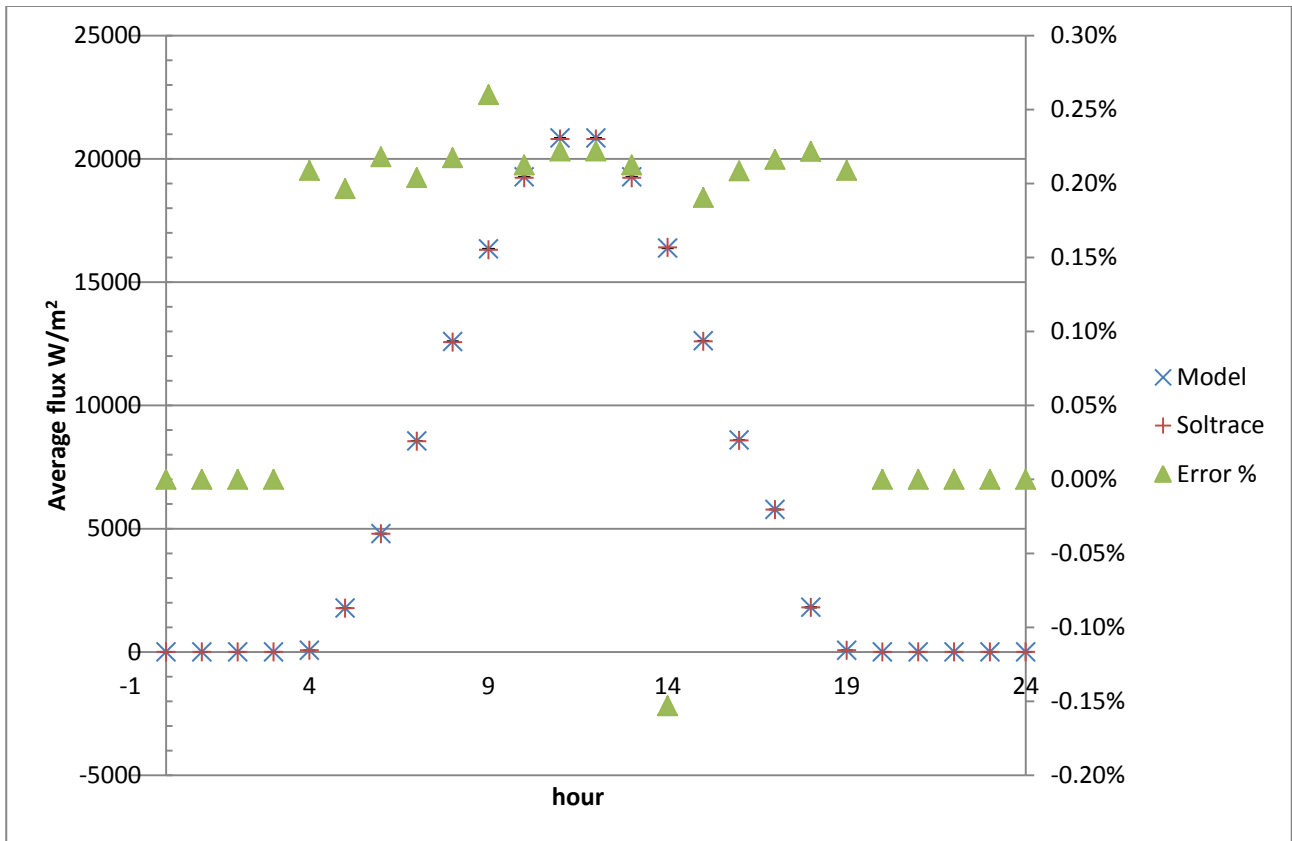


Figure 6.50 Comparison between PF2 Model and PF2 Soltrace

As it can be seen in the above graph the error evaluation (secondary axis) lead to a maximum error of 0.26% and a minimum error equal to -0.15%.

Finally after all the comparisons between the two models is possible to say that the model is almost good for the evaluation of the total quantity of solar irradiance collected by the reflectors.

## 7. ENHANCING THE MODEL

After validating the Mathcad model it was possible to enhance the research introducing new parameters to evaluate further losses.

Were implemented the:

- Characteristics of the receiver to evaluate its losses;
- Solar field piping heat losses;
- HTF energy gain;

All the above evaluation is further described below.

From here after it is possible to use the previously described (Price and Forristall) values for the optical losses involved in the absorption of the hitting rays table 7.1.

<b>Name</b>	<b>Value</b>	<b>Name</b>	<b>Value</b>
TrkTwstErr	0,99	HCEdust	0,98
GeoAcc	0,98	BelShad	0,97
MirRef	DOM	EnvTrans	0,96
MirCln	0,95	HCEabs	0,95
		HCEmisc	0,96

Table 7. 1 parameters chosen to enhance the modeling

### 7.2 Receiver Heat Loss

As the heat transfer fluid in the receiver tubes absorbs energy, its temperature will increase. This temperature increase creates a temperature difference between the bulk temperature of the fluid and the temperature of the surrounding ambient air. Heat losses from the receiver tube to the glass envelope, as well as from the glass envelope to the ambient air, are driven by this temperature difference. This parasitic heat loss can be correlated with the temperature of the heat transfer fluid, as described further below.

### 7.3 Analytical Heat Loss Derivation

Figure 7.2 shows the relevant heat transfer mechanisms responsible for losses between the collector surfaces and the ambient environment.

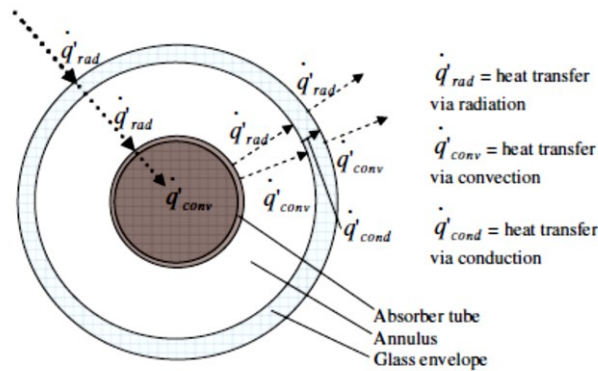


Figure 7. 1 Heat transfer mechanisms acting on HCE surfaces

The heat fluxes into each surface of the HCE must balance the fluxes leaving that surface. For a given bulk fluid temperature, insolation, ambient weather conditions, HCE dimensions, and HCE surface properties, energy balances over each surface of the HCE can be used to determine surface temperatures, the net heat flux absorbed by the fluid, and the net heat flux lost to the surroundings. Heat transfer analysis of the HCEs using simultaneous equation solving of these heat transfer rates was accomplished by Forristall (2003).

### 7.3.1 Linear Regression Heat Loss Model

To minimize the computational overhead associated with solving a dynamic heat balance to estimate receiver heat losses at each time step, a simplified model needs to be developed. The formulation of a simplified model requires identifying the dominant mechanisms that contribute to the heat loss from the heat transfer fluid through the collector. Since the heat fluxes over each surface must balance, the heat flux from the outermost HCE surface will be influenced by the incident radiation on that surface. Heat loss will also be impacted by the mass flow rate of the fluid, as convective heat transfer to the HTF improves with higher mass flow rates. The ambient air temperature will affect heat loss, as lower ambient temperature will increase temperature differences between HTF and ambient and thus increase driving potential for heat loss, while the reverse is true for higher ambient air temperatures. Finally, wind speed will affect heat loss by increasing the convection coefficient from the outermost HCE surface to the surrounding air.

The effect of wind speed on heat loss is negligible except in the case of a missing glass envelope.

While heat transfer fluid flow rate and ambient air temperature influence heat loss from the collector, the effects of these variables are small in comparison to the effect of bulk fluid temperature and DNI.

Thus, the receiver heat loss is modeled as a function of bulk fluid temperature and DNI.

The heat loss from the HCE may be expressed in a single equation by applying a linear regression analysis to the calculated heat loss from the HCE per unit length of trough [W/m] over a range of bulk fluid temperatures and DNI levels. We took the work already conducted by the NREL to quantify the heat losses and insert the results as a mean of comparison between different mirrors composition. A linear regression analysis of HCE heat loss for a UVAC tube with cermet selective coating, at an ambient temperature of 25 [°C] determines the following functional form of the heat loss equation as a function of temperature and  $Q_{\text{abs}}$ :

$$HL = A_0 + A_1(T_{HTF} - T_{amb}) + A_2T_{HTF}^2 + a_3T_{HTF}^3 + A_4(DNI_{j,n}IAM_{n,j}\cos\theta_{n,j}RowShadow_{n,j}Endloss_{n,j}\eta_{HCE}\eta_{mirrors})T_{HTF}^2 + \sqrt{V_w}(A_5 + A_6(T_{HTF} - T_{amb}))$$

where

HeatLoss	= heat loss from the outermost surface of the receiver, per unit length [W/m]
$T_{HTF}$	= bulk fluid temperature [°C]
$T_{amb}$	= environmental temperature [°C]
$\cos\theta_{n,j}$	= cosine theta
Rowshadow	= Row shadowing
Endloss	= HCE endings losses
$\eta_{HCE}$	= HCE efficiency (Schott 2008 PTR 70)
$\eta_{mirrors}$	= Mirrors efficiency
$DNI_{j,n}$	= Direct Normal irradiation [W/m <sup>2</sup> ]
$A_n$	= coefficients (see Table 5.3 – 5.4)
$V_w$	= Wind Speed [m/s]

All HCEs in the solar field are manufactured with an evacuated space between the absorber tube and the glass envelope. Field experience has demonstrated that, over time, the vacuum in the annulus can be compromised, allowing air to infiltrate the annulus. With the loss of a vacuum condition in the annulus, convective heat exchange between the receiver tube and the glass envelope substantially increases. A heat transfer analysis model is used to write heat loss correlations for the following two annulus condition cases:

- Case 1: The annulus is nearly evacuated; a small amount of air exists in the annulus at a pressure of 0.0001 [torr];
- Case 2: The annulus vacuum is completely broken; air exists in the annulus at a pressure of 760 [torr].

Coefficients for Equation, along with their standard deviations, are shown for the vacuum annulus, the air annulus, in Tables 7.2 through 7.3, respectively. Root mean square (RMS) deviation for the curve fit is shown as well in Figure 5.14, 5.15 and 5.16.

Vacuum condition	
Heat loss coefficients	2008 PTR 70
A0	4.05
A1	0.247
A2	-0.00146
A3	5.65E-06
A4	7.62E-08
A5	-1.7
A6	0.0125

**Table 7. 2 Coefficients for Receiver Heat Loss: Vacuum annulus**

Lost vacuum condition	
Heat loss coefficients	2008 PTR 70
A00	50.8
A01	0.904
A02	5.79E-04
A03	1.13E-05
A04	1.73E-07
A05	-43.2
A06	0.524

**Table 7. 3 Coefficients for Receiver Heat Loss: Air Annulus**

The receiver heat loss model, as derived by Forristall, accounts for heat loss at a constant, fixed bulk fluid temperature. As mentioned previously, the bulk temperature of the fluid will vary from the field inlet to the field outlet by as much as 100 [°C] in a HCE, (there are three in the Solar Collector Assembly). To account for this temperature variance, the previous equation is integrated from field inlet temperature to field outlet temperature, and divided by the difference in temperature between field inlet and field outlet for each case examined:

$$HL_{air,j,n} := \frac{\int_{T_{collin}}^{T_{collout}} A00 + A01 \cdot (T_{HTF} - T_{amb}) + A02 \cdot (T_{HTF})^2 + A03 \cdot (T_{HTF})^3 + A04 \cdot [(DNI_{j,n} \cdot dx_{n,j}) \cdot IAM_{n,j} \cdot Rowshadow_{n,j} \cdot Endloss_{n,j} \cdot \eta_{HCE} \eta_{mirrors}] \cdot (T_{HTF})^2 + V_w^{0.5} \cdot [A05 + A06 \cdot (T_{HTF} - T_{amb})] dT_{HTF}}{[(T_{collout} - T_{collin}) \cdot Wh]} = \dots$$

$$HL_{vac,j,n} := \frac{\int_{T_{collin}}^{T_{collout}} A0 + A1 \cdot (T_{HTF} - T_{amb}) + A2 \cdot (T_{HTF})^2 + A3 \cdot (T_{HTF})^3 + [(DNI_{j,n} \cdot dx_{n,j}) \cdot IAM_{n,j} \cdot Rowshadow_{n,j} \cdot Endloss_{n,j} \cdot \eta_{HCE} \eta_{mirrors}] \cdot (T_{HTF})^2 + V_w^{0.5} \cdot [A5 + A6 \cdot (T_{HTF} - T_{amb})] dT_{HTF}}{[(T_{collout} - T_{collin}) \cdot Wh]}$$

where

$T_{collout}$  = Solar field temperature at the outlet [°C]

$T_{collin}$  = Solar field temperature at the inlet [°C]

$T_{HTF}$  = bulk fluid temperature [°C]

$T_{amb}$  = environmental temperature [°C]

$dx_{n,j}$  = cosine theta

Rowshadow = Row shadowing

Endloss = HCE endings losses

$\eta_{HCE}$  = HCE efficiency (Schott 2008 PTR 70)

$\eta_{mirrors}$  = Mirrors efficiency

$DNI_{j,n}$  = Direct Normal irradiation [W/m<sup>2</sup>]

$A_n$  = coefficients (see Table 5.3 – 5.4)

$V_w$  = Wind Speed [m/s]

To obtain the variation of the total flux absorbed from the collector varying the typology of mirror, it's important to make some hypotheses on the above equation:

$T_{collout} = 390^\circ\text{C}$

$T_{collin} = 290^\circ\text{C}$

$T_{HTF}$	= bulk fluid temperature from 50 to 600°C [°C]
$T_{amb}$	= environmental temperature 25°C [°C]
$dx_{n,j}$	= cosine theta
Rowshadow	= Row shadowing
Endloss	= HCE endings losses
$\eta_{HCE}$	= HCE efficiency (Schott 2008 PTR 70)
$\eta_{mirrors}$	= Mirrors efficiency
$DNI_{j,n}$	= Direct Normal irradiation [W/m <sup>2</sup> ]
$A_n$	= coefficients (see Table 5.3 – 5.4)
$V_w$	= Wind Speed from 0 m/s to 5 m/s

In the next chapters will be discussed the results obtained inserting the above values into the model.

Then we will define the values of the solar field piping heat losses due to the flow of the heat transfer fluid through the pipes.

Finally will be calculated the total HTF energy gain.

### 7.3.2 Solar Field Piping Heat Losses

Thermal losses from the piping leading to and from the loops in the solar field are accounted for by the following empirical equation (Price, 2005):

$$Sf_{pipeHL} := 0.0169\Delta T - 0.0001683\Delta T^2 + 6.78 \cdot 10^{-7} \cdot \Delta T^3 =$$

where  $Sf_{pipeHL}$  is expressed per unit area of solar field aperture [W/m<sup>2</sup>], and  $T$  [°C] is the difference between the average field temperature and the ambient air temperature:

$$\Delta T := \frac{T_{collout} + T_{collin}}{2} - T_{amb}$$

Thermal losses due to piping to and from the solar field are generally small, on the order of 10 [W/m<sup>2</sup>] or less during solar field operation.

#### 7.4 Heat Transfer Fluid Energy Gain

The net energy collected by the heat transfer fluid over the field, per unit aperture area [W/m<sup>2</sup>], is the difference between the heat absorbed into the fluid by the absorber tubes and the sum of heat loss from the receivers and heat loss from the piping to and from the solar field. It was calculated for each of the cases previously considered:

$$Q_{\text{colltotair},j,n} := [Q_{\text{abs},j,n} - (HL_{\text{airtot},j,n} + S_{\text{pipe}}HL)]$$

$$Q_{\text{colltotvac},j,n} := [Q_{\text{abs},j,n} - (HL_{\text{vactot},j,n} + S_{\text{pipe}}HL)]$$

To complete this research aspect in the following will be discussed the results for the different mirrors.

#### 7.5 Heat losses evaluation

Here is examined how a different reflectance influences the total collection of solar radiation.

To obtain valuable results it's important to concentrate on a single day during the year and as done before is taken into account the 172<sup>th</sup> day the summer solstice.

Due to the composition of the formal equation the term of mirror reflectance efficiency has a very low weight, it is in the A4 and in the A04 term which are respectively A4 7.62E-08 and A04 the value of 1.73E-07 so this calculation is done once for all mirrors.

What instead varies is the Energy gain where the contribution of the mirror on the collected irradiance hasn't a correction factor so little.

In the followings this results are examined and the difference will be evaluated.

Evaluating the heat losses the parameter reflectance is not important because it has no effect on this single value but it has effect on the final balance of the HTF energy gain.

As it can be seen below (fig. 7.2) the heat losses (with or without air in the annulus) are the same, they increase as the temperature rises.

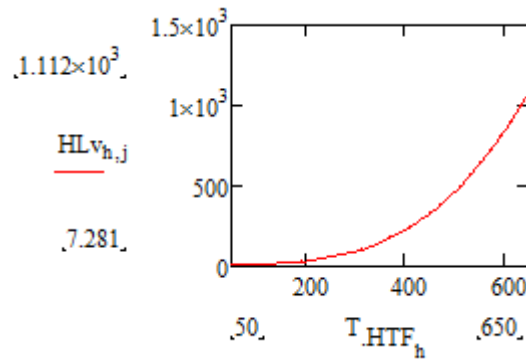


Figure 7.2 Dependence of Heat Losses on the Heat Transfer Fluid in air annulus condition

In particular the behavior of the losses are calculate for the temperature 290°C and the temperature 590 °C which are the operating values that are going to be reached with the Archimede solar plant Fig 7.3.

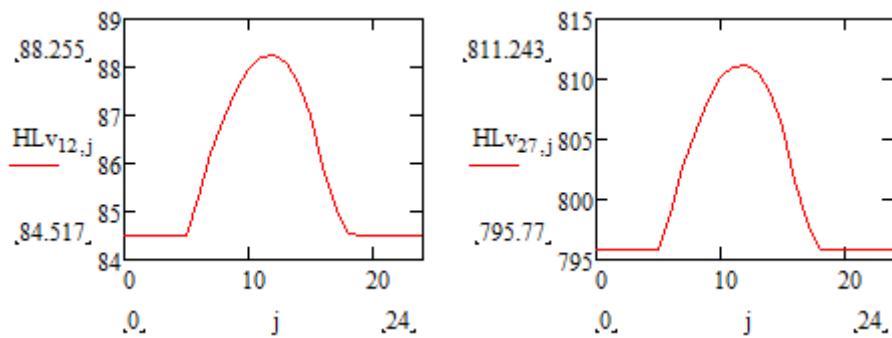


Figure 7.3 Values of Heat losse on the 172th day varying the HTF temperature in air condition

During the day as the temperature reached from the HCE raises the heat losses rises too, with a difference of 300°C is simple to see the amplification of losses in the ratio ten to one.

As it was previously done for the vacuum condition the same calculation has been done for the lost vacuum condition where the behavior with the rises of temperature is almost the same but the values are more than doubled.

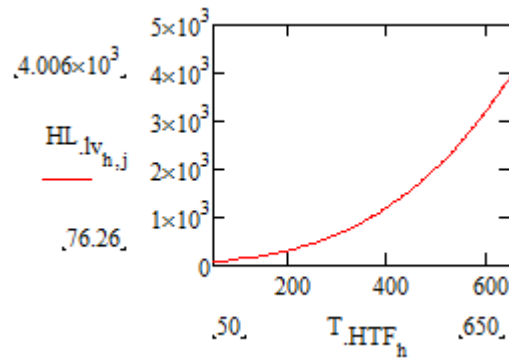


Figure 7.4 Dependence of Heat Losses on the Heat Transfer Fluid in vacuum annulus condition

The same was for the behavior calculated at 390°C and 590°C as it can be seen in the next graphs.

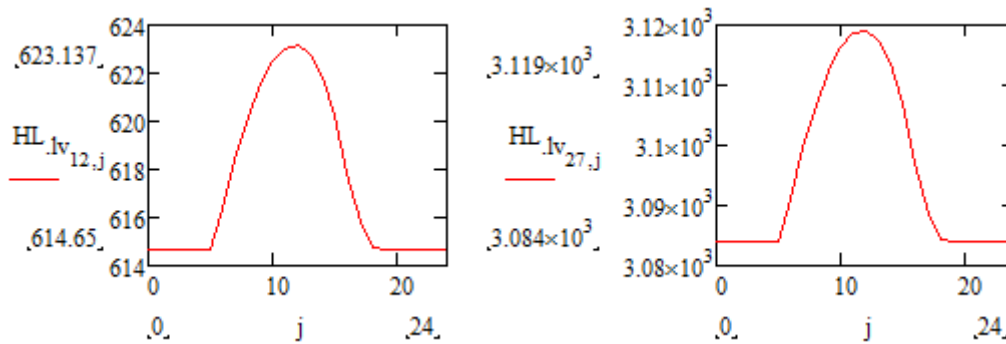


Figure 7.5 Values of Heat losses on the 172th day varying the HTF temperature in vacuum condition

### 7.5.1 Thin glass mirrors

Integrating the values as described in the previous subchapter it possible to compare the results for the TG1 mirror. These values are sensible, as it can be seen from the following graph (fig 7.6), to reflectivity value changes in this case the value of 93.27%.

In the next left graph the  $HL_{V_{12,j}}$  means Heat losses in vacuum condition at the temperature of 290 °C of the Heat Transfer Fluid varying the hour of the 172<sup>th</sup> day.

While in the  $HL_{V_{17,j}}$  means Heat losses in vacuum condition at the temperature of 390 °C of the Heat Transfer Fluid varying the hour of the 172<sup>th</sup> day.

In the next right graph the  $HL_{V_{12,j}}$  means Heat losses in lost vacuum condition at the temperature of 290 °C of the Heat Transfer Fluid varying the hour of the 172<sup>th</sup> day.

While the  $HL_{v17,j}$  means Heat losses in lost vacuum condition at the temperature of 390 °C of the Heat Transfer Fluid varying the hour of the 172<sup>th</sup> day.

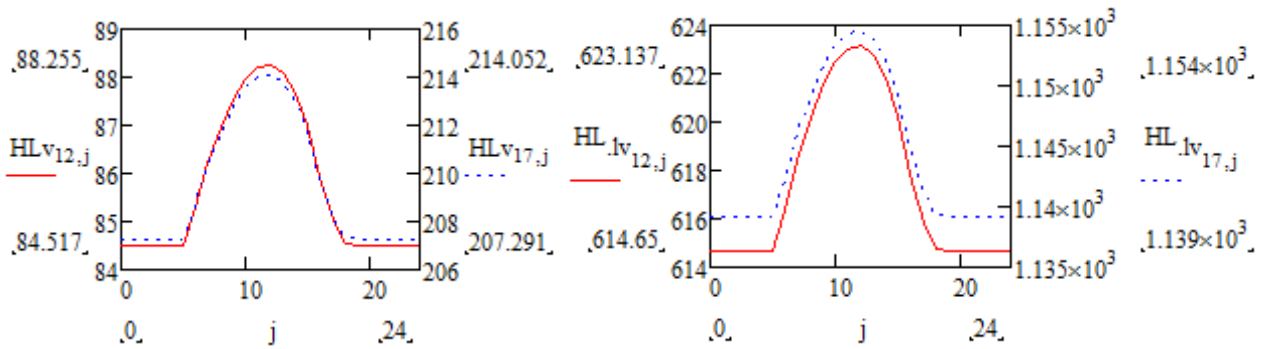


Figure 7. 6 Variation of Heat losses for TG1 reflectance value at 290°C=(12,j) and at 390°C=(17,j) in vacuum and lost vacuum condition

Where is described the losses in vacuum ( $HL_v$ ) and air ( $HL_{lv}$ ) condition at the HTF temperature of 290°C on left and at the temperature of 390°C on the right.

Integrating between  $T_{collin}$  (290°C) and  $T_{collout}$  (390°C) the above equation the values of the Heat losses in the case of the 172<sup>th</sup> day during the day results as follow:

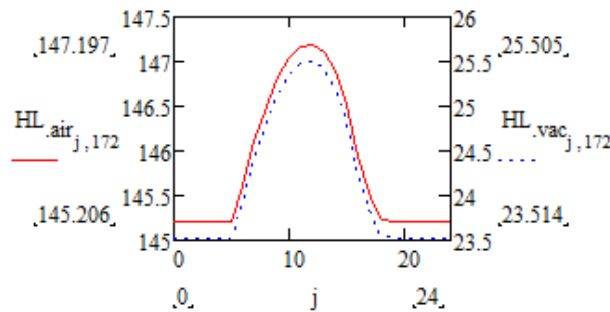


Figure 7. 7 Values of Heat Losses in air and vacuum condition for TG1 mirror

For the TG2 mirror was conducted the same modelization with its SWSR of 91.96 % obtaining the following results under the previous conditions.

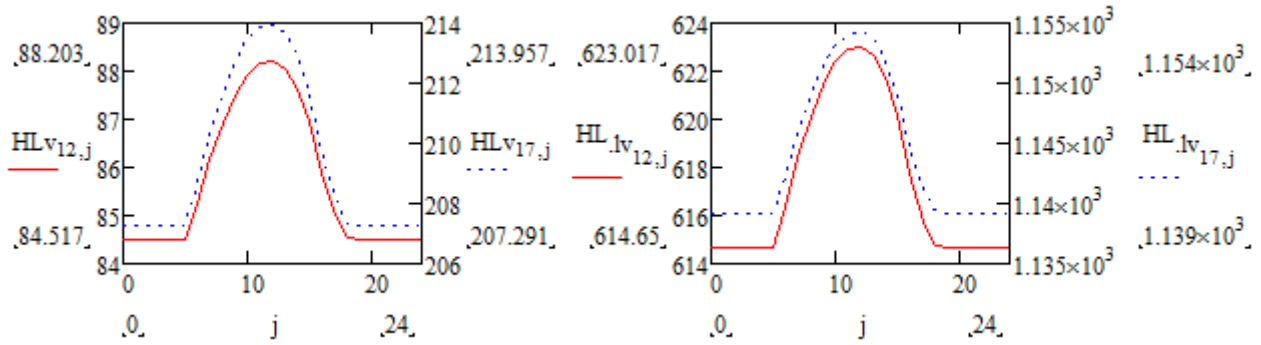


Figure 7. 8 Variation of Heat losses for TG2 reflectance value at 290°C=(12,j) and at 390°C=(17,j) in vacuum and lost vacuum condition

Integrating between Tcollin (290°C) and Tcollout (390°C) the above equation the values of the Heat losses in the case of the 172<sup>th</sup> day during the day results as follow:

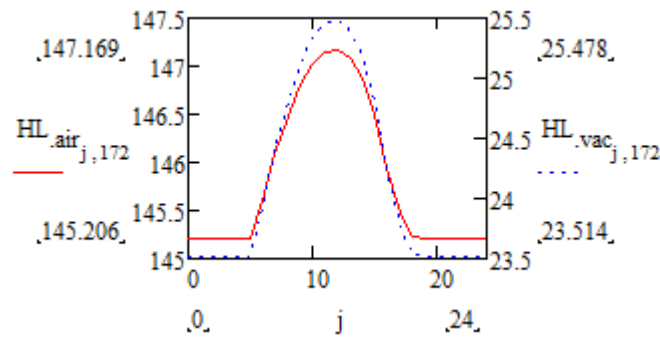


Figure 7. 9 Values of Heat Losses in air and vacuum condition for TG2 mirror

### 7.5.2 Aluminum mirrors

As above the same procedure was used to evaluate the results.

For the AL1 mirror the values of SWSR was equal to 86.55% that results in the following heat losses behavior.

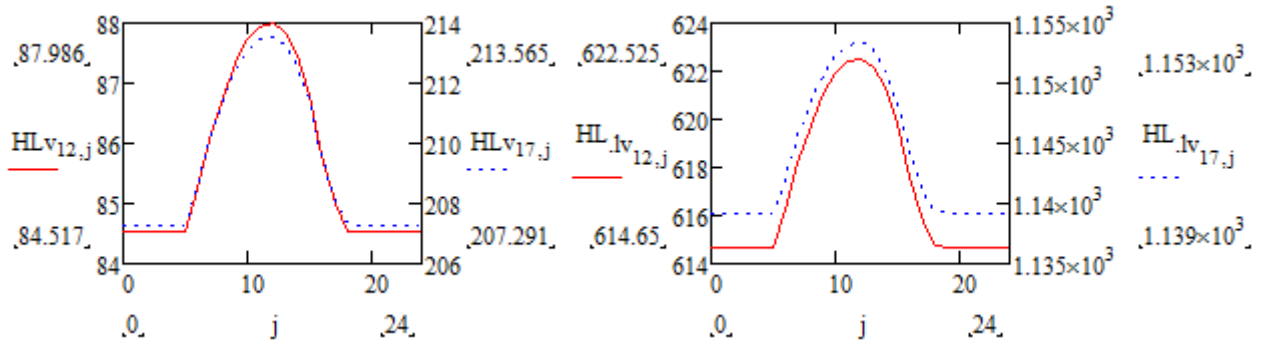


Figure 7. 10 Variation of Heat losses for AL1 reflectance value at 290°C=(12,j) and at 390°C=(17,j) in vacuum and lost vacuum condition

Integrating between  $T_{collin}$  (290°C) and  $T_{collout}$  (390°C) the above equation the values of the Heat losses in the case of the 172<sup>th</sup> day during the day results as follow:

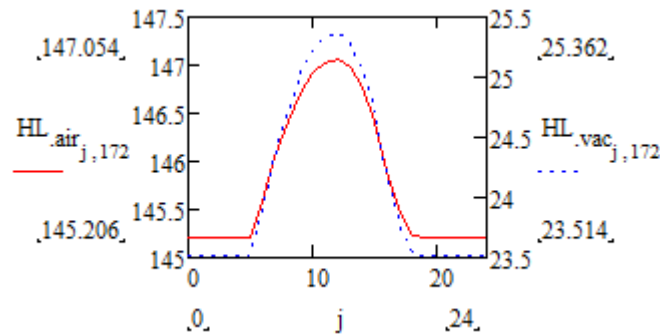


Figure 7. 11 Values of Heat Losses in air and vacuum condition for AL1 mirror

For the second aluminum mirror with a SWSR of 93.02% we obtained the following results:

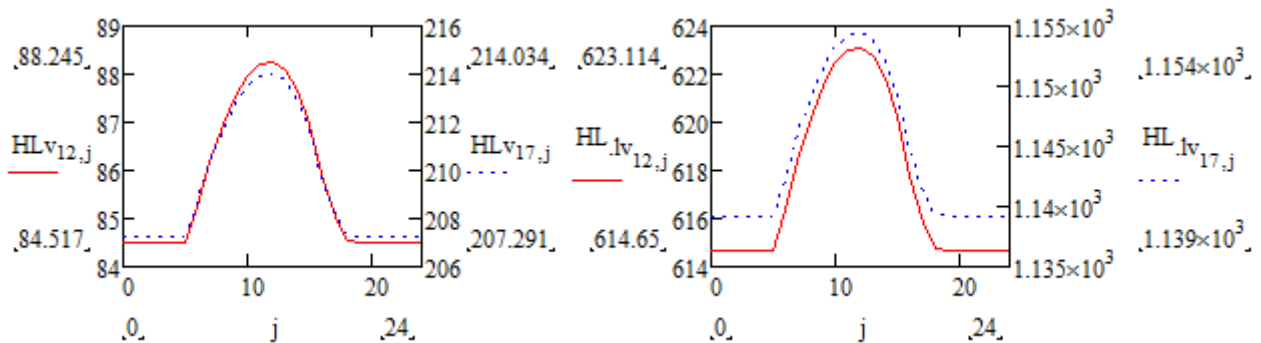


Figure 7. 12 Variation of Heat losses for AL2 reflectance value at 290°C=(12,j) and at 390°C=(17,j) in vacuum and lost vacuum condition

Integrating between  $T_{collin}$  (290°C) and  $T_{collout}$  (390°C) the above equation the values of the Heat losses in the case of the 172<sup>th</sup> day during the day results as follow:

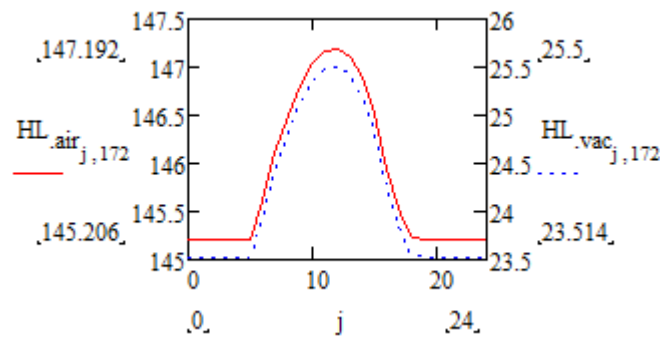


Figure 7. 13 Values of Heat Losses in air and vacuum condition for AL2 mirror

### 7.5.3 Polymeric film mirrors

For the polymeric film mirror with a SWSR of 89.59% we obtained:

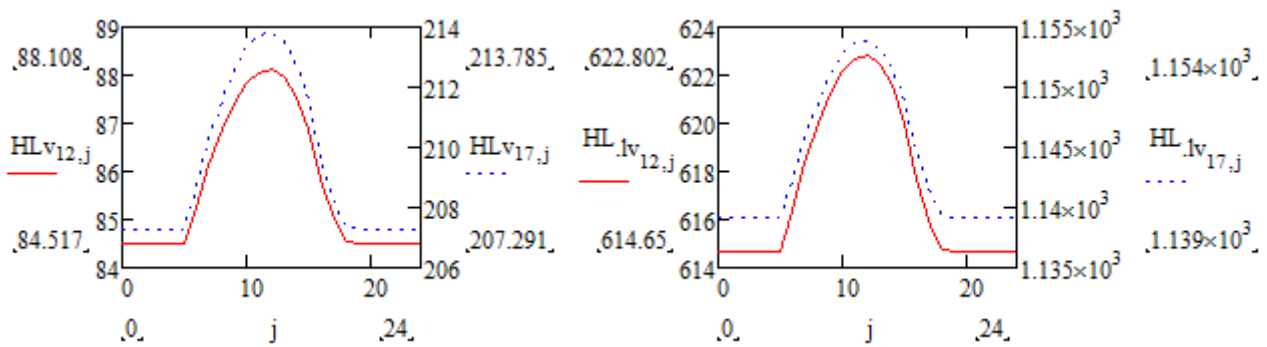


Figure 7. 14 Variation of Heat losses for PF1 reflectance value at 290°C=(12,j) and at 390°C=(17,j) in vacuum and lost vacuum condition

Integrating between  $T_{collin}$  (290°C) and  $T_{collout}$  (390°C) the above equation the values of the Heat losses in the case of the 172<sup>th</sup> day during the day results as follow:

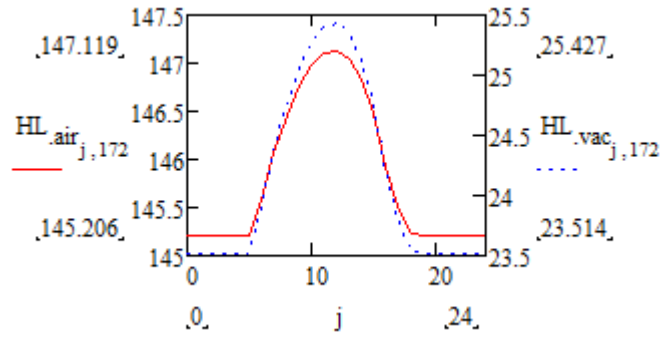


Figure 7. 15 Values of Heat Losses in air and vacuum condition for PF1 mirror

For the second polymeric mirror with a SWSR of 88.30% we obtained the following results:

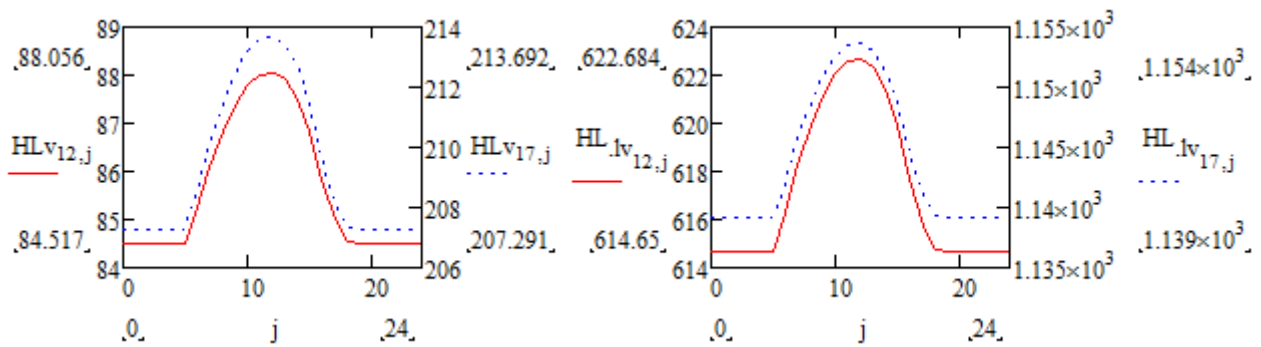


Figure 7. 16 Variation of Heat losses for PF2 reflectance value at 290°C=(12,j) and at 390°C=(17,j) in vacuum and lost vacuum condition

Integrating between Tcollin (290°C) and Tcollout (390°C) the above equation the values of the Heat losses in the case of the 172<sup>th</sup> day during the day results as follow:

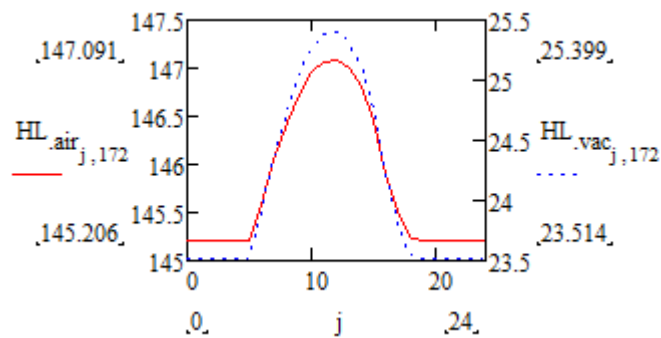


Figure 7. 17 Values of Heat Losses in air and vacuum condition for PF2 mirror

## 7.6 Results

Here in the following will be discussed the results obtained on the total heat gain of the HTF during an operational day, as mentioned before the 172<sup>th</sup> day has been taken into account.

In the following figures are described the direct normal irradiance hitting the site during the 172<sup>th</sup> day, then the solar irradiance collected by HCE after the correction of the losses described in chapter 6 above when the reflectivity calculated with the spectrophotometer has been used to evaluate the optical efficiency.

The last two curves describe the behavior of the solar irradiance collected by the HCE after the evaluation of the losses described in this chapter in the case of vacuum or lost vacuum condition.

### 7.6.1 Thin glass

The SWSR for the thin glass TG1 is 93.27% that inserted in the balance to obtain the total irradiance absorbed by the HCE has given the following results in Wh/m<sup>2</sup> per year:

$$\sum_n \left( \sum_j Q_{\text{abs}_{j,n}} \right) = 8.054 \times 10^5 \text{ ■}$$

$$\sum_n \left( \sum_j Q_{\text{colltotair}_{j,n}} \right) = 4.017 \times 10^5 \text{ ■}$$

$$\sum_n \left( \sum_j Q_{\text{colltotvac}_{j,n}} \right) = 6.884 \times 10^5 \text{ ■}$$

During a year of operation with the values of DNI inputted, according to the next graph (fig. 7.18) behavior what can be collected considering only the losses due to the row shadowing the incident angle modifier and the end losses, are also considered the losses of efficiency of the mirrors and the HCE to achieve a value of  $Q_{\text{abs}}$ .  $8.054 \times 10^5$  Wh/m<sup>2</sup> per year.

To take into account also the condition of the air or the vacuum in the annulus the values respectively obtained are:  $6.884 \times 10^5$  Wh/m<sup>2</sup> per year and  $4.017 \times 10^5$  Wh/m<sup>2</sup> per year that correspond to a percentage of respectively 85.47% and 49.88% with a corresponding losses of respectively 14.53% and 50.12%.

All of the above data is calculated in the case of 0 m/s wind speed, so it is simple to forecast that the losses will increase more as the wind speed increase.

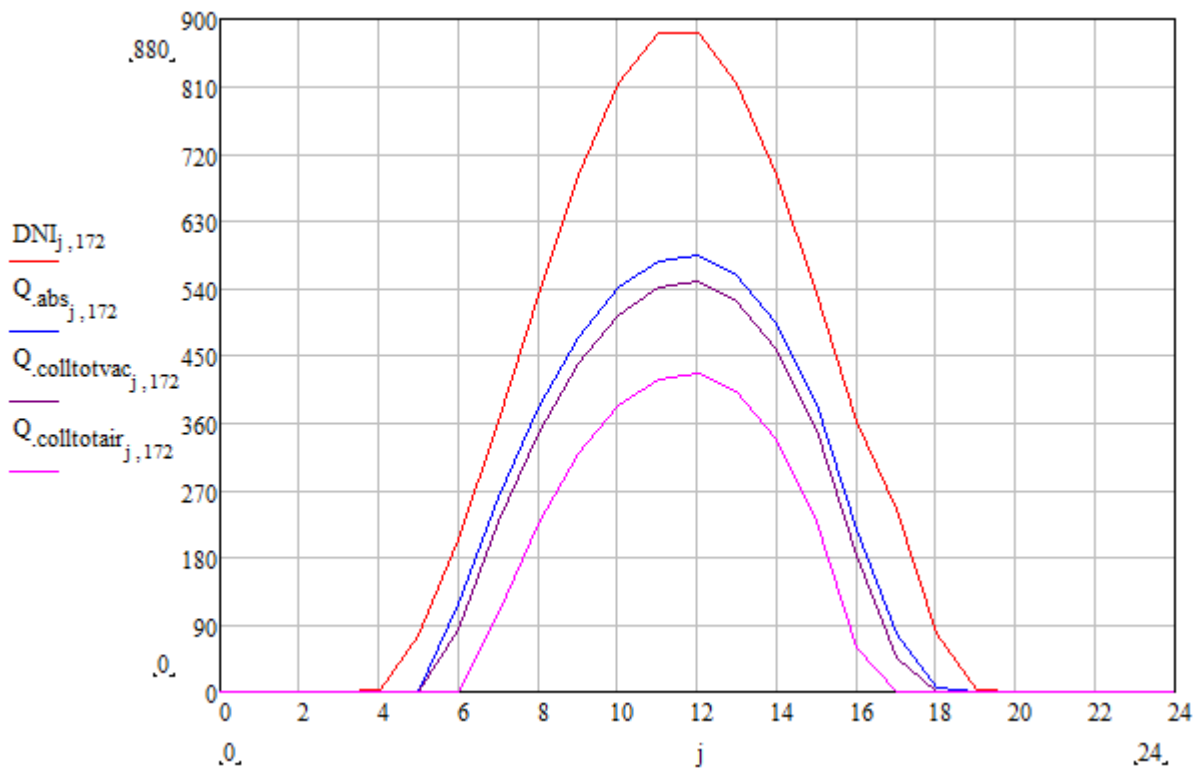


Figure 7.18 Value of total irradiance absorbed (Qabs), Total irradiance absorbed in vacuum condition (Qtotcollvac), Total irradiance absorbed in air condition (Qtotcollair) [W/m2] for the TG1 mirror

The mean value at the site of the wind speed is about 3.2 m/s calculated with a mean of the punctual values all over the year.

Were conducted calculations on different values of wind speed at different steps:

- 0.0 m/s
- 1.0 m/s
- 2.0 m/s
- 3.2 m/s
- 5.0 m/s

Here is reported the final graph to compare the results

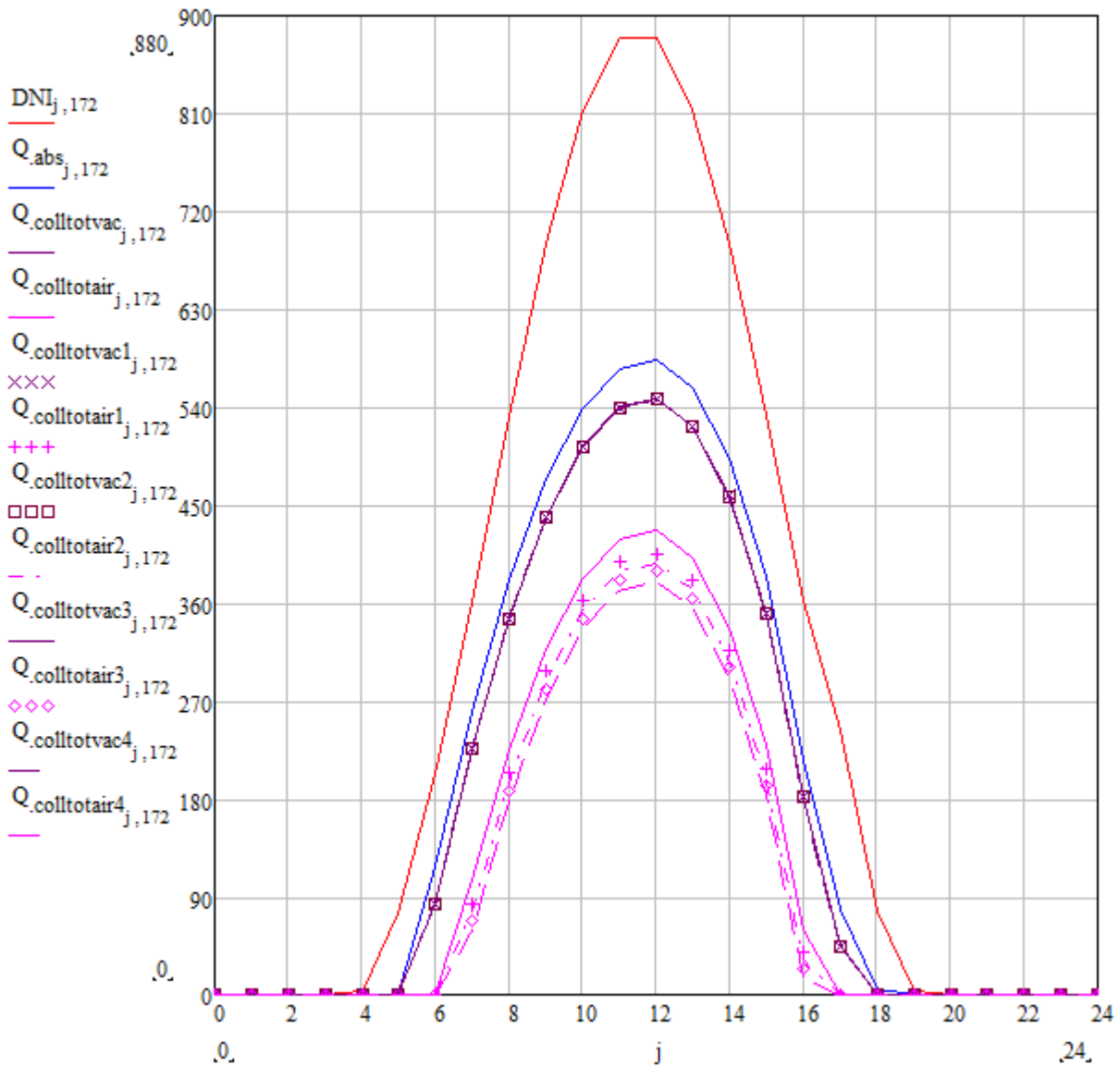


Figure 7. 19 Irradiance absorbed in different wind speed condition for the TG1 mirror

Where:

- $Q_{colltotvac}$  and  $Q_{colltotair}$  are referred to the 0.0 m/s value;
- $Q_{colltotvac1}$  and  $Q_{colltotair1}$  are referred to the 1.0 m/s value;
- $Q_{colltotvac2}$  and  $Q_{colltotair2}$  are referred to the 2.0 m/s value;
- $Q_{colltotvac3}$  and  $Q_{colltotair3}$  are referred to the 3.2 m/s value;
- $Q_{colltotvac4}$  and  $Q_{colltotair4}$  are referred to the 5.0 m/s value;

As it can be seen the increasing value of wind speed doesn't affect the calculation at the vacuum condition while there is a slightly decrease of total value of collected irradiance for what concern the air in annulus condition.

This behavior is highlighted in the next figures 7.20 and 7.21 (on the left is shown the vacuum condition while on the right is shown the air in annulus condition).

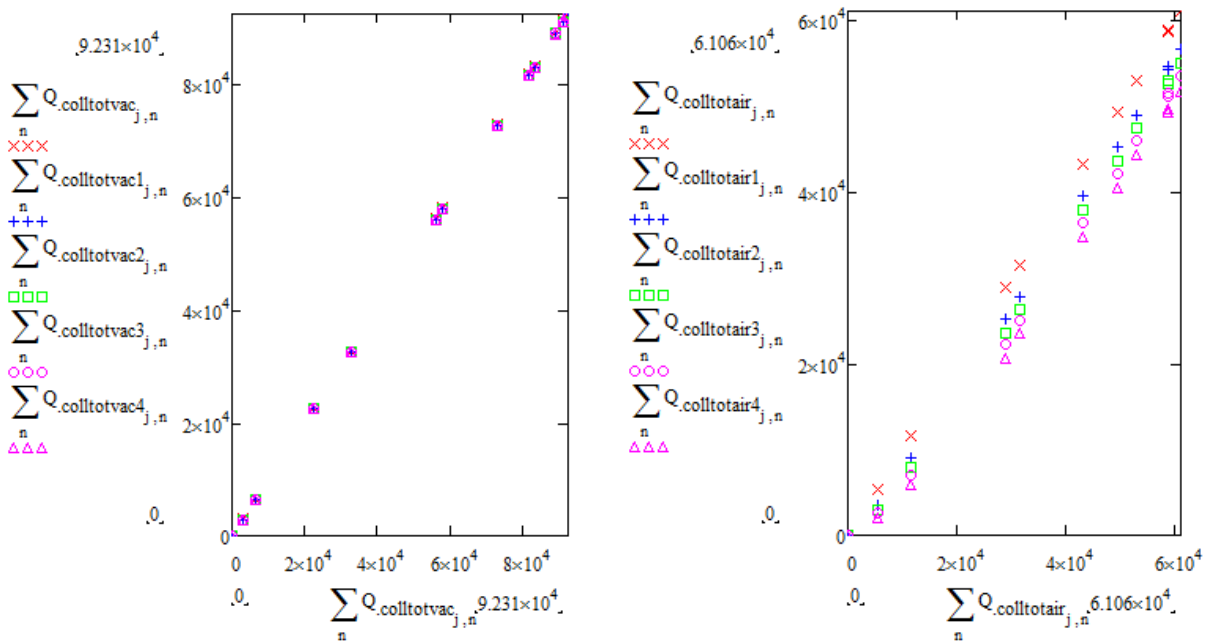


Figure 7. 20 Comparison along the year of the values of the 0.0 m/s wind speed and the different wind speed in vacuum and air condition for the TGI mirror

In all the four conditions shown above it is possible to obtain the value of the collected irradiance per year  $Wh/m^2$  per year.

$$\sum_n \left( \sum_j Q_{colltotair1_{j,n}} \right) = 3.648 \times 10^5 \text{ Wh/m}^2$$

$$\sum_n \left( \sum_j Q_{colltotvac1_{j,n}} \right) = 6.873 \times 10^5 \text{ Wh/m}^2$$

$$\sum_n \left( \sum_j Q_{colltotair2_{j,n}} \right) = 3.503 \times 10^5 \text{ Wh/m}^2$$

$$\sum_n \left( \sum_j Q_{\text{colltotvac}2_{j,n}} \right) = 6.868 \times 10^5 \text{ Wh/m}^2$$

$$\sum_n \left( \sum_j Q_{\text{colltotair}3_{j,n}} \right) = 3.374 \times 10^5 \text{ Wh/m}^2$$

$$\sum_n \left( \sum_j Q_{\text{colltotvac}3_{j,n}} \right) = 6.864 \times 10^5 \text{ Wh/m}^2$$

$$\sum_n \left( \sum_j Q_{\text{colltotair}4_{j,n}} \right) = 3.222 \times 10^5 \text{ Wh/m}^2$$

$$\sum_n \left( \sum_j Q_{\text{colltotvac}4_{j,n}} \right) = 6.858 \times 10^5 \text{ Wh/m}^2$$

In the next figure 7.21 is described a comparison between the two different conditions (air or vacuum in annulus) as the wind speed increases.

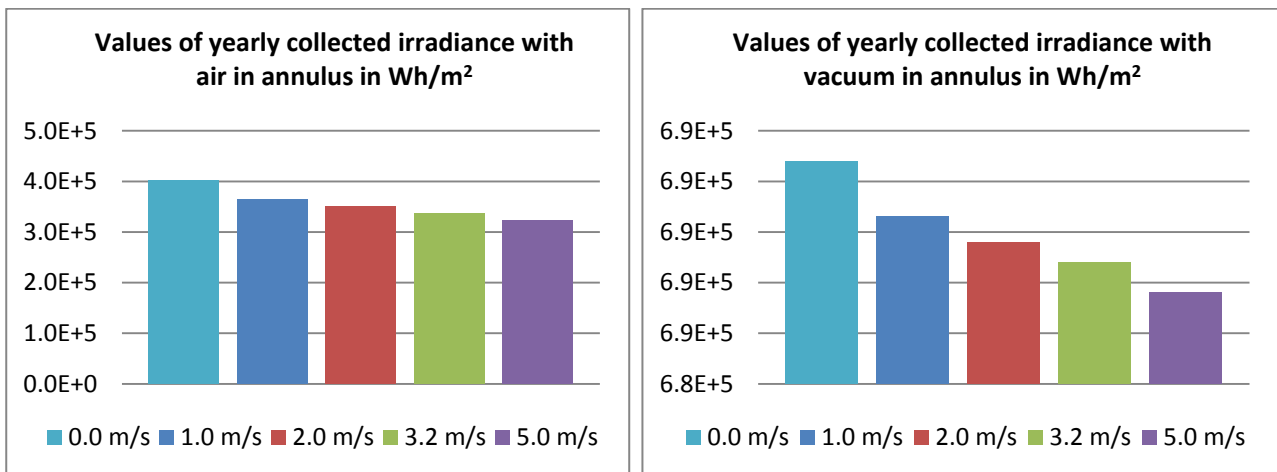


Figure 7. 21 Values of yearly collected irradiance at different wind speed and in air or vacuum condition

Making a comparison (in vacuum annulus case) between the initial condition 0.0 m/s and the 5.0 m/s wind speed case the falling of performance is evaluated in the order of -0.38%

While in the case of air in annulus the same comparison leads to a falling of performance evaluated in the order of -19.79%.

For the TG2 mirror we used its SWSR of 91.96%% that inserted in the balance to obtain the total irradiance absorbed by the HCE has given the following results in W/m<sup>2</sup> per year:

$$\sum_n \left( \sum_j Q_{\text{abs}_{j,n}} \right) = 7.941 \times 10^5 \text{ ■}$$

$$\sum_n \left( \sum_j Q_{\text{colltotair}_{j,n}} \right) = 3.92 \times 10^5 \text{ ■}$$

$$\sum_n \left( \sum_j Q_{\text{colltotvac}_{j,n}} \right) = 6.773 \times 10^5 \text{ ■}$$

During a year of operation with the values of DNI inputted, according to the next graph behavior what can be collected considering only the losses due to the row shadowing the incident angle modifier and the end losses, are also considered the losses of efficiency of the mirrors and the HCE to achieve a value of  $Q_{\text{abs}}$ .  $7.941 \times 10^5 \text{ Wh/m}^2$  per year.

To take into account also the condition of the air or the vacuum in the annulus the values respectively obtained are:  $6.773 \times 10^5 \text{ Wh/m}^2$  per year and  $3.92 \times 10^5 \text{ Wh/m}^2$  per year that correspond to a percentage of respectively 85.29% and 49.36% with corresponding losses of respectively 14.71% and 50.64%.

All of the above data is calculated in the case of 0 m/s wind speed, so it is simple to forecast that the losses will increase more as the wind speed increase.

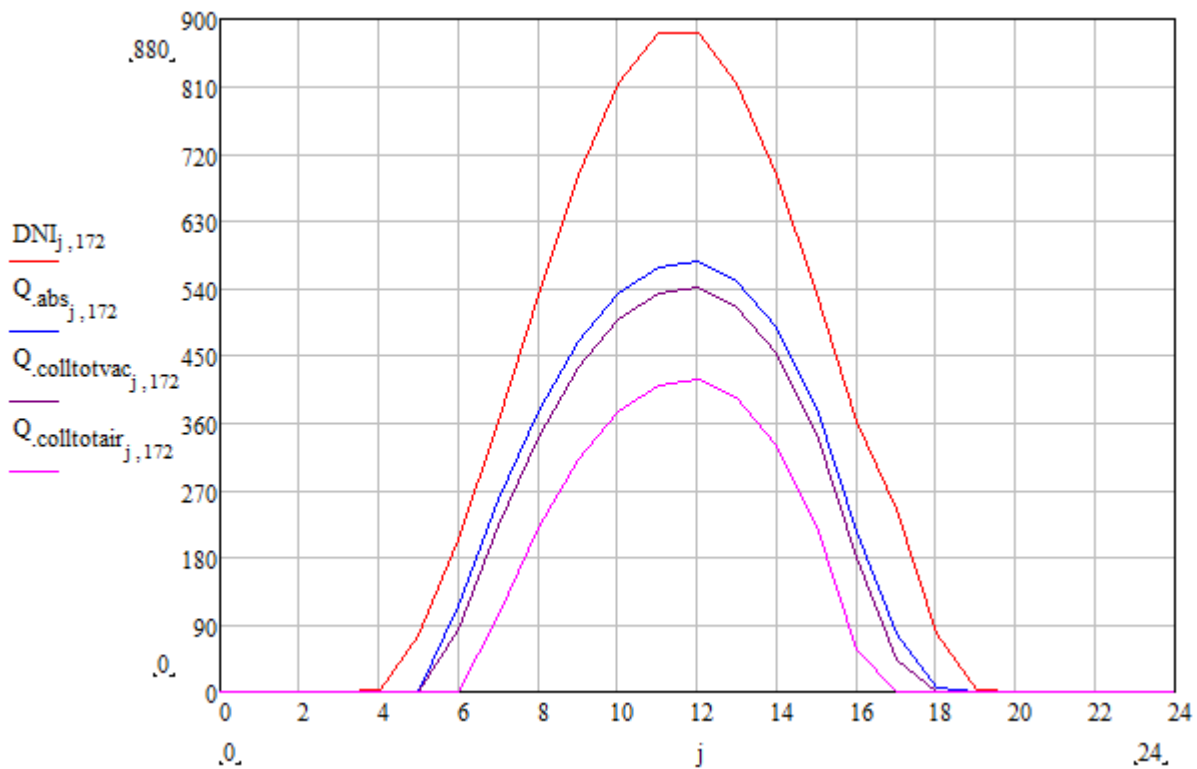


Figure 7.22 Value of total irradiance absorbed ( $Q_{abs}$ ), Total irradiance absorbed in vacuum condition ( $Q_{totcollvac}$ ), Total irradiance absorbed in air condition ( $Q_{totcollair}$ ) [W/m<sup>2</sup>] for the TG2 mirror

The mean value at the site of the wind speed is about 3.2 m/s calculated with a mean of the punctual values all over the year.

Were conducted calculations on different values of wind speed at different steps:

- 0.0 m/s
- 1.0 m/s
- 2.0 m/s
- 3.2 m/s
- 5.0 m/s

Here is reported the final graph 7.23 to compare the results

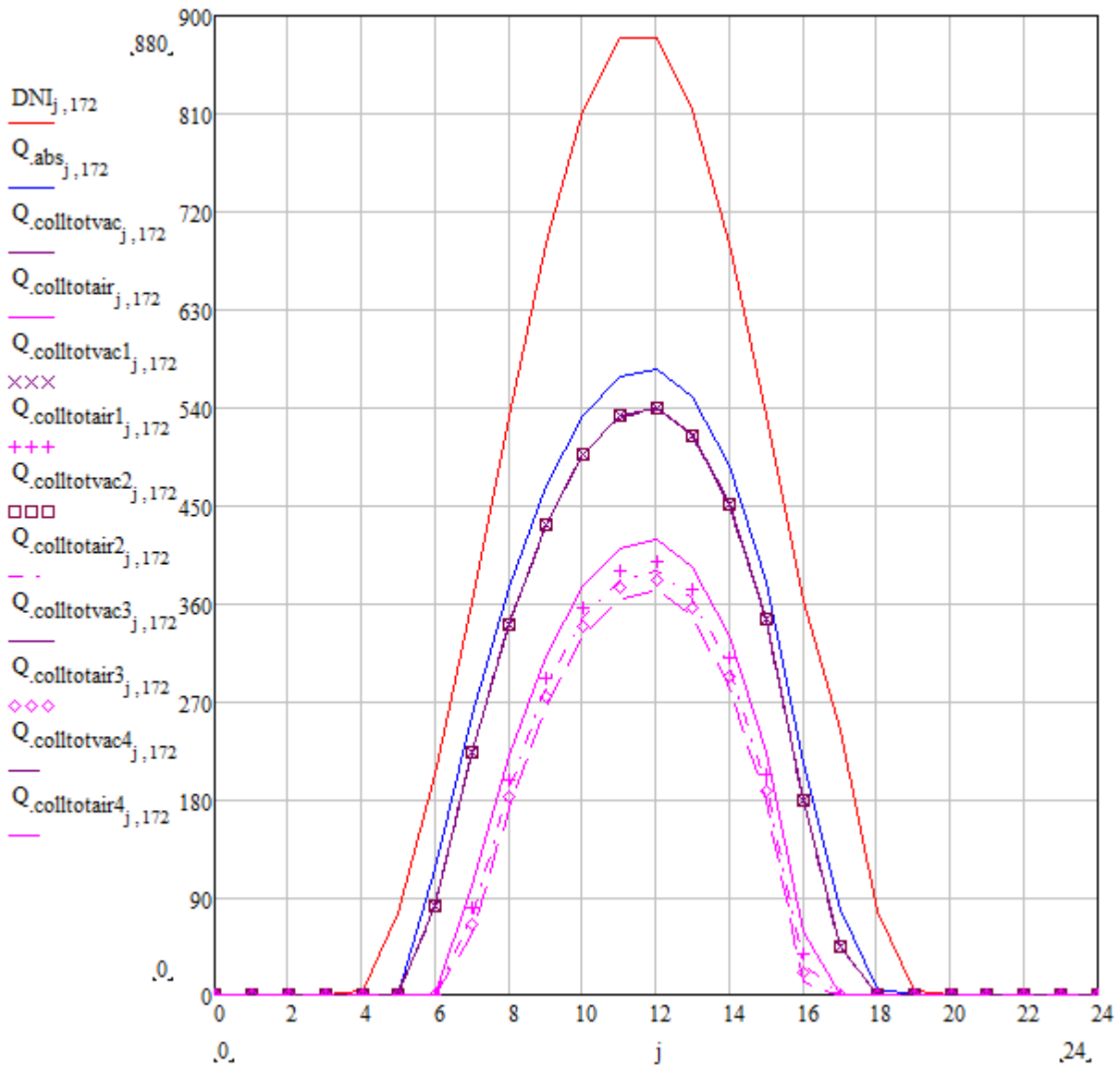


Figure 7. 23 Irradiance absorbed in different wind speed condition for the TG2 mirror

Where:

- $Q_{colltotvac}$  and  $Q_{colltotair}$  are referred to the 0.0 m/s value;
- $Q_{colltotvac1}$  and  $Q_{colltotair1}$  are referred to the 1.0 m/s value;
- $Q_{colltotvac2}$  and  $Q_{colltotair2}$  are referred to the 2.0 m/s value;
- $Q_{colltotvac3}$  and  $Q_{colltotair3}$  are referred to the 3.2 m/s value;
- $Q_{colltotvac4}$  and  $Q_{colltotair4}$  are referred to the 5.0 m/s value;

As it can be seen the increasing value of wind speed doesn't affect the calculation at the vacuum condition while there is a slightly decrease of total value of collected irradiance for what concern the air in annulus condition.

This behavior is highlighted in the next graph 7.24 (on the left is shown the vacuum condition while on the right is shown the air in annulus condition).

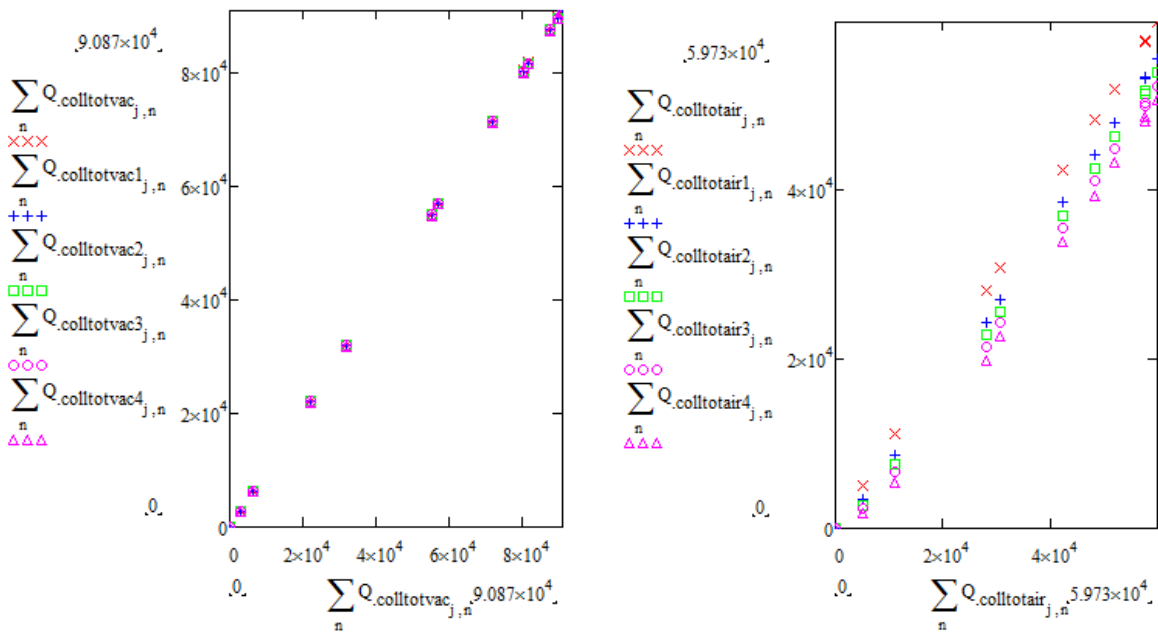


Figure 7. 24 Comparison along the year of the values of the 0.0 m/s wind speed and the different wind speed in vacuum and air condition for the TG2 mirror

In all the four conditions shown above is possible to obtain the value of the collected irradiance per year  $Wh/m^2$  per year.

$$\sum_n \left( \sum_j Q_{colltotair_{j,n}} \right) = 3.555 \times 10^5 \text{ ■}$$

$$\sum_n \left( \sum_j Q_{colltotvac_{j,n}} \right) = 6.762 \times 10^5 \text{ ■}$$

$$\sum_n \left( \sum_j Q_{colltotair_{j,n}} \right) = 3.41 \times 10^5 \text{ ■}$$

$$\sum_n \left( \sum_j Q_{\text{colltotvac}2_{j,n}} \right) = 6.757 \times 10^5 \text{ Wh/m}^2$$

$$\sum_n \left( \sum_j Q_{\text{colltotair}3_{j,n}} \right) = 3.282 \times 10^5 \text{ Wh/m}^2$$

$$\sum_n \left( \sum_j Q_{\text{colltotvac}3_{j,n}} \right) = 6.753 \times 10^5 \text{ Wh/m}^2$$

$$\sum_n \left( \sum_j Q_{\text{colltotair}4_{j,n}} \right) = 3.131 \times 10^5 \text{ Wh/m}^2$$

$$\sum_n \left( \sum_j Q_{\text{colltotvac}4_{j,n}} \right) = 6.748 \times 10^5 \text{ Wh/m}^2$$

In the next figure 7.25 is described a comparison between the two different condition (air or vacuum in annulus) as the wind speed increases.

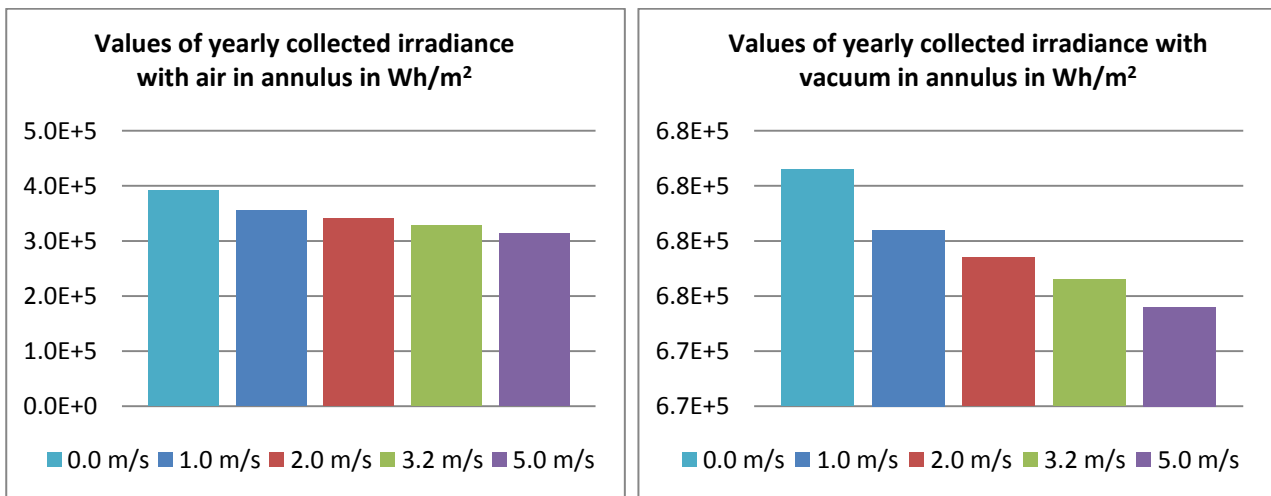


Figure 7. 25 Values of yearly collected irradiance at different wind speed and in air or vacuum condition

Making a comparison (in vacuum annulus case) between the initial condition 0.0 m/s and the 5.0 m/s wind speed case the falling of performance is evaluated in the order of -0.37%

While in the case of air in annulus the same comparison leads to a falling of performance evaluated in the order of -20.13%.

## 7.6.2 Aluminum mirrors

The SWSR for the thin glass Al1 is 86.55% that inserted in the balance to obtain the total irradiance absorbed by the HCE has given the following results in Wh/m<sup>2</sup> per year:

$$\sum_n \left( \sum_j Q_{\text{abs};j,n} \right) = 7.474 \times 10^5 \text{ Wh/m}^2$$

$$\sum_n \left( \sum_j Q_{\text{colltotair};j,n} \right) = 3.525 \times 10^5 \text{ Wh/m}^2$$

$$\sum_n \left( \sum_j Q_{\text{colltotvac};j,n} \right) = 6.315 \times 10^5 \text{ Wh/m}^2$$

During a year of operation with the values of DNI inputted, according to the next graph behavior what can be collected considering only the losses due to the row shadowing the incident angle modifier and the end losses, are also considered the losses of efficiency of the mirrors and the HCE to achieve a value of  $Q_{\text{abs}}$ .  $7.474 \times 10^5$  Wh/m<sup>2</sup> per year.

To take into account also the condition of the air or the vacuum in the annulus the values respectively obtained are:  $6.315 \times 10^5$  Wh/m<sup>2</sup> per year and  $3.525 \times 10^5$  Wh/m<sup>2</sup> per year that correspond to a percentage of respectively 84.49% and 47.16% with corresponding losses of respectively 15.51% and 52.84%.

All of the above data is calculated in the case of 0 m/s wind speed, so it is simple to forecast that the losses will increase more as the wind speed increase.

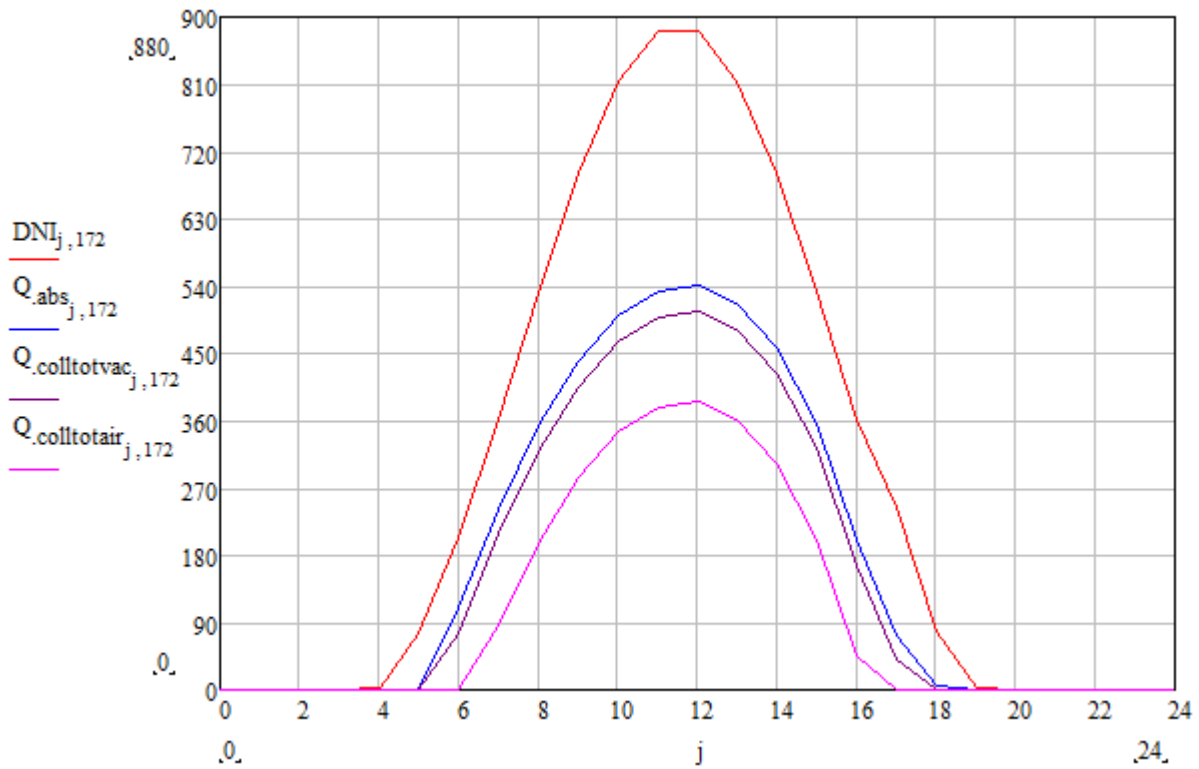


Figure 7.26 Value of total irradiance absorbed ( $Q_{abs}$ ), Total irradiance absorbed in vacuum condition ( $Q_{totcollvac}$ ), Total irradiance absorbed in air condition ( $Q_{totcollair}$ ) [ $W/m^2$ ] for the AL1 mirror

The mean value at the site of the wind speed is about 3.2 m/s calculated with a mean of the punctual values all over the year.

Were conducted calculations on different values of wind speed at different steps:

- 0.0 m/s
- 1.0 m/s
- 2.0 m/s
- 3.2 m/s
- 5.0 m/s

Here is reported the final graph to compare the results

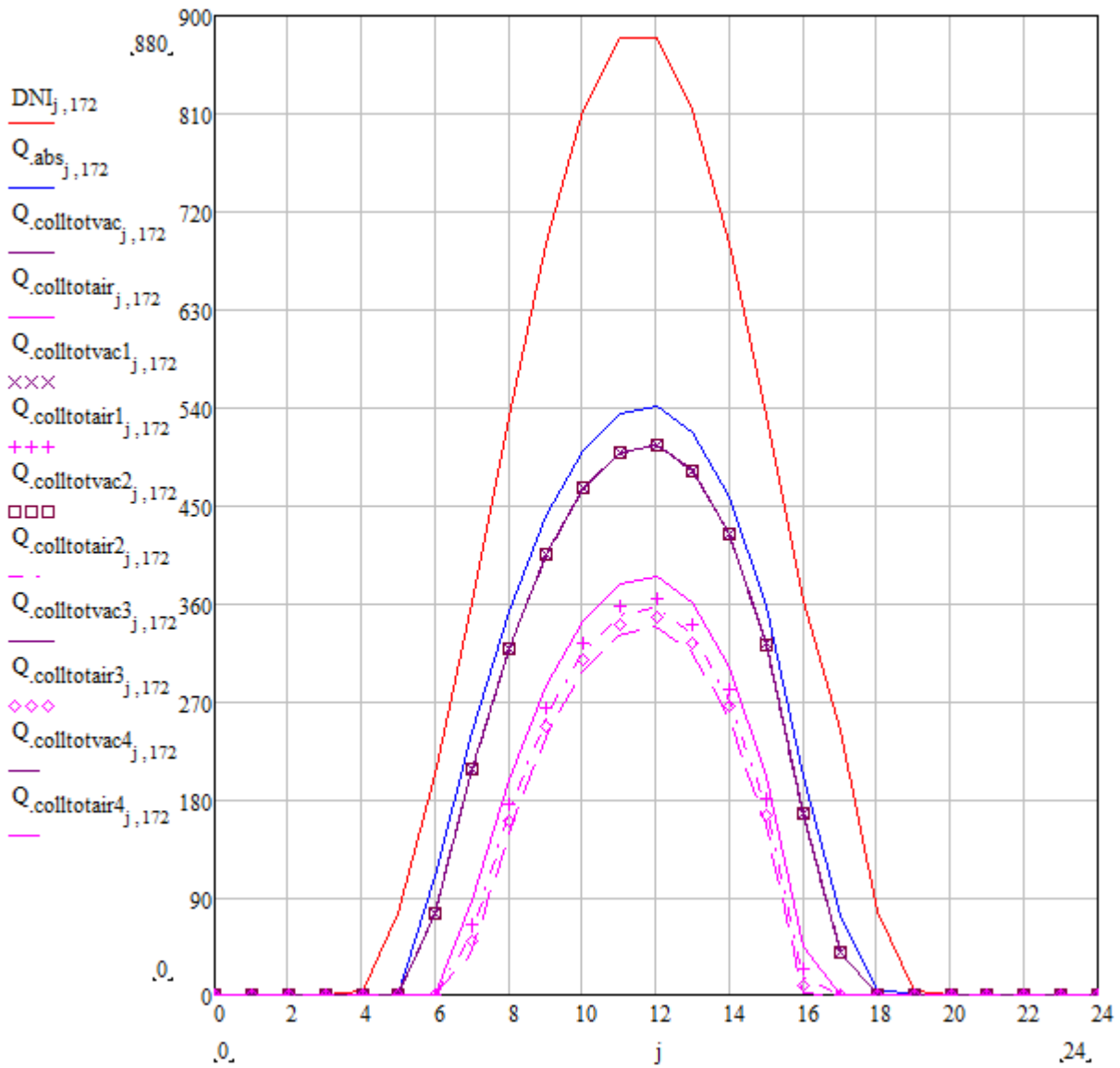


Figure 7. 27 Irradiance absorbed in different wind speed condition for the AL1 mirror

Where:

- $Q_{colltotvac}$  and  $Q_{colltotair}$  are referred to the 0.0 m/s value;
- $Q_{colltotvac1}$  and  $Q_{colltotair1}$  are referred to the 1.0 m/s value;
- $Q_{colltotvac2}$  and  $Q_{colltotair2}$  are referred to the 2.0 m/s value;
- $Q_{colltotvac3}$  and  $Q_{colltotair3}$  are referred to the 3.2 m/s value;
- $Q_{colltotvac4}$  and  $Q_{colltotair4}$  are referred to the 5.0 m/s value;

As it can be seen the increasing value of wind speed doesn't affect the calculation at the vacuum condition while there is a slightly decrease of total value of collected irradiance for what concern the air in annulus condition.

This behavior is highlighted in the next graph (on the left is shown the vacuum condition while on the right is shown the air in annulus condition).

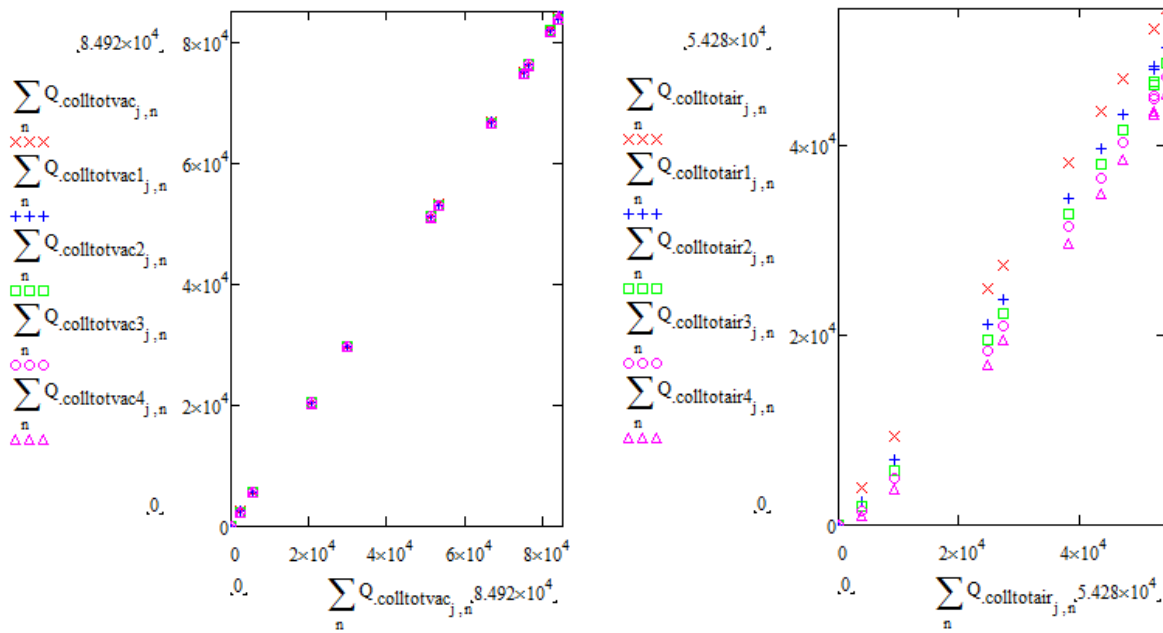


Figure 7. 28 Comparison along the year of the values of the 0.0 m/s wind speed and the different wind speed in vacuum and air condition for the AL1 mirror

In all the four conditions shown above is possible to obtain the value of the collected irradiance per year  $\text{Wh/m}^2$  per year.

$$\sum_n \left( \sum_j Q_{\text{colltotair}1,j,n} \right) = 3.171 \times 10^5 \text{ ■}$$

$$\sum_n \left( \sum_j Q_{\text{colltotvac}1,j,n} \right) = 6.304 \times 10^5 \text{ ■}$$

$$\sum_n \left( \sum_j Q_{\text{colltotair}2,j,n} \right) = 3.031 \times 10^5 \text{ ■}$$

$$\sum_n \left( \sum_j Q_{\text{colltotvac}2,j,n} \right) = 6.299 \times 10^5 \text{ ■}$$

$$\sum_n \left( \sum_j Q_{\text{colltotair}3_{j,n}} \right) = 2.906 \times 10^5 \text{ Wh/m}^2$$

$$\sum_n \left( \sum_j Q_{\text{colltotvac}3_{j,n}} \right) = 6.295 \times 10^5 \text{ Wh/m}^2$$

$$\sum_n \left( \sum_j Q_{\text{colltotair}4_{j,n}} \right) = 2.761 \times 10^5 \text{ Wh/m}^2$$

$$\sum_n \left( \sum_j Q_{\text{colltotvac}4_{j,n}} \right) = 6.29 \times 10^5 \text{ Wh/m}^2$$

In the next figure 7.29 is described a comparison between the two different conditions (air or vacuum in annulus) as the wind speed increases.

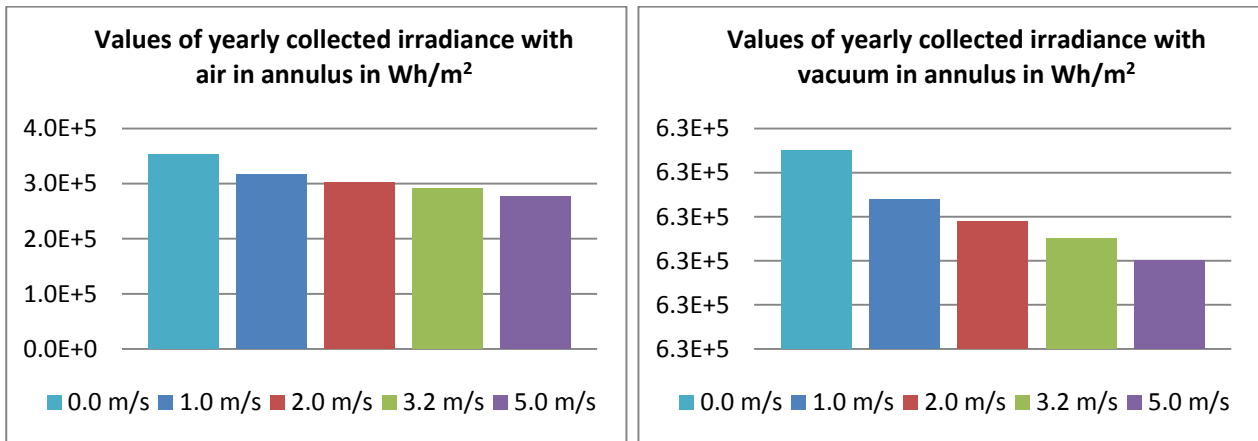


Figure 7. 29 Values of yearly collected irradiance at different wind speed and in air or vacuum condition

Making a comparison (in vacuum annulus case) between the initial condition 0.0 m/s and the 5.0 m/s wind speed case the falling of performance is evaluated in the order of -0.40%

While in the case of air in annulus the same comparison leads to a falling of performance evaluated in the order of -21.67%.

For the AL2 mirror we used its SWSR of 93.02% that inserted in the balance to obtain the total irradiance absorbed by the HCE has given the following results in Wh/m<sup>2</sup> per year:

$$\sum_n \left( \sum_j Q_{\text{abs}_{j,n}} \right) = 8.032 \times 10^5 \text{ Wh/m}^2$$

$$\sum_n \left( \sum_j Q_{\text{colltotair},j,n} \right) = 3.998 \times 10^5 \text{ Wh/m}^2$$

$$\sum_n \left( \sum_j Q_{\text{colltotvac},j,n} \right) = 6.863 \times 10^5 \text{ Wh/m}^2$$

During a year of operation with the values of DNI inputted, according to the next graph behavior what can be collected considering only the losses due to the row shadowing the incident angle modifier and the end losses, are also considered the losses of efficiency of the mirrors and the HCE to achieve a value of  $Q_{\text{abs.}} 8.032 \times 10^5 \text{ Wh/m}^2$  per year.

To take into account also the condition of the air or the vacuum in the annulus the values respectively obtained are:  $6.863 \times 10^5 \text{ Wh/m}^2$  per year and  $3.998 \times 10^5 \text{ Wh/m}^2$  per year that correspond to a percentage of respectively 85.45% and 49.78% with corresponding losses of respectively 14.55% and 50.22%.

All of the above data are calculated in the case of 0 m/s wind speed, so it is simple to forecast that the losses will increase more as the wind speed increase.

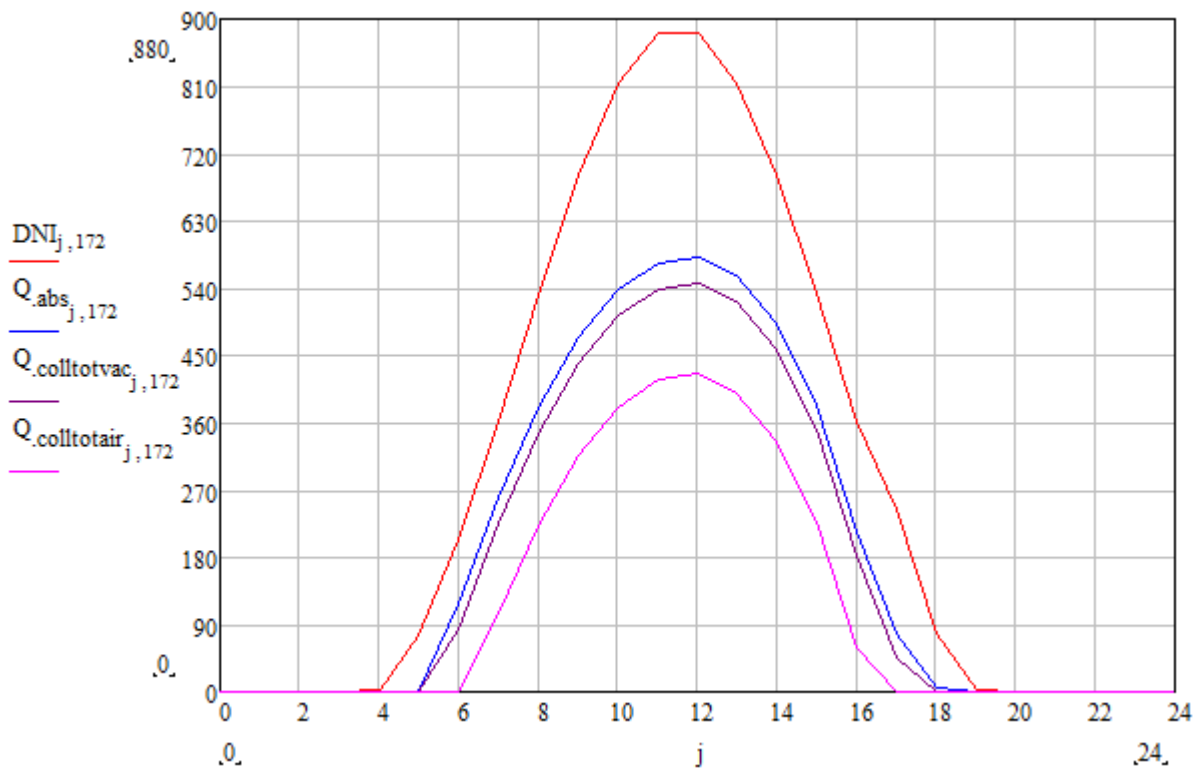


Figure 7.30 Value of total irradiance absorbed ( $Q_{abs}$ ), Total irradiance absorbed in vacuum condition ( $Q_{totcollvac}$ ), Total irradiance absorbed in air condition ( $Q_{totcollair}$ ) [W/m<sup>2</sup>] for the AL2 mirror

The mean value at the site of the wind speed is about 3.2 m/s calculated with a mean of the punctual values all over the year.

Were conducted calculations on different values of wind speed at different steps:

- 0.0 m/s
- 1.0 m/s
- 2.0 m/s
- 3.2 m/s
- 5.0 m/s

Here is reported the final graph to compare the results

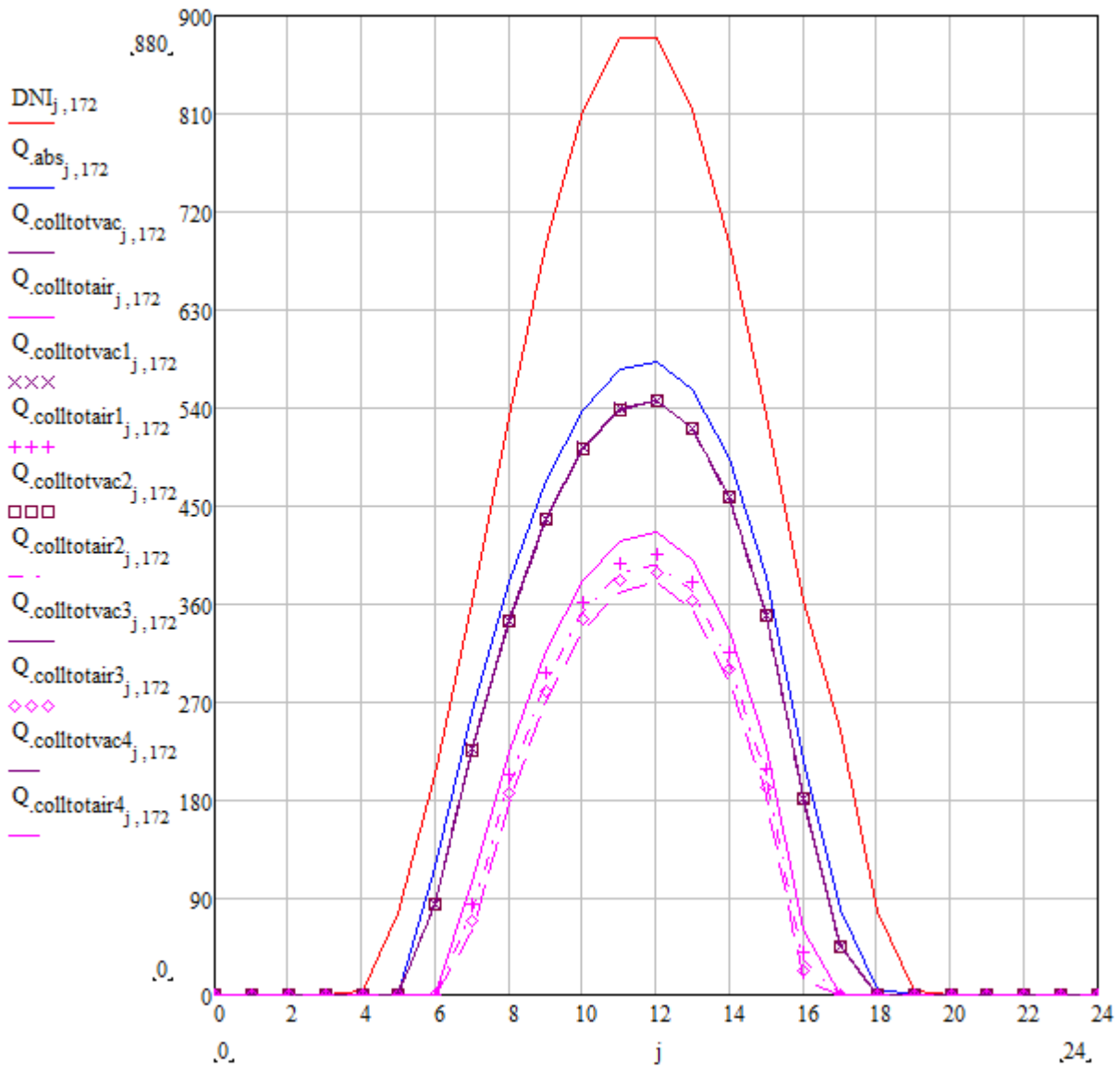


Figure 7. 31 Irradiance absorbed in different wind speed condition for the AL2 mirror

Where:

- $Q_{colltotvac}$  and  $Q_{colltotair}$  are referred to the 0.0 m/s value;
- $Q_{colltotvac1}$  and  $Q_{colltotair1}$  are referred to the 1.0 m/s value;
- $Q_{colltotvac2}$  and  $Q_{colltotair2}$  are referred to the 2.0 m/s value;
- $Q_{colltotvac3}$  and  $Q_{colltotair3}$  are referred to the 3.2 m/s value;
- $Q_{colltotvac4}$  and  $Q_{colltotair4}$  are referred to the 5.0 m/s value;

As it can be seen the increasing value of wind speed doesn't affect the calculation at the vacuum condition while there is a slightly decrease of total value of collected irradiance for what concern the air in annulus condition.

This behavior is highlighted in the next graph (on the left is shown the vacuum condition while on the right is shown the air in annulus condition).

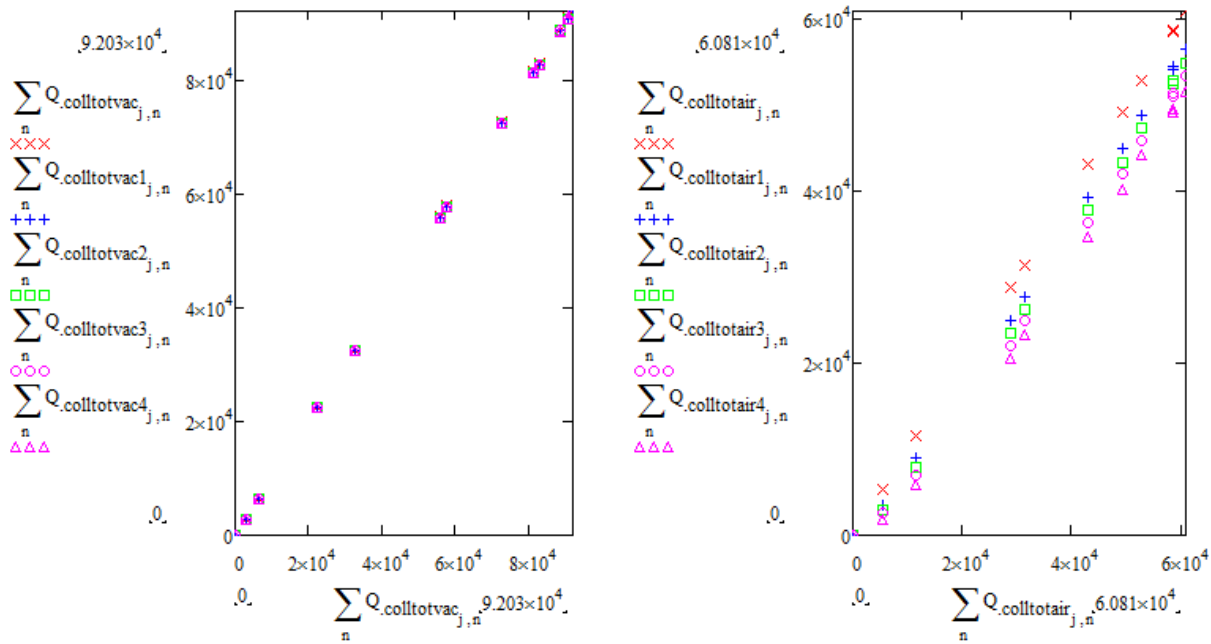


Figure 7.32 Comparison along the year of the values of the 0.0 m/s wind speed and the different wind speed in vacuum and air condition for the AL2 mirror

In all the four conditions shown above is possible to obtain the value of the collected irradiance per year  $\text{Wh/m}^2$  per year.

$$\sum_n \left( \sum_j Q_{\text{colltotair}1,j,n} \right) = 3.63 \times 10^5 \text{ ■}$$

$$\sum_n \left( \sum_j Q_{\text{colltotvac}1,j,n} \right) = 6.852 \times 10^5 \text{ ■}$$

$$\sum_n \left( \sum_j Q_{\text{colltotair}2,j,n} \right) = 3.485 \times 10^5 \text{ ■}$$

$$\sum_n \left( \sum_j Q_{\text{colltotvac}2_{j,n}} \right) = 6.847 \times 10^5 \text{ Wh/m}^2$$

$$\sum_n \left( \sum_j Q_{\text{colltotair}3_{j,n}} \right) = 3.356 \times 10^5 \text{ Wh/m}^2$$

$$\sum_n \left( \sum_j Q_{\text{colltotvac}3_{j,n}} \right) = 6.842 \times 10^5 \text{ Wh/m}^2$$

$$\sum_n \left( \sum_j Q_{\text{colltotair}4_{j,n}} \right) = 3.205 \times 10^5 \text{ Wh/m}^2$$

$$\sum_n \left( \sum_j Q_{\text{colltotvac}4_{j,n}} \right) = 6.837 \times 10^5 \text{ Wh/m}^2$$

In the next figure is described a comparison between the two different conditions (air or vacuum in annulus) as the wind speed increases.

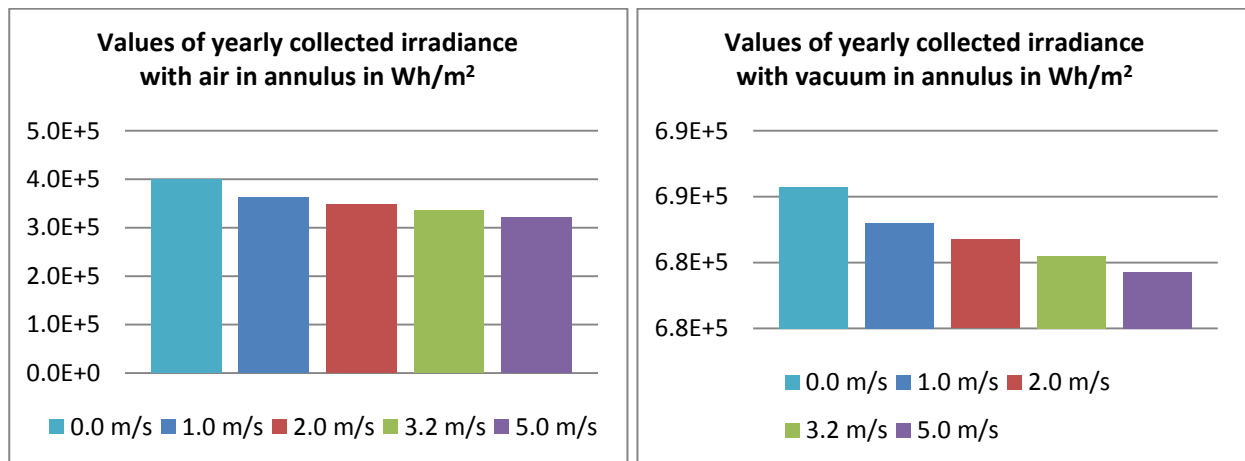


Figure 7. 33 Values of yearly collected irradiance at different wind speed and in air or vacuum condition

Making a comparison (in vacuum annulus case) between the initial condition 0.0 m/s and the 5.0 m/s wind speed case the falling of performance is evaluated in the order of -0.38%

While in the case of air in annulus the same comparison leads to a falling of performance evaluated in the order of -19.83%.

### 7.6.3 Polymeric film mirror

The SWSR for the thin glass A11 is 89.59% that inserted in the balance to obtain the total irradiance absorbed by the HCE has given the following results in Wh/m<sup>2</sup> per year:

$$\sum_n \left( \sum_j Q_{\text{abs}_{j,n}} \right) = 7.736 \times 10^5 \text{ Wh/m}^2$$

$$\sum_n \left( \sum_j Q_{\text{colltotair}_{j,n}} \right) = 3.746 \times 10^5 \text{ Wh/m}^2$$

$$\sum_n \left( \sum_j Q_{\text{colltotvac}_{j,n}} \right) = 6.573 \times 10^5 \text{ Wh/m}^2$$

During a year of operations with the values of DNI inputted, according to the next graph behavior what can be collected considering only the losses due to the row shadowing the incident angle modifier and the end losses, are also considered the losses of efficiency of the mirrors and the HCE to achieve a value of  $Q_{\text{abs}}$ .  $7.736 \times 10^5$  Wh/m<sup>2</sup> per year.

To take into account also the condition of the air or the vacuum in the annulus the values respectively obtained are:  $6.573 \times 10^5$  Wh/m<sup>2</sup> per year and  $3.746 \times 10^5$  Wh/m<sup>2</sup> per year that correspond to a percentage of respectively 84.97% and 48.42% with corresponding losses of respectively 15.03% and 51.58%.

All of the above data are calculated in the case of 0 m/s wind speed, so it is simple to forecast that the losses will increase more as the wind speed increase.

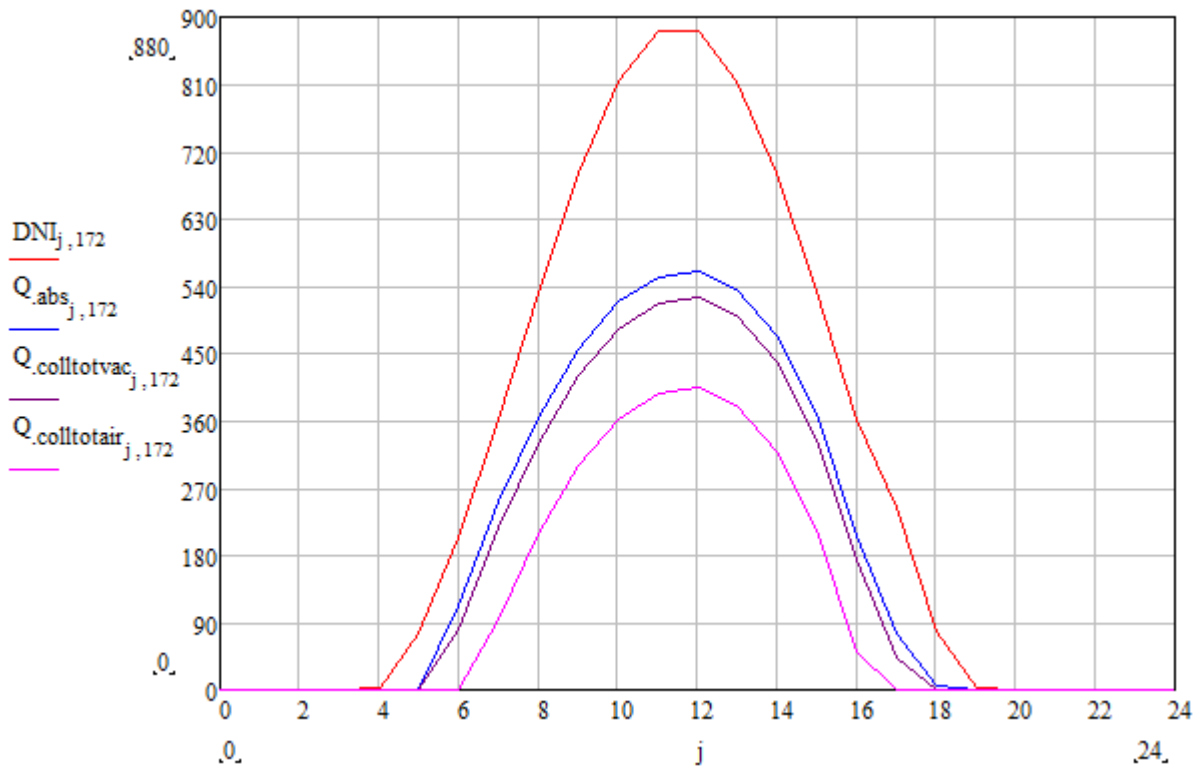


Figure 7.34 Value of total irradiance absorbed ( $Q_{abs}$ ), Total irradiance absorbed in vacuum condition ( $Q_{totcollvac}$ ), Total irradiance absorbed in air condition ( $Q_{totcollair}$ ) [ $W/m^2$ ] for the PF1 mirror

The mean value at the site of the wind speed is about 3.2 m/s calculated with a mean of the punctual values all over the year.

Were conducted calculations on different values of wind speed at different steps:

- 0.0 m/s
- 1.0 m/s
- 2.0 m/s
- 3.2 m/s
- 5.0 m/s

Here is reported the final graph to compare the results

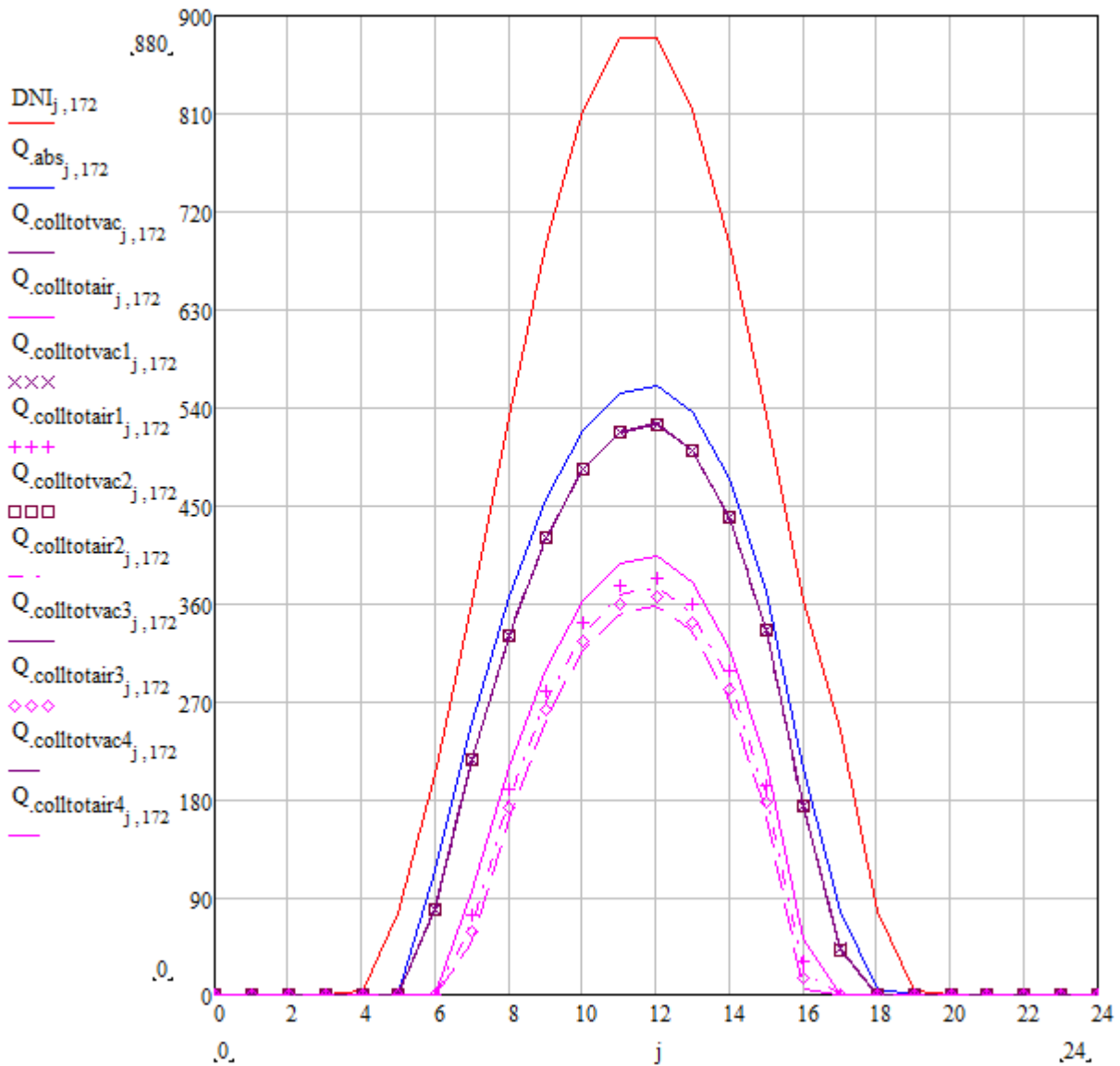


Figure 7. 35 Irradiance absorbed in different wind speed condition for the PF1 mirror

Where:

- $Q_{colltotvac}$  and  $Q_{colltotair}$  are referred to the 0.0 m/s value;
- $Q_{colltotvac1}$  and  $Q_{colltotair1}$  are referred to the 1.0 m/s value;
- $Q_{colltotvac2}$  and  $Q_{colltotair2}$  are referred to the 2.0 m/s value;
- $Q_{colltotvac3}$  and  $Q_{colltotair3}$  are referred to the 3.2 m/s value;
- $Q_{colltotvac4}$  and  $Q_{colltotair4}$  are referred to the 5.0 m/s value;

As it can be seen the increasing value of wind speed doesn't affect the calculation at the vacuum condition while there is a slightly decrease of total value of collected irradiance for what concern the air in annulus condition.

This behavior is highlighted in the next graph (on the left is shown the vacuum condition while on the right is shown the air in annulus condition).

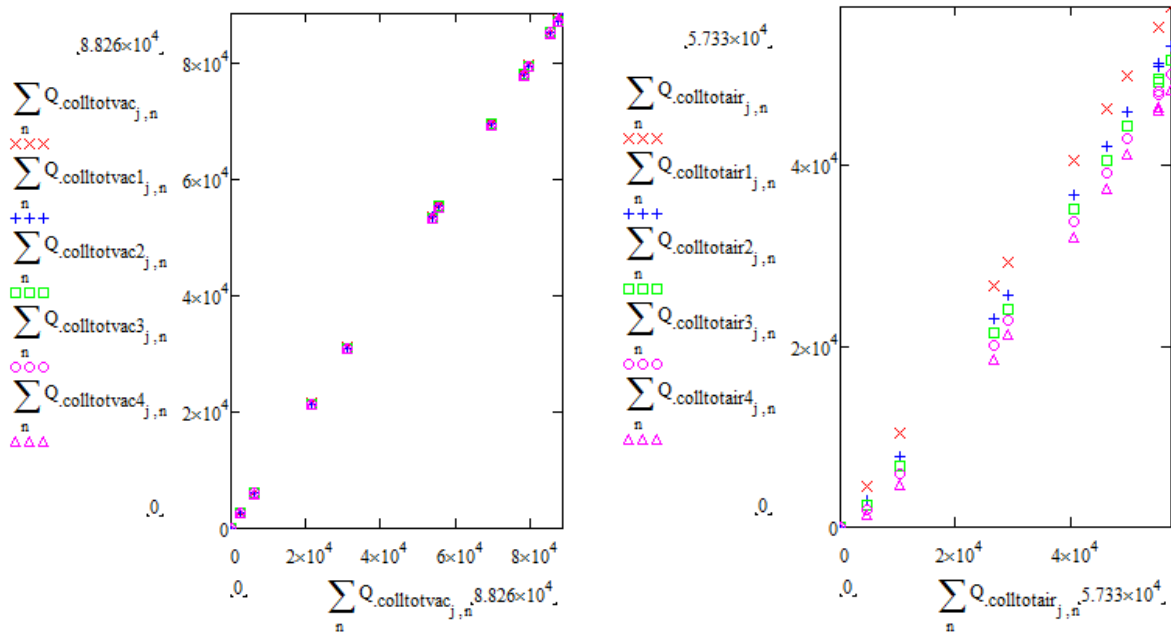


Figure 7.36 Comparison along the year of the values of the 0.0 m/s wind speed and the different wind speed in vacuum and air condition for the PF1 mirror

In all the four conditions shown above it is possible to obtain the value of the collected irradiance per year  $Wh/m^2$  per year.

$$\sum_n \left( \sum_j Q_{colltotair_{1j,n}} \right) = 3.386 \times 10^5 \text{ ■}$$

$$\sum_n \left( \sum_j Q_{colltotvac_{1j,n}} \right) = 6.561 \times 10^5 \text{ ■}$$

$$\sum_n \left( \sum_j Q_{colltotair_{2j,n}} \right) = 3.243 \times 10^5 \text{ ■}$$

$$\sum_n \left( \sum_j Q_{colltotvac_{2j,n}} \right) = 6.556 \times 10^5 \text{ ■}$$

$$\sum_n \left( \sum_j Q_{\text{colltotair}3_{j,n}} \right) = 3.116 \times 10^5 \text{ Wh/m}^2$$

$$\sum_n \left( \sum_j Q_{\text{colltotvac}3_{j,n}} \right) = 6.552 \times 10^5 \text{ Wh/m}^2$$

$$\sum_n \left( \sum_j Q_{\text{colltotair}4_{j,n}} \right) = 2.968 \times 10^5 \text{ Wh/m}^2$$

$$\sum_n \left( \sum_j Q_{\text{colltotvac}4_{j,n}} \right) = 6.547 \times 10^5 \text{ Wh/m}^2$$

In the next figure is described a comparison between the two different condition (air or vacuum in annulus) as the wind speed increases.

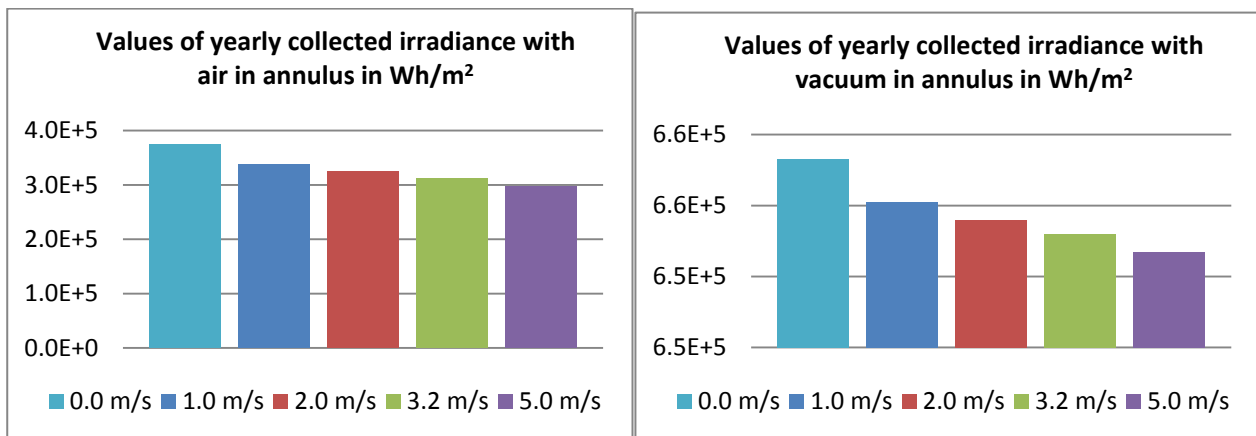


Figure 7.37 Values of yearly collected irradiance at different wind speed and in air or vacuum condition

Making a comparison (in vacuum annulus case) between the initial condition 0.0 m/s and the 5.0 m/s wind speed case the falling of performance is evaluated in the order of -0.40%

While in the case of air in annulus the same comparison leads to a falling of performance evaluated in the order of -20.77%.

For the PF2 mirror we used its SWSR of 88.30% that inserted in the balance to obtain the total irradiance absorbed by the HCE has given the following results in Wh/m² per year:

$$\sum_n \left( \sum_j Q_{\text{abs}_{j,n}} \right) = 7.625 \times 10^5 \text{ Wh/m}^2$$

$$\sum_n \left( \sum_j Q_{\text{colltotair},j,n} \right) = 3.652 \times 10^5 \text{ Wh/m}^2$$

$$\sum_n \left( \sum_j Q_{\text{colltotvac},j,n} \right) = 6.463 \times 10^5 \text{ Wh/m}^2$$

During a year of operations with the values of DNI inputted, according to the next graph behavior what can be collected considering only the losses due to the row shadowing the incident angle modifier and the end losses, are also considered the losses of efficiency of the mirrors and the HCE to achieve a value of  $Q_{\text{abs.}} 7.625 \times 10^5 \text{ Wh/m}^2$  per year.

To take into account also the condition of the air or the vacuum in the annulus the values respectively obtained are:  $6.463 \times 10^5 \text{ Wh/m}^2$  per year and  $3.652 \times 10^5 \text{ Wh/m}^2$  per year that correspond to a percentage of respectively 84.76% and 47.89% with corresponding losses of respectively 15.24% and 52.10%.

All of the above data is calculated in the case of 0 m/s wind speed, so it is simple to forecast that the losses will increase more as the wind speed increase.

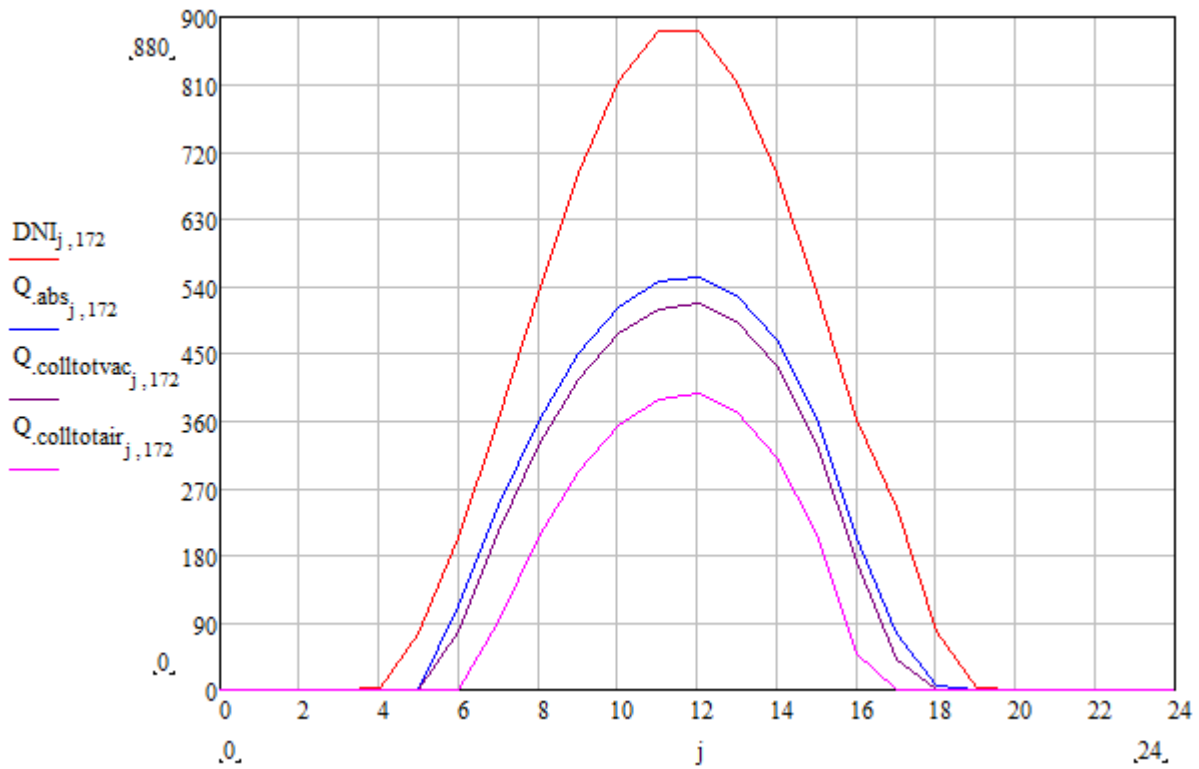


Figure 7.38 Value of total irradiance absorbed ( $Q_{abs}$ ), Total irradiance absorbed in vacuum condition ( $Q_{totcollvac}$ ), Total irradiance absorbed in air condition ( $Q_{totcollair}$ ) [W/m<sup>2</sup>] for the PF2 mirror

The mean value at the site of the wind speed is about 3.2 m/s calculated with a mean of the punctual values all over the year.

Were conducted calculations on different values of wind speed at different steps:

- 0.0 m/s
- 1.0 m/s
- 2.0 m/s
- 3.2 m/s
- 5.0 m/s

Here is reported the final graph to compare the results

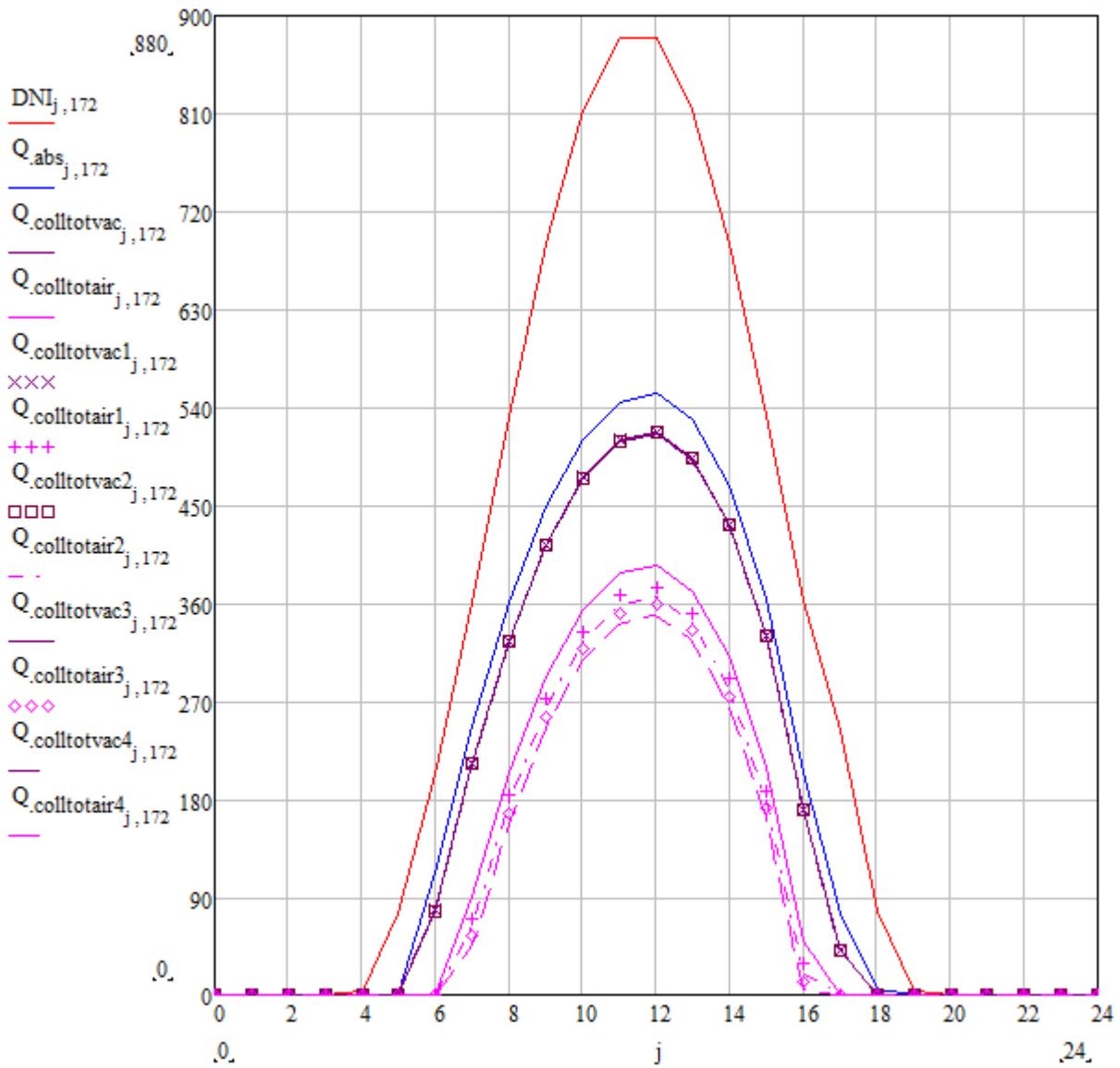


Figure 7. 39 Irradiance absorbed in different wind speed condition for the PF2 mirror

Where:

- $Q_{colltotvac}$  and  $Q_{colltotair}$  are referred to the 0.0 m/s value;
- $Q_{colltotvac1}$  and  $Q_{colltotair1}$  are referred to the 1.0 m/s value;
- $Q_{colltotvac2}$  and  $Q_{colltotair2}$  are referred to the 2.0 m/s value;
- $Q_{colltotvac3}$  and  $Q_{colltotair3}$  are referred to the 3.2 m/s value;
- $Q_{colltotvac4}$  and  $Q_{colltotair4}$  are referred to the 5.0 m/s value;

As it can be seen the increasing value of wind speed doesn't affect the calculation at the vacuum condition while there is a slightly decrease of total value of collected irradiance for what concern the air in annulus condition.

This behavior is highlighted in the next graph (on the left is shown the vacuum condition while on the right is shown the air in annulus condition).

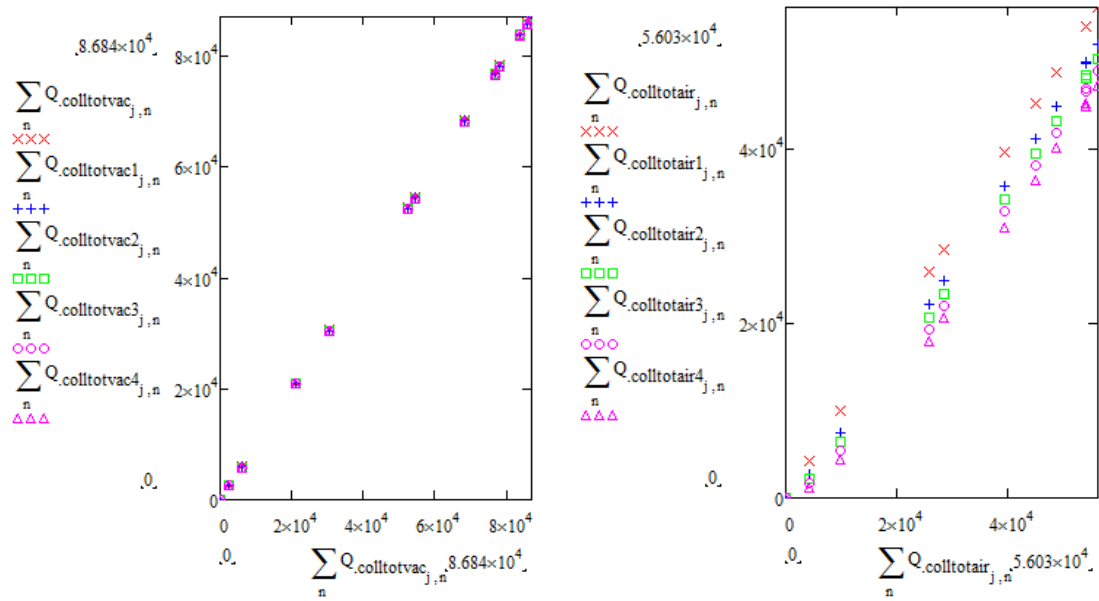


Figure 7.40 Comparison along the year of the values of the 0.0 m/s wind speed and the different wind speed in vacuum and air condition for the PF2 mirror

In all the four conditions shown above is possible to obtain the value of the collected irradiance per year  $Wh/m^2$  per year.

$$\sum_n \left( \sum_j Q_{\text{colltotair}1,j,n} \right) = 3.295 \times 10^5$$

$$\sum_n \left( \sum_j Q_{\text{colltotvac}1,j,n} \right) = 6.452 \times 10^5$$

$$\sum_n \left( \sum_j Q_{\text{colltotair}2,j,n} \right) = 3.153 \times 10^5$$

$$\sum_n \left( \sum_j Q_{\text{colltotvac}2,j,n} \right) = 6.447 \times 10^5$$

$$\sum_n \left( \sum_j Q_{\text{colltotair}3,j,n} \right) = 3.027 \times 10^5$$

$$\sum_n \left( \sum_j Q_{\text{colltotvac}3,j,n} \right) = 6.443 \times 10^5$$

$$\sum_n \left( \sum_j Q_{\text{colltotair}4,j,n} \right) = 2.88 \times 10^5$$

$$\sum_n \left( \sum_j Q_{\text{colltotvac}4,j,n} \right) = 6.438 \times 10^5$$

In the next figure is described a comparison between the two different conditions (air or vacuum in annulus) as the wind speed increases.

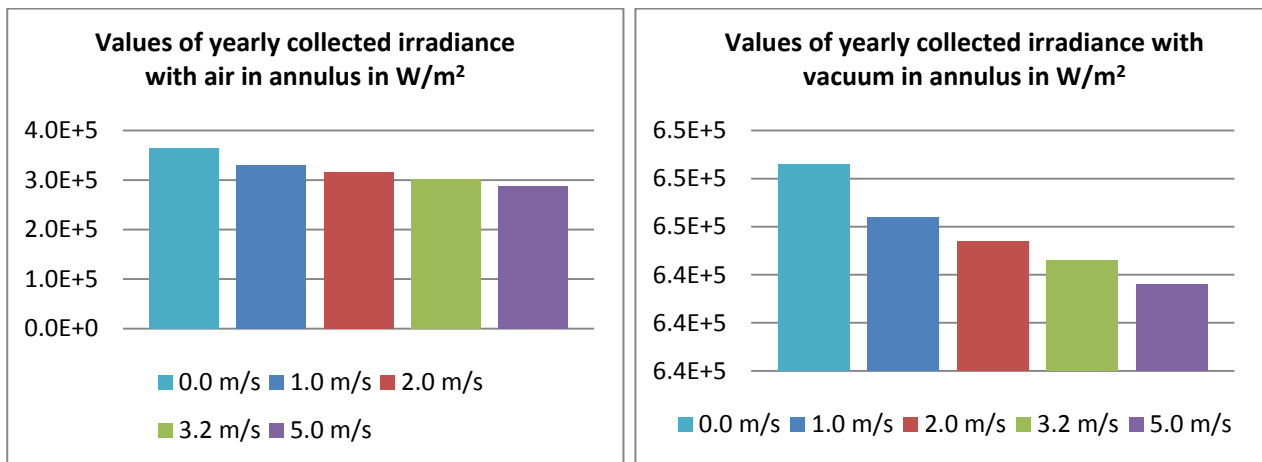


Figure 7. 41 Values of yearly collected irradiance at different wind speed and in air or vacuum condition

Making a comparison (in vacuum annulus case) between the initial condition 0.0 m/s and the 5.0 m/s wind speed case the falling of performance is evaluated in the order of -0.39%

While in the case of air in annulus the same comparison leads to a falling of performance evaluated in the order of -21.14%.

## 7.7 Result improvement

Crossing the results obtained between the VASRA and the results obtained with the Mathcad models it's possible to observe how the enhancement of mirrors reflectivity along the increasing values of the incident angle (shown in chapter 5) give us the chance to compare the different technology not only with their specular reflectance at  $6^\circ$  but varying this incidence angles as actually happens during a normal year of operation due to the sun's movement throughout the year.

Of course with the experimental data obtained using the UV/Vis spectrophotometer don't cover all the incident angles that occur during the year, but considering the value obtained with the integrating sphere (which is the lowest) it's possible to assume that in the cases not covered by the experimental data the reflectance value assumed is the lowest thus to maintain the forecast almost reliable.

According to these assumptions a discrete evaluation of the reflectance values in the Mathcad model was implemented thus to obtain the evaluation of the total collected irradiance during a year with the  $\rho(\square)$ .

The results of this evaluation are presented in the next tables.

In the first table 7.4 are summarized the values until now obtained maintaining the reflectance value constant all over the year.

Constant	TG1	TG2	AL1	AL2	PF1	PF2
Qabs [Wh/m <sup>2</sup> per year]	805,400.00	794,100.00	747,400.00	803,200.00	773,600.00	762,500.00
Qcolltotair [Wh/m <sup>2</sup> per year]	401,700.00	392,000.00	352,500.00	398,800.00	374,600.00	365,200.00
Qtotcollvac [Wh/m <sup>2</sup> per year]	688,400.00	677,300.00	631,500.00	686,300.00	657,300.00	646,300.00

Table 7.4 Value of the total energy collected along the year considering the reflectance constant at all angles of incidence

While in the next table 7.5 are summarized the values obtained using the discrete variable reflectance function.

Variable	TG1	TG2	AL1	AL2	PF1	PF2
Qabs [Wh/m <sup>2</sup> per year]	810,900.00	798,600.00	755,500.00	814,000.00	795,000.00	766,200.00
Qcolltotair [Wh/m <sup>2</sup> per year]	405,900.00	395,500.00	358,600.00	408,100.00	390,800.00	368,300.00
Qtotcollvac [Wh/m <sup>2</sup> per year]	693,800.00	681,700.00	639,400.00	696,900.00	687,100.00	650,000.00

Table 7. 5 Value of the total energy collected along the year considering the reflectance variable varying the angles of incidence

With the differences in percentage are summarized in the next table.

	TG1	TG2	AL1	AL2	PF1	PF2
Qabs	0.68%	0.57%	1.08%	1.34%	2.77%	0.49%
Qcolltotair	1.05%	0.89%	1.73%	2.33%	4.32%	0.85%
Qtotcollvac	0.78%	0.65%	1.25%	1.54%	4.53%	0.57%

Table 7. 6 Difference in percentage between the values obtained with the constant reflectance and the variable reflectance

The above values are dependent on the occurrence of each angle of incidence taken into account.

Graphically it's possible to provide the evaluation of such variation comparing the values with the constant reflectance and variable reflectance.

The next figures show individually the values “before” and “after” of Q absorbed by the heat collector element.

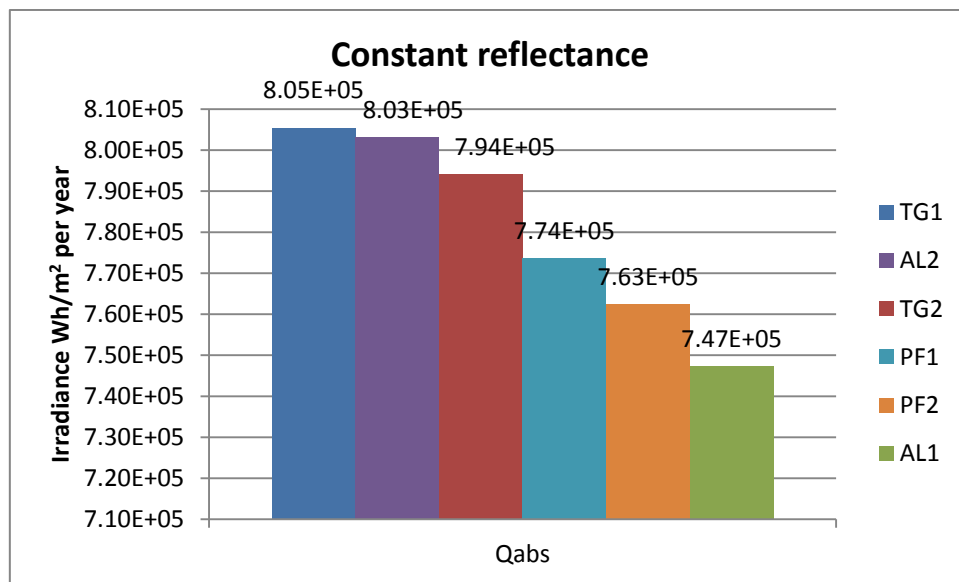


Figure 7. 42 Collected energy values along the year between the different mirrors with constant reflectance

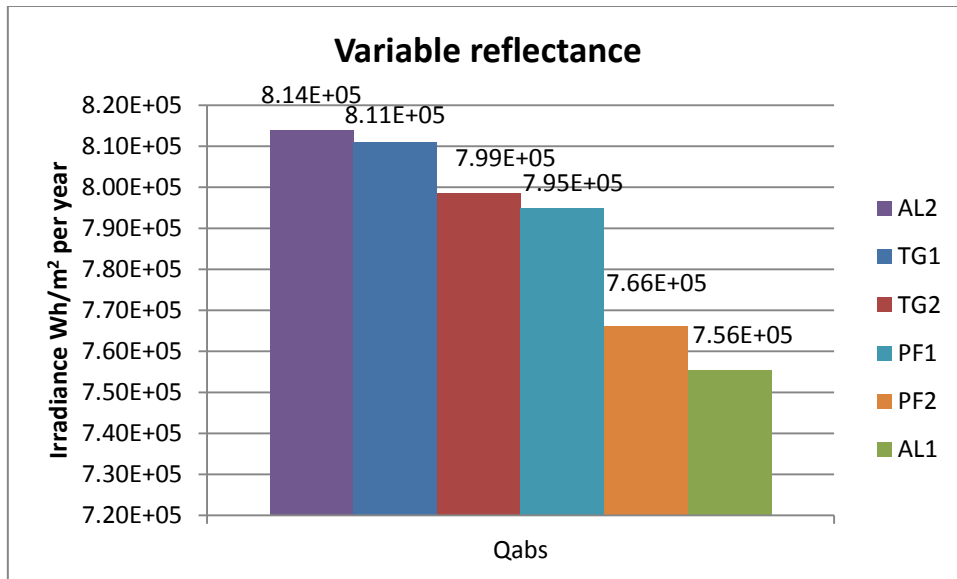


Figure 7. 43 Collected energy values along the year between the different mirrors with variable reflectance

What can be seen in first instance is that the increasing of reflectance lead to a major contribution in the values collected at the HCE, in second instance that the PF1 mirror increase consistently its efficiency in the order of 2.77% that place this mirror at the level of the best mirrors even if it's always less than the thin glass mirrors and the AL2 mirror.

This is due to its impressive reflectance increasing along the incident angles shown in chapter 5.

In the same way was possible to obtain the results for the total collected irradiance with the air in annulus case.

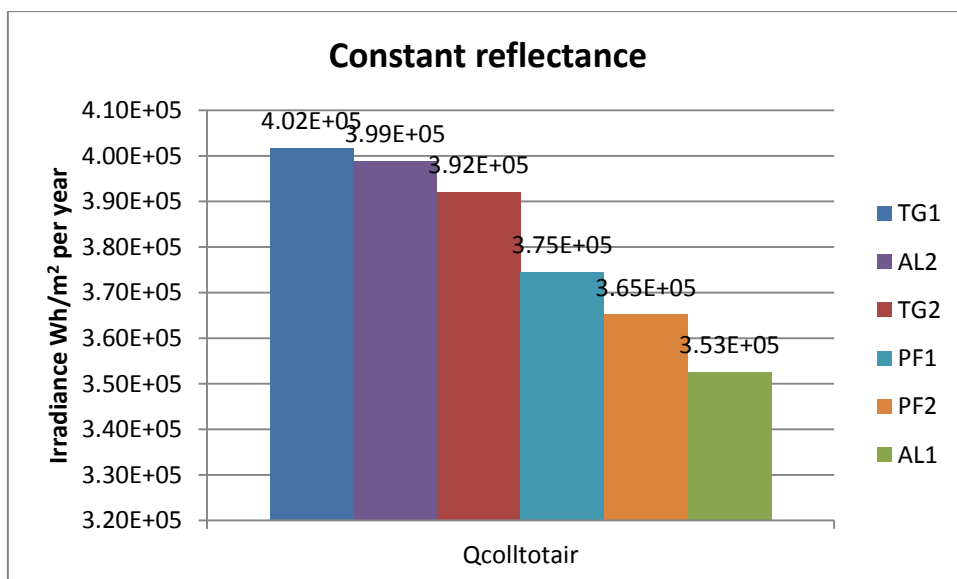


Figure 7. 44 Values of total energy collected along the year in air in annulus condition for all the typologies of mirrors

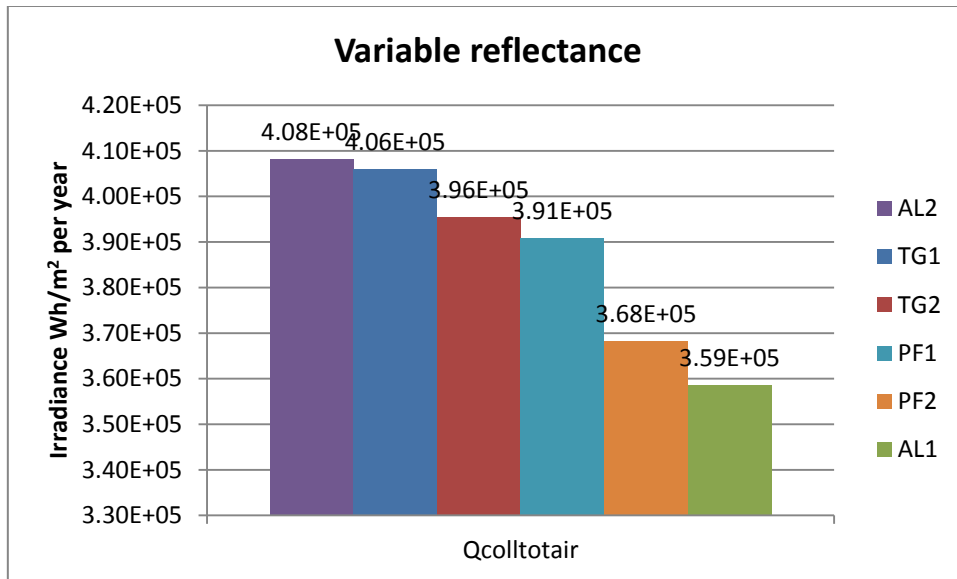


Figure 7. 45 Values of total energy collected along the year in air in annulus condition for all the typologies of mirrors

In the above graphs the same behaviour is confirmed again as it will be seen in the vacuum annulus case shown in the next two tables

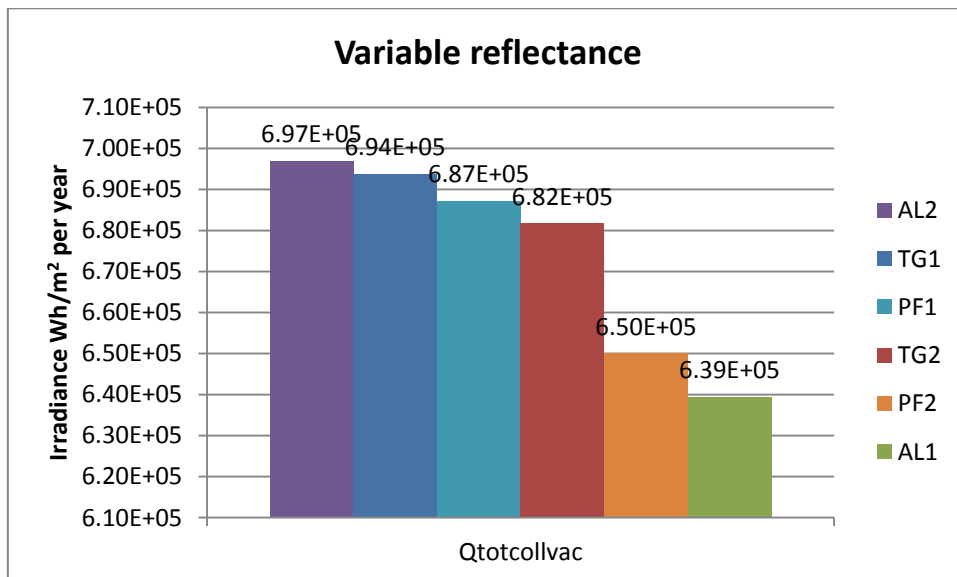
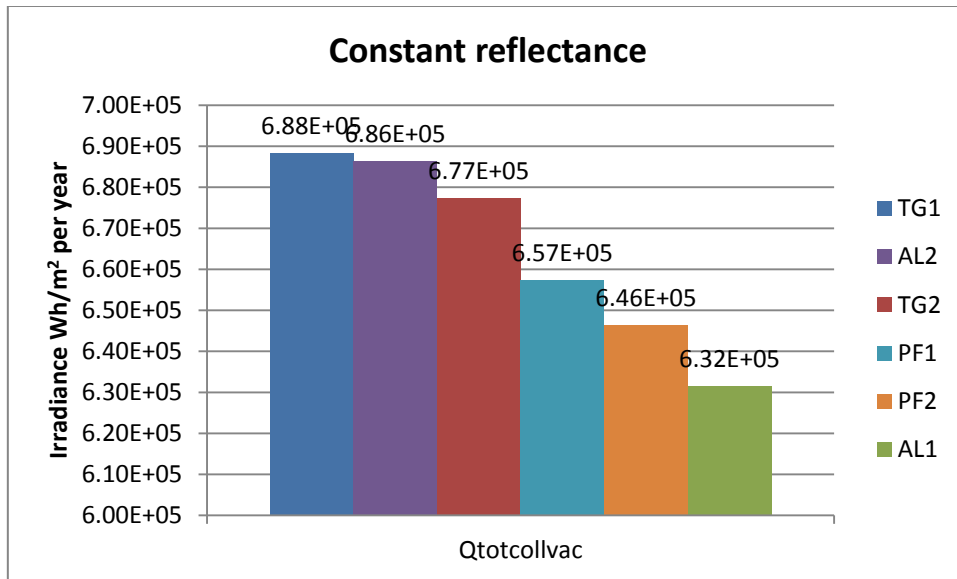


Figure 7. 46 Values of total energy collected along the year with vacuum in annulus condition for all the typologies of mirrors

In this case the increase of reflectance lead to a major contribution to the collection of irradiance from the heat collector element and in particular the PF2 mirror arrives at the third place of the overall rank.

## 8. CONCLUSION

A detailed study of new reflector technologies on the market for concentrating solar power plant was performed in this work.

It was carried on an evaluation of the clean mirrors reflectance along the spectrum in the range from 280 nm and 2500 nm with the spectrophotometer DRA to obtain the Diffuse, Hemispherical and then the Specular spectral response at  $6^\circ$  for each mirror typologies.

In order to compare the different mirror performances were calculated the solar weighted hemispherical and specular reflectance, the first ranged between 88.28% and 94.16%, while the second ranged between 86.55% and 93.27%.

The results showed how the thin glass mirrors offer the highest solar weighted specular reflectance. With the above results we implemented a model that can predicts the annual irradiance reflected ( $Q_{abs}$ ) on the heat collector element using the engineering equation solver Mathcad.

To validate the Mathcad model it was used the ray tracing software Soltrace that showed, at the same condition, a discrepancy of 0.4%, including the optical errors.

Using the VASRA we obtained the variable incidence angle specular reflectance response in the range between 280 nm and 2500 nm with an incident angle variation from  $20^\circ$  to  $70^\circ$ , to observe that:

- All the mirrors tested except for the PF1 showed an increase of reflectance values in the range between 1% and 3% till they reach their own Brewster angle after which the reflectance drops instantaneously;
- The polymeric film mirror PF1, although less performing than thin glass mirrors in the DRA measurements, showed an increase of reflectance as the incident angle increases in the order of 5%.

It was possible then to evaluate, inserting the data collected into the Mathcad model, how this reflectance enhancement in the evaluation of the irradiance reflected on the heat collector element differs from a minimum of 0.49% to a maximum value of 2.77% from the previously  $Q_{abs}$ .

The main difficulties found in this step was to link the reflectance values obtained with the DRA with the results obtained with the VASRA, without a reference mirror in fact the gap between  $6^\circ$  (DRA measurement) and  $20^\circ$  (VASRA measurement) was treated as a liner interpolation of the data to achieve comparable results between the two accessory measurements.

The above evaluation of the total irradiance reflected, offers a valuable interpretation of the results: if in the first step of research (DRA measurements) the PF1 mirror was 3.68% under the best performing mirror after the previously mentioned evaluation it raised at the TG2 level which was 1.31% under the TG1, it means that despite the lack of performances this typology of mirror has to be considered a good reflector candidate as it deserve.

It was also conducted an outdoor exposure test that revealed the non-suitability of the AL2 mirror to the main CSP applications, this type of mirror seems to be without the protection film saw in the AL1 mirror, in fact if not well insulated from the weathering elements, it presents a drop of reflectance in just a month in the order of 42.75%.

With the use of the scatterometer we were able to characterize the soiling effect on reflectance with the consequent increase of the RMS Roughness and Bi-Directional Scattering Function.

Comparing the values obtained at time 0 and after one month we revealed that:

- The RMS Roughness has grown up from a minimum value of 3.7% to a maximum value of 4.5 times the initial measurement;
- The BDSF (0,0) has grown up from a minimum of 5.17 times to a maximum value of about 17 times the initial values;
- The BDSF (50,180) has grown up from a minimum value 4.1 times to a maximum value of almost 80 times the initial value.

Unfortunately the instrument used ( $\mu$ Scan Scatterometer) has it's limitation due to the low accuracy for the reflectance measurements so only the RMS Roughness and the BDSF has to be considered reliable.

For what concern the soiling test the time at our disposal was very short but despite the time covered we obtained some information that was not achievable with a climatic chamber. The only way to observe the degradation of the AL2 mirror would have been using a salt spray chamber that at the time of our experimentation was out of order.

Furthermore the UV ageing chamber test was conducted for only one year for time limits but if continued for a longer period, the data collected would have been useful to be inserted in the Mathcad model to observe the yearly reflected irradiance degradation in the period of 20-25 years.

The use of the spectrophotometer at the laboratories allowed to obtain the spectral response of the mirrors during the various steps of research.

## BIBLIOGRAPHY

(DEW), G. W. (2004). [www.dewi.de/dewi/index.php](http://www.dewi.de/dewi/index.php).

1036, E. (s.d.).

1992, A. S.-8. (s.d.). *ASTM Standard E903-82 ~Reapproved 1992 Standard Test Method for Solar Absorptance, Reflectance, and Transmittance of Materials Using Integrating Spheres*. Philadelphia, PA: Book of ASTM Standards 1993, Vol. 12.02, American Society for Testing and Materials.

*ASTM Standard G173-03* (Book of ASTM Standards 2003 Vol. 14.04, ed.). (2003). Philadelphia, PA, USA: American Society for Testing and Materials.

*ASTM Standard G90-98 ~Reapproved 1998 Standard Practice for Performing Accelerated Outdoor Weathering of Nonmetallic Materials Using Concentrated Natural Sunlight* (Book of ASTM Standards 2004 Vol. 14.04 ed.). (2004). Philadelphia, PA: American Society of Testing and Materials.

4829, E. I. (s.d.).

al, B. e. (2006).

al, J. M. (2005). Technological learning in bioenergy systems. In Junginger M, *Learning in renewable energy technology development. PhD thesis, Universiteit Utrecht, Faculteit Scheikunde*. Utrecht.

al, N. L. (2004). Experience curves: a tool for energy policy assessment. (E. a. Department of Technology and Society, A cura di) *IMES/EESS Report No. 40*.

al, P. S. (2004). *Learning from the sun*. Energieonderzoek Centrum Nederland (ECN), Petten: ECN Report ECN-C-04-035.

ANGELA M. PATNODE. (2006). Simulation and Performance Evaluation of Parabolic Trough Solar Power Plants. National Renewable Energy Laboratory.

ASTM. (s.d.). D 4587.

- C, H. (March 2000). Experience curves of photovoltaic technology. IIASA Interim Report IR-00-014.
- Diver, S. a. (1994).
- Duffie, J. A. (1991). Solar Engineering of Thermal Processes. 2nd edition. New York, USA: John Wiley and Sons, Inc.
- Durstewitz M, H.-K. M. (1999). Using information of Germany's '250 MW Wind' programme for the construction of wind power experience curves. In V. A. Wene CO, A (eds) *Proceedings of the IEA workshop on experience curves for policy making – the case of energy technologies, Stuttgart, Forschungsbericht Band 67, Institut für Energiewirtschaft und Rationelle Energieanwendung, Universität Stuttgart* (p. p 129).
- EN, C. (s.d.). 61345.
- Forristall, R. (2003, October). Heat Transfer Analysis and Modeling of a Parabolic Trough Solar Receiver Implemented in Engineering Equation Solver. *NREL/TP-550-34169*. (N. R. Laboratory, A cura di)
- Hoffman. (2001).
- IEA. (2005). Energy balances of non-OECD countries. ©OECD/IEA, Paris.
- IEA. (2005). Energy balances of OECD countries. ©OECD/IEA. Paris.
- IEA. (2005). *Implementing agreement for a program of research, development, and demonstration on bioenergy IEA bioenergy implementing agreement and implementing agreement for the IEA Clean Coal Centre.*
- IEA. (2005). Renewable energy: RD&D priorities. Paris: ©OECD/IEA.
- Inc., V. (2011). Spectrophotometer technical guide.
- Incropera, F. P. (2002). Fundamentals of Heat and Mass Transfer. 5th edition. New York: John Wiley and Sons, Inc.
- Iqbal, M. (1983). An Introduction to Solar Radiation. Ontario: Academic Press Canada.

- J, G. (2005). *Wind as a source of energy, now and in the future*. . Amsterdam: Inter-Academy Council.
- Jorgensen, G. J. (1996). *Durability Studies of Solar Reflector Materials Exposed to Environmental Stresses and Durability Testing of Nonmetallic Materials*. (A. S. Materials, A cura di) Robert J. Herling.
- Junginger M et al. (2005). Technological learning and cost reductions in woodfuel supply chains in Sweden. In J. M, *Biomass Bioenerg, reprinted in: Learning in renewable energy technology development. PhD thesis, Universiteit Utrecht, Faculteit Scheikunde*. Utrecht.
- Junginger M, F. A. (2004). Global experience curves for wind farms. *Energ Policy* 33(2), 133–150.
- L, N. (1999). Cost dynamics of wind power *Energy* .
- Labsphere. (2010). *Techguide- A Guide to Integrating Sphere Radiometry and Photometry*. PO Box 70 231 Shaker Street North Sutton, NH 03260 USA: Labsphere.
- Labsphere. (2010). *Technical Guide - Integrating Sphere Theory and Applications*. PO Box 70 231 Shaker Street North Sutton, NH 03260 USA: Labsphere.
- Moran, M. J. (2000). *Fundamentals of Engineering Thermodynamics*. 4th Edition. John Wiley and Sons, Inc.
- Novak-Zdravkovic A, d. R. (2005 17–21 Oct). Small-scale power generation from biomass. In: *Proceedings of the 14th European biomass conference and exhibition*. Paris.
- NREL. (2011). *www.nrel.gov*. Tratto il giorno 2011 da National Renewable Energy Laboratory.
- Princiotta, F. T. (2010). *Global Climate Change - The Technology Challenge*. 109 TW Alexander Drive Research Triangle Park NC, USA: Springer.
- SES. (2006).
- Solarpaces. (2011). *MEASUREMENT OF SOLAR WEIGHTED REFLECTANCE OF MIRROR MATERIALS FOR CONCENTRATING SOLAR POWER TECHNOLOGY WITH COMMERCIALY AVAILABLE INSTRUMENTATION*. Solarpaces.
- Wongwises, K. a. (2003).